



Microgravity Science Laboratory (MSL-1) Final Report

Compiled by

M.B. Robinson

Marshall Space Flight Center, Marshall Space Flight Center, Alabama

Proceedings of the Microgravity Science Laboratory
(MSL-1) One Year Science Review Meeting held at
Marshall Space Flight Center, Huntsville, Alabama,
August 25-26, 1998

The NASA STI Program Office...in Profile

Since its founding, NASA has been dedicated to the advancement of aeronautics and space science. The NASA Scientific and Technical Information (STI) Program Office plays a key part in helping NASA maintain this important role.

The NASA STI Program Office is operated by Langley Research Center, the lead center for NASA's scientific and technical information. The NASA STI Program Office provides access to the NASA STI Database, the largest collection of aeronautical and space science STI in the world. The Program Office is also NASA's institutional mechanism for disseminating the results of its research and development activities. These results are published by NASA in the NASA STI Report Series, which includes the following report types:

- **TECHNICAL PUBLICATION.** Reports of completed research or a major significant phase of research that present the results of NASA programs and include extensive data or theoretical analysis. Includes compilations of significant scientific and technical data and information deemed to be of continuing reference value. NASA's counterpart of peer-reviewed formal professional papers but has less stringent limitations on manuscript length and extent of graphic presentations.
- **TECHNICAL MEMORANDUM.** Scientific and technical findings that are preliminary or of specialized interest, e.g., quick release reports, working papers, and bibliographies that contain minimal annotation. Does not contain extensive analysis.
- **CONTRACTOR REPORT.** Scientific and technical findings by NASA-sponsored contractors and grantees.

- **CONFERENCE PUBLICATION.** Collected papers from scientific and technical conferences, symposia, seminars, or other meetings sponsored or cosponsored by NASA.
- **SPECIAL PUBLICATION.** Scientific, technical, or historical information from NASA programs, projects, and mission, often concerned with subjects having substantial public interest.
- **TECHNICAL TRANSLATION.** English-language translations of foreign scientific and technical material pertinent to NASA's mission.

Specialized services that complement the STI Program Office's diverse offerings include creating custom thesauri, building customized databases, organizing and publishing research results...even providing videos.

For more information about the NASA STI Program Office, see the following:

- Access the NASA STI Program Home Page at <http://www.sti.nasa.gov>
- E-mail your question via the Internet to help@sti.nasa.gov
- Fax your question to the NASA Access Help Desk at (301) 621-0134
- Telephone the NASA Access Help Desk at (301) 621-0390
- Write to:
NASA Access Help Desk
NASA Center for AeroSpace Information
800 Elkridge Landing Road
Linthicum Heights, MD 21090-2934



Microgravity Science Laboratory (MSL-1) Final Report

Compiled by

M.B. Robinson

Marshall Space Flight Center, Marshall Space Flight Center, Alabama

Proceedings of the Microgravity Science Laboratory
(MSL-1) One Year Science Review Meeting held at
Marshall Space Flight Center, Huntsville, Alabama,
August 25-26, 1998

National Aeronautics and
Space Administration

Marshall Space Flight Center

Available from:

NASA Center for AeroSpace Information
800 Elkridge Landing Road
Linthicum Heights, MD 21090-2934
(301) 621-0390

National Technical Information Service
5285 Port Royal Road
Springfield, VA 22161
(703) 487-4650

Preface

This NASA Conference Publication is a compilation of experiment reports presented at the Microgravity Science Laboratory (MSL-1) One Year Science Review, which was held in Morris Auditorium at Marshall Space Flight Center August 25-26, 1998. MSL-1 first flew on Space Shuttle *Columbia* (STS-83) April 4-8, 1997, but the mission was cut short due to a fuel cell problem. The reflight of MSL-1 took place on *Columbia* (STS-94) July 1-17, 1997.

Spacelab facilities included Combustion Module-1 (CM-1), Droplet Combustion Experiment (DCE), Large Isothermal Furnace (LIF), Protein Crystal Growth (PCG), Electromagnetic Containerless Processing Facility (TEMPUS), Middeck Glovebox (MGBX), EXPRESS (EXPedite the PROcessing of Experiments to the Space Station) Rack, and four accelerometers. The PHaSE (Physics of Hard Spheres) and ASTRO/PGBA (Astro/Plant Generic Bioprocessing Apparatus) experiments were accommodated in the EXPRESS Rack, and five experiments made use of the Middeck Glovebox.

There were 29 scientific investigations associated with MSL-1: four involved combustion, 17 materials science, four fluid physics, three protein crystal growth, and one plant growth. Data from four accelerometers supported the microgravity research.

The mission was international in scope. In addition to NASA, the German Space Agency (DLR) and the National Space Development Agency (NASDA) of Japan had experiments on the mission. DLR provided the Electromagnetic Containerless Processing Facility (TEMPUS), and NASDA provided the Large Isothermal Furnace (LIF). The European Space Agency (ESA) supported microgravity experiments with its Microgravity Measurement Assembly (MMA), which provided data on the microgravity environment.

By any metric chosen the MSL-1 mission was a successful mission. The following science reports give only a foretaste of the publications which will result from the MSL-1 mission.



Michael B. Robinson
MSL-1 Mission Scientist
NASA Marshall Space Flight Center
Huntsville, Alabama

Page intentionally left blank

Table of Contents

Preface	iii
Astro/Plant Generic Bioprocessing Apparatus (ASTRO/PGBA)	1-1
Combustion Module-1 (CM-1)	
Laminar Soot Processes (LSP)	9 -2
Structure of Flame Balls at Low Lewis-Number (SOFBALL).....	23 -3
Coarsening in Solid-Liquid Mixtures (CSLM)	37 -4
Droplet Combustion Experiment (DCE)	45 -5
Large Isothermal Furnace (LIF)	
Diffusion of Liquid Metals and Alloys.....	59 -6
Diffusion in Liquid Lead-Tin-Telluride	71 -7
Impurity Diffusion in Ionic Melts.....	79 -8
Measurement of Diffusion Coefficient by Shear Cell Method.....	85 -9
Liquid Phase Sintering II (LPS-2).....	93 -10
Diffusion Processes in Molten Semiconductors (DPIMS).....	107 -11
Middeck Glovebox (MGBX)	
A Study of the Fundamental Operation of a Capillary-driven Heat Transfer Device in Microgravity (CHT)	109 -11
Bubble and Drop Nonlinear Dynamics (BDND).....	121 -12
Internal Flows in a Free Drop (IFFD).....	131 -13
Fiber Supported Droplet Combustion-2 (FSDC-2).....	141 -14
Protein Crystal Growth (PCG)	
Protein Crystal Growth Using the Protein Crystallization Apparatus for Microgravity (PCAM)	157 -15
Protein Crystal Growth Using the Hand-Held Diffusion Test Cell (HHDTTC).....	171 -16
Protein Crystal Growth Using the Second Generation Vapor Diffusion Apparatus..... (VDA-2)	173 -17
Physics of Hard Spheres Experiment (PHaSE)	185 -0

Table of Contents (cont'd)

Electromagnetic Containerless Processing Facility (TEMPUS)

Thermophysical Properties of Undercooled Metallic Melts.....	197-18
Thermophysical Properties of Advanced Materials in the Undercooled Liquid State.....	217-19
Measurements of the Surface Tension of Liquid and Undercooled Metallic Melts by Oscillating Drop Technique	231-20
Study of the Morphological Stability of Growing Dendrites by Comparative Dendrite..... Velocity Measurements of Pure Ni and a Dilute Ni-C Alloy in the Earth and Space Laboratory	243-21
Undercooled Melts of Alloys with Polytetrahedral Short-Range Order.....	253-22
Thermal Expansion of Glass Forming Metallic Alloys in the Undercooled State.....	263-23
Experiment on Nucleation in Different Flow Regimes.....	273-24
Alloy Undercooling Experiments.....	281-25
Measurement of Surface Tension Viscosity of Undercooled Liquid Metals.....	291-26
AC Calorimetry and Thermophysical Properties of Bulk Glass-Forming Metallic Liquids	303-27

Accelerometers

Orbital Acceleration Research Experiment (OARE)	315-28
Space Acceleration Measurement System (SAMS)	
Microgravity Measurement Assembly (MMA)	
Quasi-Steady Acceleration Measurement System (QSAM).....	325-29

OMIB1
THIS
13 PAGE

Astro/Plant Generic Bioprocessing Apparatus (ASTRO/PGBA)

Principal Investigator:

Dr. Louis S. Stodieck
University of Colorado
Boulder, Colorado

N 2-7 SINGLE SCAD 51-51 434838

A REVIEW OF PLANT EXPERIMENTS SUPPORTED BY THE ASTRO/PLANT GENERIC BIOPROCESSING APPARATUS ON MSL-1

A. G. Heyenga, L. Stodieck, and A. Hoehn
BioServe Space Technologies, University of Colorado
Aerospace Engineering Sciences, Boulder, CO 80309
(303) 492-4010

362137
70.

Abstract

The utilization of plant-based materials in modern human society is extensive and of considerable commercial value including the production of food, pharmaceutical, lumber, and paper products. The advent of space flight research and the means to cultivate plants in the near absence of gravity have provided a unique opportunity to expand our understanding of plant physiology, metabolism, and genetics and to develop new approaches to further utilize this resource.

An area of specific commercial interest encompasses the prospect that microgravity may be used to alter and help elucidate the control mechanisms of certain plant metabolic pathways enabling the further genetic engineering and cultivation of plants with desired traits on Earth. Particular attention is being directed towards the study of the cell structural compound lignin. A potential decrease in the production of such a compound could result in a corresponding increase in the production of metabolically related compounds including lignans and neo-lignans that are of significant medicinal value. An alteration in metabolic flux may equally extend to an enhancement in the production of compounds arising from the valuable alkaloid and terpene pathways. Additional areas in which the absence of gravity may influence plant metabolism include the production and distribution of plant growth control factors such as auxins and in the production of ligand molecules involved in the recognition system of plant symbiotic associations with microorganisms. The latter process is of significant value to agriculture in such areas as nitrogen fixation.

The implementation of the MSL-1 plant study conducted on the Shuttle mission STS-94 was directed towards establishing an initial experimental baseline in plant response and applying investigative techniques that include the use of radioisotopes and molecular markers. A number of plant species were cultivated for 16 days in the Astro/Plant Generic Bioprocessing Apparatus (Astro/PGBA) under defined environmental conditions. The principle areas of investigation involved an examination of (a) lignin and vinca alkaloid metabolism, (b) the response of an auxin inducible GH3 gene, and (c) the interactive association of wheat with Rhizobium bacteria.

OBJECTIVE

The objective of the Astro/PGBA MSL-1 plant growth study was to evaluate the use of microgravity as a means to specifically alter and help elucidate the mechanisms of control in plant-based systems with commercial interest. An emphasis was placed on

1. the specific metabolic pathways associated with the production of cell structural compounds (particularly with respect to lignin metabolism), and
2. the production of compounds involved in plant physiological responses (including plant growth regulators and mechanisms involved in plant and microbial symbiotic activity).

BACKGROUND

In affiliation with various industrial partners, BioServe Space Technologies, a Center for Space Commercialization at the University of Colorado and Kansas State University, has been involved in the development of space plant biotechnology. Based on a body of circumstantial evidence which suggests that microgravity may alter and reduce the production of the plant cell structural compound 'lignin,' an effort is being directed towards defining and characterizing the nature of this response and the potential application to commercial interests.

Lignin is a complex phenylpropanoid polymer produced and utilized by terrestrial vascular plants in various physiological roles. The deposition of lignin in the wall structure and middle lamella of a cell, and the ability of the compound to bond with cellulose and other polysaccharides gives the cell and corresponding cellular tissues considerable mechanical rigidity.

Based on the apparent role of lignin to counter the effect of mechanical loads on the cell structure, it is intriguing to speculate whether the removal of a gravity induced load might result in a corresponding reduction in the production of cellular lignin. Of even greater significance is the prospect that a microgravity state may be used to specifically influence and thus isolate the metabolic and molecular mechanisms of control involved in the 'cell load sensitive' lignin from that of lignin produced for other physiological roles. The application of such knowledge may ultimately be used to genetically engineer and cultivate plants on Earth with desired traits.

With the exception of the plant polymer cellulose, lignin is the most abundant organic material in plants. A decrease in the production of lignin may result in a corresponding increase in the production of metabolically related phenolic compounds which are of great medicinal and commercial value. An alteration in metabolic flux may equally extend to the enhanced formation of compounds derived from the valuable alkaloid (e.g., vinca alkaloids in Catharanthus roseus) and terpenoid pathways.

In reflection of the interest to evaluate a decrease in lignin production and corresponding increase of other secondary metabolites, the MSL-1 plant studies were directed towards

1. an evaluation of lignin production in pressure induced 'reaction wood' formation in Loblolly pine, Pinus taeda.
2. an evaluation of vinca alkaloid metabolism in Catharanthus roseus.
3. the application of radiolabelling techniques in metabolic studies.

To evaluate the potential influence of microgravity (and space flight conditions) on additional plant physiological and metabolic systems, further studies were conducted on

1. the interactive association and process of recognition between Rhizobium bacteria with wheat root tissue and the induction of pseudonodule structures.
2. the use of genetic markers (GH3 / GUS gene) to evaluate and elucidate the process of auxin control in tomato, Lycopersicon esculentum.

The use of microgravity as a control parameter in plant biotechnology necessitates the need to compare plants maintained in a physiologically acceptable environment in which the force of gravity is the sole variable factor. The period of time required for such studies may range from 6 to 12 months in a space flight environment. The growth of plants in space and on Earth provides a respective microgravity (μg) and gravity (1 g) control state. Due to the present limit in the capacity to cultivate plants in space flight conditions, additional attention must be placed on the design and utilization of hardware and investigative systems that support the maximum amount of test plant

material and recovery of experimental data. The Astro/PGBA chamber enabled the simultaneous support of a broad number of species and application of advanced investigative technologies.

METHODS OF DATA ACQUISITION AND ANALYSIS

The Astro/PGBA chamber used in the MSL-1 plant growth study provided the largest plant growth area presently available on Shuttle flight missions, occupying a volume of 25 cm x 30 cm x 25 cm plant shoot height and 6.5 cm root depth. The chamber provided an illumination intensity of (photosynthetic active radiation) 220 to 280 $\mu\text{mol photons m}^{-2} \text{ s}^{-1}$ at a distance of 20 cm in space flight operation with an on-orbit payload power allocation limit of 230 Watt. A 16-hour lights on and 8-hours lights off illumination cycle was used throughout the mission period. The plant chamber temperature profile was maintained at 295 K during the lights on period and 298 K during the lights off period. The relative humidity in the chamber was maintained between 75-78% using a cooled porous metal plate that removes water vapor from the chamber ventilating air stream. The collection of plant transpired water was partially recirculated back to the plant root zone via the use of replenishable 'nutrient packs.' The use of the nutrient pack system allowed the modular and compartmentalized containment of plant support media. The root matrix material (aggregate or agar) and nutrient formulation of each pack was prepared according to the specific requirements of the test plant species and experimental design. An array of 30 packs supported a total of 55 plants in the Astro/PGBA study. A basic form of the nutrient pack design was used to support plants in an agar solidified gel matrix. This design was used to incorporate radionuclide iron-59 and calcium-45 into media enabling the first radiolabel uptake studies of plants in a space flight growth chamber environment. An atmosphere control system was used to maintain carbon dioxide levels from 465-500 ppm during the plant illumination period and 565-600 ppm during the non-illumination period. The Astro/PGBA design allowed for the controlled intake of carbon dioxide-rich cabin air to replenish the carbon dioxide demand from the cultivated plants. A further atmosphere treatment system was used to scrub or decompose volatile organics, such as ethylene, which are known to affect plant growth and development.

A PC-104 computer system maintained the autonomous operations capability of the Astro/PGBA payload system. The data acquisitions and control systems enabled the relay of 32 channels of environmental data as well as digitized and or analog video signals for downlink display. The computer system also managed data communications between the Shuttle and the ground control center for real time data downlink and command uplink activity.

FLIGHT/GROUND RESULTS

An outline of results on each area of investigation is presented.

1. Lignin metabolism in Loblolly pine, Pinus taeda

The objective in establishing an experimental approach to evaluate the process of lignification in reaction wood formation in space flight and ground control conditions and establishing an initial base line of data was achieved. The various elements and prerequisites to the successful implementation of this study involved

a. the maintenance of plants in a physiologically health state,

The growth and health status of plants in both space and ground conditions was normal with no indication of stress or deterioration in plant health after the 16-day test period.

b. the elicitation of a reaction wood response,

The development of reaction wood was induced in the stems of both space and ground control plants in response to the application of a pressure clamp apparatus. A more defined analysis of the chemical composition of the reaction wood formed is presently being determined.

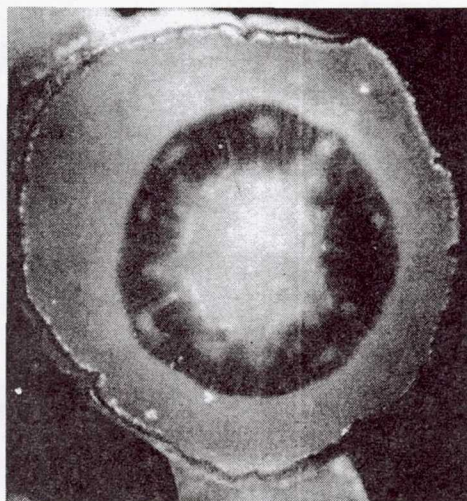


Fig. 1. Formation of reaction wood (dark crescent zone) shown in the cross section of stem tissue of P. taeda cultivated for 16 days in space flight conditions.

2. Vinca alkaloid metabolism in Catharanthus roseus

The investigative effort was directed towards establishing a profile of the vinca alkaloids present in the cultivated C. roseus plant material. The concentration of metabolites in the pathways leading to the production of the major classes of alkaloid, Vindoline, Catharanthine and Ajmalicine were low (pico molar) with no distinct difference between space and ground material. The concentration of the alkaloid Vincamine did however appear higher in the aerial tissue of flight plants than in the ground control material but not at a statistically significant level due to the limited availability of sample material.

3. The application of radiolabeling techniques in metabolite analysis

The implementation of a safe and effective protocol for the application of radionuclides in space flight conditions was successfully achieved representing the first isotope uptake studies in plants under Shuttle flight growth chamber conditions. The protocol established a means by which metabolic pathways may be radiolabeled, significantly enhancing the ability to extract, isolate, and determine the concentration of specific metabolite compounds.

The study examined the uptake of calcium-45 and iron-59 by C. roseus plants. The uptake and distribution profile of label into the aerial tissue of space and ground control plants was similar, indicating

- a. the uniformity of the growth conditions achieved in both the space and ground chambers and
- b. the apparent consistency in the uptake and transport mechanisms for calcium and iron in space flight and ground control conditions.

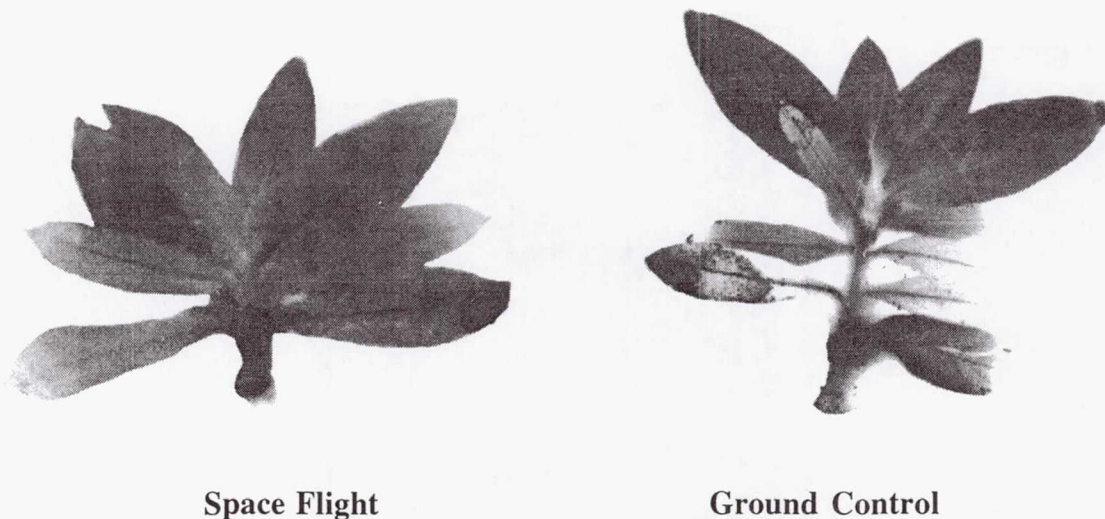


Fig. 2. Autoradiographs of the aerial tissue of *C. roseus* plants demonstrating the uptake (darkened area) of calcium-45 after a 16-day cultivation period.

4. 'Rhizobium' induced pseudonodulation in wheat Triticum aestivum

The evaluation of the potential influence of space flight and microgravity conditions on the interaction of Rhizobium bacteria and plants demonstrated an enhanced reaction and production of nodule-like structures on wheat roots during a 16-day flight period. The nodule structures were slightly larger on the space root tissue than on the ground control tissue. Most significantly, the space developed pseudonodules showed higher levels (four time that of the ground control tissue) of acetylene reduction activity, which is an indirect measure of nitrogen fixation activity. Further reisolation of Rhizobium bacteria from the space-developed pseudonodules has shown higher acetylene reduction activity in subsequent ground based studies and is presently going through further characterization.

5. The use of genetic markers in auxin studies in tomato, Lycopersicon esculentum

Histochemical staining of the GH3 promoter-GUS gene activity indicated that GH3 was specifically activated in space flight grown seedlings of tomato but not in the ground controls. The GH3 promoter/GUS gene was activated in the vascular tissue of shoots potentially reflecting the microgravity mediated changes in the growth and development patterns of shoot material. The use of such genetic markers is a valuable tool in monitoring physiological and ultimately genetic activity.

CONCLUSION AND SIGNIFICANCE AND FUTURE PLANS

The use of microgravity as a parameter in plant-based biotechnology presents the opportunity of significant benefit to a broad sector of commercial interests. The prerequisite requirements for such an endeavor encompass

- a. the ability to cultivate plants under adequate and fully defined growth conditions, which are identical in space and ground control chambers with the exception of gravity,

- b. the ability to cultivate plants under defined conditions for an extended period of time (6-12 months) in space flight conditions, and
- c. the optimal recovery of analytical data from small tissue samples through the use of advanced investigative techniques.

The MSL-1 plant study conducted on the Shuttle mission STS-94 established the necessary support requirements outlined in (a) and (c) above and providing an initial baseline response of plants cultivated for a 16-day test period. While the proposed hypothesis in which a microgravity mediated alteration of plant metabolism is based on the need for a lengthily period of microgravity exposure the present 16-day study has however shown some initial effects. A significant effect was observed with the interaction of Rhizobium bacteria and wheat root tissue with the enhanced formation of pseudonodules that are involved in nitrogen fixation. The ability to introduce a nitrogen fixation capability onto a cereal crop such as wheat would be of significant benefit to the world agricultural industry by increasing crop yield while reducing the need for soil nitrogen fertilizer.

Success in both the cultivation capability of the Astro/PGBA unit and implementation of investigative techniques has demonstrated the significant advances made in plant-based space flight research and the present capability to support valuable commercial interests.

Future work will be directed towards implementing further studies over longer duration missions and investigations on the International Space Station.

BIBLIOGRAPHIC CITATIONS OF ARTICLES/ PRESENTATIONS RESULTING FROM THE FLIGHT

Heyenga, A. G., A. Forsman, L. S. Stodieck, A. Hoehn, and M. Kliss, Approaches in the Determination of Plant Nutrient Uptake and Distribution in Space Flight Conditions (Presentation and paper submitted to the 32nd COSPAR Scientific Assembly, July 12-19, 1998, Nagoya, Japan).

Hoehn, A., J. Clawson, A. G. Heyenga, P. Scovazzo, K. S. Sterett, L. S. Stodieck, and P. W. Todd, M. H. Kliss (1998) "Mass Transport in a Spaceflight Plant Growth Chamber." SAE Paper No. 981553, 28th International Conference on Environmental Systems, Danvers, MA.

Hoehn, A., D. J. Chamberlain, S. W. Forsyth, D. S. Hanna, G. Heyenga, M. B. Horner, M. H. Kliss, P. Scovazzo, L. S. Stodieck, and P. W. Todd (1997) "On-Orbit and Ground Performance of the PGBA Plant Growth Facility." SAE Paper No. 972366, 27th International Conference on Environmental Systems, Lake Tahoe, CA.

Li, Y., Y. Wu, G. Hagen, and T. Guilfoyle, Expression of the Auxin-inducible GH3 Promoter/GUS Fusion Gene as a Useful Molecular Marker for Auxin Physiology, (submitted)

Additional papers are in preparation.

NON-TECHNICAL SUMMARY SUITABLE FOR PUBLIC AFFAIRS OFFICE USE

Plant studies in the Microgravity Science Laboratory MSL-1 may lead to the production of life-saving medicines and other important compounds.

A fundamental objective of this research is to evaluate whether microgravity may be used to alter specific metabolic pathways in plants and ultimately apply this technology for Earth-based benefit.

The concept that extended exposure of plants to microgravity may reduce their expenditure of energy on structural components, thereby increasing the flow through other metabolic pathways, many of which produce materials of important medicinal value. Of even greater significance is the possibility that corresponding changes may occur at a genetic level.

A comparison between space- and Earth-grown plants would increase the current understanding of how these metabolic pathways are controlled at the gene level. In turn, such knowledge would allow the manipulation and development of genetically engineered plants with desired metabolic traits.

For example, this information could be applied to the lumber industry in the production of trees with a low content of the structural compound lignin, greatly reducing the need to remove this compound and ultimately the cost of paper production both economically and environmentally. Conversely, it might be applied to improving timber quality in fast-growing softwoods, reducing the need to harvest slow-growing hardwoods. If this hypothesis is correct and achievable, it obviously represents the basis for a multi-billion dollar industry and certainly highlights the value of space-related research and the use of such facilities as a Space Station.

Combustion Module-1 (CM-1)

52-25
434839

141.

Laminar Soot Processes (LSP)

360138

Principal Investigator:

Dr. Gerard M. Faeth
University of Michigan
Ann Arbor, Michigan

LAMINAR SOOT PROCESSES (LSP) EXPERIMENT

G. M. Faeth*

Department of Aerospace Engineering
The University of Michigan
Ann Arbor, Michigan 48109-2140, U.S.A.

Abstract

The structure and soot properties of nonbuoyant soot-containing laminar diffusion flames were studied at microgravity within an orbiting space shuttle. Test conditions included hydrocarbon-fueled laminar jet diffusion flames burning in still air at pressures of 35-130 kPa. Measurements included luminous flame shape, soot volume fraction distributions, soot structure, soot temperature distributions, gas temperature distributions beyond the flame tip, and flame radiation. Present flames were larger and emitted soot more readily than comparable flames observed during ground-based microgravity experiments due to closer approach to steady conditions and reduced gravitational disturbances. The observations established new methods for predicting luminous flame shapes, new imaging methods for measuring soot concentrations when soot volume fractions are small (less than 1 ppm), and new information about the laminar-smoke-point properties of nonbuoyant flames. The results also support the validity of laminar flamelet concepts for soot properties in nonbuoyant diffusion flames that could substantially simplify modeling of practical nonbuoyant flames.

Nomenclature

C_f = empirical flame length parameter, d = jet exit diameter, f_s = soot volume fraction, L = laminar smoke point flame length, L_o = distance from jet exit to virtual origin, L_f = distance from jet exit to luminous flame tip, p = pressure, r = radial distance, Re = mean jet Reynolds number, Sc = mean Schmidt number, t_{ch} = characteristic residence time, $2 L_f/u_o$, u_o = streamwise velocity at jet exit, w_{MAX} = maximum laminar flame diameter, z = streamwise distance, Z_{st} = stoichiometric mixture fraction

Background

A study of the structure and soot properties of nonbuoyant soot-containing laminar nonpremixed (diffusion) flames is described based on experiments carried out at microgravity conditions on board an orbiting space shuttle. The study is motivated by the impact of soot on emissions of combustion-generated pollutants, the hazards of unwanted fires, the performance of power and propulsion systems and the feasibility of computational combustion. In particular, black exhaust plumes containing soot are an easily recognized pollutant emission that is responsible for more deaths than any other pollutant. Continuum radiation from soot is also mainly responsible for the growth and spread of unwanted fires whereas most fire deaths are caused by emission of carbon monoxide associated with the soot-containing fire plumes emitted from these flames. The deposition of flame-generated soot can foul critical combustor components whereas continuum radiation from soot is the main heat load to combustor components and controls their durability. Finally, achieving computational combustion has been frustrated by limited understanding of soot processes within hydrocarbon-fueled flames. Thus, gaining a better

*Principal Investigator.

understanding of soot processes in diffusion flames is a major unsolved problem of combustion science.

Soot processes in turbulent diffusion flames are of greatest practical interest, however, direct study of such flames is not tractable because their unsteadiness and distortion limits available residence times and spatial resolution. Thus, laminar diffusion flames are generally used as more tractable model flame systems, justified by the known similarities of gas-phase processes in laminar and turbulent diffusion flames (often referred to as the laminar flamelet concept of turbulent diffusion flames). Unfortunately, laminar diffusion flames at normal gravity are affected by buoyancy due to their relatively small flow velocities and they do not have the same utility for simulating the soot processes as they do for simulating the gas-phase processes of practical turbulent flames. In particular, effects of buoyancy are small in the soot reaction regions of practical turbulent flames; therefore, buoyant laminar diffusion flames can only provide a proper model flame system to the extent that buoyancy does not affect soot processes. Unfortunately, soot particles do not diffuse like flame gases but instead are convected at the local flow velocity; therefore, extraneous flows caused by buoyancy affect the motion of soot particles. Another difficulty is that buoyancy-induced motions distort and strain laminar flames, often causing transition to turbulent flames, which limits the spatial and temporal resolutions that are needed for definitive measurements of both soot and flame properties. In view of these considerations present attention was limited to steady nonbuoyant soot-containing laminar diffusion flames.

Complete reviews of past studies of the structure and soot properties of nonbuoyant soot-containing laminar diffusion flames are presented by Faeth (1998), Lin et al. (1998a) and Urban et al. (1998). These reviews highlight several issues concerning nonbuoyant soot-containing laminar diffusion flames, as follows: (1) have existing measurements of flame structure and soot properties been affected by unsteady development effects due to the limited test times, and the often-disturbed gravitational environments, of ground-based experiments at microgravity; (2) what is the effect of soot luminosity on observed luminous flame boundaries (flame shapes) and do classical simplified theories provide a way to predict (or correlate) their shapes; (3) what is the potential of simple flame imaging techniques for measuring soot concentrations and temperatures within these flames; (4) what is the mechanism of the onset of soot emissions and what is the effect of the absence of the intrusion of buoyancy on the conditions required for these flames to begin to emit soot; (5) do these flames exhibit simple universal correlations between the degree of mixing and the properties of soot for given fuel and air (or oxidant) stream conditions (called soot property state relationships) similar to the state relationships for other scalar properties that are exploited using laminar flamelet concepts to model practical turbulent flames?

Objectives

The present investigation sought to address the issues just enumerated, based on long-term experimental observations of steady, nonbuoyant, round, hydrocarbon-fueled laminar jet diffusion flames burning in still air at microgravity on the orbiting space shuttle Columbia. The specific objectives of the study were as follows: (1) Measure flame structure and soot properties, including luminous flame shapes, soot concentration distributions, soot temperature distributions, soot structure distributions, plume temperature distributions and flame radiative heat losses; and (2) exploit the measurements to find theoretical and experimental estimates of luminous flame shapes, estimates of soot concentrations and temperatures based on extinction and multiline emission measurements, the nature of the onset of soot emissions and corresponding laminar smoke point properties, and the potential for state relationships for soot properties.

Experimental Methods

The apparatus consisted of a laminar jet diffusion flame stabilized at the exit of a round fuel nozzle. The nozzle extended along the axis of a windowed cylindrical chamber having a nominal diameter and length of 400 and 740 mm. The chamber was filled with still dry air whereas the total consumption of oxygen during a test did not exceed 10% of the original oxygen concentration. Two fuel nozzles (1.6 and 2.7 mm dia.) were used during the tests. The flames were ignited by a hot wire coil that could be retracted from the nozzle exit once ignition was successful. Fuel flow rates at ignition were set at values larger than final test values; after ignition the fuel flow rate was automatically adjusted to the nominal test value. The crew could subsequently adjust the fuel flow rate in order to find laminar smoke point conditions and set final flame conditions. Flame and soot structure measurements were completed as follows: flame shapes were obtained using a color CCD video camera, soot volume fraction distributions were obtained by deconvoluting either laser extinction or multiline emission images of the flames recorded using CCD video cameras, soot temperature distributions were obtained by deconvoluting multiline emission images of the flames recorded using CCD video cameras, soot structure was measured by thermophoretic sampling and analysis by transmission electron microscopy (TEM), temperature distributions in the flame plume were measured using a thermocouple rake located 190 mm from the burner exit, and flame radiation was measured using a heat flux transducer directed toward the center of the flames.

The 21 experiments completed over two shuttle flights (STS-83 and 94) included ethylene- and propane-fueled flames burning in dry air, initial reactant temperatures and pressures of 300 K and 35-130 kPa, jet exit velocities of 170-1690 mm/s, jet exit Reynolds numbers of 46-172, and characteristic residence times of 40-302 ms to yield luminous flame lengths of 15-63 mm. Suffixes E and P of the test numbers denote ethylene- and propane-fueled flames, and asterisks denote the two tests completed during flight STS-83. The present flames were close to laminar-smoke-point conditions with test flames 01E*, 03E*, 01E and 10P actually emitting soot in the period when observations were made; the remaining flames contained soot but were not emitting soot.

Results and Discussion

Flame Development. Monitoring measurements for a typical flame appear in Fig. 1. These results are from Urban et al. (1998) for an ethylene/air flame at 100 kPa with the 1.6 mm diameter nozzle (test 01E*). The ignitor and soot sampler timing refers to hardware actuation periods: the period when the ignitor coil was at the burner exit and the times when the four separate soot samples were obtained. The plot shows the reduction of fuel flow rates by the crew after ignition. Another 5-10s was required after the final fuel flow rate adjustment for the flame to achieve quasisteady behavior. Subsequently, flame and chamber properties change slowly as the flame consumes oxygen and produces hot combustion products.

Flame Shapes. Results of measurements and predictions of luminous flame shapes are presented by Lin et al. (1998). The objective was to obtain a simple flame shape analysis suitable for correlating the present measurements and convenient for use by others, as opposed to a detailed analysis requiring numerical solutions on a computer. The approach was based on simplified analysis due to Spalding (1979) assuming: (1) steady, axisymmetric laminar jet diffusion flame in a still gas; (2) effects of buoyancy and potential energy are small; (3) small Mach number so that viscous dissipation and kinetic energy can be ignored; (4) large flame aspect ratio so that streamwise transport can be ignored; (5) governing equations solved for self-preserving (similarity) conditions, far from the source; (6) fast reaction in a thin flame sheet; (7) equal diffusivities of mass (all species),

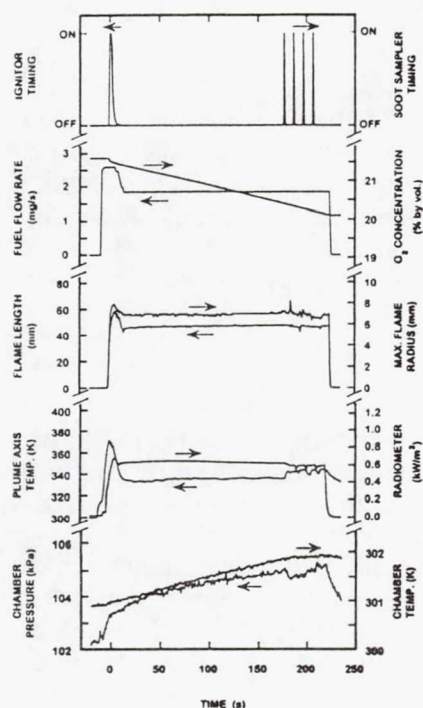


Fig. 1 Monitoring measurements as a function of time for a typical nonbuoyant hydrocarbon-fueled laminar jet diffusion flame in still air (Test 01E*, ethylene/air flame at 100 kPa, 1.6 mm jet exit diameter).

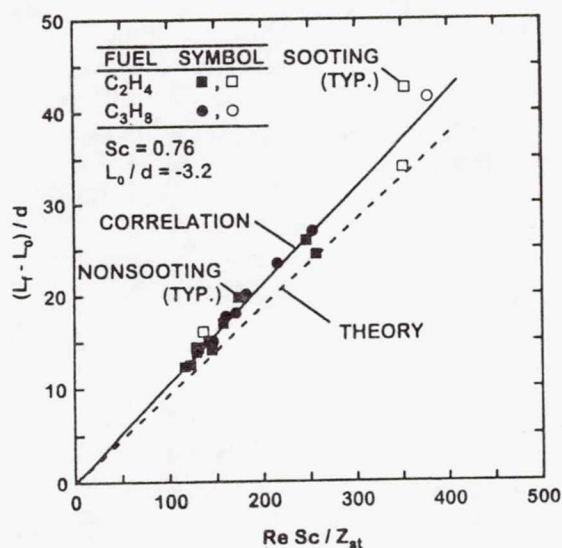


Fig. 2 Measured and predicted luminous flame lengths of nonbuoyant hydrocarbon-fueled laminar jet diffusion flames in still air.

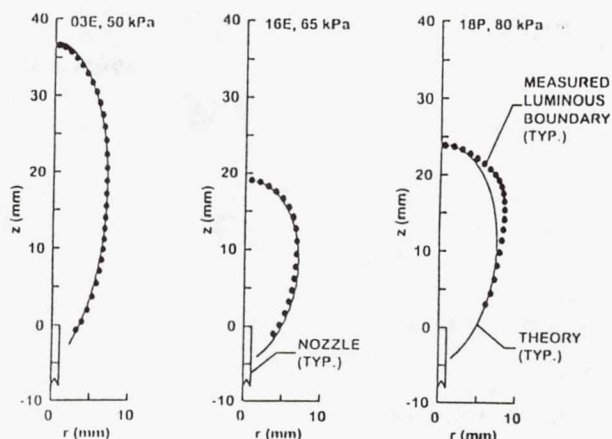


Fig. 3 Measured and predicted luminous flame shapes of typical closed-tip nonbuoyant hydrocarbon-fueled laminar jet diffusion flames in still air. (Tests 03E, 16E and 18P).

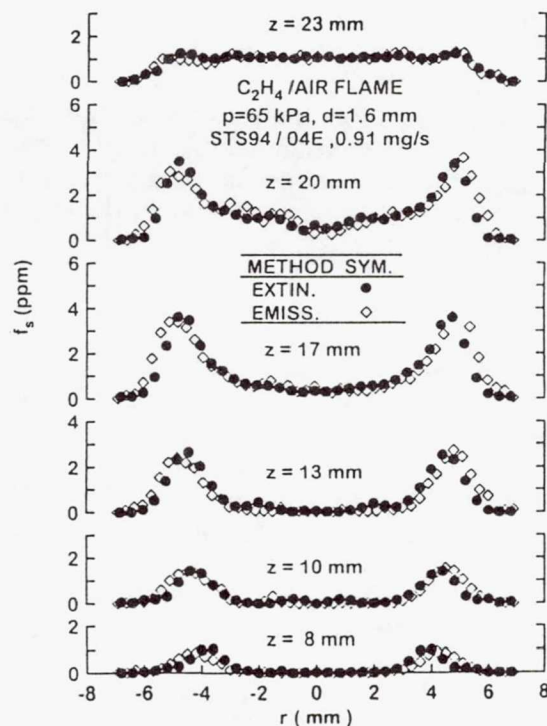


Fig. 4 Soot volume fraction distributions based on the laser extinction and multiline emission imaging methods for a typical nonbuoyant hydrocarbon-fueled laminar jet diffusion flame in still air. (Test 04E, ethylene/air flame at 65 kPa, 1.6 mm jet exit diameter).

momentum and energy; (8) all thermophysical and transport properties are constant; and (9) effects of radiation are small. These assumptions are discussed by Lin et al. (1998); most are conditions of the experiments but the last four are not satisfied by jet diffusion flames and are only adopted due to past success and the desire for a simple formulation. Solution of the governing equations yields simple expressions for the luminous flame shape (Lin et al., 1998). Introducing empirical parameters for a virtual origin (to treat flames having relatively small aspect ratios) and an empirical factor to address effects of soot luminosity (to allow for the fact that soot burns at fuel-lean conditions, somewhat downstream of the flame sheet, as laminar smoke point conditions are approached) yields the following expression for the luminous flame length:

$$(L_f - L_o)/d = (3C_f/32)Re Sc/Z_{st} \quad (1)$$

The correlation of the measurements was completed by approximating the properties needed to find Re and Sc by the properties of air at the average temperature of the flow which is reasonable because air-like gases dominate the composition of the present flames.

Typical of many past observations of soot-containing nonbuoyant laminar jet diffusion flames having a relatively large characteristic residence time, flame shapes could be grouped into closed- and open-tip configurations that were observed for fuel flow rates smaller and larger than the laminar smoke point fuel flow rates, respectively. The flame structure changes associated with these two flame configurations will be discussed later. Measured and predicted luminous flame lengths of the present flames are illustrated in Fig. 2. Non-sooting and sooting flames are denoted by closed and open symbols, respectively. Values of Sc do not change significantly over the test range; therefore, a value of $Sc = 0.76$ was adopted for all the predictions. A virtual origin at $L_o/d = -3.2$ was selected so that the fit of all the measurements passed through the origin; this value is small and negative as expected because the flames attached somewhat upstream of the jet exit. Finally, plots of Eq. (1) for $C_f = 1.00$ (denoted theory) and a best-fit correlation for $C_f = 1.13$ (denoted correlation) are shown on the plot.

The present flames were very steady and yield an excellent correlation according to Eq. (1) with little to choose between nonsooting and sooting flames. Present flames, however, were significantly longer than results from earlier ground-based measurements in the literature (Lin et al., 1998): 30% longer than soot-containing nonbuoyant laminar flames observed using drop tower (2.2s) facilities due to reduced effects of unsteadiness, 40% longer than soot-containing nonbuoyant laminar flames using aircraft (KC-135) facilities due to reduced effects of gravitational disturbances (g-jitter), roughly twice as long as soot-containing buoyant flames at normal gravity due to the absence of effects of buoyant mixing, and roughly twice as long as soot-free (blue) nonbuoyant flames observed using drop tower (2.2s) facilities due to the presence of soot luminosity and possible reduced effects of unsteadiness.

Predicted and measured flame shapes for typical closed-tip flames are illustrated in Fig. 3. The agreement between predictions and measurements is good, even extending to attachment of the flames upstream of the burner exit. This behavior is startling because predicted flame diameters cannot be fitted to the measurements by selecting conditions to find mean transport properties and by using an empirical parameter to optimize predictions, e.g., the maximum flame diameter is given by the following expression (Lin et al., 1998):

$$w_{MAX}Z_{st}/d = 9/16 \text{ @ } z/L_f = 9/16 \quad (2)$$

On the other hand, flame shapes near the tip of the open-tip flames are not predicted very well, which is expected because the present simple analysis does not consider effects of radiative quenching, that are associated with tip opening behavior (Lin et al., 1998).

Soot Property Imaging. The use of laser extinction imaging to find soot volume fraction distributions in axisymmetric flames has a long history of success, see Lin and Faeth (1998b) and Urban et al. (1998) and references cited therein. The availability of simultaneous multiline emission measurements, however, provided an opportunity to check these measurements and to develop an alternative approach to find soot concentrations by multiline imaging. The new multiline emission approach to measure soot concentrations and soot temperatures is of interest because multiline emission becomes more accurate at conditions where laser extinction is less effective; therefore, the two methods complement each other and extend the available range of measurements. Another advantage of multiline emission is that it involves a far simpler optical arrangement than laser extinction in order to carry out soot concentration measurements.

Lin and Faeth (1998b) discuss multiline emission for measuring soot concentrations and temperatures. The main approximations of these measurements were as follows: optically-thin flame conditions, Rayleigh scattering from primary soot particles, known refractive indices of soot, soot refractive indices assumed to be independent of fuel type and state of development of the soot; and soot refractive indices drawn from Dalzell and Sarofim (1969). The results for chordlike paths through the flames are deconvoluted to find radial distributions of soot concentrations and temperatures.

Typical measurements of soot volume fractions by deconvoluted laser extinction and multiline emission are illustrated in Fig. 4. This condition (Test 04E) involves an ethylene/air flame at a pressure of 65 kPa with a 1.6 mm diameter nozzle. At these conditions, maximum soot volume fractions are roughly 4 ppm so that the two methods have comparable experimental uncertainties. In order to test consistency, the left and right sides of the flame are analyzed separately while assuming that the flame is axisymmetric in each case. This approach provides a total of four estimates of soot concentration distributions at each distance from the burner exit. The soot concentration distributions by laser extinction and multiline emission are seen to be consistent for both sides of the flame and to be in good agreement with each other. Similar behavior was observed for all the flames where the two methods could be compared except for flames having large soot concentrations where the optically-thin approximation fails. An extension of the deconvolution algorithm is feasible, however, to correct for effects of optical thickness; this approach is currently being evaluated.

Soot Properties. A typical TEM image of a soot particle (aggregate) emitted from the present flames is illustrated in Fig. 5. This sample was emitted from an ethylene/air flame at a pressure of 100 kPa with a 1.6 mm diameter nozzle (Test 01E*). The structure of this aggregate is similar to soot sampled from other diffusion flames (Urban et al., 1998). The aggregates are made up of roughly spherical primary soot particles that have nearly uniform diameters at any given position in the flame. The primary soot particles are collected into open structured and branched aggregates that have rather large variations of the number of primary soot particles per aggregate (typically represented by log normal distribution functions). The main difference between present soot aggregates and those found in buoyant diffusion flames is that the present aggregates have larger primary particle diameters and aggregate sizes. Such behavior is expected, however, because present flames have unusually long residence times compared to other flames which provides an opportunity for increased soot growth.

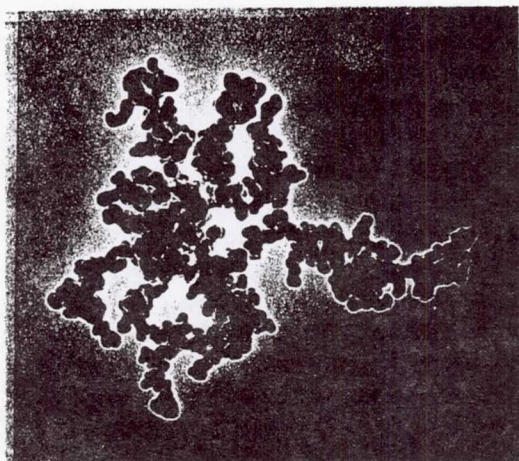


Fig. 5 TEM photograph of a typical soot aggregate emitted from an open-tip nonbuoyant hydrocarbon-fueled laminar jet diffusion flame in still air.

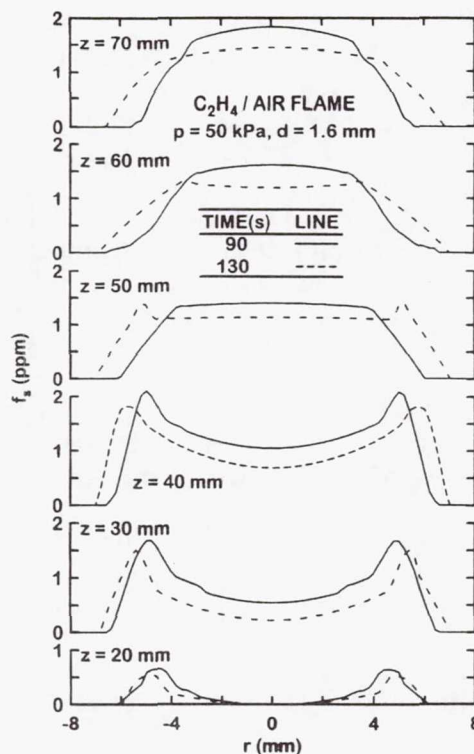


Fig. 7 Soot volume fraction distributions in a typical closed-tip nonbuoyant hydrocarbon-fueled laminar jet diffusion flame in still air

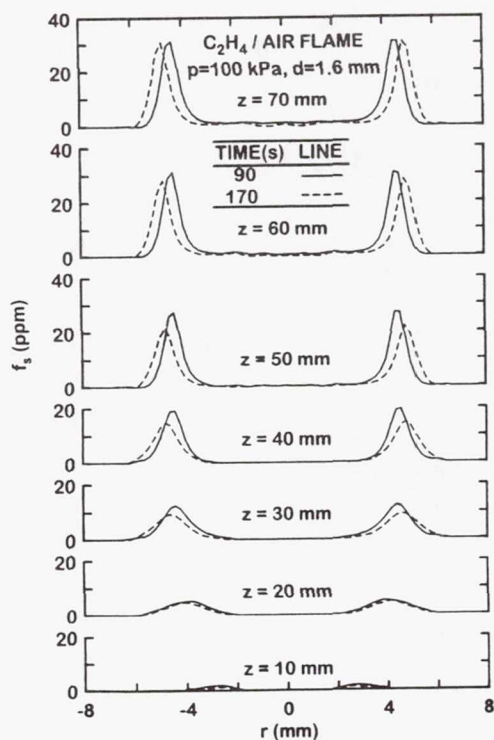


Fig. 6 Soot volume fraction distributions in a typical open-tip nonbuoyant hydrocarbon-fueled laminar jet diffusion flame in still air.

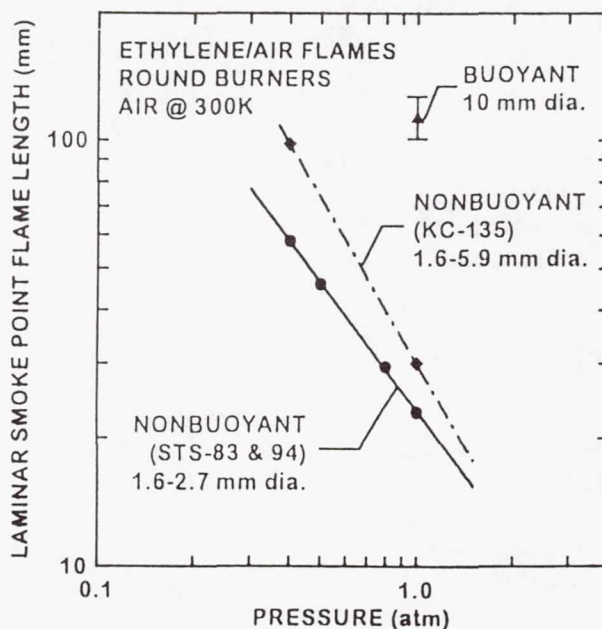


Fig. 8 Laminar smoke point flame lengths for round ethylene-fueled laminar jet diffusion flames in still air.

Typical measurements of soot volume fraction distributions at various distances from the burner exit are illustrated in Figs. 6 and 7 for ethylene/air flames having a 1.6 mm diameter nozzle at pressures of 100 and 50 kPa, respectively. The results are illustrated at two times during the quasisteady burning period, showing that the soot concentration profiles tend to become broader, with somewhat reduced peak soot concentrations, as time increases. This behavior is expected as a result of the moderately reduced ambient oxygen concentrations due to oxygen consumption by the flame. Another trend seen in Figs. 6 and 7 is the strong increase of soot concentrations with increasing pressure, e.g., maximum soot concentrations increase from roughly 2 to 32 ppm for an increase of pressure from 50 to 100 kPa. This behavior is consistent with earlier observations of effects of pressure on soot concentrations in diffusion flames, see references cited by Urban et al. (1998).

An interesting feature of the soot concentration profiles illustrated in Figs. 6 and 7 is the tip-opening phenomena mentioned earlier. Figure 6 is representative of a soot emitting tip-opened flame where all the soot at each cross-section of this flame is contained within a narrow annular ring and soot is never observed along the axis of the flame. Corresponding temperature measurements for this flame show that temperatures in the soot layer become relatively small near the tip of the luminous portion of the flame, approaching 1000 K where combustion and soot oxidation reactions are expected to be quenched. This implies that unreacted fuel is escaping along the flame axis. The results illustrated in Fig. 7 are representative of closed-tip flames where the annular regions of high soot concentrations merge toward the axis and the soot is eventually oxidized completely. This behavior is also supported by temperature measurements that generally indicate soot temperatures greater than 1300 K in this flame. The reasons for the differences between these two flames is the smaller characteristic residence time (63 as opposed to 121 ms) and larger jet exit velocities (1630 as opposed to 820 mm/s) of the low pressure flame compared to the high pressure flame. These changes reduce effects of radiative quenching and thermophoresis that tend to promote tip-opening behavior.

Measurements of laminar smoke points are plotted as a function of pressure for ethylene-fueled flames in Fig. 8. Corresponding results for propane-fueled flames can be found in Sunderland et al. (1998). Three sets of measurements are illustrated in the figure: results for nonbuoyant flames for burner diameters of 1.6 and 2.7 mm from the present space shuttle experiments, results for nonbuoyant flames for burner diameters of 1.6-5.9 mm based on aircraft (KC-135) experiments and results for buoyant flames for a burner diameter of 10 mm. In each case, effects of burner diameter over the range indicated are small. Clearly, the laminar smoke point flame lengths of the nonbuoyant flames from the space-based experiments are significantly smaller than the rest. This behavior follows because present flames have large characteristic residence times (120-300 ms compared to values less than 10 ms for buoyant flames at atmospheric pressure) which implies much greater potential for radiative heat losses leading to quenching and effects of thermophoresis leading to tip opening and emission of soot. Another interesting aspect of laminar smoke point flame lengths is the strong effect of pressure. In particular, laminar smoke point flame lengths decrease roughly inversely proportional to pressure for the present nonbuoyant flames with the effect of pressure being even stronger for the aircraft KC-135 experiments. It was also found that soot concentrations and primary particle diameters at the laminar smoke point decrease substantially as the pressure is decreased; this behavior highlights the fact that laminar smoke points are caused by the relative rates of soot formation and oxidation, and not the absolute magnitudes of either (Urban et al., 1998).

Laminar Flamelet Concepts. Results discussed in connection with Figs. 2 and 3 suggest that the simplified analysis of the shapes of nonbuoyant laminar jet diffusion flames due to Spalding (1979) provides a reasonable description of the mixing properties of

the present flames. A well known property of this formulation is that various paths through the flame from the burner exit have the same variation of scalar properties as a function of time. Exceptions to this behavior involve a small region near the burner exit associated with effects of flame attachment, conditions where flame residence times are large so that radiative heat losses become relatively more important for paths near the axis, and conditions where flow velocities are small so that thermophoretic effects modify velocities along the various paths through the flame. Barring these conditions, soot particles convecting along various paths through the flame should be subject to the same variation of reactive environment as a function of time so that soot properties should vary in a universal manner as a function of mixture fraction. Another feature of such conditions is that scalar properties as a function of time become independent of the burner exit velocity. Taken together, this behavior implies universal state relationships for soot properties for given jet exit and ambient conditions so that the laminar flamelet concept for soot properties is satisfied.

Present results for nonbuoyant laminar jet diffusion flames provide an opportunity to test the laminar flamelet concept for soot properties, because if scalar properties as a function of time are similar for various paths through the flame, it follows that maximum soot concentrations should be identical for the various paths as well. Such behavior is not observed for test flame 01E* having the soot distributions plotted in Fig. 6 where maximum soot concentrations in the annular region progressively increase with increasing distance from the jet exit while a path along the axis would never encounter any soot. This exception is expected, however, because this flame has a large residence time and small flow velocities leading to radiative quenching and thermophoretic effects associated with the tip-opening phenomena. The results plotted in Fig. 7 for test flame 03E*, however, exhibit different behavior from the results plotted in Fig. 6. In this case, maximum values of soot volume fractions for all paths through the flame (except for the near burner exit region) are in the range 1.5-2.0 ppm which at least roughly satisfies the necessary condition for the existence of a soot volume fraction state relationship. This difference comes about because flame 03E* involves much smaller characteristic residence times and larger jet exit velocities than flame 01E*.

The evaluation of the potential for soot property state relationships for nonbuoyant laminar jet diffusion flames was extended over the data base. The flames considered involved the smallest characteristic residence times (less than 70 ms), the largest burner exit velocities (greater than 600 mm/s) and reasonably large flame aspect ratios (greater than 11). The results revealed relatively modest variations of maximum soot concentrations (std. dev. $\leq 20\%$) for various paths through a given flame, which also is supportive of the validity of the laminar flamelet concept for soot properties, see Faeth et al. (1998).

Conclusions

The structure and soot properties of steady, nonbuoyant, round hydrocarbon-fueled laminar jet diffusion flames burning in still air were studied based on long term (100-230s) experiments at microgravity carried out on an orbiting space shuttle. The major conclusions of the study are as follows:

1. The present nonbuoyant and steady flames at microgravity were larger than earlier observations from ground-based experiments, as follows: 30% longer than soot-containing nonbuoyant flames observed using aircraft (KC-135) facilities due to reduced effects of gravitational disturbances (g-jitter), roughly twice as long as soot-containing buoyant flames at normal gravity due to the absence of effects of buoyant mixing; and roughly twice

as long as soot-free (blue) nonbuoyant flames observed using drop tower (2.2s) facilities due to the presence of soot luminosity and possible reduced effects of unsteadiness.

2. Similar to earlier observations of soot-containing nonbuoyant laminar jet diffusion flames having large characteristic residence times, present flame shapes could be grouped into closed- and open-tip configurations, which were observed at fuel flow rates smaller and larger than the laminar smoke point fuel flow rate, respectively. Measured soot temperatures near the tip of open-tipped flames approach 1000 K, suggesting that tip opening is caused by quenching of flame reactions due to radiative heat losses; this behavior implies significant emissions of unburned fuel along with soot.

3. The simplified theoretical analysis of nonbuoyant laminar jet diffusion flames due to Spalding (1979) generally yielded excellent predictions of flame shapes upon adjusting an empirical flame length parameter to account for effects of soot luminosity in the fuel-lean portions of the flame as the laminar smoke point is approached. Remarkably, the simplified analysis of Spalding (1979) remains reasonably effective for open-tipped flames even through it does not account for effects of radiative quenching.

4. The present laser extinction imaging measurements of soot concentrations agreed with corresponding multiline emission imaging measurements of soot concentrations for conditions where both methods have comparable accuracy. Multiline emission imaging has substantial advantages compared to laser extinction imaging for measurements of soot concentrations, however, because it is more accurate at small soot concentrations (less than 1 ppm) and it involves a much simpler optical arrangement.

5. The present nonbuoyant and steady flames at microgravity emitted soot more readily than earlier observations from ground-based experiments, based on smaller laminar smoke point flame lengths, as follows: 40% smaller than nonbuoyant flames observed using aircraft (KC-135) facilities due to reduced effects of gravitational disturbances (g-jitter) and up to five times smaller than buoyant flames at normal gravity due to reduced effects of buoyant mixing. These changes come about due to the absence of mixing from effects of flow development, disturbances and buoyancy, combined with larger effects of radiation due to the rather long characteristic residence times of the present flames.

6. Finally, flames having small characteristic residence times, large burner exit velocities and large aspect ratios, yielded nearly the same maximum soot concentrations along all paths through the flame, except for a small region near the burner exit. At such conditions, effects of radiative extinction and thermophoresis are small, typical of practical nonbuoyant laminar jet diffusion flames, and theory shows that the flame environment as a function of time is identical for all paths through the flame except near the jet exit. Such "paradigm flame" conditions should lead to similar maximum soot concentrations as observed which supports the potential existence of universal state relationships for soot properties (or the validity of the laminar flamelet concept for soot properties) for practical nonbuoyant diffusion flames.

In addition to directly contributing to improved understanding of soot-containing diffusion flames, the present findings provide both new experimental methods and directions for future research concerning the structure and soot processes of nonbuoyant hydrocarbon-fueled diffusion flames. First of all, reliable predictions of flame shapes based on the present application of the Spalding (1979) theory will simplify the design of test apparatus and imaging systems for future experiments with nonbuoyant laminar jet diffusion flames. The successful development and evaluation of the multiline imaging approach for measuring both soot concentrations and temperatures provides new capabilities for measurements over a broader range of test conditions (including flames

having soot concentrations less than 1 ppm) with a much simpler optical system than laser extinction imaging. Additional information about laminar smoke point properties also improves the selection of test conditions so that soot emissions that could compromise experimental observations by fouling windows and instrumentation can be avoided. Finally, improved insight about effects of flame residence times on radiative quenching and thermophoresis, and conditions needed to observe the "paradigm flames" that are most relevant to practical nonbuoyant flames, suggest new directions for experimentation needed to evaluate laminar flamelet concepts for soot properties in nonbuoyant diffusion flames.

Articles/Presentations Resulting from Flight

Journal Articles:

Faeth, G.M. (1998) Gaseous Laminar Diffusion Flames. *Microgravity Combustion Science* (H.D. Ross, ed.), Academic Press, New York, invited.

Faeth, G.M., Lin, K.-C., Sunderland, P.B., Urban, D.L. and Yuan, Z.-G. (1998) Laminar Flamelet Concept for Soot Properties in Nonbuoyant Laminar Jet Diffusion Flames. Combust. Flame, in preparation.

Lin, K.-C. and Faeth, G.M. (1998a) Shapes of Nonbuoyant Round Luminous Hydrocarbon/Air Laminar Jet Diffusion Flames in Coflowing Air. AIAA Journal, submitted.

Lin, K.-C. and Faeth, G.M. (1998b) Soot Volume Fraction and Temperature Distributions in Laminar Diffusion Flames by Extinction and Multiline Emission Imaging. AIAA Journal, in preparation.

Lin, K.-C., Faeth, G.M., Sunderland, P.B., Urban, D.L. and Yuan, Z.-G. (1998) Shapes of Nonbuoyant Round Luminous Hydrocarbon/Air Laminar Jet Diffusion Flames. Combust. Flame, in press.

Sunderland, P.B., Urban, D.L., Yuan, Z.-G., Lin, K.-C. and Faeth, G.M. (1998) Laminar Smoke Point Properties of Ethylene/Air and Propane/Air Nonbuoyant Laminar Jet Diffusion Flames. Combust. Flame, in preparation.

Urban, D.L., Yuan, Z.-G., Sunderland, P.B., Linteris, G.T., Voss, J.E., Lin, K.-C., Dai, Z., Sun, K. and Faeth, G.M. (1998) Structure and Soot Properties of Nonbuoyant Ethylene/Air Laminar Jet Diffusion Flames. AIAA Journal, Vol. 36, No. 8, pp. 1346-1360.

Conference Papers and Reports:

Dai, Z., Lin, K.-C., Sunderland, P.B., Xu, F. and Faeth, G.M. (1997) Laminar Soot Processes (LSP). Report No. GDL/GMF 97-01, Department of Aerospace Engineering, The University of Michigan, Ann Arbor.

Faeth, G.M. (1999) The Reactive and Radiative Properties of Soot in Flame Environments. *Proceedings of the 5th ASME/JSME Joint Thermal Engineering Conference*, San Diego, CA, March 1999, invited.

Lin, K.-C. and Faeth, G.M., Sunderland, P.B., Urban, D.L. and Yuan, Z.-G. (1988) Shapes of Nonbuoyant Round Luminous Hydrocarbon/Air Laminar Jet Diffusion Flames.

Proceedings of the Spring Technical Meeting, Central States Section of the Combustion Institute, Pittsburgh, pp. 357-362.

Urban, D.L., Yuan, Z.-G., Sunderland, P.B., Linteris, G.T., Voss, J.E., Lin, K.-C., Dai, Z., Sun, K. and Faeth, G.M. (1998) Structure and Soot Properties of Nonbuoyant Ethylene/Air Laminar Jet Diffusion Flames. 36th Aerospace Sciences Meeting, Reno, AIAA Paper No. 98-0568.

Xu, F., Lin, K.-C., Faeth, G.M. and Sunderland, P.B. (1997) Laminar Soot Processes. *Proceedings of the Fourth International Microgravity Conference Workshop*, NASA Conf. Pub. No. 10194, Washington, pp. 199-204

Oral and Poster Presentations:

Faeth, G.M. (1997a) Soot Growth in Laminar Premixed and Diffusion Flames. UIC Spring Seminar Series, Mechanical Engineering Department, University of Illinois-Chicago, Chicago.

Faeth, G.M. (1997b) LSP Science Results. CM-1 Awards Ceremony, NASA Lewis Research Center, Cleveland.

Faeth, G.M. (1997c) Academic Perspectives on Combustion Research in the 21st Century. ASME, Winter Annual Meeting, Houston, plenary lecture.

Faeth, G.M. (1998) Space Shuttle Observations of Soot-Containing Round Laminar Jet Diffusion Flames. Mechanical Engineering Seminar, University of Connecticut, Storrs.

Lin, K.-C., Faeth, G.M., Sunderland, P.B., Urban, D.L. and Yuan, Z.-G. (1998) Shapes of Nonbuoyant Round Luminous Hydrocarbon/Air Laminar Jet Diffusion Flames. *27th Symposium (International) on Combustion*, The Combustion Institute, Pittsburgh, Poster Paper No. W5A03.

Appendix: Nontechnical Summary

Soot-containing flames were studied at microgravity in the orbiting Space Shuttle Columbia. The objective was to complete measurements that are not possible at normal laboratory conditions due to the intrusion of Earth's gravity. Study of soot formation in flames is motivated by several important problems of society, as follows: particulate soot emitted from flames causes more deaths than any other pollutant, toxic gases associated with soot are responsible for most deaths in unwanted fires, heat radiated from soot is the main mechanism for both the spread of unwanted fires and the limited life of combustion chambers used for power and propulsion systems, and limited understanding of soot inhibits methods of computational combustion needed to avoid costly cut and try methods of developing combustion systems. The observations showed that the present flames were larger and emitted soot more readily than flames studied using ground-based microgravity facilities due to reduced disturbances. These findings help establish new theories to predict flame properties and provide new insight about effects of flame disturbances on soot emissions. The observations also disclosed a surprising potential for universality of soot formation in complex flame environments that was not recognized earlier due to extraneous gravitational disturbances. This finding helps explain the uniform sizes of soot particles emitted from flames and suggests new ways of reducing pollutant soot emissions from combustion processes.

Page intentionally left blank

OMIT THIS
PAGE

Combustion Module-1 (CM-1)

Structure of Flame Balls at Low Lewis-Number (SOFBALL)

Principal Investigator:

Dr. Paul D. Ronney
University of Southern California
Los Angeles, California

SINGLE
SCAN

53-25
434840

Structure Of Flame Balls At Low Lewis-number (SOFBALL): Preliminary Results from the STS-83 and STS-94 Space Flight Experiments

Paul D. Ronney, Ming-Shin Wu and Howard G. Pearlman
Department of Aerospace and Mechanical Engineering
University of Southern California, Los Angeles, CA 90089

Karen J. Weiland
Microgravity Science Division
NASA Lewis Research Center, Cleveland, OH 44135

362139
121

ABSTRACT

Results from the Structure Of Flame Balls At Low Lewis-number (SOFBALL) space flight experiment conducted on the MSL-1 Space Shuttle missions are reported. Several new insights were obtained, including: much lower buoyancy-induced drift speed than anticipated pre-flight; repulsion of adjacent flame balls due to their mutual interaction; remarkable sensitivity of flame balls to small accelerations resulting from Orbiter attitude control maneuvers; and very similar net heat release for all flame balls in all mixtures tested. Comparison of experimental results to computational predictions reveals limitations in current models of H_2 - O_2 chemistry for very lean mixtures. It is discussed how the results of these space experiments may provide an improved understanding of the interactions of the two most important phenomena in combusting materials, namely chemical reaction and transport processes, in the unequivocally simplest possible configuration.

INTRODUCTION

Flames are typically classified as "premixed" flames, where all reactants (for example fuel and air) are intimately mixed on the molecular level before the combustion process is started, and "nonpremixed" or "diffusion" flames, where the fuel and oxidant must mix before combustion can take place. Premixed flames include the familiar laboratory Bunsen burner as well as the flames inside of a gasoline-fueled internal combustion engine. It is well known that premixed gas flames containing too little fuel ("lean mixtures") or too much fuel ("rich mixtures") will not burn. Despite many years of study, these lean and rich "flammability limits" and the behavior of weakly burning flames near these limits are not well understood. For example, the best available predictions of the burning velocities of very lean hydrogen-air mixtures near flammability limits are higher than the experimental measurements by a factor of 2 (Ref. 1). Away from these limits, the agreement between model and experiment is much more satisfactory. Understanding combustion under lean conditions is critical to the design of efficient, clean-burning combustion engines. Lean-burning hydrogen-fueled engines are frequently considered as a means of meeting California's upcoming ultralow emission vehicle standards and the proposed federal emission standards for beyond the year 2000. Also, knowledge of near-limit behavior of flames is necessary for the assessment of fire and explosion hazards in mine shafts, oil refineries and chemical plants².

It has been known for many years² that most near-limit phenomena are influenced by gravity through the effects of buoyant convection on the transport rates of thermal energy and reactants to/from the chemical reaction zones. This has motivated a number of recent experiments on flame propagation in a μg environment^{3,4}. It has been found that in a μg environment the absence of buoyant convection emphasizes other transport mechanisms, including the unequal rates of diffusion of thermal energy and diffusion of molecular reactants (the Lewis number effect) and the spectral radiation emitted from the gaseous combustion products. As a consequence of the change in the relative magnitudes of various transport mechanisms at μg , a number of new near-limit phenomena have been observed. Perhaps the most unusual of these are "flame balls," which are the subject of the SOFBALL flight experiment.

SCIENTIFIC BACKGROUND

Over 50 years ago, Zeldovich⁵ showed that the steady heat and mass conservation equations admit a solution corresponding to a stationary spherical flame or "flame ball" (Fig. 1), just as the same governing

equations in planar geometry admit a steadily propagating flame as a solution for every mixture. In the former case the solutions are characterized by a radius (r) and in the latter case by the burning velocity. The mass conservation equation in a steady spherically symmetric system with no sources or sinks, $\nabla \cdot (\rho \mathbf{u}) = 0$, where ρ is the density and \mathbf{u} the fluid velocity vector, requires that \mathbf{u} be identically zero everywhere. In spherical geometry, the solution to steady, convection free diffusion equations for temperature and chemical species, $\nabla^2 T = 0$ and $\nabla^2 Y$, where T is the temperature and Y the fuel mass fraction, are of the form $c_1 + c_2/r$, where r is the radial coordinate and c_1 and c_2 are constants. This form satisfies the requirement that T and Y be bounded as $r \rightarrow \infty$. For cylindrical and planar geometry the corresponding forms are $c_1 + c_2 \ln(r)$ and $c_1 + c_2 r$, respectively, which are obviously unbounded as $r \rightarrow \infty$. For this reason theory admits steady flame ball solutions, but not "flame cylinder" or "flame slab" solutions. Zeldovich showed that for an adiabatic flame ball, the energy and species conservation equations could be combined to infer the temperature at the surface of the flame ball (T_s):

$$T_s = T_\infty + (T_{ad} - T_\infty)/Le \quad (1),$$

where T_∞ is the ambient temperature, T_{ad} the adiabatic flame temperature and Le the Lewis number, defined as ratio of the mixture thermal diffusivity (α) to the mass diffusivity (D) of the stoichiometrically limiting reactant (which is always the fuel for the purposes of the discussion here.) Thus, the temperature profile is given by $T(r) = T_\infty + (T_s - T_\infty)r/r$, where r is the flame ball radius. Zeldovich also showed that flame ball solutions are unstable and thus probably would not be physically observable, just as planar flames are frequently subject to instabilities which prevent them from remaining planar.

Forty years later after Zeldovich's analysis, seemingly stable flame balls were accidentally discovered in drop-tower experiments⁶ in lean hydrogen-air mixtures ($Le \approx 0.3$) and subsequently observed in drop-tower and aircraft experiments⁷ in H_2 - O_2 - CO_2 ($Le \approx 0.2$), H_2 - O_2 - SF_6 ($Le \approx 0.06$) and CH_4 - O_2 - SF_6 mixtures ($Le \approx 0.3$). The μg environment of the drop tower was needed to obtain spherical symmetry and to avoid buoyancy-induced extinction of the flame balls. The following sequence of phenomena was observed as the mixtures were progressively weakened by addition of air, inert gas or chemical inhibitor. For mixtures sufficiently far from flammability limits, flame balls consistently split into more flame balls, resulting in an expanding spherical front composed of many individual cells, similar to the cellular fronts resulting from the diffusive-thermal instability widely observed at 1g in mixtures with low Le . For weaker mixtures closer to the flammability limits, stable flame balls were observed. For still weaker mixtures all flames extinguished. It was concluded that flame balls would probably occur in all combustible mixtures with low Le for mixtures close to the extinction limits, however, the short duration of drop tower experiments and the substantial fluctuations in the acceleration level in aircraft μg experiments precluded definite conclusions.

These results were found to be qualitatively the same over the range $0.06 < Le < 0.3$, with H_2 and CH_4 fuels, with or without added CF_3Br (a chemical inhibitor) and at pressures from 0.5 to 3 atm, indicating that variations in Lewis number over this range, chemical mechanisms, and radiation spectra do not qualitatively influence these phenomena.

The apparent discovery of stable flame balls motivated a search for a stabilizing mechanism. Zeldovich⁵ had noted the possibility of heat losses stabilizing flame balls. The effects of volumetric radiative losses (e.g., due to gas radiation) on flame balls were analyzed by Buckmaster and collaborators^{8,9}. When the heat losses are not too strong, two stationary flame ball radii are predicted (Fig. 2), a "large" flame ball that is strongly affected by heat loss and a "small" flame ball that is nearly adiabatic, and when the losses are sufficiently strong no solutions exist, indicating a flammability limit. As the limit is approached, the difference between the radii of the "large" and "small" balls decreases to zero. Stability analyses^{8,9} showed that all small flame balls are unstable to radial disturbances, i.e., the flame will either grow outward from the equilibrium radius (and possibly develop into a propagating flame) or collapse inward and extinguish. Large flame balls with weak heat loss effects, i.e., far from the flammability limits, are predicted^{8,9} unstable to three-dimensional disturbances, which is consistent with the observation of splitting cellular flames in these mixtures. Consequently, a portion of the large flame branch close to the extinction limits is stable to both types of disturbances, which is consistent with the experimental observations.

It has also been predicted¹⁰ that stable flame balls can only exist for mixtures with mixtures having Le less than a critical value which is less than unity, which explains why flame balls are not observed for

mixtures with Le less than but close to unity (e.g. CH_4 -air) or larger than unity (e.g. C_3H_8 -air), even for near-limit mixtures at μg . Instead, conventional propagating flames are observed under these conditions.

Flame balls have several unique and interesting properties which indicate a number of practical applications. Since they are one-dimensional, steady and convection-free, they are the simplest possible type of premixed flame structure and therefore provide a useful test-bed for theoretical and numerical models of the interaction between chemical and transport processes in flames, especially near flammability limits. Some of these interactions are not predicted well even by the best currently available models. For example, numerical simulations of flame ball properties^{11,13} employing detailed chemical, radiation and transport models in a spherically symmetric system show that different published chemical reaction models for hydrogen-oxygen oxidation predict widely varying flame ball characteristics (Fig. 3), even though all of these models can accurately predict the burning velocities of flames in hydrogen-air mixtures farther away from the extinction limits (Fig. 4). This is particularly significant because models of hydrocarbon combustion chemistry must have an accurate H_2 - O_2 sub-mechanism if they are to be able to model hydrocarbons accurately. Also, since flame balls can be observed in mixtures that are well outside the conventionally defined extinction limits, microgravity can be a more hazardous environment from the point of view of fire safety. Flame balls warrant particular concern because they do not propagate; this makes fire detection and suppression more difficult. This potential problem is compounded because hydrogen burns without visible radiation or smoke, and because sources of hydrogen abound on spacecraft (e.g., in propulsion and fuel cell systems). Flame balls may also be relevant to the turbulent combustion of mixtures with low Lewis number because flame balls are more robust than plane flames (the computed¹¹ radiation-induced extinction limit of flame balls in lean H_2 -air mixtures is 3.43% H_2 , whereas for plane flames it is 11.1%.) Consequently, sufficiently strong turbulence may extinguish planar flames, whereas flame balls could persist under the same conditions. Hence, structures reminiscent of flame balls could be the prevalent ones in near-limit turbulent combustion of lean hydrogen-air mixtures in engines.

EXPERIMENTAL APPROACH

Based on the above discussion, the objectives of the SOFBALL experiment can be summarized as follows:

- Determine whether steady, stationary flame balls can exist in an extended-duration μg environment
- Assess the influence of gaseous radiation on flame ball size and stability
- Determine whether flame ball motion (if observed) is due to the non-zero gravity level (present to a small extent even in the Spacelab environment)
- Determine the effect of Lewis number and radiation on flame balls through the use of mixtures employing different diluent gases

The drop-tower and aircraft μg experiments indicate that a very long duration and high quality μg environment is necessary to assess the steady properties and stability limits of flame balls. A theoretical estimate of the time required can be made in the following way. The response time of flame balls is on the order of the time for thermal diffusion of energy from the near-field region of the flame ball to the far-field region. Theory^{8,9} shows that the former region is characterized by radii of the order of r , and the latter region is characterized by radii of the order of θr , where $\theta \equiv E/RT_*$ is the non-dimensional activation energy, E the dimensional overall activation energy of the heat release reactions and R the gas constant. Consequently, the far-field time scale is of the order $(\theta r)^2/\alpha$. Since typical values of r , θ and α are 5 mm, 10 and 20 mm^2/s , respectively, for lean H_2 -air mixtures, a representative time scale for flame ball evolution is 125 s - much longer than the time available from drop-tower or aircraft facilities. This evolution time scale is confirmed by numerical simulations^{11,13}. Another consideration is that the gravity level must be small enough that the flame balls are not significantly affected by convection. The drift velocity of flame balls based on aircraft μg data was found⁷ to be $1.5(g_r)^{1/2}$, where g_r is the gravitational acceleration. Since velocities on the order of α/r are sufficient to disturb flame balls¹², $g \ll 1.5 \times 10^{-4} g_0$, where g_0 is earth gravity, is required to obtain diffusion-dominated flame balls (as opposed to convection-dominated flames.) To insure that the conductive flux, represented by α/r , is significantly less than the convective flux, represented by the drift velocity, the acceleration level should be a factor of θ less than this, or $1.5 \times 10^{-5} g_0$. Another requirement is that the acceleration is small enough that the flame balls do not drift into the walls

of the combustion chamber before at least one characteristic evolution time has elapsed. This coincidentally also requires a gravity level of $1.5 \times 10^{-5} g_0$ or lower in the combustion chamber employed, which has a radius of 160 mm. This required time and quality of μg indicate the need for space experiments. The SOFBALL experiment on MSL-1 provided the requisite μg environment.

The SOFBALL experiments were performed in the Combustion Module-1 facility, developed by the NASA-Lewis Research Center in Cleveland, Ohio. A cylindrical chamber of 320 mm inside diameter and 320 mm length was filled from one of 14 bottles containing a pre-specified weakly combustible H_2 -air, H_2 - O_2 - CO_2 or H_2 - O_2 - SF_6 gas mixture and ignited using electric sparks of variable deposited energy up to 700 mJ with spark gaps variable from 0.35 to 10 mm. The optimal energy and gap were determined pre-flight by aircraft μg tests. The flame balls evolving from this ignition source were observed using two intensified video cameras (sensitive to visible and near-IR emissions from 400 to 900 nm) with orthogonal views, a set of six thermocouples to measure gas temperature, and four radiometers (two unfiltered and two with a $5 \mu m - 7.5 \mu m$ band-pass filter to detect only H_2O radiation) to measure the radiant heat flux emitted from the flames. Additionally, the chamber pressure was recorded during the test and the pre- and post-combustion gas compositions were measured using a gas chromatograph. The on-orbit acceleration levels were measured by the four different on-board accelerometer systems (OARE, MMA, SAMS and QSAM). The PI Microgravity Services (PIMS) team provided the SOFBALL team with OARE acceleration data transformed to the combustion chamber location; the accelerations reported below use these specially processed data.

EXPERIMENTAL RESULTS

Two of the fifteen scheduled SOFBALL experiments were successfully conducted during the shortened STS-83 mission. A total of seventeen test points were performed on STS-94, including all fifteen planned combustion tests plus two additional tests (obtained by creating gas mixtures from bottle residuals), of which sixteen of these seventeen mixtures ignited. These mixtures tested on STS-83 and STS-94 produced from one to nine flame balls, with the mixtures having more fuel producing multiple flame balls. Most of the tests burned for 500 seconds, until the experiment timed out and a mixing fan extinguished the flames. As discussed later, it had not been expected that any flame balls would last this long. Unfortunately, it was not possible to change the experiment duration after the STS-83 mission but before the STS-94 mission, mostly due to the time that would have been required to re-verify the control software. Ten of the mixtures from STS-94 were ignited a second time (since there was ample remaining fuel in many cases) and eight of these burned for an additional 500 seconds.

A typical image of the flame balls is observed in H_2 -air mixtures is shown in Fig. 5. For this and most of the H_2 -air tests, unlike most H_2 - O_2 - CO_2 and H_2 - O_2 - SF_6 tests, all flame balls extinguished before the 500 s experiment time-out. This is mainly because the flame balls are larger in H_2 -air mixtures and the fuel (hydrogen) diffusivity is higher in N_2 than in CO_2 or SF_6 . Both of these factors led to more volume of fuel being consumed per unit time in H_2 -air tests for the same number of flame balls.

Figure 6 shows measured flame ball radii for H_2 -air mixtures as a function of the fuel concentration. The radius is arbitrarily defined as the half-width of the flame ball intensity profile and one-third of the maximum intensity. Data obtained in the space experiments is very consistent with data obtained in the 10-second drop tower at the Japan Microgravity Center (JAMIC)²¹ as well as recent aircraft²¹ tests. (Other properties, notably temperature profiles and radiative emission, are very different in the drop tower, aircraft and space experiments.) The flame ball radii are in poor agreement with our computational predictions, mainly because of uncertainties in the chemical reaction rates (Fig. 3), and in fact none of the mechanisms predict radii in agreement with experimental observations.

A typical image of the flame balls is observed in H_2 - O_2 - CO_2 mixtures is shown in Fig. 7. The flame balls drifted several tens of mm away from each other during this test, but the imaginary point at the "center of mass" of the three balls hardly moved at all during the 500 s test period. Thus, the flame ball movement is likely due to an interaction of the balls rather than buoyancy-induced drift. Both of these mechanisms of flame ball drift are discussed in the following section.

Figure 8 shows measured flame ball radii for H_2 - O_2 - CO_2 mixtures as a function of the fuel concentration. Again, data obtained in the space experiments is very consistent with data obtained in the JAMIC and aircraft tests. Note that our numerical model¹³ predicts that no mixtures below 5.8% H_2 are flammable, and even for 5.8% H_2 and higher, the predicted flame ball radii are much smaller than those observed in drop tower and aircraft μg experiments. The discrepancies are believed to be due to the effect of

reabsorption of emitted radiation by the CO_2 diluent gas, which is neglected in current models^{11,13}. Reabsorption is expected to be important for the CO_2 -diluted mixture because the Planck mean absorption length (L_p) for CO_2 at 1 atm and 300K is 42 mm, which is much smaller than the radius of the combustion chamber. These effects are also important for the $\text{H}_2\text{-O}_2\text{-SF}_6$ mixtures ($L_p \approx 3.5$ mm) but not for H_2 -air mixtures, where the only radiating specie is the product H_2O where $L_p \approx 1$ m. Consequently, for $\text{H}_2\text{-O}_2\text{-CO}_2$ and $\text{H}_2\text{-O}_2\text{-SF}_6$ mixtures much of the radiation emitted from within or near the flame ball will not be lost to the chamber walls but instead will be reabsorbed within the gas. An approximate theoretical model of flame balls including radiative reabsorption effects¹⁴ predicts that as the absorption length scale decreases, the flame ball size increases and the flammability limit shifts to weaker mixtures, which is consistent with the observed discrepancies. A computational estimate of an upper bound for reabsorption effects in $\text{H}_2\text{-O}_2\text{-CO}_2$ mixtures was obtained¹³ by artificially neglecting CO_2 radiation entirely in the numerical model, which is equivalent to assuming zero absorption length. Figure 8 shows that the actual flame ball radii are much closer to that predicted assuming this upper bound for reabsorption effects rather than that predicted without reabsorption.

The gas temperature data obtained from the H_2 -air test shown in Fig. 5 are given in Fig. 9, and the chamber pressure and radiometer data are given in Fig. 10. These data are much more dynamic than that from the previous test, which is expected since 5 balls of varying size were observed and all extinguished at varying times during the test. The maximum temperature observed was 576°C, which compares to the maximum predicted¹³ temperature of 862°C. This discrepancy is not surprising considering that no flame ball was observed to make a "direct hit" on a thermocouple junction.

DISCUSSION

Buoyancy-induced flame ball drift

It had not been expected that the flame balls would last more than about half of the 500 s experiment time-out period because the drift velocity (v) of flame balls was expected to be given by the formula⁷

$$v \approx 1.5 \sqrt{gr_*} \quad (2).$$

This empirical relation was inferred from data on drift velocity obtained in KC-135 μg aircraft experiments, where accelerations are on the order of $10^{-2} g_0$. According to Eq. (2), even at 1 μg , a flame ball with radius 3 mm will drift 129 mm, nearly the radius of the chamber, in 500 s. The form of Eq. (2), $v \sim \sqrt{gr_*}$, is that of a bubble rising in an inviscid fluid¹⁵, which implies viscosity effects are negligible. This is reasonable for the conditions in the aircraft experiments, where 50 is a typical Reynolds number (Re) based on the observed g -induced drift velocity and the "equivalent buoyant radius" of the flame ball, inferred to be about five times the visible radius⁷. (The high-temperature, low density region of the flame ball extends far beyond the visible radius, as implied by Fig. 1, thus the volume of buoyant gas is much larger than the volume of the flame ball itself.) In contrast, at 1 μg , Re will be much less than unity and the viscous, creeping-flow relation for bubbles¹⁵

$$v = \frac{1}{3} \frac{gr_b^2}{v_o} \left(\frac{\rho_b}{\rho_o} - 1 \right) \frac{\mu_o + \mu_b}{\mu_o + 1.5\mu_b} \quad (3),$$

where the b subscript refers to the bubble properties, should be employed instead of Eq. (2). Modeling the flame ball as a bubble whose radius is the equivalent buoyant radius ($= 5r_*$) mentioned above and using temperature-averaging of gas properties based on a maximum temperature of 1200K, Eq. (3) becomes

$$v = 2.4 \frac{gr_*^2}{v_o} \quad (4).$$

While the validity of Eq. (4) has not yet been confirmed, this appears to be an example of circumstances where ground-based μg experiments led to inaccurate predictions of the behavior of a space experiment.

With very low drift velocities, it is possible that in many cases the flame balls could continue to burn until their fuel supply has been depleted sufficiently that the remaining mixture was no longer flammable, rather than drifting into the chamber wall first. In a few of the Estimates for the maximum possible burn duration developed based on mechanism suggest that in the 3 atm $\text{H}_2\text{-O}_2\text{-SF}_6$ mixtures which produced only one flame ball, the ball could burn for about 17 hours!

Flame ball mutual repulsion

It was found that in both tests the flame balls drifted apart from each other throughout the duration of the burn. This had been seen in drop tower tests, but the test durations had been too short to obtain meaningful data on separation rates. In the space experiments it was found that the drift rate continually decreased with time. Figure 11 shows the mean separation between the three flame balls seen in Fig. 7 as a function of time, and the mean radius of separation, determined by finding the radius of the circle passing through all three flame ball centers. The camera view (not shown) orthogonal to that seen in Fig. 7 shows three practically collinear balls, which indicates that in the view shown in Fig. 7, the plane of the flame balls is orthogonal to the axis of the camera lens, which in turn indicates that the measure of flame spacing seen in this view is a reasonably accurate indication of the true spacing.

A proposed mechanism of flame ball drift based on the mutual depletion of total enthalpy (chemical plus thermal) by two flame balls in the region between them is presented here. When two flame balls are in close proximity, they have two influences on each other: first, they deplete each other of reactants from the region between them (decreased chemical enthalpy) and two, they increase the temperature in the region between them (increased thermal enthalpy). Because of the enthalpy gradient, one side of the flame ball will have a temperature slightly greater than T , while the other will be slightly lower, thus leading to differences in heat release rate on the two sides of the ball. It is proposed that the ball must drift in the direction of increasing total enthalpy at a rate whereby the convective transport of enthalpy to the ball balances this difference in heat release rate. A model of flame ball drift has been developed, resulting in the prediction¹⁶

$$S = \left[\frac{9\alpha_o r_* t}{1 - Le} \right]^{1/3} \quad (5).$$

The prediction of Eq. (5) with the representative parameters for Test #1 ($T_* \approx 1200\text{K}$, $T_o = 300\text{K}$, $\alpha_o \approx 10 \text{ mm}^2/\text{s}$, $r_* = 3 \text{ mm}$, $Le = 0.2$) are shown in Fig. 11, where the formula has been multiplied to by $(8/\sqrt{3})^{1/3}$ to account for the additional gradient caused by presence of three rather than two flame balls as well as transformation of the prediction from mean spacing to mean radius of separation. The agreement between theory and experiment is fairly close, and so may indicate some validity for the proposed mechanism.

The flame balls were found to be much more sensitive to Orbiter Vernier Reaction Control System (VRCS) thruster firings than expected pre-flight. These firings produced a noticeable change in the flame ball position, drift speed, and especially radiometer data (Fig. 12). The strong effect of microgravity disturbances on radiation is probably due to the fact that the visible flame ball is surrounded by a much larger volume of hot but non-reacting gas. Most of the radiation is emitted from this large gas volume rather than from within the flame ball itself¹¹. This large ball of gas is extremely susceptible to buoyancy-induced motion resulting from even the smallest VRCS impulses (on the order of $50 \mu\text{g}$ for 1 sec = 0.5 mm/sec). (Careful inspection of the two data sets from STS-83 also showed this trend, but it was much less noticeable in these cases because both STS-83 tests produced multiple flame balls with more widely dispersed hot gas regions that, as a group, are much less affected by the VRCS firings than tests producing only one or two flame balls.) Note that Fig. 12 shows that only VRCS firings, which cause a net change in the Orbiter momentum, had any effect; vibrations resulting from crew and Orbiter systems operations, which do not affect the net momentum of the Orbiter, had practically no effect. Once the effects of the VRCS firings were seen, "free drift" (suppression of VRCS firings) was requested during the remaining experiments and was granted in many cases. When free drift could be maintained for the entire test period, the disturbances to the radiometer readings did not occur.

Preliminary inspection of the flight data suggest that the flame balls respond ballistically to the VRCS impulses, that is, the impulse (change in velocity) imparted to the ball is the same as the acceleration impulse. This change in velocity then decays on a time scale of tens to hundreds of seconds, comparable to the viscous time scale associated with the flame ball and its surrounding hot gas field.

SUMMARY AND CONCLUSIONS

Two space-based experiments on STS-83 and 24 experiments on STS-94 have shown that flame balls are in fact stable for very long periods of time in a μg environment. The rate at which the flame balls drift due to the small acceleration levels on the spacecraft was far smaller than that expected before the mission. A modified mechanism of buoyancy-induced drift is proposed based on the difference between the flow regimes in the aircraft and space experiments (nearly inviscid flow vs. creeping flow), and a new mechanism of flame ball drift induced by mutual interaction of adjacent flame balls is proposed. Flame ball properties, especially radiative emission, were found to be strongly affected by orbiter Vernier Reaction Control System thruster firings. This may have important implications for combustion experiments to be performed on the International Space Station.

Another finding of these experiments is that the differences between computer models and experiments found based on earlier short-duration μg tests were also found in the space experiments. Different models of H_2-O_2 chemistry yield different predictions for flame ball properties, and it is expected that detailed evaluation of the results of the space experiments will help lead to the identification of the most appropriate chemical models for lean-limit combustion of hydrogen and hydrocarbon fuels.

A reflight of the SOFBALL experiment is planned for STS-107 in the fall of 2000. Among the changes planned for SOFBALL-2 include longer test durations, since most flame balls were still burning at the end of the 500 s tests on STS-83 and STS-94. A third intensified video camera with a smaller field of view but greater spatial resolution will be added. A higher energy ignition system will be used to study still-leaner mixtures, particularly in the H_2 -air family. Optical filters will be used on some of the intensified video cameras in order to determine if the emission wavelength has an impact on the apparent flame ball sizes.

PUBLICATIONS AND PRESENTATIONS

Refereed journal publications:

- Abid, M., Wu, M. S., Liu, J. B., Ronney, P. D., Ueki, M., K. Maruta, K., Kobayashi, H., Niioka, T. and VanZandt, D. M., "Experimental and Numerical Study of Flame Ball IR and UV Emissions," to appear in *Combustion and Flame* (1998).
- Wu, M.-S., Liu, J. B. and Ronney, P. D., "Numerical Simulation of Diluent Effects on Flame Ball Structure and Dynamics," to appear in the *Twenty-Seventh International Symposium on Combustion* (1998).
- Buckmaster, J. D. and Ronney, P. D., "Flame Ball Drift in the Presence of a Total Diffusive Heat Flux," to appear in the *Twenty-Seventh International Symposium on Combustion* (1998).
- Ronney, P. D., "Understanding Combustion Processes Through Microgravity Research," to appear in *Twenty-Seventh International Symposium on Combustion*, Combustion Institute, 1998 (**invited paper**).
- Ronney, P. D., "Premixed Laminar and Turbulent Flames at Microgravity," to appear in *Space Forum* (1998).
- Ronney, P. D., Wu, M. S., Pearlman, H. G. and Weiland, K. J., "Experimental Study of Flame Balls in Space: Preliminary Results from STS-83," *AIAA Journal*, Vol. 36, pp. 1361-1368 (1998).

Presentations:

- Wu, M.-S., Ronney, P. D., "Computation of Flame Ball Properties with Detailed Chemical and Transport Models," SIAM Numerical Combustion Conference, York, England, March 30-April 1, 1998.
- Ronney, P. D., Wu, M.-S., Weiland, K. J. and Pearlman, H. G., "Structure of Flame Balls At Low Lewis-number (SOFBALL): Preliminary Results from the STS-83 and STS-94 Space Flight Experiments," 36th Aerospace Sciences Meeting, Reno, NV, January 12 - 15, 1998.
- Buckmaster, J. D. and Ronney, P. D., "Flame Ball Drift," Fall Technical Meeting, Combustion Institute, Eastern States Section, Hartford, CT, October 27-29, 1997.

ACKNOWLEDGMENTS

The authors wish to thank the CM-1 Project Managers, Mr. Roy Hager (retired) and Ms. Ann Over, the CM-1 Project Engineer, Mr. Ron Chucks (retired) and the entire CM-1 engineering and operations team for their tremendous effort in designing, constructing, testing and operating the CM-1 facility. Angel Abbud-Madrid, Mohammed Abid, Quin Blackburn and Jian-Bang Liu assisted with the data analysis during and after the missions. Special thanks is owed to the STS-83/94 crew for conducting the experiments, and the MSFC mission management team, led by Ms. Teresa Vanhooser and Dr. Michael Robinson, for coordinating experiment operations. This work was supported by NASA grants NAG3-1242, NAG3-1523 and NAG3-2124.

REFERENCES

- ¹Eolfopoulos, F. N. and Law, C. K., "An Experimental and Computational Study of the Burning Rates of Ultra-lean to Moderately-rich $H_2/O_2/N_2$ Laminar Flames with Pressure Variations," Twenty-Third Symposium (International) on Combustion, Combustion Institute, Pittsburgh, 1990, pp. 333-340.
- ²Coward, H., Jones, C., "Flammability Limits of Gases and Vapors," U. S. Bureau of Mines Bulletin 503, 1952.
- ³Ronney, P. D., "Effect of Chemistry and Transport Properties on Near-Limit Flames at Microgravity," Combustion Science and Technology, Vol. 59, 1988, pp. 123-141.
- ⁴Abbud-Madrid, A. and Ronney, P. D., "Effects of Radiative and Diffusive Transport Processes on Premixed Flames Near Flammability Limits," Twenty-Third Symposium (International) on Combustion, Combustion Institute, Pittsburgh, 1990, pp. 423-431.
- ⁵Zeldovich, Ya. B., Theory of Combustion and Detonation of Gases, Academy of Sciences (USSR), 1944.
- ⁶Ronney, P. D. "Near-Limit Flame Structures at Low Lewis Number," Combustion and Flame, Vol. 82, 1990, pp. 1-14.
- ⁷Ronney, P. D., Whaling, K. N., Abbud-Madrid, A., Gatto, J. L. and Pisowicz, V. L., "Stationary Premixed Flames in Spherical and Cylindrical Geometries," AIAA Journal, Vol. 32, 1994, pp. 569-577.
- ⁸Buckmaster, J. D., Joulin, G. and Ronney, P. D., "Effects of Heat Loss on the Structure and Stability of Flame Balls," Combustion and Flame, Vol. 79, 1990, pp. 381-392.
- ⁹Buckmaster, J. D., Joulin, G. and Ronney, P. D., "Structure and Stability of Non-adiabatic Flame Balls: II. Effects of far-field losses," Combustion and Flame, Vol. 84, 1991, pp. 411-422.
- ¹⁰Lee, C. and Buckmaster, J. D., "The Structure and Stability of Flame Balls: a Near-Equidiffusional Flame Analysis," SIAM Journal on Applied Mathematics, Vol. 51, 1991, pp. 1315-1326.
- ¹¹Wu, M. S., Ronney, P. D., Colantonio, R. and VanZandt, D., "Detailed Numerical Simulation of Flame Ball Structure and Dynamics," to appear in Combustion and Flame (1998).
- ¹²Buckmaster, J. D. and Joulin, G., "Flame Balls Stabilized by Suspension in Fluid with a Steady Linear Ambient Velocity Distribution," Journal of Fluid Mechanics, Vol. 227, 1991, pp. 407-427.
- ¹³Wu, M. S. and Ronney, P. D., Twenty-Seventh Symposium (International) on Combustion, Combustion Institute, Pittsburgh, 1998, to appear.
- ¹⁴Lozinski, D., Buckmaster, J. D., Ronney, P. D., "Absolute Flammability Limits and Flame Balls in Optically Thick Mixtures," Combustion and Flame, Vol. 97, 1994, pp. 301-316.
- ¹⁵Batchelor, G. K., An Introduction to Fluid Dynamics, Cambridge University Press, Cambridge, U.K., 1967.
- ¹⁶Buckmaster, J. D. and Ronney, P. D., "Flame Ball Drift in the Presence of a Total Diffusive Heat Flux," Twenty-Seventh Symposium (International) on Combustion, Combustion Institute, 1998, to appear.
- ¹⁷Frenklach, M., et al., "An Optimized Kinetics Model for Natural Gas Combustion," Twenty-Fifth Symposium (International) on Combustion, Poster 26, Session 3, 1994.
- ¹⁸Peters, N. in: Reduced Kinetic Mechanisms for Applications in Combustion Systems, N. Peters and B. Rogg (Eds.), Springer-Verlag, Berlin-Heidelberg, 1993, Chapters 1 and 5.
- ¹⁹Yetter, R. A., Dryer, F. L. and Rabitz, H., "A Comprehensive Reaction Mechanism For Carbon Monoxide/Hydrogen/Oxygen Kinetics," Combustion Science and Technology, Vol. 79, 1991, pp. 97-128.
- ²⁰Mauss, F., Peters, N., Rogg, B. and Williams, F. A., in: Reduced Kinetic Mechanisms for Applications in Combustion Systems, N. Peters and B. Rogg (Eds.), Springer-Verlag, Berlin-Heidelberg, 1993, Chapter 3.
- ²¹Abid, M., Wu, M. S., Liu, J. B., Ronney, P. D., Ueki, M., K. Maruta, K., Kobayashi, H., Niioka, T. and VanZandt, D. M., "Experimental and Numerical Study of Flame Ball IR and UV Emissions," to appear in Combustion and Flame (1998).

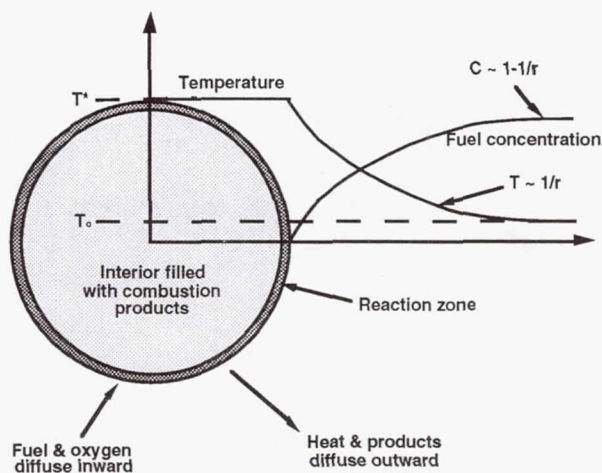


Figure 1. Schematic diagram of a flame ball, illustrated for the case of fuel-limited combustion at the reaction zone. The oxygen profile is similar to the fuel profile except its concentration is non-zero in the interior of the ball. The combustion product profile is identical to the temperature profile except for a scale factor.

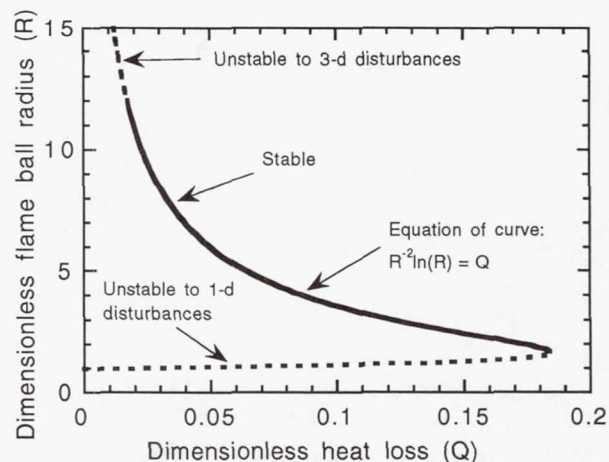


Figure 2. Theoretical prediction⁸ of the effect of heat loss on flame ball radius and stability properties with single-step Arrhenius chemistry, constant thermodynamic and transport properties and volumetric heat loss from the interior of the ball.

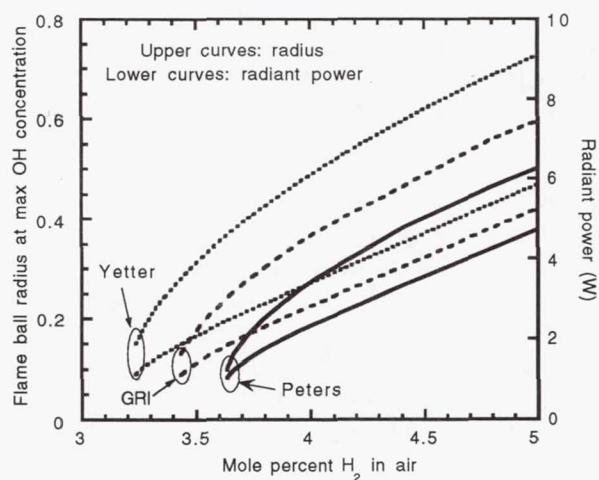


Figure 3. Predicted¹³ steady flame ball radii and radiant emission in H_2 -air mixtures using the GRI¹⁷, Peters¹⁸ and Yetter¹⁹ chemical models.

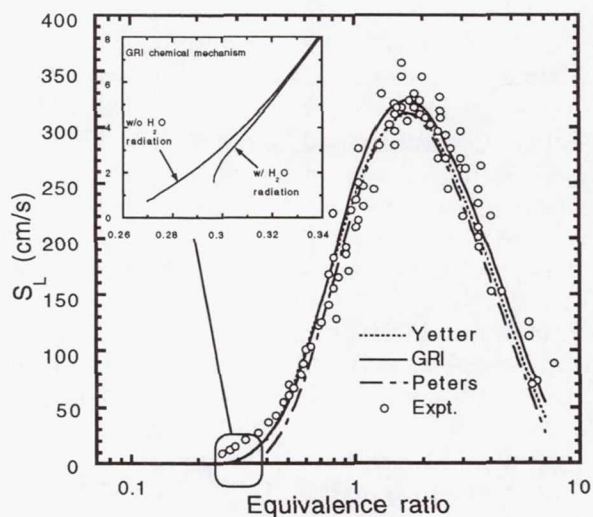


Figure 4. Predicted¹³ steady burning velocities (S_L) of H_2 -air mixtures using the GRI¹⁷, Peters¹⁸ and Yetter¹⁹ chemical models. A compilation²⁰ of experimental results from several sources is also shown.

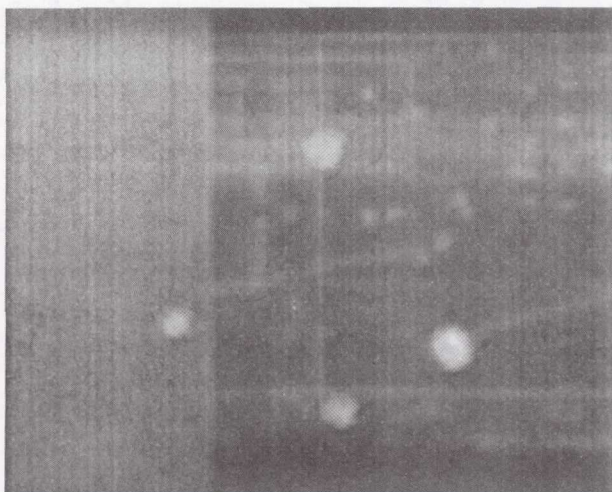


Figure 5. Image of flame balls obtained in 3.85% H_2 / 96.15% air mixture, taken 25 s after ignition. Field of view is 112 mm x 150 mm.

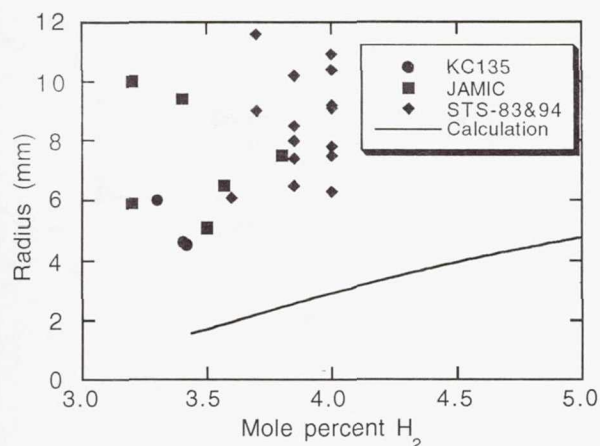


Figure 6. Predicted¹³ flame ball radii in H_2 -air mixtures along with measured flame ball radii from aircraft μg experiments²¹, JAMIC drop-tower experiments²¹, and the STS-83/94 space experiments.

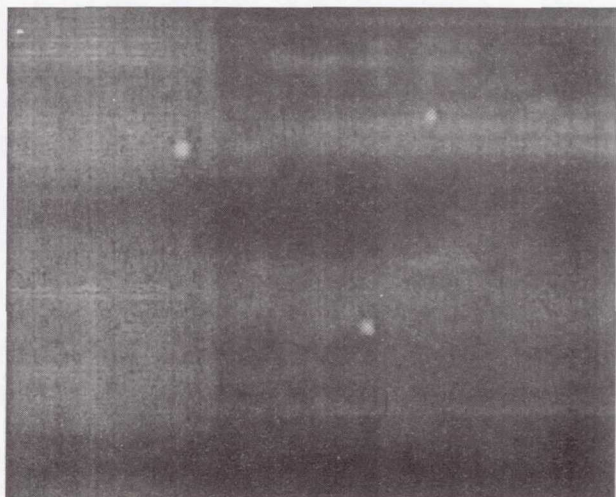


Figure 7. Image of flame obtained in 4.9% H_2 / 9.8% O_2 / 85.3% CO_2 mixture, taken 130 s after ignition. Field of view is 112 mm x 150 mm.

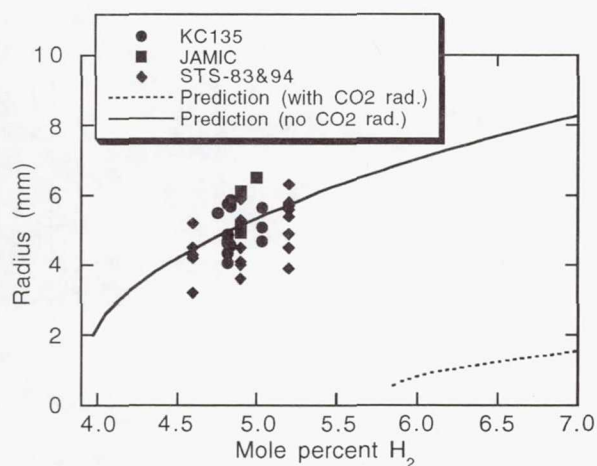


Figure 8. Predicted¹³ flame ball radii in H_2 - O_2 - CO_2 mixtures ($H_2:O_2 = 1:2$) including and excluding CO_2 radiation, along with measured flame ball radii from aircraft μg experiments²¹, JAMIC drop-tower experiments²¹, and the STS-83/94 space experiments.

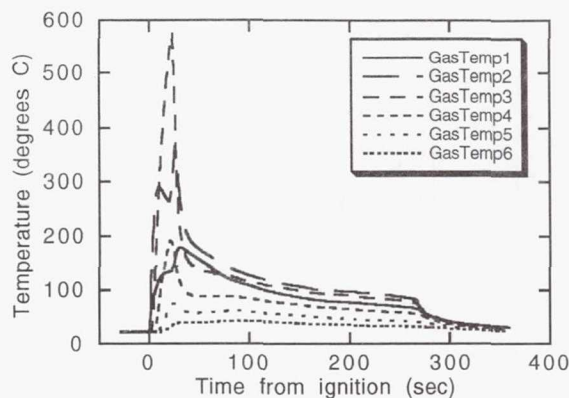


Figure 9. Measured gas temperatures for Test #2. Thermocouple locations corresponding to GasTemp1 through GasTemp6 are 30, 50, 70, 90, 110 and 130 mm from spark gap, respectively.

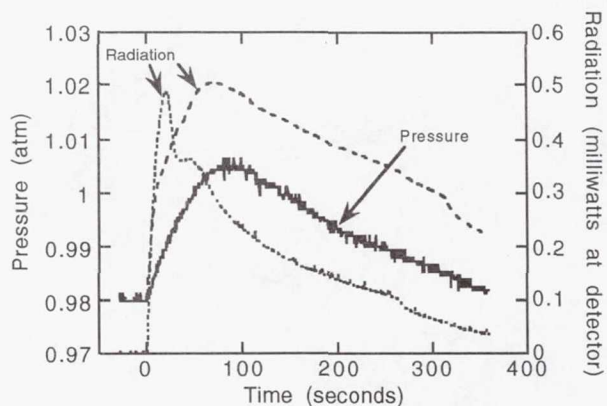


Figure 10. Measured chamber pressure and radiant emissions for Test #2.

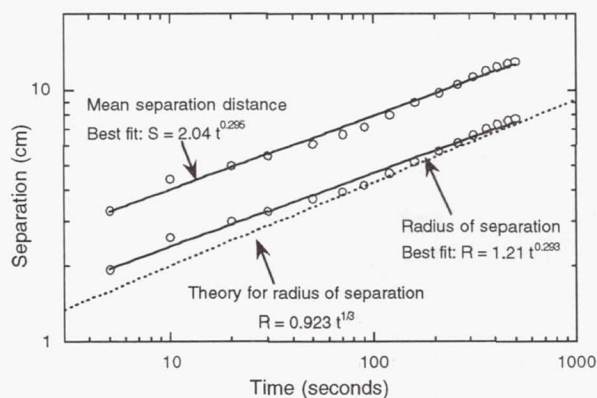


Figure 11. Observed radius of separation and mean separation of the three flame balls seen in Fig. 7 as a function of time, and comparison to theoretical predictions¹⁶.

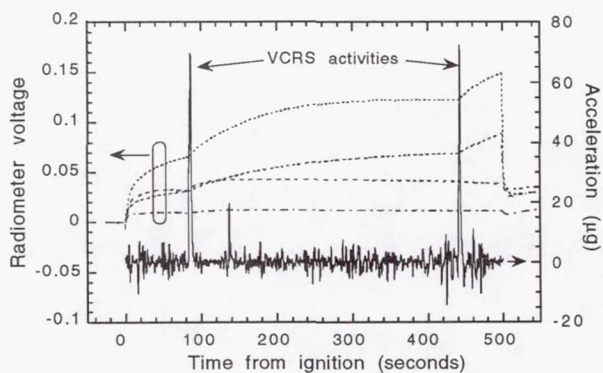


Figure 12. Example correlation of radiometer readings with Orbiter acceleration environment during STS-94 mission showing impact of VRCS thruster firings. For clarity, only the Orbiter z-axis (vertical) acceleration component is shown. Mixture: 6.50% H_2 - 13.00% O_2 - 80.50% SF_6 , 1 atm initial pressure.

Structure Of Flame Balls At Low Lewis-number (SOFBALL): Results from space flight experiments on STS-83 and STS-94

Paul D. Ronney, Principal Investigator
University of Southern California, Los Angeles, CA

The objective of the Structure Of Flame Balls At Low Lewis-number (SOFBALL) experiment is to study the behavior and properties of a newly discovered premixed-gas flame phenomena called "flame balls." These spherical, stable, stationary flame structures, observed only in microgravity, provide the opportunity to study the interactions of the two most important processes necessary for combustion (chemical reaction and heat/mass transport) in the simplest possible configuration. The previously unobtainable experimental data collected during the STS-83 and STS-94 missions provide a comparison with models of flame stability and flame propagation limits that are crucial both for fire safety assessment on earth and in orbiting spacecraft as well as for the design of lean-burn combustion engines which provide improved fuel economy and lower pollutant formation.

The tests were conducted by filling a 26-liter chamber with a weakly combustible gas (hydrogen and oxygen highly diluted with an inert gas) and igniting the mixture with a spark. The flames were imaged using four video cameras. Radiometers, thermocouples and pressure transducers were used to determine the heat release from the flame balls. The experiments were performed in the Combustion Module-1 facility on the Microgravity Science Laboratory (MSL-1) Spacelab missions.

Two successful tests (out of two attempts) were conducted on STS-83 and 16 successful tests (out of 17 attempts) were conducted on STS-94. Most of the tests burned for 500 sec, until the experiment timeout extinguished the flames. Over 3 hours of test data were collected.

SOFBALL highlights:

- **First premixed gas combustion experiment ever performed in space**
- **Weakest flames ever burned**, either on the ground or in space. Flame ball powers as low as one watt were measured. By comparison, a birthday candle releases about 50 watts.
- **Longest-lived gas flames ever burned in space** (many mixtures burned for the entire 500 sec test duration and were still burning at the timeout.)
- **Conclusive evidence of limitation of existing models of lean hydrogen-oxygen combustion chemistry**, which predict many ground-based experimental results accurately but yield conflicting predictions of flame ball properties, none of which agree with the experiments. Improved models of lean combustion are currently being developed based on the SOFBALL results.
- **First conclusive demonstration of the effect of reabsorption of emitted radiation on the burning characteristics of a flame**, either on the ground or in space. This factor is insignificant for most laboratory-scale experiments, but of key importance in practical flames at high pressure (as in automotive and jet engines) or at large scale (as in industrial boilers).
- **First conclusive demonstration of the impact of accelerations caused by Orbiter vernier thruster firings and water dumps** on science data obtained during a shuttle flight.

Work supported by the SOFBALL project has led to 27 journal papers and 7 invited conference presentations by the PI and his associates since SOFBALL was approved for flight in 1991.

Page intentionally left blank

54-55
H34841

8P.

Coarsening in Solid-Liquid Mixtures (CSLM)

362140

Principal Investigator:

Dr. Peter W. Voorhees
Northwestern University
Evanston, Illinois

Coarsening in Solid-Liquid Mixtures (CSLM)

J. Alkemper, V. Snyder, P.W. Voorhees

Department of Material Science and Engineering
Northwestern University

Abstract

The CSLM experiment examines the dynamics of particle-coarsening in a two-phase mixture. The evolution of the average particle size and particle size distribution of dispersed Sn-particles in a Pb-Sn liquid was measured with respect to time. Samples were heat treated at 185°C where a mixture of liquid Pb-Sn and Sn-rich solid exist with varying volume fractions of solid. Initially, the solid was present in the form of small, dispersed particles with average sizes of ca. 10 μ m. Presented here are the results of the samples from the MSL-1 mission which have been analyzed at this time. Initially we concentrated our analysis on samples with 10% solid volume fraction, only a few samples with other volume fractions have been analyzed. It is found that the kinetics of the process follow the theoretical predictions within the uncertainties of the materials parameters. We also found an increasing coarsening rate with increasing volume fraction which is in agreement with existing theories. A full evaluation of the existing theories based on the results of the CSLM experiments is not possible at this point.

Objectives

There are numerous theories in the field of Ostwald Ripening, none of which has ever been verified in a quantitative manner. The predicted evolution of the average particle size was found in many experiments qualitatively (see equation 1), but a quantitative comparison was usually not possible because the thermophysical parameters were unknown. In some cases these parameters were determined from coarsening experiments through the use of one theory. However, starting from the early work of Ardell [1,2] to today [3] the measured particle size distributions (PSD) do not agree with the theoretical predictions. The objective of the CSLM experiment is to close this gap and prove or disprove the existing theories. The system of solid Sn-rich particles in a liquid Pb-Sn matrix was chosen because it allows a fast coarsening process, spherical particles, and knowledge of the necessary thermophysical parameters. The problem of particle sedimentation could be overcome through the use of microgravity (see section *Flight results compared with ground results*).

Background

In a dispersion of particles in a matrix phase where diffusion between the particles is permitted, the larger particles grow at the expense of smaller particles resulting in a reduction of interfacial area and thus minimizing the total energy. This coarsening process is known as Ostwald ripening[4]. Ostwald ripening is a phenomenon that occurs in many metallurgical systems and other systems. For example, the second-phase particles in high temperature materials used in turbine blades undergo coarsening at the operating temperature of the turbine. The coarsening process degrades the strength of the

blade since alloys containing many small particles are stronger than those containing a few large ones. Other systems that show coarsening are liquid-phase sintered materials such as tungsten carbide-cobalt alloys, iron-copper alloys, dental amalgam alloys used for fillings, and porcelain.

The kinetics of the coarsening are controlled by diffusional mass flow. The classical work by Lifshitz, Slyosov[5] and Wagner[6] (LSW) predicts that the average particle size R is proportional to the cube root of time t .

$$R(t)^3 - R(0)^3 = K_{LSW}t \quad (1)$$

K_{LSW} is a constant which includes all relevant materials parameters. Unfortunately, the theory is only valid in the limit of a vanishingly small volume fraction of coarsening phase. More recent theories that include the effect of finite volume fraction, and thus particle-particle diffusional interactions, predict that the exponent of the temporal power law will not be a function of the volume fraction, but the amplitude of the temporal

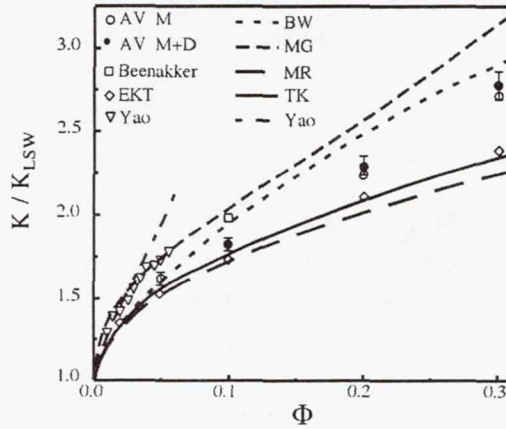


Figure 1: The dependence of the coarsening rate on the volume fraction. Shown are predictions by Akaiwa and Voorhees [7], Beenakker [8], Enomoto *et al.* [9], Yao *et al.* [10], Brailsford and Wynblatt [11], Marsh and Glicksman [12], Marquessee and Ross [13], and Tokuyama and Kawasaki [14].

power law, the rate constant, will depend on the volume fraction. The dependence of the rate constant as well as the particle size distribution (PSD) on the volume fraction is different for each theory. This dependence is usually written in terms of K_{LSW} as

$$K(\Phi) = K_{KLW}f(\Phi) \quad (2)$$

where Φ is the volume fraction. Figure 1 shows $f(\Phi)$ for different theories. Each of the theories shown reproduces the LSW-theory in the limit of $\Phi \rightarrow 0$. For increasing volume fractions the theories predict an increasing coarsening rate. The higher the volume fraction, the closer the particles are together leading to an increasing diffusional interaction between particles and thus increasing coarsening rate. Since most theories assume spherical, separated particles the plot stops at a volume fraction of 0.3. For higher volume fractions the particles will touch each other and can no longer be spherical. Figure 2 shows the changes in the PSD with increasing volume fraction based on the theory of Tokuyama and Kawasaki[14]. The PSD become wider and more symmetric with increasing Φ . This behavior is the same for all theories.

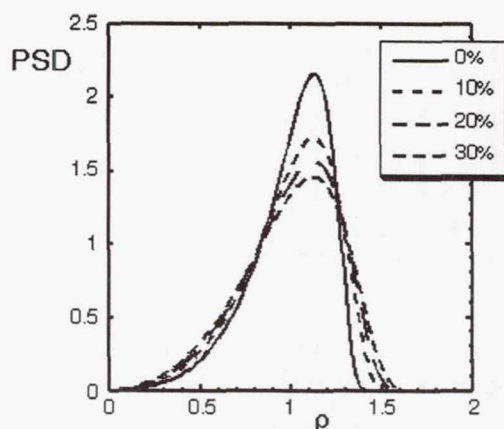


Figure 2: The PSD for different volume fractions of coarsening phase as predicted by the Tokuyama and Kawasaki theory [14]

Methods of data acquisition and analysis

Cylindrical samples of 10mm in diameter and 5mm in length were placed in a sample holder plate (see figure 3) in a 3 x 3 matrix arrangement. The assembly was closed from both sides with heater plates and contained in a vacuum chamber. Each sample position in the sample holder plate was assigned to a different sample composition. The compositions of the samples were chosen to give volume fractions of solid ranging from 5% to 80% at the coarsening temperature. The experimental procedure is basically shown by figure 4: The samples are heated up to 185°C, held for a predetermined amount of time Δt , and then quenched to room temperature. This was done for different Δt . This allows the study of the coarsening behavior over time for different volume fractions of coarsening phase. During the experiments the temperature at five different locations in the sample holder plate (see figure 3) was measured and stored.

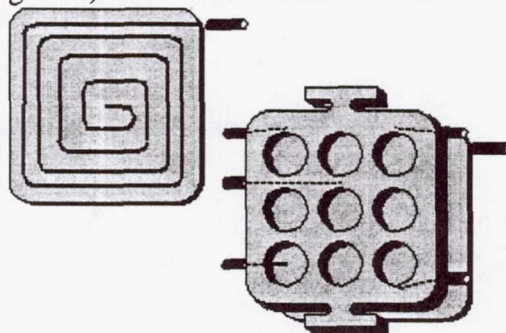


Figure 3: Sample holder plate with nine holes for the samples. Five thermistors are placed in the sample holder plate to monitor the temperature over time. Two heater plates close the assembly.

For the analysis of the microstructure the samples were cut, etched, and photographed. The cutting was done with a Reichert-Jung (Leica) Polycut E micro-milling machine. It allows the samples to be cut in predetermined steps and gives scratch-free surfaces. The etched microstructure was photographed with a digital scanning camera (Leaf Micro-Lumina) which was attached to a microscope. The pictures were taken with a resolution of ca. 2000 x 1600 pixel. In order to get a resolution of at least 100μm for a particle of average size different objectives were used. Individual images were put together to form a montage of a cross-section of a sample (see figure 5). Between 22 and 70 images were

combined to give a high resolution picture of the complete cross-section. Standard image analysis routines were used for these pictures to extract the average particle size and the particle size distributions.

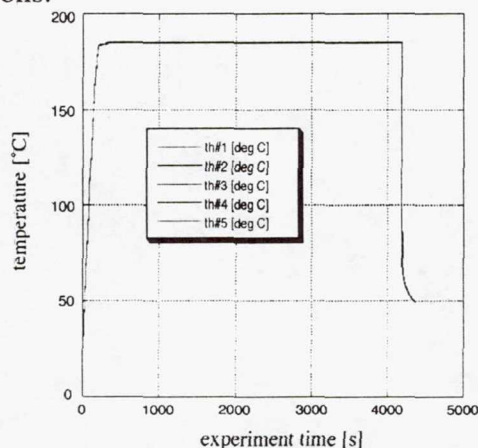


Figure 4: Temperature vs. time for one experiment. The samples were heated to 185°C (2K above the eutectic temperature), hold at that temperature for a preset amount of time and then quenched.

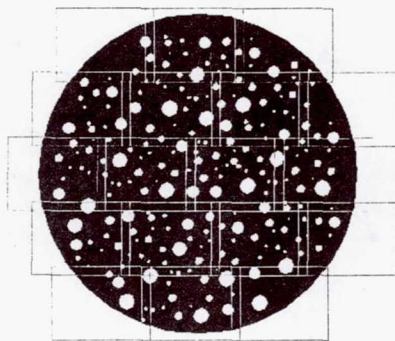


Figure 5: schematic drawing on how individual images of a cross-section were taken and later montaged to one high resolution picture of the entire cross-section.

Flight results compared with ground results

In ground based experiments the sedimentation of the Sn particles can only be avoided through the use of high volume fractions. This was done by Hardy and Voorhees [15] for different volume fractions $>65\%$. For low volume fractions (like 10%) the sedimentation leads to a microstructure shown in figure 6a. All Sn particle are collected at the top of the sample splitting the sample into a high volume fraction region (ca. 80%) and a particle free region. In microgravity the sedimentation does not take place (figure 6b). The particles are evenly distributed throughout the sample. Valid ground data for low volume fraction samples (like 10%) does not exist for this sample system. A comparison can only be made for high volume fractions. Figure 7 shows the measured average particle sizes for the samples that have been analyzed at this time. Samples with coarsening times shorter than 545 seconds are excluded from the plot since the steady coarsening temperature had not been established for shorter times. For the samples with 10% and 20% coarsening phase equation 1 is fitted to the data giving good agreement with the experimental findings. The coarsening rates for the average particle size in the planar sections (PS) are:

$$K_{ps}(\Phi = 0.1) = 2.47 \pm 0.05 \mu m^3 / \text{sec}.$$

$$K_{ps}(\Phi = 0.2) \approx 3.3 \mu m^3 / \text{sec}.$$

$$K_{ps}(\Phi = 0.7) \approx 6.9 \mu m^3 / \text{sec}.$$

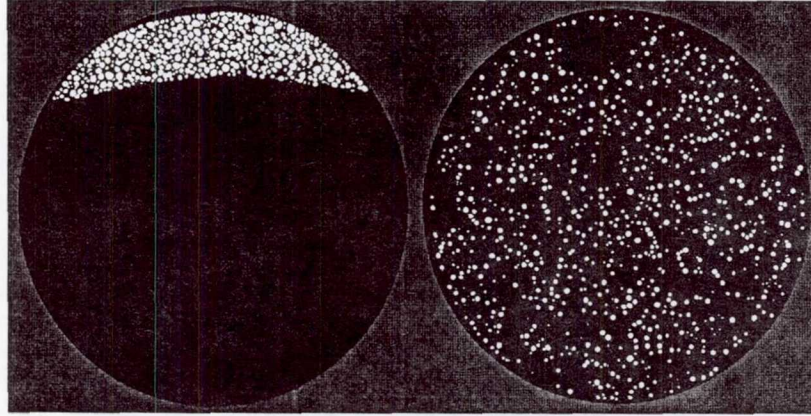


Figure 6: coarsened sample with 10% coarsening phase. The left image (a) shows a cross-section through a sample which was coarsened on ground. All Sn-particles (white) are sedimentated to the top of the sample. The right image (b) shows a sample treated the same way in space.

The values at $\Phi=0.7$ and $\Phi=0.2$ are rough estimates due to the limited number of data points.

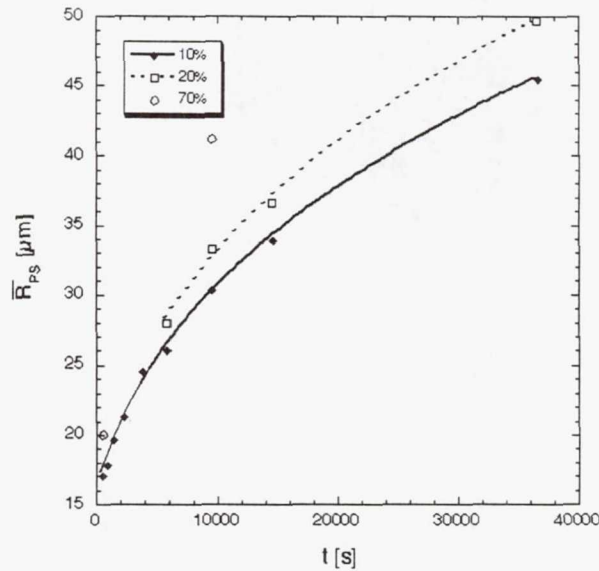


Figure 7: The average particle radii measured in planar sections for the at this time analyzed samples. The fits are done with equation 1.

Measurements of grain boundary groove experiments by Hardy *et. al.* [16] determine $K_{LSW} = 1.01 \mu m^3 / \text{sec}$. Similar experiments performed as part of the CSLM experiment show a large scatter but are consistent with Hardy's results. Using the value given by Hardy we get $K(\Phi = 0.1) / K_{LSW} \approx 4.1$. This is approximately twice as high as the theories predict. Since Hardy *et. al.* used flux to reduce the oxide on the surface of the samples it is likely that this introduced impurities into the samples. These impurities may have lowered the surface tension and thus K_{LSW} . Never-the-less an agreement within a factor of two is reasonable.

Conclusions

The present results indicate the validity of the existing theories in general. They do not, however, allow us to distinguish between the different theories. This might be possible once all samples are analyzed. The coarsening rates are higher than expected. The reason is likely the uncertainty of the existing materials parameters. With respect to future plans it would be helpful to measure the materials parameters again. It is now possible to repeat the grain boundary groove experiments without the impurities which Hardy *et. al.* could not avoid. One problem encountered during the MSL-1 flight was the long time interval to reach thermal equilibrium (545 seconds). A reflight with the possibility of longer experiments will allow us to circumvent this problem.

Summary

The coarsening process of an ensemble of particles in a matrix was successfully studied. The samples are partially analyzed. The results at this point show agreement with the existing theories that describe this process to within the uncertainties of the materials parameters. A distinction between the different existing theories is not possible at this time.

Bibliography

- [1] A.J. Ardell and R.B. Nicholson, *J. Phys. Chem. Solids* **27**, 1793-1804 (1966)
- [2] P.K. Rastogi and A.J. Ardell, *Acta Metallurgica* **19**, 321-330 (1971)
- [3] W. Bender and L. Ratke, *Zeitschrift für Metallkunde* **83**, 541-547 (1992)
- [4] W. Ostwald, *Zeitschrift für physikalische Chemie* **34**, 495-503 (1900)
- [5] I.M. Lifshitz and V.V. Slyozov, *Journal Phys. Chem. Solids* **19**, 35-50 (1961)
- [6] C. Wagner, *Zeitschrift für Elektrochemie* **65**, 581-591 (1961)
- [7] N. Akaiwa and P.W. Voorhees, *Physical Review E* **49** (5), 3860-3880 (1994)
- [8] C.W.J. Beenakker, *Physical Review A* **33** (6), 4482-4485 (1987)
- [9] Y. Enomoto, K. Kawasaki and M. Tokuyama, *Acta Met.* **35** (4), 907-913 (1987)
- [10] J.H. Yao, K.R. Elder, H. Guo and M. Grand, *Phys. Rev. B* **47** (14), 110 (1993)
- [11] A.D. Brailsford and P. Wynblatt, *Acta Metallurgica* **27**, 489-497 (1978)
- [12] S.P. Marsh and M.E. Glicksman, *Modelling of coarsening and grain growth*, TMS, Warrendale (1992)
- [13] J.A. Marqusee and J. Ross, *Journal of chemical Physics* **80** (1), 536-543 (1984)
- [14] M. Tokuyama, K. Kawasaki and Y. Enomoto, *Physica* **143A**, 323-338 (1986)
- [15] S.C. Hardy and P.W. Voorhees, *Metallurgical Transactions A* **19A**, 2713-2721 (1988)
- [16] S.C. Hardy, G.B. McFadden, S.R. Coriell, P.W. Voorhees and R.F. Sekerka, *Journal of Crystal Growth* **114**, 467-480, (1991)

Page intentionally left blank

55-25
434842

362141

Droplet Combustion Experiment (DCE)

17P.

Principal Investigator:

Dr. Forman A. Williams
University of California, San Diego
La Jolla, California

DROPLET COMBUSTION EXPERIMENT

John B. Haggard, Jr. and Vedha Nayagan
NASA Lewis Research Center
21000 Brookpark Road
Cleveland, OH 44135

Frederick L. Dryer
Department of Mechanical and Aerospace Engineering
Princeton University
Princeton, NJ 08544

Forman A. Williams
Center for Energy and Combustion Research
University of California, San Diego
La Jolla, CA 92093

Abstract

The first space-based experiments were performed on the combustion of free, individual liquid fuel droplets in oxidizing atmospheres. The fuel was heptane, with initial droplet diameters ranging about from 1 mm to 4 mm. The atmospheres were mixtures of helium and oxygen, at pressures of 1.00, 0.50 and 0.25 bar, with oxygen mole fractions between 20% and 40%, as well as normal Spacelab cabin air. The temperatures of the atmospheres and of the initial liquid fuel were nominally 300 K. A total of 44 droplets were burned successfully on the two flights, 8 on the shortened STS-83 mission and 36 on STS-94. The results spanned the full range of heptane droplet combustion behavior, from radiative flame extinction at larger droplet diameters in the more dilute atmospheres to diffusive extinction in the less dilute atmospheres, with the droplet disappearing prior to flame extinction at the highest oxygen concentrations. Quasisteady histories of droplet diameters were observed along with unsteady histories of flame diameters. New and detailed information was obtained on burning rates, flame characteristics and soot behavior. The results have motivated new computational and theoretical investigations of droplet combustion, improving knowledge of the chemical kinetics, fluid mechanics and heat and mass transfer processes involved in burning liquid fuels.

Introduction

The general objectives of the droplet combustion experiment (DCE) are to improve understanding of the mechanisms of burning of liquid fuel droplets. These objectives are important for both scientific and practical reasons. Scientifically, the conservation equations of combustion, especially in the presence of phase changes, are too complex to be solved in arbitrary configurations and contain many detailed chemical-kinetic, transport and radiative parameters having uncertain values. These equations, however, now can be solved in the one-dimensional, spherically symmetrical, time-dependent situations established in DCE, so that comparisons of predictions with experimental results can be made to improve knowledge of uncertain parameters that control combustion mechanisms. Practically, fossil fuels provide 85% of our energy needs and liquid fuels more than 95% of energy usage in the transportation sector. Improvements in methods of combustion gained from knowledge generated in DCE studies can help to conserve these natural resources, reduce rates of emission of greenhouse gases and decrease air pollution associated with combustion processes. An additional practical motivation for DCE lies in the realm of fire and explosion safety of liquid fuels, which can be quite different in microgravity compared with normal gravity and which could be improved by knowledge obtained in such experiments.

The DCE fuel, n-heptane, is a representative liquid hydrocarbon constituent of transportation fuels, a higher normal alkane that has been studied most extensively in earlier combustion experiments, including ground-based experiments on droplet burning. It was selected for DCE because this extensive earlier data base facilitates the comparisons with ground results and the development of new, firmly based, fundamental knowledge; the aforementioned uncertainties in chemical-kinetic, transport and radiative parameters all apply to heptane, so that there are things to be learned.

The first microgravity droplet combustion experiment, performed by Kumagai¹, in fact employed heptane. His apparatus provided about 1 second of microgravity, enabling him to burn to completion in air droplets of initial diameters slightly less than 1 mm. Since the burning time increases as the square of the initial diameter in these diffusion-controlled processes, the largest ground facility currently available, the 10-second drop shaft in Hokkaido, can be used to study the entire history of heptane droplets burning in air only up to initial droplet diameters of about 3 mm. Maintaining good spherical symmetry in droplet combustion requires the gravity levels, below 10^{-4} to 10^{-6} earth gravity, obtainable in drop towers and in space; experiments in aircraft flying parabolic trajectories, which in principle could provide longer test times, generate degraded data as a consequence of their higher gravity levels. The only other alternative to space-based experiments, namely the use of sounding rockets, could provide the longer test times at excellent gravity levels but has not been implemented for droplet combustion because of the associated time and expense. Experiments on droplets larger than 3 mm in initial diameter are desirable because of the additional physical phenomena, such as strong influences of radiative energy loss, that occur at these sizes.

Most previous droplet-combustion experiments had air at 1 bar as the atmosphere. Some DCE data points were obtained in air at 1 bar, facilitating comparison with earlier results. Most DCE data, however, employed helium-oxygen atmospheres, designed to facilitate measurements by increasing burning rates and diffusive extinction diameters while reducing soot formation. The use of helium rather than nitrogen as the inert adds a new dimension, enabling effects of different Lewis numbers to be explored more thoroughly.

The DCE experiment was developed over a period of many years. The first space-based droplet-combustion experiment, flown on STS-73, was fiber-supported droplet combustion (FSDC), a glovebox experiment that employed fibers to tether the droplet in spacelab cabin air within the field of the measurement system in the glovebox. That experiment provided data for a number of different fuels, not including heptane, in the same general initial droplet size range as the DCE experiments. On STS-94, FSDC-2 was tested, this time including heptane among the fuels for which data were acquired. To help in comparison with FSDC results, two DCE tests were performed with tethered droplets in cabin air. The intent was to ascertain in detail the influences of the fiber on the combustion by comparing the tethered results with those for free droplets. Since tethered experiments are easier to perform, sufficient fidelity of results with fiber support can reduce the amount of testing needed with free droplets, saving time and expense.

Measurements

Besides ordinary measurements of combustion-chamber pressures and temperatures, camcorder video images of the overall view of each droplet combustion sequence were downlinked. The main data, however, were obtained from magnified backlit images of the droplet recorded on 35 mm motion-picture film and from ultraviolet (UV) images of the flame recorded by a CCD camera equipped with a narrow-band interference filter centered at 310 nm, one of the bands of OH emission characteristic of the flame. The droplet and flame views were selected to be orthogonal to provide three-dimensional information. The UV images were downlinked, but the main data reduction awaited return of the motion-picture film. The combustion chamber contained a crew-view port through which 35 mm still color photographs were taken of some of the tests.

Figure 1 shows a typical backlit sequence of the experiment. In this figure, a droplet of 4 mm initial diameter is burned in an oxygen-helium atmosphere of 35% oxygen at 1 bar. The droplet is formed by injecting the liquid fuel through a pair of opposed and slightly retracting needles to form a bridge. The first frame shows the droplet centered between the needle tips and two opposed hot-wire igniters in place on opposite sides of the droplet. In the second frame, the droplet has been stretched just prior to deployment; the stretching results in more symmetrical deployment with smaller droplet drift velocities. The drift velocities in the present experiments typically were on the order of 1 mm/s, about one order of magnitude lower than those achieved in earlier experiments. This small level of motion is attained by rapid extraction of the needles after stretching, between the second and third frames. Needle extraction induces droplet oscillation in the first spherical harmonic mode which, however, viscously damps to immeasurable amplitudes, always in less than 1 s. The third frame shows the droplet oscillation at maximum amplitude.

After droplet deployment, the hot-wire igniters are activated to initiate combustion. The fourth frame shows the beginning of combustion and demonstrates that there is buildup of soot, the dark speckled elliptical region around the sphere, during ignition. After ignition, the igniters are withdrawn slowly to minimize associated gas flow currents. The last two frames are illustrative of the free-droplet combustion process that continues after igniter withdrawal. Initially the sooting intensifies, and some agglomerated soot escapes as chains in the directions of needle withdrawal, seen in the penultimate frame. As combustion proceeds, the region of high soot concentration becomes more spherical, and agglomeration leads to larger soot particles, the largest of which escape in random directions through the flame, as seen in the final frame. The field of view in these photographs is smaller than the flame diameter so that the flame, a sphere concentric with the droplet, cannot be seen. The condition of the test shown here, one of the largest droplets at the highest pressure and highest oxygen concentration at that pressure, was selected to maximize the visible details of sooting behavior; sooting is less intense for smaller droplets, lower pressures or lower oxygen concentrations.

Figure 2 shows two typical UV flame-image sequences as downlinked. In this figure, the droplets burn in an oxygen-helium atmosphere of 30% oxygen at 1 bar. The frames shown are at 2 s intervals, beginning at ignition. The energized hot-wire loops are visible in each of the initial frames (a). In each sequence, the droplet burns for about 10 s, exhibiting remarkably spherical flames. In Fig. 2A, the initial droplet diameter d_0 was 3 mm and the maximum flame diameter, frame (c), about 21 mm. The droplets are not visible at all in these UV images. Figure 2A illustrates diffusive extinction in that the flame initially expands then contracts increasingly rapidly, extinguishing at a small diameter, just after the last frame (f), at which time the droplet has just reached zero diameter and disappeared. In Fig. 2B, the droplet initially was 4 mm in diameter, and the maximum flame diameter, frame (d), was about 25 mm; the magnification is slightly different in the two sequences, as can be seen by comparing the sizes of the igniter wires. Figure 2B illustrates radiative extinction in that the flame can be seen to be extinguishing in the last frame (f), while the flame diameter is still near its maximum value, and at this time the droplet diameter is found from the backlit view to still be roughly 40% of its initial value. In this atmosphere, therefore, initially small droplets extinguish diffusively and large ones radiatively, as discussed more thoroughly in the following section.

The backlit and UV images are digitized and analyzed by a computer-based image-analysis system that identifies edge locations on the basis of gradations in intensity. Diameters are obtained from the area of a circle having the area measured by the image-analysis system. Results for droplet diameters were checked by visual measurements of some film frames and by direct measurement of two orthogonal diameters with the image-analysis system, indicating accuracies better than 5%. Flame images are quite round with well-defined edges marking the outer boundary of the very thin, hottest reaction zone, as seen in Fig. 2. Time histories of droplet and flame diameters and of ratios of flame to droplet diameters are obtained from these results.

Results and Comparisons

Figure 3 shows a representative set of results from STS-83. This figure pertains to droplets burning in oxygen-helium mixtures having 35% oxygen at 1 bar. Many details of the results shown in this figure are given in a publication,² which also makes extensive reference to earlier ground-based results. These earlier results all pertain to initial droplet diameters d_0 less than 2 mm. The space-based experiments thus extend the ground-based results to diameters larger by more than a factor of 2. The first observation to be made from Fig. 2 is the nearly linear decrease in droplet diameter squared (d^2) with time (t) after the initial stage. This decrease extends essentially to zero droplet diameter, that is, the droplet essentially disappears prior to extinction in this atmosphere. The same is inferred to be true² for $d_0 = 4$ mm, although that is not seen in the figure because the droplet passes out of the backlit view before completion of combustion; the flame remained in view for the entire combustion history in this test and exhibited an excursion at time $t=6$ s, apparently caused by ignition of a large soot agglomerate passing through the flame. The 15s duration of the flame in this test is well beyond measurement capabilities of any ground-based experiments. The flame-diameter histories in Fig. 3 clearly do not obey the d^2 law, that is, the curves are not linear. This indicates that the flames are in the outer transient region rather than the inner quasisteady region.² The flames exhibit measurable nonzero (but small) diameters at extinction. Relevant chemical-kinetic information about combustion may be obtained from these flame diameters at extinction. Diffusive extinction occurs in these high-oxygen atmospheres; it is diffusive energy loss, rather than radiative energy loss, that is responsible for extinction.²

Figure 4, also from STS-83, pertains to the same conditions as Fig. 3, except that the oxygen mole fraction was 25%; again the 4 mm droplet passes out of the backlit view prior to extinction, although this did not occur for the 4 mm droplet in 30% oxygen² (not shown here). The droplets in Fig. 4 again exhibit a regime of d^2 -law burning, while the flames do not, as expected.² The main difference between Figs. 3 and 4 is that in Fig. 4 the flames extinguish at their maximum diameters or slightly thereafter. The extinction in these cases, at the end of the flame-diameter traces, is caused by radiative rather than diffusive energy loss.² After flame extinction, the droplets are seen in Fig. 4 to vaporize more slowly in the residual hot gas; the d^2 slope decreases. Both flame and droplet diameters at extinction seen in these tests can be employed to extract chemical-kinetic information about the combustion process. Radiative extinctions of this kind have not previously been observed for heptane droplets in ground-based (or any other) experiments.

Tests from STS-83 in 30% oxygen exhibited radiative extinction for $d_0=4$ mm but diffusive extinction for $d_0=3$ mm, as was shown in Fig. 2. This indicates that this intermediate dilution is close to the boundary between diffusive and radiative extinction and that larger droplets have a greater tendency towards radiative extinction. Modeling calculations, still continuing, verify this general behavior. Figure 5 shows comparisons of numerical modeling results with experimental results for tests at 1 bar in 30% oxygen, for the time dependence of the square of the droplet diameter.³ The computations were performed for 4 different initial diameters. It is seen that the modeling predicts diffusive extinction with zero droplet diameter at extinction for $d_0 < 3$ mm and radiative extinction with appreciable droplet diameter at extinction for $d_0 > 4$ mm. The two experimental data runs from STS-83 lie between these computational conditions and exhibit intermediate behavior consistent with the calculations. The slopes of the curves, that is, the burning rates, also are in reasonable agreement with the predictions.

Figure 6 provides a more detailed comparison between predicted and measured burning rates under various conditions at 1 bar, for both space-based and ground-based experiments.³ It is seen from this figure that the burning-rate constant K in the formula

$$d^2 = d_0^2 - Kt \quad (1)$$

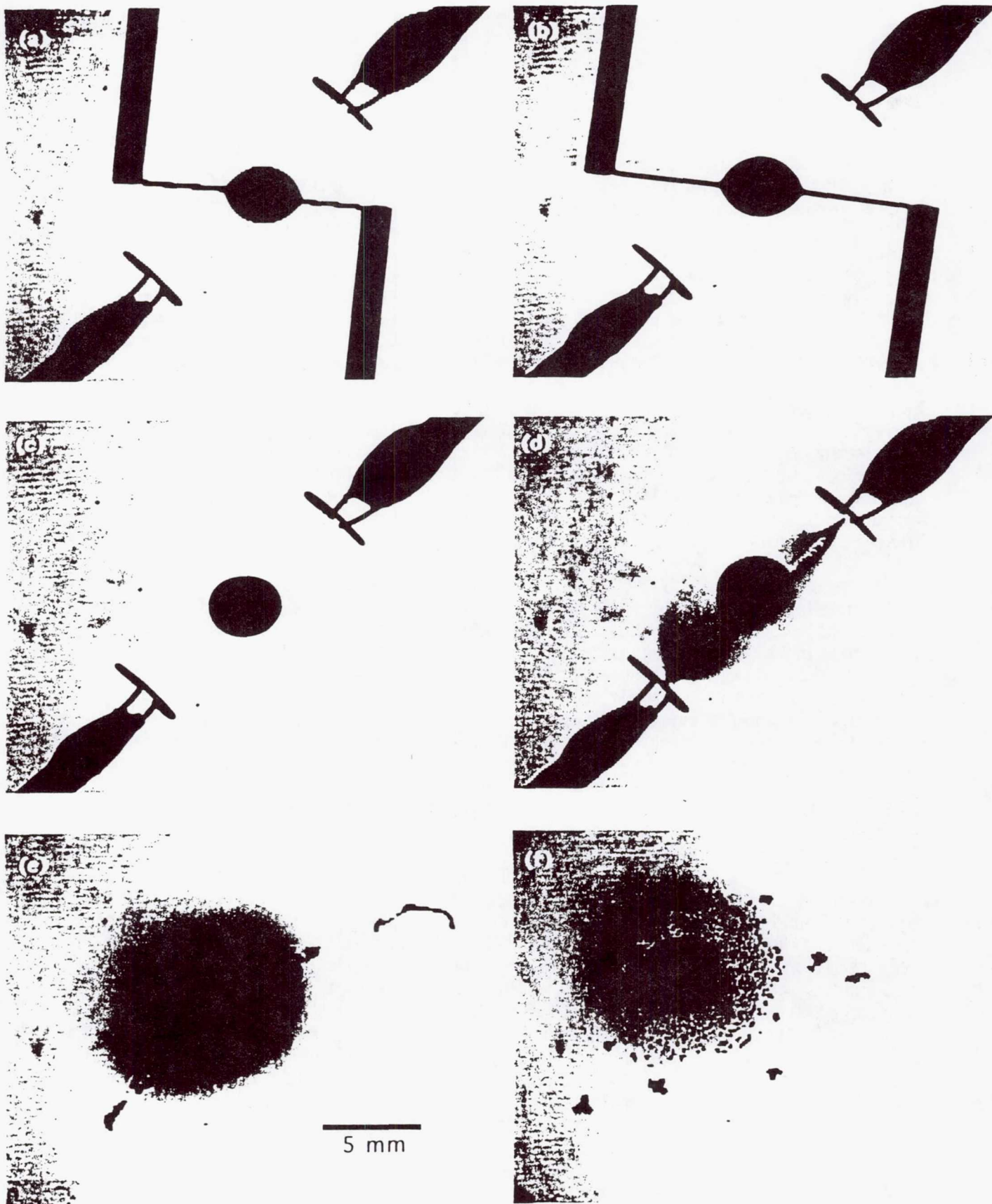
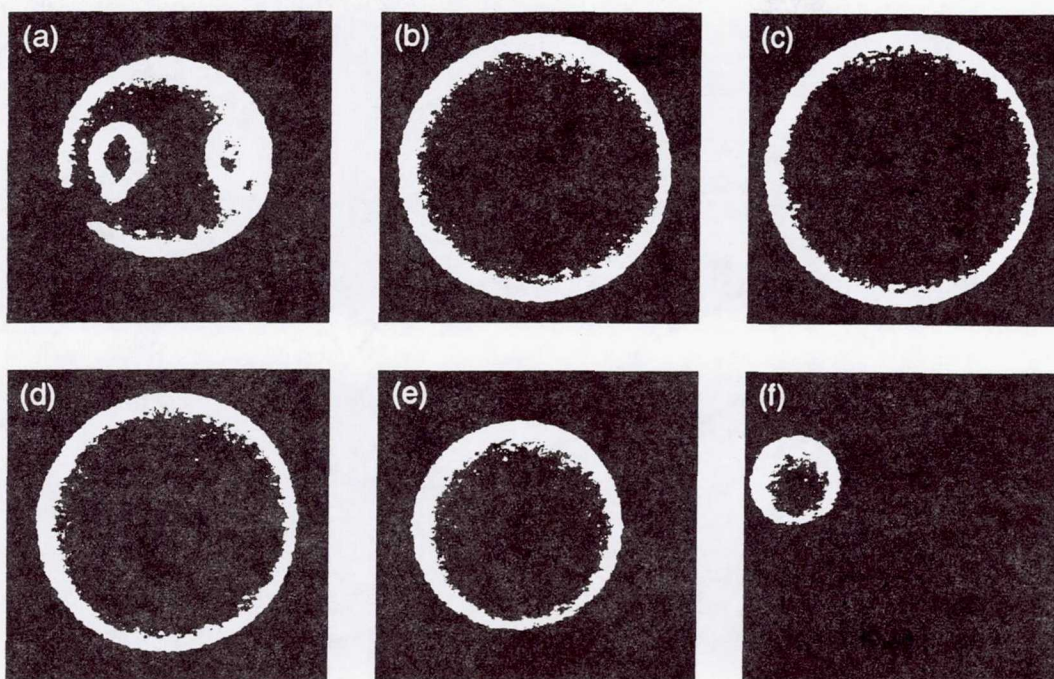
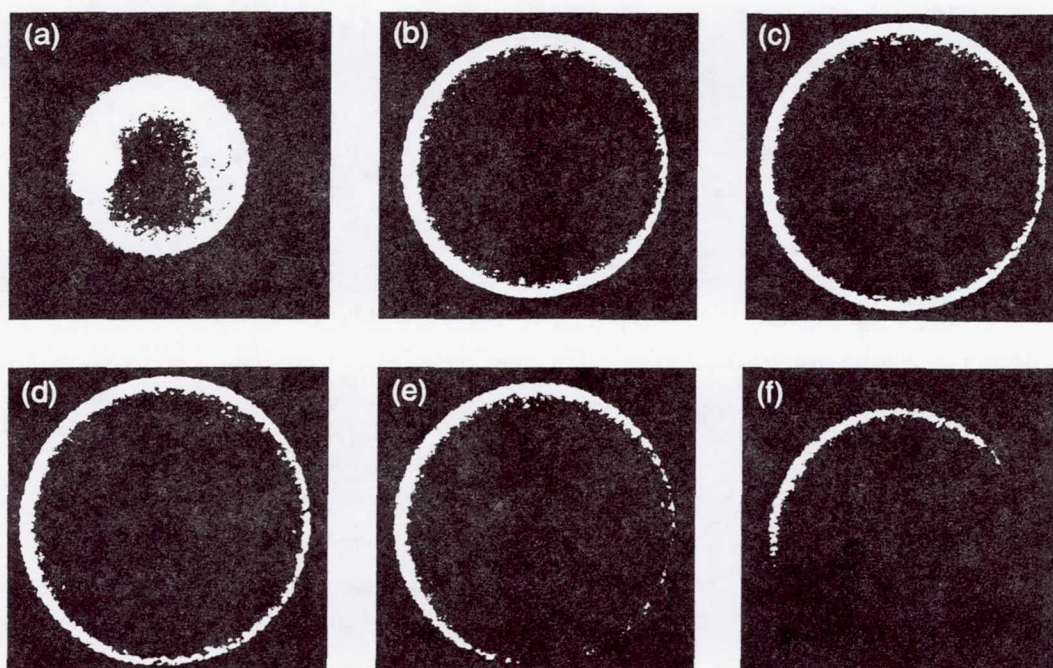


Figure 1 Representative sequence of events in the backlit view of the DCE experiment (35% O₂, 65% He, 1 bar, d₀=4mm).



A



B

Figure 2 Two representative UV flame-image sequences (30% O_2 , 70% He, 1 bar) at 2s intervals, starting from ignition, for (A) $d_0=3\text{mm}$, illustrating diffusive extinction, and (B) $d_0=4\text{mm}$, illustrating radiative extinction; both droplets burned for about 10s.

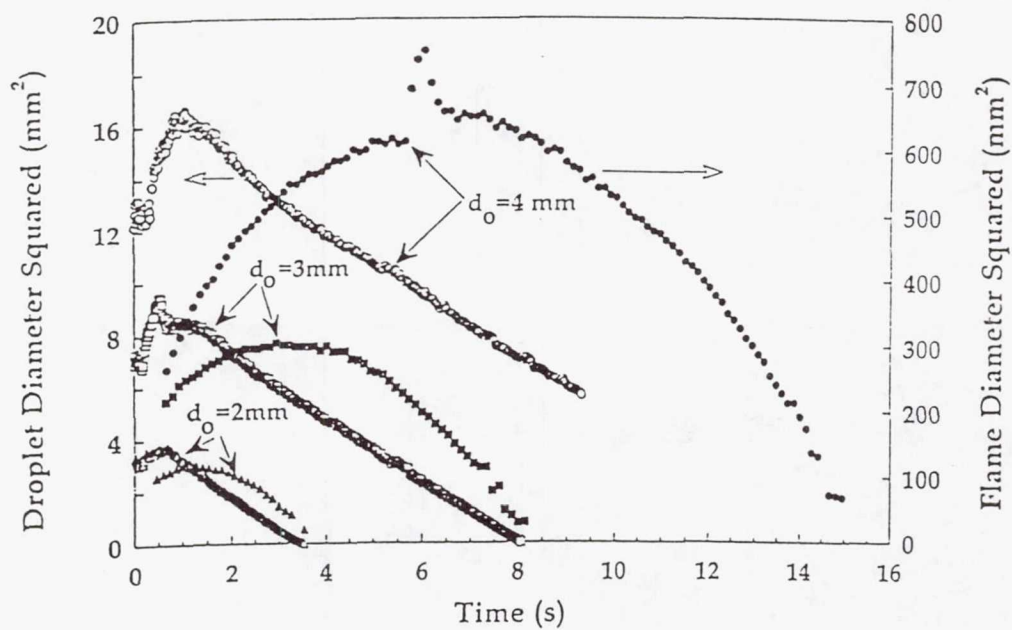


Figure 3 Squares of droplet and flame diameters as functions of time (STS-83, 35% O_2 , 65% He, 1 bar).

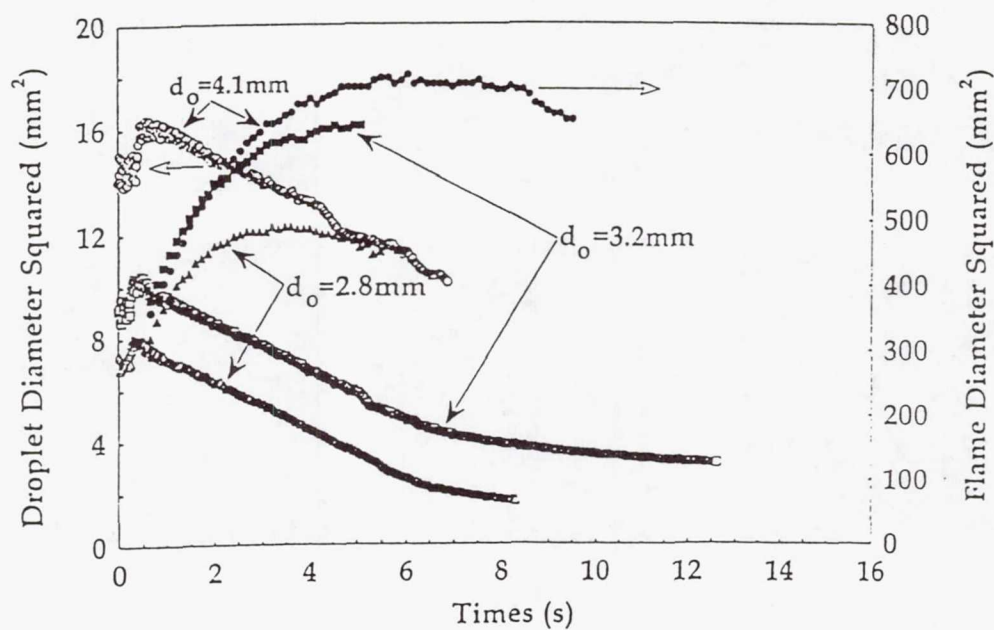


Figure 4 Squares of droplet and flame diameters as functions of time (STS-83, 25% O_2 , 75% He, 1 bar).

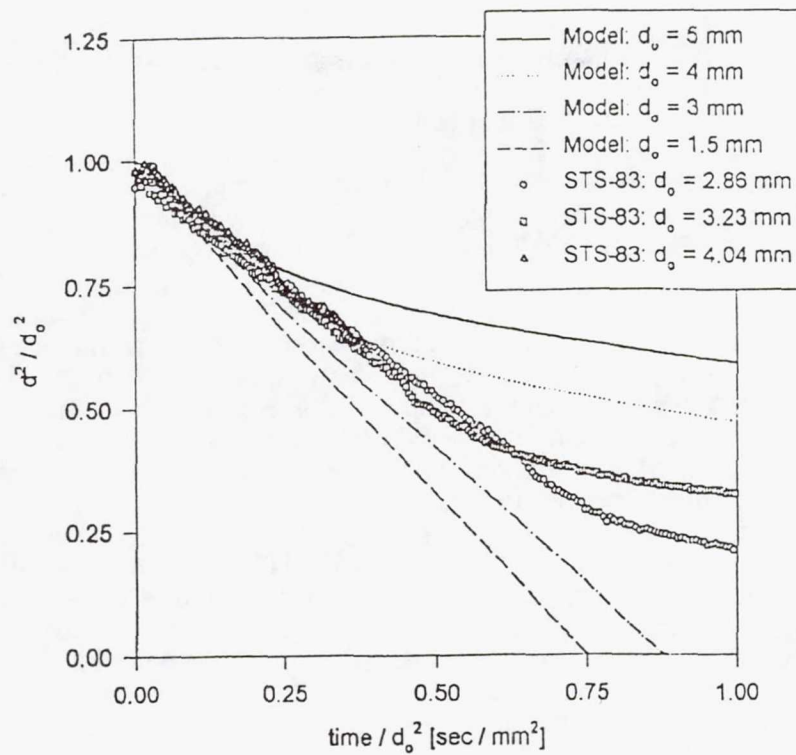


Figure 5 Calculated (curves) and measured (points) normalized d^2 plots for droplet diameters (30% O_2 , 70% He, 1 bar).

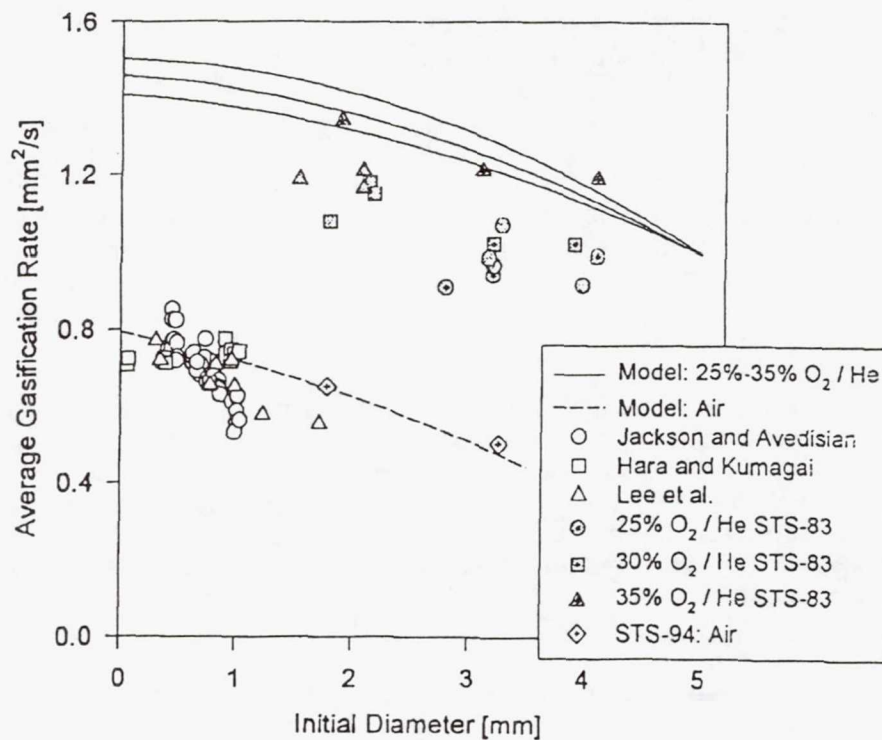


Figure 6 Calculated and measured burning-rate constants K as functions of initial diameter d_0 at 1 bar, for both ground-based and space-based experiments.

is larger in helium-oxygen mixtures than in air. This is due largely to the higher diffusivity of helium. The computational results for air are in excellent agreement with experiment for both ground-based measurements and the measurements of larger droplets in STS-94. In helium-oxygen mixtures, the results agree well in 35% oxygen, but at lower oxygen concentrations the predicted values of K exceed the measured values. This may be caused by inaccuracies in available diffusivities of helium under these conditions.³ Such inaccuracies are known to exist for both helium and hydrogen. Computations with improved transport properties are needed to test this explanation.

Figure 7 compares computed and measured histories of flame diameters for droplets burning in helium-oxygen mixtures having 30% oxygen at 1 bar.³ As with the droplet diameters, the flame diameters are seen to lie between the computed diameters for $d_0=3$ mm and $d_0=5$ mm. In general, then, our knowledge is sufficient to provide good qualitative agreement. More work is needed to provide better tests of our abilities to describe these droplet-combustion processes, especially with respect to flame diameters at extinction.

Much of the extensive data obtained by DCE in STS-94 has not yet been fully analyzed and compared with predictions. The data in atmospheres at reduced pressures in particular need further attention. As is typical in detailed scientific investigations, these analyses are time-consuming, and definitive results are to be expected in five-year rather than one-year periods. It is fortunate that STS-94 has provided so much reliable DCE data that study of it will be able proceed for an extended time in the future. Pursuit of this future research may be expected to further improve our knowledge of droplet combustion.

Conclusions

The DCE experiments have provided a great deal of information on the combustion of heptane droplets, especially in helium-oxygen mixtures. In particular, both radiative and diffusive extinctions were obtained, and the boundary between them was delineated approximately.

It was established that, at one atmosphere and about 300 K ambient temperature in oxygen-helium atmospheres, heptane droplet combustion experiences diffusive extinction for 35% oxygen and radiative extinction for 25% oxygen for droplets of initial diameters between about 2 and 4 mm. At 30% oxygen diffusive extinction occurs for small droplets (less than about 3 mm initial diameter) and radiative extinction for large droplets (greater than about 4 mm initial diameters). After ignition the square of the droplet diameter decreases linearly with time even through the flame diameter behaves in a more complex manner that is consistent with current understanding of the dynamics of droplet combustion.

Average burning-rate constants increase with increasing oxygen content of the atmosphere and exhibit some variations with initial droplet diameter and with droplet motion. Soot production experiences a rich variety of evolutionary behavior and is much stronger in 35% oxygen than in 25% oxygen. Soot-cloud diameters divided by droplet diameters (not shown above) increase somewhat with time and correlate approximately with time from ignition scaled by the burning time for different initial diameters. Many additional details of the droplet-combustion process were observed and explained.

Much more research remains to be done on the basis of these results. Radiative extinctions need to be analyzed in a quantitative manner theoretically, as do diffusive extinctions for situations in which the flame is influenced by the outer transient zone surrounding the quasisteady burning region. Fuel pyrolysis in the gas and the potential for absorption of pyrolysis products by the liquid require further quantitative study. Many aspects of soot production and soot-particle histories deserve further attention. As with many fundamental scientific investigations, the present work thus has uncovered an appreciable number of additional areas worthy of further study.

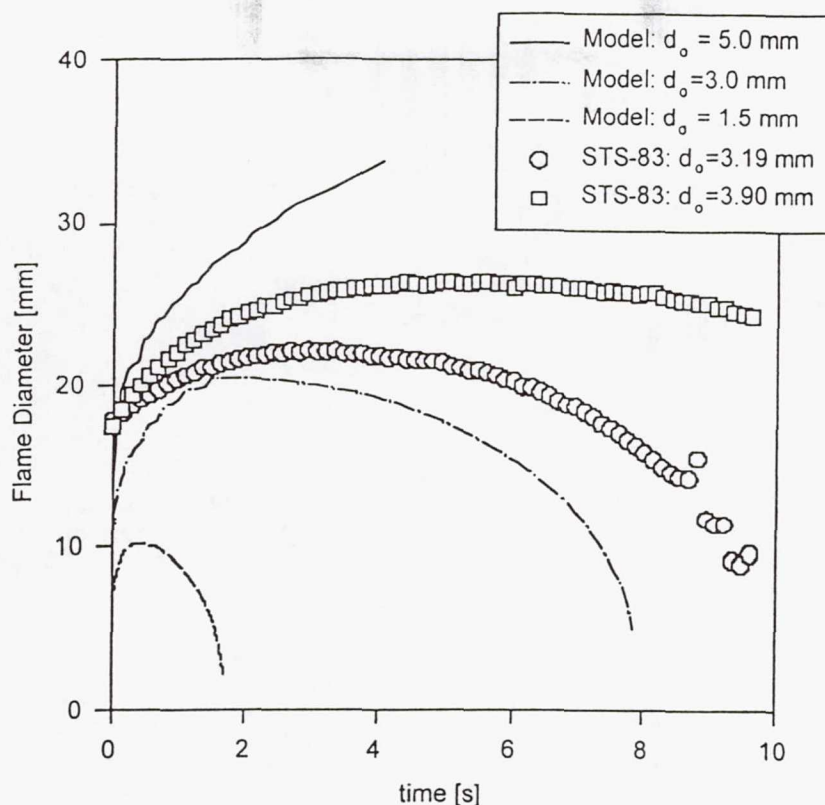


Figure 7 Calculated and measured flame-diameter histories (25% O₂, 70% He, 1 bar).

Acknowledgment

We extend sincere thanks to the MSL-1 crew members, in particular, to Roger Crouch, Greg Linteris, and Janice Voss for conducting the experiments. Tony Marchese and Bai-Li Zhang participated strongly in the Science Team and completed their PhD's at Princeton and UCSD, respectively, through this research. We also thank the many individuals at the Payload Operation Control Center at Marshall Spaceflight Center in Huntsville, Alabama for their support help throughout the mission. Without the dedicated efforts of the Engineering Team at the NASA Lewis Research Center this flight experiment would not have been possible. Renato Colantonio helped greatly with the data acquisition, and Malissa Ackerman and Brad Urban with the data analysis. The research was sponsored by the NASA Microgravity Combustion Science program.

References

1. Kumagai, S., "Combustion of Fuel Droplets in a Falling Chamber with Special Reference to the Effects of Natural Convection", *Jet Propulsion*, Vol. 26, 1956, pp. 786-790.
2. Nayagam, V., Haggard, J.B., Jr., Colantonio, R.O., Marchese, A.J., Dryer, F.L., Zhang, B.L. and Williams, F.A., "Microgravity N-Heptane Droplet Combustion in Oxygen-Helium Mixtures at Atmospheric Pressure", *AIAA Journal*, Vol. 26, 1998, pp. 1369-1378.
3. Marchese, A.J., Dryer, F.L. and Nayagam, V., "Numerical Modeling of Isolated n-Alkane Droplet Flames: Initial Comparisons with Ground and Space-based Microgravity Experiments", *Combustion and Flame*, in press, 1998.

Bibliography

PUBLICATIONS:

1. Nayagam, V., Haggard, J.B., Jr., Colantonio, R.O., Marchese, A.J., Dryer, F.L., Zhang, B.L. and Williams, F.A., "Microgravity N-Heptane Droplet Combustion in Oxygen-Helium Mixtures at Atmospheric Pressure", AIAA Journal, Vol. 26, 1998, pp. 1369-1378.
2. Marchese, A.J., Dryer, F.L. and Nayagam, V., "Numerical Modeling of Isolated n-Alkane Droplet Flames: Initial Comparisons with Ground and Space-based Microgravity Experiments", Combustion and Flame, in press, 1998.

PRESENTATIONS:

1. Marchese, A.J., "Microgravity Droplet Combustion", Fluid, Particulate and Environmental Seminar Series, University of Delaware, Newark, DE, October 15, 1997.
2. Marchese, A.J., "Detailed Kinetic Modeling of Microgravity n-Alkane Droplet Flames", Eastern States Sectional Meeting of the Combustion Institute, East Hartford, CT, October 28, 1997.
3. Dryer, F.L., "Recent Studies of Liquid Hydrocarbon Droplet Combustion Aboard the Columbia Space Shuttle", University of Wisconsin, Madison, WI, November 19, 1997.
4. Williams, F.A., "Experiments on Droplet Combustion in the Space Shuttle", National Fire Prevention Association (NFPA) Meeting, San Diego, CA, December 8, 1997.
5. Zhang, B.L., "Theoretical Analysis of Heptane Droplet Combustion for Comparison with Results from the Shuttle Spacelab During the MSL-1 Mission", 36th AIAA Aerospace Sciences Meeting, Reno, NV, January 13, 1998.
6. Marchese, A.J., "Detailed Numerical Modeling of Liquid Droplet Combustion Experiments Conducted Aboard Microgravity Science Laboratory-1", 36th AIAA Aerospace Sciences Meeting, Reno, NV, January 13, 1998.
7. Dryer, F.L., "Liquid Hydrocarbon Droplet Combustion Aboard the Columbia Space Shuttle", Vanderbilt University, Nashville, TN, February 20, 1998.
8. Dryer, F.L., "Combustion in Low Gravity. Isolated Droplet Burning on the Shuttle", Mechanical and Aerospace Engineering, Princeton, NJ, April 24, 1998.

Non-Technical Summary

Fire is one of humankind's oldest tools yet one of the least understood. The DCE project helps to improve understanding of droplet burning – fires of liquid fuels – an important topic because such fuels account for more than 95% of energy usage in the transportation sector. In the DCE tests on MSL-1, the liquid fuel studied was normal heptane, a representative hydrocarbon whose combustion characteristics are relevant to those of all petroleum-derived fuels. Improved understanding of heptane droplet combustion ultimately can contribute to reduction of air pollution, better fire safety of liquid fuels and conservation of precious fossil-fuel resources.

In DCE, measurements were made of the combustion histories of individual spherical fuel droplets burning in different atmospheres. Free droplets were formed by injection of the liquid fuel through two opposed hypodermic needles and retraction of the needles to leave the droplet stationary in the combustion chamber. Because of the weightlessness in Space Shuttle the droplet does not fall. The droplet is ignited by two hot wires, which also are retracted to leave the burning spherical droplet alone in the field of view of the measurement system. The principal measurements made were motion-picture views of the history of the droplet diameter and spectroscopic views of the history of the flame diameter. Again because of weightlessness, the flame surrounding the droplet remains spherical instead of rising buoyantly into a familiar teardrop shape.

The combustion history was found to depend on the initial droplet size and the atmosphere in which the droplet burned. In sufficiently oxygen-rich atmospheres, the liquid droplet eventually vaporized completely and the flame around it first grew in size then decreased to a very small diameter, at which point it extinguished. We call this behavior diffusive extinction because the heat loss causing extinction occurs by diffusion. In sufficiently oxygen-poor atmospheres, the flame grows then extinguishes near its maximum diameter, leaving unburnt liquid fuel behind in the droplet. We call this behavior radiative extinction because the heat loss occurs by radiation. In intermediate-oxygen atmospheres, the initially larger droplets exhibited radiative extinction and the smaller ones diffusive extinction. Radiative extinction had not been observed before for heptane droplet combustion because it was not possible to burn large enough droplets in ground-based microgravity facilities. The observed burning times of ten to twenty seconds are too long to be studied in earthbound facilities without influences of buoyancy and therefore needed these Spacelab experiments.

The experiments provided a large amount of data on droplet combustion, including data on the formation of soot during burning, an important process in air pollution. Analysis and interpretation of this data are expected to continue for about another five years. It is through long-term, careful study of experimental results like these that scientific investigation improves our knowledge of the physics and chemistry of combustion.

Page intentionally left blank

56-26
434843

Large Isothermal Furnace (LIF)

362142

12P.

Diffusion of Liquid Metals and Alloys

Principal Investigator:

Dr. Toshio Itami
Hokkaido University
Sapporo, Japan

Diffusion of Liquid Metals and Alloys

- The study of self-diffusion under microgravity in liquid Sn
in the wide temperature range-

T.Itami^{a,b)}, H.Aoki^{a)}, M.Kaneko^{c)}, M.Uchida^{d)}, A.Sisa^{d)}, S.Amano^{d)}, O.Odawara^{e)},
M.Masaki^{f)}, T.Ooida^{f)}, H.Oda^{f)}, S.Yoda^{f)}

a) Division of Chemistry, Graduated School of Science, Hokkaido University

b)Invited Researcher of National Space Development of Agency in Japan(NASDA)

c)Ishikawajima Jet service

d)Ishikawajima-Harima Heavy Industry

e)Department of Materials and Engineering, Tokyo Institute of Technology

f)National Space Development of Agency in Japan(NASDA)

Abstract

In the MSL-1 mission the self-diffusion coefficient, D , in liquid Sn was investigated at five temperatures in the wide temperature range up to 1622K. The long capillary (LC) method was adopted with the use of stable isotope ^{124}Sn as a tracer. The concentration profiles of ^{124}Sn were determined by the SIMS analysis. The D was determined with the use of the analytic solution of the Fick's second law and the effective time, t_{eff} . In this effective time the effect of diffusion on both the heating and cooling periods was taken into account properly in addition to the keeping time. In practical application the iteration method was adopted. The obtained self-diffusion coefficients remain to be small enough even at 1622K contrary to the abrupt increase of the ground data in the literature due to the same LC method. The present data at 1622K was in good agreement with D obtained by the shear cell technique, which was adopted in the present MSL-1 mission by NASDA. The extrapolation of present data to the low temperature range is in good agreement with the microgravity data of D due to Froberg et al. The power index in the temperature dependence of D is 1.81 for the present data and 2.04 for the all microgravity data of D though the latter index seems to be much affected by the data due to Froberg et al. Obtained data was analyzed by the hard sphere model. Agreement between calculations and experiments is qualitatively good though 1.77 was obtained as the power index for the calculated temperature dependence of D . The prediction of the viscosity of some liquid metals was successfully performed by the present improved hard sphere model, in which the present experimental information of D under microgravity is taken into account.

Objectives

Because of no convection the microgravity condition in space is the ideal circumstance to investigate the diffusion of liquids with the high melting temperature, T_m , for which experimentals on the ground have been seriously suffered from the thermal convection due to the presence of inevitable temperature difference in the sample even in the keeping period in addition to heating and cooling periods. This advantage of microgravity circumstance for the diffusion experiments was for the first time made clear in the self-diffusion measurement of liquid Sn in the D1 mission by Frohberg et al[1], though it was limited to the rather low temperature range. In this study the self-diffusion, D , of liquid Sn under microgravity was planned to be studied in the wide temperature range on the flight chance of space shuttle "Columbia" in the MSL-1 mission. One reason for this selection is that it is easy to confirm the validity of microgravity for the study of diffusion in melts with high T_m because of the presence of excellent reference data[1]. Another reason is that the temperature dependence can be discussed in the extremely wide temperature range based on the "exact diffusion data under microgravity", which can be constructed with the combination of present data with the excellent reference data[1].

Background

For recent two decades the intentions of the researchers to study the atomic transport in melts with high T_m have been suppressed because of the difficulty in experiments due to high temperature conditions. The importance of atomic transport itself has been recognized deeply from fundamental and applied points of view. However, on the ground with gravity, the thermal convection is always accompanied in liquid samples even in the process for keeping at a constant temperature in addition to the heating and cooling processes. The study of diffusion of such melts on the ground has been seriously spoiled because of the significant effects of convection on the experimental accuracy. The microgravity is the fascinating condition for the study of diffusion of melts with high T_m because of its "no convection" property. In fact Frohberg et al[1] presented the striking results for the D of liquid Sn; the temperature dependence obeys the square law; isotope effects can be detected even for the mass of Sn; the diffusion coefficient under microgravity has a tendency to become smaller in the high temperature range compared with data on the ground in the literature.

Recently one of present authors[2] presented a simple analytic form of hard sphere model, in which the "exact self-diffusion data under microgravity" play an important role for its discussion.

Method of data acquisition and analysis

In table 1 is shown the planned five experimental conditions. MET1 corresponds to the experiment in the temperature range studied by Frohberg et al[1]. The other four conditions correspond to

experiments at the higher temperatures up to 1800K beyond their experimental temperature range. In the actual MSL-1 mission, unfortunately, the experimental condition for MET5 was replaced by that of MET1 due to some slight trouble. The D was planned to be measured by the long capillary (LC) method. In Figure 1 is shown the construction of sample container. The carbon spring provides the application of the slight compression to the liquid sample throughout the course of experiments with considerable volume changes due to the thermal expansion and shrinkage, melting and solidification. This mechanism is required to prevent the Marangoni convection in liquids, which appears easily under microgravity if the free surface or void in liquids is present. The selection of strength and length of spring was performed based on theories of capillary phenomena[3] by taking into account of the precise data about the dimension of sample container, inner lid and sample. For this mechanism the material for the sample container must be "non-wetted" by liquid Sn. The graphite showed the excellent such a property, which was confirmed by the observation of almost constant contact angle, 160 degree, between graphite and liquid Sn over 1400K.

The stable isotope, ^{124}Sn , was employed as the tracer. After the diffusion run the concentration profile of ^{124}Sn in the sample was analyzed by the SIMS analysis. Measured concentration profile is shown in Figure 2. The self-diffusion coefficient was determined as a function of temperature by using the iterative method, in which the exact solution of the Fick's second law[3], $n(x, t_{i, \text{eff}})$, and the effective time[3], t_{eff} , was employed. In Figure 3 is shown the flow chart of this iteration method and the explicit form of $n(x, t_{i, \text{eff}})$ and t_{eff} respectively(see also Ref.[3]). In this iterative method the calculated concentration profile can reproduce the experimental one with $t = t_{\text{eff}}$, in which the diffusion coefficient is included. The convergency of this iteration is excellent.

Flight results compared with ground results

In Figure 2 is included also the calculated concentration profile, which is calculated by this iterative method. In this method considerably good agreement between experiments and calculations is obtained. It is to be noted that all concentration profiles at various temperatures were fitted by using a common temperature dependence of diffusion coefficient.

In Figure 4A is shown the temperature, T , dependence of self-diffusion coefficient, D , obtained by the LC method in the present MSL-1 mission. If this T dependence is summarized by the power law of T , that is $D=AT^B$, 1.81 can be obtained as the power index B . In Figure 4B this experimental result under microgravity was compared with the data of other data sources. At first, comparisons should be performed between the present microgravity data and the previous data (Ma & Swallin) obtained on the ground for liquid Sn due to the same LC method. It can be known that this ground data shows an abrupt increase in the temperature range over 1100K. The present data never shows such an abrupt increase even in the temperature range up to 1622K. The present data are well situated on the

extrapolated tendency of data due to Froberg et al[1] under microgravity. In addition the present data at 1622K well agrees with the data due to the shear cell method performed by NASDA in the present MSL-1 mission. As is well known, the shear cell technique is free from the convection in liquids and the most promising method for the determination of D for melts with high T_m . The LC method in the present MSL-1 mission may be performed considerably freely from the effect of convection.

The power index was determined to be 2.02 by using these a t'all microgravity self-diffusion data for liquid Sn", in which data in lower temper ure range due to Frohberg et al[1] seem to be much influenced on this determination.

Following to the previous paper the hard sphere model in an analytic form was employed to explain the behaviour of D obtained under microgravity. As can be seen in Figure 4C, the calculated values agree with experimental ones particularly in the low temperature range. In this model the hard sphere diameter, σ , plays an essential roles together with the packing fraction, $y (= (\pi n \sigma^3) / 6 (n: \text{number density}))$. In this calculation conventionally $y=0.464$ was assumed and the empirical equation of Protopapas et al[4] was adopted as the T dependence of σ (see the Ref.[2])). The power index for this calculated curve is 1.77, which is rather closer to 1.81 determined only by the present data due to the LC method in the present MSL-1 mission.

An "universal" relation was tried to be determined for the T denpence of σ by using "all microgravity self-diffusion data for liquid Sn". This relation was determined so that the calculated hard sphere model may reproduce the experimental D. Determined relation is as follows:

$$\frac{\sigma(T)}{\sigma(T_m)} = -4.43944 \times 10^{-3} \left(\frac{T}{T_m} - 1 \right)^2 - 5.6337 \times 10^{-2} \left(\frac{T}{T_m} - 1 \right) + 1 \quad (1)$$

Here equation (1) was tried to be applied to predict the physical properties, which is free from the problem of convection. One such a candidate is the viscosity, which is usually measured under the forced flow. In the case of hard sphere dense fluids it is known that the Stokes-Einstein relation with the slip boundary condition may be established[2]. Therefore, the viscosity can be written as follows:

$$\eta = \frac{k_B T}{2\pi\sigma D} \quad (2)$$

In this equation k_B is the Boltsmann constant. The viscosity was calculated for liquid Sn, Pb, In and Sb. The agreement between calculations and experiments is rather good except for liquid Sb(See Figure 5). This indicates that the hard sphere model is valid as an universal model for liquid In, Sn and Pb and possibly many liquid simple metals. On the other hand, this model fails to predict the

viscosity of liquid Sb. In the case of liquid state of semi-metals, such as liquid Sb, and semiconducting matters, such as liquid Ge[3], the hard sphere model is not valid at least in a straight manner. The effect of covalency in this kinds of liquids may be responsible to this disagreement. In near future these points will be discussed in more detail.

Finally, compared with the case of "previous" Protopapas et al equation, the prediction of viscosity is better in the case of "present" equation (1) newly determined with the use of microgravity data(see Figure 5). This indicates that the aquisition of accurate data under microgravity may contribute to the fundamental science at least for the diffusion of melts with high melting temperature.

Conclusions including the significance and future plans

The self-diffusion coefficient, D , in liquid Sn was measured by the long capillary method under microgravity in the MSL-1 mission. Obtained D remains to be small even at 1622K contrary to the abrupt increase over 1100K for ground data in literature due to the same long capillary method as the present case. The power index for the temperature, T , dependence of D for liquid Sn is 1.81 for the present data and 2.02 if "all self-diffusion data of liquid Sn under microgravity" are included. The T dependence was reproduced qualitatively by the hard sphere model with the power index 1.77. New equation is proposed for the T dependence of hard sphere diameter by using "all self-diffusion data of liquid Sn under microgravity". The adoption of this equation in the hard sphere model is succesful to predict the viscosity of some liquid metals except for liquid Sb. Thus the validity of microgravity has been established. In future the atomic transport in melts with the high melting temperature must be intensively studied under microgravity with the relation to complexities and structures of melts.

Biographic citations of articles/presentations resulting from the flight

- [1] G.Frohberg, K.H. Kraatz and H.Weber, in Proc. Vacancies and Interstitials in Metals, 1986.
- [2] T.Itami and K.Sugimura, Phys. Chem.. Liq., 1995, Vol.29,31-41.
- [3] T.Itami et al, JASMA, 1997, Vol.14, 323-330.
- [4] P.Protopapas et al, J.Chem.Phys., 1973, Vol.59, 15.

Acknowledgement

One of authors(T.I.) is grateful to Dr. H.Tamura for the guidance and the help of the SIMS analysis in the early stage of the present experiment. Authors are also thankful to Tore Research Center(Mr. Hasegawa and Mr.Hatada) for SIMS analysis. In addition to these this project has been supported by the help and cooperation with many oraganizations and scientists. Authors are much appreciated with ISAS, JSUP and JAMSS, Mr.T.Fukazawa, Ms.K.Sugimura, Mr.T.Onogi, Mr.N.Higashimoto. Finally authors are grateful to Mr. T.Kiya and T.Miura for the beautiful quartz work for ampoules.

Table 1 Planed experimantal condition

Exp.No.	Experimental temperature condition				
	keeping temp. /K	heating duration /min	keeping time /min	rapid cooling duration /min	cooling duration /min
MET1	900	10	432	10	139
MET2	1191	17	276	17	145
MET3	1423	23	198	23	162
MET4	1622	28	162	28	156
MET5	1800	32	138	32	164

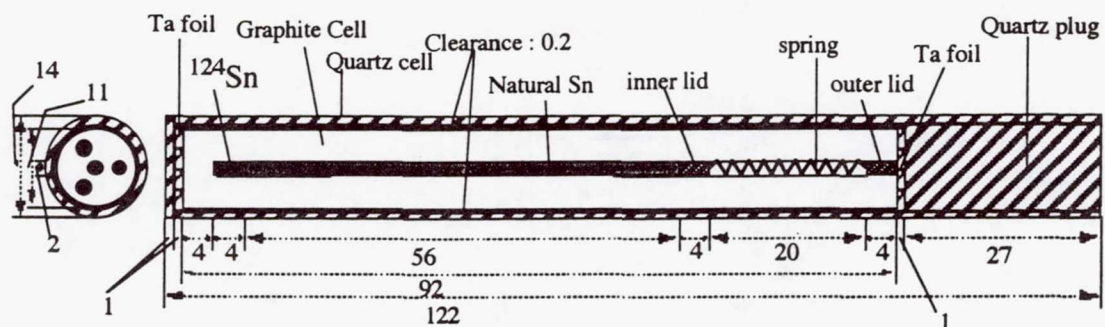


Figure 1 Constitution of sample container for diffusion coefficient measurement due to the long capillary method

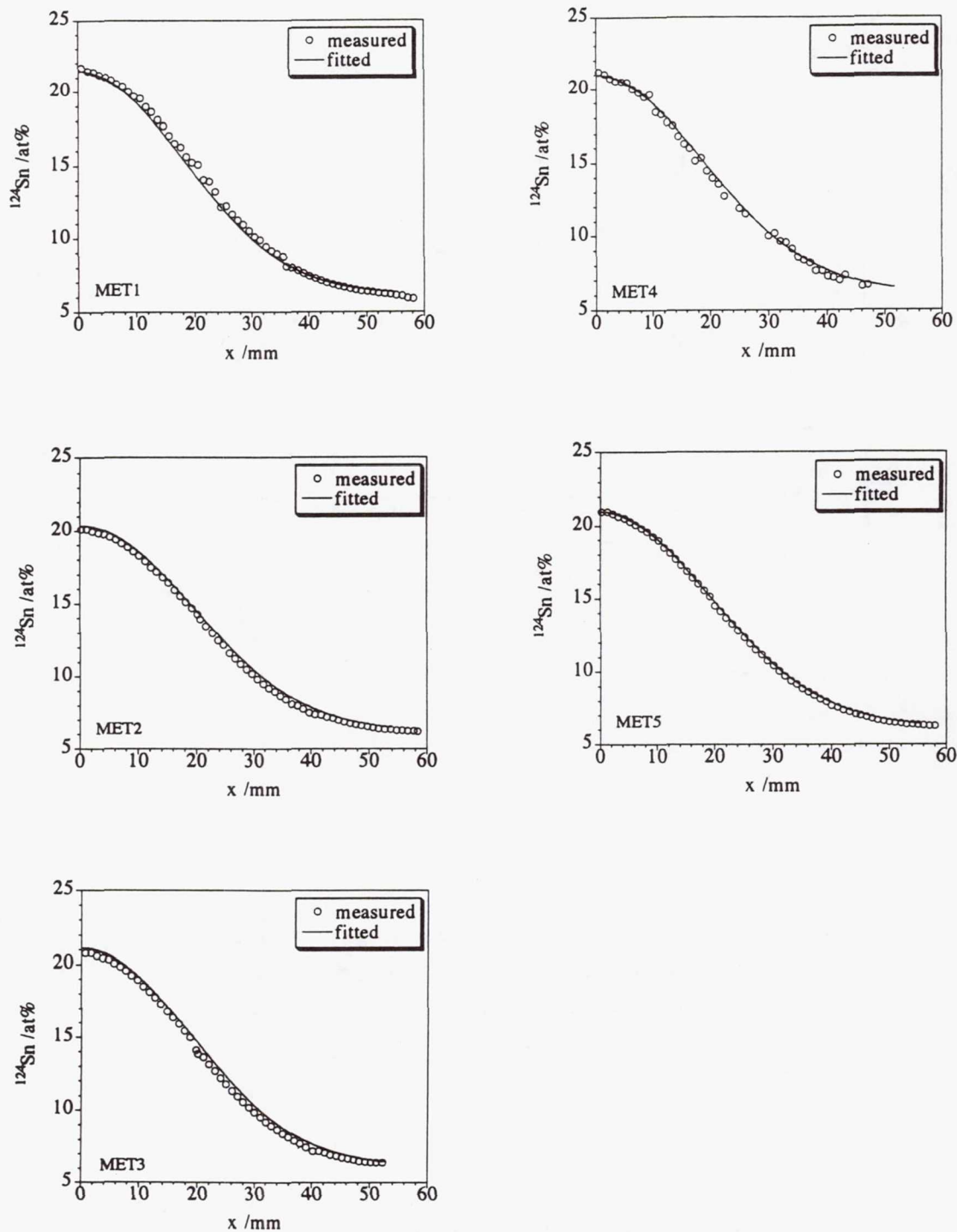


Figure 2 Comparison of ^{124}Sn concentration between measured and calculated by the fitting procedure

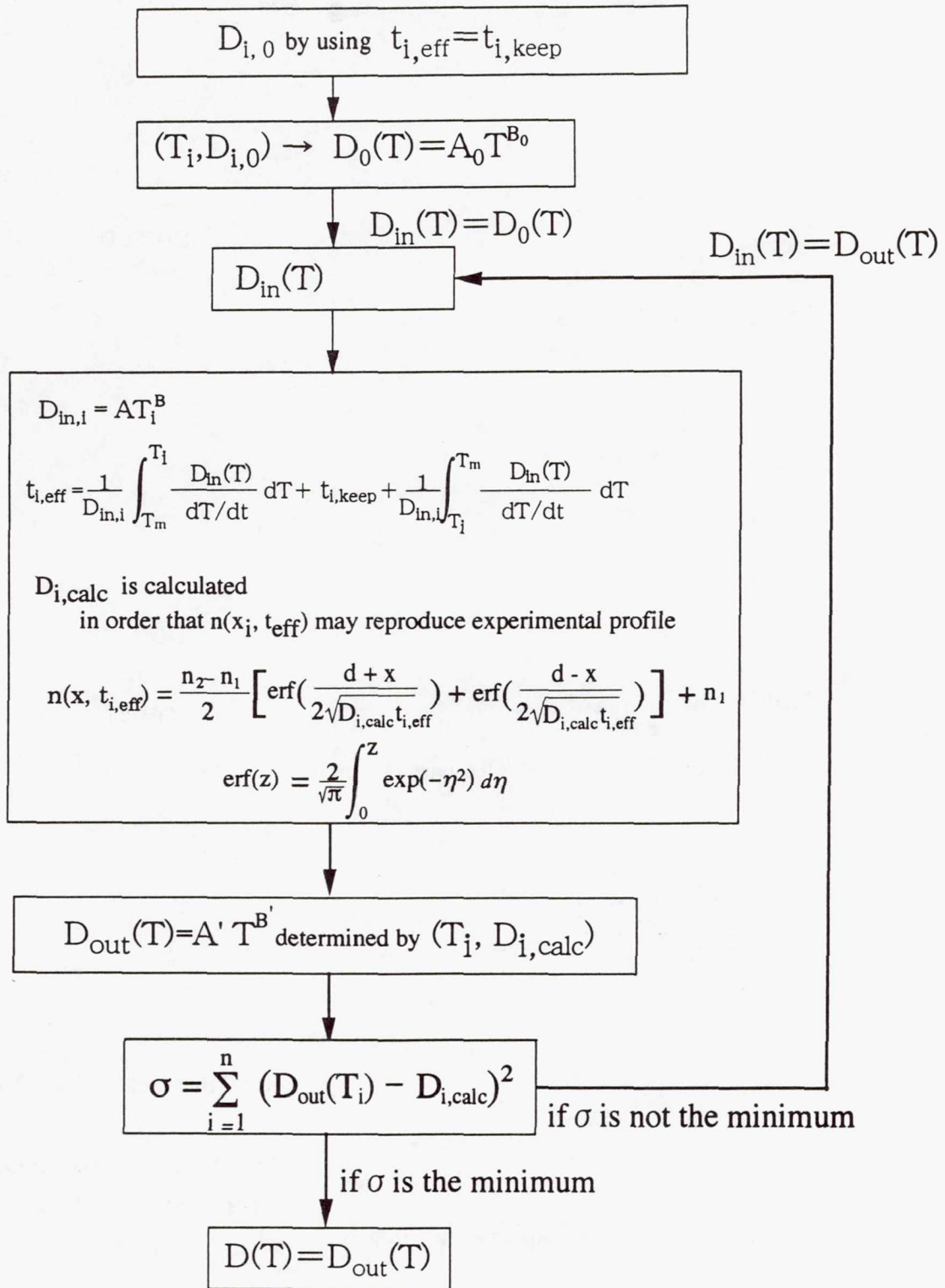
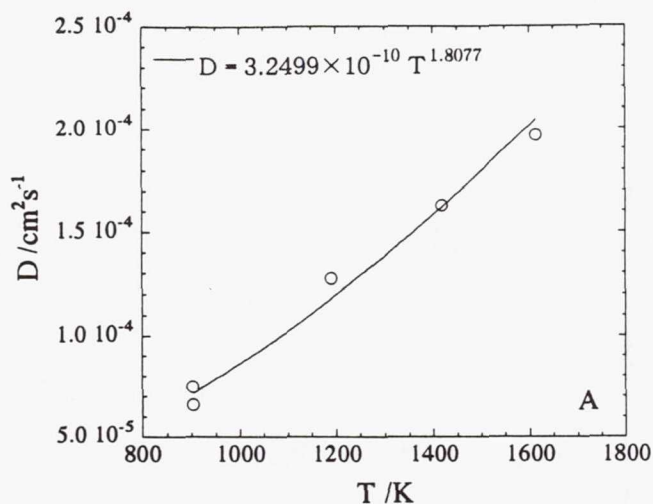
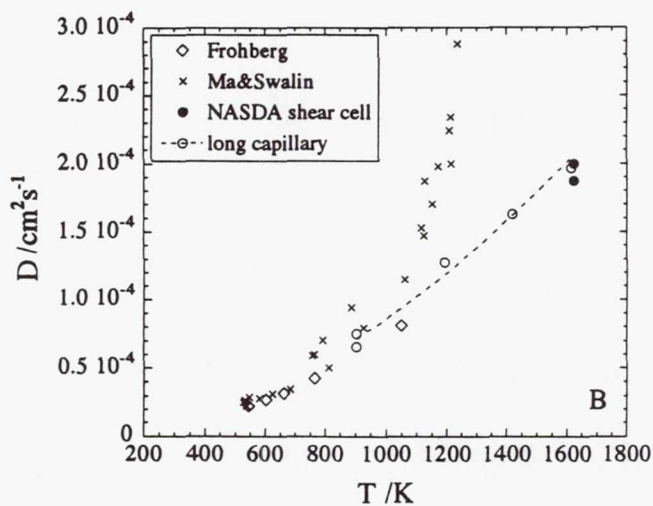


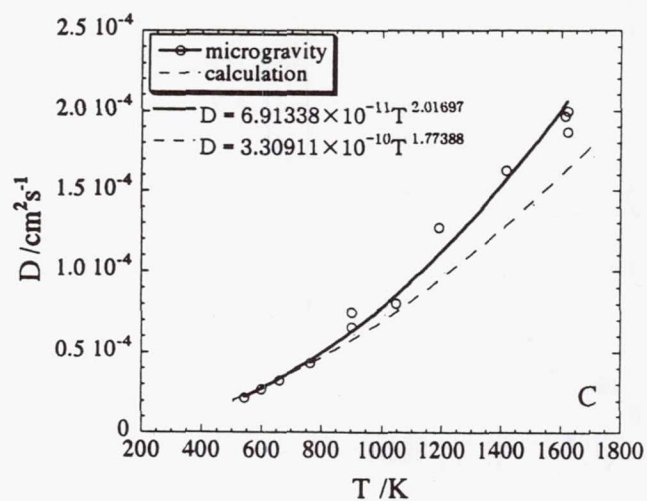
Figure 3 Flow chart of iteration for the determination of diffusion coefficients



present



present
and
others



all microgravity data
and
calculations due to the
hard sphere model

Figure 4 The self-diffusion coefficient of liquid Sn

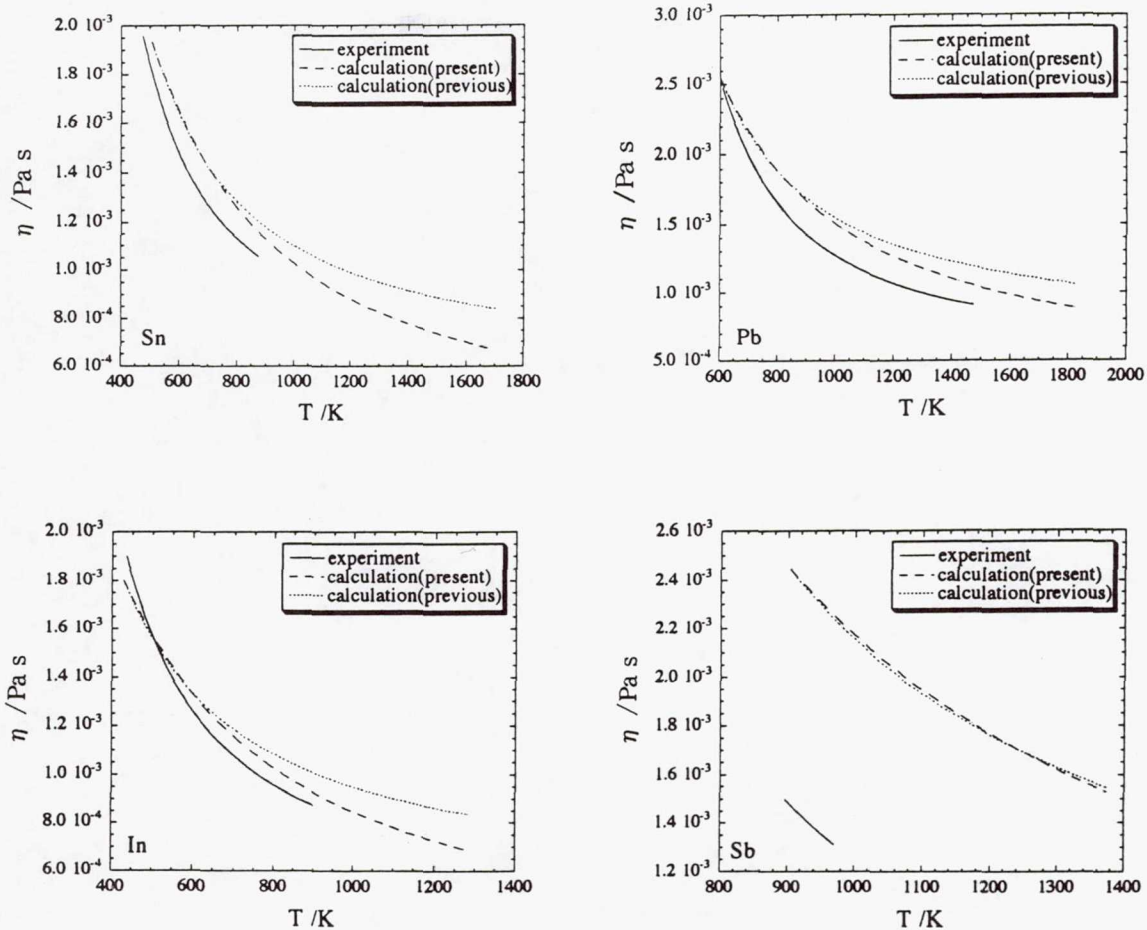


Figure 5 Comparison between calculated viscosity due to the hard sphere model and experimental one

Page intentionally left blank

Emul TH17
PAGE

Large Isothermal Furnace (LIF)

Diffusion in Liquid Lead-Tin-Telluride

Principal Investigator:

Dr. Misako Uchida
IHI
Tokyo, Japan

MICROGRAVITY DIFFUSION EXPERIMENTS FOR THE MELT OF COMPOUND SEMICONDUCTOR LEAD-TIN-TELLURIDE

Misako Uchida¹⁾, Minoru Kaneko²⁾, Toshio Itami³⁾ and Shinichi Yoda⁴⁾

- 1) Materials Technology Dept., Research Inst.
Ishikawajima-Harima Heavy Industries Co., Ltd.
3-1-15 Toyosu, Koto-ku, Tokyo 135 Japan
Phone : +81-3-3534-4140 Fax : +81-3-3534-3388
e-mail : uchidam@rimat.ty.ihl.co.jp
- 2) Ishikawajima Jet Service Co., Ltd.
3-1-15 Toyosu, Koto-ku, Tokyo 135 Japan
Phone : +81-3-3534-3675 Fax : +81-3-3534-3676
- 3) Dept. of Chemistry Faculty of Science, Hokkaido University
N10 W8, Kita-ku, Sapporo 060 Japan
Phone : +81-11-706-3532 Fax : +81-11-746-2548
e-mail : itami@science.hokudai.ac.jp
- 4) National Space Development Agency of Japan
2-1-1 Sengen, Tsukuba-shi, Ibaragi 305 Japan
Phone : +81-298-52-2775 Fax : +81-298-52-1594

SINGLE SCAN

57-26

434844

362352

7P.

ABSTRACT

In order to obtain the "true" temperature dependence of diffusion coefficient of liquid lead-tin-telluride, microgravity experiments were conducted in MSL-1 mission. The diffusion temperature of each experiments was 1223 K, 1273 K, 1373 K, 1473 K and 1573K. The diffusion couple ($\text{Pb}_{0.8}\text{Sn}_{0.2}\text{Te} - \text{Pb}_{0.7}\text{Sn}_{0.3}\text{Te}$) of a 2 mm diameter cylinder was melted at each diffusion temperature and quenched by injecting helium gas. The cooling was controlled to avoid the axial directional solidification, which was confirmed to spoil diffusion experiments from ground experiments. For the experiment at 1573K, the diffusion during heating and cooling periods was included in an analytical solution of Fick's second law with the assumption of $D=A(T/T_m)^n$ (A and n are constants, and T_m is the melting temperature). The temperature dependence of diffusion coefficients was calculated by using the results of MSL-1 experiment results and the rocket experiments which were previously carried out.

INTRODUCTION

$\text{Pb}_{(1-x)}\text{Sn}_x\text{Te}$ is known to be an important material for infrared detectors and lasers. But it is difficult to make high quality crystals of this semiconductor compound by the directional solidification. One difficulty is to obtain an uniform element distribution in an ingot, which is essentially determined by the solutal diffusion at the liquid - solid interface [1]. However the "true" diffusion coefficient of liquids has not yet been obtained because the buoyancy-driven convection is inevitable in liquid samples. One technique to remove such a convection is to use the capillary method in which the convection can be suppressed by the viscosity of liquid itself.

Table 1 Experimental condition for each experiment

diffusion temperature	1223 K	1273 K	1373 K	1473 K	1573K
holding time at diffusion temperature	5000 s	4500 s	4000 s	3600 s	3300 s

The diffusion coefficient of a liquid lead-tin-telluride has been measured [2,3], for example by this method using 2 mm diameter samples, though it was not known whether there was some convection or not. A more elegant way might be a space experiment. It was reported that the temperature dependence of the diffusion coefficient was different between space and ground experiments, and its accuracy could be better in space [4].

We have done microgravity experiments in MSL-1 mission with the space shuttle Columbia STS83 in April and STS94 in July, 1997, and conducted using the German sounding rockets TEXUS 26 and 29 in 1990 and 1992, the Japanese rocket TR-1A in 1995.

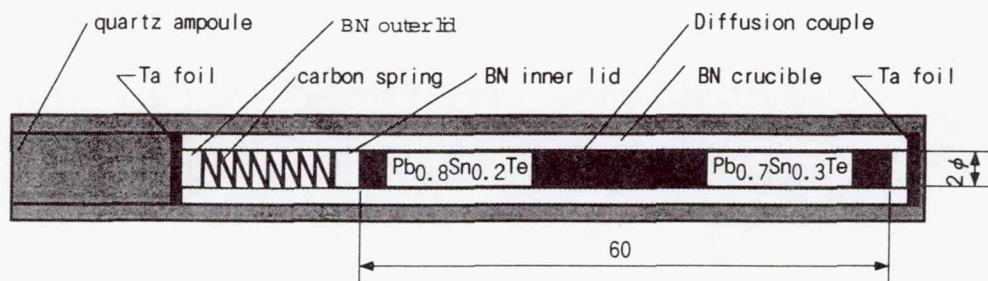
In the TEXUS 26 experiment, we found a strong directionality in the solidified structure of the sample, which brought another complexity in the solutal distribution and in the analysis of the diffusion coefficient [5]. We did some ground experiments to confirm the influence of solidification on diffusion measurements[6]. The cooling condition was controlled to avoid the axial directional solidification in the later diffusion experiments in space.

This paper describes the results of MSL-1 experiments analyzing with those of diffusion experiments by TEXUS29 rocket and TR-1A4 rocket.

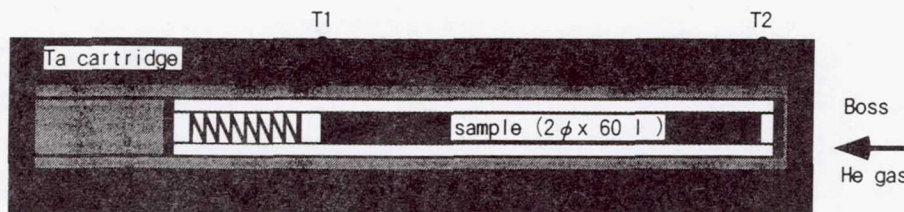
EXPERIMENTAL

Diffusion experiment

Diffusion couples of $\text{Pb}_{0.8}\text{Sn}_{0.2}\text{Te}$ and $\text{Pb}_{0.7}\text{Sn}_{0.3}\text{Te}$, which was 2 mm diameter and 60 mm length, were used in the experiments. Fig. 1 illustrates the inside configuration of the cartridge used for the present experiment. The diffusion couple was placed in a BN crucible, and subsequently sealed in a quartz ampoule with argon gas. The ampoule was sealed in a tantalum cartridge on which two thermocouples were put to measure temperature change during the experiments. The couple was slightly pressed by a graphite spring in terms of the crucible lid throughout the experiment in order to ensure the interface contact, and not to



(a) Ampoule configuration



(b) Cartridge configuration

Fig. 1 Diffusion sample configuration

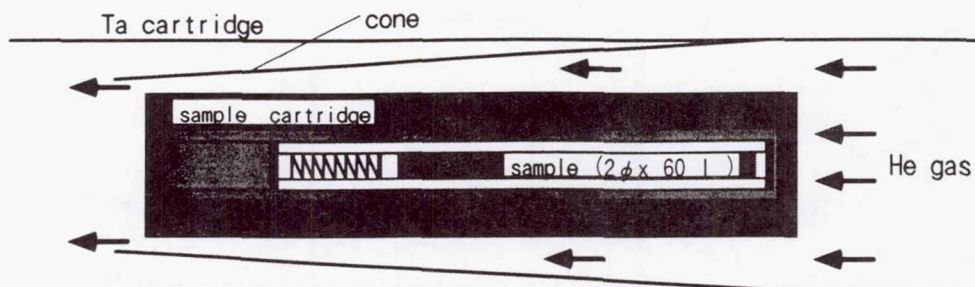


Fig. 2 Cartridge configuration and gas flow during cooling

generate the Marangoni convection due to the void formation[7]. The diffusion experiment was designed to melt and to keep the sample at the each diffusion temperature for each holding time shown in table 1, followed by quenching by helium gas coolant. To avoid large temperature difference between the top and the bottom during the cooling, we used a cone to accelerate heat transportation as shown in Fig.2.

The longitudinal (diffusion direction) surfaces of the solidified sample were polished about 0.1 mm deep, and the microstructure was observed by backscattered electron image of EPMA (Electron Probe Microanalyses). The distribution of Sn atoms on the polished surfaces was analyzed by EPMA.

RESULTS AND DISCUSSIONS

The temperature hysteresis during the experiment at 1573 K is shown in Fig. 3. T1 and T2 are the temperatures on the ampoule around the diffusion interface, and the T2 is on the gas inlet side. To improve the heating rate over melting point, the sample was preheated at 1073 K. It was confirmed that the sample was not melt at the pre-heating stage. The average cooling rate and the temperature gradient was around 19 K/s and 3 K/mm, and it seems to be sufficient cooling condition for diffusion measurement[6]. The solidified microstructure of the MSL-1 experiment at 1223 K is shown in Fig. 4. The structure is a dendritic structure at high solidification rate. The dendrite was homogeneous in the sample and axially directional dendrite was not observed.

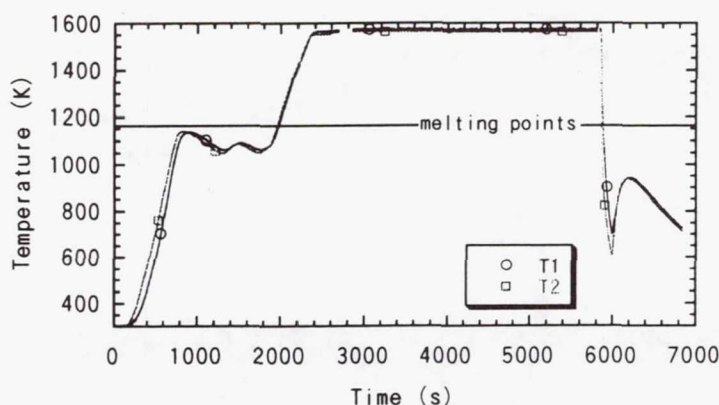


Fig. 3 Temperature hysteresis during the experiment at 1573 K

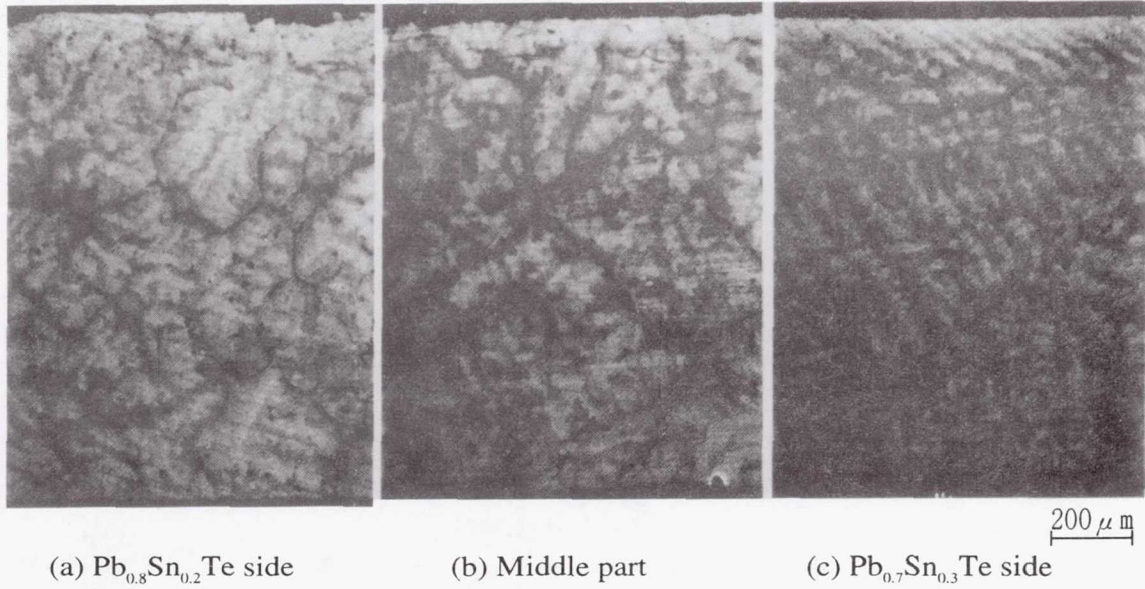


Fig. 4 Backscattered electron image of solidified samples after the MSL-1 experiment at 1223 K

Since the concentration profiles of Sn were measured at room temperature after solidification, we need to calculate the profiles of Sn at the diffusion temperature. For this purpose were taken into account the volume change on melting, volume shrinkage, etc. Then we evaluated the diffusion coefficient from the corrected profiles of Sn concentration.

The diffusion occurred not only while the samples were kept at the diffusion temperature, but also while they were heated up and cooled down. In the experiments at lower temperature than 1473 K, the holding time for the diffusion temperature was long enough to be able to neglect the diffusion during heating and cooling period. But in the experiment at 1673 K, we need to calculate the diffusion coefficient including the effect of the temperature change. We can employ an analytical solution with the effective time, t_{eff} , instead of the holding time. The effective time, t_{eff} , is defined as follows [7].

$$t_{eff} = \frac{1}{D_{keep}} \int_{T_m}^{T_{keep}} \frac{D(T)}{\left(\frac{dT}{dt}\right)} dT + t_{keep} + \frac{1}{D_{keep}} \int_{T_{keep}}^{T_m} \frac{D(T)}{\left(\frac{dT}{dt}\right)} dT \quad (2)$$

where D_{keep} is the diffusion coefficient at the diffusion temperature, T_{keep} , and t_{keep} is the holding time at the diffusion temperature. T_m is the melting temperature, 1163 K.

We assume that the diffusion coefficient is in proportion to the n th power of the absolute temperature.

$$D = A(T/T_m)^n \quad (A \text{ and } n \text{ are constants}) \quad (3)$$

The solution of Fick's second law for the diffusion couple considered here is

$$c(x,t) = \frac{c_2 - c_1}{2} \left[1 - \operatorname{erf} \left(\frac{x}{2\sqrt{D_{keep} t_{eff}}} \right) \right] + c_1 \quad (4)$$

where c_1 and c_2 are the initial Sn concentrations on one side and another side of the diffusion couple, respectively.

We calculated temperature dependence of the diffusion coefficient from the concentration profiles of MSL-1 experiments at 1273 K, 1273 K, 1373 K, 1473 K and 1573 K, and from those of the TEXUS rocket experiment at 1227 K and TR-1A rocket experiment at 1277 K. For the MSL-1 experiment at 1573 K and two rocket experiments, the diffusion coefficients were calculated from temperature hysteresis and concentration distributions of the three experiments using the iteration method [9] for above equations. First the temperature dependence was calculated from the diffusion coefficients of the MSL-1 experiments at lower temperature than 1473 K. Then the diffusion coefficient was calculated with the equation (2), (4) and (3) with the temperature dependence for the MSL-1 experiments at 1573 K and two rocket experiments. Next the temperature dependence was calculated with the all of diffusion coefficients and the constants A and n in equation (3) was determined. With the calculated temperature dependence, we obtained the diffusion coefficient for each experiment again. The calculation was 'iterated' until the solutions converged.

Fig.5 shows typical concentration profiles of Sn and calculated curves. The temperature dependence was calculated as $(6.7 \times 10^{-9} \text{ m}^2/\text{s}) \times (T/T_m)^{2.6}$ (T_m is the melting temperature) as shown in Fig.6. The diffusion coefficient at the melting temperature, $6.7 \times 10^{-9} \text{ m}^2/\text{s}$ was a little larger than the results of Kinoshita et. al., in which the diffusion coefficient was estimated from the distribution of Sn atoms for frozen sample after stopping the crystal growth[2].

The more direct method for the measurement of diffusion was performed by Clark, et. al.[3]. They measured the concentration dependence of diffusion coefficient at 1213 K and obtained $7.4 \times 10^{-9} \text{ m}^2/\text{s}$ for $\text{Pb}_{0.8}\text{Sn}_{0.2}\text{Te}$ even though the scatter at the interface was large. The value from the MSL-1 experiments at 1213 K is $7.5 \times 10^{-9} \text{ m}^2/\text{s}$, and was almost the same value as Clark et al. obtained. In this MSL-1 mission, the diffusion coefficient for lead-tin-telluride was determined accurately in the wide temperature range.

CONCLUSIONS

The diffusion experiments for liquid lead-tin-telluride were carried out in MSL-1 mission with controlling the cooling condition. The Sn concentration profiles were analyzed considering the influence of the diffusion during heating and cooling process. The temperature dependence was determined from the results of MSL-1 experiments and of the rocket experiments as $(6.7 \times 10^{-9} \text{ m}^2/\text{s}) \times (T/T_m)^{2.6}$ (T_m is the melting emperature).

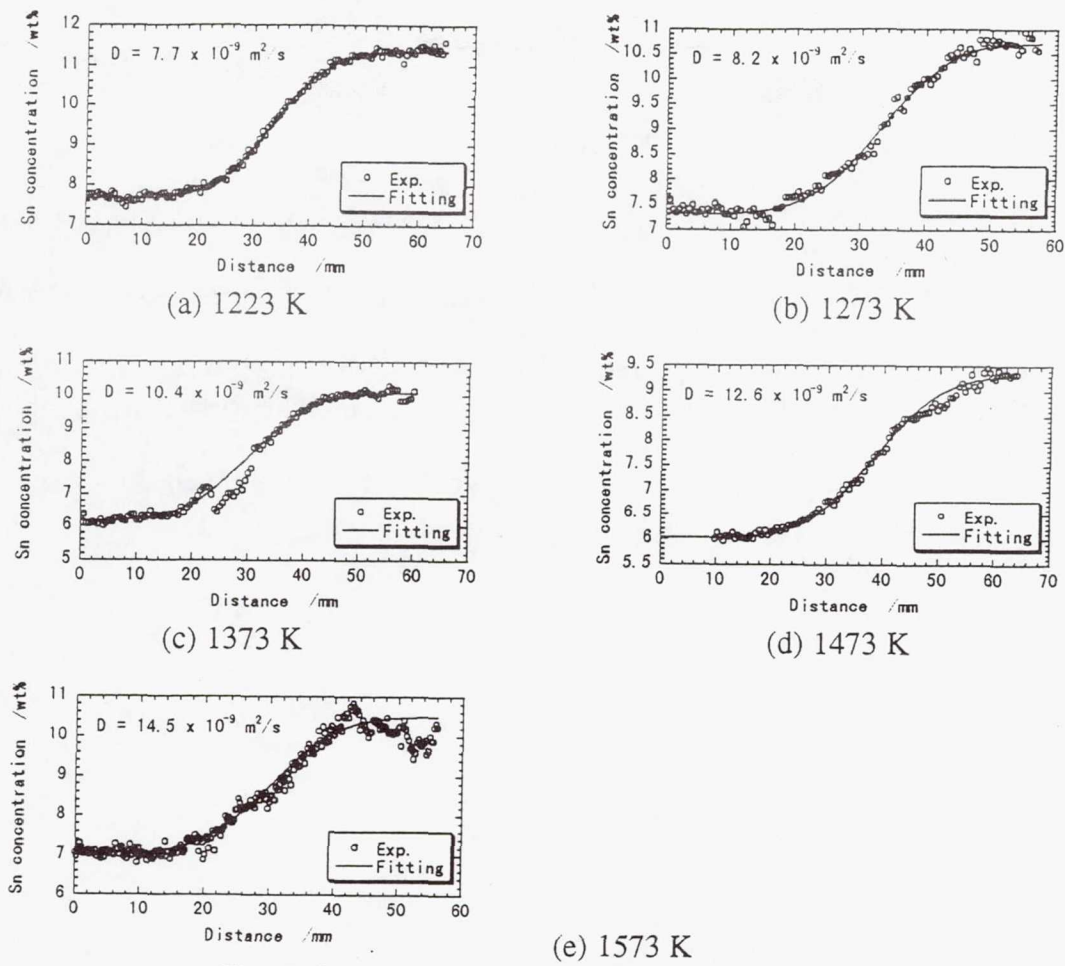


Fig. 5 Sn concentration distribution after MSL-1 experiments

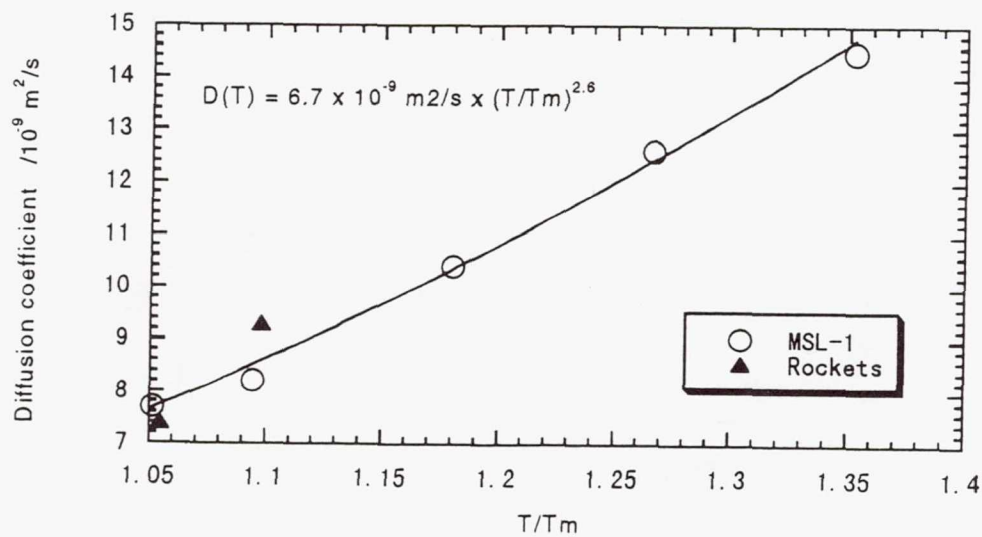


Fig. 6 Calculated temperature dependence of diffusion coefficient

REFERENCES

- [1] W. A. Tiller, K. A. Jackson, J. W. Rutter and R. Chalmers, *Acta Met.* 1 (1953), p. 428
- [2] T. Kinoshita and K. Sugii, *J. Crystal Growth* 67 (1984), pp. 375-379
- [3] I. O. Clark, A. L. Fripp, W. J. Debnam, Jr., R. Crouch and W. D. Brewer, *J. Electrochem. Soc.* 130 (1983), pp. 164 - 167
- [4] G. Froberg, K. H. Kraatz and H. Wever, *Proc. of the Norderney Symposium on Scientific Results of German Spacelab Mission D1* (1986)
- [5] M. Uchida, M. Kaneko, T. Horitomi and Y. G. Nakagawa, *Proc. of Diffusion in Materials DIMAT-92* (1992), pp. 1007 - 1012
- [6] M. Katayama, M. Kaneko, T. Sato and Y. G. Nakagawa, *Proc. of the Ninth International Conference on Crystal Growth* (1989), p. 181
- [7] M. Uchida et. al., *J. Jpn. Soc. Microgravity Appl.* Vol. 14, No. 1 (1997) pp. 42-47
- [8] M. Uchida et. al., *Proc. of the 9th International Symposium on Experimental Methods for Microgravity Materials Science*
- [9] T. Itami, et. al., *J. Jpn. Soc. Microgravity Appl.* Vol. 14, No. 4 (1997) pp. 323-330

*omit THIS
PAGE*

Large Isothermal Furnace (LIF)

Impurity Diffusion in Ionic Melts

Principal Investigator:

Dr. Tsutomu Yamamura
Tohoku University
Sendai, Japan

Measurements of Impurity Diffusion Coefficients in Ionic Melts
with High Accuracy under Microgravity

T. Yamamura, S. Yoda, T. Ohida and M. Masaki

SINGLE SCAN

58-26

434845

362358 51

(1) Abstract

In order to determine the impurity (tracer) diffusion coefficients in high temperature melts accurately, the diffusion coefficients of silver ions in the eutectic LiCl-KCl melt was measured by a chronopotentiometric technique under microgravity so as to avoid the natural convection, which has been widely considered as the important source of errors accompanying diffusion coefficient measurements on the ground. The results obtained have been analysed to elucidate the accuracy of the measurements, and the accurate diffusion coefficients of silver ion in the eutectic LiCl-KCl melt have been derived over the temperature range of 640 and 860K.

(2) Objective

Present study aims to determine the impurity(tracer)diffusion coefficients in molten salts accurately by the use of the microgravity so as to avoid the effects of the convective flow in liquids. A typically ionic eutectic LiCl-KCl melt was chosen as the solvent. This melt has been widely used as an ionic solvent for the electrochemical study and engineering. Silver ion was chosen as the tracer. The chronopotentiometry was adopted for the measurement of the impurity diffusion coefficients, because this method had been considered as the most suitable for attaining appropriate boundary conditions and for remote science. The results obtained have been analyzed to elucidate the relative importance of the sources of errors to establish the precise diffusion coefficients of silver ion in the eutectic LiCl-KCl melt.

(3) Background

Diffusion coefficients of high temperature melts are indispensable for the analysis of the high temperature processes such as the crystal growth from the melts as well as the test of the liquid theories. But, it is widely known that the discrepancies found among the literature values of diffusion coefficients of high temperature melts are enormous. While details of the origins of the discrepancy have not been elucidated, it has been pointed out that the effects of the thermally induced natural convection would be the most significant as the error sources. Therefore, the measurements under microgravity, in which case the effects of the convection could be avoided, would produce accurate results.

(4) Method of data acquisition and analysis

The impurity diffusion coefficients of silver ions have been determined by the chronopotentiometry. A trace amount of silver chloride was added into the eutectic LiCl-KCl solvent. The electrochemical cell consists of the three electrodes such as working, reference and counter electrodes as shown in Fig.1.

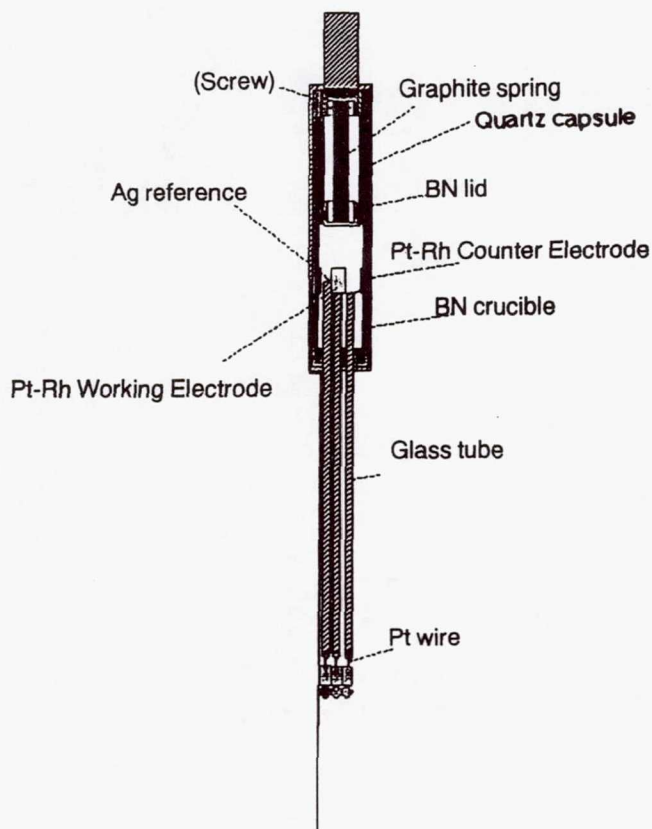


Fig.1 Electrochemical Cell for Chronopotentiometry

A constant current is applied between the working and counter electrodes, and the chronological change in the potential of the working electrode relative to the reference electrode is observed. A typical potential-time curve is shown in Fig.2. The potential rises sharply to the negative direction, then stays for a while and rises again sharply. The period while the potential stays is called the transition time. During this period all of the current is carried by the diffusion of the silver ions. If the current is limited by the diffusion of the electrochemically active ions, in this case silver ions, transition time τ and current i satisfies the following relation.

$$i \tau^{1/2} / C = n F D^{1/2} \pi^{1/2} / 2 \quad (1)$$

where C and D are content and diffusion coefficient of silver ions, respectively.

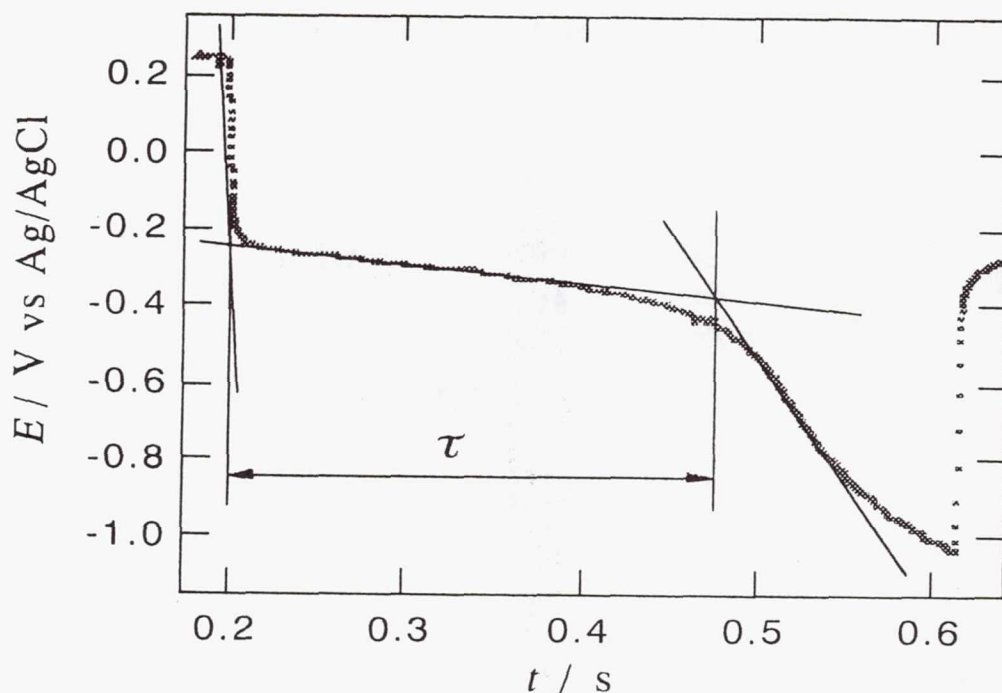


Fig.2 A typical Chronopotentiogram of Ag^+ in Molten LiCl-KCl on Pt Electrode. $i=573 \text{ Am}^{-2}$, $T=765\text{K}$.

the diffusion coefficient of the tracer can be determined from the transition time observed by eq.(1). But, when we do the experiment on the ground, the natural convection disturbs the diffusion limited boundary conditions. Particularly, when the current is small, this means the diffusion layer extends long, the relation expressed by the eq.(1) fails. This phenomena are usually observed in the ground experiments. But in the microgravity experiments, the relation of eq.(1) would hold even at the small current region, because the effect of the convection would be suppressed, and the precise measurement of diffusion coefficient is expected.

(6) Flight results compared with ground results

To see the effects of the natural convection flow on the determination of the diffusion coefficients, the current dependence of the transition time constant $i \tau^{1/2}$ was examined for both microgravity and ground experiments. Figures 3 and 4 show the results of the microgravity and ground experiments, respectively. As clearly shown in Fig.3, the curve for 640K stays constant as low as $60/(\text{Am}^{-2})$. On the other hand, as shown in Fig.4, the transition time constant starts to increase with decreasing current at the current less than $160/(\text{Am}^{-2})$. These results show the more accurate and precise

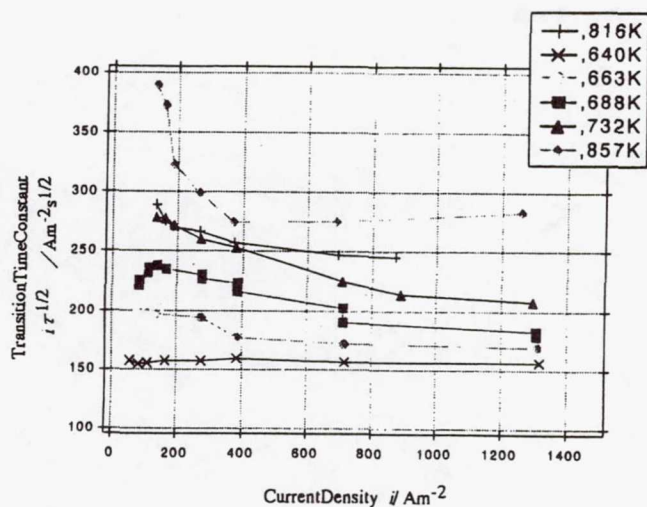


Fig.3 Relation between Current Density and Transition Time Constant for ION1

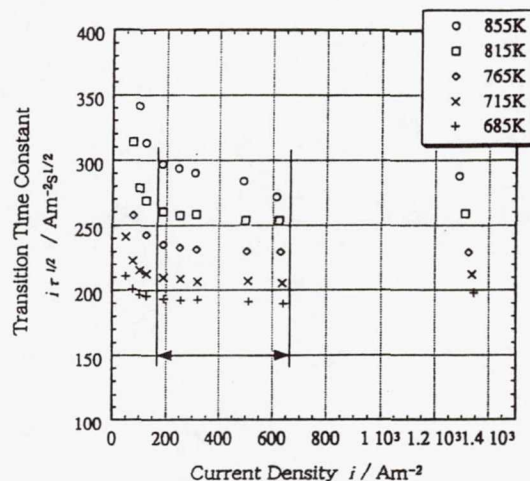


Fig. 4 Relation between Current Density and Transition Time Constant on Pt Plate Electrode.

determination can be attained under microgravity.

As shown in Fig.3, the transition time constant taken at 857K starts to increase at $380/(\text{Am}^{-2})$ with decreasing current. The surface of the electrodes were inspected by a scanning electron microscope. The observation revealed that the electrode surfaces were rough. This was due to repeated usage of working electrode. Therefore, the measurements done at early stage provide more accurate results than taken at the last stage. At each run, the current was reversed to recover the after effects, but after repetition of the experimental runs, the recovery became incomplete, and deposited silver stayed on the electrode surface.

The logarithm of diffusion coefficients determined are plotted against inverse temperature in Fig.5. There found a linear relation at the temperature range observed within experimental error. In the figure, the literature values and authors' data taken by the ground experiments have been compared. Although there are large difference among the literature values, present results agrees with the values reported by Poignet and Barbier[1], and the data taken by ground experiments by the authors group.

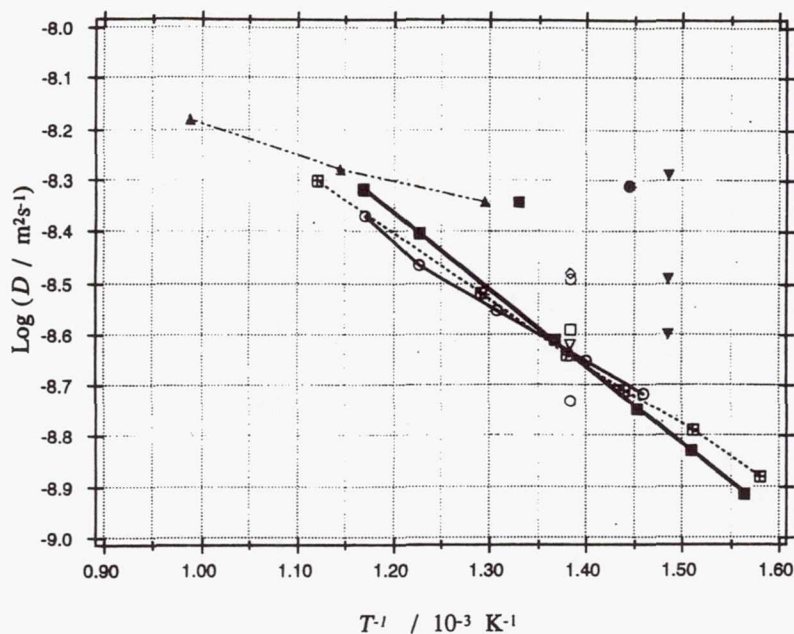
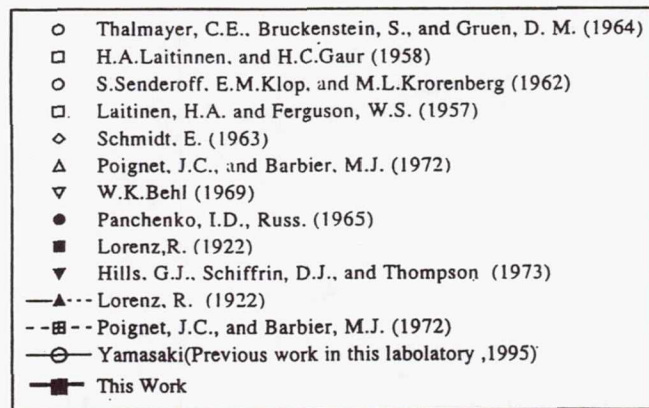


Fig.5 Relation between diffusion coefficient and temperature



figure, the literature values and authors' data taken by the ground experiments have been compared. Although there are large difference among the literature values, present results agrees with the values reported by Poignet and Barbier[1], and the data taken by ground experiments by the authors group.

(7)Reference

[1] Poignet, J.C. and Barbier, M.J., *Electrochim.Acta*,17(1972),1227.

59-76
434846

Large Isothermal Furnace (LIF)

362 359

8p.

Measurement of Diffusion Coefficient by Shear Cell Method

Principal Investigator:

Dr. Shinichi Yoda
NASDA
Tsukuba, Japan

Measurement of Diffusion coefficient by Shear Cell method

Shin-ichi Yoda, Tadahiko Masaki, Hirohisa Oda
National Space Development Agency of Japan

Abstract

Diffusion coefficient is necessary to decide most suitable condition for crystal growth, but diffusion coefficient can not be measured accurately because of thermal convection on the ground. Shear cell method which is modified from long capillary method was used for measurement of diffusion coefficient of tin and lead-tin-telluride in this investigation. Diffusion coefficient of tin at 1000°C was found to be $1.8 \times 10^{-4} \text{ cm}^2/\text{s}$ from flight experiment result which was performed in MSL-1 mission. Result of lead-tin-telluride varied widely because of crystal segregation.

1. Background and Objective

Diffusion coefficient is a fundamental property, and it is necessary to decide most suitable parameter for crystal growth. So far, diffusion coefficient was measured for many kind of material. But, thermal convection occur on ground, so Long capillary method is used to avoid this disturbance. Diffusion coefficient of tin was measured under micro-gravity environment in D-1 project by Froberg, and it was found that diffusion coefficient under micro-gravity environment indicate 20~30% lower than under 1-g environment. This result indicate that measurement of

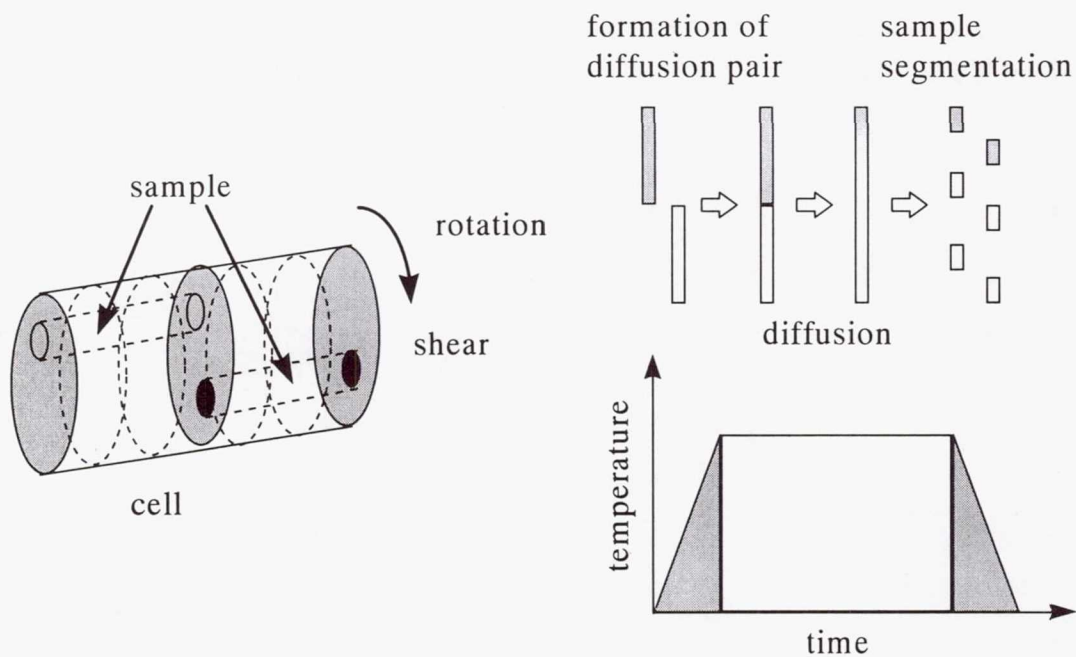


Fig.1 Concept of Shear cell method

diffusion coefficient is suffered effect of thermal convection, even if that measurement method is most suitable on ground. So, importance of measurement of diffusion coefficient under micro-gravity was recognized by this result.

Long capillary method is widely used because that method is convenience. In this method, two materials which have different concentration are joined, diffusion will start by melt of material, diffusion coefficient is measured from concentration distribution of that material. But this method has a following fault. Diffusion coefficient is depended on temperature, so diffusion must progress in a fixed temperature to make clear that dependency. But, diffusion progress when material melt in this method. So, Long capillary method has a fault that diffusion progress in heating and cooling region.

Shear cell method was invented to overcome this fault. Concept of shear cell is indicated to Fig.1. In this method, samples are not joined before melting, and are joined when temperature get target value. Diffusion progress in certain time, and sample is divided to several small segments by rotating shear cell before cooling. So, diffusion in heating and cooling region is prevented in this method. High accurate measurement of diffusion coefficient is expected by shear cell method. But shear cell method has not been used widely so far, because of problems as following. First one is that shear cell has complicated structure. Second one is that convection will occur by rotating of shear cell, and this convection will disturb concentration distribution in sample. So object of this investigation is development of high accurate measurement of diffusion coefficient by shear cell method under micro-gravity environment.

2.Experimental method

This experiment was performed in MSL-1 (First Material Science Laboratory), LIF (Large Isothermal Furnace) was used for this experiment. Tin and lead-tin-telluride are used for experiment sample. Size of experiment sample is indicated in Table 1. Two samples were set in one cartridge. Fig.2 shows a configuration of shear cell cartridge. BN (Boron Nitride) was used for material of shear cell. This reason is that BN has excellent mechanical and lubricant property in high temperature.

Table 1. Dimension of experiment sample

sample	composition	diameter/mm	length/mm
tin	tin isotope ^{124}Sn	2	4
	natural tin	2	56
lead-tin-telluride	$\text{Pb}_{0.7}\text{Sn}_{0.3}\text{Te}$	2	30
	$\text{Pb}_{0.8}\text{Sn}_{0.2}\text{Te}$	2	30

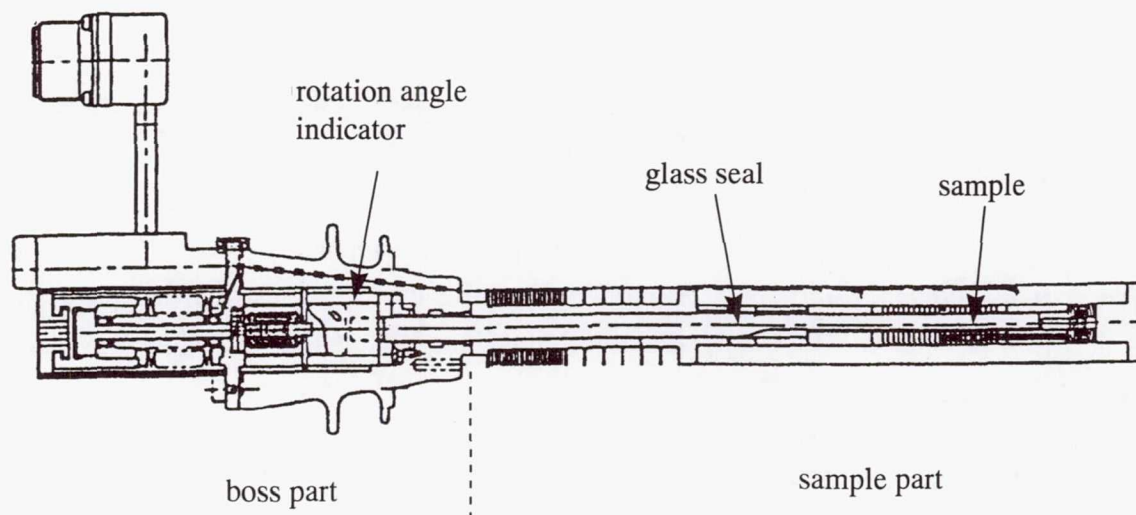


Fig.2 Configuration of shear cell cartridge

Lead-tin-telluride has a high vapor pressure. So, following problem was occurred in ground experiment, that almost all lead-tin-telluride sample was vaporized in experiment temperature and deposited on lower temperature part in cartridge. So, helium gas is enclosed in cartridge to decrease this evaporation. And glass seal is also used to prevent this evaporation. This glass seal prevent a transfer of vaporized sample from high temperature part to low temperature part. And necessity of glass is that there is a rotation axis in cartridge to transmit rotation power, and seal must not disturb this rotation power.

And indicator of rotating angle is also set to measure rotation angle of rotation axis in the end of cartridge boss part. This reason is as following. Rotated angle of handle from outside cartridge is not always consist with the real rotated angle of shear cell, because rotate movement is changed into linear movement in cartridge boss part.

Table 2 shows experiment condition of each experiment sample. Rotation of shear cell was performed using handle which was operated by crew. Cartridge was resolved after flight experiment, and cutting statement of sample was confirmed, and rotation angle of shear cell was measured. After that, sample weight was measured and amount of evaporation was calculated. Then experiment sample was re-heated on ground and concentration in each cell was unified to measure average concentration in each cell. This re-heating condition was 500°C and 1 hour for tin, and 950°C and 1 minute for lead-tin-telluride. Concentration of these samples was measured by SIMS (Secondary Ion Mass Spectrometry) and ICP (Inductively Coupled Plasma mass spectrometry) for tin, and EPMA (Electron Probe Micro Analyzer) for lead-tin-telluride.

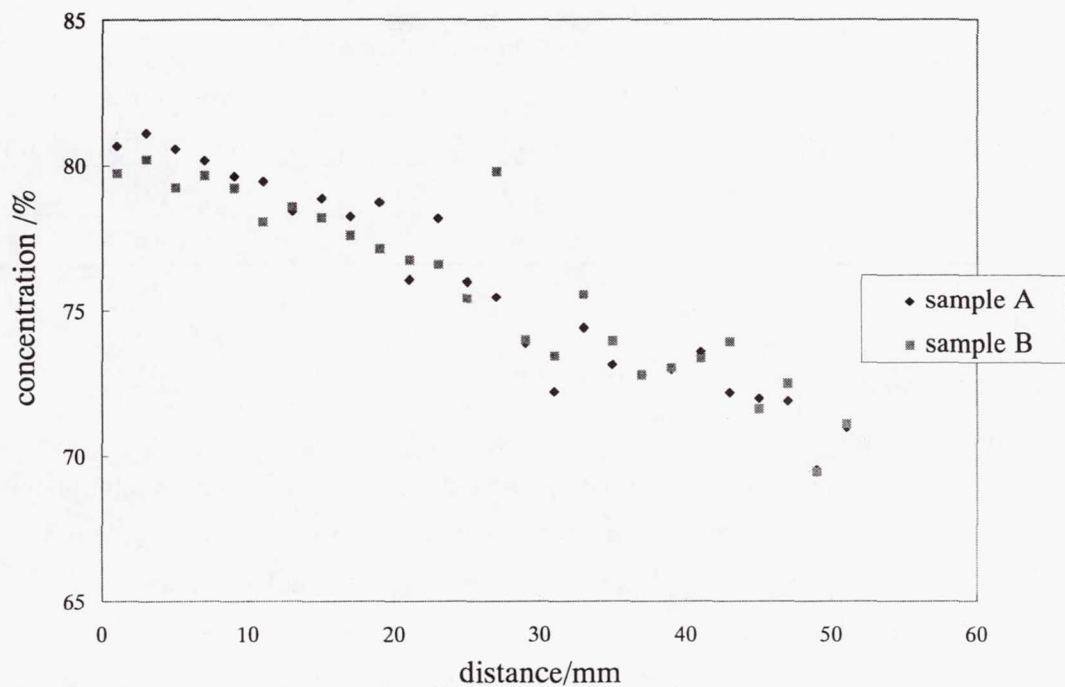


Fig.3-1 Result of concentration measurement (Pb)

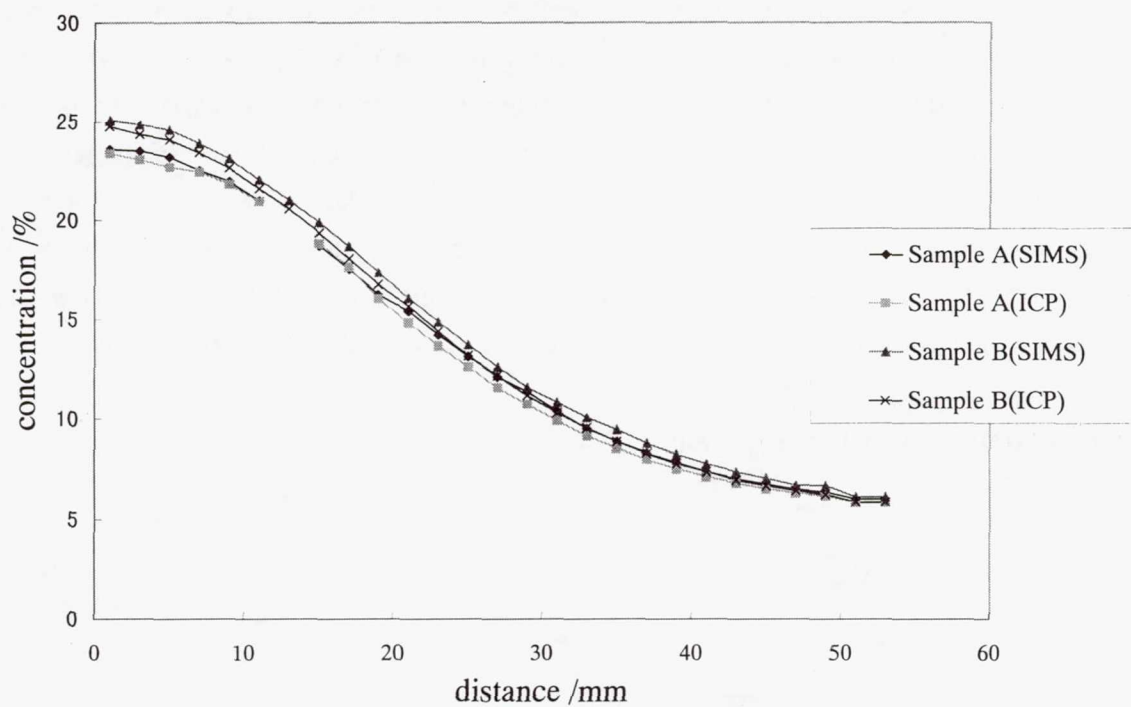


Fig.3-2 Result of concentration measurement (tin)

Fig.3 shows the results of concentration profile. Measurement results was varied widely in

Table 2. Experiment condition

sample	experiment temperature /°C	diffusion time /min
tin	1000	170
	1349	140
lead-tin-telluride	950	65

3.Results and Discussion

3.1.Inspection of sample

Cutting statement of sample was investigated, and cutting was not performed completely for tin sample (1000°C). Rotation angle of rotation axis was measured from rotation angle indicator, and that was found to be 31 degree. This rotation angle was normal, so reason of failure was presumed as following. Shear cell itself did not rotate as expected because a gap between shear cell and rotation axis was larger than expected value, although rotation axis itself rotated normally.

Evaporation rate of lead-tin-telluride sample was 20% in flight experiment, on the other hand evaporation rate was 4% on ground experiment, so evaporation rate in flight experiment was higher than that of ground experiment. It was found that glass seal worked well and almost all vaporized sample deposited on inner wall of cartridge. So, reason of this evaporation is presumed as following. Evaporation of sample will occur in cooling step of experiment. In flight experiment, cooling is dominated by radiation and conduction from outer wall of cartridge. So outer wall of cartridge become relatively low temperature in cartridge, then sample trends to deposit. On the other hand, in ground experiment temperature in cartridge is unified by thermal convection of helium gas which is enclosed in cartridge, then sample does not trend to deposit.

3.2.Calculation of diffusion coefficient

lead-tin-telluride. This reason is as following. Lead-tin-telluride has an inclination to generate crystal segregation at solidification, so concentration of sample vary widely. So more measurement point is required to decide concentration of this sample accurately.

Measurement result of tin did not vary widely compared with that of lead-tin-telluride. Diffusion coefficient was calculated from this concentration profile. Fick's second law was used to calculate diffusion coefficient, experiment result was fitted to decide most suitable value. Diffusion coefficient was $1.8 \times 10^{-4} \text{cm}^2/\text{s}$ from this calculation. Fig.4 shows the comparison between this result and usual results. Fig.4 indicate that this result is well consist with Frohberg's result which was performed in D-1 mission. Many models about temperature dependency of diffusion coefficient was suggested second power law about temperature dependency of diffusion coefficient. This result supports Frohberg's suggestion. More investigation about modeling of diffusion mechanism which is based on this result is needed in the future.

4. Conclusion

Diffusion coefficient measurement experiment using shear cell method about tin (experiment temperature 1000°C , 1349°C) and lead-tin-telluride (experiment temperature 950°C) was performed in MSL-1 mission.

(1) tin (1000°C)

Cutting sample was not performed completely. This reason is presumed that a gap between shear cell and rotation axis was larger than expected value.

(2) tin (1349°C)

Cutting of sample was performed completely, and normal concentration profile was got. Diffusion coefficient was found to be $1.8 \times 10^{-4} \text{cm}^2/\text{s}$ from concentration profile. This value is well consist with Frohberg's results, and supports their suggestion about temperature dependency of diffusion coefficient.

(3) lead-tin-telluride (950°C)

Cutting of sample was performed completely. Measurement results of concentration varied widely because of crystal segregation at solidification and lack of measurement points. More measurement is required to determine diffusion coefficient.

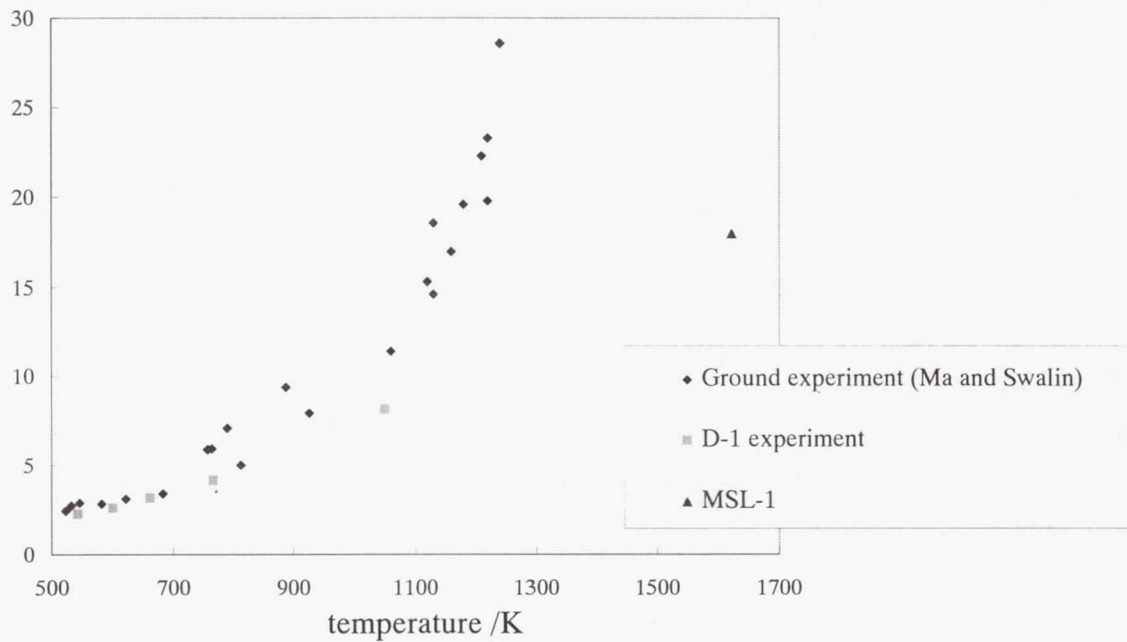


Fig.4 Comparison between this result and usual results

OP 159
THIS
PAGE

Large Isothermal Furnace (LIF)

Liquid Phase Sintering II (LPS-2)

Principal Investigator:

Dr. Randall M. German
Pennsylvania State University
University Park, Pennsylvania

Gravitational Role in Liquid Phase Sintering

Anish Upadhyaya,* Ronald G. Iacocca,** and Randall M. German***

* Director, Materials Development
** Director, Materials Characterization
*** Brush Chair Professor in Materials

P/M Lab, 118 Research West
The Pennsylvania State University
University Park, PA 16802-6809

Abstract

To comprehensively understand the gravitational effects on the evolution of both the microstructure and the macrostructure during liquid phase sintering, W-Ni-Fe alloys with W content varying from 35 to 98 wt.% were sintered in microgravity. Compositions that slump during ground-based sintering also distort when sintered under microgravity. In ground-based sintering, low solid content alloys distort with a typical elephant-foot profile, while in microgravity, the compacts tend to spheroidize. This study shows that microstructural segregation occurs in both ground-based as well as microgravity sintering. In ground-based experiments, because of the density difference between the solid and the liquid phase, the solid content increases from top to the bottom of the sample. In microgravity, the solid content increases from periphery to the center of the samples. This study also shows that the pores during microgravity sintering act as a stable phase and attain anomalous shapes.

Introduction

Liquid phase sintering (LPS) is a common process for the fabrication of dense, net-shape structures. Despite extensive industrial use, several processing difficulties trace to gravity. One easily recognized problem is solid-liquid separation. Like sand settling in water, differences in densities between the solid and liquid phases induce microstructure and compositional segregation. Consequently, only alloys with small quantities of liquid are fabricated on Earth. The tungsten heavy alloys (W-Ni-Fe or W-Ni-Cu) are particularly sensitive to gravitational effects since the liquid-solid density difference is nearly 9 g/cm^3 . In this research, we have documented that after sintering on Earth there is a significant gradient in grain coordination number, grain size, grain shape, and solid phase contiguity with the position in the compact. Further, there is a slight difference in grain size due to the compressive stresses during Earth-based sintering. Grain coalescence occurs at gravity induced contacts, giving gradients from the stress in the microstructure due to gravity. It was on the basis of these observations that microgravity and parallel ground-based experiments were performed.

Gravity effects are evident at the macroscale as compact distortion. An excess of liquid causes shape loss, with the formation of the elephant foot geometry or even puddles of solid-liquid. The factors causing distortion in LPS are not understood.

Previous work suggested that it was simply due to the solid-liquid ratio; however, experiments have produced compacts with more than 60 vol.% liquid that retain shape. Compositions that slump on Earth also distorted in microgravity, but in the latter case they spheroidized. Our analysis and modeling efforts now explain distortion during sintering (from both gravitational and surface tension stresses, thus is applicable to both ground-based and microgravity samples) as arising from three features - solid-liquid ratio, dihedral angle, and solubility change when the liquid forms.

Microgravity LPS experiments have been performed in recent years, and the Penn State research team was involved in analysis of samples from flights starting in 1992 (SLJ, IML-2, MSL-1, and MSL-1R). Each investigator has adopted different questions, compositions, and sample preparation techniques. Although each study provides insight, a unified view is missing. Therefore, one goal of the research was to perform cross-study experiments where these various alloys will be processed under similar conditions. This showed the lack of care in prior sample preparation greatly affected the findings and compromised final conclusions. Further, reports from ground-based experiments often proved inadequate to fully document sintering and microstructure findings. One success was the stability of the Large Isothermal Furnace and the support hardware. No malfunction of the flight hardware directly involved in the liquid phase sintering experiments was encountered in microgravity. In this regard, the original plan to use microgravity experiments to isolate gravitational effects on microstructure evolution during liquid phase sintering was very successful. The contrast and comparison of ground-based and microgravity samples, processed from the same powders, in the same furnace, using the same cycles provided the needed separation of variables. Modeling efforts conducted in parallel with the experiments provide a basis for assessing current understanding. The initial phase of the microgravity research was focused on variations in sintering time and solid content using W-Ni-Fe compositions with a constant Ni:Fe ratio of 7:3, but varying W content from 35 to 98%. With improved understanding of the LPS system, we were successful in extending the flight samples to new composition regions with high liquid contents.

Experimental Procedure

Table I summarizes the compositions W-Ni-Fe and W-Ni-Cu alloys used for this investigation. The tungsten heavy alloy samples were cold isostatically pressed, presintered, and then dry-machined in the form of cylindrical pellets of height and diameter 8.29 ± 0.02 mm. The dimensions were so chosen that in case of subsequent sintering performed under microgravity, the compact should not have any constraint on spheroidization. The machined samples were placed in individual alumina crucibles. Samples were grouped in sets of seven, as they had to be sintered under identical conditions. The crucibles were so designated that the bottom of one acted as the top of other. Each set of seven crucibles (with sample in it) were then placed in a BN cartridge tube which was then sealed with a screw cap. The BN ampoule was enclosed in a triple layered Ta tubing. The inner surface of each Ta containment tube is coated with a thin layer of alumina to protect the Ta from attacks by vapors from the sample. All Ta containers were evacuated and sealed using electron beam welding.

Table I. Summary of the compositions used for the MSL-1 experiments.

Cartridge One, 1 min at 1500°C

Cartridge Three, 180 min at 1500°C

Cartridge Four, 600 min at 1500°C

sample number	composition, wt%
1	78W-15.4Ni-6.6Fe
2	65W-24.5Ni-10.5Fe
3	50W-35Ni-15Fe
4	35W-45.5Ni-19.5Fe
5	88W-9.6Ni-2.4Cu
6	88W-7.2Ni-4.8Cu
7	50W-30Ni-20Cu

Cartridge Two, 45 min at 1500°C

sample number	composition, wt%
1	78W-15.4Ni-6.6Fe
2	50W-40Ni-10Cu
3	50W-35Ni-15Fe
4	35W-45.5Ni-19.5Fe
5	88W-9.6Ni-2.4Cu
6	88W-7.2Ni-4.8Cu
7	50W-30Ni-20Cu

Cartridge Five, 120 min at 1500°C

sample number	composition, wt%	preparation
1	78W-15.4Ni-6.6Fe	hot isostatic pressed
2	78W-15.4Ni-6.6Fe	argon presinter
3	78W-15.4Ni-6.6Fe	green cold isostatic pressed
4	78W-15.4Ni-6.6Fe	hydrogen presinter
5	93W-4.9Ni-2.1Fe	green die pressed
6	78W-15.4Ni-6.6Fe	vacuum presinter
7	78W-15.4Ni-6.6Fe	liquid phase sintered

The presintered and machined W-Ni-Fe samples were liquid phase sintered at 1500°C for duration ranging from 1 to 600 min in a Large Isothermal Furnace (LIF)

supplied by Ishikawajima-Harima Heavy Industries Co. Ltd. (IHI) under a collaborative agreement with the National Space Development Agency of Japan (NASDA). Two sets of samples, each with five cartridges, were prepared. One set was for the microgravity experiments, while parallel ground-based experiments were conducted on the second set of samples.

The microgravity sintering experiments were performed aboard the space shuttle *Columbia* as a part of the Microgravity Space Lab 1 and 1R (STS 83 and STS94 missions, respectively) in April 1997 and July 1997. After the samples were sintered, the ground and flight samples were analyzed, and the results were documented in accordance with a well-established protocol. The sintered samples were then quantified using a coordinate measuring machine for distortion and were subsequently sectioned for metallography. The data obtained from these experiments, in combination with parallel Earth-based experiments, provided insight into the effects of gravity on both macrostructural and microstructural development.

Results

All the experiments were successfully completed and met scheduled timeline requirements. Figures 1a and 1b compare the distortion W-Ni-Fe alloys with different liquid volume fractions sintered in ground-based (1g) and microgravity (μg) for 120 min. Prior to sintering, the alloys were presintered at 1400°C for 1 h to nearly full density. Note that slumping decreases with increasing solid (tungsten) volume fraction. The 93W or 98 wt.% W did not slump. Samples containing less than 93 wt.% W distort during both 1g as well as μg sintering. An interesting point to note is that the composition that did not slump during ground-based (1g) sintering, retained their shapes even when sintered in μg .

Ideally, a high liquid content alloy when sintered in μg will try to minimize its energy by attaining a spherical shape. Figure 2a shows the photograph of a 78W-15.4-6.6Fe alloy liquid phase sintered at 1500°C in microgravity for 120 min. Prior to liquid phase sintering, the alloy was presintered at 1400°C for 1 h to 100% density in vacuum. During μg sintering, the cylindrical presintered sample underwent reshaping and completely spheroidized. Figure 2b shows the same composition sintered under unconstrained condition on Earth. Note that the alloy when sintered in 1g condition undergoes slumping and attains the characteristic elephant-foot profile. Figures 3a and 3b show the photographs from the periphery and the center region of the μg sintered 78W samples. Similarly, Figures 3c and 3d show the micrographs from the top and the bottom region of the 1g sintered 78W alloy. Evidently, the alloys sintered in both 1g and μg conditions show microstructural gradients. The degree of segregation, θ , in the microstructure was quantified using following expression:

$$\theta = \frac{X_p^{\max} - X_p^{\min}}{\sum_{i=1}^N X_p^i} N \quad (1)$$

where P is the locally measured mean attribute (e.g. grain size, solid content, connectivity, or contiguity), and R is the range of the measured variation, which is the difference between the maximum and the minimum numerical value for that attribute.

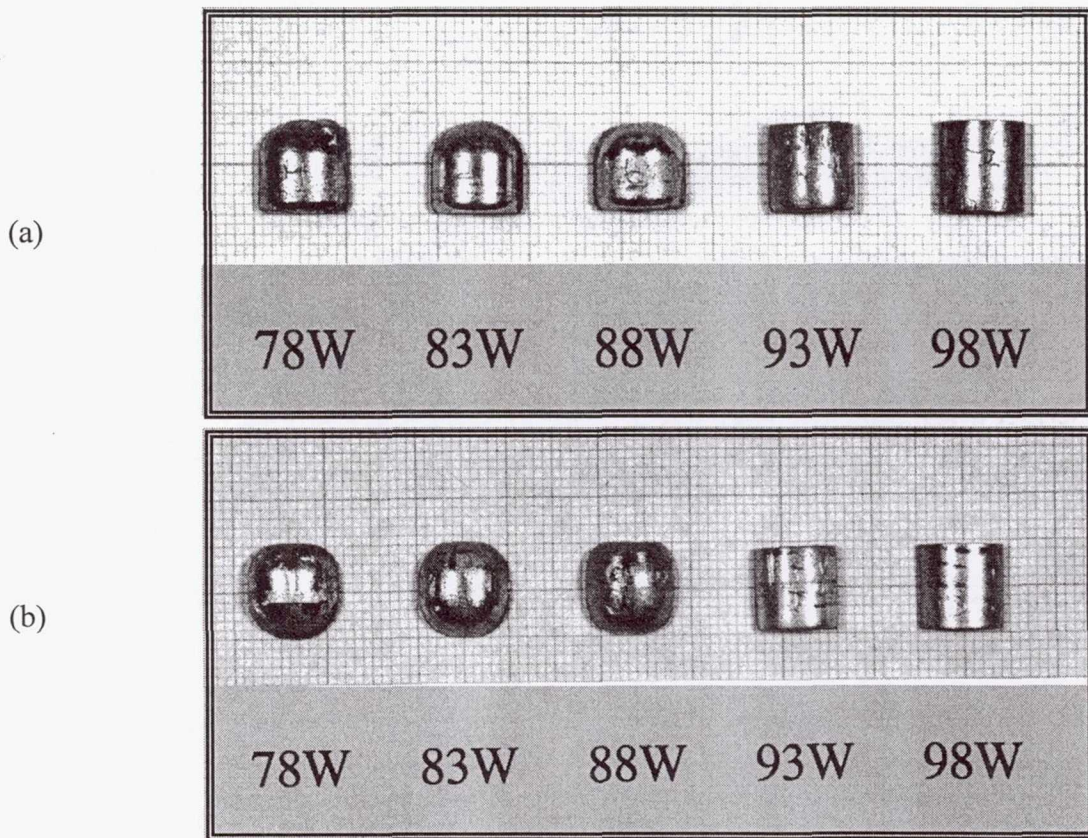
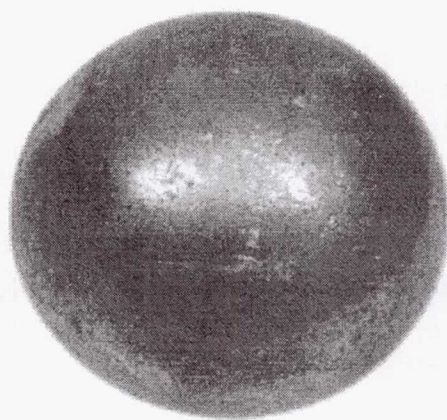
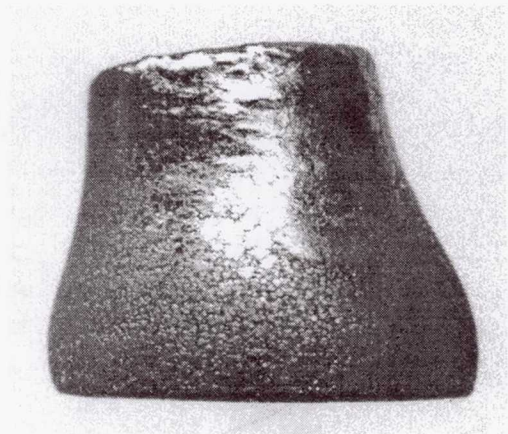


Figure 1. Photograph of W-Ni-Fe alloys with varying W content after liquid phase sintering at 1500°C for 120 min in (a) ground-based and (b) microgravity condition.



(a)



(b)

Figure 2. Shape distortion in 78W-15.4Ni-6.6Fe alloy liquid phase sintered at 1500°C for 120 min in (a) microgravity and (b) ground-based condition.

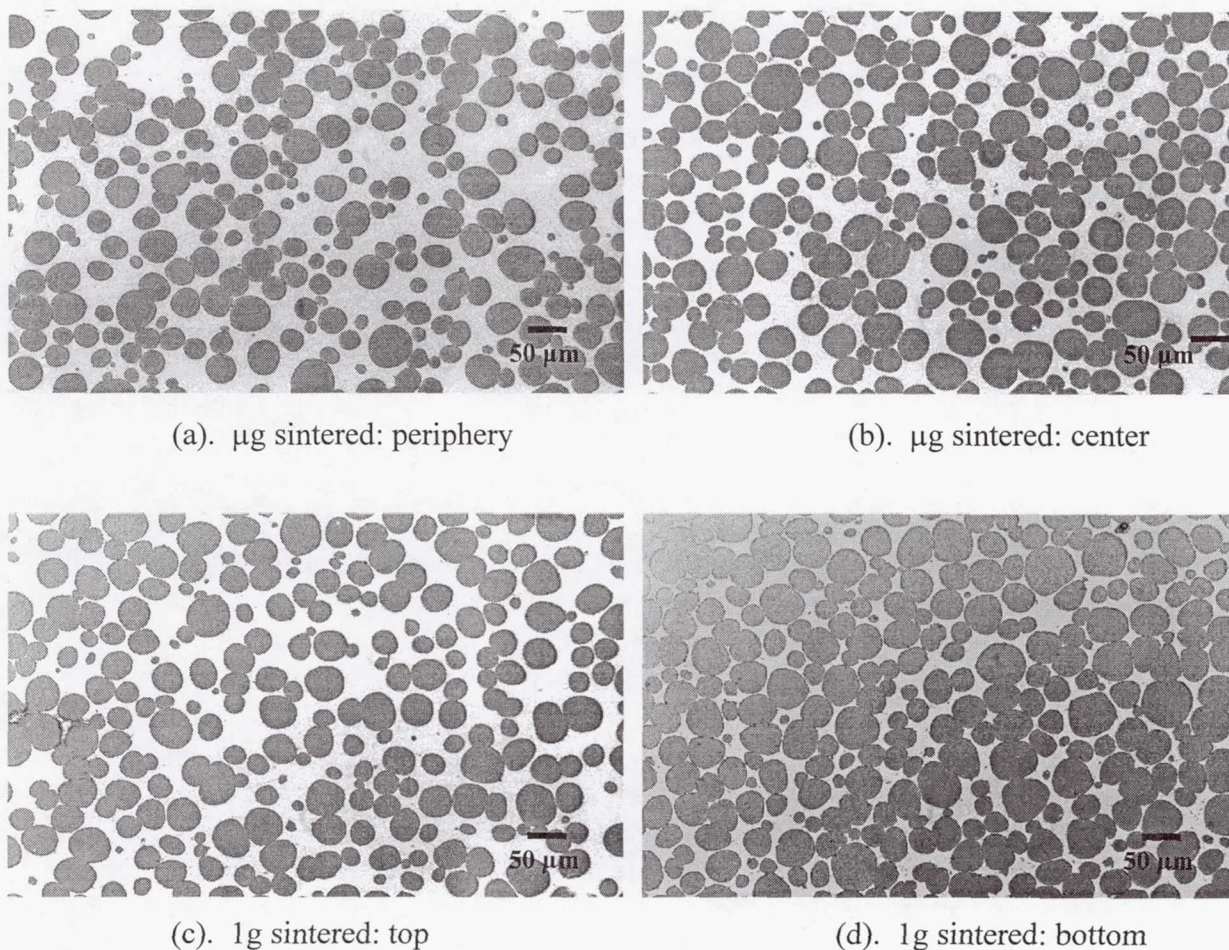


Figure 3. Optical micrographs showing microstructure at various regions of a 78W-15.4Ni-6.6Fe alloy sintered under microgravity (μg) and ground-based (1g) environment.

The range is normalized by the average value to yield a dimensionless measure of segregation.

The corresponding degree of segregation in the 1g and μg sintered 78W alloy- as calculated from Equation 1- is presented in Table II. An interesting fact that comes to light is that microstructural segregation is prevalent in both 1g and μg sintered alloys.

Under microgravity conditions, the pores proved unexpectedly stable and showed anomalous faceting and distorted morphologies. Figure 4a shows a spherical pore in a the center of a 78W alloy liquid phase sintered at 1500°C for 180 min. Figure 4b is an example of a an irregular dog-bone pore that is apparently pinned into a highly distorted shape by tungsten grains. Figures 4c and 4d are scanning electron micrographs showing several grains coalescing and entrapping liquid with a pore inside the grain loop. Figures 5a and 5b compare the pore location in a liquid phase sintered 78W alloy in ground-based and microgravity. Note that when sintered on Earth the pores are located at the top of the sample, where as in microgravity the pores are localized at the center of the sample.

Table II. Influence of gravity on the degree of microstructural segregation, θ , for 78W-15.4Ni-6.6Fe alloy liquid phase sintered at 1500°C for 120 min.

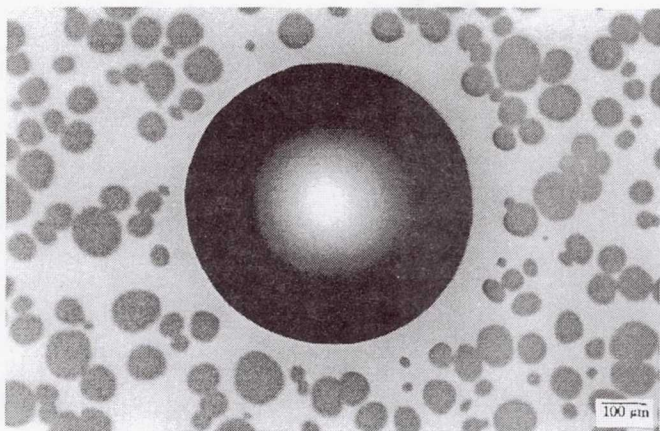
Property	Degree of Segregation, θ	
	ground-based	microgravity
solid content, V_s	0.35	0.47
grain size, \bar{G}	0.27	0.96
connectivity, C_g	0.75	0.62
contiguity, C_c	0.38	0.78

Discussion

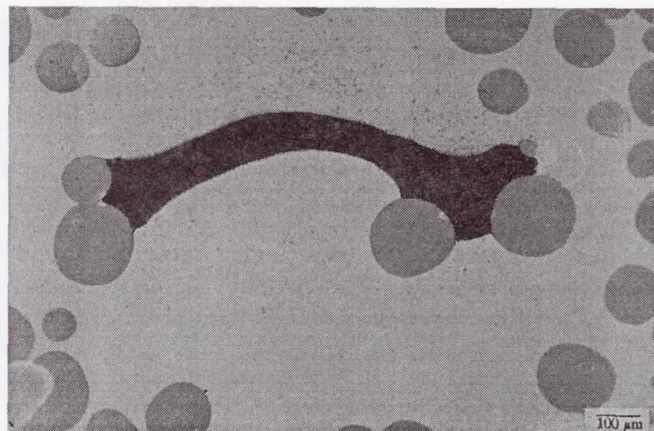
On comparing the macrostructure the W-Ni-Fe alloys sintered on Earth *versus* that sintered in microgravity, one finds that compositions that distort in 1g sintering undergo distortion when sintered in μg . However, the distorted shapes differ from each other. The low solid content (<60 vol.%) solid alloys attain a typical elephant-foot shape on Earth, whereas in microgravity, the compacts tend to reshape into a spheres. This suggests a link between the microstructural segregation and distortion. In systems with large density difference between the solid and the liquid phase, gravity-induced grain settling increases the packing coordination number at the bottom of the compact. A larger packing coordination number will subject the grains at the bottom to self-compressive stresses, which will cause accelerate slumping.

The microstructure of the ground-based sintered alloys show gradient in the microstructural attributes along the gravity vector. An intriguing feature however was the observance of microstructural segregation even under microgravity. For instance, in the spheroidized 78W-15.4Ni-6.6Fe alloy, the solid content, contiguity, grain size, and connectivity increased from the periphery to the center of the compact. The movement of solid grains in the solid-liquid mixtures can be induced by the shear stress as a result of reshaping event from cylinder to a sphere under the action of surface tension. This reshaping of the compacts from cylinder into a sphere indicates that viscous flow occurred even under the small surface tension forces that act on the samples during microgravity. Compact spheroidization results in the minimization of the gradients in these surface tension forces. Aside from this, the microstructural segregation in microgravity can also lead to spheroidization. The microstructure of the microgravity sintered W-Ni-Fe compact shows an increasing liquid content as we approach towards the periphery. A high liquid content at the periphery will in turn reduce the resistance to flow and promote reshaping and preferential deformation of the peripheral region. To explain microstructural segregation in microgravity, a model based on the total energy of the system has recently been proposed by us. The model calculations suggest that agglomeration and bonding lower system energy and are therefore energetically favored. Thus, a weak agglomeration tendency is inherent in liquid phase sintered systems.

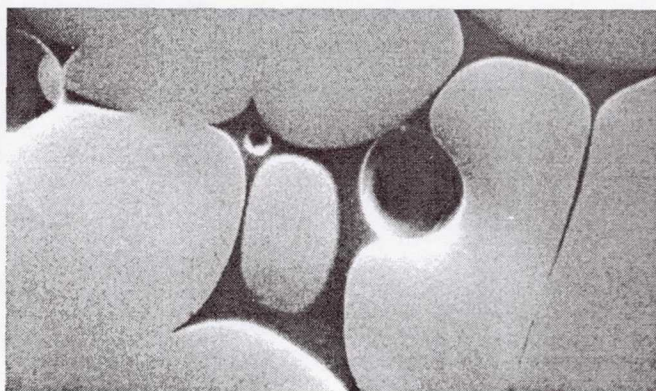
The microstructural examination of the liquid phase sintered W-Ni-Fe sample show a lack of pore buoyancy in microgravity conditions. The lack of buoyancy restricts



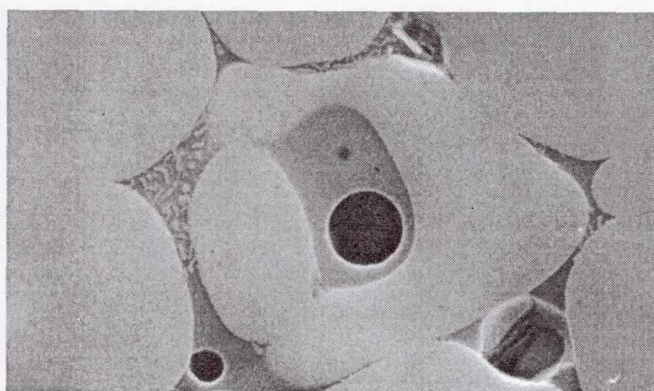
(a)



(b)

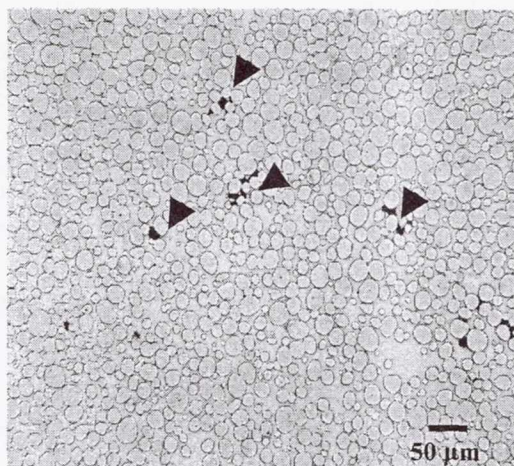


(c)

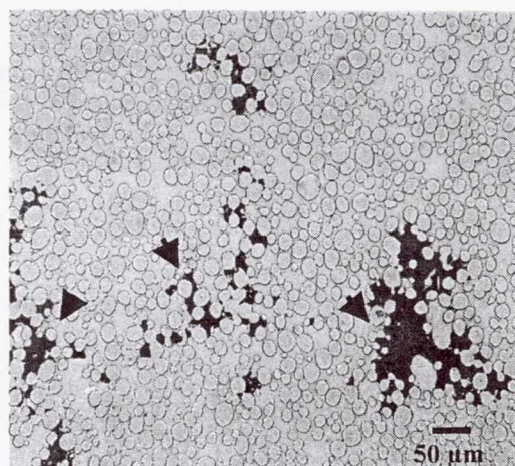


(d)

Figure 4. Anomalous pore structures in microgravity sintered 78W-15.4Ni-6.6Fe alloy.



(a). 1g sintered: top



(b). μ g sintered: bottom

Figure 5. Porosity in the 78W-15.4Ni-6.6Fe alloy sintered at 1500°C for 180 min under (a) ground-based and (b) microgravity condition.

pore migration and makes the pore as a stable phase. The stable pores caused solid-grain distortion, which indicates a contact angle equilibrium more complex than that treated by Young's equation. Liu and German observed that under microgravity the solid-liquid-vapor equilibrium significantly differs from that observed in the presence of gravity. They found discrepancy in Gibb's analysis of surface energy balance (Young's equation) which did not include the gravity term in the treatment, consequently, Young's equation is not suitable for μg condition.

Conclusions

This research shows important aspects concerning liquid phase sintering on Earth and under microgravity conditions. This study investigates the role of gravity on microstructural evolution and compact shape retention. The results indicate that samples that distort in ground-based sintering undergo distortion in microgravity. In the former, distortion is accompanied by solid-liquid segregation and formation of a typical elephant-foot profile, whereas, in the latter the compacts tend to spheroidize. This proves that the conditions that cause the loss in structural rigidity prevail even in a microgravity environment. The current study shows that during ground-based sintering, gravitational segregation increases with an increasing solid-liquid density difference. Consequently, microstructural links are used to predict the degree of grain settling in dilute alloys sintered in Earth. Microstructural investigation of microgravity sintered W-Ni-Fe alloys disprove the premise that absence of gravity will lead to homogeneous microstructure during sintering. Low solid content alloys, when sintered in microgravity, exhibit microstructural gradients from periphery to the center of the compact. These results suggest that agglomeration is a natural event, even in microgravity. The microstructure also points out to lack of buoyancy-induced pore migration during microgravity sintering.

Summary of Key Findings

A universal grain size distribution for LPS materials has been isolated and described mathematically, and this distribution agrees with recent independent findings. The volume fraction of liquid has been mathematically linked to the grain growth rate constant and solid-liquid density difference for LPS materials, giving the first universal coarsening law applicable to the solid contents characteristic of LPS.

A model has been created for slumping and distortion during LPS. This model describes the role of gravity, component size, substrate friction, and surface tension on reshaping processes. Analysis has shown an important role of grain connectivity and dihedral angle on shape preservation during LPS. Evidence exists that grain boundary wetting by newly formed liquid is a key factor in distortion.

Grain agglomeration has been predicted and observed in dilute solid content systems. The weak agglomeration force was first modeled for LPS, but may be applicable to many situations including solid-liquid, liquid-liquid, solid-vapor, and liquid-vapor systems. The agglomeration event was observed in microgravity samples sintered by Kohara and Ekbom.

Based on pore stabilities in the microgravity samples, we have revisited the derivation of Young's equation and found Gibbs' original treatment is incorrect since a gravity term was dropped from the derivation.

Coalescence has been documented in a zero dihedral angle LPS system conclusively to prove Ostwald ripening theories are incorrect in ignoring this effect. Further, grain rotation as part of coalescence has been measured during long time LPS. Electron channeling experiments will show the emergence of preferred grain orientations for coalescence during long term LPS.

Early evidence shows a non-random radial distribution function in the grain size of LPS heavy alloys.

The settled region of Earth-based LPS samples has been analyzed for the density difference effect and the terminal skeletal structure for no solid-liquid density difference. A model for the solid content versus position in the settled solid structure accurately explains all previous observations.

A new generalized idea of grain coordination number versus effective pressure has emerged that may have applicability to loosely packed particles. The model expresses the mean coordination number as a function of the effective pressure. Ground-based experiments are being performed to test this model.

Pore structure observations in microgravity LPS samples show a high stability. This suggests buoyancy may be important to densification during LPS on Earth. A complication is the lack of a reducing atmosphere during microgravity sintering, but under identical ground-based LIF experiments a gravity role is evident.

Acknowledgement

The funding for this research was provided by the National Aeronautical and Space Administration (NASA). Data from these experiments are available by accessing the P/M Lab website at <http://pmlab.esm.psu.edu/pmhome.htm>.

Some Publications for In-Depth Study

1. C. M. Kipphut, A. Bose, S. Farooq and R. M. German, "Gravity and Configurational Energy Induced Microstructural Changes in Liquid Phase Sintering," *Metallurgical Transactions A*, 1988, vol. 19A, pp. 1905-1913.
2. R. M. German and S. Farooq, "An Update on the Theory of Liquid Phase Sintering," *Sintering '87*, vol. 1, S. Somiya, M. Shimada, M. Yoshimura, and R. Watanabe (eds.), Elsevier Applied Science, London, UK, 1989, pp. 459-464.
3. S. C. Yang, S. S. Mani and R. M. German, "The Effect of Contiguity on Growth Kinetics in Liquid Phase Sintering," *JOM*, 1990, vol. 42, no. 5, pp. 16-19.
4. S. C. Yang and R. M. German, "Gravitational Limit of Particle Volume Fraction in Liquid Phase Sintering," *Metallurgical Transactions A*, 1991, vol. 22A, pp. 786-791.
5. S. S. Mani and R. M. German, "Gravitational Effects on Microstructural Parameters During Liquid Phase Sintering," *Advances in Powder Metallurgy*, 1991, vol. 4, Metal Powder Industries Federation, Princeton, NJ, pp. 195-212.
6. S. C. Yang and R. M. German, "Generic Grain Size Distribution for Liquid Phase Sintering," *Scripta Metallurgica*, 1992, vol. 26, pp. 95-98.
7. R. M. German, A. Bose and S. S. Mani, "Sintering Time and Atmosphere Influences on the Microstructure and Mechanical Properties of Tungsten Heavy Alloys," *Metallurgical Transactions A*, 1992, vol. 23A, pp. 211-219.

8. R. G. Iacocca and R. M. German, "Experimental Design for Liquid Phase Sintering in Microgravity," Advances in Powder Metallurgy and Particulate Materials, 1993, vol. 2, Metal Powder Industries Federation, Princeton, NJ, pp. 181-194.
9. R. M. German, "Microstructure of the Gravitationally Settled Region in a Liquid Phase Sintered Dilute Tungsten Heavy Alloy," *Metallurgical Materials Transactions A*, 1995, vol. 26A, pp. 279-288.
10. R. Raman and R. M. German, "A Mathematical Model for Gravity-Induced Distortion During Liquid Phase Sintering," *Metallurgical Materials Transactions A*, 1995, vol. 26A, pp. 653-659.
11. Y. Liu, D. F. Heaney and R. M. German, "Gravitational Effects on Solid Grain Packing in Liquid Phase Sintering," Tungsten and Refractory Metals, A. Bose and R. Dowding (eds.), Metal Powder Industries Federation, Princeton, NJ, 1995, pp. 121-128.
12. Y. Liu, D. F. Heaney and R. M. German, "Gravity Induced Solid Grain Packing during Liquid Phase Sintering," *Acta Metallurgica Materialia*, 1995, vol. 43, pp. 1587-1592.
13. R. M. German, R. G. Iacocca, J. L. Johnson, Y. Liu and A. Upadhyaya, "Liquid-Phase Sintering Under Microgravity Conditions," *JOM*, 1995, vol. 47, no. 8, pp. 46-48.
14. Y. Liu, R. Iacocca, J. L. Johnson, R. M. German, and S. Kohara, "Microstructural Anomalies in a W-Ni Alloy Liquid Phase Sintered under Microgravity Conditions," *Metallurgical Materials Transactions A*, 1995, vol. 26A, pp. 2485-2486.
15. R. G. Iacocca, Y. Liu, and R. M. German, "Microstructural Examination of Tungsten Heavy Alloys Sintered in a Microgravity Environment," Advances in Powder Metallurgy and Particulate Materials, 1995, vol. 1, pp. 4.239-4.249.
16. D. F. Heaney, R. M. German, and I. S. Ahn, "The Gravitational Effects on Low Solid-Volume Fraction Liquid-Phase Sintering," *Journal Materials Science*, 1995, vol. 30, pp. 5808-5812.
17. Y. Liu and R. M. German, A Relationship Between Contact Angle and Surface Tensions, Sintering 1995, R. M. German, G. L. Messing, and R. Cornwall (eds.), Marcel Dekker, New York, NY, 1996, pp. 229-236.
18. R. M. German, "Grain Agglomeration in Solid-Liquid Mixtures Under Microgravity Conditions," *Metallurgical Materials Transactions B*, 1995, vol. 26B, pp. 649-651.
19. Y. Liu and R. M. German, "Contact Angle and Solid-Liquid-Vapor Equilibrium," *Acta Materialia*, 1996, vol. 44, pp. 1657-1663.
20. R. M. German and Y. Liu, "Grain Agglomeration in Liquid Phase Sintering," *Journal Material Synthesis Processing*, 1996, vol. 4, pp. 23-34.
21. J. L. Johnson and R. M. German, "A Solid-State Contributions to Densification during Liquid Phase Sintering," *Metallurgical Materials Transactions B*, 1996, vol. 27B, pp. 901-909.
22. A. Upadhyaya and R. M. German, "Control of Distortion during Liquid Phase Sintering," Proceedings of 14th International Plansee Seminar-1997, vol. 2, G. Keneringer, P. Rödhammer, and P. Wilhartitz (eds.), Plansee AG, Reutte, Austria, 1997, pp. 68-85.
23. A. Upadhyaya and R. M. German, "Densification and Distortion in Liquid Phase Sintered W-Cu Alloys," *International Journal Powder Metallurgy*, 1998, vol. 34, pp. 43-55.

24. . J. L. Johnson, A. Upadhyaya, and R. M. German, "Microstructural Effects on Distortion and Solid-Liquid Segregation during Liquid Phase Sintering under Microgravity Conditions," *Metallurgical Materials Transactions B*, 1998, vol. 29B, pp. 857-866.
25. A. Upadhyaya and R. M. German, "Shape Distortion in Liquid Phase Sintered Tungsten Heavy Alloys," *Metallurgical Materials Transactions A* (in press)
26. A. Upadhyaya, "A Microstructure-Based Model for Shape Distortion during Liquid Phase Sintering," *Ph.D. Thesis*, The Pennsylvania State University, University Park, PA, 1998.

Page intentionally left blank

OPPOSITE
THIS
PAGE

Large Isothermal Furnace (LIF)

Diffusion Processes in Molten Semiconductors (DPIMS)

Principal Investigator:

Dr. David H. Matthiesen
Case Western Reserve University
Cleveland, Ohio

Declined to provide input.

omit this
211-27
PAGE

Middeck Glovebox (MGBX)

**A Study of the Fundamental Operation of a Capillary-driven
Heat Transfer Device in Microgravity (CHT)**

Glovebox Investigator:

Dr. Kevin P. Hallinan
University of Dayton
Dayton, Ohio

CAPILLARY PUMPED HEAT TRANSFER (CHT) EXPERIMENT

K. P. Hallinan¹ and J. S. Allen²

¹University of Dayton, Dayton, Ohio, 45469-0210, khallina@engr.udayton.edu

²National Microgravity Research Center, 2100 Brookpark Rd., Cleveland, OH, 44135, jeff.allen@lerc.nasa.gov

SINGLE SCAN 511-34
434848

ABSTRACT

The operation of Capillary Pumped Loops (CPL's) in low gravity has generally been unable to match ground-based performance. The reason for this poorer performance has been elusive. In order to investigate the behavior of a CPL in low-gravity, an idealized, glass CPL experiment was constructed. This experiment, known as the Capillary-driven Heat Transfer (CHT) experiment, was flown on board the Space Shuttle Columbia in July 1997 during the Microgravity Science Laboratory mission.

362411 10P

During the conduct of the CHT experiment an unexpected failure mode was observed. This failure mode was a result of liquid collecting and then eventually bridging the vapor return line. With the vapor return line blocked, the condensate was unable to return to the evaporator and dry-out subsequently followed. The mechanism for this collection and bridging has been associated with long wavelength instabilities of the liquid film forming in the vapor return line. Analysis has shown that vapor line blockage in present generation CPL devices is inevitable.

Additionally, previous low-gravity CPL tests have reported the presence of relatively low frequency pressure oscillations during erratic system performance. Analysis reveals that these pressure oscillations are in part a result of long wavelength instabilities present in the evaporator pores, which likewise lead to liquid bridging and vapor entrapment in the porous media. Subsequent evaporation to the trapped vapor increases the vapor pressure. Eventually the vapor pressure causes ejection of the bridged liquid. Recoil stresses depress the meniscus, the vapor pressure rapidly increases, and the heated surface cools. The process then repeats with regularity.

Objective

The Capillary-driven Heat Transfer (CHT) experiment was designed and conducted to gain insight into the physical behavior of CPL devices in low gravity in an attempt to explain some of the anomalous behavior that has been observed in previous low gravity technology demonstrations.

Background

The first Capillary-Pumped Loop (CPL) was developed in the 1960's at the NASA Lewis Research Center in Cleveland, Ohio (Stenger, 1966). Since then a significant number of low gravity evaluations have followed. The first of these was the Capillary Pumped Loop GAS Experiment (G-471), flown in June, 1985. The low-gravity results of this experiment are still unclear; though initial reports indicated success. The CAPillary Pumped Loop (CAPL) experiment was flown in February, 1994 on board STS-60 as part of the Hitchhiker payload. This experiment tested a starter pump concept designed to clear the vapor lines of liquid prior to start-up of the CPL evaporators. Douglass (1997) reported that vapor penetrated the wick of the starter pump during operation yielding a temperature there above that of the system temperature. Further, the starter pump was never able to fully clear the vapor lines of liquid. The CAPL experiment was reflown as CAPL-2 with a redesigned starter pump in July, 1995 on board STS-69. Preliminary findings indicated performance within the thermal requirements of the EOS program (CAPL2, 1995). In November 1996, the Visualization In an Experimental Water Capillary Pumped Loop (VIEW-CPL) experiment was flown on the middeck of STS-80. This was the first experiment specifically designed to investigate the internal physics of CPL's in low gravity (Kolos and Herold, 1997). Finally, the Two Phase Flow (TPF) experiment, designed to address problems encountered during the CAPL experiment, was flown in August, 1997 on STS-85 during the Technology, Application and Science (TAS) mission. The TPF experiment incorporated a new type of starter pump as well as a "capillary flow valve". Initial reports indicate a few difficulties in start-up (Ottenstein, 1997).

In general, capillary-pumped loops have not been started from a cold state successfully without the use of a starter pump (Ku, 1995b). In most instances, the starter pump is a heated wicking structure that is used to clear the vapor lines of liquid. Often, especially during startup, the temperature data has indicated that the liquid was flowing in reverse inside the evaporator. These experiments have also exhibited pressure oscillations accompanied by

evaporator deprime (Ku and Huang, 1995a). The fundamental mechanism of the unstable operation, however, has not been identified.

METHODS OF DATA ACQUISITION AND ANALYSIS

The main component of the Capillary-driven Heat Transfer (CHT) experiment is a Pyrex test loop shown schematically in Figure 1. The loops were designed to ideally model CPLs. All glass construction was used to permit observation of the fluid orientation within the whole of the CPL during testing.

Two such loops were fabricated and tested in low gravity. These loops were mounted within an enclosed experimental housing. Each was designed with an evaporator and condenser leg, having respective evaporator inner diameters of 1mm and 4mm and a 10mm inner diameter condenser. A partition wall was used to isolate these legs from each other. The vapor return line likewise had a 10mm internal diameter. The liquid return line was equal in diameter to the evaporator inner diameter. Within the loop a three-way valve was used to direct liquid (ethanol) from the 10cc reservoir into the condenser leg and/or the evaporator leg of the test loop. Conical transition sections connected the vapor leg to the capillary tubing. The conical sections were designed as capillary traps in low gravity and preferentially located the evaporator meniscus. The test fluid was spectroscopic grade ethanol.

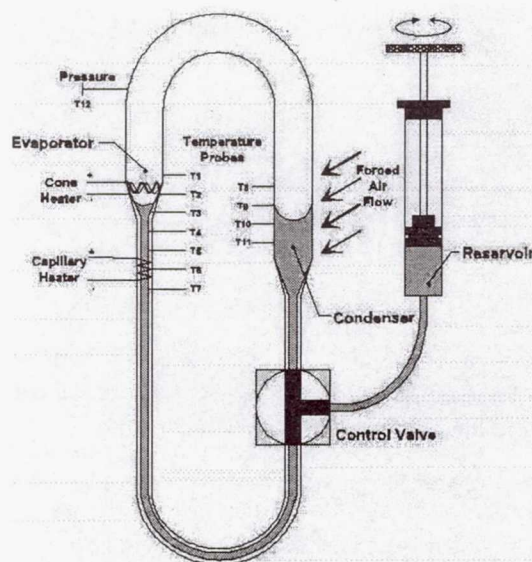


Figure 1 Schematic of experimental CPL model.

The loops were designed to prevent evaporator dry-out due to surface tension differences between the evaporator and the condenser alone even at the maximum temperature expected.

During the testing, heat could be applied to the evaporator by either of two heaters. The first, called the cone heater, was a serpentine wire attached to the evaporator conical transition section. The second, called the capillary heater, was a spiral wound wire located on the capillary tubing approximately 10 mm from the cone heater. Both heaters were constructed from 0.25mm Kanthol wire, rolled flat to insure good contact with the glass surface. A brushless fan mounted over an opening (fan vent) in the experiment module housing provided cooling for the condenser. This cooling air was exhausted through two additional openings (condenser vents) in the condenser side of the experiment module housing.

The loop was instrumented with 7 thermocouples (Type T, 40 AWG) along the length of the evaporator leg and 4 thermocouples along the length of the condenser leg. The thermocouples were located 0.25 mm from the inside wall in small diameter holes drilled into the Pyrex tubing. This proximity to the inside wall coupled with the fine gauge of the thermocouples provided a very quick response to wall temperature changes. An additional thermocouple and a pressure transducer were connected to the vapor leg to allow for a determination of the vapor properties. The loops were backlit to permit video recording of the internal phenomenon.

Four types of CHT experiments were conducted on the MSL-1 mission. The two relevant to the present paper were conducted as follows. In the first, liquid was added to the loop to the condenser to near the top of the straight section. Capillarity insured that the liquid in the evaporator was at the top of the evaporator conical section. Power was initiated to one of the two heaters. During the transient, evaporator meniscus stability and overall liquid orientation within the loop was observed.

The second type of experiment was referred to as the re-wetting experiments. In these, the liquid was withdrawn to the bottom of the straight section of the evaporator capillary tubing. Power was then applied to the capillary heater. After a set waiting period, the control valve was rotated to free liquid flow from the condenser to the evaporator. The subsequent re-wetting of the evaporator meniscus was then observed. Several waiting times and therefore initial temperatures were investigated.

FLIGHT RESULTS

Liquid Slug Formation in the Vapor Return Lines

One of the first experimental observations was the formation of a continuous liquid film over the entire length of the vapor return leg. Immediately after applying heat, a liquid film could be seen advancing along the wall of the vapor leg on the evaporator side due to condensation of vapor on the cooler walls of the loop. Capillary forces "drain" the liquid film in the regions where the vapor tubing bends. The process of low-gravity liquid pooling in the elbow of the vapor tube and the eventual formation of a liquid slug is illustrated in Fig. 2. During each experiment run, the liquid accumulated in the outer radius of the bend in the vapor section of the test loop. This pool of liquid would collect into a lobe that would grow until a slug of liquid would form, completely bridging the vapor line.

Figures 3 and 4 show the formation of the liquid slug in the vapor leg and the subsequent recession of the condenser meniscus after the slug has formed. In Figure 3 the liquid film begins to pool in the outer radius of the bend and eventually bridges. Prior to complete bridging of the vapor line, the pooling of the liquid in the bend of the vapor leg does not adversely effect the CPL operation. However, after the liquid slug forms, condensation to the condenser meniscus is completely disrupted. Subsequently, as liquid is continually fed to the evaporator, the condenser meniscus begins to recede as shown in Figure 4. Eventually, it recedes into the capillary tube thereby eliminating the pressure difference feeding liquid into the evaporator. At this point the evaporator dries out and the system fails.

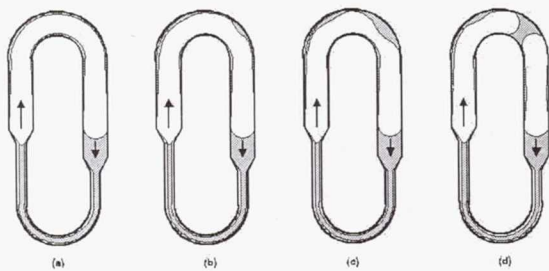


Figure 2. Illustration of liquid accumulation and slug formation in the test loop vapor leg during low-gravity CHT experiments. The arrows indicate the direction of liquid and vapor flows.

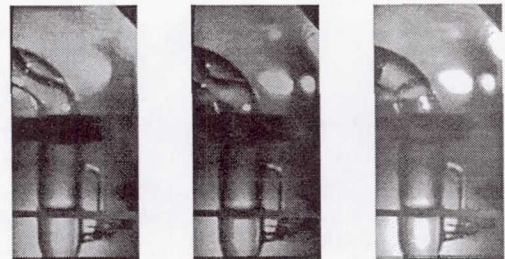


Figure 3. Formation of a liquid slug in the bend of the vapor leg.

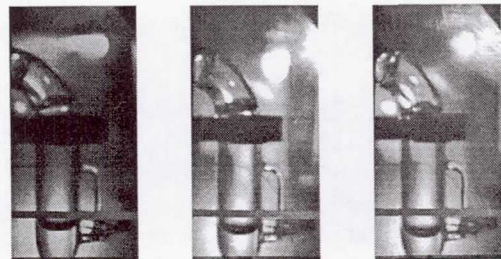
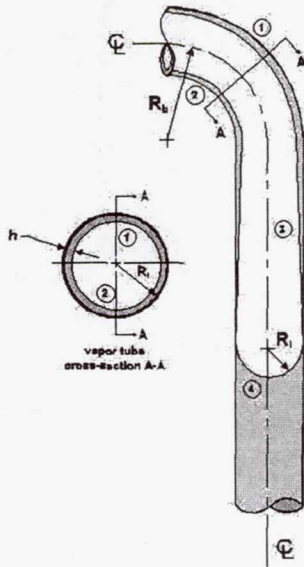


Figure 4. Recession of the condenser meniscus after formation of a liquid slug.

The formation of this slug is primarily the result of an instability arising from a long-wave disturbance of the annular liquid film in the vapor return line. Gauglitz and Radke(1990), Aul and Olbricht (1990) and Hu and Joseph (1989) have shown that an annular film within a straight tube is fundamentally unstable to long-wave disturbances. Such a liquid film will always breakup and form periodically spaced annular lobes when the length of the liquid film exceeds a critical length. For thick liquid films, the annular liquid lobes will bridge the tube and form liquid slugs. Though this long wavelength instability is ultimately responsible for the slug formation shown in Figures 3 and 4, the liquid flow to the outer portion of the tubing bend is caused by another mechanism.

In a low Bond number (i.e., low gravity) environment, liquid in an annular film will flow from the inner to outer radius of a bend because of differences in the interfacial curvature and, therefore, liquid pressure between these two regions. These pressure differences and the liquid flow that develops are analyzed by examining four distinct regions of the annular liquid film (see Figure 5). The first region is the outer portion of the tubing bend where the liquid accumulates. Region 2 is the inside radius of the tubing bend and is located 180° from region 1 at the same centerline location. Regions 1 and 2 are highlighted in the cross sectional view of the annular liquid film at section A-A. Region 3 comprises the straight portion of the vapor line. Region 4 is the condenser meniscus. For the purposes of this analysis, the condenser meniscus is presumed to be far from the bend (See Allen et al., 1998, for results obtained by relaxing this requirement) and the liquid film is assumed to be of uniform thickness, h .



The pressure drop across a liquid-vapor interface is known from the Laplace-Young equation. One of the principal radii of curvature is the same for each of the four regions and is equal to the tubing inside radius minus the film thickness, $R_i - h$. The second principal radius curvature varies from region to region. In region 1 that radius of curvature is $R_b + R_i - h$. Similarly, $-R_b + R_i - h$, ∞ , and $R_i - h$ are the second principal radius of curvature for regions 2, 3, and 4, respectively.

A dimensionless film thickness ratio and bend radius are defined as respectively $\delta = h/R$ and $\Gamma = (R_i - h)/R_b$. Substituting these and the appropriate principal radii of curvature into the Laplace-Young equation results and computing the pressure differences in the annular film between each of the regions results in the following

Figure 5 Geometry of the annular liquid film.

$\Delta P_{l 2-1} = \frac{\sigma}{R_i(1-\delta)} \left(\frac{2\Gamma}{1-\Gamma^2} \right)$	$\Delta P_{l 3-1} = \frac{\sigma}{R_i(1-\delta)} \left(\frac{\Gamma}{1+\Gamma} \right)$
$\Delta P_{l 2-3} = \frac{\sigma}{R_i(1-\delta)} \left(\frac{\Gamma}{1-\Gamma} \right)$	$\Delta P_{l 3-1} = \frac{\sigma}{R_i(1-\delta)}$

The potential for liquid flow can be rewritten in terms of the Capillary number. Neglecting the aspect ratio of the annular liquid film, the Capillary number is defined as $Ca = \mu U / \sigma$. Using a lubrication approximation to describe the liquid film flows, the pressure drops and the characteristic lengths, L , between each region are combined to determine the respective velocity scales, U . The length scales and resulting capillary numbers for each of these regions are shown in Table 1.

Table 1 Length scales and Capillary numbers characterizing liquid film flows between each of the regions

Region	Length Scale	Capillary number
2-1	$\frac{\pi}{2} R_i (1-\delta) 2$	$\frac{2}{\pi} \left(\frac{\delta}{1-\delta} \right)^2 \left[\frac{\Gamma}{1-\Gamma^2} \right]$
3-1	$\frac{\pi}{2} R_i (1-\delta) \frac{1+\Gamma}{\Gamma}$	$\frac{2}{\pi} \left(\frac{\delta}{1-\delta} \right)^2 \left[\frac{\Gamma}{1+\Gamma} \right]^2$
2-3	$\frac{\pi}{2} R_i (1-\delta) \frac{1-\Gamma}{\Gamma}$	$\frac{2}{\pi} \left(\frac{\delta}{1-\delta} \right)^2 \left[\frac{\Gamma}{1-\Gamma} \right]^2$
3-4	$\frac{\pi}{2} R_i (1-\delta)$	$\frac{2}{\pi} \left(\frac{\delta}{1-\delta} \right)^2$

During the CHT experiments, the annular liquid film thickness was estimated to be 350 microns. Based upon these parameters, these Capillary numbers are represented pictorially in Figure 6, where the length of the arrow is representative of the magnitude of the liquid flows. Liquid flow into the bend is much larger than the flow out of the bend. Therefore, liquid will accumulate in the outer region of the tubing bend in any low Bond number system. Also, the liquid flow into the condenser meniscus is higher than any other liquid film flows in the system. This implies that there is always significant drainage into the condenser meniscus even in low gravity systems. It also explains why the formation of the slug often took as many as 10 minutes to form. But as reported by Aul and Olbricht (1989), drainage by the meniscus will only occur over a length of $2\pi R_i$. When the condenser meniscus receded to near the conical section after a slug formed, another lobe was observed to form in region 4, since the length above the condenser meniscus to the bend approach this critical length.

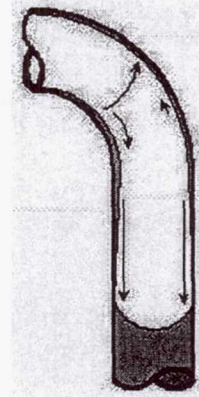


Figure 6 Vectors representing magnitude and direction of liquid film flow in CHT experiment

Characteristic Time Scales and Evaporator Meniscus Oscillations

An annular liquid film in a straight tube has been shown to be unstable when the film length exceeds a critical length of $2^{3/2} \pi R_i$ (Aul and Olbricht, 1990, Gauglitz and Radke, 1990). This long wavelength instability, driven by surface tension, results in the liquid film collecting into periodically spaced, axisymmetric "lobes". When $\delta > 0.1$ enough liquid is present that the lobes will "pinch off" and bridge the tube, forming slugs of liquid. When δ is less than 0.1, only lobes will form.

The effect of the capillary-driven flow in the bend relative to the long wavelength instability can be gauged through a comparison of the characteristic times for each of the flow potentials. The characteristic time associated with the long wave length instability is given by Aul and Olbricht (1989) as

$$t_\lambda = \frac{\mu_1 R_i}{\sigma \delta^3},$$

where μ_1 is the absolute viscosity of the liquid. This time scale characterizes the growth rate of the lobe or slug of liquid.

The circumferential flow only occurs when there is a bend in the tubing. When $\delta \ll 1$, the film can be treated as planar and the characteristic flow time for the circumferential flow is $\mu_1 R_i / \sigma \delta^2$. For thicker films, the radial dependence of the annular film must be retained. At times during the conduct of the CHT experiment, δ exceeded 0.1, preventing use of the simpler formulation.

The radial and circumferential velocities and velocity scales in the liquid film are represented respectively by u, U and v, V . By non-dimensionalizing the radial dimension as $r = R_i(1 - \delta r^*)$, the annular liquid film thickness is scaled from 0 at the wall to 1 at the liquid-vapor interface. Applying these scales to the continuity equation yields $U \sim \delta V$. Retaining only those terms of order δ or greater reduces the conservation of momentum equations to

$$\frac{\delta^2}{R_i} \mu_i V \left(\frac{1}{1 - \delta r^*} \right) \frac{\partial P}{\partial \theta} = \frac{\partial^2 v^*}{\partial r^{*2}} - \delta \left(\frac{1}{1 - \delta r^*} \right) \frac{\partial v^*}{\partial r^*}$$

Using the no-slip condition at the wall and the free shear condition at the liquid surface, the dimensionless velocity profile, v^* , after eliminating terms $o(\delta)$, can be expressed as

$$v^* = \frac{\delta^2 R \Delta P_\sigma}{\pi \mu_i V} \left\{ \left(r^* - \frac{1}{2} r^{*2} \right) + \delta \left(\frac{1}{2} r^{*2} - \frac{1}{3} r^{*3} \right) + \dots \right\}.$$

Setting r^* and v^* equal to 1 results in a velocity scale equal to

$$V \sim \frac{\delta^2 R \Delta P_\sigma}{\pi \mu_i} \left(\frac{1}{2} + \frac{1}{6} \delta \right).$$

The characteristic time for the capillary flow from the inner portion of the bend to the outer portion of the bend, t_σ , is found by dividing the distance for liquid flow, πR_i , by the velocity scale, V . Substituting the expression for the capillary pressure drop from region 2 to region 1, $\Delta P_{|2-1}$ into the velocity scale, V , results in the following expression for the characteristic time of the capillary-driven flow:

$$t_\sigma \sim \frac{\pi^2 \mu_i R_i}{\sigma \delta^2} \frac{1 - \Gamma^2}{1 + 1/3 \delta}$$

The two time scales, t_λ and t_σ , characterize the rate of liquid accumulation in the vapor line. Liquid flow in the axial direction (scaled by t_λ) will always tend to form liquid lobes whenever the film length exceeds $2^{3/2} \pi R_i$. When there is a bend in the tube, circumferential flow (scaled by t_σ) will result in liquid collecting in the outer portion of the tubing bend. **The bend does not eliminate the long wavelength instability, but rather, it provides a perturbation to the liquid film that augments the long wavelength instability.**

The importance of t_λ relative to t_σ can be examined by expressing the time scales as a ratio,

$$t_{\lambda\sigma} = \frac{t_\lambda}{t_\sigma} \sim \frac{1}{\pi^2} \left[\frac{1 + \delta^3}{\delta(1 - \delta)} \right] \left(\frac{\Gamma}{1 - \Gamma^2} \right)$$

The ratio of tube radius to bend radius, Γ , varies from 0 to 1. The limits on Γ vary from 0 for a straight tube to 1 for a toroid with zero inside radius. The effect of Γ on the liquid lobe formation is illustrated in Figure 7. At $\Gamma \sim 0$ (i.e., for straight tubing), $t_{\lambda\sigma} \sim 0$ and the liquid forms axisymmetric lobes. As $\Gamma \sim 1$, and $t_{\lambda\sigma} \rightarrow \infty$, a uniform liquid film forms on the outer radius of the bend. At $0 < \Gamma < 1$, $t_{\lambda\sigma} \sim 1$ and the liquid forms into non-axisymmetric lobes on the outer region of the bend. For the CHT experiments, $t_{\lambda\sigma}$ is typically around 0.4, so the formation of non-axisymmetric lobes in the bend is expected.

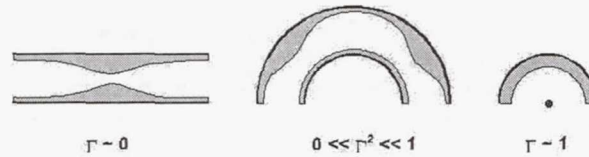


Figure 7 Types of liquid accumulation in the bend of the vapor line for various values of Γ with $\delta < 0.1$.

During the CHT experiment, the liquid nearly always accumulated in the same location on the condenser side of the vapor leg. The most probable explanation for liquid accumulation in this particular location is that the radius of curvature of the bend in the glass tubing was slightly smaller at this point than at other points along the vapor leg. The non-uniform radius of curvature occurred as a result of the test loop fabrication process. The smaller radius of curvature, R_b , reduces the characteristic flow time, t_λ . Therefore, liquid accumulates in the outer region of the bend more quickly at this location resulting in a larger film thickness, δ . Since, the characteristic time for the lobe formation, t_λ , is proportional to δ^3 , any small perturbation in the film thickness is greatly amplified by the long wavelength instability.

Evaporator Meniscus Oscillations

During the low-gravity CHT experiments, the evaporator meniscus did oscillate and a direct correlation of meniscus position to vapor pressure was established. Portions of two CHT rewetting experiment runs are provided which illustrate this relationship.

Figure 8 shows a small time segment (12 seconds) taken from the first rewetting experiment run, near the beginning of the test run when the system was far from steady-state. In Fig. 8 the upper graph shows the evaporator wall temperatures TC5 and TC6 against time. The major time divisions are in 30 frame (1 second) increments. TC6 is located in the center of the capillary heater and TC5 is located just beyond the capillary heater towards the vapor side of the loop. The center graph is a plot of the vapor pressure versus time. The lower graph plots the evaporator meniscus position against time. The meniscus position is referenced from thermocouple 3. The horizontal grid lines on the bottom graph are the locations of thermocouples 1 through 7.

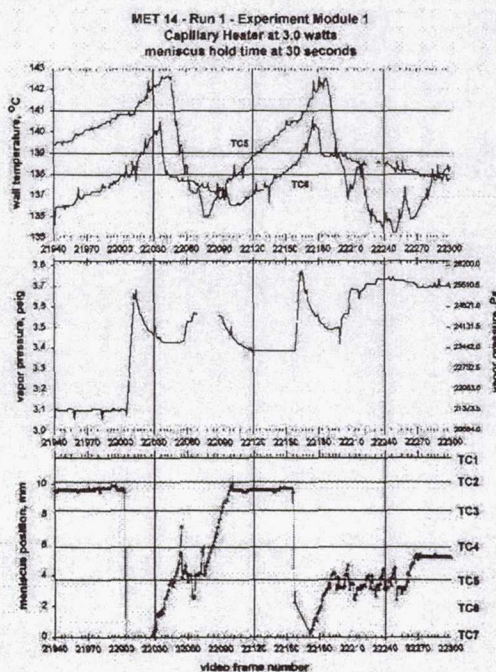


Figure 8 Time slice of evaporator wall temperatures, vapor pressure, and evaporator meniscus position from the CHT rewetting experiment - run 1.

Figure 9 shows a 12 second time slice from the second rewetting experiment run, taken near the end of the test run where quasi-steady-state operation is being approached. At the beginning of this time slice, the evaporator meniscus was oscillating with a very small amplitude (~ 500 microns) near the TC5 location. The frequency of these oscillations was about 6 Hz. The small oscillations produced vapor pressure changes that could not be resolved by the pressure transducer. At frame number 7542, the evaporator meniscus suddenly stabilized and advanced to the TC2 location. Simultaneously, the vapor pressure began to drop as the evaporation was reduced and the wall temperatures increased, especially at TC5. After 1.2 seconds (frame 7578) the meniscus violently destabilized and once again began to oscillate about the TC5 location. As the evaporation increased the vapor pressure also increased and the wall temperature at TC5 decreased dramatically. This cycle is repeated again starting at frame 7680.

In Figure 8 the meniscus was stable and located near TC 2 until frame 22000. Complete rewetting had occurred. Then the meniscus violently destabilized. Vapor recoil depressed the meniscus below thermocouple 7. Simultaneously, the vapor pressure jumped 4000 Pa, and after a one second time lag the wall temperatures TC6 and TC5 began to drop. These two temperatures begin to decline again once the meniscus began to move back into the evaporator.

After another 100 frames, the evaporator meniscus restabilized near TC2. Once the meniscus stabilized, the vapor pressure begins to drop, eventually leveling off, and the wall temperatures began to rise. At frame 22156, the process repeated. In all cases, the vapor pressure spikes were directly attributable to the destabilization of the evaporator meniscus (characterized by a dramatic and rapid recession).

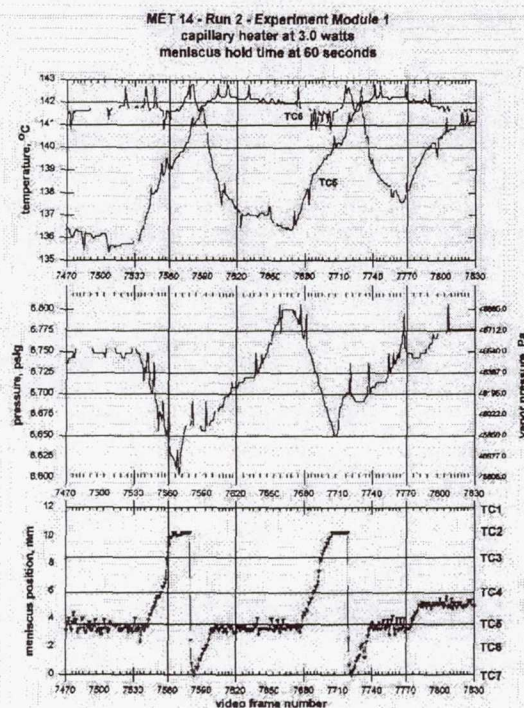


Figure 9 Time slice of evaporator wall temperatures, vapor pressure, and evaporator meniscus position from the CHT rewetting experiment - run 2.

The previous results establish the link between vapor pressure oscillations and the meniscus destabilization and show that these oscillations are periodic. However, these do not reveal their source. One potential mechanism can be eliminated from consideration. Nucleate boiling was not observed in any of the tests.

For some of these oscillations, a liquid bridge was observed to form upstream of the intrinsic meniscus in the capillary tube. When this occurs, evaporation to the entrapped vapor bubble increases the pressure within. Eventually the liquid bridge is ejected. Given that the length in the capillary tube above the intrinsic meniscus was greater than $2^{3/2}\pi R_c$, where R_c is the internal radius of the evaporator capillary, the possibility of a long wavelength instability could not be ignored.

To see if the characteristic frequency of the observed oscillations can be explained by this mechanism, the time scale, t_λ for the formation, growth, and coalescence of lobes in the evaporator capillary is determined. To accomplish this, an estimate for the dimensionless film thickness, δ , is required. Generally, in ground tests, the initial lobe and slug formation was slowest. After the first incidence, however, the observed rate of formation increased rapidly, suggesting that much of the liquid ejected from the liquid bridge when the vapor pressure becomes sufficient to blow through the liquid bridge, finds its way to the wall of the capillary. The initial liquid film thickness after ejection of the bridge can then be estimated from the volume in the liquid bridge. Presuming the bridge volume to be roughly equal to one half of the cross-sectional area of the evaporator capillary times the critical length, $(\pi^2 R_c^3 2^{1/2})$, the dimensionless liquid film thickness after ejection of the bridge can be estimated as:

$$\delta \sim h/R_c = 2^{-1/2} \pi R_c / L$$

where L is the length of the evaporator capillary length above the bridge (~ 1 cm). This dimensionless film thickness is estimated to be 0.11, suggesting that liquid bridging is likely (Aul and Olbricht, 1990).

Now, the time scale t_λ is estimated. Evaluating the thermophysical properties at TC5, the time scale for lobe formation and bridging is on the order of 0.08s. Since this period is less than that associated with the oscillations, the possibility that the long wave instability contributes to their occurrence cannot be discounted. Further, since the time

scale is very small, the absence of visual observation of liquid bridging prior to the meniscus oscillations for every occurrence may be a consequence of aliasing introduced by the 1/30 second video recording rate.

CONCLUSIONS

The CHT experiment has provided significant insight into of the fundamental operation of a capillary pumped loop heat transfer device in low-gravity. Above all, it has revealed that the present criteria used to design such systems which ignores the presence of liquid in the so-called adiabatic vapor transport region and that ignores the dynamics within the evaporator pores is inadequate for low-gravity systems. The present research has shown that the liquid film forming along the walls of the *adiabatic* region will inevitably de-stabilize due to a long wavelength instability mechanism, particularly given the long transport lines characteristic of CPL's. The present research has further shown that bends in these lines will amplify the long wavelength disturbances due to the accumulation of liquid at the outer radius of the bend due to capillary pumping. Given that CPL's rely have multi-pass heat exchangers comprising the condensers, the significance of this result is clear. In time, a liquid slug will form in each and every bend. While these vapor slugs do not inevitably lead to CPL failure, they may if the liquid volume in the CPL is insufficient. Secondly their presence has a significant impact on the maximum heat transport of such systems.

The present research has also offered a plausible explanation for the vapor pressure oscillations that have been observed in CPL's in the past. Analysis reveals that long wavelength instabilities present in the evaporator pores can lead to liquid bridging and vapor entrapment in the porous media. Subsequent evaporation to the trapped vapor increases the vapor pressure. Eventually the vapor pressure causes ejection of the bridged liquid. Recoil stresses dramatically depress the meniscus. As the meniscus attempts to rewet, the process then repeats. At high enough temperatures, wetting degradation is observed to coincide with these cyclic oscillations.

Future work will focus on the design of CPL systems that can tolerate and sustain the formation of the slugs of liquid in the vapor return lines as well as the oscillations present in the evaporator.

BIBLIOGRAPHIC REFERENCES AND ARTICLES/PRESENTATIONS RESULTING FROM THE FLIGHT

References

- Allen, J. S., Hallinan, K. P., and Lekan, J., "A Study of the Fundamental Operations of a Capillary Driven Heat Transfer Device in Both Normal and Low Gravity," presented at the 1998 STAIF Conference, Albuquerque, NM, January 27-29.
- Aul, R.W. and Olbricht, W.L., 1990, "Stability of a Thin Annular Film in Pressure-Driven, Low-Reynolds Number Flow Through a Capillary," *J. of Fluid Mechanics*, 215, pp. 585-599.
- Butler, D., 1986, "The Capillary Pumped Loop (CPL) GAS Experiment, G-471," Post Flight Data Report.
- CAPL-2 Experiment Team, 1995, CAPL-2 Final Mission Status Report, Posted by the Goddard Space Flight Center -- Thermal Engineering Group at World Wide Web site <http://sspp.gsfc.nasa.gov/capldata.html>.
- Douglas, D. and Ku, J. and Schlager, L., 1997, "Investigation of the Starter Pump Purge Superheat Observed in the CAPL 1 Flight," AIAA 97-3871, presented at the 1997 National Heat Transfer Conference, Baltimore, Maryland.
- Gauglitz, P.A. and Radke, C.J., 1990, The Dynamics of Liquid Film Breakup in Constricted Cylindrical Capillaries, *Journal of Colloid and Interface Science*, 134, No. 1, pp. 14-40.
- Hu, H. H. and Joseph, D. D., 1989, "Lubricating Pipelining: Stability of Core-Annular Flow. Part 2," *Journal of Fluid Mechanics*, 205, pp. 359-396.
- Kolos, K. R. and Herold, K. E., "Low Frequency Temperature and Fluid Oscillations in Capillary Pumped Loops," AIAA 97-3872, Presented at the 1997 National Heat Transfer Conference, Baltimore, Maryland.
- Ku, J. and Hoang, T., 1995a, "An Experimental Study of Pressure Oscillation and Hydrodynamic Stability in a Capillary Pumped Loop," Presented at the 1995 National Heat Transfer Conference, Portland, Oregon.
- Ku, J., "Start-up Issues in Capillary Pumped Loops," Presented at the 9th International Heat Pipe Conference, Albuquerque, New Mexico.
- Ottenstein, L., 1997, "Two-Phase Flow Post Mission Briefing," Presentation Handout.
- Stenger, F. J., "Experimental Feasibility Study of Water-Filled Capillary-Pumped Heat Transfer Loops," NASA Lewis Research Center, Cleveland, Ohio, NASA TM X-1310.

Presentations/Articles Resulting from the Flight

Allen, J.S., Behavior of Capillary-Pumped Loops in Low Gravity, Ph.D. Dissertation, University of Dayton, May, 1998.

Allen, J. S., Hallinan, K. P., and Lekan, J., " A Study of the Fundamental Operations of a Capillary Driven Heat Transfer Device in Both Normal and Low Gravity," presented at the 1998 STAIF Conference, Albuquerque, NM, January 27-29.

Hallinan, Kevin P. and Allen, J.S., "Comments on the Operation of Capillary Pumped Loop Devices in Low Gravity," presented at the 3rd Microgravity Fluids Conference, Cleveland, Ohio, August 12-14.

Non-Technical Summary

The Capillary-driven Heat Transfer (CHT) experiment, was flown on board the Space Shuttle Columbia in July 1997 during the Microgravity Science Laboratory mission. The experiment was designed and conducted to gain insight into the physical behavior of capillary pumped heat transfer devices in low gravity in an attempt to explain some of the anomalous behavior that has been observed in previous low gravity technology demonstrations of these systems. These device

The CHT experiment has provided significant insight into of the fundamental operation of a capillary pumped loop heat transfer device in low-gravity. Above all, it has revealed that the present criteria used to design such systems which ignores the presence of liquid in the so-called adiabatic vapor transport region and that ignores the dynamics within the evaporator pores is inadequate for low-gravity systems. The present research has shown that the liquid film forming along the walls of the *adiabatic* region will inevitably de-stabilize due to a long wavelength instability mechanism, particularly given the long transport lines characteristic of CPL's. The present research has further shown that bends in these lines will amplify the long wavelength disturbances due to the accumulation of liquid at the outer radius of the bend due to capillary pumping. Given that CPL's rely have multi-pass heat exchangers comprising the condensers, the significance of this result is clear. In time, a liquid slug will form in each and every bend. While these vapor slugs do not inevitably lead to CPL failure, they may if the liquid volume in the CPL is insufficient. Secondly their presence has a significant impact on the maximum heat transport of such systems.

The CHT experiment has also offered a plausible explanation for the vapor pressure oscillations that have been observed in CPL's in the past. Analysis reveals that long wavelength instabilities present in the evaporator pores can lead to liquid bridging and vapor entrapment in the porous media. Subsequent evaporation to the trapped vapor increases the vapor pressure. Eventually the vapor pressure causes ejection of the bridged liquid. Recoil stresses dramatically depress the meniscus. As the meniscus attempts to rewet, the process then repeats. At high enough temperatures, wetting degradation is observed to coincide with these cyclic oscillations.

Page intentionally left blank

S/2-29
434849

Middeck Glovebox (MGBX)

362712

10P.

Bubble and Drop Nonlinear Dynamics (BDND)

Glovebox Investigator:

Dr. L. Gary Leal
University of California, Santa Barbara
Santa Barbara, California

BUBBLE AND DROP NONLINEAR DYNAMICS (BDND)

E.H. Trinh¹, L.G. Leal², D.A. Thomas³, and R.K. Crouch⁴

¹ Jet Propulsion Laboratory, California Institute of Technology

² Department of Chemical Engineering, University of California, Santa Barbara

³ Astronaut Office, Johnson Space Center

⁴ NASA Headquarters, Washington DC

ABSTRACT

Free drops and bubbles are weakly nonlinear mechanical systems that are relatively simple to characterize experimentally in 1-G as well as in microgravity. The understanding of the details of their motion contributes to the fundamental study of nonlinear phenomena and to the measurement of the thermophysical properties of freely levitated melts. The goal of this Glovebox-based experimental investigation is the low-gravity assessment of the capabilities of a modular apparatus based on ultrasonic resonators and on the pseudo-extinction optical method. The required experimental task is the accurate measurements of the large-amplitude dynamics of free drops and bubbles in the absence of large biasing influences such as gravity and levitation fields. A single-axis levitator used for the positioning of drops in air, and an ultrasonic water-filled resonator for the trapping of air bubbles have been evaluated in low-gravity and in 1-G. The basic feasibility of drop positioning and shape oscillations measurements has been verified by using a laptop-interfaced automated data acquisition and the optical extinction technique. The major purpose of the investigation was to identify the salient technical issues associated with the development of a full-scale Microgravity experiment on single drop and bubble dynamics.

1. BACKGROUND

The principal difficulty in the analysis of experimental results of measurements of the nonlinear dynamics of levitated single drops and bubbles on Earth arises from the interference of the levitation fields. Because of the high intensity required to overcome gravity, secondary effects such as shape distortion, strong restraining force, internal flows, and field-induced onset of instability must be separated from the strictly nonlinear effects under scrutiny. This is also important in the context when a specific material property of the liquid is to be inferred from the measured fluid particle motion. For example, a well-established method for the non-contact measurement of surface tension is the determination of the resonance frequencies of drop or bubble shape oscillations [1,2]. Unfortunately, these resonance frequencies are also dependent on the mechanical state of the particle such as the static equilibrium shape, the magnitude of internal flows, the rotational state, and the magnitude of the restraining force of the levitation field. In addition, because of nonlinearity, these resonant frequencies are also dependent on the shape oscillation amplitude [3]. For Earth-based investigations, one or several of these effects can be present during any particular measurement, and their impact must be taken into account in order to arrive at an accurate value for the surface tension.

The judicious combination of different levitation methods having mutually synergistic effects can mitigate these problems. Such an instance would be provided by the combination of electrostatic and ultrasonic levitation methods where the uncontrolled flows and rotation associated with ultrasonic fields are reduced at the expense of the addition of surface charges and a high electric field. A much more rigorous approach, however, would be to carry out the measurements in low-gravity where the field effects can be drastically reduced or even virtually eliminated. Under these circumstances, measurements of the thermophysical properties in Microgravity, or the calibration of the various theoretical

analyses dealing with the field effects would both be productive research tasks. The BDND investigation addresses the problem of developing a compact and low-cost modular approach for the direct measurement of the nonlinear dynamics of both drops and bubbles at ambient temperature and in Microgravity. The emphasis has been placed on using the *same instrumentation* as that would be found in an Earth-based laboratory, and on keeping as much of *the same empirical experimental methodology* as allowable.

2. EXPERIMENTAL OBJECTIVES

State-of-the-arts techniques for the levitation of drops and trapping of gas and vapor bubbles have already been successfully implemented in Earth-based laboratories to obtain quantitative information on the nonlinear characteristics of oscillating drops and the rheological properties of gas bubbles [4,5]. Adapting such methods to the Microgravity environment is the principal motivation of this Glovebox investigation. The specific objectives were thus defined as:

1. The testing of the on-orbit performance of a single-axis ultrasonic levitator in combination with a photodetector-based optical pseudo-extinction method for the precise measurement of drop shape oscillation frequency and relative amplitude. The measurement of the relative change in the *free-decay* fundamental resonance frequency for drop shape oscillations with increasing amplitude *at zero acoustic field intensity*.
2. The measurements of the *driven* resonance frequencies of the first three modes and of the change in the fundamental resonance frequency as a function of the trapping acoustic pressure amplitude.
3. The evaluation of a closed resonant liquid chamber for the stable trapping of single air bubbles in water.
4. The excitation and measurement of large-amplitude bubble shape oscillations and the measurement of the amplitude dependence of the fundamental resonance frequency.

3. EXPERIMENTAL METHOD

An approach using a common optical mounting assembly for both drop levitator and bubble resonant cell has been chosen. The same laser-based illumination and silicon photodetector are used to monitor the dynamics of either single drops and bubbles depending upon the nature of the levitation module placed on the optical assembly. A collimated and expanded beam from a battery-powered 670 nm diode laser is aligned to project an image of a drop (bubble) shadow at a pinhole in focal plane of a focusing lens. A silicon photodetector is placed behind the pinhole to detect the light scattered due to the fluid particle shape oscillations [6,7]. The output of the photodetector is sent to a PCMCIA card in the Shuttle Laptop computer and the analog data is digitized and processed by the Labview software to display the time series and Fourier spectrum of the shape oscillations optical signal.

The drop levitator is the same device used for IFFD (Internal Flows in Free Drops), a related Glovebox investigation, and uses a 23 kHz transducer to generate a standing wave. Spherical drops with diameter between 0.1 and 0.6 cm can be stably positioned in the Shuttle environment with relatively low acoustic power. The electrical drive is supplied by a manually-operated Electronic Control Unit which is capable of generating 15 Volts rms at the input of the piezoelectric transducer. A third-harmonic signal can also be generated, and a variable-frequency (5 to 150 Hz) amplitude modulation of either or both

signals is available. This amplitude modulation function is used to excite the various resonant modes of drop and bubble shape oscillations.

The bubble trapping resonator is a water-filled square cross-section cell used to generate a 23 kHz standing wave as well as its third harmonic. Using the 23 kHz wave, such a device is capable of trapping air bubbles with diameter up to 1 cm at positions along the cell axis and in an Earth-based laboratory. Experimental evidence suggests that gravity plays an important role in the determination of the trapping positions of gas bubbles within the standing wave: An equilibrium bubble position near the cell center may not be available under Microgravity conditions. On the other hand, the third-harmonic standing wave has been shown to be effective at trapping gas bubbles with diameter up to 1 cm in low-gravity [8]. An appropriate combination of the fundamental and third-harmonic resonant pressure distribution should allow trapping of a gas bubble towards the center of the cell and away from the walls. Amplitude modulation of either waves also allows the excitation of bubble resonant shape oscillation modes. **Figure 1a** is a photograph of the BDND flight experiment apparatus with the liquid cell installed on the optical support assembly. **Figure 1b** shows video images of a levitated water drop in air and of an air bubble in water.

4. MSL-1 FLIGHT EXPERIMENTAL RESULTS

4.1 Performance of the apparatus and resonance nonlinearity measurement

The accuracy of the pseudo-extinction optical technique for shape oscillation frequency measurement is roughly independent of the position of the drop or bubble as long as the fluid particle resides within the central portion of the 1.1 cm diameter illuminating laser beam. When ambient transient acceleration impulses within the Space Shuttle-Spacelab environment perturb the sample from its equilibrium position, however, translational oscillations will be excited and the recorded waveform will be a superposition of the translational oscillation frequency upon the shape-dependent signal. The results of an FFT operation will yield the two separate frequencies within the available resolution limit.

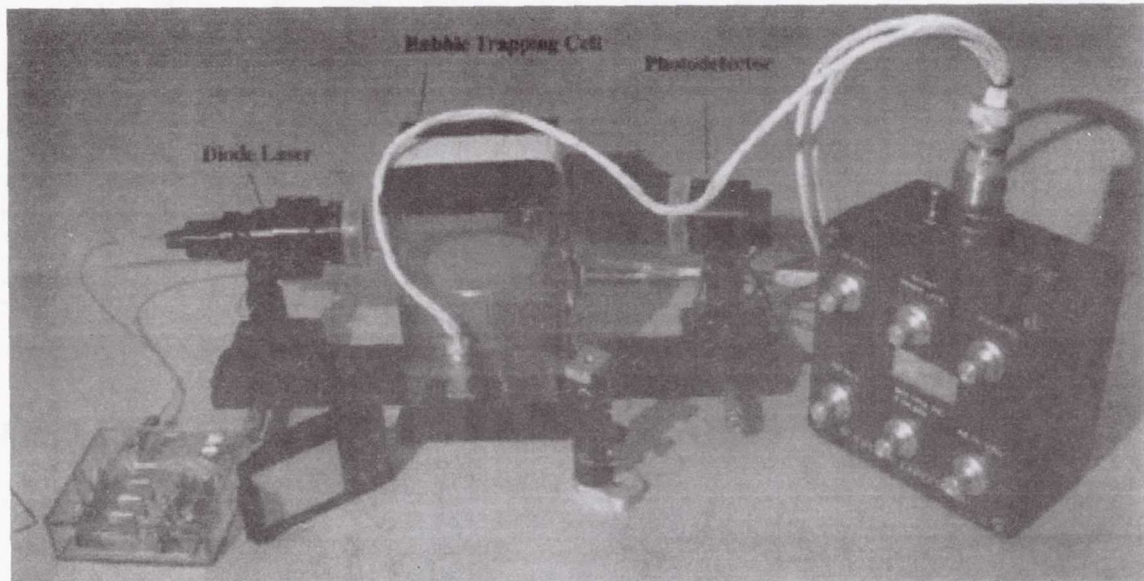


Figure 1a. BDND flight investigation apparatus with Bubble trapping cell.

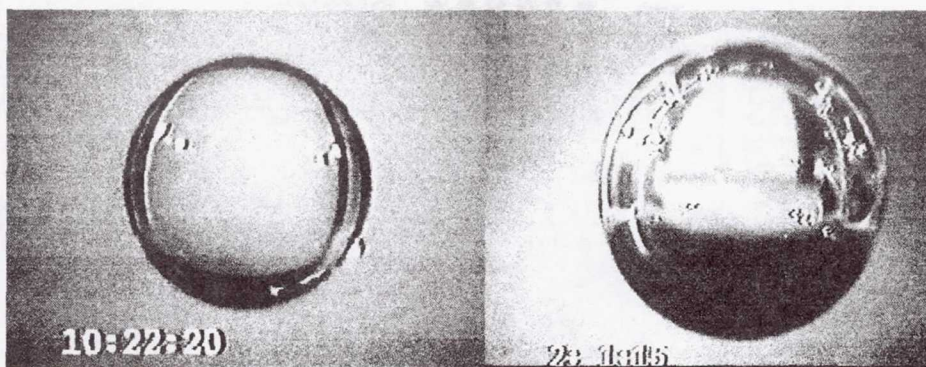


Figure 1b: Single video frames of a 5 mm diameter water drop in air (left) and a 5.5 mm air bubble in water (right). Both were trapped in Microgravity by ultrasonic fields.

The optical detection technique is fundamentally nonlinear, and the measurement of large-amplitude drop or bubble oscillations invariably results in the appearance of higher harmonics of the oscillation frequency. The approach is therefore not appropriate for the quantitative analysis of the frequency spectrum of large amplitude oscillations. The measured value of the *fundamental* oscillation frequency, however, has been verified to be accurate to within 0.2 %. It is thus possible to obtain a near instantaneous measurement of the oscillatory response of a drop or bubble to acoustic excitation both in the continuously driven or free-decay modes.

Reliable results of the measurement of the *free-decay* frequency of drops have been obtained for four different samples. The data were obtained by first driving the drop oscillations through amplitude modulation of the acoustic field and subsequently shutting off the acoustic power and recording the optical signal onto the laptop computer. The use of a manual toggle switch on the levitator housing to suddenly null the acoustic force appears to cause an initial disturbance to the positioned drop for the free decay measurement. This introduces a non-constant baseline for the electrical signal from the photodetector monitoring the drop shape oscillations. This did not preclude, however, the measurement of the free-decay *frequency*. **Figure 2** is a sample 1-G data set obtained for a 4.5 mm diameter drop. The first display gives the time-series of the drop oscillations in real-time, the second is the FFT plot of the same time series data set. The number of total samples and the sample rate can be varied between 1,000 to 5,000. The third trace is the display of a previously captured data set plotted as a function of time, and shows a free-decay trace for a drop levitated in 1-G. The free-decay frequency is a more desirable measurement because of the absence of any acoustic restraining field. It provides the means for real-time measurement of the surface tension of the drop liquid if the density and drop diameter can be measured or are known. Using the MSL-1 flight results, it has been derived that the fundamental free-decay resonance frequency can be determined with a relative accuracy of ± 0.5 %. In turn, the surface tension can be measured with a relative accuracy of ± 1 % since the drop diameter and the density can be determined to within ± 0.1 %. The decay rate also provides a measure of the liquid viscosity.

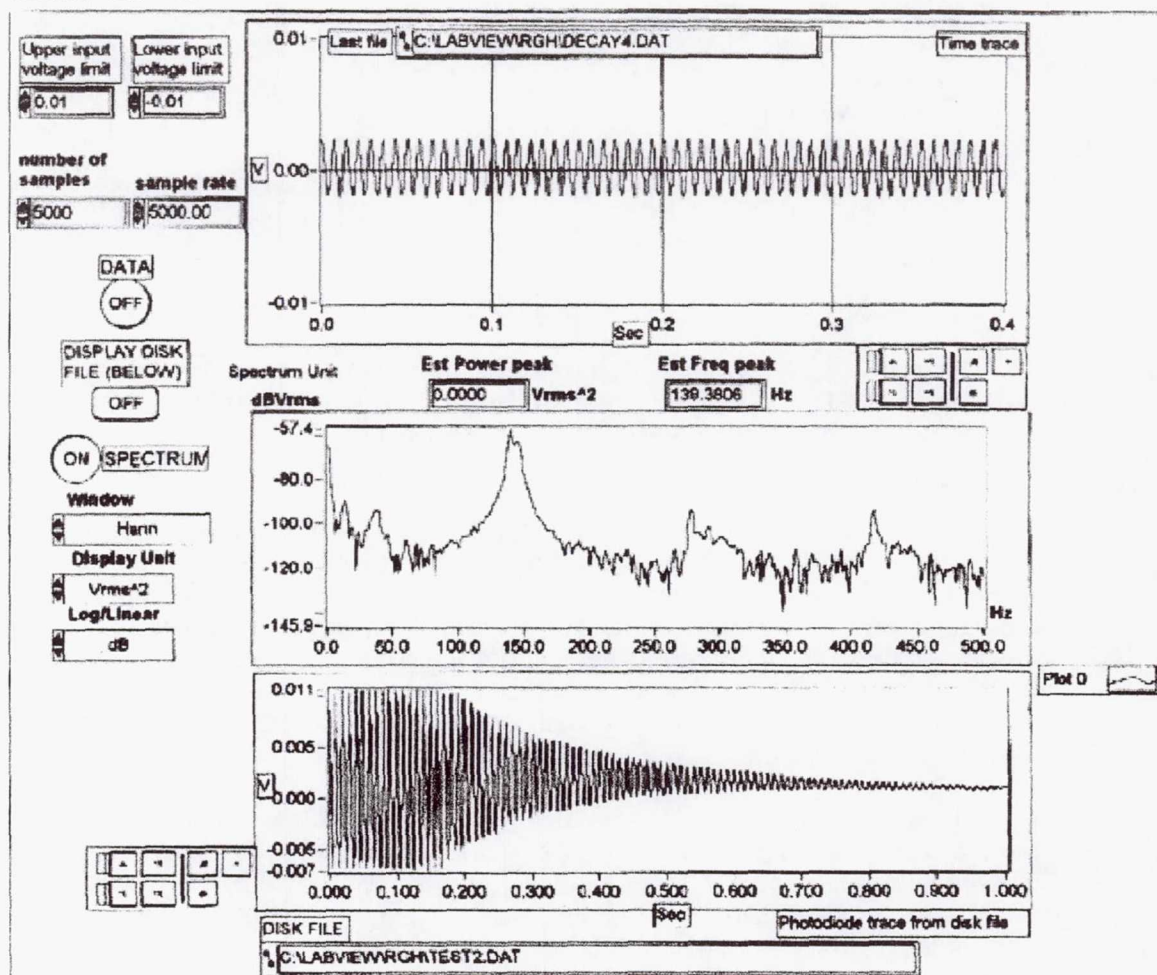


Figure 2. Print-out of the BDND LabView data acquisition display page

Figure 3 is a sample of the MSL-1 data sets obtained in Microgravity. The drop was *initially driven* at 34.8 Hz through amplitude modulation of the acoustic field. The power was then cut-off to the levitator, and the oscillations decay were recorded. The *free-decay* frequency was measured to be a *constant* and equal to 34.2 Hz (+/- 0.1 Hz). No soft-nonlinearity was therefore detected.

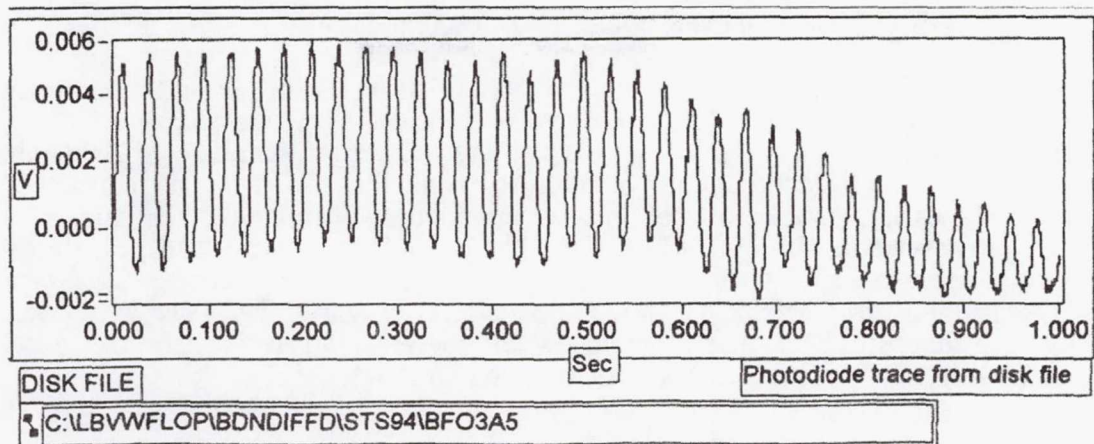


Figure3: Sample time series data set from the MSL-1 results.

4.2 Measurement of first resonance frequencies of drop shape oscillations

Manual measurement of the fundamental resonance frequency for drop and bubble shape oscillations was demonstrated in the driven as well as free-decay approaches. The manual procedure for resonance determination was the visual monitoring of the video image or measuring the amplitude of the time-series signal from the photodetector on the laptop LabView display as the modulation frequency was manually varied. The fundamental mode of shape oscillations was straightforward to excite through amplitude modulation of the acoustic pressure, and its frequency was also successfully measured in the continuously driven mode. The residual rotation of the drop was minimized, but the rotation axis was always nearly perpendicular to the z-axis along which the acoustic pressure was modulated. This residual rotation interfered with the clean excitation of large-amplitude oscillations and prevented the substantial driving of the next higher modes which are more heavily damped due to viscous effects.

4.3 Evaluation of a closed resonant chamber for bubble trapping

Contrarily to Earth-based experimental observations, the fundamental (23 kHz) standing wave did not allow the trapping of air bubbles in water at positions away from the cell walls in the Microgravity environment. Because large gas bubbles (with radii larger than 300 μm) are driven by radiation pressure to acoustic nodal regions, it becomes evident that the desirable bubble trapping positions are found in regions centered along the cell axis between the pressure nodal and anti-nodal planes. The observed capability for centered and long-duration trapping of air bubbles in 1-G is due to buoyancy which causes the equilibrium trapping position to shift to a position above the pressure nodal plane.

The results from the MSL-1 runs confirmed previous observations obtained during the STS-50 flight during which a similar cell was used in the third-harmonic mode to trap single air bubbles [7]. A few stable trapping positions could be empirically found at various locations within the bulk of the liquid. The positioning stability at each of these locations is bubble volume dependent, and varies significantly with the chamber frequency tuning.

4.4 Large-amplitude bubble shape oscillations

Bubbles were trapped near the bottom of the cell using the third harmonic mode, and were also successfully driven into significant amplitude shape oscillations. The fundamental mode of shape oscillations was measured manually by maximizing the oscillation amplitude through the variation of the amplitude modulation frequency. Because the bubbles are trapped at a local pressure minimum in Microgravity (as opposed to above the pressure nodal plane in 1-G), the morphology of the oscillatory shapes is symmetrical with respect to the bubble equator. **Figure 4** shows the strobed configuration of a bubble oscillating in the fundamental mode in Microgravity and in 1-G. The asymmetry of the prolate shape in 1-G is quite pronounced, and reveals a larger excursion of the lower pole during the maximum prolate deformation of the oscillatory cycle.



Figure 4: Comparison of the shape at maximum prolate deformation for a bubble oscillating at 1-G and in low-G.

SUMMARY

The results of the MSL-1 experiment runs have provided the hard experimental data required for the *evaluation* of the current experimental approach, and new definite directions for redesign have been obtained. *The method for the measurement of the fundamental free-decay frequency has been validated*, and consequently, a *real-time technique for the measurement of the surface tension of low-viscosity liquids* has been developed. The controlled investigation of large-amplitude shape oscillations dynamics requires the complete elimination of all residual drop rotation, or the capability to excite drop oscillations in the direction of the rotation axis. Although mechanical adjustments of the levitator were allowed, they were not found to be completely effective at eliminating all residual rotation. No new data for large-amplitude bubble shape oscillations were obtained, but conclusive information on the effect of gravity on the trapping capabilities of a resonant ultrasonic cell was derived. *The basic feasibility of the experimental approach has been confirmed*, and a redesign will allow the complete experimental study of the nonlinear dynamics of single bubbles in Microgravity. The ultimate objectives of the Glovebox investigation were to test and to refine the experimental approach. We believe that these objectives were achieved.

ACKNOWLEDGMENTS

This research was sponsored by the NASA Microgravity Research Division. We would like to thank the invaluable support of the Glovebox Project Office, of the MSL-1 mission team, and of the Marshall Space Flight Center POCC team.

REFERENCES

1. E.H. Trinh, P.L. Marston, J.L. Robey, "Acoustic Measurement of the Surface Tension of Levitated Drops," *J. of Colloid and Interf. Science* **124**, 9S, (1988)..
2. T. J. Asaki, P.L. Marston. and E.H. Trinh, "Shape oscillations of bubbles in water driven by modulated ultrasonic radiation pressure: observation and detection with scattered laser light", *J. Acoust. Soc. Am.* **93**, 706 (1993)
3. E.H. Trinh, R.G. Holt, and D.B. Thiessen, " The dynamics of levitated drops in an electric field", *Phys. Fluids* **8**, 43 (1996)
4. E.H. Trinh, D.B. Thiessen, and R.G. Holt, " Oscillations of bubbles and drops immersed in a liquid", *J. Fluid Mech.*, (1998) at press)
5. T. Asaki, P.L. Marston, D.B. Thiessen, " Effect of an insoluble surfactant on capillary oscillations of bubbles in water: Observation of a maximum in damping", *Phys. Rev. Lett.* **75**, 2686-2689 (1995)
6. T. Asaki, P.L. Marston, "Free-decay of shape oscillations of bubbles acoustically trapped in water and sea water", *J. Fluid Mech.* **300**, 149-167 (1995)
7. P.L. Marston, E.H. Trinh, J. Depew, and T.J. Asaki, "Response of bubbles to ultrasonic radiation pressure: Dynamics in low gravity and shape oscillations", in *Bubble Dynamics and Interface Phenomena*, 343-353, J.R. Blake et al. (eds.) Kluwer Academic Publishers, the Netherlands 1994

Page intentionally left blank

5/3-29
434 850

10P.

Middeck Glovebox (MGBX)

362416

Internal Flows in a Free Drop (IFFD)

Glovebox Investigator:

Dr. Satwindar S. Sadhal
University of Southern California
Los Angeles, California

INTERNAL FLOWS in FREE DROPS (IFFD)

E.H. Trinh ¹, S.S. Sadhal ², D.A. Thomas ³, and R.K. Crouch ⁴

¹ Jet Propulsion Laboratory

² University of Southern California

³ Astronaut Office, Johnson Space Center

⁴ NASA Headquarters, Washington DC

ABSTRACT

Within the framework of an Earth-based research task investigating the internal flows within freely levitated drops, a low-gravity technology development experiment has been designed and carried out within the NASA Glovebox facility during the STS-83 and STS-94 Shuttle flights (MSL-1 mission). The goal was narrowly defined as the assessment of the capabilities of a resonant single-axis ultrasonic levitator to stably position free drops in the Shuttle environment with a precision required for the detailed measurement of internal flows. The results of this entirely crew-operated investigation indicate that the approach is fundamentally sound, but also that the ultimate stability of the positioning is highly dependent on the residual acceleration characteristic of the Spacecraft, and to a certain extent, on the initial drop deployment of the drop. The principal results are: the measured dependence of the residual drop rotation and equilibrium drop shape on the ultrasonic power level, the experimental evaluation of the typical drop translational stability in a realistic low-gravity environment, and the semi-quantitative evaluation of background internal flows within quasi-isothermal drops. Based on these results, we conclude that the successful design of a full-scale Microgravity experiment is possible, and would allow accurate the measurement of thermocapillary flows within transparent drops. The need has been demonstrated, however, for the capability for accurately deploying the drop, for a quiescent environment, and for precise mechanical adjustments of the levitator.

1. BACKGROUND

The fundamental importance of thermocapillary (or Marangoni) flows in a low-gravity environment has been firmly established by many theoretical and experimental investigations [1-3]. It is also clear that the rigorous separation of these surface tension-driven flows from buoyant convection is not achievable in a ground-based laboratory when the additional requirement for accurate velocity field measurement is also imposed. Although a substantial effort has been expended by NASA in the study of Marangoni convection in recent years, little work has been devoted to the case of a totally free, three-dimensional liquid-gas interface such as that presented by freely levitated drops. The recently developed experimental techniques for drop levitation has allowed the acquisition of notable new understanding in scientific subjects in fluid dynamics, surface phenomena, and fundamental material science [4-9]. Access to low-gravity allows the most effective exploitation of this levitation-based experimentation approach because it allows the drastic reduction of the detrimental influence of the high-intensity fields required for levitation against 1-G.

The side effects of levitation fields in Earth-based laboratories are the principal subjects our ground-based research task: The outer streaming flows and the induced internal circulation associated with ultrasonic levitation are investigated, and their impact on the measurement of thermocapillary flows is to be assessed. In addition, experimental measurements of buoyant thermocapillary flows in laser-heated electrostatically levitated drops are to be carried out in 1-G in order to develop the techniques for Microgravity implementation. The opportunity to develop and to carry out a preliminary Glovebox

investigation should lead to the generation invaluable new information for the planning and development of a potential flight experiment.

Even though our Earth-based experimental studies utilize electrostatic levitation, this approach is quite elaborate and no proven technique has yet been tested for operation in Microgravity. Ultrasonic levitation, on the other hand, is a mature technology, and it has been demonstrated to operate equally well on Earth and in microgravity. This latter method also has the advantage to require a modest level of instrumentation, and has been shown to be relatively simple to operate. A major deficiency, however, arises from the uncontrolled drop rotation which has been attributed to the induced streaming flows associated with high-intensity sound waves. The goal of the Glovebox investigation is thus to test a single-axis resonant ultrasonic levitator in low-gravity by measuring the residual uncontrolled drop rotation under minimal power level and using adjustable mechanical controls in an isothermal condition as well as under differential heating.

The specific objectives are then defined as:

- The demonstration of the feasibility of using a simple non-contact single-axis ultrasonic positioner to study thermocapillary flows in low-gravity.
- The evaluation of the interfering effects due to ultrasonic levitation forces.
- The measurement of the drop equilibrium shape and residual rotation as a function of the acoustic power level
- The performance of the first experimental observation of thermocapillary flows in a free drop due to non-uniform surface heating (this objective was not carried out on STS-94 or 83, but it will be implemented for a reflight on STS-95).

2. EXPERIMENT DESCRIPTION

The test for the non-contact positioning of a drop in microgravity was carried out by using an ultrasonic resonant levitator [5] operating at 23 kHz. Manual tuning of the resonance conditions was performed by adjusting both the frequency of the electronic drive as well as the mechanical gap separation for optimizing the standing wave intensity. The levitator was designed to fit on an optical assembly also used to hold a diode laser and beam expander and a solid-state photodetector with focusing lens assembly. **Figure 1** shows the IFFD apparatus components. The entire optical assembly is placed on the work area inside the Glovebox, but both the Electronic Control Unit (ECU) and the laser battery packs remain outside. The Glovebox doors remain open except for the front one which holds the front view video camera. A second video camera is mounted on the Glovebox panel in order to display a top view of the drop through a window placed in the reflector component of the ultrasonic levitator. Internal flow and rotational motion of the drop are observed through suspended tracer particles dispersed in the test liquid (Pliolite tracers).

A drop is manually injected and deployed inside the levitation region using a syringe and either Teflon or steel needle. Drops of water and an aqueous solution of glycerin with diameter between 2 and 4 mm were deployed during the flight. The adjustable sound field parameters were the drive frequency and the amplitude. The analog electronic instrumentation was custom designed and has previously flown as a part of the STS-50 science payload in 1992.

The data to be acquired are:

- The drop video images (providing a measurement of the diameter and shape deformation using the calibration image of a ruler),
- The motion of the suspended particles inside the drop (providing the internal flow and the rotation rate),
- The ultrasonic power level.
- Video data are recorded on the Glovebox 8mm VCR tapes

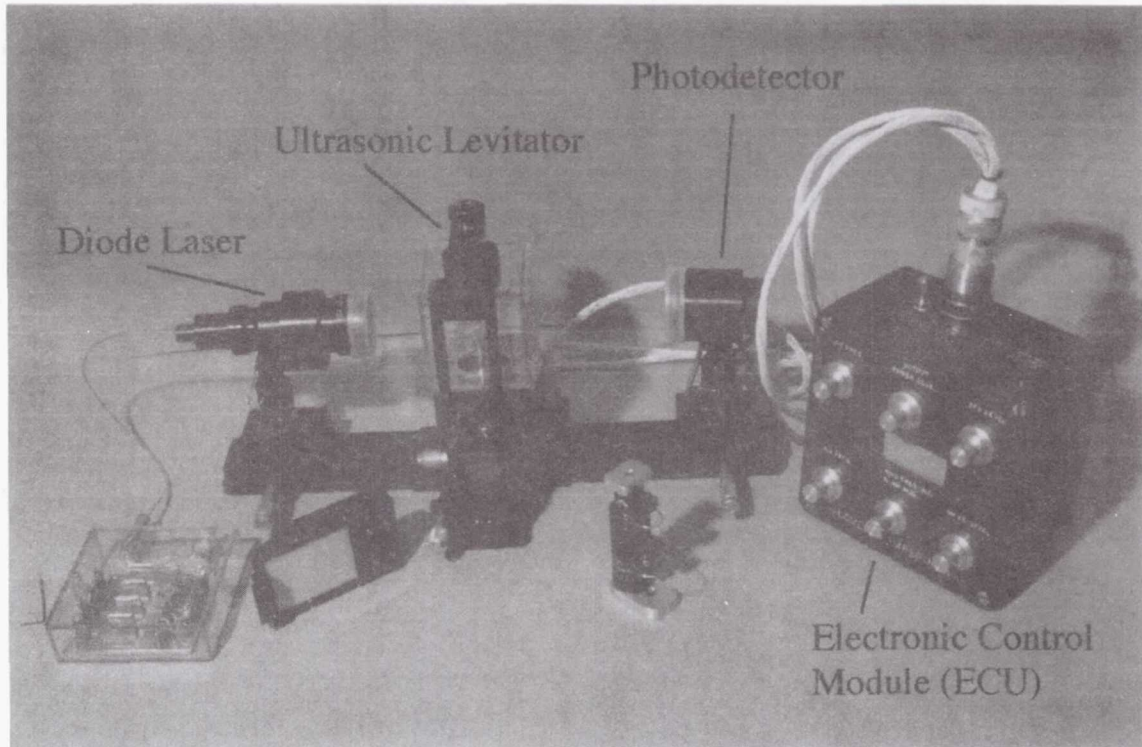


Figure 1. IFFD flight investigation apparatus

3. EXPERIMENTAL PROCEDURE

The most crucial part of the experimental procedure is the manual drop injection and deployment process. This is primarily because manual tuning of the standing wave is required prior to injecting a drop from a syringe and needle assembly. The process involves both frequency setting on the electronic control module and the mechanical adjustment of the spatial gap where the ultrasonic standing wave is established. The visual feedback for the quality of the resonance tuning is provided by the distortion of the droplet by the ultrasonic radiation pressure.

After successful deployment of a free drop within the levitation volume, a waiting period is required for sample stabilization. A rough alignment of the mechanical components of the levitator is required for optimal sample stability. In addition, at low ultrasonic drive power the restoring force of the acoustic well is diminished, and a minimization of all external continuous and transient acceleration is required. For typical Earth-based conditions, the resonant translation mode of a 3 mm diameter drop in the acoustic well has a frequency in the vicinity of 40 Hz. In low gravity this resonance would

be on the order of 5 Hz; any disturbance with a similar frequency component would drive oscillatory motion.

Limited adjustment of lighting using the 1.1 cm diameter diode laser beam and the Glovebox internal lights is required for optimization of both the drop contour for shape and dimension measurements, and for the visualization of the suspended tracer particles. Adjustments to the front and top view Glovebox video cameras are also required for sharp focus and centering of the drop image.

The determination of the controlling parameters for the minimization of the uncontrolled drop rotational motion requires the adjustment of micrometers setting the relative alignment of the driver and reflector components of the ultrasonic levitator. *The principal objective of the investigation is to establish the minimum required acoustic power for stable sample positioning and the measuring the resulting minimum rotational velocity.* Once those conditions are obtained, observation of the internal flow through suspended particle tracking can be accomplished.

4. EXPERIMENTAL RESULTS

4.1 Drop Translational Stability

Drops of water and water-glycerin mixtures with diameter between 0.2 and 0.6 cm have been deployed and restrained within the ultrasonic positioning well. Once the drop positioning controls are adjusted for optimum and quiescent conditions in the Spacelab module, the sample translational oscillations have been observed to be restricted to excursions *smaller than $0.1 R_{DROP}$* for low acoustic power and spherical equilibrium shape. Because of the smaller required field of view, this kind of positional stability allows a high enough optical magnification to resolve the details of the motion of tracer particles within the drop bulk with a *relative position resolution of better than 0.5 %*. The Sound Pressure Level (SPL) required to keep 5 mm diameter drops stationary within this restricted excursion window is *45 dB lower* in the microgravity environment than in 1-G.

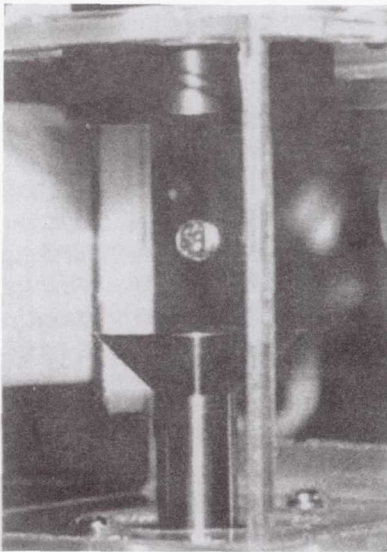


Figure 2: A positioned drop in the IFFD in μG .

4.2 Drop Rotational Stability

The IFFD ultrasonic levitator incorporates a cubical chamber surrounding the immediate drop trapping volume. The primary purpose for this transparent lucite enclosure is to shield the drop from external forced convection, but the hard, acoustically reflecting walls also introduce extraneous resonances that interfere with the primary positioning standing wave. This cavity also shapes the acoustically-driven convective flow fields which generate the aerodynamic torque on the freely levitated drop. The characteristic convective (or streaming) velocity is proportional to the square of the acoustic pressure amplitude, and a substantial uncontrolled drop rotational motion results due the aerodynamic drag exerted by the air flow on the drop surface. A limited control over the direction and magnitude of this resulting aerodynamic torque can be exercised by making fine mechanical adjustments of the relative alignment of the reflector and acoustic driver components of the levitator. A drastic reduction of the convective velocity, however, can be directly effected by reducing the acoustic pressure. The above mentioned decrease in the required microgravity positioning acoustic power also greatly lowers the uncontrolled drop rotational velocity.

Figure 3 reproduces the data obtained from the residual rotational velocity on a 4.5 mm diameter glycerin-water drop and a 5.1 mm diameter thick glycerin-water-air shell (drop with a suspended air bubble). As observed, a minimum rotation rate of 0.1 rps can be measured at the lowest acoustic drive levels in both cases. The residual rotation rate measurements were carried out after all mechanical alignments of the reflector and driver have been effected by the crew. These adjustments have invariably resulted in setting the drop rotation axis in a plane normal to the levitator symmetry axis, yielding a rotation roughly normal to the front camera viewing axis

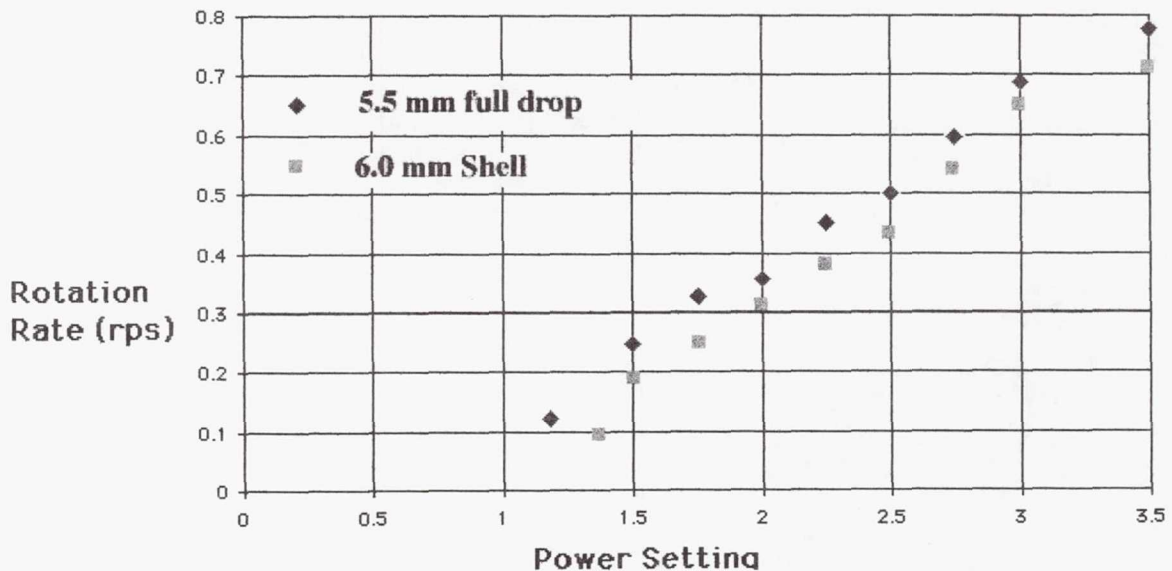


Figure 3. Residual rotation rate as a function of the acoustic power

4.3 Controlled Drop Deformation Measurements

Because the drop is positioned at an acoustic pressure nodal plane in microgravity, it becomes feasible to carry out detailed measurement of the *symmetrical* acoustically-induced drop deformation in order to perform a quantitative evaluation of existing theoretical predictions. It also becomes possible to carry out measurement at very low acoustic pressure and for *electrically uncharged* free drops. A quantitative validation of

theoretical treatments will allow their use in the development of reliable non-contact methods for the measurement of surface tension of viscous liquids which do not allow measurements of dynamic oscillations.

The STS-94 data yielded drop deformation with axial ratio ranging between 1.0 (spherical drops) to 2.3 (drastically flattened drops). The linear dimensions of the drop contour could be determined to better than 0.5 %, allowing a relative accuracy of better than 1% for the drop axial ratio. **Figure 4** displays results of the low-gravity measurements together with Earth-based data. The axial ratio is plotted as a function of the relative change in acoustic pressure level for both ground-based [10] and microgravity data. In addition to extending to very low relative acoustic pressure, the low-gravity data show a larger deformation for the same acoustic pressure ratio. The droplet size relative to the acoustic wavelength was larger in microgravity than on Earth ($kR=2\pi R/\lambda=1.1$). The range of the measurements has been greatly extended in microgravity both for droplet size and deformation (both at the high and low deformation values).

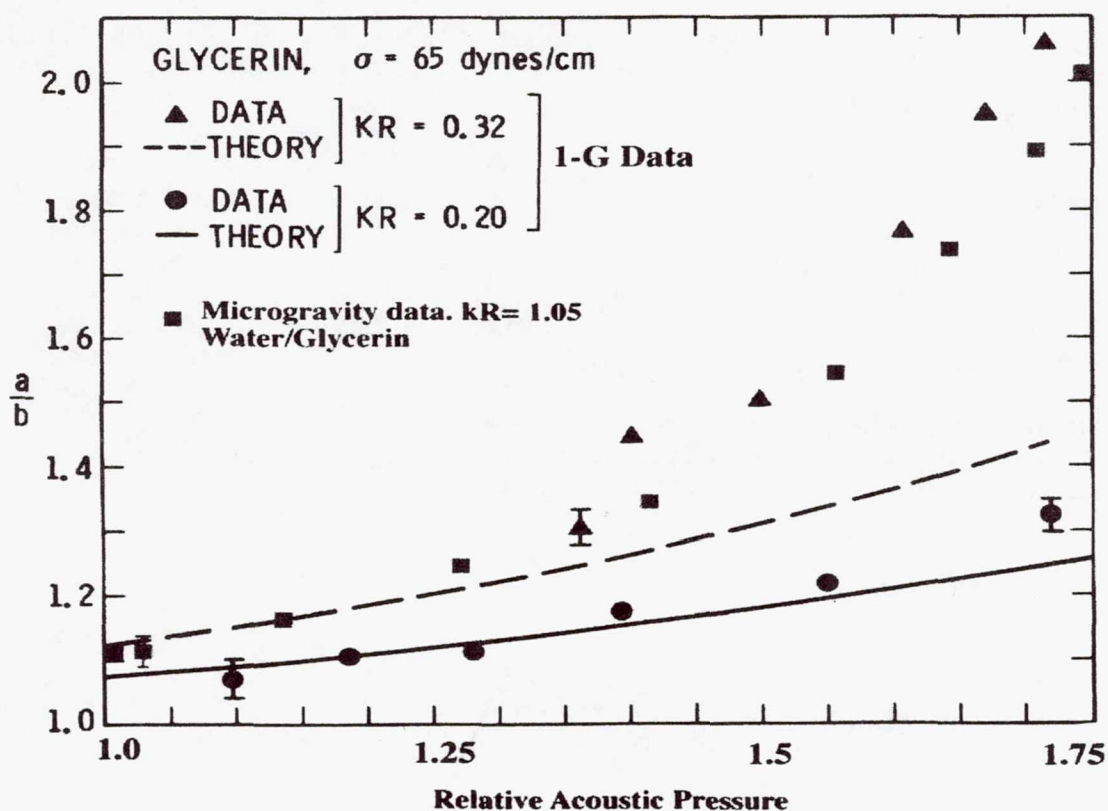


Figure 4. Measurement of drop deformation as a function of the acoustic pressure amplitude.

4.4 Residual internal flow in a quasi-isothermal drop

A state of very slow drop rotation has allowed the measurement of the residual internal flow within freely positioned droplets in a quasi-isothermal environment. Such a

measurement is required in order to determine the base state within the drop prior to inducing thermocapillary flows using spot-heating. The analysis of three different sets of video images for three different drops has resulted in a quantitative evaluation of the average residual convective flow within free drops in microgravity. The data indicate that any residual convection velocity could not be greater than 0.05 mm/minute. These results were obtained by using two-camera tracking of visible tracer particles within droplets undergoing slow rotation under minimal acoustic drive.

5.0 SUMMARY

An unbiased assessment of the results of the IFFD flight investigation would be generally positive: All of the objectives have been addressed and conclusive and reliable data have been obtained. The practical capabilities of a simple single-axis drop levitator have been reasonably well tested in the Shuttle environment, and some conclusive evidence for the feasibility of performing accurate thermocapillary flow measurements in the moderate Marangoni number region has been obtained. Very low acoustic power is required for stable positioning, leading to negligible drop deformation and a low residual rotation rate. In addition, the first set of data on acoustically-induced drop deformation has been obtained in low gravity, under conditions which make it feasible to compare with theoretical predictions.

The scope of a Glovebox investigation significantly limits the resources and sophistication needed to design and to implement a well controlled flight experiment. The lack in capabilities for full automation and intelligent control of the experiment, however, can be compensated by the availability of skilled operators. The IFFD investigation was designed for complete flexibility for manual control and adjustment to unanticipated observations. The intent was to test the experimental approach, but also to document the various details associated with the unpredictable behavior of a free drop within an ultrasonic restraining force potential. We believe that in spite of the difficulty encountered during operations of the experiment, substantial new knowledge has been acquired that will allow the design of a more substantial and automated apparatus that would be a useful and productive containerless experimentation facility for fluid dynamical studies.

ACKNOWLEDGMENTS

This research was sponsored by the NASA Division of Microgravity Research, and was performed at the Jet Propulsion Laboratory with phases carried out with the indispensable participation of the Glovebox Project Office and the POCC team at the Marshall Space Flight Center and the integration team at the Kennedy Space Center.

REFERENCES

1. Y. Kamotani, J. Mastad, and A. Pline, *J. Thermophysics & Heat Transfer*, **10**, 102-108 (1996)
2. M.K. Smith and S.H. Davis, *J. Fluid Mech.* **132**, 119-144 (1983)
3. Y. Kamotani, S. Ostrach, and J. Mastad, in *Proceedings of the Fourth Microgravity Fluid Physics and Transport Phenomena Conference*, 263-368 (1998)
4. R.E. Apfel, Y. Tian, J. Jankovsky, T. Shi, X. Chen, R.G. Holt, E. Trinh, A. Croonquist, K.C. Thornton, A. Sacco, C. Coleman, F.W. Leslie, and D.H. Matthiesen, *Physical Review Letters* **78**, 1912 (1997)

5. T.G. Wang, A.V. Anilkumar, and C.P. Lee, J. Fluid Mech. **308**, 1-14 (1996)
6. Rhim W.K., Chung, S.K., Barber, D., Man, K.F., Gutt, G., Rulison, A, and Spjut, Rev. Sci. Instrum. **64**, 2961-2970 (1993)
7. E.H. Trinh, ESA Publications **SP-295**, 503 (1990).
8. E.H. Trinh, Rev. Sci. Instr., **56**, 2059, (1985).
9. E.H. Trinh, R.G. Holt, and D.B. Thiessen, Phys. Fluids **8**, 43 (1996)
10. E.Trinh and C.J.Hsu, J. Acoust. Soc. Am. **79**, 1335 (1986)

Page intentionally left blank

514-25
434851

Middeck Glovebox (MGBX)

362717
16P.

Fiber Supported Droplet Combustion-2 (FSDC-2)

Glovebox Investigator:

Dr. Forman A. Williams
University of California, San Diego
La Jolla, California

FIBER SUPPORTED DROPLET COMBUSTION-2

Renato Colantonio, Daniel Dietrich, John B. Haggard, Jr. and Vedha Nayagan
National Center for Microgravity Research
NASA Lewis Research Center
21000 Brookpark Road
Cleveland, OH 44135

Frederick L. Dryer
Department of Mechanical and Aerospace Engineering
Princeton University
Princeton, NJ 08544

Benjamin D. Shaw
University of California, Davis
Davis, CA 95616

Forman A. Williams
Center for Energy and Combustion Research
University of California, San Diego
La Jolla, CA 92093

Abstract

Experimental results for the burning characteristics of fiber supported, liquid droplets in ambient Shuttle cabin air (21% oxygen, 1 bar pressure) were obtained from the Glove Box Facility aboard the STS-94/MSL-1 mission using the Fiber Supported Droplet Combustion - 2 (FSDC-2) apparatus. The combustion of individual droplets of methanol/water mixtures, ethanol, ethanol/water azeotrope, n-heptane, n-decane, and n-heptane/n-hexadecane mixtures were studied in quiescent air. The effects of low velocity, laminar gas phase forced convection on the combustion of individual droplets of n-heptane and n-decane were investigated and interactions of two droplet-arrays of n-heptane and n-decane droplets were also studied, with and without gas phase convective flow. Initial diameters ranging from about 2mm to over 6mm were burned on 80-100 μm silicon fibers. In addition to phenomenological observations, quantitative data were obtained in the form of backlit images of the burning droplets, overall flame images, and radiometric combustion emission measurements as a function of the burning time in each experiment. In all, 124 of the 129 attempted experiments (or about twice the number of experiments originally planned for the STS-94/MSL-1 mission) were conducted successfully.

The experimental results contribute new observations on the combustion properties of pure alkanes, binary alkane mixtures, and simple alcohols for droplet sizes not studied previously, including measurements on individual droplets and two-droplet arrays, inclusive of the effects of forced gas phase convection. New phenomena characterized experimentally for the first time include radiative extinction of droplet burning for alkanes and the "twin effect" which occurs as a result of interactions during the combustion of two-droplet arrays.

Numerical modeling of isolated droplet combustion phenomenon has been conducted for methanol/water mixtures, n-heptane, and n-heptane/n-hexadecane mixtures, and results compare quantitatively with those found experimentally for methanol/water mixtures. Initial computational results qualitatively predict experimental results obtained for isolated n-heptane and n-heptane/n-hexadecane droplet combustion, although the effects of sooting are not yet included in the modeling work. Numerical modeling of ethanol and ethanol/water droplet burning is under development. Considerable data remain to be fully analyzed and will provide a large database for comparisons with further numerical and analytical modeling and development of future free droplet experiments aboard space platforms.

Background

Isolated, spherically symmetric, single droplet burning is the simplest example of non-premixed combustion that involves large molecular species typically found as components in liquid hydrocarbons used as transportation fuels. The simple, symmetrical, experimental configuration that can be obtained by removing the complicating effects of buoyancy provides an ideal venue for investigating, in fundamental detail, the complex physical and chemical processes involved in diffusion/mixing limited combustion of liquid fuels. These phenomenon include the effects of the multi-component nature of the liquid fuel, liquid phase internal circulation effects (effective liquid phase diffusivities), liquid phase combustion product absorption, diffusion flame dynamics, soot interactions in diffusion flame configurations, and radiative and diffusively controlled extinction processes. Furthermore, the spherically symmetric configuration can be perturbed in systematic and simply quantifiable fashion by imposing a slow gas phase convective flow relative to the droplet, and/or by introducing neighboring droplets in an array to investigate in a simple configuration the drop and flame interactions encountered in spray combustion.

Another paper in this L+1 proceedings describes the background and development of a full facility experiment, the Droplet Combustion Experiment (DCE), which can be utilized to investigate many of the above issues with experimental rigor¹. For

example, this facility was used on the MSL-1 mission to study the combustion of isolated n-heptane droplets in helium/oxygen at various oxidizer concentrations and ambient pressures and in shuttle cabin air at atmospheric pressure. The successful operation of DCE on a particular fuel and various ambient conditions is strongly dependent on developing experimental experience with large initial droplet diameters, larger than those which can be studied successfully in ground-based (droptower) or parabolic flight experiments. The Fiber Supported Droplet Combustion (FSDC) experiment was conceived as a much simpler, complementary facility that could not only provide the source of such data, but would permit cursory results on a myriad of liquid fuel compositions and droplet configurations, all within one flight mission. The use of fiber supported droplet combustion methods permits the study of large initial diameter droplets under quiescent conditions, as well as in the presence of forced gas phase convection. In addition, to studying individual droplet combustion phenomena, the interactions of multiple droplet flames with one another and with forced gas phase convection can also be investigated.

An FSDC experiment, FSDC-1, was first manifested as a multi-investigator endeavor during the STS-73/USML-2 mission in 1995. The mission profile consisted of seven separate sets of experiments: n-heptane single droplet combustion without forced flow, n-heptane droplet combustion with forced flow, methanol droplet combustion, methanol droplet-array combustion, methanol/dodecanol miscible binary-fuel mixture combustion, n-heptane/n-hexadecane binary-fuel droplet combustion, and methanol/water mixture droplet combustion. Due to crew-time limitations and safety considerations on the amount of liquid flammables that can be carried on board the Space Shuttle, each of these investigations were allotted a maximum of five droplet burns, with only two different mixture compositions for the bi-component fuels and two different flow velocities for the forced convection experiments. Although two sets of the planned experiments were unable to obtain data because of hardware malfunctions (n-heptane single droplet combustion without forced flow, methanol droplet-array combustion), the remaining components of the test matrices were very successful. The details of the experimental observations are reported and discussed in several publications^{2,3,4,5,6,7,8,9}.

The present FSDC-2 experiments were conducted aboard MSL-1 with slightly re-configured hardware to gather further scientific data on droplet combustion phenomenon and to extend the range of parameter values over which data were obtained during the USML-2 mission, both in terms types of fuels and initial droplet size.

Objectives

The general objectives of the droplet combustion experiments at the large diameters reported here focus on improving understanding of the mechanisms and the dynamics of burning liquid fuel droplets. The scientific justifications for these objectives are fully detailed elsewhere. The specific objectives of the FSDC-2 experiments themselves were as follows:

- a) *Obtain new (first) data on the isolated droplet combustion behavior of n-heptane, n-decane, and ethanol over a range of initial droplet sizes from 2 to 6mm, in quiescent air, and to investigate the effects of relative gas phase convection on the combustion on individual droplets of n-heptane and n-decane.*
- b) *Obtain new (first) data from droplet array experiments performed using n-heptane, and n-decane as fuels, and for a range of L/D ratios (where D is the droplet diameter and L is the distance between the droplets).*
- c) *Obtain additional and complementary data (at mixture ratios not studied in FSDC-1) for isolated n-heptane/n-hexadecane and methanol/water droplet combustion in air, and new data on the isolated droplet combustion on ethanol/water azeotrope in air, over a range of droplet sizes from 2 to 6 mm.*

The co-investigators of each of these related projects and the relationship of each to other ongoing microgravity combustion projects are listed in Table 1. In addition to the FSDC-2 investigators, Drs. A. J. Marchese, and Bi-Li Zhang, former graduate students involved in this research at Princeton University and the University of California, San Diego, participated as FSDC Science Team Members during the MSL-1 mission.

Experiment Description

All experiments were carried out in the Glovebox Facility on board the Spacelab using the FSDC-2 experimental apparatus (Fig. 1). Fuels were contained in fourteen modified, airtight commercial syringe cartridges. Because of fuel volatility, the loaded fuel cartridges were stowed in the shuttle only 24-h before launch. To operate the experiment, the fuel cartridge is screwed into the base of the experiment module. The crew turns a plunger screw, forcing fuel through two opposed hypodermic needles to the deployment site on a silicon fiber located between the needles and perpendicular to them. Numbered needle pairs, the fiber stretched between them and fuel cartridges may be seen in Fig. 1. After the fuel coalesces into a droplet of the desired size, the needles are slowly retracted to minimize contact of the liquid with the needle surfaces. The stretched droplet is then deployed by rapidly retracting the needles into the bottom of the chamber. Motions of the deployed droplet are allowed to dampen before the ignition button is depressed. This automatically raises a replaceable igniter wire into place on one side of the droplet (parallel to the fiber), approximately 3.5 mm from the fiber, and simultaneously provides DC electric current to the igniter. The igniter, seen on the chamber floor in Fig. 1, is a coiled loop of an aluminum alloy wire (resistivity 0.04 Ω/mm) with a diameter of 0.25 mm and total length about 35 mm, carrying a current of approximately 3 amps. When the crew operator detects ignition visually, the igniter button is released, automatically retracting the igniter to the bottom of the test chamber.

Imaging data are provided by two video views, one a backlit view of the droplet and the other a perpendicular view of the flame. The backlight is comprised of five LEDs (620–670 nm), which reflect off a mirrored lens in the bottom of the experiment module. The video camera for the droplet view is attached to the Glovebox microscope. The second video camera, with a view essentially orthogonal to the microscope, records the droplet, the fiber, and the flame. All of the data were recorded using three 8 mm VCR's.

The taped camera images were analyzed using microcomputer-based imaging analysis systems. Reference 10 describes a typical example of the type of system employed. A frame grabber board is used to transfer video images of the backlit droplet to a microcomputer for analysis. The droplet image is differentiated from the background using various threshold-intensity-based algorithms. A two-dimensional projected area (A_p) is determined by counting individual pixels within the envelope of the droplet image. An equivalent droplet diameter, D_{AP} , can be determined as the diameter of a circle that yielded the measured projected area. In some cases a volume-equivalent diameter D_v , based on the assumption that the droplet is symmetric about the fiber has also been used to define the equivalent droplet diameter. In other cases, measurements of the major and minor axes of the droplet have been used to calculate an equivalent drop diameter. Each of the above reduction techniques have specific advantages and disadvantages, and the multi-investigator team continues to make cross-comparisons of the methodologies. For the purposes of the present paper, differences amongst results produced by the various methods are not relevant to the conclusions drawn.

In addition to the imaging data, two radiometers were employed in the experiments to measure radiant fluxes from the flame zone as a function of burning time. One radiometer (denoted as Radiometer 1) was used to detect radiant power fluxes in the wavelength range 0.6 - 40 microns. The other radiometer (denoted as Radiometer 2) was used to detect radiant power fluxes in the wavelength range 5.1 - 7.5 microns, which corresponds approximately to the wavelength range for thermal radiation emission from water vapor.

In experiments investigating the effects of forced flow, a dc fan (Fig. 1) generates an imposed forced flow. The fan induces airflow through a honeycomb (ten-to-one cell aspect ratio) inlet section and the experiment module, with the vectored direction collinear with the supporting droplet fiber. Uniform forced air speeds from 30 mm/s to 250 mm/s can be produced. When forced convection is imposed during an experiment, the droplets tend to move along the fiber. In order to "anchor" the droplet within the field of view of the imaging cameras, small ceramic (alumina glue) beads were placed along the SiC fibers at a spacing of 5 mm. This spacing also fixed the droplet separation distance during linear array tests at 5 mm for all the experimental runs. These beads were not present in the FSDC-1 experimental configuration. Further details of the apparatus and the experiment operation procedures can be found in Reference 4.

Each droplet combustion test occurred at pressures (0.996–1.107 bar), oxygen mole fractions (0.204–0.222), and relative humidity (39–46%) of the Spacelab environment.

Experimental Results Comparisons with Ground Based Data, and Analyses

Below, we summarize our initial findings and analyses concerning the study of pure alkane, binary alkane mixture, and alcohol isolated droplet burning in quiescent atmospheres, two-droplet array combustion in quiescent gas surroundings, and the effects of forced convection on droplet burning phenomenon. Much of the data presented are preliminary in nature, and further analyses are continuing. The qualitative features of results presented and discussed below are clear and independent of the continuing evaluations of the quantitative nature of the results. Quantitative interpretations may be modified by the continuing work. We therefore caution readers to contact the authors should they have interest in using the results from the experiments presented here quantitatively.

Isolated Droplet Quiescent Gas Phase Studies

Pure Alkanes

Isolated droplet studies without convection were performed using both pure n-heptane and n-decane as fuels. Normal heptane and decane are molecular species characteristic of liquid fuel carbon numbers found for species in gasoline, gas turbine, and diesel fuels. Burning n-heptane droplets allows a direct comparison between the fiber-supported data and the Droplet Combustion Experiment (DCE) obtained in the MSL-1 mission. This comparison includes examining the effects of the fiber on gasification rates and extinction, comparing the potential effects of the reduced gas volume surrounding the burning droplet in FSDC-2 (in comparison to that in DCE), and a comparison of burning heptane in air versus burning heptane in a helium-oxygen environment. Through several efficiencies in conducting tests in DCE, some tests not originally planned were conducted with cabin air rather than helium-oxygen mixtures. DCE experiments included tests using a similar filament suspension technique (that had no ceramic beads mounted on the filament). Thus, the combined FSDC-2 and DCE tests with n-heptane permit a number of cross-comparisons of results. Experiments with n-decane have never been performed in space environments before, although n-decane is a fuel that could be studied in DCE in the future. The quiescent, isolated droplet studies of n-heptane and n-decane also provide base cases for comparison with studies involving forced convection and 2-droplet arrays (discussed below). Both FSDC-2 and DCE tests result in excellent opportunities to evaluate the relationship of initial droplet size to gasification rate, flame dynamics, and extinction phenomena, particularly flame extinction induced by radiative heat loss from the droplet flame.

Fifteen single droplets of n-heptane were successfully ignited and burnt under quiescent gas conditions. Views of the droplets and radiometers exist for all the tests; no visible flame appears in the tests. However, the flame location can be estimated from local position of maximum radiation from the silicon fiber passing through the flame and the droplet surfaces. In some of the tests, bubbles formed inside the droplet while it was still burning. Initially, small bubbles usually grew to large bubbles (This growth maybe caused by small bubbles combining or by droplet heating.). The bubbles left the droplet at various times during the burning, but often a bubble with a volume approximately equal to the remaining fluid volume broke free in the last one or two seconds of the burn. Bubbles were present in studies with other fuels as well, and this observation appears to be more pervasive in the FSDC-2 experiments than was reported for FSDC-1 studies. Furthermore, the presence of the ceramic bead (FSDC-2 configuration only) appeared to enhance bubble formation, particularly in forced convection studies. The exact cause of these bubbles is still being investigated.

Preliminary measurements of droplet diameter as a function of burning time and extinction diameter as a function of initial droplet diameter have been made using the droplet views. These measurements cover a variety of initial droplet diameters ranging from 2.48 millimeters to 6.26 millimeters.

Figure 2 compares some of the FSDC-2 and DCE measurements of average gasification rate for n-heptane droplet combustion in air with ground-based experimental data and recent numerical modeling results¹³. One notes that the average gasification rate decreases with increasing initial droplet size, both experimentally and computationally. Furthermore, the FSDC-2 and DCE experimental measurements at about 4-mm initial droplet size are in excellent agreement with one another. Consistent with the interpretation of similar behavior for methanol droplet combustion¹¹ and DCE data for n-heptane¹², Marchese et al.¹³ conclude that this result is due to energy losses from the flame structure from both luminous (soot) and non-luminous radiation (hot gas products). At initial drop sizes larger than about 3.5 mm, non-luminous effects appear to dominate. The non-luminous loss reduces the flame temperatures sufficiently that the formation rate of gas phase soot formation is suppressed, and the resulting flame is non-sooting.

However, other average gasification rates measured for n-heptane drops in the FSDC-2 experiments, particularly those which contained substantial numbers of bubbles, appear to be much larger than expected from the results presented in Fig. 2. It should be noted that bubbles appeared in the liquid phase in the DCE tests only as a result of introduction through the fuel supply needles themselves, while bubbles appeared to form and grow in size throughout the burning history in some of the FSDC-2 experiments. The source for these peculiarities continues to be investigated.

Normal heptane droplets were observed to burn for as little as six seconds in some tests, and longer than thirty seconds in other test. The droplet burning time does not always increase as the square of the initial drop diameter. While experiments at smaller initial droplet sizes burned to completion, as initial droplet size was increased, the droplet flame was observed to extinguish with a finite diameter droplet remaining. Figure 3 displays the "extinction" diameter found in different initial diameter experiments. Theory would predict that one should observe the qualitative relationship shown in Figure 3, based upon the increased radiative loss effects with increasing drop diameter. Further evaluation of these results and comparisons with theory are continuing.

Successful experiments were also performed using isolated pure n-decane droplets, and some results are presented here, primarily for comparison with two-drop array observations discussed below. Figure 4 compares the burning histories of three single n-decane droplets of different initial in FSDC-2. The quality of the experimental data for the variation of the square of droplet diameter with burning time is typical of FSDC-2 experiments with n-decane as well as with the other fuels studied. The observed scatter in the data results from two factors: 1) difficulty in determining the edge of the droplet because of flame radiation (especially close to ignition) and non-uniform backlighting combined with soot generation; 2) vibration of the droplet due to the nucleation and growth of the vapor bubbles. The slope of the curve at any point in Figure 4 is the instantaneous gasification rate constant, k . The average gasification rate constant, k_{avg} , reported in Fig. 1 and elsewhere in this paper, is the average slope over a burning period of linear behavior in the data, typically, 10% to 90% of the total droplet burn time. The initial burning time is defined to be when the droplets anchor after ignition. From the results in Fig. 4, the average gasification rate constant for n-decane in air clearly decreases with increasing diameter, similar to the behavior noted in studies of n-heptane described above. The average gasification rate for the smallest droplet, $0.76 \text{ mm}^2/\text{s}$, is close to the average gasification rate constant for smaller 1 mm initial diameter droplets ($k_{avg} \sim 0.7 \text{ mm}^2/\text{s}$) burned in drop tower experiments. During combustion, bubbles were observed to nucleate within the fuel droplet near the bead of the droplet. These bubbles grew during combustion and became a significant volume of the droplet near the end of the burn. Many of the bubbles burst near the end of combustion, which caused a sharp, drop off in droplet diameter measurements at the end of a test (Figure 4).

N-heptane/n-hexadecane Mixtures

Liquid fuels used in practical devices such as internal combustion engines and gas turbines are blends of several hundred molecular structures, having a wide range of chemical and physical properties. These binary component alkane experiments address the effects on gasification rate, flame dynamics, and extinction phenomenon which are related to the fuel component interactions resulting from volatility differences among molecules of similar structural type (normal alkanes). Normal heptane and hexadecane differ widely in volatility, with heptane being the more volatile species. The large volatility difference allows study of phenomena associated with transient liquid species diffusion and component volatility differences. After ignition of a heptane-hexadecane droplet, heptane is initially preferentially vaporized from the droplet with most of the hexadecane remaining in the liquid phase. As the droplet decreases in size, the liquid surface mass fraction of hexadecane increases with time, causing rapid droplet heating as the surface mass fraction of hexadecane closely approaches unity. This heating reduces the droplet vaporization rate and causes the flame to contract until liquid heating is completed, at which time vigorous vaporization of both droplet components begins and the flame grows in size again. The onset time for a flame contraction can be used to estimate liquid species diffusivities in burning droplets¹⁴. In addition, transient processes associated with flame contractions can apparently cause extinction of large droplets⁴ as well as variations in sooting¹⁵ and gasification rates¹⁴.

The present experiments complement previous ones⁴ that were performed in FSDC-1 during the STS-73/USML-2 flight in 1995. As with FSDC-1, the FSDC-2 experiments focused upon studying initially large droplets, allowing the study of chemical and physical phenomena over length and time scales that cannot be achieved in ground-based experiments. The FSDC-2 experiments were performed with the following specific objectives:

1. *The initial liquid compositions in FSDC-1 were limited to initial heptane mass fractions (Y) of 0.90 and 0.60. To more fully test theories on bi-component droplet combustion, other compositions needed to be investigated. The FSDC-2 experiments utilized Y = 0.95 and Y = 0.80.*

2. Measurements of flame radiant energy output rates were made with FSDC-2 (this measurement was not available in FSDC-1). These measurements provided new and useful data on radiant outputs of the weak flames associated with combustion of large heptane-hexadecane droplets, and the measurements allowed determination of whether flames had actually extinguished. Because of the very dim flames encountered with FSDC-1, it was not possible to determine when flame extinction had occurred. The radiometer data also provided information on the occurrence of flame contractions.
3. Unexpected extinction and sooting behaviors were observed during the FSDC-1 experiments. For example, larger droplets appeared to soot weakly only shortly after ignition, with sooting becoming negligible prior to extinction. In addition, extinction in larger droplets seemed to be induced by flame contractions. These phenomena merited further study.

Twenty-two droplets were deployed, ignited and burned in the FSDC-2 heptane-hexadecane experiments, with 11 droplets having $Y = 0.95$ and the remainder $Y = 0.8$. Initial droplet sizes ranged from about 1.8 mm to about 6 mm. The larger initial droplets extinguished at large diameters (a few mm). These droplets could be re-ignited after extinction, much as is described for the ethanol results reported below. Only limited representative data and results are presented here, as analyses are continuing.

In both the FSDC-1 and FSDC-2 experiments, flames were detected by the video cameras only for times shortly after ignition, after which the flame luminosity was too low to record. Even glowing of support fiber was not evident in the video images after the initial ignition transients. These factors suggest that flame temperatures were very low for the mixture fractions and droplet sizes studied here. The square of the droplet diameter (d) and radiometer data as a function of burning time are shown in Fig. 5 for a droplet ($Y = 0.95$) initially about 1.8 mm in diameter. After ignition, the d^2-t plot is essentially linear until an interior bubble exits the droplet, causing a sudden decrease in droplet size. As in the case of the pure alkane studies, small bubbles were present in many of the heptane-hexadecane droplets prior to ignition. After the bubble exits, the d^2-t plot is again essentially linear with nearly the same slope as prior to the bubble exit. The plot also exhibits a temporary decrease in slope at about 3.5 s, likely associated with the flame contraction phenomenon typical of bi-component combustion. The gasification rate prior to the flame contraction is about $0.64 \text{ mm}^2/\text{s}$. This gasification rate, in conjunction with asymptotic theory¹⁴ yields the effective liquid-phase species diffusivity $D \approx 9 \times 10^{-9} \text{ m}^2/\text{s}$.

The radiometer data presented in Fig. 5 show increases after the igniter was turned on, with very sharp increases after droplet ignition. Following ignition, the radiant heat fluxes grow and then decrease, with slight increases apparent after the flame contraction has occurred. Interestingly, the shapes of curves in these radiometer data are qualitatively similar to flame diameter data published for drop-tower experiments with heptane-hexadecane droplets initially about 1 mm in diameter¹⁴.

Figure 6 report similar data for a larger droplet, 2.9 mm diameter. After an initial the bubble exits, the d^2-t plot is again essentially linear until a flame contraction appears at about 10.5 s. The gasification rate prior to the flame contraction is about $0.66 \text{ mm}^2/\text{s}$ for this droplet. A similar analysis with asymptotic theory yields $D \approx 8 \times 10^{-9} \text{ m}^2/\text{s}$. The D values corresponding to the data in Figs. 5 and 6 are very close to the D values determined from the FSDC-1 experiments.

Unlike the data in Fig. 5, the radiometer values for the droplet in Fig. 6 did not increase after the flame contraction. Rather, the data decreased to low values prior to the disappearance of the droplet (from complete evaporation) at about 16.5 s. Cusps are apparent in the radiometer data at flame contraction as well as shortly after the droplet had completely vaporized. Radiometer data following the latter set of cusps indicates that cooling rates of the gas increased substantially after the droplet had completely vaporized.

While not shown here, it is noted that droplet diameter data indicate the largest droplets extinguished at large diameters corresponding to the droplet sizes expected at the onset times for flame contractions. The radiometer data show cusps at these same times, followed by strong decreases in radiometer outputs, indicating that gas-phase chemical heat release had abruptly stopped and that the gases were rapidly cooling. Gasification rates were also observed to decrease as droplets became larger, with the largest droplet exhibiting gasification rate constants roughly 30 % lower than the smaller droplets (prior to flame contractions). Finally, it is noted that interesting soot shell dynamics were observed in these experiments; these behaviors are presently being evaluated.

Further data analyses remain to be performed. The droplet diameter data will be analyzed to determine the liquid species diffusivities that apply to all droplets burned in the experiments. In addition, the radiometer data will be further analyzed and compared with theoretical predictions of radiant heat losses from spherical droplet flames with particular attention being paid to the transient effects caused by transient liquid species diffusion. Recent numerical modeling of the n-heptane/n-hexadecane droplet combustion, including detailed gas phase chemistry and non-luminous radiation¹³, qualitatively shows many of the phenomena observed in the FSDC experiments and that observations are particularly responsive to liquid phase transport within the droplets and radiative loss from the flame structure. Additional modeling efforts will be necessary to produce quantitative predictions of both ground and flight microgravity data.

Simple Alcohol and Alcohol/Water Mixtures

Methanol and methanol/water have been extensively investigated in drop towers and FSDC experiments primarily because the fuel itself is a relatively simple hydrocarbon for which physical and chemical properties are relatively well known, and the material has no propensity to form soot. Methanol also offers a unique opportunity to study dissolution of combustion products in the liquid phase (primarily water) and binary multicomponent combustion behavior with one of the components being non flammable. Methanol/water droplet combustion experiments from FSDC-1 and FSDC-2 have recently been analyzed and compared against the predictions of a detailed numerical model⁹. In FSDC-2, two additional levels of water content (15% and 30% by mass) were studied by performing experiments at several different initial drop sizes (a total of thirteen successful experiments in all).

Overall, both pure methanol and methanol/water droplets of 2 to 7 mm were studied. In some cases, droplets burned for over 40 seconds and flame extinction was observed at small but finite droplet diameters. In other cases, droplets ignited, but the flames rapidly extinguished. Numerous asymptotic and numerical modeling studies have addressed the prediction of droplet burning phenomena in microgravity for methanol, particularly the extinction phenomena^{6,8,9,16}. In the most recent work⁹, both FSDC-1 and FSDC-2 experiments are compared against the results of a detailed numerical model, which simulates the time-dependent, spherically symmetric combustion of a multi-component liquid droplet in an infinite oxidizing environment. The model includes detailed chemistry, multi-component molecular diffusion and non-luminous radiative heat transfer. The model quantitatively reproduces (without modifications or adjustments) measured gasification rate, flame position and extinction diameter for a wide range of initial diameters and initial water contents. Radiative heat loss is significant in experiments with initial diameters greater than 3 mm, resulting in a decreased gasification rate and a non-linear increase in extinction diameter. Figure 6 shows that, both numerically and experimentally, the extinction diameter increases with increasing initial droplet size. At smaller initial sizes, the dissolution of water (a combustion product) into the liquid fuel droplet leads to the increased extinction diameter. At larger initial diameters, radiative loss from the flame structure becomes an important factor. Moreover, at 6-mm initial diameter, radiative losses result in entirely transient burning, with extinction occurring after only a few seconds of combustion. The critical extinction diameter of 6 mm, predicted numerically in a previous study for methanol droplet combustion⁸ in 1-atm air, was verified experimentally. Figure 7 shows that importance of considering non-luminous radiative loss in predicting the flame diameter for large-diameter methanol droplet combustion. Non-luminous radiative effects also result in decreased gasification rate with increasing initial drop diameter even at initial diameters smaller than 3.0 mm.

Ethanol and Ethanol/water azeotrope mixture were also studied in FSDC-2 experiments. Ethanol has been proposed as a fuel for investigating the droplet combustion behavior of azeotropes¹⁷ and sooting effects in microgravity droplet combustion¹⁸. As in the case of methanol, the physical and chemical properties of ethanol itself, as well as the intermediates present in its combustion are reasonably well known, compared to those of liquid alkanes. The azeotrope mixture is mostly ethanol (96% ethanol, 4% water), limiting the amount of water that can be absorbed as combustion products of absolute ethanol droplets. Finally, the sooting nature of this fuel has pressure sensitivities qualitatively similar to that of n-heptane, but shifted to a higher range of pressures. For example, droplet combustion of this fuel produces no soot at atmospheric pressure and 21% oxygen index in nitrogen. At three atmospheres, however, sooting is profuse at the same oxygen index. The present FSDC-2 experiments provide first observations of ethanol combustion in microgravity at large drop sizes.

Figures 9 and 10 display the average gasification rate and extinction diameters for ethanol as functions of initial droplet size. Figure 10 includes average gasification rate data taken on ethanol in the NASA-Lewis 2.2 s droptower¹⁹. The results show that both average gasification rate and extinction diameter are related to the initial droplet size in manners similar to n-alkanes and methanol. However, ethanol does not soot at these conditions (as does n-heptane), and cannot absorb large amounts of combustion products during its combustion history (as does methanol). The ethanol experiments were particularly interesting in that large initial droplets that burned and underwent extinction could be re-ignited. The gasification rate of the re-ignited droplet was reduced in comparison to the prior burn. The re-ignited droplet was observed to sometimes burn to extinction again, with an extinction droplet size that could again be re-ignited. The observed gasification rate would again be slower than for the prior burn. Eventually, the re-ignited droplets would burn to completion. In one case, the initial droplet burned and extinguished, and this sequence was repeated 5 times until the droplet was fully consumed. The extinction diameters for droplets that were re-ignited were quite similar in their relationship to the ignited initial drop diameter, as were similar data for droplets ignited only once. Apparently, the amount of water dissolved into the liquid phase over multiple burns does not accumulate sufficiently on a volume-averaged basis to affect extinction. The averaged water content cannot be more than that in the azeotrope mixture (4% water). Even slight increases in average water content, however, appears to reduce the average gasification rate. Data analyses are continuing and a numerical model to for to compare results with the data is in development.

Two Droplet Array Studies

While the results of single droplet studies are relevant to practical combustion devices, in practice, droplets, do not burn in an isolated manner. Instead, droplets interact with each other during combustion. Droplet arrays represent the next logical building block in the development of a spray model. During the FSDC-2 experiments, several experiments on two-droplets arrays of droplets at a known distance from each other were conducted. The results from binary droplet tests with n-decane as fuel are compared here with single droplet experiments with decane reported earlier. Both experiments were in a quiescent ambient.

In general, the droplets studied were near-spherical with slight elongation along the axis of the fiber (the ratio of the maximum and minimum diameters was typically no more than 1.2). The two droplets moved on the fiber as a result of combustion interactions, and this combustion-induced phenomenon was coined the Thomas "twin" effect. The droplets initially moved apart along the fiber during ignition and anchored to the fiber ceramic bead on the side of the droplet nearest to each other. After ignition, the droplets drifted together and became anchored to the bead on the side facing away from each other. During many of the tests, soot particles formed during ignition. The soot gave evidence of unexpected recirculating flow patterns in the vicinity of the droplets. Between the droplets in the array, soot particles were observed to approach the droplets somewhat parallel to the fiber and then rapidly move radially away from the droplets. The motion of the soot particles suggests the existence of strong liquid-phase motion during combustion. Internal, liquid phase flow patterns have also been observed in the single droplet experiments discussed earlier, but generally were less developed.

Figure 11 shows the gasification rate history for both droplets in the two-droplet array (separation distance, ~7-mm between the center of the droplets, anchored immediately after ignition. The burning is relatively symmetric in the present case, with a

lack of symmetry in other tests typically due to the bubble nucleation and growth, especially for smaller size (< 3 mm initially) droplets.

Figure 11 also shows the instantaneous gasification rate constant, K , for the two drops. In general, significant errors are encountered when differentiating experimental data. Both Miyasaka and Law²⁰ and Mikami *et al.*²¹ differentiated a polynomial fit of the experimental data to determine K . We found, however, that the polynomial fit did not accurately describe the experimental data over the entire burning history and could produce errors in K when differentiated. Also, simply smoothing and differentiating the data produced very scattered plots of $K(t/D_0^2)$. The K values in Figure 11 are determined by performing a modified cubic spline curve fit on the experimental data. In the present case, the data are divided into equal increments of $(t/D_0^2) = 0.15$. Third order polynomial fits are then performed on the data in each interval subject to the constraint that the values along with the first and second derivatives are continuous at each node point.

Figure 11 shows that K is nearly constant or just slightly increasing over a significant portion of the burn. This is in contrast with previous work^{20,21} which show that the gasification rate constant increases continuously as the relative separation distance (inter-droplet spacing, L , normalized by the instantaneous droplet diameter, D) increases during burning. The results are, however, consistent with recent droptower work that shows that most of the curvature in the droplet history (D^2 vs. t) occurs early in the lifetime and that K is nearly constant over (most of) the droplet lifetime.

Figure 12 shows a comparison of the burning histories and gasification rate constants for one of the droplets in Figure 11 (left) with a nearly identical sized single droplet (initially). Clearly, the average gasification rate of the droplet in the array is smaller than for an isolated single droplet. The interaction effect is the largest when the normalized separation distance, L/D (L/D increases with increasing t/D_0^2) is largest. The difference decreases as L/D increases, approaching zero at the end of the burn. The surprising point in Fig. 12 is that the gasification rate constant for the single droplet also decreases with time.

Forced Convective Studies

Relative droplet/gas velocities exist in practical, spray combustion applications. The influences of slow, purely forced convective velocities on the burning characteristics of two-droplet linear arrays of *n*-decane in air are discussed here. Droplet gasification rates and flame dynamics were experimentally measured for a range of imposed velocities, and droplet initial sizes. The results are compared here with single droplet combustion under similar flow conditions. The separation distance between the two droplets were nominally 5 mm, and the upstream and downstream droplet initial sizes were varied independently between 2 and 5 mm. Figure 13 shows the gasification rate histories of isolated, single droplets as a function of imposed flow velocities. The instantaneous droplet diameter is obtained by measuring the major and minor diameter of the droplet from the backlit images and then computing D as the cube root of the major diameter times the square of the minor diameter. The D^2 versus time curves in Fig. 13 are not linear. However, the noise in the data precluded us from obtaining instantaneous gasification rates. The average gasification rate constant, $K = d(D^2)/dt$, computed from linear least-square curve fits to the portion of the curve prior to the vapor bubble explosion (to be discussed below) are 1.3, 1.4, 1.5, 1.5, and 1.4 mm²/s for the imposed flow velocities of 11, 15, 15, 20, and 25 cm/s, respectively. The gasification rate in general increases with the increasing flow velocity. There are insufficient data to derive a statistically significant correlation between K and other independent dimensionless numbers, such as the Reynolds number. During the experiments, it was observed that the droplet anchored itself on the ceramic bead at its forward leading edge. A few seconds into burning, a small vapor bubble formed on the ceramic bead and continued to grow before bursting. The time at which the bubbles burst is marked with a vertical line in Fig. 13. The vapor bubble formation was rapid and vigorous during the forced convective burning. In this case, the anchoring bead is less shielded by the liquid droplet than under quiescent burning conditions where the bead is centered within the droplet. With reference to Fig. 13, we note that two competing effects influence the observed droplet size and d^2 - t history displayed in the figure. The size decreases due to vaporization, but increases due to bubble growth. The actual mass vaporization rate is likely somewhat higher than that implied by the average K determined from Fig. 13.

Figure 14 shows the burning histories for a typical 2-droplet array test. As in the case of single droplet combustion, the ceramic beads cause vapor bubble nucleation and growth within both the upstream and downstream droplets. The time at which the vapor bubbles break is marked by a vertical line. The average gasification rate constants calculated prior to the vapor bubble release are plotted against the Reynolds number for the single droplet and the linear array droplets in Figure 15. This plot clearly shows that droplet interaction reduces the individual gasification rates of both the upstream and downstream droplets. The downstream droplet, which is embedded in the wake of the upstream droplet most of its lifetime, shows a larger reduction in gasification rate, as much as 30%, compared to a single droplet burning under the same imposed velocity.

Conclusions

FSDC-2 planned to conduct 52 total experiments, using single droplets and nine different fuels or fuel mixtures. Each experiment was to have involved the combustion of a single isolated droplet of between 2mm and 6 mm in diameter in cabin air. One-hundred-twenty-seven (127) experiments were conducted, of which 123 resulted in producing test data. In addition to investigating the full range on initial droplet sizes with each fuel, seventeen experiments were conducted using two droplets, spaced about 1 cm apart, to study droplet-droplet interactions during combustion. These experiments yielded science that was originally planned for the flight of FSDC-1 on the STS-73 USML-2 mission in 1995. In the two-drop array studies, the drops were forced apart by ignition process, and then as the drops burn, they are forced together by the reduced vaporization on the adjacent sides of the drop. We named this effect, the "Thomas Twin Effect", after Don Thomas who was operating the experiment. Single droplet studies have yielded extensive and new information for gasification rate and extinction phenomena for the various fuels studied and on the effects of forced convection on droplet burning. Three presentations of this work to the science community have occurred over the last twelve months, and results from the methanol/water droplet combustion studies

have been published archivally. Analyses of single droplet pure and binary mixture, forced convective, and two-droplet array studies are continuing and will be the subject of future archival publications

Acknowledgments

The authors are indebted to the MSL-1 crewmembers, in particular to R. Crouch and D. Thomas, who conducted the FSDC-2 experiments. We also thank the many individuals at the Payload Operation Control Center, Marshall Spaceflight Center, for their support, and Drs. B. Zhang and A. Marchese, for their participation in the Science Team direction of the experiments throughout the mission. Without the dedicated efforts of the Engineering Team at the NASA Lewis Research Center, particularly S. Motil, this flight experiment would not have been possible. The contributions of university students and technical staff - M. Ackerman (University of California, San Diego), M. Calvert (U. of Alabama, Birmingham), B. Clark (University of California, Davis), J. Conley, Y. Stein, and B. Urban (Princeton University) - and Mr. Peter Struk of the National Center for Microgravity Research to data reduction and analysis efforts is also gratefully acknowledged. Drs. M. King and H. Ross also provided valuable suggestions and support during the MSL-1 mission.

Bibliography

Archival Publications

1. Marchese, A.J., Colantonio, R.O., "Radiative Effects in Space-Based Methanol/Water Droplet Combustion Experiments", 27th Symposium (Int'l) on Combustion, The Combustion Institute, Pittsburgh, PA. 1998. In Press.
2. Marchese, A.J., Dryer, F.L. and Nayagam, V., "Numerical Modeling of Isolated n-Alkane Droplet Flames: Initial Comparisons with Ground and Space-based Microgravity Experiments", *Combust. Flame*, 1998. In Press.

Other Preprints and Presentations

1. Nayagam, V., Calvert, M.E., Colantonio, R.O., and Dietrich, D.L., "Forced Convection Burning of Two-Droplet n-Decane Linear Arrays in Microgravity", Proceedings of the 1998 Central States Section of the Combustion Institute.
2. Marchese, A. J., "Microgravity Droplet Combustion", University of Delaware Fluid, Particulate and Environmental Seminar Series, Newark DE, October, 1997.
3. Marchese, A.J. and Dryer, F.L., "Detailed Kinetic Modeling of Microgravity n-Alkane Droplet Flames", Eastern States Sectional Meeting of the Combustion Institute, East Hartford CT, October 1997.
4. Dryer, F.L., "Recent Studies of Liquid Hydrocarbon Droplet Combustion Aboard the Columbia Space Shuttle", University of Wisconsin, Madison, Nov. 19, 1997.
5. Williams, F.A., "Experiments on Droplet Combustion in the Space Shuttle", National Fire Prevention Association (NFPA) Meeting, San Diego, CA, December 8, 1997.
6. Zhang, B.L., "Theoretical Analysis of Heptane Droplet Combustion for Comparison with Results from the Shuttle Spacelab During The MSL-1 Mission", 36th AIAA Aerospace Sciences Meeting, Reno, NV, January 13, 1998.
7. Marchese, A.J. and Dryer, F.L. "Detailed Numerical Modeling of Liquid Droplet Combustion Experiments Conducted Aboard Microgravity Science Laboratory-1", 36th Annual Aerospace Sciences Meeting, Reno, NV, January 13, 1998.
8. Dryer, F.L., "Liquid Hydrocarbon Droplet Combustion Aboard the Columbia Space Shuttle", Vanderbilt University, Nashville, TN, February 20, 1998.
9. Dryer, F.L., "Combustion in Low Gravity: Isolated Droplet Burning on the Shuttle", Mechanical and Aerospace Engineering, Princeton University, Princeton, NJ, April 24, 1998.
10. Nayagam, V. and Williams, F. A., "Dynamics of Diffusion Flame Oscillations Prior to Extinction During Low Gravity Droplet Combustion," 7th International Conference on Numerical Combustion, 30th March - 1st April, 1998, York, England.

Table 1. FSDC-2 Investigators and their relationship to funded projects

<i>Investigator</i>	<i>Experiment Responsibility</i>	<i>Relationship to funded microgravity research programs</i>
Prof. Forman A. Williams University of California, San Diego	Principal Investigator of overall program	Droplet Combustion Experiment (DCE)
Prof. Frederick L. Dryer Princeton	n-heptane - no flow, methanol/water mixtures ethanol/water mixtures	DCE
Prof. Benjamin D. Shaw University of California, Davis	n-heptane/n-hexadecane, internal circulation visualization	Bi-Component Droplet Combustion
Dr. Daniel Dietrich NASA Lewis Research Center	n-heptane and n-decane two-droplet arrays	Droplet Array Interactions
Mr. John Haggard NASA Lewis Research Center	n-heptane - no flow	DCE, FSDC-1 co-Investigator
Dr. Vedha Nayagam Analex Corporation	forced flow effects, n-heptane, n-decane	DCE - Project Scientist FSDC-1 co-Investigator
Dr. Ron Colantonio NASA Lewis Research Center	ethanol/water azeotrope	DCE - Deputy Project Scientist*

- Current responsibilities are: High Speed Systems Office, NASA-Lewis Research Center

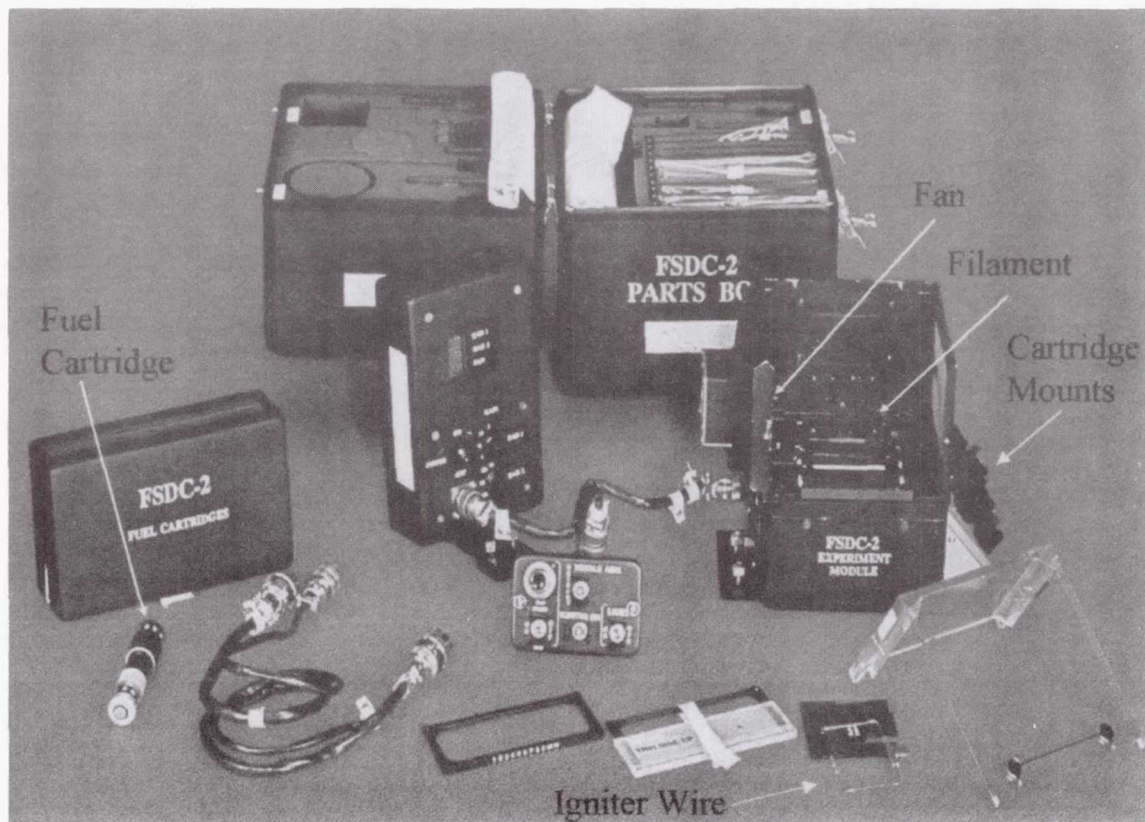


Figure 1 FSDC-2 Hardware

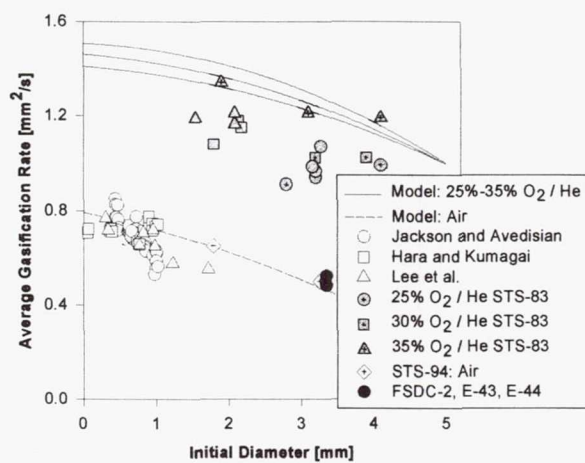


Figure 2 Average burning rate as a function of initial diameter for n-heptane burning in air.

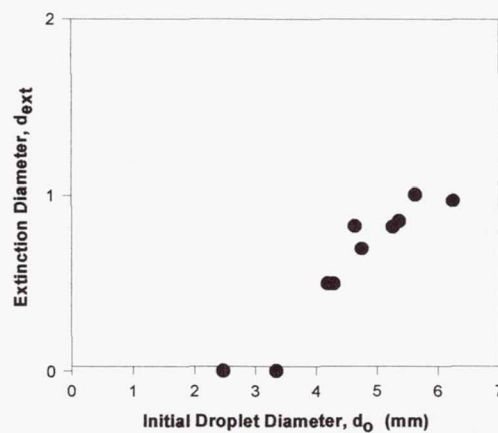


Figure 3 Extinction diameter as a function of initial diameter for n-heptane combustion in air.

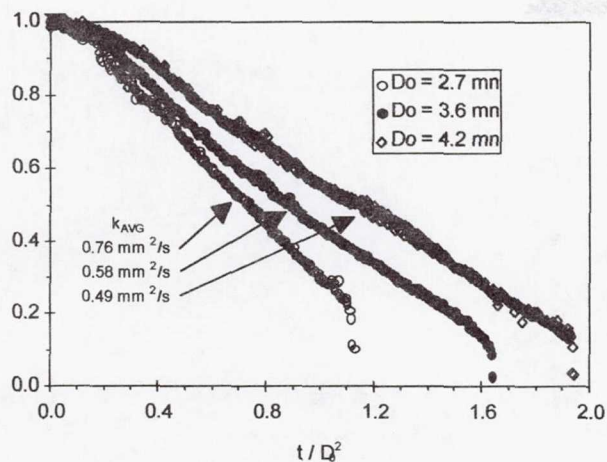


Figure 4 Single n-decane droplets burning in FSDC-2.

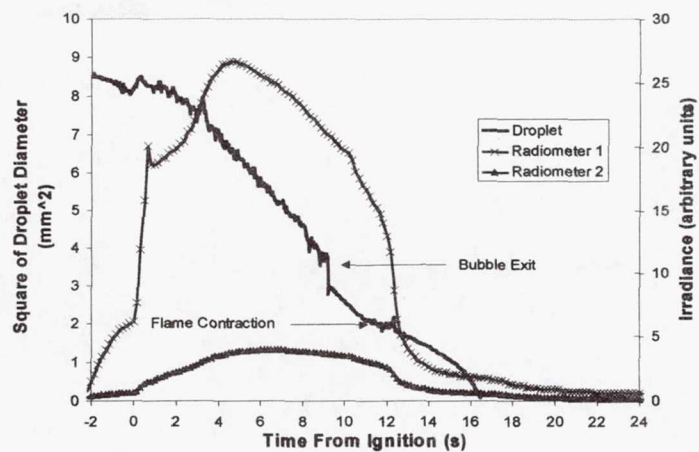


Figure 5 Droplet diameter and radiometer data for a heptane-hexadecane mixture droplet burned in the FSDC-2. The initial heptane mass fraction (Y) was 0.95.

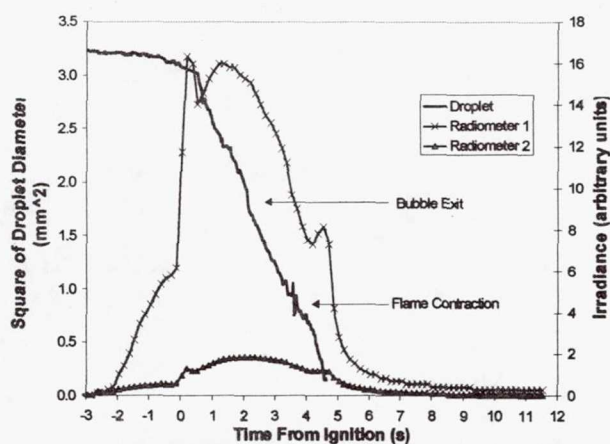


Figure 6 Droplet diameter and radiometer data for a heptane-hexadecane mixture droplet burned in the FSDC-2. The initial heptane mass fraction (Y) was 0.95.

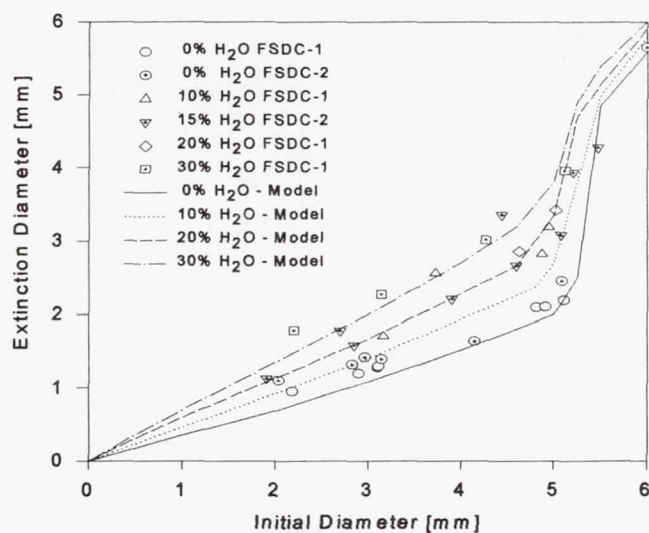


Figure 7 Extinction diameter as a function of initial diameter for methanol/water mixtures.

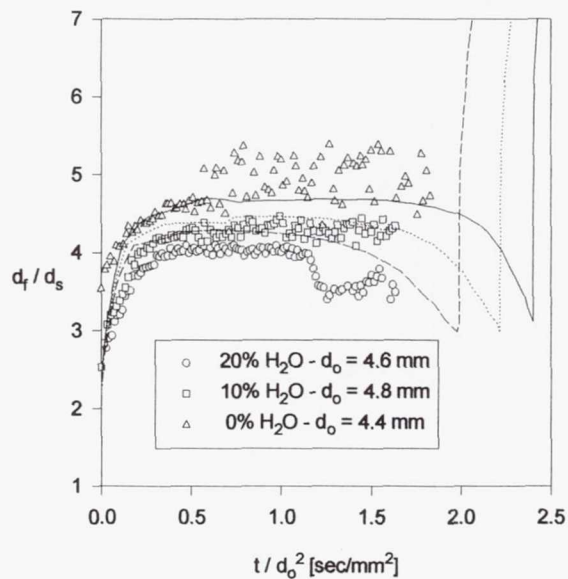


Figure 8 Measured and calculated flame position for 5 mm methanol/water droplets with varying initial water content.

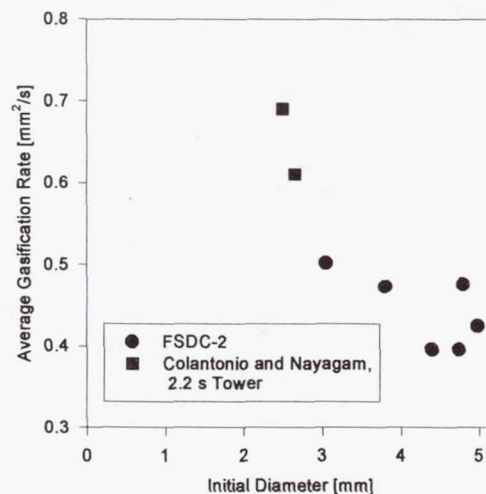


Figure 9 Extinction diameter as a function of initial diameter for ethanol in FSDC-2.

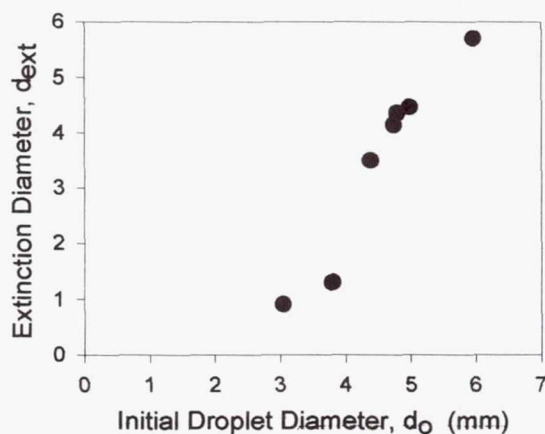


Figure 10 Average burning rate as a function of initial diameter for ethanol burning in air.

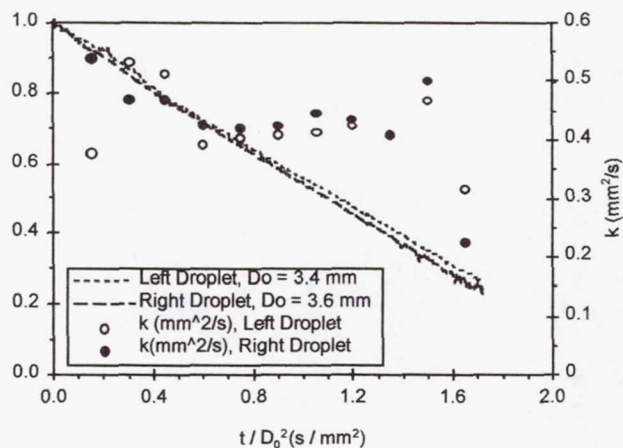


Figure 11 Burning rate history for both n-decane droplets of a two-droplet array with an initial separation distance of approximately 7 mm.

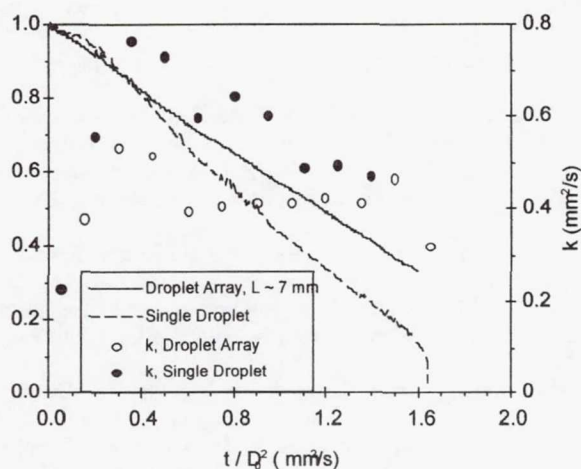


Figure 12 Burning history and instantaneous burning rate comparison of a single droplet and droplet array in FSDC-2. The initial droplet size was approximately 3.7 mm for both droplets in the array and the single droplet.

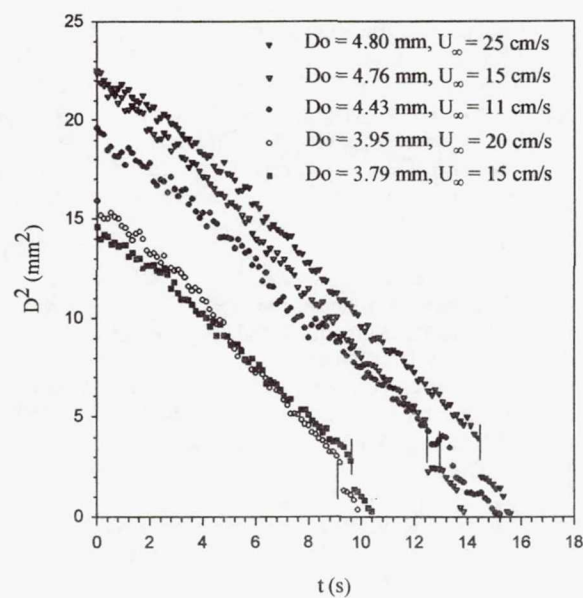


Figure 13 Droplet diameter squared versus time for single n-decane droplets in a forced convective field.

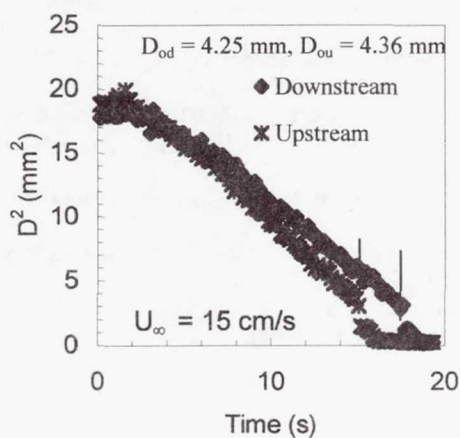


Figure 14 Burning history of a two-droplet linear Array under forced convection.

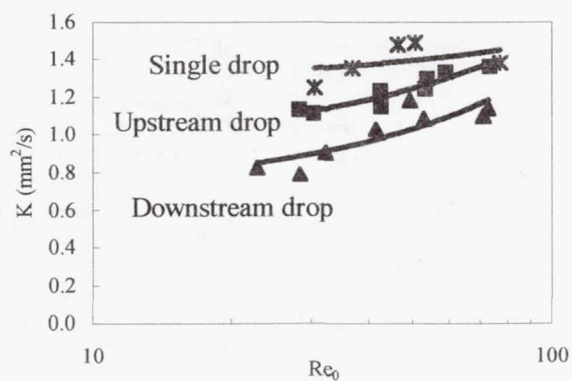


Figure 15 Average burning rates for single and two-droplet, linear arrays as a function Reynolds

References

- ¹ Haggard, J.B., Jr., Nayagan, V., Dryer, F.L., Marchese, A.J., Williams F.A., and Zhang, B., "Droplet Combustion Experiment", This Proceedings.
- ² Marchese, A.J., and Dryer, F. L., "Effect of Liquid Mass Transport on the Combustion and Extinction of Bi Component Liquid Droplets of Methanol and Water", *Combust. Flame*, 105, 104 (1996).
- ³ Zhang, B. L., Card, J., and Williams, F. A., "Application of Rate-Ratio Asymptotics to the Prediction of Extinction for Methanol Droplets", *Combust. Flame*, 105, 267 (1996).
- ⁴ Dietrich, D.L., Haggard, J.B. Jr., Dryer, F.L., Nayagam, V., Shaw, B. D., and Williams, F. A., "Droplet Combustion Experiments in Spacelab", 26th International Symposium, The Combustion Institute, Pittsburgh, PA, 1996. p. 1201.
- ⁵ Dietrich, D.L., Dryer, F.L., Haggard, J.B., Jr., Nayagam, M. V., Shaw, B. D., and Williams F. A., "Fiber Supported Droplet Combustion, L+1 Symposium for USML-2 Shuttle Mission", National Academy of Sciences, February, 10-11, 1997. Published in Proceedings.
- ⁶ Zhang, B. L. and Williams, F. A., "Theoretical Studies of Methanol Droplet Combustion Based on Results from the Shuttle Spacelab during the USML-2 Mission", *Acta Astronautica* 40, 829 (1997).
- ⁷ Marchese, A.J. and Dryer, F.L., "Science Support for Space-Based Droplet Combustion: Drop Tower Experiments and Detailed Numerical Modeling", Presented at the Fourth International Microgravity Conference, Cleveland Ohio, May 21, 1997. Published in the Proceedings.
- ⁸ Marchese, A.J. and Dryer, F.L., "The Effect of Non-luminous Thermal Radiation in Microgravity Droplet Combustion, *Combust. Sci. and Tech.*, 124, 373 (1997).
- ⁹ Marchese, A.J., Dryer, F.L., and Colantonio, R., "Radiative Effects in Space-Based Methanol/Water Droplet Combustion Experiments, 27th Symposium (Intn'l) on Combustion, The Combustion Institute, Pittsburgh, PA, 1998. In Press.
- ¹⁰ Klimek, R. B., Wright, T. W., and Sielken, R. S., NASA TM 107144, February 1996.
- ¹¹ Marchese, A.J., "The Effect of Non-luminous Thermal Radiation in Microgravity Droplet Combustion", *Combust. Sci. Tech.*, 124, 373 (1997).
- ¹² Nayagam, V., Haggard, J.B., Jr., Colantonio, R.O., Marchese, A.J., Dryer, F.L., Zhang, B.L. and Williams, F.A., "Microgravity N-Heptane Droplet Combustion in Oxygen-Helium Mixtures at Atmospheric Pressure", *AIAA Journal*, 36, 1369 (1998).
- ¹³ Marchese, A.J., Dryer, F.L. and Nayagam, V., "Numerical Modeling of Isolated n-Alkane Droplet Flames: Initial Comparisons with Ground and Space-based Microgravity Experiments", *Combustion and Flame*, 1998. In Press.
- ¹⁴ Aharon, I. and Shaw, B. D., "Estimates of Liquid Species Diffusivities from Experiments on Reduced-Gravity Combustion of Heptane-Hexadecane Droplets", *Combust. Flame* 113:507 (1998).
- ¹⁵ Chen, A.G. and Shaw, B. D., "Laser Attenuation Measurements of Soot Volume Fractions During Reduced-Gravity Combustion of Heptane and Heptane/Hexadecane Droplets", *Combust. Sci. Tech.* (submitted) 1998.
- ¹⁶ Zhang, B. L., Card, J., and Williams, F. A. (1996). Application of Rate-Ratio Asymptotics to the Prediction of Extinction for Methanol Droplets, *Combust. Flame*, 105, 267.
- ¹⁷ Kim, J.S., Lee, A., Law, C.K., On the Gasification of Droplets of Azeotropic Mixtures: Theory and Experiment, 23rd Symposium (International) on Combustion, The Combustion Institute, Pittsburgh, PA., 1990. p. 1423.
- ¹⁸ Choi, M.Y. and Dryer, F.L., "Experiments and Model Development for Investigation of Sooting and Radiation Effects in Microgravity Droplet Combustion", University of Illinois Chicago and Princeton University, proposal to NASA NRA-97-HEDS-01, 1998. Award in preparation, August, 1998.
- ¹⁹ Colantonio, R.O., and Nayagam, V., "Radiative Heat Loss Measurements During Microgravity Droplet Combustion, Proceedings of the 1997 Central States Section of the Combustion Institute.
- ²⁰ Miyasaka, K. and Law, C.K., "Combustion of Strongly-Interacting Linear Droplet Arrays," 18th Symposium (International) on Combustion, The Combustion Institute, Pittsburgh, PA., 1981. p. 283.
- ²¹ Mikami, M., Kato, H., Sato, J. and Kono, M., "Interactive Combustion of Two Droplets in Microgravity," 25th Symposium (International) on Combustion, The Combustion Institute, Pittsburgh, PA., 1995. p. 423.

Non- Technical Summary

Fiber Supported Droplet Combustion-2

Renato Colantonio, Daniel Dietrich, John B. Haggard, Jr. and Vedha
Nayagan

National Center for Microgravity Research
NASA Lewis Research Center
21000 Brookpark Road Cleveland, OH 44135

Frederick L. Dryer

Princeton University
Department of Mechanical and Aerospace Engineering
Princeton, NJ 08544

Benjamin D. Shaw

University of California, Davis
Davis, CA 95616

Forman A. Williams

University of California, San Diego
Center for Energy and Combustion Research
La Jolla, CA 92093

Liquid hydrocarbons supply the majority of the energy utilized in transportation. In North America last year we utilized about 2.5 tons of liquid fuels per capita, or about 2.5 times the world average. Combustion in general is the major methodology for converting the chemical energy in these fuels to useful thermal and/or mechanical forms. Combustion is **also** a major contributor to air pollution, including nitrogen oxides, carbon monoxide, unburned hydrocarbons, and particulates (we normally think of these as "soot" or "smoke"). In addition, carbon dioxide - a "greenhouse gas" - also is produced by the combustion of hydrocarbons. It is relatively easy to produce a highly efficient conversion of the chemical energy in the fuels to thermal energy when there are no imposed constraints of the emissions, which are produced. It is much harder to optimize the conversion of the thermal energy to useful mechanical energy, particularly with minimum emissions. Minimized emissions and the best "miles per gallon", if you will, require us to carefully control and tailor the combustion process. Whereas in earlier times, much of this could be accomplished by solely experimental R & D, today, very sophisticated computational design tools are necessary to guide this R & D. However, even small improvements in the fuel conversion to useful work with reduced emissions has very large economic impact on the economies of our nation and the world, as well as on both national, international, and global health issues. All of the fundamental combustion experiments aboard MSL-1 impact the fundamental sciences necessary to construct better computational design tools for internal combustion engines, including those in trucks, cars and aircraft, as well as in the industrial and electrical utility sectors. The droplet Combustion Experiment (DCE) and Filament Supported Droplet Combustion Experiment (FSDC-2) aboard MSL-1 address these science issues for the large hydrocarbon molecular structures characteristic of those found in the liquid fuels utilized in the transportation sector.

FSDC operates in the Mid-Deck Glove Box Facility, and can only use cabin air as the combustion environment. However, this experiment can utilize a number of different fuel types. On FSDC-2, we studied methanol, two methanol water mixtures, ethanol, n-heptane, n-decane, and two mixtures of n-heptane/n-hexadecane. Experiments are much less sophisticated than those, which can be conducted in DCE, but give us "first looks" at combustion behavior in microgravity. In addition to yielding some important science over a more limited range of parameters for each fuel, results are extremely helpful in developing test conditions for future work that can be conducted using DCE.

FSDC-2 planned to conduct 52 total experiments, using single droplets and nine different fuels or fuel mixtures. These were pure methanol, 85% methanol/15% water, 70% methanol/30% water, pure ethanol, 96% ethanol/4% water, n-heptane, n-decane, 95% n-heptane/5% n-hexadecane, and 80% n-heptane/20% n-hexadecane. Each experiment was to have involved the combustion of a single isolated droplet of between 2mm and 6 mm in diameter in cabin air. Although the nominal mission was to have used eleven fuel cartridges, all 14 fuel cartridges were utilized to perform experiments. Each cartridge contains approximately 0.5 ml or about 1/60 of an ounce of liquid. One-hundred-twenty-seven (127) experiments were conducted, of which 123 resulted in producing test data. In addition to investigating the full range on initial droplet sizes with each fuel, seventeen experiments were conducted using two droplets, spaced about 1 cm apart, to study droplet-droplet interactions during combustion. These experiments yielded science that was originally planned for the flight of FSDC-1 on the STS-73 USML-2 mission in 1995. In the two-drop array studies, the drops were forced apart by ignition process, and then as the drops burn, they are forced together by the reduced vaporization on the adjacent sides of the drop. We named this effect, the "Thomas Twin Effect", after Don Thomas who was operating the experiment.

Acknowledgments

We want to especially thank the members of the STS-94 crew who conducted experiments on FSDC and DCE for us, notably, Roger Crouch, Greg Linteris, Don Thomas, and Janice Voss, and the cadre at MSFC which provided terrific support for our experiments during the mission. We are especially grateful as well to the other Science team members (Ron Colantonio, Anthony Marchese, Be-Li Zhang) and the Engineering team members from NASA-Lewis who have assisted in controlling the operation of DCE and FSDC-2 during this mission.

Page intentionally left blank

OMIT THIS
PAGE

Protein Crystal Growth (PCG)

Protein Crystal Growth Using the Protein Crystallization Apparatus for Microgravity (PCAM)

Principal Investigator:

Dr. Daniel C. Carter
New Century Pharmaceuticals
Huntsville, Alabama

SINGLE SCAN

S15-76

434852

Highlights from the Protein Crystallization Apparatus for Microgravity (PCAM) Experiments Conducted during MSL-1

362418

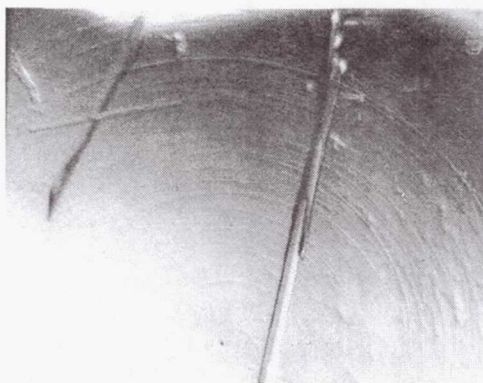
13A

D. C. Carter, B. Wright, J. Chapman, T. Miller, L. Adcock-Downey, J.-P. Declercq, and C.H. Chang

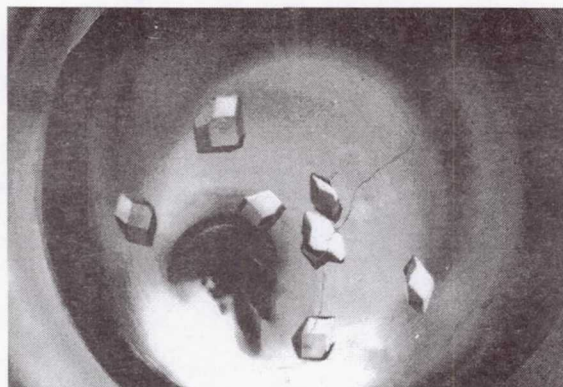
PCAM is a facility-based apparatus used for the optimization and production of protein crystals in microgravity for application in structural biology. Crystals produced in the facility also support fundamental crystal growth research with an emphasis on establishing the role of microgravity in the improvements in size and quality. PCAM experiments on MSL-1 supported 10 co-investigator groups studying 13 proteins involving research from academic and industrial laboratories. Highlights from this mission include one of the highest resolution protein structures to be produced as a result of microgravity and the first example of microgravity enablement for a neutron diffraction study.

The PCAM (Protein Crystallization Apparatus for Microgravity) is a large capacity facility for the production of protein crystals of improved quality for application in structural biology and to support fundamental studies in crystal growth (Carter & Dowling, 1997; Carter et al., 1998a,b,c). PCAM occupies a single middeck locker and utilizes the STES (Single-locker Thermal Enclosure System) for temperature control. Each STES houses six PCAM cylinders for a total of 378 individual vapor equilibration experiments. Four additional cylinders were stowed at ambient temperature in a mid-deck locker to give a total of 630 experiments for each flight. Previous PCAM experiments have produced numerous examples of protein crystals with improved size and quality (Carter et al., 1998b,c; Skinner et al., 1997; Wardell et al., 1997; Evrard et al., 1997; Evrard et al., 1998; Declercq et al., 1998). Ten different co-investigator groups studying 13 proteins were flown on the combined MSL-1 and MSL-1R missions (Tbl. 1). Figures 1 and 2 illustrate the spectrum of crystals produced on the two missions.

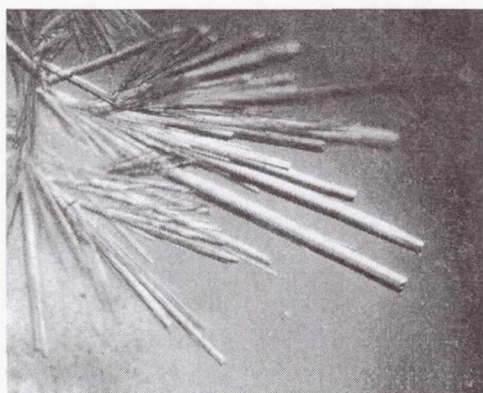
Despite the disappointing early termination of the mission for STS-83, significant results were obtained. One result related to hardware performance. This represented the first flight of the improved activation mechanism for PCAM which performed perfectly. Five of the proteins produced crystals of suitable size for x-ray diffraction: lysozyme (two different forms), respiratory syncytial virus (rsv) Fab, HIV protease/inhibitor complex, transcription initiation factor, and parvalbumin (Fig. 1). However, the overall yield was much lower than expected for the full growth period. The remaining five proteins exhibited microcrystals which were too early in the growth stage for x-ray analysis.



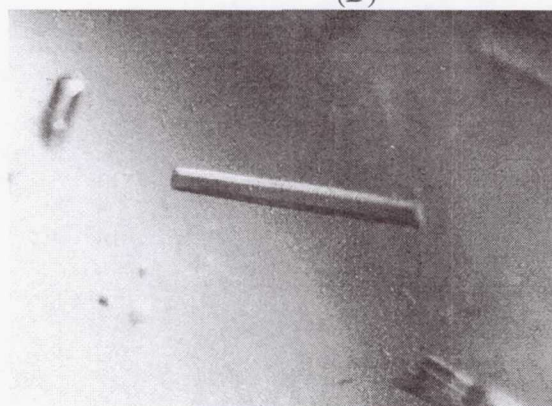
(A)



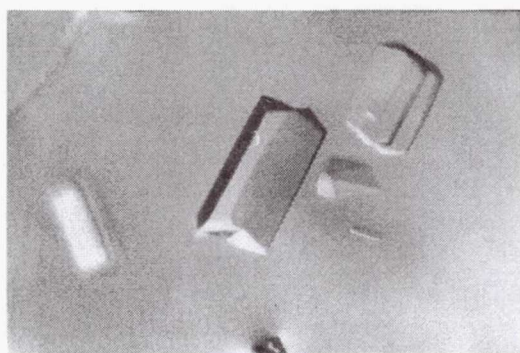
(B)



(C)

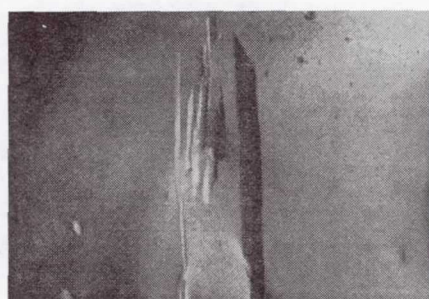


(D)

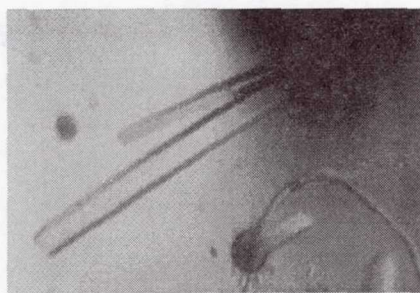


(E)

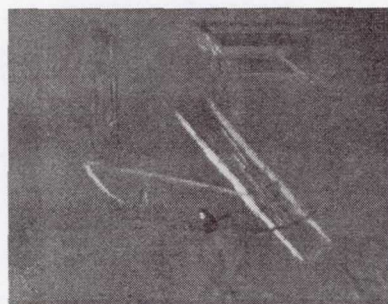
Figure 1. Protein crystals grown in microgravity on the abbreviated STS-83 mission: (A) HIV Protease/Inhibitor Complex, (B) Lysozyme, (C) Pike Parvalbumin, (D) Respiratory Syncytial Virus Fab, (E) Transcription Initiation Factor



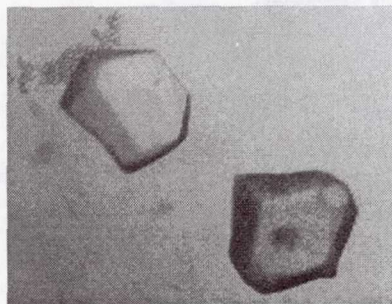
(A)



(B)



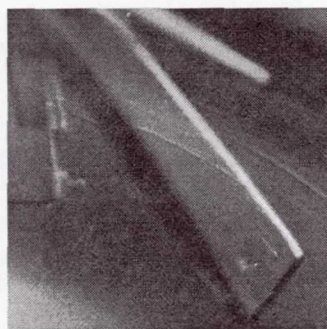
(C)



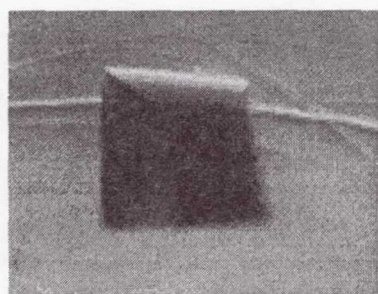
(D)



(E)



(F)



(G)



(H)

Figure 2. Protein crystals grown on STS-94 (the reflight of STS-83): (A) Pike Parvalbumin; (B) Respiratory Syncytial Virus Fab; (C) Human Antithrombin III; (D) Bacteriophage PRD1; (E) Cytomegalovirus Assemblin Complex; (F) Lysozyme; (G) Ferritin; (H) E. coli Gro EL

TABLE 1

MSL-1 STS-83 Protein List and Guest Investigators

Investigator	Protein	Affiliation	Application
Dr. Daniel Carter (Principal Investigator)	Respiratory Syncytial Virus Antibody Lysozyme	New Century Pharmaceuticals (NCP)	Therapy and Vaccine development Crystal growth: model system
Dr. William Stallings/ Dr. Anna Stevens	Cytomegalovirus Assemblin Complex	Monsanto/Searle	Herpes therapeutic research and development
Dr. Mark Wardell	Human Antithrombin III	University of Washington at St. Louis	Fundamental & therapeutic: Stroke
Dr. B.C. Wang/ Dr. John Rose	T7 RNA Polymerase	University of Georgia	Fundamental Life Process
Dr. John Rosenberg	E.coli Gro EL	University of Pittsburgh	Fundamental virus structure and function
Dr. Jean-Paul Declercq	Parvalbumin	University of Louvain, Belgium	Fundamental Biochemistry
Dr. Dennis Bamford	Bacteriophage PRD1	University of Helsinki, Finland	Biotechnology & Biochemistry
Dr. C.H. Chang	HIV protease-inhibitor complex	Dupont Pharmaceuticals	AIDS therapeutic research & development
Dr. Ubo Heinemann	Translation Initiation factor	Max-Delbruck Center for Mol. Med. Germany	Fundamental Biochemistry

MSL-1 STS-94 Protein List and Guest Investigators

Investigator	Protein	Affiliation	Application
Dr. Daniel Carter (Principal Investigator)	Respiratory Syncytial Virus Antibody Lysozyme	New Century Pharmaceuticals (NCP)	Therapy and Vaccine development Crystal growth: model system
Dr. William Stallings/ Dr. Anna Stevens	Cytomegalovirus Assemblin Complex	Monsanto/Searle	Herpes therapeutic research and development
Dr. Mark Wardell	Human Antithrombin III	University of Washington at St. Louis	Fundamental & therapeutic: Stroke
Dr. B.C. Wang/ Dr. John Rose	Augmenter of Liver Regeneration	University of Georgia	Accelerates Liver cell regeneration
Dr. John Rosenberg	E.coli Gro EL	University of Pittsburgh	Fundamental virus structure and function
Dr. Jean-Paul Declercq	Parvalbumin	University of Louvain, Belgium	Fundamental Biochemistry
Dr. Dennis Bamford	Bacteriophage PRD1	University of Helsinki, Finland	Biotechnology & Biochemistry
Dr. Franz Rosenberger/ Dr. Bill Thomas	Ferritin/Apoferritin	University of Alabama in Huntsville	Fundamental Biochemistry & Crystal growth model system

Many of the experiments were flown back to back on missions STS-83, STS-94, through STS-85. Several of the protein crystallization conditions were optimized for microgravity crystal growth during this flight series culminating with optimal growth conditions on STS-85. Two of the proteins, lysozyme and ferritin, were in support of research emphasizing the role of microgravity in the production of protein crystals with improved size and perfection which together with experiments utilizing DCAM aboard Mir NASA increment 5 have lead to important findings (Carter et al., 1998a). The importance of the continuity of experimentation supports the value of the ability to conduct and optimize experiments in microgravity on the future International Space Station. Selected highlights from the experiment series are given below and referenced in recent publications (Carter et al., 1998b; Declercq et al., 1998).

Highlights from MSL-1

Co-Investigator: Dr. Jean-Paul Declercq, Laboratoire de Chimie Physique et de Cristallographie, Université Catholique de Louvain, Belgium

Pike Parvalbumin

Background & Objective: to grow crystals of improved size and resolution, and to attempt growing extremely large crystals for application in neutron structure determination.

Crystals of Pike Parvalbumin (PPA) grown during STS-83 and STS-94 gained improvements which moved the resolution into the Ultra-high resolution category diffracting X-rays beyond 0.9 Å at the Hamburg synchrotron. Prior work by the co-

investigator group indicated a diffraction limit of 1.7 Å for pike parvalbumin and the Brookhaven Protein Data Bank contains 13 parvalbumin structures of which the highest resolution is 1.5 Å. The data indicate this will result in one of the highest resolution protein structures over 100 amino acids determined to date. Since the data in the highest resolution shell are observed at 97.3%, clearly usable diffraction data exist well below 0.9 Å potentially to 0.6 Å. Future flight experiments planned for STS-95 later this year will focus on higher resolution x-ray and neutron studies. Statistics on the diffraction data collected at the synchrotron facility at Hamburg, Germany are presented in Table 2. Quite remarkably, the $R_{\text{merge}}(I) = 3.6\%$ for 481,972 reflections (63,763 unique). Preliminary refinement has revealed the high quality of the resulting structure and answered many questions concerning conformational states in the protein structure and calcium binding (Fig. 3). Additionally, as a result of the longer duration of STS-94 (MSL-1R), the largest crystal to date was produced of this protein (Declercq et al., 1998) which has provided the first example of microgravity enablement for neutron diffraction.(Fig. 2).

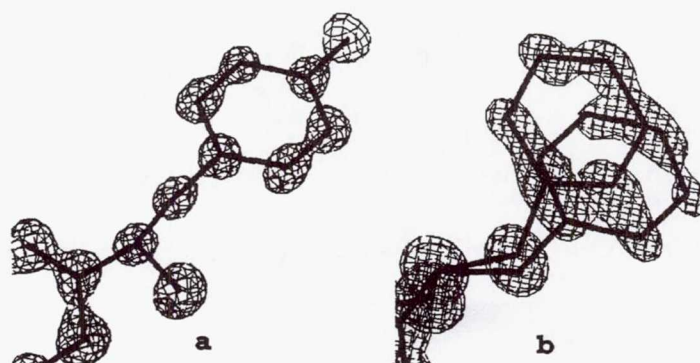


Figure 3. (a) Example of electron density for PPA (Tyr 48) showing the atomic resolution; (b) Electron density corresponding to two alternate conformations of the side-chain of Phe 30.

TABLE 2

Pike Parvalbumin Crystal Data and Data Collection Statistics

Crystal system		Orthorhombic
Space group		P2 ₁ 2 ₁ 2 ₁
a, b, c (Å)		51.026, 49.807, 34.570
Mw (Dalton)		11,390
Z		4
Vm (Å ³ /Dalton)		1.93
Temperature of data collection (K)		100
Resolution range (Å)		25.0 – 0.91
Reflections collected		481,972
Unique reflections		63,763
Rmerge(I)	overall	3.6%
	highest resolution shell	12.4%
	(0.92 – 0.91 Å)	
Completeness	overall	99.8%
	highest resolution shell	97.3%
<I/s(I)>	overall	14.2
	highest resolution shell	3.3

Co-Investigator: Dr. Chong Hwan Chang, DuPont Pharmaceuticals, Inc.

HIV Protease complex with Proprietary Inhibitor(s)

Background & Objective: The objective is to improve the quality of the crystals of selected protease/inhibitor complexes for increased resolution in the design of new therapeutics against HIV.

Crystallization experiments performed on STS-83 grew diffraction size crystals that were twinned (Fig.1). Unfortunately, insufficient protein was available to support the reflight on STS-94. The conditions from STS-83 were used to optimize experiments on STS-85. Previous terrestrial crystals were of insufficient size for x-ray analysis. The microgravity crystals from STS-85 were the largest grown to date (Fig.4) and provided data to 1.8 Å. A detailed image of the inhibitor bound to the active site was obtained from the microgravity data. (Fig. 5).

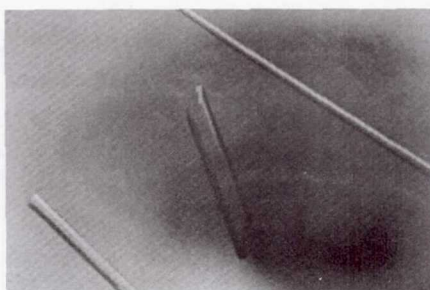


Figure 4. Crystals of HIV protease complex with proprietary inhibitor grown aboard STS-85.

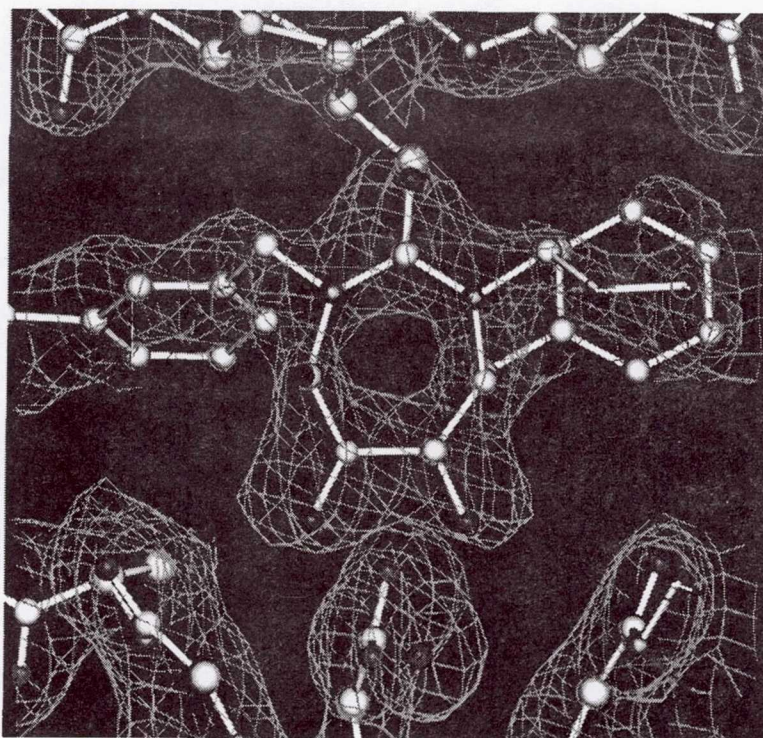


Figure 5: Initial 2Fo-Fc of mutant HIV protease coupled with proprietary inhibitor. Model has been altered to avoid compromising proprietary data.

Summary and Conclusions

Numerous crystals were successfully produced in support of macromolecular structure determinations and basic crystal growth studies for several proteins. However, crystals of human antithrombin III while of superior quality on previous PCAM experiments (Wardell et al., 1997) were of insufficient size, as were crystals of the Augmenter of Liver Regeneration (ALR) protein. Crystals of two of the proteins, lysozyme and ferritin were utilized to support basic research in understanding the underlying role of microgravity in protein crystal growth (Carter et al., 1998a). Others, such as the rsv antibody and HIV protease complex produced useful results which were optimized on the sequential STS-85. Perhaps the most

striking result was that of pike parvalbumin, a calcium binding protein which showed improved diffraction from 1.7 Å to less than 0.9 Å. Larger crystals grown on STS-94 provided the first example of microgravity enablement for neutron diffraction studies (2.0 Å) at ILL, Grenoble, France. Future crystallization experiments currently manifested on STS-95 will provide crystals for continuing and completing selected studies, such as higher resolution structure refinements and impurity partitioning studies.

REFERENCES

- Carter, D. C., and T. E. Dowling, Protein Crystal Growth Apparatus For Microgravity, U.S. Patent No. 5,643,540 (1997).
- Carter, D. C., K. Lim, J. X. Ho, B. S. Wright, P. D. Twigg, T. Y. Miller, J. Chapman, K. Keeling, J. Ruble, P. G. Vekelov, B. R. Thomas, F. Rosenberger, and A. A. Chernov, submitted to *J. Cryst. Growth* (1998).
- Carter, D. C., B. Wright, T. Miller, J. Chapman, P. Twigg, K. Keeling, K. Moody, M. White, J. Click, J. R. Ruble, J. X. Ho, L. Adcock-Downey, and T. Dowling, "PCAM: A Multi-user Facility-based Protein Crystallization Apparatus for Microgravity," *J. Cryst. Growth* in press (1998).
- Carter, D. C., B. Wright, T. Miller, J. Chapman, P. Twigg, K. Keeling, K. Moody, M. White, J. Click, J. R. Ruble, J. X. Ho, L. Adcock-Downey, and T. Dowling, "PCAM: A Multi-user Facility-based Protein Crystallization Apparatus for Microgravity," Poster presentation at the 7th International Conference on Protein Crystal Growth (1998).
- Declercq, J.-P., and D. Deforge "Comparison of L-Alanine Dehydrogenase from *Bacillus Subtilis* on Earth and Under Microgravity Conditions," recent Advances in Macromolecular Crystallization (International Meeting: Le Bischoffberg, France, 1996).
- Declercq, J.-P., C. Evrard, D. Carter, B. Wright, G. Etienne, J. Parello, "A Crystal of a Typical EF-hand Protein Grown Under Microgravity Diffracts X-rays Beyond 0.9Å Resolution," *J. Cryst. Growth* in press (1998).
- Declercq, J.-P., C. Evrard, D. Carter, B. Wright, G. Etienne, J. Parello, "A Crystal of a Typical EF-hand Protein Grown Under Microgravity Diffracts X-rays Beyond 0.9Å Resolution," Poster presentation at the 7th International Conference on Protein Crystal Growth (1998).
- Evrard, C., P. Soumillion, J.-P. Declercq, and J. Fastez, "Crystallization of Bacteriophage Lysozyme after Incorporation of Non-Natural Amino Acid in the Protein," Recent Advances in Macromolecular Crystallization (International Meeting: Le Bischoffberg, France, 1996).
- Evrard, C., J.-P. Declercq, and J. Fatsrez, *Acta Cryst.* D53 (1997) 217-219.
- Evrard, C., "Structural Study of Bacteriophage Lambda Lysozyme," Ph.D. Thesis, University Catholique de Louvain (1997).
- Evrard, C., J.-P. Declercq, and J. Fastez, submitted to *J. Crystal Growth* (1998).
- Skinner, R., "Structural Biology of Antithrombin," A dissertation submitted to the University of Cambridge for the degree of Doctor of Philosophy, Hughes Hall, Cambridge, May 1996).
- Skinner, R., J.-P. Abrahams, J. C. Whisstock, A. M. Lesk, R. W. Carrell, and M. R. Wardell, *J. Mol. Biol.* 266 (1997) 601.
- Wardell, M. R., R. Skinner, D. C. Carter, P. D. Twigg, and J.-P. Abrahams, *Acta Cryst.* D53 (1997) 622.

PAO

PCAM (Protein Crystallization Apparatus for Microgravity) is a facility-based apparatus emphasizing the optimization and production of protein crystals in microgravity for application in structural biology. Crystals produced in the facility also support fundamental crystal growth research with an emphasis on establishing the role of microgravity in the improvements in size and quality. PCAM experiments on MSL-1 supported 10 co-investigator groups studying 13 proteins involving research from academic and industrial laboratories. Highlights from this mission include one of the highest resolution protein structures to be produced as a result of microgravity and the first example of microgravity enablement for a neutron diffraction study.

omit DPN
PAGE

Protein Crystal Growth (PCG)

Protein Crystal Growth Using the Hand-Held Diffusion Test Cell (HHDTC)

Principal Investigator:

Dr. Alexander McPherson
University of California, Irvine
Irvine, California

L+1 Report on HHDTTC Investigation on MSL-1

by

S. Koszelak and A. McPherson
University of California, Irvine
Department of Molecular Biology & Biochemistry
Irvine, CA 92697-3900

Our investigation on MSL-1 was based on an apparatus of our design and construction referred to as the Hand Held Diffusion Test Cell (HHDTTC). The device is designed to carry out the crystallization of macromolecules in a microgravity environment, as well as the crystallization of conventional organic molecules. The device employs a methodology known as liquid-liquid diffusion, a process which is initiated in this case by rotating a stopcock to establish continuity between a chamber of about 0.4 ml containing protein with a chamber of about 0.8 ml containing a precipitating agent such as ammonium sulfate in water, or solutions of polyethylene glycol. Complete, multi-chambered cells are organized in sets of eight within Lucite containers so that they can be activated in sets by a hand cranked ganging mechanism. The activation is carried out once microgravity is achieved by a crew member. The cells are also equipped with backlights so that events within can be recorded using a hand held video camera manipulated by a crew member.

The experiments we conducted on MSL-1 had two major objectives: one was to explore certain crystallization systems (proteins and precipitant combinations) for their value in more advanced studies, and the second was to further evaluate the design and fabrication of the crystallization cells and the procedures used to prepare and load them for flight. The HHDTTC is a precursor experiment for a considerably more advanced instrument under construction for the International Space Station known as the Observable Protein Crystal Growth Apparatus (OPCGA). The cells investigated in these HHDTTC experiments, and the protein systems as well, are the same as those that will be used in the later OPCGA investigations. The OPCGA studies are intended to definitively answer the question of how the absence of gravity affects macromolecular crystal growth.

On MSL-1, thirty two samples were investigated in individual cells of the HHDTTC. These included the proteins thaumatin (3 cells), canavalin (4 cells), lysozyme (3 cells), satellite tobacco mosaic virus (3 cells), bacterial lipase (2 cells), horse spleen ferritin (2 cells), apoferritin (2 cells), fungal cellulase (2 cells), catalase (3 cells), concanavalin B (2 cells), and horse myoglobin (2 cells). An additional 4 cells were also utilized to grow crystals of a small organic molecule, triglycine sulfate (TGS), which serves as a model crystallization system for conventional crystals grown from solution. Precipitants included solutions of sodium tartrate, ammonium sulfate, sodium chloride, sodium formate, nickel chloride, and PEG monomethylester (PEG-MME). The total time available for crystallization was approximately two weeks.

The protein crystals grown in the experiment aboard MSL-1 were returned to the University of California at Riverside for examination and analysis and for comparison with corresponding crystals grown in the conventional laboratory. The crystals of TGS were taken to the Marshall Space Flight Center for similar examination and analysis. There, polarized light microscopy and photography, along with atomic force microscopy and X-ray diffraction analysis, were applied where appropriate to obtain quantitative data.

Of the eleven proteins attempted, eight produced crystals of some form or size. These included thaumatin, canavalin, lysozyme, bacterial lipase, horse ferritin, apoferritin, and horse myoglobin. Triglycine sulfate was also successfully crystallized. Of the crystals grown, all myoglobin crystals

were microcrystals. Both the ferritin and apoferritin crystals exhibited rounded edges and poor face development characteristic of too rapid growth. Lipase crystals, though of reasonable size, were generally twins and multiple crystals. All of the other crystals were somewhat disappointing in size and quality compared both to crystals grown in our conventional laboratory and compared to corresponding crystals that we have grown in previous microgravity experiments using a variety of crystallization apparatus and instruments, including previous experiments in the HHDTC itself. Triglycine sulfate crystals were of good size and quality and represented a definitive demonstration that the HHDTC was an acceptable device for crystallizing conventional organic materials from solution.

The most important result of the HHDTC investigation was not so much with any improvement in crystal quality and size, but with improvements in the design and performance of the HHDTC cells, the overall instrument design, and the procedures employed. All ganged activation mechanisms operated perfectly, crystallization was achieved in a high percentage of cells, no leakage or anomalous effects were noted, and the device performed nominally across a spectrum of engineering considerations. The appearance of bubbles in the crystallization chambers was substantially less than in any previous experiments, reflecting modifications that we made in loading procedures and minor changes to the design and fabrication of the cells. In terms of proving the cell design and fabrication for later inclusion in the OPCGA, the experiment was an unqualified success. Those cells and the activation mechanics of the HHDTC have now, in fact, been fully integrated into the prototype OPCGA.

We believe that the failure to grow significantly improved crystals on this mission may have been due to sample aging over the period between the initial and reflight of STS-94, though we have no direct evidence that this was true. Crystals of canavalin, thaumatin, satellite tobacco mosaic virus, and lysozyme have been grown to greater size and improved quality on several past missions. The only alternate explanation we could offer is that minor modifications to the buffers and precipitant solutions might be responsible, but we feel that is unlikely.

Protein Crystal Growth (PCG))

omit
THIS
PAGE

Protein Crystal Growth Using the Second Generation Vapor Diffusion Apparatus (VDA-2)

Principal Investigator:

Dr. Lawrence J. DeLucas
University of Alabama at Birmingham
Birmingham, Alabama

SINGLE SCAN

517-76

434854

36242081 10A.

FINAL REPORT

VDA-2 PROTEIN CRYSTAL GROWTH EXPERIMENTS

MSL-1

Principal Investigator: Lawrence J. DeLucas, O.D., Ph.D., University of Alabama at Birmingham

Guest Investigators: Christian Betzel, Ph.D., University of Hamburg; Gabriella Bombieri, Ph.D., University of Milano; Louis Delbaere, Ph.D., University of Saskatchewan; Yancho Devedjiev, Ph.D., University of Alabama at Birmingham; Volker Erdmann, Freie Universität Berlin; Mark Jedrzejewski, Ph.D., University of Alabama at Birmingham; Siegfried Lorenz, Ph.D., Freie Universität Berlin; Karen Moore, Ph.D., University of Alabama at Birmingham; Glaucius Oliva, Ph.D., University of São Paulo; Pier Giorgio Righetti, Ph.D., University of Milano; Jozef Sevcik, Ph.D., Slovak Academy of Sciences; Wolfgang Weber, Ph.D., University of Hamburg

Abstract

The vapor diffusion crystal growth experiments conducted by the Center for Macromolecular Crystal growth at the University of Alabama at Birmingham involved ten macromolecular compounds. The experiments were conducted in the second-generation Vapor Diffusion Apparatus (VDA-2) stored in a Commercial Refrigerator/Incubator Module, at 22° C. The macromolecular compounds included in the experiments were proteinase K complex, human serum albumin, PEP carboxykinase, NAD synthetase complex, 5S rRNA, hyaluronidase, glyceraldehyde-3-phosphate dehydrogenase, lectin KM+, glucoamylase and grass pollen allergen.

The VDA-2 experiments were successful in producing diffraction-sized crystals of eight of the ten compounds flown. Five of the macromolecular compounds produced crystals that yielded the best x-ray diffraction data ever collected for these compounds. X-ray diffraction data from the microgravity crystals was used to produce a new three-dimensional structure of one of the compounds and to significantly refine the structures of four additional compounds.

Objectives

The objectives of the VDA-2 experiments aboard MSL-1 were:

1. to produce large, well ordered crystals of ten different proteins for use in x-ray diffraction studies

2. to continue to develop the technology of microgravity protein crystal growth.

Background

The first launch of MSL-1 was the 32nd flight of a protein crystal growth payload from the Center for Macromolecular Crystallography. The CMC's microgravity protein crystal growth program was initiated with vapor diffusion experiments in 1985, and has been expanded to accommodate large-scale, temperature-induced crystallization experiments as well as improved flight hardware for vapor diffusion experiments at 4 °C and 22 °C.

The vapor diffusion crystal growth experiments aboard MSL-1 involved ten macromolecular compounds in the second-generation vapor diffusion apparatus hardware (VDA-2). This hardware consisted of 80 crystal growth experiments contained in a CRIM, stored in the shuttle middeck. The experiments were conducted at 22° C.

STS-83, the first launch of MSL-1, developed a fuel cell problem and was terminated on Flight Day four. The macromolecular crystal growth experiments were deactivated on orbit, and the flight hardware was returned to Birmingham after landing. The experimental system was installed in the laboratory at the CMC and the experiments were reactivated. The experiments were allowed to run the remainder of the sixteen days. The temperature of the experiments was maintained at 22° C from turnover through analysis of the experiments.

STS-94 was a reflight of MSL-1, and the experimental complement was essentially the same as STS-83. Table 1 contains information on the compounds selected for the VDA-2 payload aboard MSL-1.

Data Acquisition and Analysis

Acquisition of in-flight information for the VDA-2 payload is minimal because the payload operates passively from activation to deactivation. Daily status checks on the CRIM were performed by the shuttle crew and called down to the POCC team. The post-activation photography session was cancelled because of problem with the photography equipment. A work-around was arranged and mid-mission and deactivation photography sessions were completed.

After MSL-1 landed, the VDA-2 hardware was returned to the CMC's laboratory, and the macromolecular crystal growth experiments were analyzed. The crystals were removed from each experiment chamber, photographed and stored for x-ray diffraction data collection. The crystals were then turned over to the individual guest investigators. Some of the crystals were taken to crystallography laboratories for

immediate analysis by area detector and image plate systems. Others were preserved and stored for data collection at a synchrotron radiation source.

After x-ray diffraction data was collected on the microgravity-grown crystals, each guest investigator analyzed the data and compared it to data on comparable ground-grown crystals. This comparison is presented as a plot of x-ray diffraction data intensity versus resolution range.

Results

The hybrid $\mu\text{g}/1\text{-g}$ experiments conducted on STS-83 provided an interesting technical experience but were not successful crystal growth experiments. Crystals of several proteins were recovered from the experiments aboard STS-83, but none of these crystals provided better x-ray diffraction data than that collected from ground-grown crystals. These results are understandable considering events the experiments experienced: very short crystal growth time in microgravity, deactivation of the experiments, shuttle landing, transport to the CMC, reactivation of the experiments, and significant growth time in the 1-g environment.

The experiments conducted aboard STS-94, however, were extremely successful and will be discussed in detail as the true results of MSL-1. The results of the initial analysis of the STS-94 experiments are shown in Table 2.

Table 2

PRELIMINARY ANALYSIS

MACROMOLECULE	RESULTS
Proteinase K	Many large, single, icosohedral crystals, up to 0.7 mm in length
Human Serum Albumin	Very small rod-shaped crystals; crystals are too small for x-ray data collection.
PEP Carboxykinase Complex	Rectangular plates and rod-shaped crystals up to 0.5 mm in length

NAD Synthetase	Rectangular plates, up to 0.8 mm in length; some crystals appeared stacked or twinned.
5S rRNA	Well-formed triangular and hexagonal plates with significant thickness
Hyaluronidase	Very well-formed crystals up to 0.5 mm in length
Glyceraldehyde-3-phosphate Dehydrogenase	Collection of rod-shaped crystals, rectangular and hexagonal plates, up to 0.4 mm in length
Lectin KM+	Diamond-shaped and rectangular plates up to 0.7 mm in length
Glucoamylase	Well-formed rectangular crystals up to 0.75 mm
Grass Pollen Allergen Phlp 5b	Some single, rod-shaped crystals; clusters of twinned crystals

The preliminary analysis indicated that the vapor diffusion experiments aboard MSL-1 were very successful, producing diffraction-quality crystals of eight of the ten macromolecular compounds flown. The VDA-2 hardware operated nominally and the CRIM maintained the command temperature of 22 ° C to $\pm 0.1^{\circ}$ C throughout the entire mission. The post-activation photography session was canceled because there was a problem interfacing the shuttle camera lens assembly to the UAB-supplied focusing aid/light source assembly. It was determined that the wrong polarizing filter was stored with the camera by JSC personnel when the photography equipment was re-stowed in preparation for STS-94. The UAB team and the JSC Photo-TV operations group devised an alternative method for attaching the camera to the focusing aid/light source assembly, and the mid-mission and deactivation photography sessions were successfully completed.

The human serum albumin crystals grown on MSL-1 were too small for x-ray diffraction data collection, but they were used in seeding experiments to grow larger crystals in the 1-g laboratory. Crystals of the remaining nine macromolecular compounds were prepared for x-ray diffraction studies. The PEP carboxykinase crystals proved marginal for data collection on the laboratory area detector, and no usable diffraction data was collected. Crystals of glucoamylase and grass pollen allergen were stored for synchrotron studies. Unfortunately, the crystals of the allergen

were damaged during the freezing process, and the glucoamylase crystals deteriorated before data could be collected at the synchrotron.

Hyaluronidase crystals grown on MSL-1 produced x-ray data 0.2 Å higher resolution than the best data collected from earth-grown crystals. This data was used to refine the structure that is being used in a structure-based drug design study to develop a vaccine against bacterial infections.

Glyceraldehyde 3-phosphate dehydrogenase (GAPDH) is a target for the development of drugs to treat Chagas' Disease, which is a serious and ultimately fatal condition that affects nearly 20 million people in Central and South America. The GAPDH crystals grown aboard MSL-1 belonged to a different space group and proved to be much higher quality than the ones previously grown in the laboratory. The space grown crystals diffracted to greater than 2.0 Å, using a rotating anode x-ray generator and R-axis image plate detector system. Previous x-ray data, collected on the best earth-grown crystals, diffracted only to 2.8 Å. However, after MSL-1, laboratory crystallization conditions were improved, based on the microgravity results, and produced crystals of the new space group which diffracted to 2.2 Å. Thus, the microgravity experiments with GAPDH contributed to this project in two ways. The microgravity-grown crystals produced improved x-ray diffraction data that contributed significantly to the refinement of the protein structure. Further, the microgravity experiments induced this protein to crystallize in a new space group, and these crystals were far superior to the previous crystals.

The MSL-1 experiments involving 5S rRNA produced the best crystals ever grown of this ribosomal RNA. X-ray diffraction data was collected at the synchrotron ELETTRA. The crystals diffracted to 7.5 Å and yielded the first complete data set ever collected on crystals of this macromolecule. The best data previously collected on earth-grown crystals was measured to 9.0 Å. The space group of 5S rRNA was determined from the data collected on the microgravity-grown crystals.

NAD synthetase is a key enzyme in NAD biosynthesis and is the target for structure-based design of antibacterial drugs. The MSL-1 experiments included a complex of NAD synthetase with an inhibitor. The crystals produced in these experiments were large, rectangular plates that yielded x-ray diffraction data 0.3 Å better than data collected from the best laboratory-grown crystals. (Figure 1)

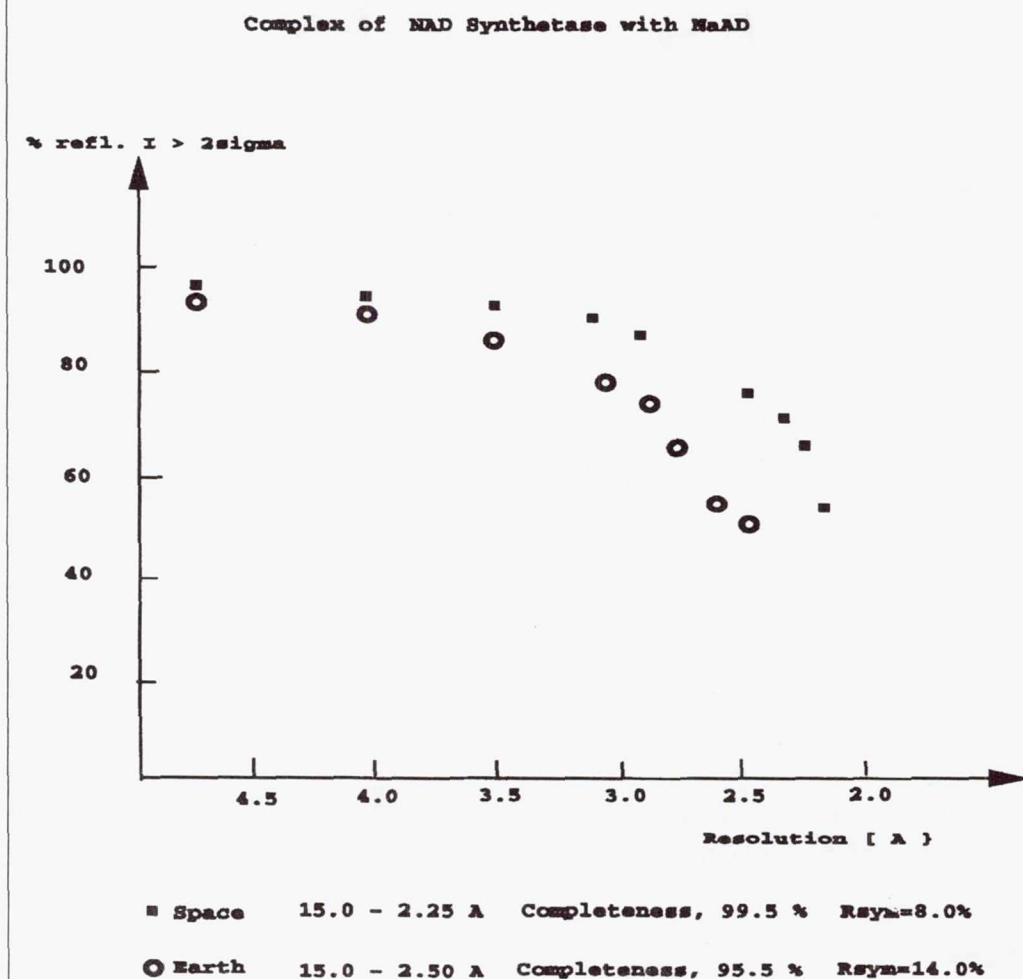
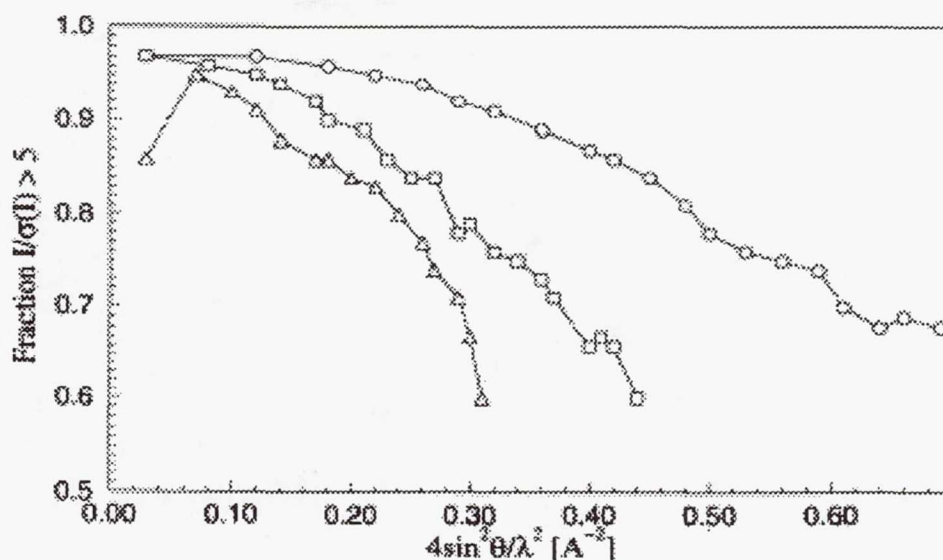


Figure 1: Comparison of x-ray diffraction data for space (■) and earth-grown (●) crystals of NAD synthetase complex. (Plot contributed by Dr. Yancho Devedjiev)

X-ray diffraction data from the microgravity crystals was used to determine the structure of the protein/inhibitor complex. This structure is currently being used to design high affinity inhibitors of NAD synthetase.

The VDA-2 experiments on MSL-1 also produced high quality crystals of proteinase K in complex with a substrate analogue. The microgravity crystals were perfectly shaped and significantly larger than typical ground-grown crystals. X-ray diffraction data was collected from these crystals using synchrotron radiation. The space-grown crystals diffracted to 0.3 Å higher resolution, giving a strong increase in measurable data and a significant improvement in signal-to-noise ratio throughout the resolution range as shown in Figure 2.



Comparison of x-ray diffraction data sets for space (O) and ground (□, Δ) crystals

Figure 2: Comparison of x-ray diffraction data for space (O) and earth-grown (□, Δ) crystals of Proteinase K complex. (Plot contributed by Dr. Christian Betzel)

Conclusions

The macromolecular crystal growth experiments conducted in the VDA-2 hardware aboard MSL-1 were very successful, producing diffraction-sized crystals of eight of the ten compounds flown. Five of these macromolecular compounds produced crystals that yielded the best x-ray diffraction data ever collected. The three-dimensional structures of four of the compounds were significantly enhanced and refined, and one new molecular structure was determined from the microgravity data. The VDA-2 hardware performed flawlessly.

MSL-1 provided a long span of quiet growth time for the macromolecular crystal growth experiments and produced the best results yet accomplished by this payload. It is hoped that future flights of long duration will be available to build on these results.

Citations of articles/presentations resulting from MSL-1

Eschenburg, S., Degenhardt, M., Moore, K., DeLucas, L., Peters, K., Fittkau, W., Weber, W., Betzel, C., "Crystallization on US Space Mission STS-94 of Proteinase K

Complexed with a Substrate Analogue Heptapeptide", Submitted to Journal of Crystal Growth, 1998.

Moore, K., and DeLucas, L., "Vapor Diffusion Crystal Growth in Microgravity", presented at 7th International Conference on the Crystallisation of Biological Macromolecules, Granada, Spain, May 3-8, 1998.

Lorenz, et al., "Crystallization of Engineered *Thermas flavus* 5S rRNA on Ground and under Microgravity and their Diffraction Studies", in preparation.

Non-Technical Summary

The macromolecular crystal growth experiments conducted by the Center for Macromolecular Crystal growth at the University of Alabama at Birmingham involved ten macromolecular compounds. The experiments, conducted in the second-generation Vapor Diffusion Apparatus (VDA-2) at 22° C, were stored in a Commercial Refrigerator/Incubator Module in the shuttle middeck. The macromolecular compounds included in the experiments are implicated in many diseases and conditions including bacterial infections, diabetes, Chagas' disease, and allergies. Many of these compounds are the targets for development of new drugs.

The VDA-2 experiments were successful in producing diffraction-sized crystals of eight of the ten compounds flown. Five of the macromolecular compounds produced crystals that yielded the best x-ray diffraction data ever collected for these compounds. X-ray diffraction data from the microgravity crystals was used to produce a new three-dimensional structure of one of the compounds and to significantly refine the structures of four additional compounds.

Table 1

STS-94 PROTEIN CRYSTAL GROWTH EXPERIMENTS

PROTEIN	CO-INVESTIGATOR	AFFILIATION	SCIENTIFIC SIGNIFICANCE
Proteinase K Proteinase K/substrate Complex	Dr. Christian Betzel	DESY, Hamburg, Germany	The goal of this project is to get crystals of the native protein that diffract to atomic resolution, and to obtain high resolution crystals of the complex for determination of the protonation state in the active site of the protein.
Domain C of Human Serum Albumin Domain A of Human Serum Albumin	Dr. Gabriella Bombieri	Instituto Di Chimica Farmaceutica, Milano, Italy	Human serum albumin is a plasma protein that binds a variety of drugs. These two domains of human serum albumin bind drugs but provide a simpler approach to studying the three-dimensional structure and binding mode of the native protein.
PEP Carboxykinase Complex	Dr. Louis Delbaere	University of Saskatchewan, Saskatchewan, Canada	The structure of this enzyme will provide a starting point for the design of therapeutic agents against diabetes mellitus.
NAD Synthetase	Dr. Yancho Devedjiev	Center for Macromolecular Crystallography	NAD Synthetase is the key enzyme in NAD biosynthesis and is the target for the structure-based design of antibacterial drugs.
5S rRNA	Dr. Volker Erdmann/Dr. Siegfried Lorenz	Freie Universitat Berlin, Berlin, Germany	5S rRNA is an essential component of ribosomes; the three-dimensional structure will help in understanding the process of protein biosynthesis.

Hyaluronidase	Dr. Mark Jedrzejak	Center for Macromolecular Crystallography	This enzyme is involved in the degradation of extracellular matrix during bacterial pathogenesis, and is a target for the development of a vaccine against bacterial infections.
Glyceraldehyde-3-phosphate Dehydrogenase	Dr. Glaucius Oliva	University of São Paulo, São Carlos, Brazil	Glyceraldehyde-3-phosphate Dehydrogenase is a drug target for the treatment of Chagas' disease. The three dimensional structure of this mutant will help elucidate the catalytic mechanism of the native enzyme.
Lectin KM+ from Artocarpus integrifolia	Dr. Glaucius Oliva	University of São Paulo, São Carlos, Brazil	This lectin stimulates neutrophil migration and serves as a model system for studying inflammatory processes in mammals.
Glucoamylase	Dr. Jozef Sevcik	Slovak Academy of Sciences, Bratislava, Slovak Republic	Glucoamylases are important industrial enzymes in the conversion of starch to glucose.
Grass Pollen Allergen Phl p 5b	Dr. Wolfgang Weber	University of Hamburg, Hamburg, Germany	This allergen induces allergic rhinitis and bronchial asthma. Therefore, it is an important target for the design of drugs to block allergic reactions

Page intentionally left blank

omit
THIS
PAGE

Physics of Hard Spheres Experiment (PHaSE)

Principal Investigator:

Dr. Paul M. Chaikin
Princeton University
Princeton, New Jersey

SINGLESCAN
518-25
434922

The Dynamics of Disorder-Order Transitions in Hard Sphere Colloidal Dispersions

Paul M. Chaikin, Jixiang Zhu, Zhengdong Cheng
Department of Physics
Princeton University

See-Eng Phan and William B. Russel
Department of Chemical Engineering
Princeton University

362421
101

Christian T. Lant, Michael P. Doherty,
William V. Meyer, Richard Rogers
NASA Lewis Research Center

D.S. Cannell
Department of Physics
UC Santa Barbara

R.H. Ottewill
School of Chemistry
Bristol University

PHaSE Team
Crew of Space Shuttle Columbia, STS-73
Crew of Space Shuttle Columbia, STS-83, STS-94

Abstract – The Physics of Hard Spheres Experiment (PHaSE) seeks a complete understanding of the entropically driven disorder-order transition in hard sphere colloidal dispersions. The light scattering instrument designed for flight collects Bragg and low angle light scattering in the forward direction via a CCD camera and performs conventional static and dynamic light scattering at 10-160° through fiber optic cables. Here we report on the kinetics of nucleation and growth extracted from time-resolved Bragg images and measurements of the elastic modulus of crystalline phases obtained by monitoring resonant responses to sinusoidal forcing through dynamic light scattering. Preliminary analysis of the former indicates a significant difference from measurements on the ground, while the latter confirms nicely laboratory experiments with the same instrument and predictions from computer simulations.

INTRODUCTION

The simplest colloidal dispersion consists of hard spheres, which interact through hydrodynamic and Brownian forces but feel no direct force before an infinite repulsion at contact. The hard sphere phase diagram, including the disorder-order transition, has been well established (Pusey & van Megen 1987), but many-body interactions complicate the understanding of the transport properties at higher concentrations in both disordered/metastable fluids and the ordered solid.

Recent studies of the kinetics of nucleation and growth with colloidal hard spheres (Schatzel and Ackerson 1992, 1993; Harland, et al. 1995; He, et al. 1996; Harland and van Megen 1997) monitor either the small angle scattering that reflects the form factor for growing crystallites or the intensity, position, and width of the main interlayer Bragg reflection as a function of time. From these the amount of crystalline phase, the average linear dimension and number density of the crystallites, and the volume fraction within the crystallites are deduced. In the coexistence region the observations are compatible with the classic picture of sequential nucleation and growth of isolated crystals, though diffusion processes create a region around the growing crystallite at a lower concentration than the bulk fluid. Above melting nucleation events seem to become correlated, accelerated nucleation and suppressing growth. Coarsening begins as crystallization is completed, increasing the average crystallite size and reducing the number of crystallites. However, the process is quite complex and far from fully understood.

Most previous studies of rheological properties of hard spheres under both steady (Krieger 1972; Mewis, et al. 1989; van der Werff & deKruif 1989) and oscillatory shear (van der Werff, et al. 1989; Frith, et al. 1990; D'Haene, et al. 1992; Shikata & Pearson 1994) examined the fluid phase below the freezing transition and in the metastable region above. Many rheological studies also exists for colloidal crystals, but focus on aqueous dispersions dominated by electrostatic forces (Benzing & Russel 1981; Buscall, et al. 1982; Lindsay & Chaikin 1982; 1985; Chen, et al. 1994; Chow, et al. 1995; van der Vorst, et al. 1995). The main difficulty in determining the elasticity is that colloidal crystals are orders of magnitude weaker than conventional atomic solids and, thus, easily melt under shear. Oscillatory shear of small amplitude slightly perturbs the microstructure and is suitable for measuring the linear viscoelasticity of colloidal crystals.

Frenkel and Ladd (1987) computed the static elastic constants for hard sphere crystals from molecular dynamics simulations of slightly distorted unit cells at several concentrations and then averaged over all orientations to obtain the static shear modulus G' . Nunan and Keller (1984) calculated the orientation-dependent effective viscosity of periodic arrays of spheres in an incompressible Newtonian fluid and averaged over all orientations. Colloidal particles undergo Brownian fluctuations within the crystal lattice, whereas Nunan and Keller assumed the particles to be fixed on the lattice. Interactions at smaller separations imply a higher viscosity, so their predictions represent a lower bound.

Here we report the kinetics of nucleation and growth extracted from the time evolution of the main Bragg peak and rheological measurements for colloidal crystals of nonaqueous hard spheres by exciting shear waves and detecting the response via dynamic light scattering. The nucleation and growth data and the shear modulus and dynamic viscosity from experiments performed in microgravity on NASA space shuttle missions STS-83 and STS-94 are compared with simulations and models as well as measurements under normal gravity.

COLLOIDAL SPHERES

R.H. Ottewill and his group at University of Bristol synthesized and graciously supplied samples of poly-(methyl methacrylate) (PMMA) spheres with a grafted comblike layer of poly-(12-hydroxy stearic acid) (PHSA) chains that we dispersed in a refractive index matching mixture of 1,2,3,4-tetrahydronaphthalene (tetralin, $n=1.541$) and 1,2,3,4-cis-decahydronaphthalene (decalin, $n=1.4815$). Tetralin is a good solvent for PMMA and swells the particles, significantly increasing the size. Index matching suppresses the van der Waals forces and is necessary for performing light scattering, but the associated swelling increases the effective hard sphere volume fraction ϕ . The particle diameter from dynamic light scattering on a dilute sample is 655 ± 15 nm. Previous measurements of the equation of state demonstrate them to be near hard spheres (Phan, et al. 1996). Polydispersity affects the freezing transition (Bolhuis & Kofke 1996), but the error in determining the concentration (± 0.007) exceeds the correction for the 5% polydispersity of our samples. Thus, the effective volume fractions reported here do not include the effect of polydispersity.

EXPERIMENT

A multipurpose light scattering instrument was designed by NASA Lewis Research Center, ADF Corporation, NYMA Corporation, Titan Spectron, and Princeton University for the Physics of Hard Sphere Experiments or PHaSE (Lant, et al. 1997). This instrument performs both static and dynamic light scattering and also oscillates the sample for determining the rheological properties. Specially designed glass sample cells, whose refractive index ($n=1.511$) matches that of our PMMA-PHSA suspensions, consist of two pieces, a face plate and a hemispherical cap. The cap has a parabolic skirt and a cylindrical cavity, 10 mm in radius and 10 mm high, that requires approximately 3 mL of sample. The face plate is screwed into the cap to seal the sample. To allow for expansion and contraction due to temperature fluctuations, we incorporate a rubber diaphragm in the sample cell. All surfaces of the sample cell are highly polished and coated with anti-reflective material.

A 100 mW Adlas diode laser Model DPY313II supplies a 532 nm green beam, which is split into two, one for static light scattering and the other for dynamic. Each beam is routed with Newport mirrors and holders into single mode, polarization maintaining (PM) fiber optic cables terminated on both ends with a quarter-pitch gradient index (GRIN) lens. The GRIN lens restricts the k -vector of the collected light and focuses the beam to a 100 μ m Gaussian waist. For Bragg scattering the optics produces an 8 mm collimated beam with a Gaussian profile that passes axially through the sample cell. Light scattered by the crystalline or crystallizing sample within the cell is focused by the hemispherical exit surface of the cell onto a concentric

fluorescent screen, while unscattered light is focused by the same optics onto a beam dump in the center of the screen. A CCD camera mounted on the far wall of the enclosure records a 10-bit image of the screen covering angles of 0-60°. The cable for dynamic light scattering directs the beam onto the parabolic skirt and through the center of the cell. The beam is totally internally reflected from the skirt radially through the sample. The two single-mode pick-up fibers, 180° apart, are attached to a motorized stage, allowing the scattered intensity to be collected at angles $\theta=10-169^\circ$ with 0.1° resolution. A sensitive avalanche photodiode detector (APD) converts the scattered intensity into binary data from which two Brookhaven BI9000 correlators compute autocorrelation functions.

The sample cell is mounted into a circular holder, whose outer edge has ridges that grip a rubber belt that also hugs the gear of a PMI ServoDisc DC motor. The motor transmits sinusoidal oscillations at frequencies between 0.2 to 10 Hz to the sample cell through the rubber belt. Because our samples crystallize and, thus, are nonergodic, we ensemble average by rotating the cell slowly (<1°/minute) through many configurations.

DATA ANALYSIS

For nucleation and growth studies high resolution CCD images taken at regular intervals beginning shortly after shear melting of a sample quantify the growth of the Bragg peaks with 0.2° resolution. These are averaged azimuthally to obtain the intensity as a function of wavenumber and stored for analysis. The first step is to estimate the particle form factor $P(q)$ and the instrument factor $\alpha(q)$ by dividing the intensity detected immediately after shear melting by the static structure factor $S_{py}(aq)$ for an equilibrium fluid at the appropriate volume fraction as approximated by the Percus-Yevick theory. Then for partially crystalline samples we obtain the static structure factor by dividing the measured intensity by $\alpha(q)P(aq)$. The contribution from the disordered fluid phase is then subtracted as $\beta(t)S_{py}(aq)$ with $\beta(t)$ chosen to bring the residual crystal structure factor $S_c(aq)$ to zero as $q \rightarrow 0$ (Figure 1a). Since $S_c(aq)$ generally reflects the random stacking of hexagonal planes, the main Bragg peak is accompanied by shoulders not present in the face-centered cubic structure (Figure 1b). Consequently the main peak is truncated at the shoulders and value of q at the maximum, the integral under the curve, and width at half maximum are recorded. These provide quantitative measures of the particle volume fraction within the crystallites, the crystalline fraction, and average crystallite size, respectively.

For the rheology measurements we obtain the autocorrelation function

$$g_1(q, \tau) = \langle E(q, 0)E^*(q, \tau) \rangle / \langle I(q, 0) \rangle$$

that decays from unity toward zero at a rate that depends on the driving frequency ω , the relaxation of the suspension without any forcing, and the response of the sample to the oscillatory forcing. If the sample were a rigid solid, $g_1(q, \tau)$ would be completely correlated at the inverse of the driving frequency or $\omega\tau=2\pi$ and would follow the shape of the forcing, i.e., sinusoidal. Since our sample is not totally rigid and we ensemble average by superimposing a slow rotation onto the oscillation, crystallites return close but not exactly to their original positions after one oscillation.

At shorter times, even for small amplitude oscillations, the angular rotation alone fully decorrelates the signal. Therefore, we measure the autocorrelation function at different driving frequencies at a scattering angle just off Bragg reflections and scale the delay time by the driving frequency and the amplitude of angular rotation to determine the resonant response. The detector sees the center of the sample, detecting the motion propagated inward from the boundaries and, therefore, the bulk rheological properties of the whole sample.

We extract the shear modulus G' and dynamic viscosity η' of our concentrated dispersions from solutions to the equation of the motion of a finite cylinder of a viscoelastic solid with radius and height R in oscillatory shear. The amplitude of the response at the center of the cylinder depends on the reduced frequency $\Omega = \omega R (\rho/G')^{1/2}$ and the reduced viscosity $\xi = \eta'/R(\rho G')^{1/2}$.

RESULTS

Nucleation and Growth

Reduction of the Bragg images during nucleation and growth as described above determines the time evolution of the average crystallite diameter $\langle L \rangle$ (from the width at half maximum), the crystalline fraction f (from the area under the primary Bragg peak), the number density of crystallites n_c (from the area divided by the crystallite volume), and the volume fraction ϕ_c within the crystallites (from the position of the Bragg peak). Figures 2 a-d display the results for one of the samples examined, positioned just below melting at $\phi = 0.552$. Since our analysis of the data is still in the early stages, we focus the following discussion on this sample, for which the trends are most clear.

The data from normal gravity suggests a critical nucleus L_c of 11-12 particle diameters. In microgravity we see three phases in the process. In Figures 1 a-c the initial slow transient for times $t < 150$ s is controlled by nucleation, while the period $150 \text{ s} < t < 300$ s reflects diffusion-limited growth. When the crystalline fraction becomes significant, $f \approx 0.1$, the volume fraction within the fluid phase begins to drop, allowing that within the crystallites to relax toward melting or coexistence, i.e. $\phi_c \rightarrow 0.545$. In the meantime, coarsening takes over and proceeds in two stages joined by a transition at roughly 6000 s. Note that the crystallites are significantly larger in microgravity, while the overall rate of crystallization remains the same. Presumably this indicates breakage of growing crystallites and leads to an over estimate of the rate of nucleation in normal gravity.

A simple model suffices to explain the nucleation and growth phase of this data. Assume the rate of nucleation to be constant and the rate of growth to be diffusion limited such that

$$n_c = \frac{dn_c}{dt} t \quad \frac{dL^3}{dt} = \frac{L_c^2}{\tau} L$$

with τ the time scale for growth. From these the average crystallite size $\langle L \rangle$ and the crystalline fraction f follow as continuous functions of time with the limits

$$\begin{aligned} t/\tau \ll 1 \quad f &\approx L_c^3 \frac{dn_c}{dt} t & t/\tau \gg 1 \quad f &\approx 0.07 L_c^3 \frac{dn_c}{dt} \frac{t^{5/2}}{\tau^{3/2}} \\ \langle L \rangle &\approx L_c \left(1 + \frac{4}{9} \frac{t}{\tau} + \dots \right) & \langle L \rangle &\approx 0.8 L_c \left(\frac{t}{\tau} \right)^{1/2} \end{aligned}$$

These correspond qualitatively with the observed behavior

$$\begin{array}{llll} t/\tau \ll 1 & f \propto t^{0.72} & t/\tau \gg 1 & f \propto t^{2.24} \\ \langle L \rangle \propto t^{0.15} & & & \langle L \rangle \propto t^{0.47} \end{array}$$

though further analysis is needed to assess whether the magnitudes are reasonable relative to the predictions from classical and more sophisticated theory.

Rheology

The autocorrelation functions obtained during the small amplitude oscillations of an individual sample are normalized to one at early delay times and the delay times are scaled with the driving frequency. For each frequency, we then estimate the response of the sample to oscillatory shear by rescaling the delay time with a factor $\Lambda(\omega)/\Lambda(\omega_0)$ that collapses each onto the correlation function at the lowest measured frequency ω_0 . Thus, the scaled correlation functions at the various driving frequencies should form a master curve. This works well for frequencies above 0.6 Hz so we force those correlation functions to coincide at $g_1=0.5$.

The response of Sample 4 as a function of driving frequency (Figure 3) for measurements made in normal and microgravity environments clearly exhibit the same resonance. Using the model, we choose $\Lambda(\omega_0)$, G' , and η' so that the position and shape of the resonance best fit the data. The resonance frequency mainly determines the shear modulus G' and the amplitude and width control the dynamic viscosity η' .

For hard spheres the storage and loss moduli are naturally scaled as Ga^3/kT and η'/μ . Our measurements for the elastic moduli (Figure 4) compare well with the static shear moduli that Frenkel and Ladd (1987) obtained from simulations for an FCC crystal and lie well below the values predicted by Lionberger and Russel (1994) and measured by Shikata and Pearson (1994) for the metastable fluid. The static modulus is an equilibrium property that allows the structure to re-equilibrate to the applied strain and is unaffected by hydrodynamic interactions, while the high frequency modulus measures the instantaneous response to a strain. Consequently, the high frequency modulus always exceeds the static limit, though generally not by much for colloidal crystals. Thus our results are quite reasonable and agree with the measurements of van der Vorst, et al. (1995, 1996) on aqueous latex dispersions which also showed little variation in the modulus with frequency.

The dynamic viscosity scaled by the solvent viscosity exceeds both Nunan and Keller's (1984) calculations for the high frequency viscosity of an FCC crystal and the values measured by Shikata and Pearson (1994) and van der Werff, et al. (1989) for the metastable fluid. The high value may result from nonlinear effects. Frith, et al. (1987) found the loss modulus to pass through a maximum with increasing strain amplitude, while the storage modulus remained constant in the range of our measurements. If our strain amplitude lies near the maximum in the loss modulus, that would explain a higher value for the dynamic viscosity that falls close to the high shear limit for disordered dispersions.

CONCLUSIONS

Decomposition of the time-resolved Bragg peaks during nucleation, growth, and coarsening of hard sphere crystals at $\phi = 0.552$ suggests a constant rate of nucleation throughout the growth

period and diffusion-limited growth of the individual crystallites. Toward the end of growth the volume fraction within the crystallites relaxes toward the equilibrium value, as the volume fraction within the fluid falls toward the value at freezing. Coarsening also yields well defined trends but not ones that we are prepared to interpret. Gravity clearly affects the process reducing the crystallite size below that seen in microgravity and, thereby, leading to an over estimate of the number or density of crystallites. This may be responsible for significantly higher rates of nucleation deduced from laboratory experiments, relative to predictions from simple theories.

The resonance detected with dynamic light scattering gives reasonable values for the high frequency shear modulus of our colloidal crystals, representing the first data on viscoelastic properties of the nonaqueous hard sphere colloidal crystals. The high frequency dynamic viscosity seems a bit high, perhaps due to a nonlinear response. In this case the results for micro- and normal gravity are indistinguishable.

ACKNOWLEDGEMENTS

We thank the PHaSE team at NASA Lewis Research Center in Cleveland, OH for their work on the instrument and Sal Torquato for his advice on the orientationally averaged modulus. This research was funded by a NASA grant (NAG 3-1762) and Graduate Student Researchers Program Fellowship (NGT 3-52301).

REFERENCES

- Benzing, D.W., and W.B. Russel *J. Colloid Interface Sci.* **83** 178 (1981).
 Bolhuis, P., and D. Kofke *Phys. Rev. E* **54** 634 (1996).
 Buscall, R., J.W. Goodwin, M. Hawkins, and R.H. Ottewill *J. Chem. Soc. Faraday Trans. 1* **78** 2873 (1982).
 Chen, L., B.J. Ackerson, and C.F. Zukoski **38** 193 (1994).
 Chow, M., and C.F. Zukoski *J. Rheol.* **39** 33 (1995).
 D'Haene, P. *Rheology of Polymerically Stabilized Suspensions* (Katholieke Universiteit Leuven, Netherlands, 1992).
 Frenkel, D., and A. Ladd *Phys. Rev. Lett.* **59** 1169 (1987).
 Frith, W., J. Mewis, and T. Strivens *Powder Technol.* **51** 27 (1987).
 Frith, W., T. Strivens, and J. Mewis *J. Colloid Interface Sci.* **139** 55 (1990).
 Harland, J.L., and W. van Megen *Phys. Rev. E* **55** 3054 (1997).
 Harland, J.L., S.I. Henderson, S.M. Underwood, and W. van Megen *Phys. Rev. Lett.* **75** 3572 (1995).
 He, Y., B.J. Ackerson, W. van Megen, S.M. Underwood, and K. Schatzel *Phys. Rev. E* **54** 5286 (1996).
 Krieger, I.M. *Adv. Colloid Interface Sci.* **3** 111 (1972).
 Lant, C.T., A.E. Smart, D.S. Cannell, W.V. Meyer, and M.P. Doherty *Appl. Opt.* **36** 7501 (1997).
 Lindsay, H., and P.M. Chaikin *J. Chem. Phys.* **76** 3774 (1982).
 Lindsay, H., and P.M. Chaikin *J. Physique* **46** C3 (1985).
 Lionberger, R.A., and W.B. Russel, *J. Rheol.* **38** 1885 (1994).
 Mewis, J., W. Frith, T. Strivens, and W.B. Russel *AIChE J.* **35** 415 (1989).
 Nunan, K., and J. Keller *J. Fluid Mech.* **142** 269 (1984).
 Phan, S.-E., W.B. Russel, Z. Cheng, J. Zhu, P.M. Chaikin, J.H. Dunsmuir, and R.H. Ottewill *Phys. Rev. E* **54** 6633 (1996).

Pusey, P., and W. van Megen *An Exxon Monograph: Physics of Complex and Supramolecular Fluids*, (edited by S.A. Safran and N.A. Clark) John Wiley & Sons, New York, 1987, pp.673-698.

Schatzel, K., and B.J. Ackerson *Phys. Rev. E* **68** 337 (1992).

Schatzel, K., and B.J. Ackerson *Phys. Rev. E* **48** 3766 (1993).

Shikata, T., and D. Pearson *J. Rheol.* **38**, 601 (1994).

van der Werff, J., C.G. de Kruif, C. Blom, and J. Mellema *Phys. Rev. A* **39** 795 (1989).

van der Werff, J., and C.G. de Kruif *J. Rheol.* **33** 421 (1989).

van der Vorst, B., D. van den Ende, and J. Mellema *J. Rheol.* **39** 1183 (1995).

van der Vorst, B., D. van den Ende, and J. Mellema *Physica B* **228** 180 (1996).

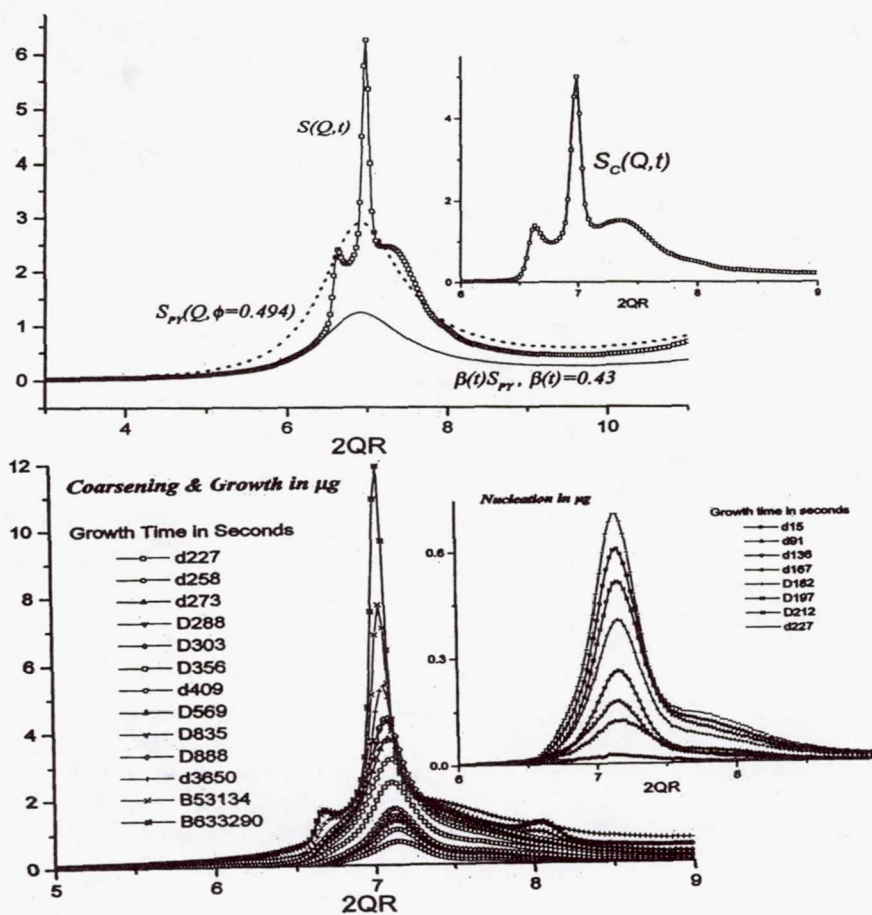


Figure 1 - Static structure factors for (a) a mixture of fluid and crystal demonstrating the subtraction of the corresponding S_{PP} weighted by $\beta(t)$ and (b) the resulting structure factors for the crystallites at a series of times.

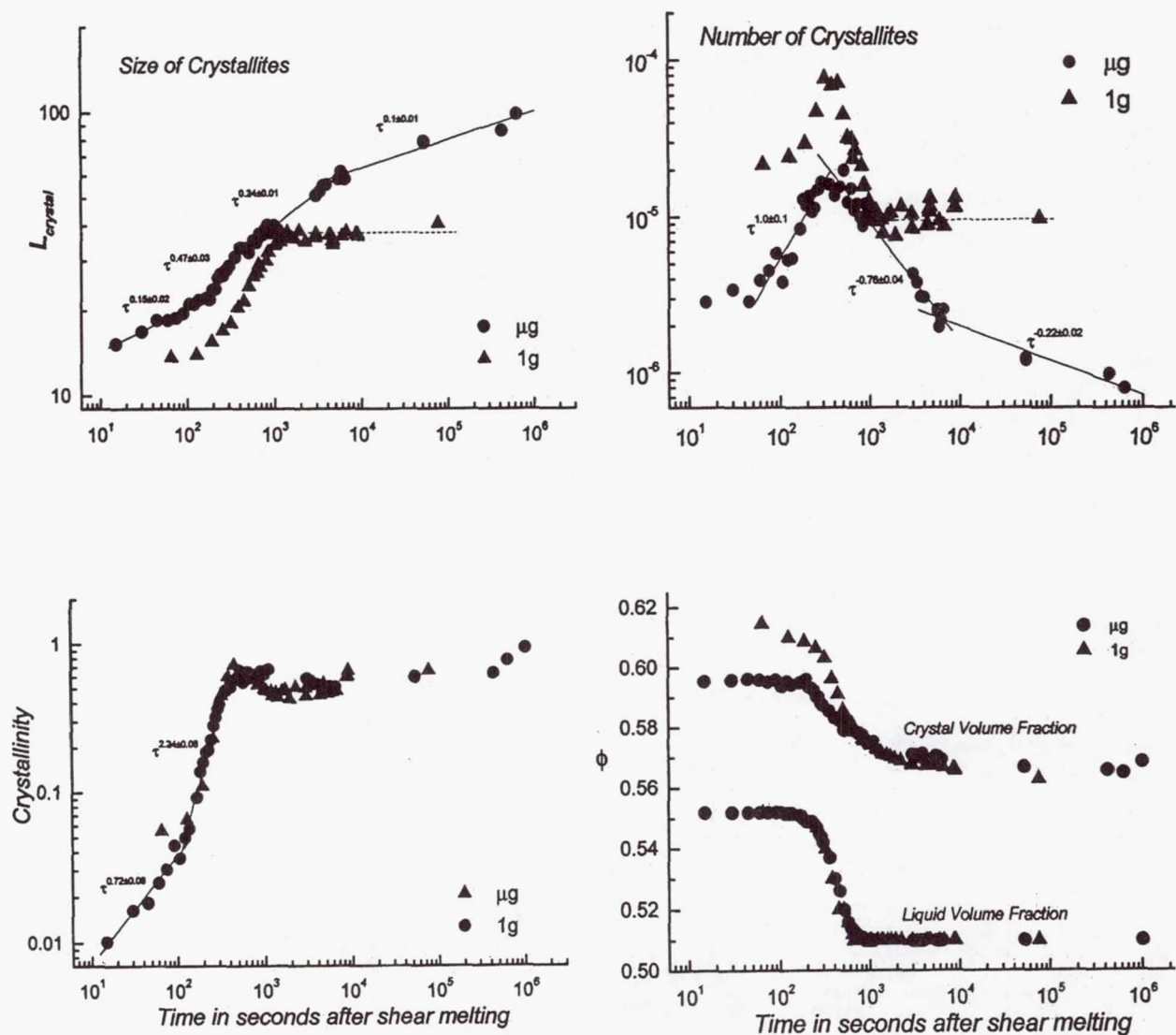


Figure 2 – The time evolution of (a) the average crystallite size $\langle L \rangle$, (b) the crystalline fraction f , (c) the number density of crystallites $n_c = f/\langle L \rangle^3$, and (d) the volume fractions within the crystalline and fluid phases for $\phi = 0.552$.

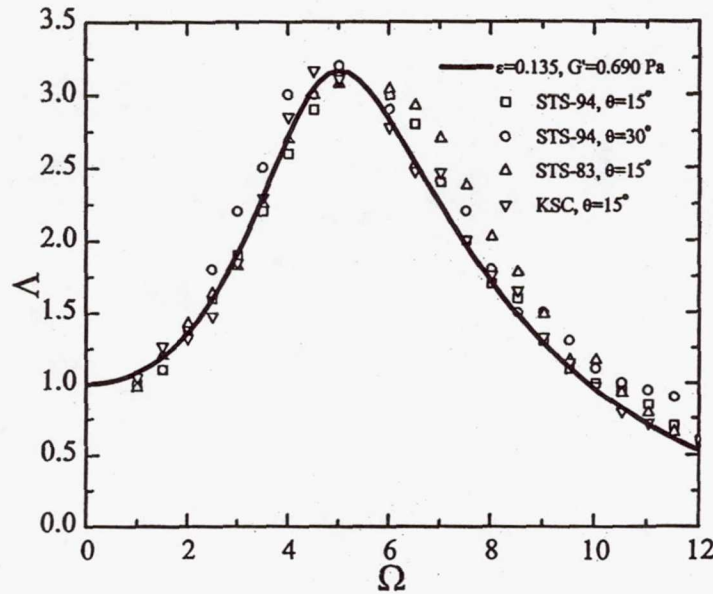


Figure 3 - Resonant response of Sample 4 STS-94 at various angles under gravity and microgravity vs driving frequency compared with the frequency independent model $\xi=0.135$.

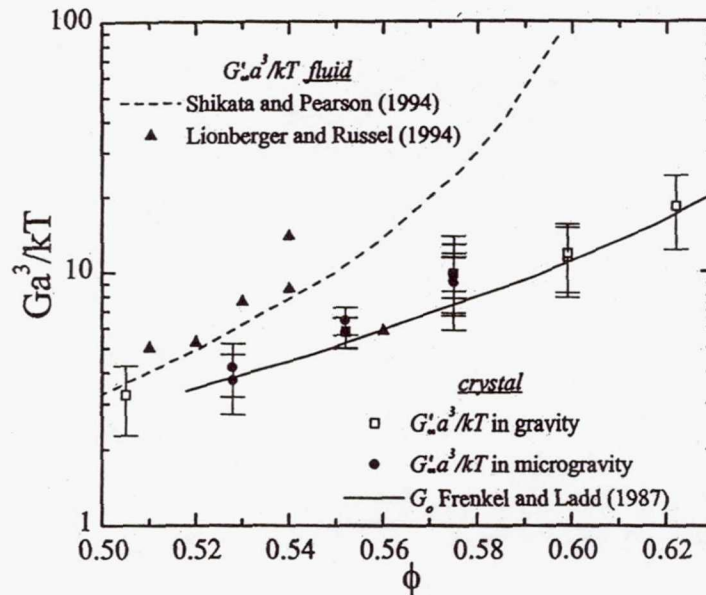


Figure 4 - The shear moduli of hard sphere crystals compared with measurements and theory for the high frequency moduli of the metastable fluid (Shikata & Pearson 1994, big triangleup; Lionberger & Russel 1994, ---) and Frenkel and Ladd's prediction (1987, ----) for the static moduli of an FCC crystal.

Page intentionally left blank

*omit this
page*

Electromagnetic Containerless Processing Facility (TEMPUS)

Thermophysical Properties of Undercooled Metallic Melts

Principal Investigator:

Dr. Ivan Egry
DLR
Cologne, Germany

181.

SINGLE SCAN!

3-19-26

434 855

Viscosity and surface tension measurements in

microgravity

362422

T H E R M O

TEMPUS MSL -1

Final Science Report

I. Egry, G. Lohöfer, I. Seyhan, B. Feuerbacher

Institute for Space Simulation

DLR

Cologne, Germany

ABSTRACT

Viscosity and surface tension of liquid metals can be measured by observing the oscillations of a levitated drop. The frequency is related to the surface tension, while the viscosity determines the damping of the oscillations. If no external forces are present, like in microgravity, these relations are particularly simple and precise. During the recent Spacelab mission MSL-1 such experiments have been performed on $\text{Co}_{80}\text{Pd}_{20}$ and $\text{Pd}_{78}\text{Cu}_6\text{Si}_{16}$ using the electromagnetic levitation facility TEMPUS. It was possible to obtain data over a wide temperature range, including the undercooled regime. While the temperature dependence of the surface tension remains linear throughout, the temperature dependence of the viscosity is much more pronounced and is discussed in terms of different models.

In addition, the electrical conductivity of liquid $\text{Co}_{80}\text{Pd}_{20}$ was measured, including the undercooled regime by a new, non-contact, inductive method. The results indicate the onset of magnetic ordering in the undercooled liquid.

1 Introduction

The thermophysical properties of liquid metals and alloys are difficult to measure; yet they play an important role in many phenomena relevant to both, fundamental science, and technological applications. In particular, surface tension and viscosity are of interest. The oscillating drop method has been used widely to measure the surface tension of levitated liquid metals. This method makes use of the fact that the frequency of the surface oscillations of a liquid drop is related to the surface tension by Rayleigh's formula. If the radius R of a spherical droplet undergoes oscillations of the form:

$$R = R_0 (1 + \delta \cos(\omega t) e^{-\Gamma t}) \quad (1)$$

where δ is the amplitude of the oscillation, ω is the frequency and Γ is the damping, then the frequency ω is given by:

$$\omega^2 = (32\pi\gamma)/(3m) \quad (2)$$

where γ is the surface tension and m is the mass of the drop.

Unfortunately, Rayleigh's formula cannot be applied to oscillations of drops levitated on earth. The influence of the external electromagnetic and gravitational fields must be taken into account. However, under microgravity both fields are negligibly small, and Rayleigh's formula can be applied directly.

In addition, the oscillating drop technique also yields the viscosity of the droplet. This idea is based on Kelvin's work on the oscillations of viscous drops. He derived the following expression for the damping constant Γ :

$$\Gamma = \frac{20\pi}{3} \frac{\eta R_0}{m} \quad (3)$$

where η is the viscosity. Like Rayleigh's formula, this equation is only correct for spherical drops in the absence of external fields.

Based on the experience gained during IML-2, the TEMPUS facility was modified and reflown on Spacelab mission MSL-1 in 1997. For this flight, we have proposed to measure surface tension and viscosity of two different alloys, namely $\text{Co}_{80}\text{Pd}_{20}$ and $\text{Pd}_{76}\text{Cu}_6\text{Si}_{18}$. While the first system is a low viscosity alloy with excellent undercooling capabilities, the latter is a eutectic system which is a good glass former and has, consequently, a high viscosity. The reported

values for the viscosity of $\text{Pd}_{76}\text{Cu}_6\text{Si}_{18}$ at the eutectic temperature differ by a factor of 100. In this paper, we present the results obtained during MSL-1. While no previous data exist for the viscosity of $\text{Co}_{80}\text{Pd}_{20}$, our results confirm that the lower of the two values reported for $\text{Pd}_{76}\text{Cu}_6\text{Si}_{18}$ is correct.

Even though TEMPUS has not been designed for a measurement of the electrical resistivity of the levitated samples, it was under certain conditions possible to extract this quantity from the monitored housekeeping data of the coil current and voltage. This enabled us for the first time to determine the electrical conductivity of a liquid droplet in the undercooled regime using the $\text{Co}_{80}\text{Pd}_{20}$ sample.

2 Experiments and Results

2.1 Surface Tension and Viscosity

We prepared spherical samples of 8 mm diameter. The $\text{Pd}_{76}\text{Cu}_6\text{Si}_{18}$ sample was placed into a sample holder consisting of a wire cage made of W-Re and a pedestal of SiC, whereas the $\text{Co}_{80}\text{Pd}_{20}$ sample was placed into a cup-type sample holder made of SiC. This cup served as an evaporation shield to protect the levitation coil from the expected strong evaporation of the sample. For viewing purposes, it had a lateral slit. Both sample holders were integrated into the TEMPUS facility, where they were kept under inert gas atmosphere until launch. The experiments on $\text{Pd}_{76}\text{Cu}_6\text{Si}_{18}$ were performed in 100 mbar argon of 6N purity, while those on $\text{Co}_{80}\text{Pd}_{20}$ were performed in 100 mbar He-4%H₂ atmosphere. Temperature was measured by a pyrometer equipped with an InAs detector covering the range between 600 K and 2000 K. The temperature data were acquired with 100 Hz resolution, while the coil current was monitored with 10 Hz. The sample oscillations were observed radially with a video camera, operating at 30 Hz. Using the time stamps on both, the temperature signal, and the video frames, the two data sets could be synchronised with an accuracy better than 0.1 s.

After stable positioning, the samples were melted and overheated by 100-400 K. Then, the heating fields were switched off, allowing the sample to cool

down due to cooling by radiation and heat conduction. During cooling, a short current pulse was sent through the heating coils, leading to a lateral compression of the sample and subsequent oscillations. Although observing the oscillations during cooling introduces a temperature error of about 5 - 10 K, it has the advantage that the electromagnetic fields are reduced to a minimum, eliminating any fluid flow effects. During one cooling cycle, such an excitation pulse was applied every 50 K, until the sample solidified. The video images were analyzed frame by frame and the radius of the sample was determined as a function of time. The damping constant was obtained from the time signal directly, whereas the frequency was obtained from the Fourier transform of the signal.

2.1.1 $\text{Co}_{80}\text{Pd}_{20}$

$\text{Co}_{80}\text{Pd}_{20}$ has a liquidus temperature of $T_l = 1610$ K and a solidus temperature of $T_s = 1565$ K, and therefore only a small temperature region where solid and liquid phase coexist. This makes this alloy easy to handle in electromagnetic levitation. During MSL-1, 30 melt cycles could be performed. After initial in situ purification by overheating, it could be undercooled by more than 340 K, which means that the hypercooling limit was exceeded and the Curie temperature $T_c = 1257$ K of the liquid phase was approached. The temperature trace of one typical thermal cycle is shown in figure 1. Melting, undercooling, recalescence and solidification are clearly visible. Note the absence of a recalescence plateau and the fact that, upon recalescence, the liquidus temperature is not reached. This is a consequence of hypercooling. The graph also shows the electrical current through the heating coils. The distinct spikes correspond to the pulses which were used to excite surface oscillations. From the video signal, the onset and decay of these oscillations can be observed. This is shown in Figure 2. Using eqns (2) and (3) to convert frequencies and damping constants into surface tension and viscosity, we have analyzed all oscillations and obtained surface tension and viscosity as functions of temperature. The results are shown in figures 3 and 4,

respectively. The surface tension data have been fitted to a linear relation and we obtain:

$$\gamma_{\text{Co-Pd}} = 1675 - 0.17 (T - 1610) \text{ [mN m}^{-1}\text{]} \quad (4)$$

where temperature T is in K. The viscosity was fitted to an Arrhenius type expression, and we obtain:

$$\eta_{\text{CoPd}} = 0.15 \exp(9.37 \cdot 10^{20}/kT) \text{ [mPa s]} \quad (5)$$

Here, Boltzmann's constant k is given in J K^{-1} , and temperature in K. The viscosities measured range from 5 to 30 mPas, covering nearly an order of magnitude. An undercooling of approximately 300 K leads to an increase in viscosity by a factor of 3.

2.1.2 $\text{Pd}_{76}\text{Cu}_6\text{Si}_{18}$

At the chosen composition, PdCuSi forms a eutectic at a temperature of $T_e = 1033$ K. This means that melting and solidification takes place at a fixed temperature, which can be used to calibrate the pyrometer reading. The addition of Cu to the binary Pd-Si system is supposed to improve the glass-forming ability of the alloy. Unfortunately, its presence limits the undercoolability under quasi-isothermal conditions to approximately 70 K, due to the formation of CuO.

The experiments on $\text{Pd}_{76}\text{Cu}_6\text{Si}_{18}$ were all carried out during the MSL-1 Spacelab mission, however during two different Space Shuttle flights, STS-83 and STS-94. STS-83 was a minimum duration flight of 4 days only. Three thermal cycles could be performed on $\text{Pd}_{76}\text{Cu}_6\text{Si}_{18}$ during STS-83, and additional 16 cycles were run on STS-94.

The experiments on PdCuSi were analysed in complete analogy as described above for CoPd. The data obtained for the surface tension are shown in Figure 5. They can be fitted to following linear relation:

$$\gamma_{\text{PdCuSi}}(T) = 1399 + 0.26 (T-1033) \text{ [mN m}^{-1}\text{]} \quad (6)$$

As before, temperature is in K. Full squares correspond to data taken during STS-83, empty squares represent measurements during STS-94. As can be seen, there is considerable scatter in the data. We attribute this as well as the

positive temperature coefficient to the formation of Cu-O at the surface.

The data obtained for the viscosity are shown in Figure 6. The scatter of the STS-94 data set is higher than that of STS-83, which may be due to microgravity disturbances. We have fitted the data to different theoretical models for the viscosity, namely to a simple Arrhenius-type exponential, $\eta = \eta_0 e^{\Delta E/kT}$, corresponding to an activated (hopping) process, as well as to the Vogel-Fulcher formula for the viscosity of a glass-forming alloy, $\eta = \eta_0 \exp\{\Delta E/k(T-T_0)\}$. These two fits are shown in Figure 7. We have also fitted our data to a power-law, $\eta = A (T-T_0)^{-\alpha}$, as predicted by the mode-coupling theory. For clarity, this fit is not shown. In the temperature range considered, it is indistinguishable from the Arrhenius fit. Figure 6 also shows the fit obtained by Lee and coworkers indicating the temperature range of their measurements. There is good agreement, but our data extend to much higher temperatures, allowing a more reliable fit. In summary, our fitting procedure yields the following expressions for the viscosity of $\text{Pd}_{76}\text{Cu}_6\text{Si}_{18}$:

$$\eta = 0.134 \exp(8.35 \cdot 10^{-20}/kT) \text{ [mPa s]} \quad \text{Arrhenius} \quad (7)$$

$$\eta = 1.97 \exp(1.82 \cdot 10^{-20}/k(T-630)) \text{ [mPa s]} \quad \text{Vogel-Fulcher} \quad (8)$$

$$\eta = 7.49 \cdot 10^7 (T-630)^{-2.38} \text{ [mPa s]} \quad \text{Power-law} \quad (9)$$

All dimensions are the same as in eqn. 5. The measured viscosities range from 10 mPa s at 1400 K to 50 mPa s at 1100 K, very similar to the case of Co-Pd. Therefore we expect that viscosities in the range from 1 mPa s to 100 mPa s can be measured using the oscillating drop technique.

2.2 Electrical Resistivity

The changing sample resistivity influences the total resistance and inductance of the TEMPUS heating coil and thus also the voltage U_0 and current I_0 through the heating circuit. The amplitudes of voltage and current are, however, housekeeping data of the facility and are monitored with a 10 Hz data rate only. Together with the phase difference ϕ between voltage and current, which is essentially controlled by the heating current generator dependent on its voltage, i.e., $\cos\phi = f(U)$, it is possible to determine the sample resistivity from

$$\frac{I_0}{U_0} \cos \varphi = \frac{C}{L} (R + \alpha R_s(\rho)) \quad (10)$$

where C , L , and R are the capacity, inductance and resistance of the RF heating circuit without sample, respectively, and $R_s(\rho)$ the additional resistance of the sample, which is a well known function of its resistivity ρ . The constants C , L , R , are determined from a calibration run without sample, and the constant α from data of the Gold (FO12), Nickel (FO17), and Zirconium (FO10) experiments, which deal with materials of known resistivity.

The current and voltage data monitored during the cooling phase of a normal $\text{Co}_{80}\text{Pd}_{20}$ experiment cycle, see Fig. 1, where the excitation spikes had to be cut out however, have been used to determine the electrical resistivity of the sample in the liquid state above and below the melting temperature and in the solid state from Eq. (10). Figure 7 shows the measured resistivity data of $\text{Co}_{80}\text{Pd}_{20}$ in the liquid state (spheres) and in the solid state (diamonds) together with the corresponding linear fits

$$\begin{aligned} \rho_{sol} &= 120.5 + 0.044(T - 1560) \quad [\mu\Omega\text{cm}] \\ \rho_{liq} &= 163.2 + 0.058(T - 1610) \quad [\mu\Omega\text{cm}] \end{aligned} \quad (11)$$

Below about 1350 K the drastic increase of the data indicate the onset of magnetic ordering in the solid as well as in the liquid state of the sample. In this region, our analysis which is valid for non-magnetic materials only, breaks down. Therefore, the increase of the data points cannot be interpreted as an increase in electrical resistivity.

3 Conclusion

The oscillating drop technique is a useful tool for measuring surface tension and viscosity of high temperature melts, in particular in the undercooled region. In microgravity, the drop is spherical, and simple formulae can be used to derive these data from the oscillation spectrum. We have demonstrated the feasibility of this approach and were able to resolve a long standing controversy regarding the viscosity of $\text{Pd}_{76}\text{Cu}_6\text{Si}_{18}$. Future

experiments will concentrate on the application of this technique to technologically relevant materials.

For the first time, we were also able to measure the electrical conductivity of undercooled liquid metals. Despite the limitations imposed by the hardware, reliable values could be derived and even the onset of magnetic ordering could be observed. This measurement technique has a great potential for future experiments, because the measurement of the electrical conductivity in combination with the Wiedemann-Franz law offers an elegant alternative to direct measurements of the thermal conductivity.

4 Publications

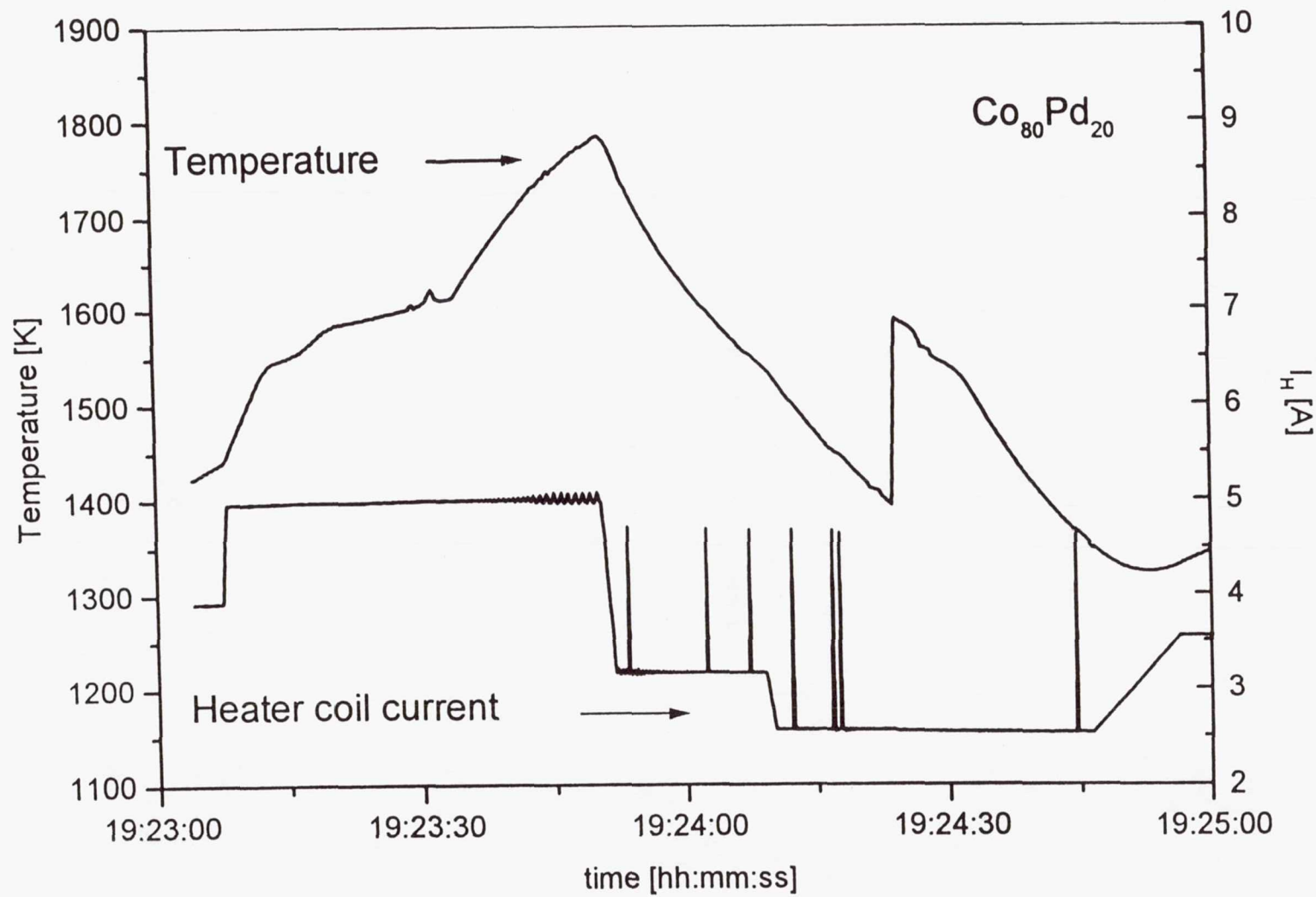
- [1] I. Egry, G. Lohöfer, I. Seyhan, S. Schneider, B. Feuerbacher:
Viscosity of eutectic $Pd_{78}Cu_6Si_{16}$ measured by the oscillating drop technique in microgravity, Appl. Phys. Lett. **73** (1998), 462
- [2] I. Egry, G. Lohöfer, I. Seyhan, S. Schneider, B. Feuerbacher:
Viscosity and surface tension measurements in microgravity,
submitted to Int. J. Thermophys.

5 Figure captions

- Figure 1 One thermal cycle of $\text{Co}_{80}\text{Pd}_{20}$ indicating hypercooling. The lower curve shows the current through the levitation coil. The spikes correspond to pulses used to excite surface oscillations.
- Figure 2 Excitation and decay of a surface oscillation, as detected in the video signal.
- Figure 3 Surface tension of $\text{Co}_{80}\text{Pd}_{20}$ as function of temperature. The vertical line represents the liquidus temperature.
- Figure 4 Viscosity of $\text{Co}_{80}\text{Pd}_{20}$ as function of temperature. The vertical line represents the liquidus temperature.
- Figure 5 Surface tension of $\text{Pd}_{76}\text{Cu}_6\text{Si}_{18}$ as function of temperature.
- Figure 6 Viscosity of $\text{Pd}_{76}\text{Cu}_6\text{Si}_{18}$ as function of temperature.
- Figure 7 Electrical resistivity of $\text{Co}_{80}\text{Pd}_{20}$ in the liquid state (spheres) and in the solid state (diamonds) together with the corresponding linear fits as a function of temperature. T_s and T_l indicate the solidus and liquidus temperatures, respectively.

Figure 1 One thermal cycle of $\text{Co}_{80}\text{Pd}_{20}$ indicating hypercooling.

The lower curve shows the current through the levitation coil. The spikes correspond to pulses used to excite surface oscillations.



copdiic-temp&u_H

Figure 2 Excitation and decay of a surface oscillation, as detected
in the video signal.

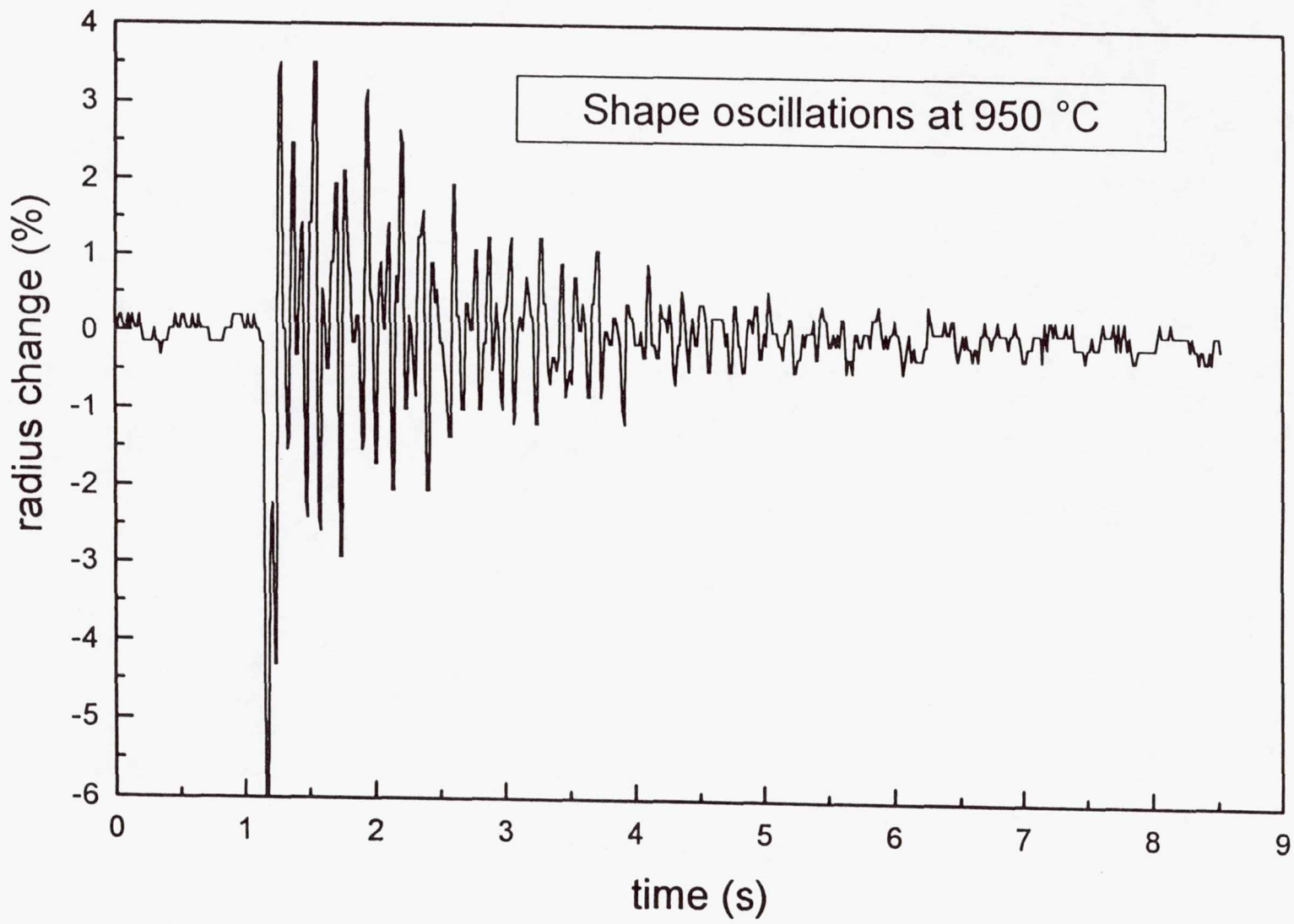
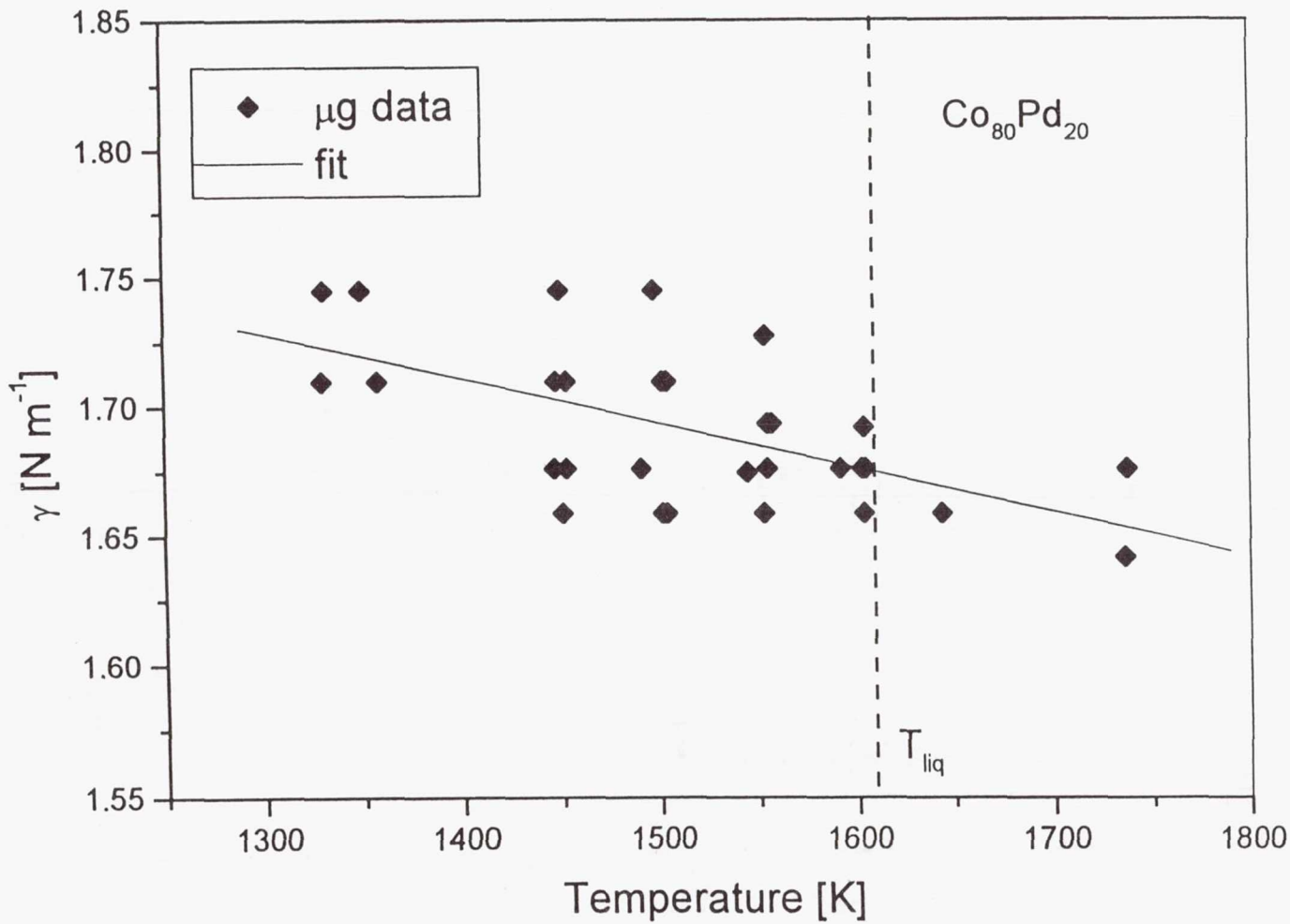


Figure 3

Surface tension of $\text{Co}_{80}\text{Pd}_{20}$ as function of temperature.
The vertical line represents the liquidus temperature.



Copdgamma[K]

Figure 4 Viscosity of $\text{Co}_{80}\text{Pd}_{20}$ as function of temperature. The vertical line represents the liquidus temperature.

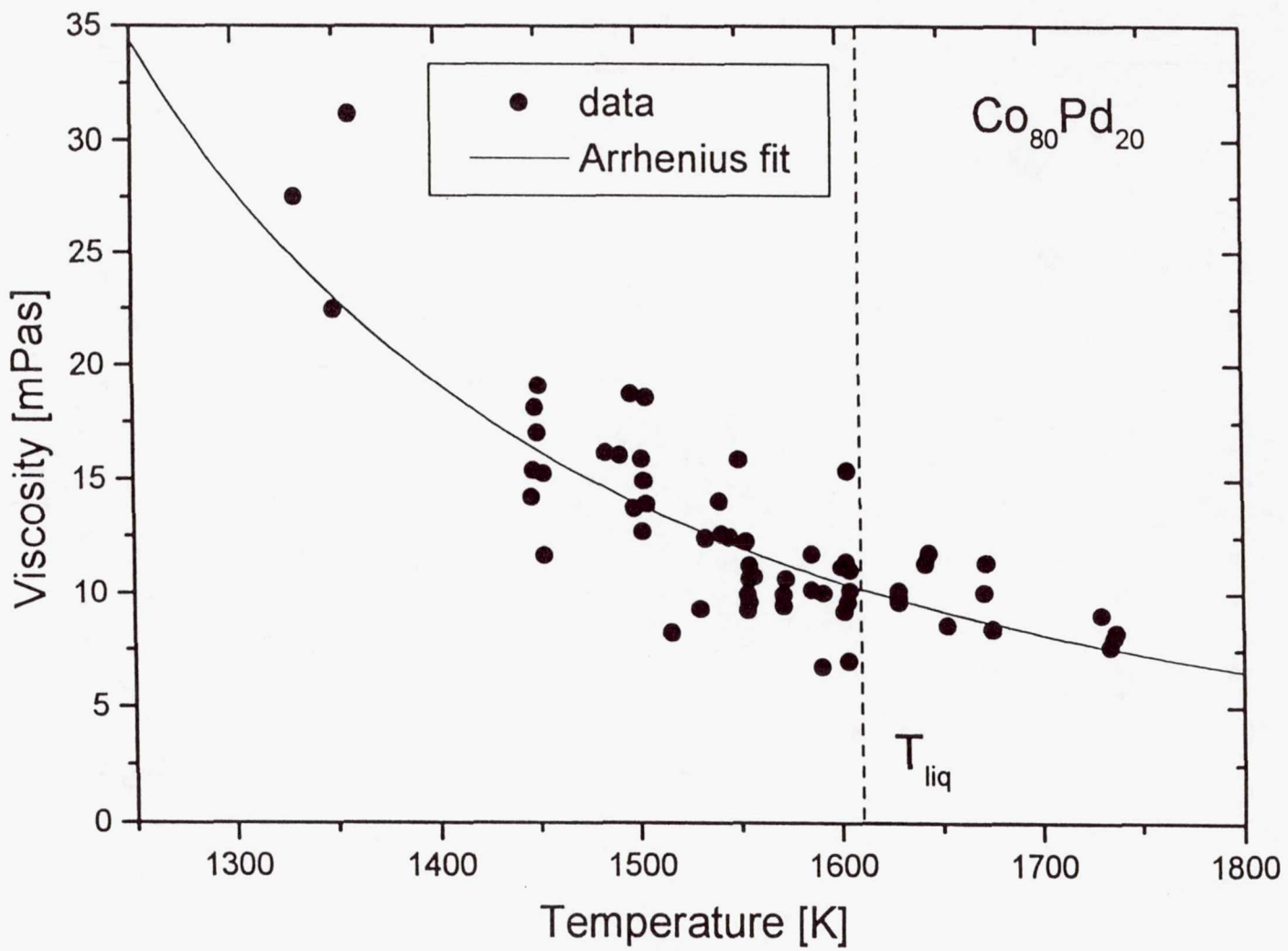


Figure 5 Surface tension of $\text{Pd}_{76}\text{Cu}_6\text{Si}_{18}$ as function of temperature.

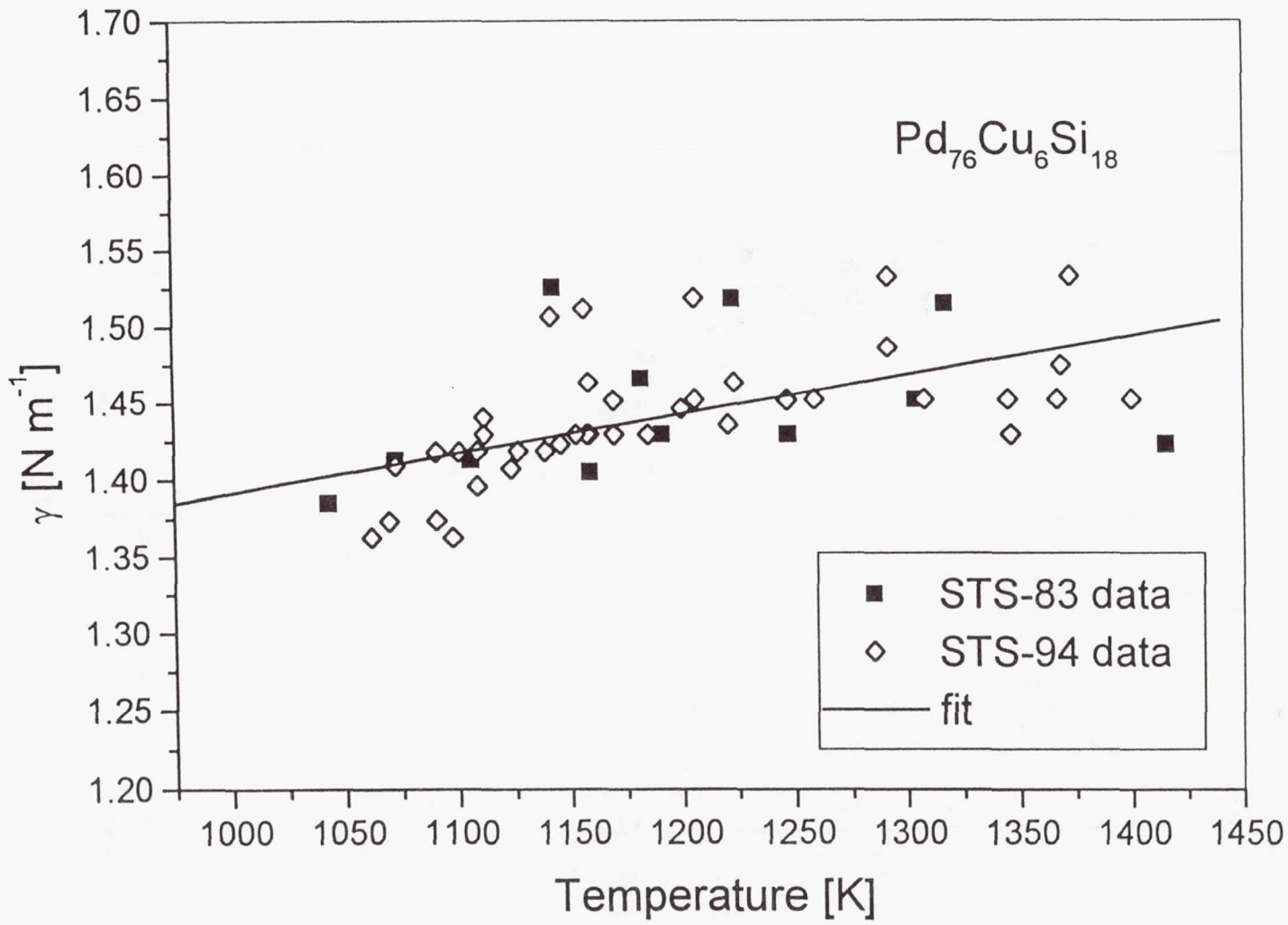


Figure 6 Viscosity of $\text{Pd}_{76}\text{Cu}_6\text{Si}_{18}$ as function of temperature.

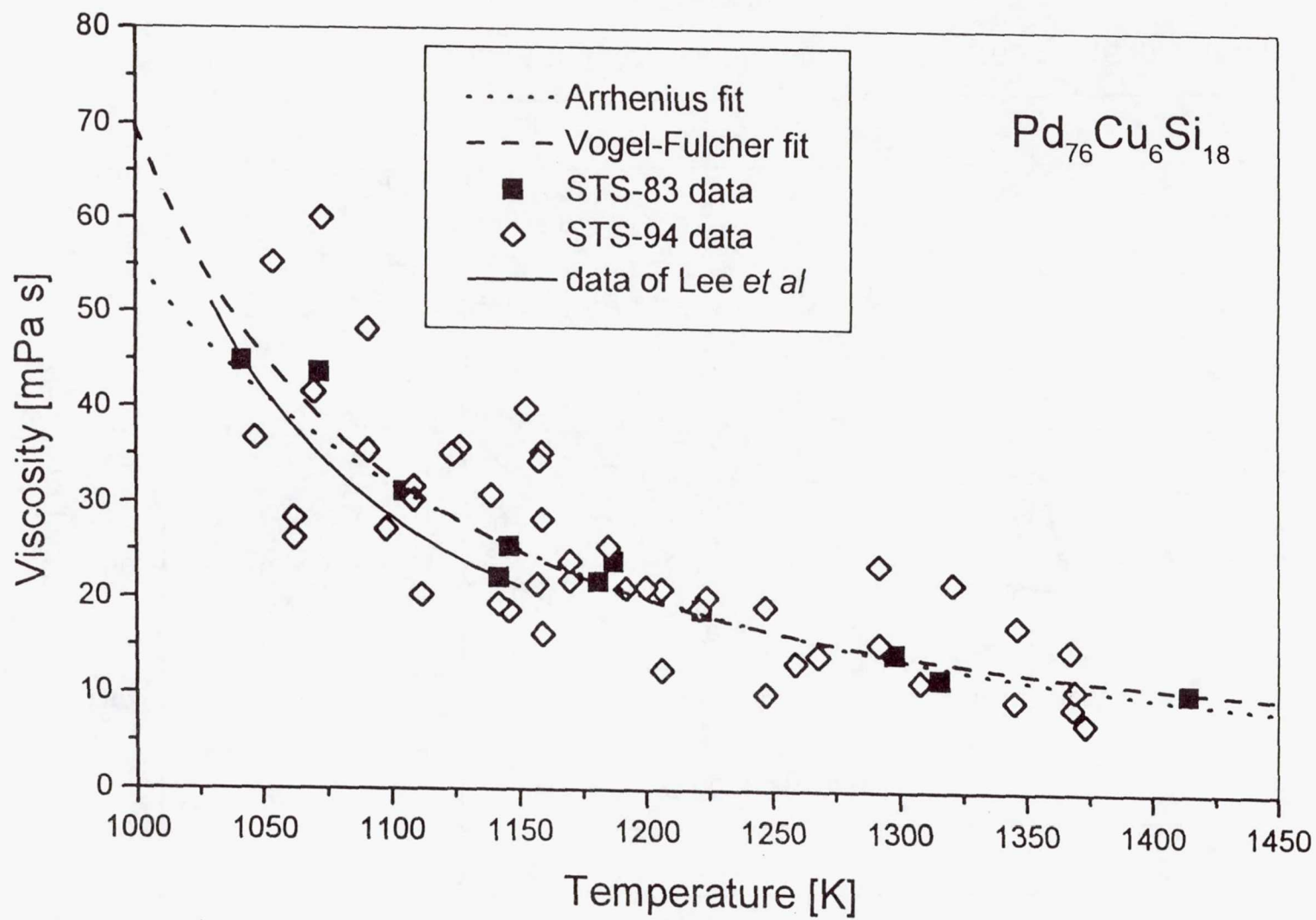
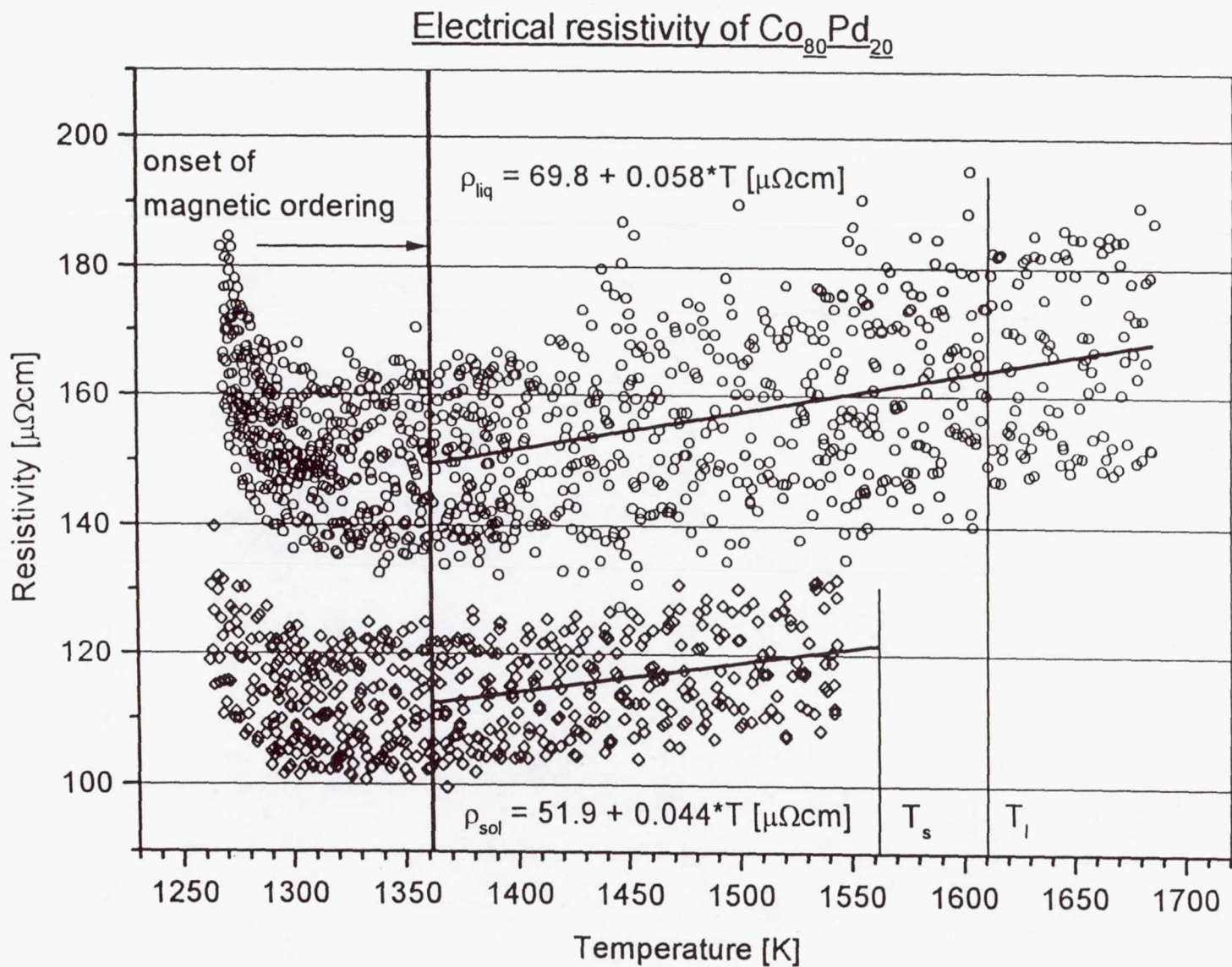


Figure 7

Electrical resistivity of $\text{Co}_{80}\text{Pd}_{20}$ in the liquid state (spheres) and in the solid state (diamonds) together with the corresponding linear fits as a function of temperature. T_s and T_l indicate the solidus and liquidus temperatures, respectively.



T H E R M O

Non-technical Summary

I. Egry

For many industrial processes like welding or casting it is important to know the properties of liquid metals and alloys with great precision. Such measurement cannot be done in conventional containers due to the high temperatures involved. The liquid metal would react with the container walls, leading to contamination of the material studied and to erroneous results. Therefore, containerless methods like electromagnetic levitation, have to be used. Here the liquid droplet is floating on strong electromagnetic fields without any contact to material container walls. Unfortunately, these strong fields have undesirable side effects on the liquid droplet: they deform its shape and induce strong fluid motion inside the droplet. Again, these effects lead to measurement errors. In microgravity, only small electromagnetic fields are needed to position the droplet against residual accelerations. Consequently, the sample is undisturbed and high precision measurements can be carried out.

We have measured surface tension, viscosity and electrical conductivity of two alloys, namely $\text{Co}_{80}\text{Pd}_{20}$ and $\text{Pd}_{78}\text{Cu}_6\text{Si}_{16}$. Surface tension is the force which keeps liquid bubbles in shape and prevents them from flowing apart. In welding, the quality of the weld seam depends on the surface tension. Viscosity is a quantitative measure of the resistance of a fluid against shear flow. Water has low viscosity, honey has high viscosity. Liquid metals have low viscosities like water above their melting point, but their viscosity increases dramatically as the temperature is lowered and they become undercooled. When the viscosity exceeds a certain value, no motion is any longer possible within the fluid, and it freezes into an amorphous solid, a glass. The electrical conductivity indicates how well a material can conduct electrical current. In the solid phase, most metals are very good conductors, but their conductivity gets poorer in the liquid state, because the electrons, who carry the current, are now scattered more often by the irregular structure and movement within the liquid.

The two materials studied have interesting properties. $\text{Pd}_{78}\text{Cu}_6\text{Si}_{16}$ is known to be a good glass-former, i.e. it has a high viscosity and we were able to measure the temperature dependence of the viscosity over a temperature range of more than 400 K, which was not possible before. A 20% change in temperature leads to a viscosity change by 300%.

In the solid state, $\text{Co}_{80}\text{Pd}_{20}$ is a very good (ferro)magnet below its Curie temperature (1250 K). There have been suggestions and experiments which indicated that also liquid $\text{Co}_{80}\text{Pd}_{20}$ would become magnetic if it is sufficiently undercooled. We have been able to undercool $\text{Co}_{80}\text{Pd}_{20}$ by 340 K, and we could in fact observe the onset of magnetic ordering in the liquid. Note that no liquid magnet exists in nature. We have thereby proved that this is not impossible *a priori*, i.e. there is no physical law which prohibits a liquid from becoming magnetic, it just happens that the Curie temperature is always lower than the melting temperature. Therefore, under equilibrium conditions, a material always becomes first non-magnetic before it melts.

Page intentionally left blank

omit
THIS
PAGE

Electromagnetic Containerless Processing Facility (TEMPUS)

Thermophysical Properties of Advanced Materials in the Undercooled Liquid State

Principal Investigator:

Dr. Hans Fecht
University of Ulm
Ulm, Germany

SINGLE SCAN

520-26
434856

Final Science Report MSL-1

131.

Thermophysical Properties of Undercooled
Metallic Glass Forming Liquid Alloys

362426

Prof. Dr. H. -J. Fecht

Institute for Electric and Magnetic Materials
Department of Materials Sciences
University of Ulm

and

Dr. R. K. Wunderlich
Institute for Metal Physics
Technical University of Berlin

Abstract

Thermophysical properties of glass forming metallic alloys are important for a systematic assessment of the inherent factors determining the ability of different alloy compositions to form metallic glasses within a wide range of critical cooling rates. According to classical nucleation theory these critical cooling rates are basically determined by the viscosity (mobility), the interfacial tension and, the difference in Gibbs free energy between the undercooled melt and crystalline phase combining the kinetic and thermodynamic aspects of undercooling and nucleation. In particular, measurements of the specific heat of undercooled liquid alloys allow evaluation of the Gibbs free energy difference between the liquid and crystalline phase and thus of the thermodynamic stability of the undercooled melt. In order to make the undercooled liquid state accessible to specific heat measurements under clean, quiescent isothermal conditions experiments were performed in microgravity with the containerless electromagnetic processing device TEMPUS. For these investigations the new method of non-contact ac-calorimetry was developed and applied successfully for the first time during the IML-2 mission.

In continuation of our experiments on IML-2 where we have measured the specific heat of binary eutectic glass forming liquid alloys with critical cooling rates in the order of 10^{-5} K/sec in MSL-1 we have investigated the specific heat of liquid multicomponent bulk metallic glass forming alloys, ZrAlCuNi and ZrAlCuNiCo, having critical cooling rates for glass formation in the range of $5 \cdot 10^2$ sec. The specimen showed excellent stability in the undercooled melt making possible for the first time measurements of the specific heat in an extended temperature range from the stable into the undercooled liquid regime.

The experiments were performed in close collaboration with the groups of Prof. W.L. Johnson, Caltech, who processed bulk metallic glass forming alloys of different compositions and the group of Prof. K. Samwer from the University of Augsburg who measured the coefficient of thermal expansion in the liquid phase of these alloys.

2. Objectives

The primary scientific objective of the experiments conducted in the MSL-1 spacelab mission was the measurement of the specific heat in the stable and undercooled liquid of the two bulk metallic glass forming alloys $\text{Zr}_{65}\text{Al}_{7.5}\text{Cu}_{17.5}\text{Ni}_{10}$ and $\text{Zr}_{60}\text{Al}_{10}\text{Cu}_{18}\text{Ni}_9\text{Co}_3$. In addition, the method of contactless modulation calorimetry allows also determination of thermal transport coefficients such as the total hemispherical emissivity and the effective thermal conductivity of the specimen. The third specimen to be investigated, the binary eutectic alloy $\text{Zr}_{64}\text{Ni}_{36}$, was already processed in the IML-2 mission. Here the objective was to provide a calibration specimen for the calorimetric measurement method and to ensure reproducibility and thus the consistency of the data analysis and calibration method employed for evaluation of the specific heat. Furthermore, this sample was intended to investigate fluid flow as function of the applied electromagnetic heating and positioning fields by the group of Dr. G. Trapaga from MIT.

The experiments performed in MSL-1 were conducted in close collaboration with the group of Prof. W. L. Johnson from the California Institute of Technology regarding the choice of alloy compositions and the group of Prof. K. Samwer from the University of Augsburg who measured the coefficient of thermal expansion in the stable and undercooled liquid of these alloys.

3. Background

The formation of metallic glasses by cooling of metallic melts from temperatures above the equilibrium melting point depends critically on the cooling rate. Binary eutectic alloys such as $\text{Zr}_{64}\text{Ni}_{36}$ require cooling rates as high as 10^5 K / sec while the recently discovered bulk metallic glass forming alloys such as ZrTiNiCuBe or ZrAlCuNiCo require critical cooling rates ranging from 10 K/sec to $5 \cdot 10^2$ K/sec. According to classical nucleation theory the nucleation rate and thus the critical cooling rate for glass formation where nucleation is altogether suppressed is determined by the viscosity, the interfacial tension between the melt and the crystalline nucleus and the difference in the Gibbs free energy between the undercooled liquid and the crystalline phase. In addition, other factors such as the

ability to either dissolve or passivate heterogenous nucleants present in the melt may influence the ability to form a metallic glass upon cooling with a given alloy composition.

The Gibbs free energy difference can be evaluated from measurements of the specific heat of the undercooled liquid allowing to differentiate between these factors and to assess the thermodynamic contribution to glass formation as a function of alloy composition. Furthermore, the temperature dependence of the specific heat in the stable and undercooled melt may reveal structural changes in the liquid state. These changes, regarding different states of chemical nearest neighbour ordering have been suggested in particular for melts with a strong temperature dependence of the mixing enthalpy of the constituent alloy components. However, so far there is no convincing experimental evidence of a nonmonotonous temperature dependence of the liquid specific heat for metallic alloys has been presented.

In order to avoid heterogenous nucleation by contact of these reactive alloy melts with container walls the experiments were performed with the containerless electromagnetic processing TEMPUS. Reduced gravity is required to avoid excessive heating levels associated with electromagnetic levitation under one-g conditions thus allowing to process under ultrahigh vacuum conditions.

For the specific heat measurements the method of non-contact ac-calorimetry was developed by Fecht and Johnson and successfully applied during the IML-2 spacelab mission with the TEMPUS device. In short, the specimen is positioned with the quadrupole field and heated with the dipole field of the TEMPUS two oscillating circuits. The heating and positioning frequencies are chosen such as to decouple the heating effects of the positioner and heater. Temperature measurement is performed by an optical pyrometer calibrated for the specific alloy in ground based experiments. After heating the specimen to a given temperature T_0 the heating field is sinusoidally modulated at frequencies ranging typically from 0.05 Hz - 0.20 Hz. From the resulting temperature modulation, ΔT_{mod} , the specific heat, c_P , is evaluated according to:

$$c_P = \frac{P_{mod}}{\omega \Delta T_{mod}} f(\omega, \tau_1, \tau_2)$$

where ω is the modulation frequency and P_{mod} is the modulation power component. $f(\omega, \tau_1, \tau_2)$

is a correction function accounting for the finite thermal conductivity of the specimen with internal relaxation time τ_2 and heat loss with external relaxation time τ_1 . Due to the typically large difference in the external and internal relaxation times for metallic specimen there is a frequency where $\Delta T_{\text{mod}}(\omega)$ is position independent characterizing the isothermal regime with $1 - f(\omega, \tau_1, \tau_2) < 10^{-2}$. Experimentally this regime can be identified by a phase shift of 90° between heater and temperature response and, $\Delta T_{\text{mod}}(\omega) \approx \text{const.}$ as a function of ω in a certain frequency intervall. The isothermal frequency range was determined in ground based experiments and verified by variation of the modulation frequency in the course of the space experiment. Furthermore, an increase of the modulation frequency outside the isothermal regime allows determination of τ_2 while τ_1 can be determined from analysis of the temperature decay function following a small step function change in heater input power. Knowing the specific heat the total hemispherical emissivity can be evaluated from τ_1 . The effective thermal conductivity can be obtained from τ_2 with a specific heat flow model.

4. Methods of Data Acquisition and Analysis, Conduction of Experiment

Primary ingots for processing in MSL-1 were prepared from low oxygen metals in an arc melter under a purified argon atmosphere. At each step of the alloying process the oxygen content of the ingot was verified by the LECO hot gas extraction method. The final MSL-1 batch specimen had a typical oxygen content of 400 ppm increasing to 600 ppm after processing in TEMPUS.

In Fig. 1 a typical MSL-1 experimental run for the ZrAlCuNi alloy. is shown. The

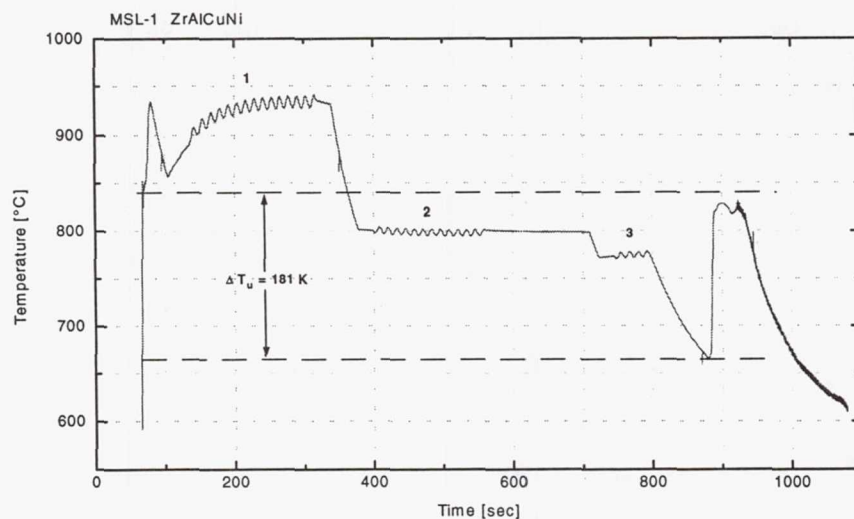


Fig.2 . Typical experiment run during MSL-1 with processing in the stable and undercooled melt and recalescence.

specimen was melted by a fast heating pulse and heated to equilibrium temperature in the stable melt while performing modulation calorimetry (1). Subsequently the sample was cooled by a fast cooling pulse to a temperature in the undercooled melt performing again modulation calorimetry at equilibrium temperature (2). This step was repeated (3) at another temperature plateau in the undercooled melt with subsequent undercooling and recalescence. With regard to nucleation the specimen exhibited excellent stability in the undercooled melt allowing for the first time extended specific heat and thermal expansion measurements in this regime. However due to increasing sample deformation as function of processing time in the liquid the cp measurement (3) had to be interrupted. The deformation is caused by an increasing rotational speed of the specimen and was quantitatively analyzed with the high resolution camera operated by the Samwer. The raw temperature signal (2) with modulation frequency $\omega = 0.08$ Hz is shown in Fig. 2a. The signal is further processed by application of a drift correction to compensate for a change in the bias temperature before reaching temperature equilibrium at $t \approx 500$ sec. ΔT_{mod} is then obtained from subsequent Fourier analysis as shown in Fig 2b. In addition, ΔT_{mod} is calculated from a running average over modulation cycles after application of a 0.80 Hz low pass FFT filter to remove the high frequency modulation components caused by harmonic oscillations in the potential of the positioning field. ΔT_{mod} values obtained by both methods agree within better 0.15 K. As such the precision of ΔT_{mod} determination is typically $< 4\%$.

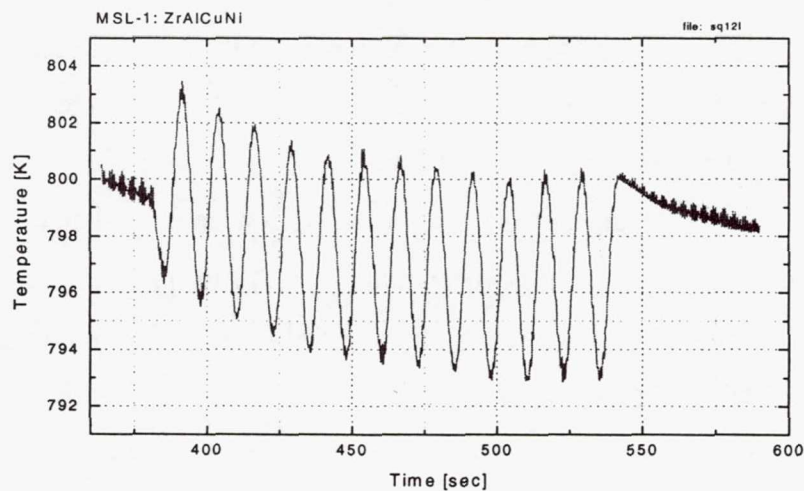


Fig.2a . Modulated temperature response in undercooled melt for cp measurement.

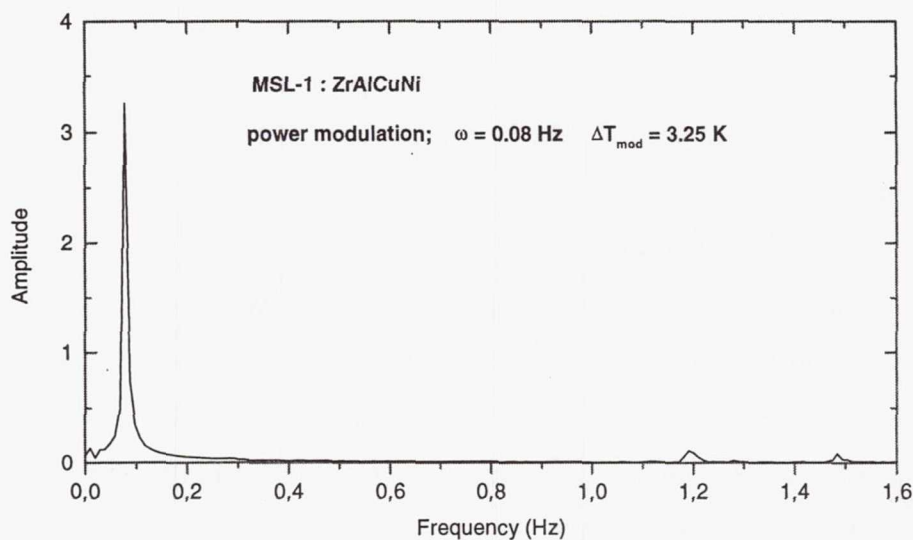


Fig. 2b. Fourier transform of temperature signal shown in Fig.2a after correcting for signal drift

The external relaxation time is obtained either by tracing the time dependence of the modulation maxima shown in Fig.2 or by measuring the decay to equilibrium after turning off the modulation. Because of the T_0^{-3} dependence of τ_1 the accuracy depends strongly on the time available for the measurement. At $T_0 = 850^\circ\text{C}$ and $\tau_1 \approx 40$ sec accuracy is typically better 3 %. The phase shift between heater and temperature response is obtained after application of a suitable FFT filter to the temperature and current signal to eliminate short time scale temperature variations and a low frequency oscillation in the temperature signal . The low frequency drift is caused by a nutational motion of the specimen and shows up in the the low frequency peak near 0.007 Hz in the FFT spectrum. This low frequency motion was also detected in the optical analysis by the Samwer group.

Quantitative determination of the heat capacity from measurements of ΔT_{mod} require proper calibration of the modulated power component, P_ω . P_ω is obtained by performing a calibration experiment in the solid phase with known heat capacity at a modulation frequency independently verified to be within the isothermal regime. This approach is similar to conventional DSC measurements. In particular, calibration experiments of good quality could be performed for the ZrNi and ZrAlCuNi alloys. Scaling of the electromagnetic coupling constant thus obtained to the liquid phase is performed by optical measurement of the volume change with the high resolution camera and, by evaluating the change in resistivity from the

oscillating circuit current and voltage data. As such we obtain for the ZrNi specimen the specific heat data the shown in table Table.1 where comparision is made with with equivalent data from the IML-2 mission. Considering the new heating coil design in the TEMPUS device for the MSL-1 missions resulting in different electromagnetic coupling efficiencies the very good reproducibiliy

Tab. 1 $\text{Zr}_{64}\text{Ni}_{36}$ liquid specific heat capacity, c_p in $\text{J K}^{-1}\text{mol}^{-1}$

T [°C]	MSL - 1	IML - 2
1020	45.3	44.4
1110	43.8	43.5

of the specific heat data demonstrates the consistency of the calibration and scaling proceeedure and the accuracy of data evaluation. Typical error in these data points is < 4%.

5. Flight results compared with ground results

As a particular result specific heat values of the ZrAlCuNi specimen obtained in the space experiment for the stable and undercooled liquid are shown in Fig. 3. In additon the corresponding values in the crystalline phase and those obtained by heating the glassy phase above the calorimetric glass transition in a laboratory DSC using the step heating method are shown. The temperature range of the of the latter measurement is limited by the onset of crystallization. These results seem to indicate a nonmonotonous behavior of the liquid specific heat exhibiting a maximum in the undercooled regime. Compared to other available data of lower melting point alloys where conventional DSC experiments can be performed in the stable liquid and just above the calorimetric glass transition this result is singular. It is however compatible with one result published recently where the specific heat of the stable liquid was measured and compared with that just above the glass transition. These data were however obtained by measurements of the heat of crystallization of the undercooled melt which is subject to the formation of metastable crystalline phases. Considering the wide

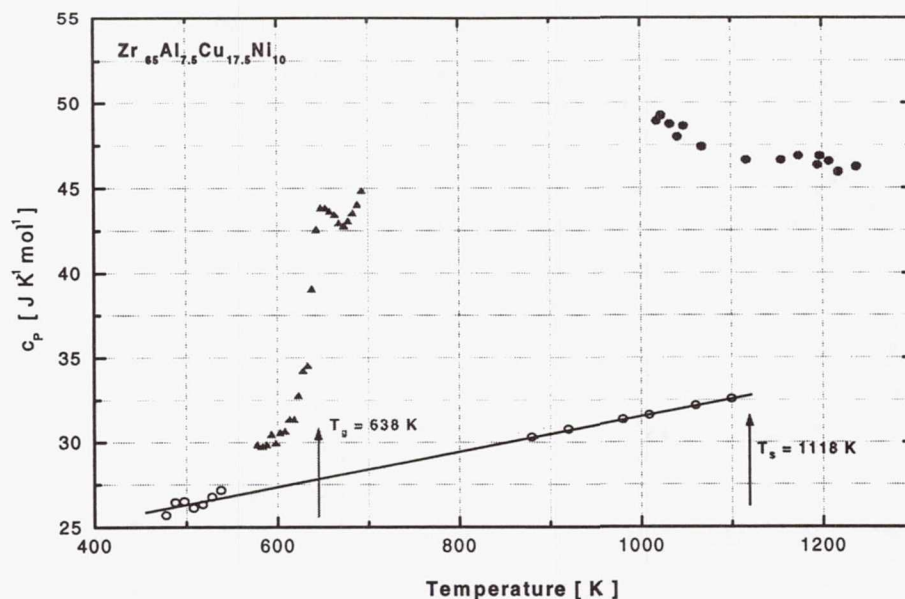


Fig.3. Specific heat capacity of ZrAlCuNi . \bullet : MSL-1 results in stable and undercooled melt. Δ : glassy phase below and above the calorimetric glass transition, T_g . \circ : crystalline phase

specific heat just above the calorimetric glass transition measured in different laboratories care must be exercised for a final evaluation our result giving support to models of temperature dependent structural changes in the undercooled liquid. As such careful c_p measurements near the glass transition will be performed for further clarification of this point which is of considerable scientific interest. As mentioned above the specimen showed an increasing elliptical deformation in the course of processing in the liquid state. The effect of this deformation on the electromagnetic coupling constant is not yet taken into account in the scaling of P_ω . This work is currently under way. It is interesting to note that in the five component ZrAlCuNiCo alloy the temperature dependence of the specific heat does not appear to exhibit similar features.

Measurements of the external and internal relaxation time have been performed. Variation of the modulation frequency for determination of τ_2 was however limited by specimen stability at higher modulation frequencies and by limitations in P_ω at lower processing temperatures. In Tab. 2 phase shift measurements in the crystalline (x) and liquid phase (l) for the ZrAlCuNi alloy are shown from which the internal relaxation time and the thermal conductivity were evaluated. The value of the thermal conductivity in the solid phase

corresponds closely to what is expected by application of the Wiedemann - Franz law. Scaling of τ_2 from the solid to the liquid phase using again the Wiedemann - Franz law and the measured liquid specific heat results in $\tau_2 = 0.34$ sec and $\Delta\phi = 106^\circ$ well above the observed phase shift of 98° corresponding to an internal relaxation time of just $\tau_2 = 0.18$ sec. The increased thermal conductivity is due to internal electromagnetically driven convection thus demonstrating the effects of fluid at low undercooling. It is interesting to note that in this temperature range pulse excitation of the liquid specimen for measurements of surface tension and viscosity by the oscillating drop method as applied by the group of Prof. I. Egry from

Tab.2. Phase shift heater current - temperature for solid and liquid ZrAlCuNi

To [°C]	w [Hz]	$\Delta\phi$ [deg]	τ_2 [sec]	κ [W cm ⁻¹ K ⁻¹]
760 ^x	0.20	104±2	0.19±0.15	0.19
840 ^l	0.16	96±2	0.17±0.15	'0.34'

did not produce measurable effects due to the inherent high viscosity of these alloys. As such it appears that modulation calorimetry combined with temperature measurement at different spots on the sample surface and numerical modeling may be an interesting method to infer fluid flow motions and place limits on the Reynolds number in high viscosity liquids.

Furhter work conducted currently in our laboratory includes the analysis of the solidification microstructure and phase selection in the space specimen and comparison with the phase selection observed at the onset of crystallization in the highly undercooled melt.

6. Conclusions and further plans

The specific heat of two bulk metallic glass forming alloys was measured in the stable and undercooled liquid phase. Results for the alloy ZrAlCuNi seem to indicate a specific heat anomaly in the undercooled melt Calibration experiments performed with the ZrNi alloy which was already processed in the IML-2 spacelab mission proved the very good

reproducibility of specific heat data obtained with the new method of non-contact calorimetry which this far has been only applied to liquid specimen in microgravity experiments. In addition, sensitive measurements of the effective thermal conductivity of liquid specimen could be performed. We plan to use these results as input for numerical modelling of fluid flow and temperature distribution with the intention to devise experimental methods i.e. variation of modulation frequency, changing the ratio of heater to positioner field at constant temperature and increasing the number of measurement points for temperature to separate fluid flow from pure thermal conductivity and thus obtain values for the Reynolds number and identify different fluid flow regimes. In this regard it is also of practical importance that in an electromagnetic device resistivity measurements can be performed in situ thus providing the electromagnetic coupling coefficient.

Future plans for our microgravity research are geared towards application of the techniques demonstrated successfully in the IML-2 and MSL-1 mission to investigate the thermophysical properties industrially relevant alloys in order to input parameters for modeling of casting processes. This work will be in close cooperation with the group of Prof. Samwer from the University of Augsburg for measurement of thermal expansion and volume change during melting and with Prof. I. Egry from DLR in Cologne for the measurement of surface tension and viscosity.

Thermophysical Properties of Undercooled Metallic Glass Forming Alloys

H. -J. Fecht and A. Sagel , Department of Materials Science, University of Ulm

and R. K. Wunderlich, Department of Materials Science , Technical University of Berlin

Compared to usual crystalline materials metallic glasses are characterized by the absence of any long range atomic order and grain boundaries resulting in improved material properties such as increased tensile strength and corrosion resistance. Until quite recently metallic glasses could only be produced with small dimensions by rapid cooling techniques with cooling rates as high as 10^5 K/sec. With the recent introduction of metallic glass forming alloys requiring much lower cooling rates for glass formation it became possible to produce metallic glasses in bulk dimensions. The factors which determine the glass forming ability of a specific alloy can be divided loosely in kinetic, regarding the mobility of atoms in the melt and thermodynamic regarding the stability of a melt cooled below its thermodynamic freezing point with regard to the competing crystalline phase. The stability of an undercooled melt is one important factor in the formation of metallic glasses because it determines the critical cooling rate necessary to produce a metallic glass.

In the MSL-1 spacelab mission we performed measurements of the specific heat of liquid metallic alloys of bulk glass forming composition in the stable and undercooled melt. From the results of these measurements the glass forming ability of these alloys can be inferred and compared with that of other alloy compositions. Experiments were performed in the containerless processing device TEMPUS in order to allow for a large range of liquid undercooling not possible under 1-g conditions.

Two alloys, ZrAlCuNi and ZrAlCuNiCo were processed. Sample selection and conduction of the experiment was performed in close cooperation with other research groups from the California Institute of Technology in the US and the University of Augsburg in Germany thus providing a larger range of specimen and additional thermophysical information regarding the thermal expansion and volume change on melting. For the measurement of the specific heat a newly developed calorimetric method, non-contact acalorimetry, was applied. Besides the specific heat, this method also allows determination of the thermal conductivity and total hemispherical emissivity. The specimen exhibited excellent stability in the undercooled melt making possible for the first time extended specific heat measurements at intermediate undercooling. In addition the effective thermal conductivity of

the melt could be determined at several temperatures. Combined with measurements of the thermal expansion and surface tension integrated into the TEMPUS device this method can provide thermophysical properties of metallic melts useful for modelling of industrially relevant casting processes.

521-26

434 857

Electromagnetic Containerless Processing Facility (TEMPUS)

100

362701

Measurements of the Surface Tension of Liquid and Undercooled Metallic Melts by Oscillating Drop Technique

Principal Investigator:

Dr. Martin Froberg
Technische Universität Berlin
Berlin, Germany

Measurements of the Surface Tension of Liquid and Undercooled Metallic Alloys by Oscillating Drop Technique

Michael Rösner-Kuhn; Gunnar Kuppermann; Martin G. Froberg

In cooperation with the entire TEMPUS Team.

Technical University of Berlin, Institute of Metallic Materials, General Metallurgy, Berlin 10719 Germany.

1. Abstract

The surface tension of liquid metallic alloys is an important parameter for the understanding of surface phenomena in metallurgical processes; eg. interpretation of metal - slag reactions, wettability of refractory materials, filtration of melts, hot sintering of metallic powders, production of metal matrix composites, welding processes. Containerless electromagnetic levitation conditions are tend to cause surface oscillations on liquid droplets. The oscillations are detectable with the temperature-time signal of pyrometers and the corresponding frequencies can be obtained by fast Fourier transformation (FFT) of those signals. The performance of an on-line analysis of these data during the Spaceshuttle Mission MSL-1 provided the need for additional experimental procedures in the electromagnetic levitation facility TEMPUS. Investigations have been carried out on high viscous metallic glassformers, pure zirconium and stainless steels. Restrictions of the method have been found by the glassforming alloys where surface oscillations only occur at elevated temperatures of about 150°C above the melting points.

2. Objectives

It was the aim of the project to realize a real-time analysis of the surface oscillations of liquid levitated droplets by fast Fourier transformation of the temperature-time profiles obtained by pyrometric measurement from various materials which were melted and processed in the TEMPUS levitation facility during MSL-1 Spacelab mission in April and July 1997. The on-line analysis should provide additional experimental procedures (pulsing of the heating field) to guarantee clear frequency spectra from the oscillating surface.

3. Background

Based on the general theory of Rayleigh [1] for a free-falling drop, equating the change in the surface energy with the kinetic energy of motion as the consequence of the surface oscillations, the electromagnetic levitation technique for the determination of the surface tension of molten metals was first introduced by Lu and co-workers [2-4]. Rayleigh's formula, expressing the surface tension, σ , by the mass of the droplet, M , and the oscillation frequency of the fundamental mode $\lambda = 2$, $\nu_{\lambda=2}$, is given by

$$\sigma = \frac{3}{8} \pi M \nu_{\lambda=2}^2 \quad (1)$$

The validity of Eq. (1) is restricted to an inviscid spherical droplet. Under terrestrial levitation conditions, the sample is distorted due to the electromagnetic field and the Rayleigh frequency is split into either three, or in case of nonaxisymmetric rotation five (two pairs of the five peaks are doubly degenerate), unequally spaced peaks called split modes, m . This effect is caused by the aspherical equilibrium shape of the oscillating droplet. Theoretical work to solve this problem has been performed by Cummings and Blackburn [5]. They interpreted the influence of the electromagnetic field as a magnetic pressure on the surface and derived the following frequency sum rule as a correction formula to obtain the Rayleigh frequency from the split modes:

$$v_{\lambda=2}^2 = \frac{1}{5} \left(v_{\lambda=2, m=0}^2 + 2 v_{\lambda=2, m=\pm 1}^2 + 2 v_{\lambda=2, m=\pm 2}^2 \right) - 1.9 v_t^2 - 0.3 v_t^{-2} \left(\frac{g^2}{R^2} \right) \quad (2)$$

where v_t is the translation frequency and R the radius of the droplet. Under microgravity conditions the oscillation spectra are characterized by only one peak, i.e. the splitting of the $\lambda = 2$ mode does not occur. The validity of Eq. (2) was shown by Egry et al. [6]. Their comparison of surface tension values under terrestrial conditions (high magnetic field strength) and consideration of the magnetic pressure according to Eq. (2) with values from microgravity (approximately force-free) and use of Eq. (1)) for the IML-2 Spacelab flight data using the containerless electromagnetic processing facility TEMPUS shows very good agreement.

Various procedures to detect and analyse the surface oscillations have been developed:

- high-speed photography [2-4,7],
- use of a photodetector and oscilloscopic observation of the signal [8-12],
- use of a photocell in combination with an on-line Fourier wave analyzer [13-18],
- use of a photodetector and off-line fast Fourier transformation (FFT) [19],
- digital image processing and FFT afterward [6, 20-25], and
- use of a pyrometer in combination with an on-line Fourier wave analyzer [26-28].

4. Data Acquisition and Analysis

Temperature measurement was performed with a resolution of 100Hz via a two colour pyrometer operating in the wavelength range 1–2.5 μ m and 3–4 μ m and a silicon pyrometer operating at 632nm. During the experiments the incoming telemetry data of the temperature reading was taken from a database management system called "DAVIS" (Data, Audio, and Video Information System developed by the Microgravity User Support Center "MUSC" from the German Aerospace Center) and converted into a binary format to provide fast data handling for the FFT analysis program. The data was written into a separate file for each experimental cycle where one cycle consists of a maximum number of 5 possible processing steps for the sample. The time slot between end of the experimental cycle and analysis of the temperature - time profile with the resulting frequency spectra of the surface oscillations was in the range of 1 - 2 min. Thus, depending on the result, the next cycle was planned without great time delay with respect to the temperature profile in general, the pulse amplitudes necessary to excite the surface oscillations, and the quality of the spectra obtained.

Fig. 1 shows a typical temperature-time profile of a surface tension experiment on a Fe72Cr12Ni16 alloy. After an overheating of about 80°C, the heating field was switched off and the sample was cooled to the desired temperature in the undercooled state. Setting the pulse the heating field was directly ramped to a certain amount in 0.1s and the temperature plateau (as the result of constant positioner and chosen heater voltage) was adjusted for a period of about 6s. Finally the heating field was switched off again and the sample cooled down with subsequent solidification. Curve A of the subplot represents the temperature range directly before and after the pulse. Curve B, representing the oscillating signal given as relative deviation between the original signal and lowpass filtered signal, shows the reaction of the temperature signal as the result of the surface oscillations.

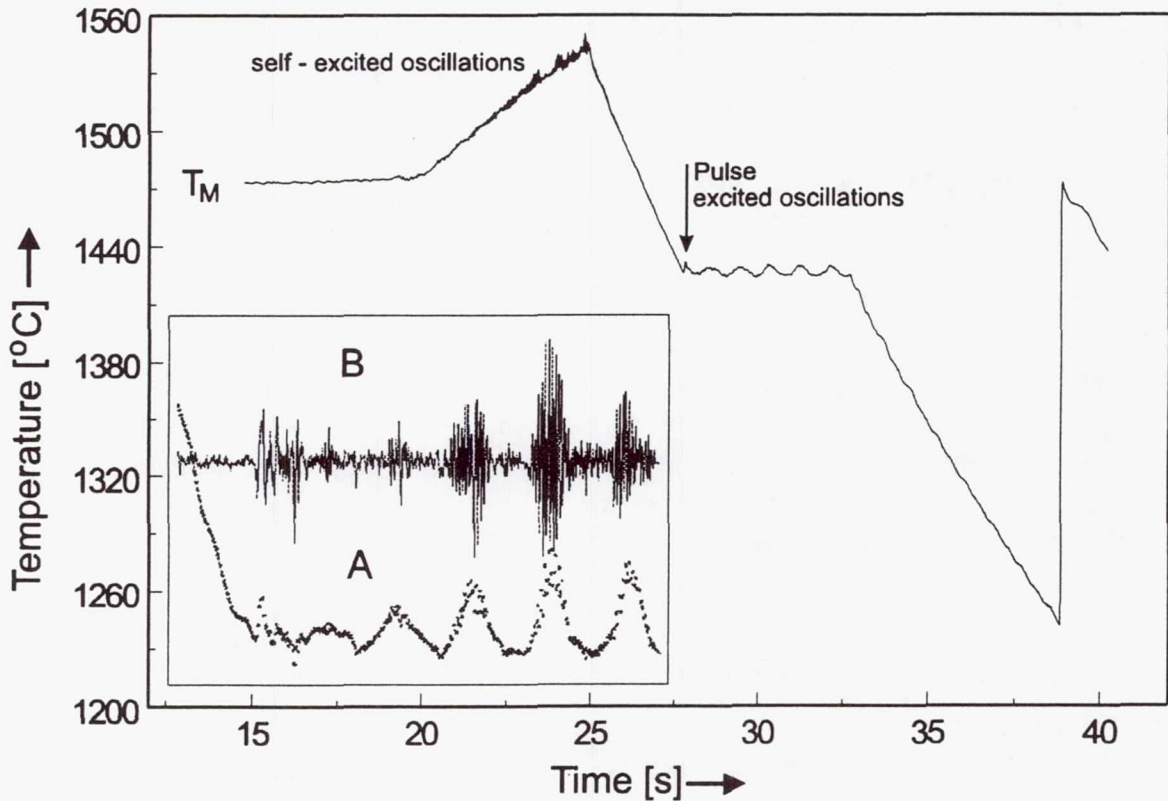


Fig. 1 Temperature-time profile of a surface tension experiment on Fe72Cr12Ni16 alloy. Curve A of the subplot represents the temperature intervall directly before and after the pulse. Curve B represents the oscillating signal given as relative deviation between the original signal and lowpass filtered signal.

Fig. 2 shows the corresponding frequency spectrum of the surface oscillations (highpass filtered for the range 15-50Hz) and the translation spectrum of the sample (lowpass filtered for the range 1-15Hz) on the temperature plateau after the pulse. Both spectra were obtained with a 512-point Fourier transform. Based on the 100Hz temperature signal, the resulting resolution is 0.2Hz. The single peak at 34Hz represents the frequency of the $\lambda = 2$ surface oscillation mode and was inserted into the Rayleigh formula Eq. (1).

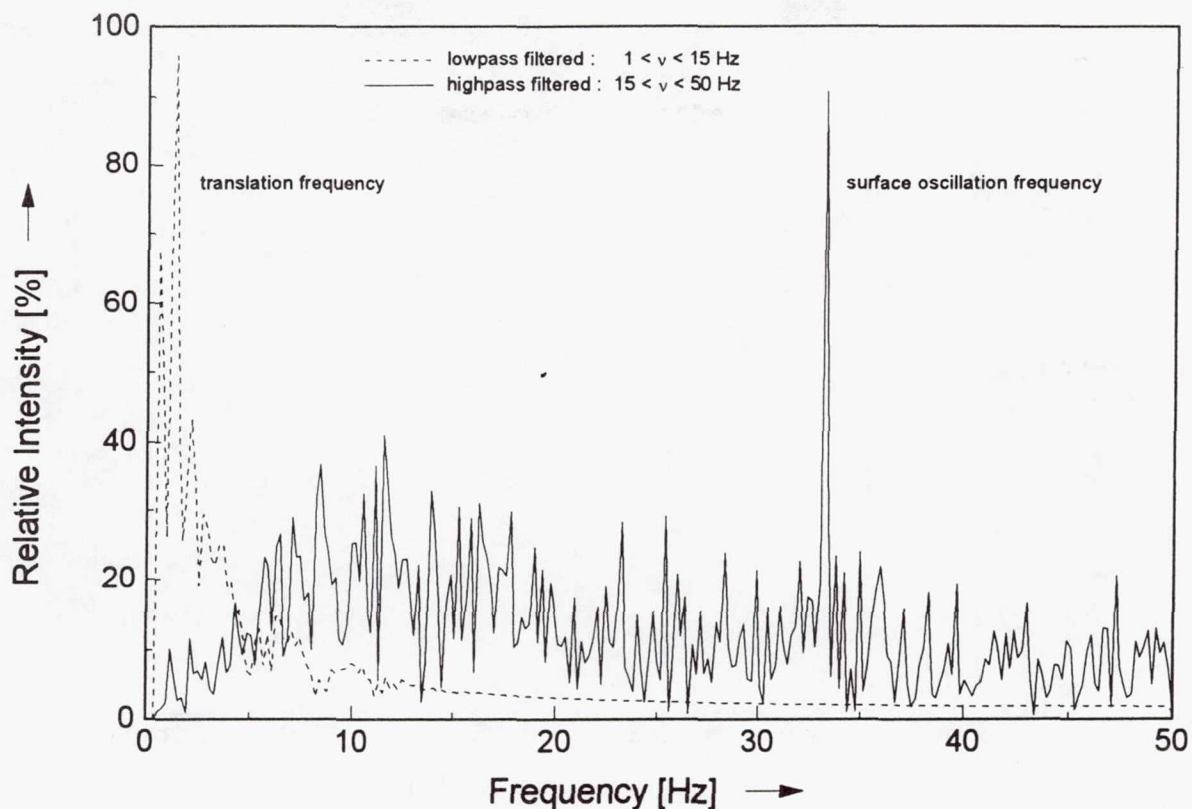


Fig. 2 Corresponding frequency spectrum of the surface oscillations (highpass filtered for the range 15 - 50Hz) and the translation spectra of the sample (lowpass filtered for the range 1 - 15Hz) on the temperature plateau after the pulse.

5. Flight Results

5.1 Steel Alloys Fe72Cr12Ni16 and Fe72Cr16Ni12

Fig. 3 shows the results obtained for the surface tension of the Fe72Cr12Ni16 alloy. The filled points represent the values obtained from spectra on temperature plateaus and the corresponding least-squares fit yields (solid curve)

$$\sigma(T) = 1878 + 1.01(T_M - T) \quad (3)$$

where $\sigma(T)$ is in $\text{N} \cdot \text{m}^{-1} \cdot 10^{-3}$ and T is in $^{\circ}\text{C}$. The open points represent results obtained on cooling curves performed for solidification experiments. These results include values obtained with and without pulsing. The cooling rate was on average $40^{\circ}\text{C} \cdot \text{s}^{-1}$. The fit to the data yields (dashed curve)

$$\sigma(T) = 1877 + 1.05(T_M - T) \quad (4)$$

Both functions are almost identical. This fact was taken as a basis for the analysis of temperature profiles of other samples where no temperature plateaus were available.

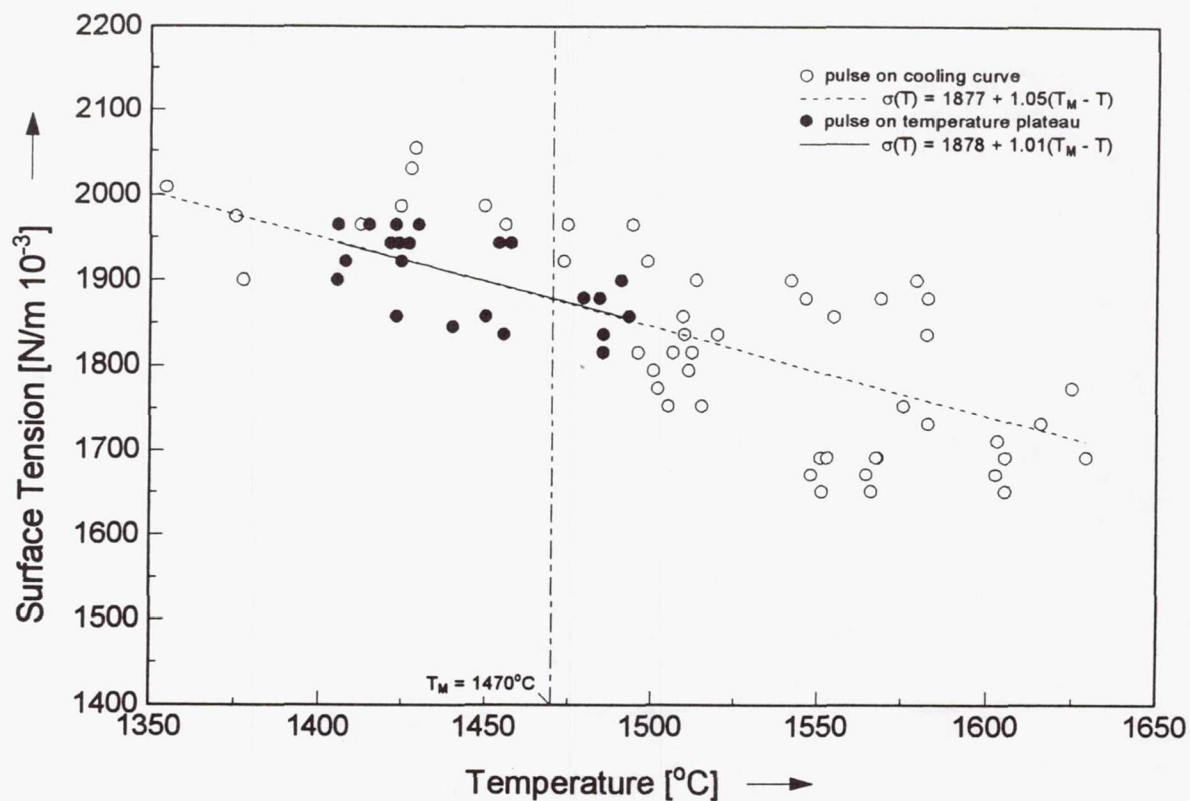


Fig. 3 Temperature dependence of the surface tension of Fe₇₂Cr₁₂Ni₁₆ alloy.

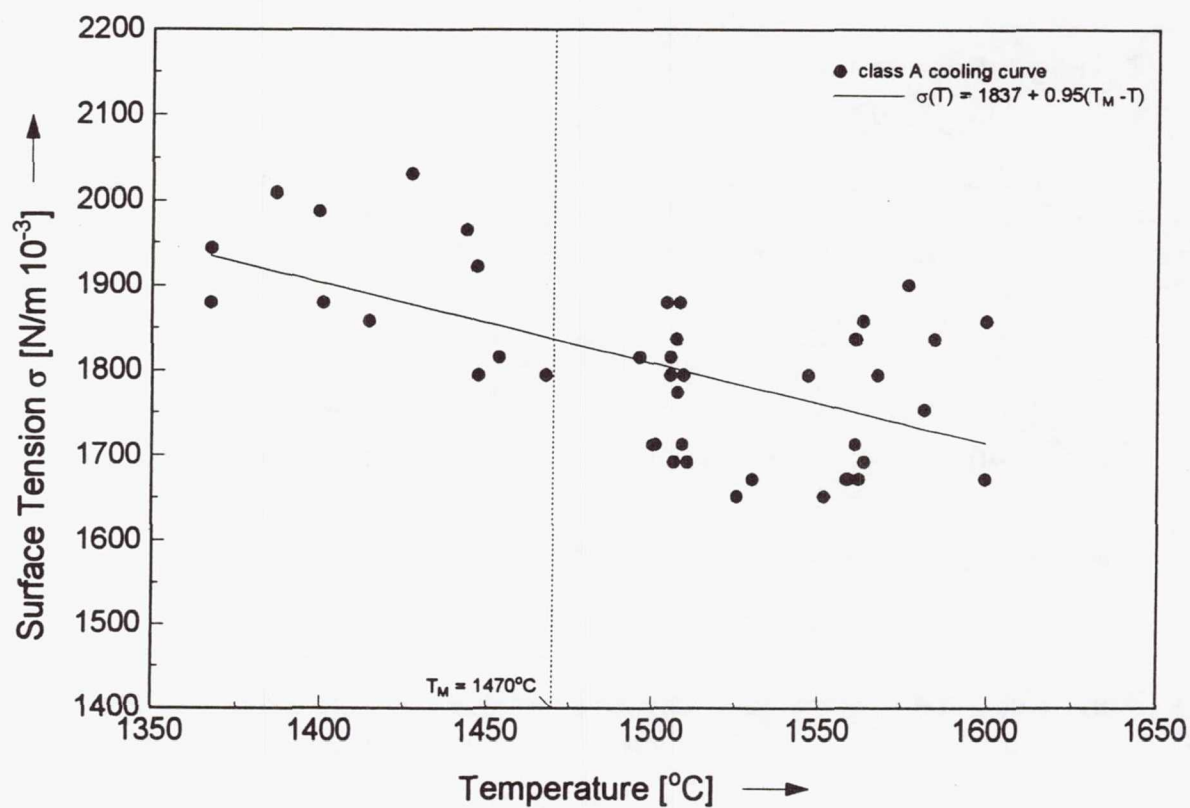


Fig. 4 Temperature dependence of the surface tension of Fe₇₂Cr₁₆Ni₁₂ alloy.

Fig. 4 shows the surface tension obtained for the higher chromium alloy Fe72Cr16Ni12. All values were obtained on cooling curves. Comparing the results for the two alloys it can be seen that the higher chromium alloy is characterised by a lower surface tension. This result is in qualitative agreement with a sessile drop investigation by Mori et al. [29].

5.2 Zirconium

Fig. 5 shows the surface tension obtained on zirconium and compares μg and 1g measurements. The filled points represent the microgravity values based on an analysis of 297 spectra obtained from about 100 cooling curves. The cooling rate was on average $60^{\circ}\text{C}\cdot\text{s}^{-1}$. The spectra were obtained performing 256-point Fourier transforms with a resulting resolution of 0.4Hz. The earthbound measurements have been carried out on temperature plateaus performing 1024-point Fourier transforms with a corresponding resolution of 0.01Hz. Calculating the corresponding least squares fits, we have obtained for the μg data (solid curve)

$$\sigma(T) = 1512 + 0.37(T_M - T) \quad (5)$$

and for the 1g measurements (dashed curve)

$$\sigma(T) = 1543 + 0.66(T_M - T) \quad (6)$$

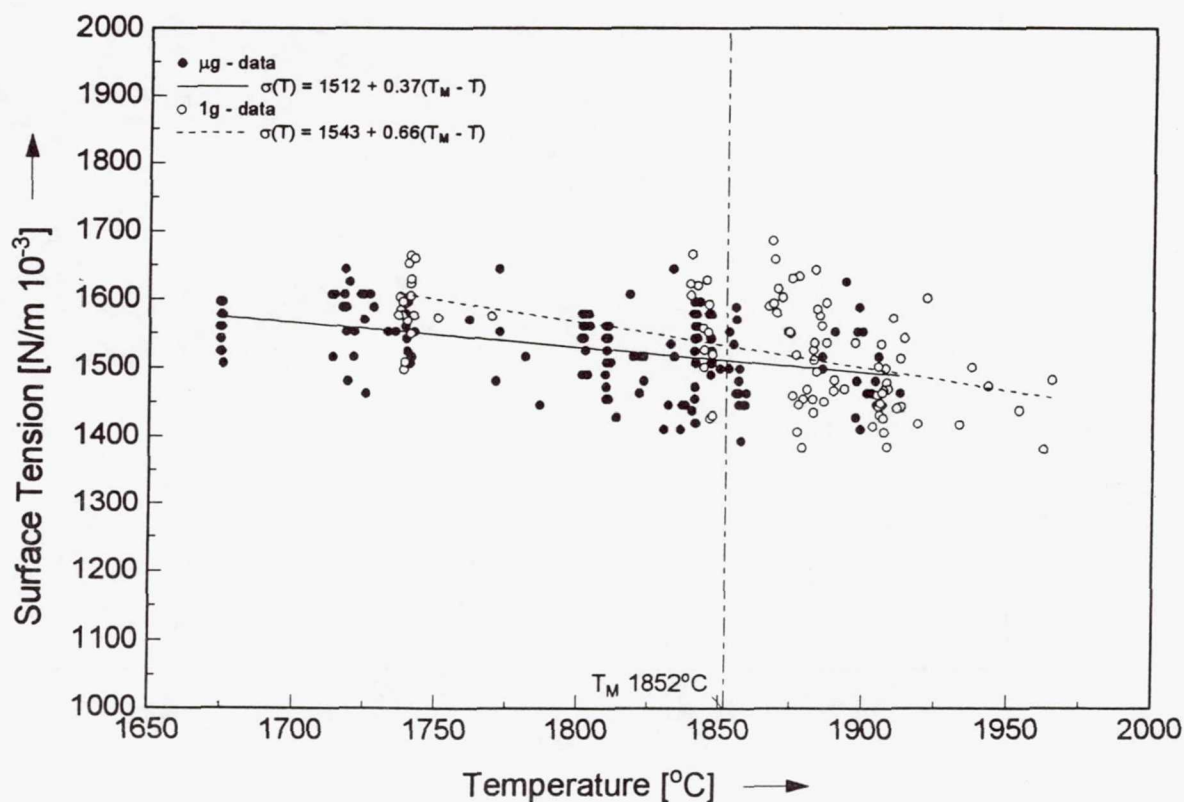


Fig. 5 Temperature dependence of the surface tension of pure zirconium.

The scatter in the data does not support any difference in the least square fits to provide different slopes. But, the difference between the two results may be due to the fact that the use of the correction formula Eq. (2) for the earthbound measurements requires the consideration of the temperature dependence of the density of the material. The values presented had been obtained with a constant density of $5.93 \text{ g}\cdot\text{cm}^{-3}$ for the liquid zirconium at the melting point. Qualitatively, considering a decreasing density with increasing temperature it can be seen from Eq. (2) that above the melting point an increasing radius will yield higher Rayleigh frequencies and the surface tension values will raise for a small amount whereas below the melting point a decreasing radius leads to the contrary effect. Thus, the 1g curve of the surface tension will tend to be the same as the microgravity curve. An analysis of the density will be done by Damaschke and Samwer [30] from the University of Augsburg analysing the thermal expansion with a high resolution camera [31] which was part of TEMPUS.

Fig. 6 shows a typical spectrum obtained on a non-rotating zirconium sample levitated under 1g conditions. In comparison to the microgravity spectrum, Fig. 2, the Rayleigh frequency is split. The splitting indicates the influence of high magnetic field strength (necessary to levitate under 1g) resulting in a distorted shape of the droplet.

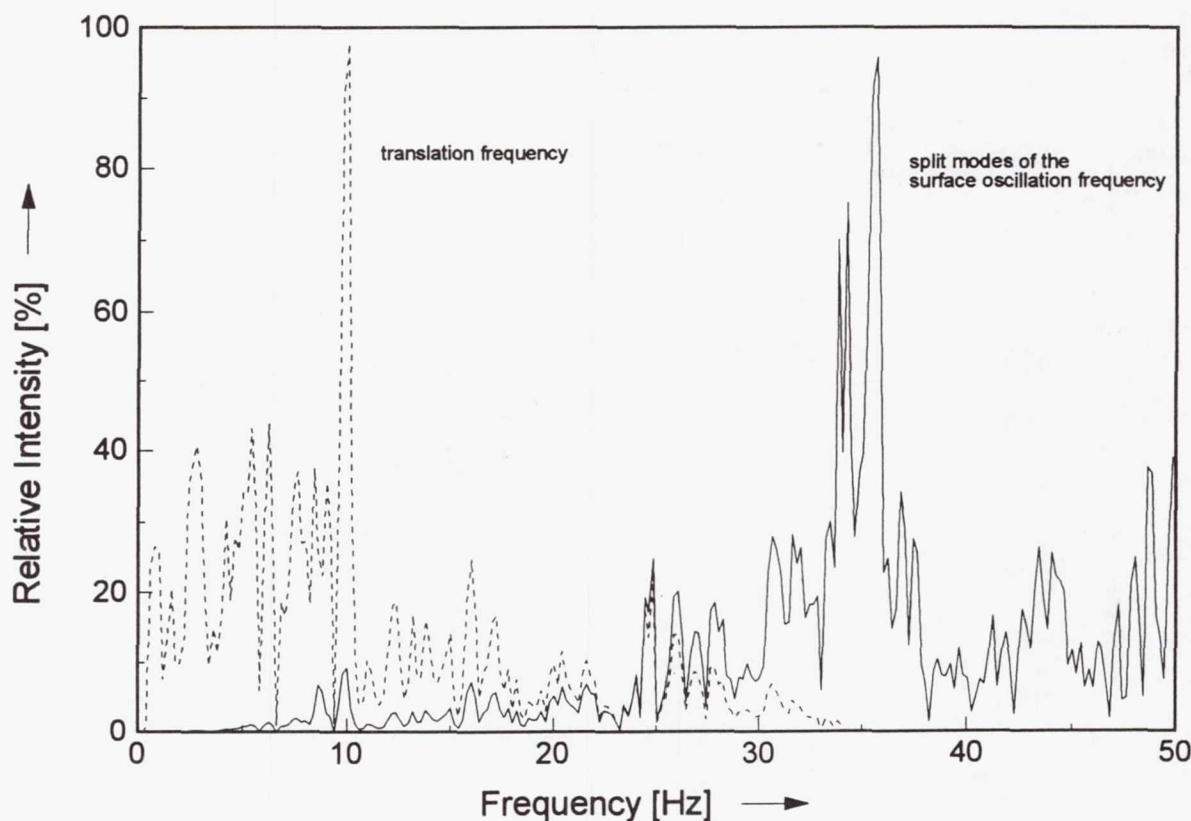


Fig. 6 Earthbound spectrum of the surface oscillations of a non-rotating Zr sample.

5.3 Glassforming Alloys $Zr_{11}Ti_{34}Cu_{47}Ni_8$ and $Zr_{57}Cu_{12.6}Ni_{15.4}Nb_5Al_{10}$

Fig. 7 shows the result for the strong glassforming Johnson alloys $Zr_{11}Ti_{34}Cu_{47}Ni_8$ and $Zr_{57}Cu_{12.6}Ni_{15.4}Nb_5Al_{10}$ with melting points of 842°C and 819°C, respectively. Due to the high viscosity of the material ($\approx 200 \text{ mPa} \cdot \text{s}$) no excitation of surface oscillations was possible at temperatures lower than 1000°C. Thus, one of the major goals of the project, to look at the trend of the surface tension of such high viscosity material in the undercooled range, failed. Nevertheless, the five component alloy (closed curve) shows a spectacular behaviour; the strong decrease in the surface tension obtained with decreasing temperature represents a dramatic change in the surface composition of this alloy. The absence of any surface tension decreasing impurity like oxygen or sulphur leads to the assumption that surface segregation of aluminum took place. Its surface tension is in the range of $900 \text{ mN} \cdot \text{m}^{-1}$, which is nearly the value achieved at 950°C. This interpretation is underlined by the fact that in general the element with the lowest surface tension is the surface active part in a liquid alloy system.

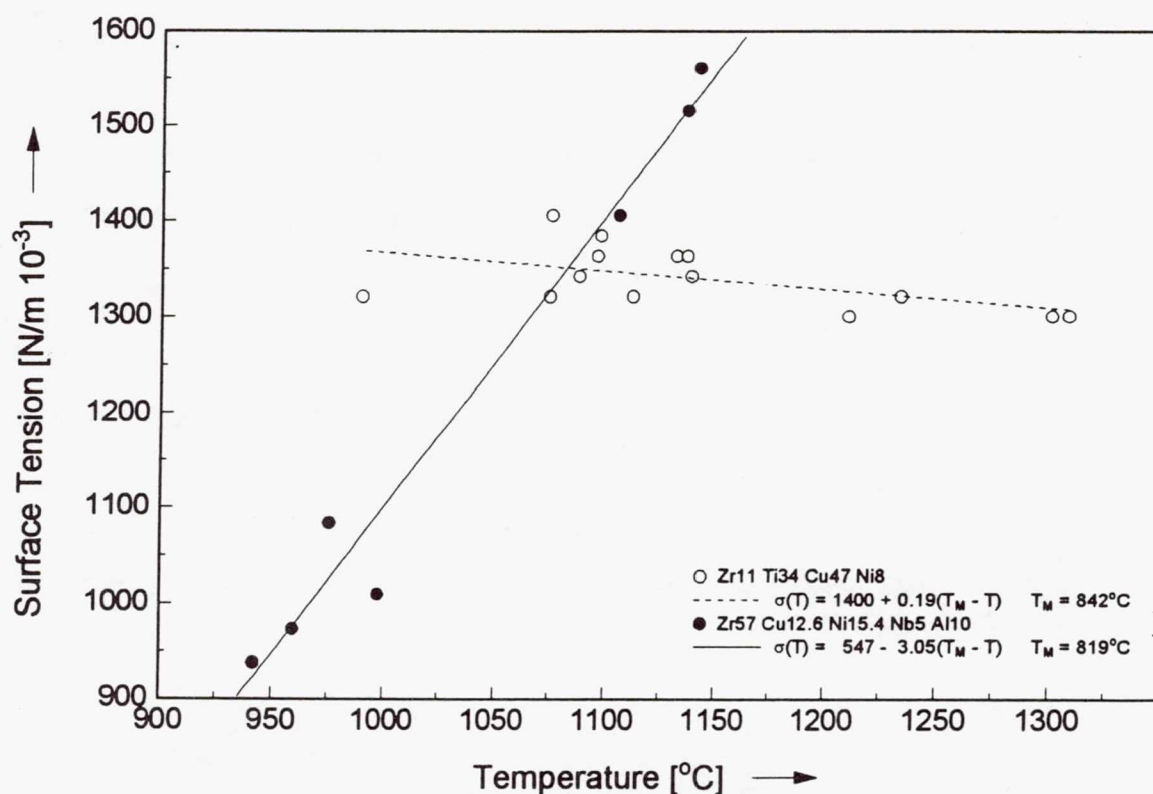


Fig. 7 Temperature dependence of the surface tension of the strong glassforming alloys $Zr_{11}Ti_{34}Cu_{47}Ni_8$ and $Zr_{57}Cu_{12.6}Ni_{15.4}Nb_5Al_{10}$.

6. Conclusion

Summarizing the quality of the spectra and the results obtained it can be stated that the method to analyse temperature-time profiles from pyrometric measurement

Acknowledgements

The authors acknowledge the excellent cooperation and efforts of W. H. Hofmeister, C. T. Morton, and R. J. Bayuzick on the zirconium (Vanderbilt University), D. S. Lee, S. C. Glade, and W. L. Johnson on the glassformers (Caltech), and D. M. Matson and M. C. Flemings on the steels (MIT). The MUSC team from DLR is thanked for the great support on the preparation of the experimental setting. The tremendous engineering from Dornier (DASA) is acknowledged and many hands from MSFC and NASA have to be thanked for their contribution. We gratefully acknowledge the financial support from German Aerospace Center (DLR Grant 50 WM 9578). M. Rösner-Kuhn personally thanks R. K. Wunderlich from TU-Berlin for the cooperation and discussions on microgravity research.

7. Articles and Presentations

- R. K. Wunderlich, M. Rösner-Kuhn, G. Kuppermann:
Berührungslose Messung thermodynamischer Eigenschaften reaktiver Metallschmelzen unter Schwerelosigkeit.
TU - Berlin International 38/39 (1997) 4 - 6.
- U. Thiedemann, M. Rösner-Kuhn, D. M. Matson, G. Kuppermann, K. Drewes, M. C. Flemings, M. G. Froberg:
Mixing Enthalpy Measurements in the Liquid Ternary System Iron-Nickel-Chromium and Its Binaries.
steel research 69 (1998) 3 - 7.
- M. Rösner-Kuhn, D. M. Matson, K. Drewes, U. Thiedemann, G. Kuppermann, M. C. Flemings, M. G. Froberg:
Enthalpies and Heat Capacities of Liquid Fe-Cr-Ni Alloys with the Focus on Pure Liquid Chromium.
Thermochimica Acta 314 (1998) 123 - 129.
- M. Rösner-Kuhn, G. Kuppermann, I. Egry, M. G. Froberg:
Measurements of the Surface Tension of Liquid and Undercooled Metallic Alloys by Oscillating Drop Technique.
Proceedings of the 10th International Symposium on Experimental Methods for Microgravity Materials Science, February 16th -17th, 1998, San Antonio, Texas.
- M. Rösner-Kuhn, G. Kuppermann, M. G. Froberg:
Measurements of the Surface Tension of Liquid and Undercooled Metallic Alloys by Oscillating Drop Technique.
Workshop: Nucleation and Thermophysical Properties of Undercooled Melts, March 4th - 6th, 1998, Bad Honnef, Germany.

8. Summary

The surface tension of liquid metallic alloys is an important parameter for the understanding of surface phenomena in metallurgical processes; eg. interpretation of metal - slag reactions, wettability of refractory materials, filtration of melts, hot sintering of metallic powders, production of metal matrix composites, welding processes. The surface tension measurements performed under microgravity yield unique conditions with respect to the accuracy of the results, the speed of the evaluation, the temperature ranges obtainable, and the expansion to investigations on high viscous metallic materials.

on electromagnetically levitated droplets is successful. Especially the speed of the evaluation should be of interest thinking about a possible reflight of TEMPUS on Spacehab or the Spacestation. The procedure is easy and enables fast reactions on the experiments. For the valuation of the oscillating drop technique and the detection method presented regarding its applicability to high viscosity material, it will be necessary to perform a bench marked experiment on a material with wellknown temperature dependence of the viscosity. Moreover, further ground based research will concentrate on the influence of chromium to the surface tension of the FeCrNi steels [32] and on the influence of oxygen and nitrogen to the surface tension of Zr [33].

References

- [1] J. W. S. Rayleigh, *Proc. Royal Soc.* **29**: 71 (1879).
- [2] M. E. Fraser, W. K. Lu, A. E. Hamielec, and R. Murarka, *Metall. Trans.* **2**: 817 (1971).
- [3] R. Murarka, W. K. Lu, and A. E. Hamielec, *Metall. Trans.* **2**: 2949 (1971).
- [4] R. Murarka, W. K. Lu, and A. E. Hamielec, *Can. Met. Quart.* **14**: 11 (1975).
- [5] D. L. Cummings and D. A. Blackburn, *J. Fluid Mech.* **224**: 395 (1991).
- [6] I. Egry, G. Jacobs, E. Schwartz, and J. Szekely, *Int. J. Thermophys* **17**: 1181 (1996).
- [7] S. Krishnan, G. P. Hansen, R. H. Hauge, and J. L. Magrave, *Metall. Trans. A* **19**: 1939 (1988).
- [8] H. Soda, A. McLean, and W. A. Miller, *Mat. Trans. JIM* **18**: 445 (1977).
- [9] H. Soda, A. McLean, and W. A. Miller, *Metall. Trans. B* **9**: 145 (1978).
- [10] A. Kasama, A. McLean, and W. A. Miller, *Can. Met. Quart.* **19**: 399 (1981).
- [11] A. Kasama, A. McLean, W. A. Miller, Z. Morita, and M. J. Word, *Can. Met. Quart.* **22**: 9 (1983).
- [12] B. J. Keene, K. C. Mills, J. W. Bryant, and E. D. Hondros, *Can. Met. Quart.* **21**: 393 (1982).
- [13] B. J. Keene, *The Use of a Fourier Analyser for Determination of the Surface Tension of Liquid Metals by Levitating-Droptechique*; NPL Report DMA(A) 56, (Teddington, U.K., 1982).
- [14] B. J. Keene, K. C. Mills, and R. F. Brooks, *Mat. Sci. Tech.* **1**: 568 (1985).
- [15] J. Schade, A. McLean, and W. A. Miller: in *Undercooled Alloy Phases*; E. W. Collins, C. C. Koch (Eds.), *Proc. 115th Annual Meeting of TMS-AIME* (1986), p. 233..
- [16] B. J. Keene, K. C. Mills, A. Kasama, A. McLean, and W. A. Miller, *Metall. Trans. B* **17**: 159 (1986).
- [17] K. Nogi, K. Ogino, A. McLean, and W. A. Miller, *Metall. Trans. B* **17**: 163 (1986).
- [18] K. Nogi, W. B. Chung, A. McLean, and W. A. Miller, *Mat. Trans. JIM* **32**: 164 (1992).
- [19] E. Eckler, I. Egry, and D. M. Herlach, *Mat. Sci. Eng. A* **133**: 718 (1991).
- [20] I. Egry, *Surface Tension Measurements of Liquid Metals by the Oscillating Drop Technique*; DLR Report, IB333-90/4, (Cologne, Germany, 1990).
- [21] I. Egry, *J. Mat. Sci.* **26**: 2997 (1991).
- [22] I. Egry, G. Lohhöfer, P. Neuhaus, and S. Sauerland, *Mat. Sci. Forum* **77**: 257 (1991).
- [23] S. Sauerland, K. Eckler, and I. Egry, *J. Mat. Sci. Letters* **11**: 330 (1992).
- [24] I. Egry, G. Lohhöfer, P. Neuhaus, and S. Sauerland, *Int. J. Thermophys.* **13**: 65 (1992).
- [25] S. Sauerland, *Messung der Oberflächenspannung an levitierten flüssigen Metalltropfen*. Dr. thesis, (RWTH Aachen, Germany 1993).
- [26] H.-K. Lee, M. G. Froberg, and J. P. Hajra, *steel research* **64**: 191 (1993).
- [27] H.-K. Lee, M. G. Froberg, and J. P. Hajra, *ISIJ Int.* **33**: 833 (1993).
- [28] H.-K. Lee, M. G. Froberg, and J. P. Hajra, *Can. Met. Quart.* **32**: 289 (1993).
- [29] K. Mori, M. Kishimoto, S. Toshinori, and Y. Kawai, *J. Jpn. Inst. Met.* **39**: 1301 (1975).
- [30] B. Damaschke and K. Samwer, in preparation.
- [31] B. Damaschke and K. Samwer, *Rev. Sci. Instr.*, in press.
- [32] M. Rösner-Kuhn, G. Kuppermann, D. M. Matson, M. C. Flemings, and M. G. Froberg, to be published.
- [33] M. Rösner-Kuhn, G. Kuppermann, W. H. Hofmeister, R. J. Bayuzick, and M. G. Froberg, to be published.

Page intentionally left blank

amt
THIS
PAGE

Electromagnetic Containerless Processing Facility (TEMPUS)

Study of the Morphological Stability of Growing Dendrites by
Comparative Dendrite Velocity Measurements of Pure Ni and a
Dilute Ni-C Alloy in the Earth and Space Laboratory

Principal Investigator:

Dr. Dieter Herlach
DLR
Cologne, Germany

SINGLE SCRA
522-76
434858

FINAL SCIENCE REPORT

Dendrite growth velocity measurements
in undercooled Ni and Ni-C melts in space

M. Barth¹, D. Holland-Moritz¹ and D. M. Herlach¹
D. M. Matson² and M. C. Flemings²

¹ German Aerospace Centre (DLR), D-51170 Cologne, Germany

² Massachusetts Institute of Technology, Cambridge, MA 02139, USA

(1) ABSTRACT

Under terrestrial processing conditions, convection in the melt shows a major impact on metallic solidification, especially at small crystal growth velocities. Previous studies of dendrite growth in undercooled Ni melts on earth show systematic deviations of experimental data and predictions of dendrite growth theory at small undercoolings. The discrepancy is partly reduced if convection is taken into consideration. The present experimental studies in space aimed to test, under the conditions of reduced convection in microgravity, the predictions of dendrite growth models by measurements of the growth velocities in pure Ni and dilute Ni-0.6 at.% C alloy melts. A comparison of velocity data of the pure metal and the dilute alloy is used to investigate the prediction of marginal stability theory that for growing dendrites, the addition of a strongly partitioning element may lead to an enhancement of the growth velocity. The experiments were performed during the MSL-1-R mission in July 1997 using the electromagnetic levitation facility TEMPUS.

(2) OBJECTIVES

The present studies aimed to investigate the influence of fluid flow on dendritic growth by comparative measurements of dendrite growth velocities on pure Ni and dilute Ni-0.6 at.% C alloy melts under terrestrial and microgravity conditions.

(3) BACKGROUND

Numerous theoretical and experimental investigations are dealing with the dendritic growth in undercooled metallic melts. The crystal growth velocities in undercooled melts are correlated to the composition, to the dimensions and to the spacings of the dendrites, i.e. to the resulting segregation pattern that determines several physical properties of the material. Despite its importance, there is still a lack of knowledge at melt undercoolings where the solidification velocity is equal or even smaller than the fluid flow velocities. A better understanding of the regime of small solidification velocities is especially of relevance for manufacturing processes like casting or welding. Undercoolings and crystal growth velocities in industrial processes are usually small, and convection during solidification shows, through the microstructure, a major impact on the properties of the resulting material.

As a model system, the transition metal Ni has been frequently studied with respect to dendrite growth behavior. Predictions for the velocity-undercooling relation by modern theories of dendrite growth have been compared with experimental data, and it turned out that the presence of forced or natural convection in the melt cannot be generally neglected. There are systematic deviations of experimentally measured dendrite growth velocity versus undercooling curves from the behavior predicted by current

theories of dendrite growth that only consider diffusion-controlled heat and mass transport at the solid-liquid interface. The deviations are for Ni strongest at small undercoolings where the growth velocity is comparable to the speed of fluid flow in the melt.

According to dendrite growth theory, the addition of a solute element to a pure metal causes the appearance of a constitutional undercooling which reduces the growth velocity. On the other hand, marginal stability hypothesis predicts that a steep composition gradient in front of the solid-liquid interface leads to the formation of very thin dendrites. They may propagate faster than the comparatively thick dendrites in pure metals controlled by thermal diffusion exclusively. In the case of alloys it should be possible to increase the dendrite growth velocity by the addition of a small amount of a strongly partitioning solute. However, in the undercooling range at which this effect may become observable the enhancement of growth velocity by convection may conceal the theoretically predicted increase of growth velocity in the dilute alloy. Comparative measurements of growth velocities both on a pure metal and a dilute alloy under the conditions of highly reduced convection in microgravity are mostly favourable to experimentally test the predictions of dendrite growth theory and marginal stability analysis. Ni-C was selected as a suitable alloy because it is characterized by its small partition coefficient and, moreover, C shows a high chemical diffusion coefficient in liquid Ni. There is a critical solute composition below which the velocity-increasing effect dominates the counteracting impact of constitutional interface undercooling. The C-composition was chosen such that the effect was expected to be largest following results of calculations within the frame of theories on dendrite growth [1] and marginal stability analysis [2].

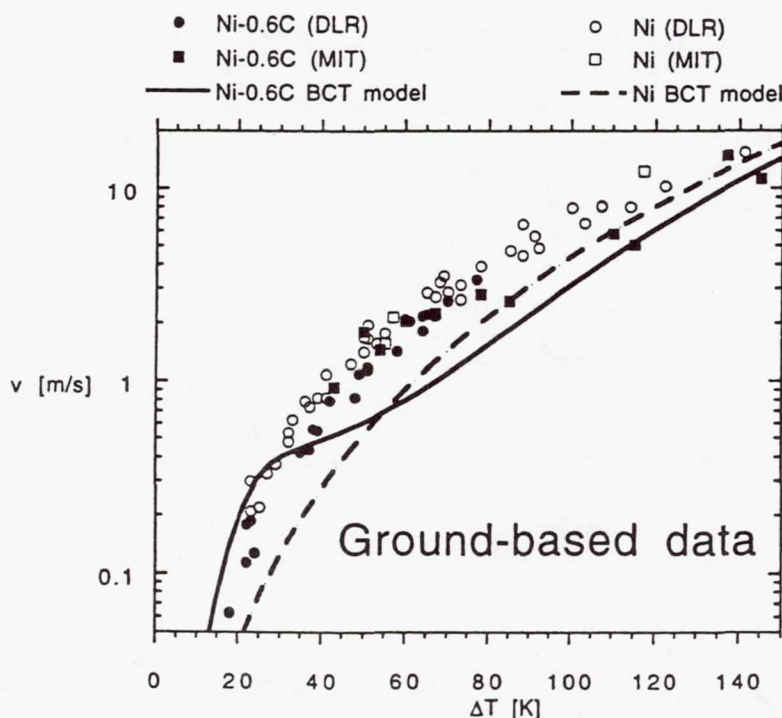


Figure 1: Ground-based dendrite growth velocity V versus undercooling ΔT data on pure Ni (open symbols) and a dilute Ni-0.6 at.% C alloy (black symbols). Circles/dots refer to the capacitance sensor technique applied at DLR in Cologne [3, 4], squares to new unpublished data obtained by the video method of MIT in Cambridge. Calculated curves according to the predictions of the BCT model [1] are plotted for Ni (dashed line) as well as for Ni-C (full line).

Fig. 1 shows growth velocity versus undercooling data on pure Ni and dilute Ni-0.6 at.% C alloy melts obtained in earth-bound electromagnetic levitation experiments (taken from references [3, 4] as well as new unpublished results). Calculations of dendrite growth velocities have been performed within the model by Boettinger, Coriell and Trivedi (BCT) [1]. The smaller ΔT is, the larger the deviations of

theoretically predicted and experimentally measured growth velocities, in particular for pure Ni. These discrepancies might be a consequence of the influence of strong fluid flow induced by natural convection under 1g and, additionally, by strong electromagnetically induced stirring of the melt due to the high electromagnetic fields needed for levitation of metallic samples under terrestrial conditions. El-Kaddah et al. [5] determined numerically the fluid flow velocities, induced by electromagnetic stirring, in levitated pure Fe droplets ranging up to 0.3 ms^{-1} . For comparison, the growth velocities of pure Ni are larger than 1 ms^{-1} for $\Delta T > 50 \text{ K}$, and the influence of convection on solidification is therefore expected to be most pronounced for $\Delta T < 50 \text{ K}$.

Glicksman et al. [6] have measured the growth kinetics of the transparent model system succinonitrile under microgravity conditions. They found reduced growth velocities at small undercoolings compared to data that had been obtained with the same experimental equipment on earth. The reduction in space growth velocity was attributed to the absence of convective effects. Glicksman et al. were able to describe well the μg -data, even at smallest undercoolings, by using the Ivantsov paraboloidal diffusion solution. The system succinonitrile is, as far as its physical properties are concerned, quite different from metallic systems.

Tong et al. [7] applied the phase field method to dendritic growth with convection in two dimensions. They found that the growth velocity depends considerably on the direction of the fluid flow with respect to the moving solid-liquid interface. In particular, the velocity may be increased or even decreased compared to the pure diffusion case if the fluid flow is in the opposite or in the same direction as crystal growth.

(4) METHODS OF DATA ACQUISITION AND ANALYSIS

The ground-based dendrite growth velocity data on Ni and Ni-C, that are shown in fig. 1, have been obtained by electromagnetic levitation experiments at DLR in Cologne and MIT in Cambridge. The circles and dots refer to the DLR capacitance sensor technique [3, 4]. Another series of experiments was run using the MIT digital imaging equipment. A description of this technique is given in ref. [8].

The TEMPUS facility is an electromagnetic levitation apparatus that has been constructed for experiments under microgravity conditions [9]. In addition to 16 other samples for different scientific purposes, one Ni-0.6 at.% C and one pure Ni sample were processed in the multi-user facility during the MSL-1-R Spacelab mission aboard the Columbia flight STS-94 in July 1997.

The maximum power outputs of the two RF positioner and heater fields in TEMPUS were 0.85 and 1.08 kW at frequencies between 150 and 350 kHz. A quadrupole field was used for positioning, a dipole field for inductively heating of the sample. The temperature of the droplet was measured by a two-color pyrometer that was calibrated during melting at the liquidus temperature and that was working with a maximum sampling rate of 1 MHz. Top- and side-view video observation was available with sampling rates of 120 Hz and 30 Hz, respectively.

A metallic W-Re trigger needle coated at the tip with ZrO_2 (in order to decrease the sticking tendency while touching the melt) was used for external stimulation of nucleation at selected undercoolings. The whole undercooling range of interest could be studied by means of this method. It also enabled quantitative growth velocity determination with an error of approximately 20%. The information about velocity was extracted from the measured temperature-time profiles during recalescence, i.e. during rapid release of the heat of fusion. Since, for a selected nucleation point, the geometry of the growth direction of the moving solid-liquid interface was well defined, the velocity could be evaluated from the calculated solidification path through the pyrometer spot divided by the measured time duration of recalescence. The main source of uncertainties of this photosensing method arises from morphological irregularities of the growth front at small undercoolings. If solidification started spontaneously, it was only possible to estimate the growth velocity with an error of about 100% in the determination of the absolute value due to the uncertainty in the relationship between the nucleation point and the sensor position. Because of a high evaporation rate of the materials, the experiments were performed in gas atmosphere, either in Ar (Ni-C, Ni) or in He/H₂ (Ni).

For sample preparation, material of purities of 99.998% (Ni, delivered from "Johnson&Matthey") and 99.9999% (C, delivered from "Koch Chemicals") was used. The rod material was repeatedly melted in a terrestrial levitation facility and solidified from deep melt undercoolings.

(5) FLIGHT RESULTS COMPARED WITH GROUND RESULTS AND THEORETICAL PREDICTIONS

Fig. 2 shows growth velocity data of Ni-0.6 at.% C and Ni that have been obtained by the experiments in TEMPUS, as well as theoretical curves. An arrow marks the resolution limit of the 100 Hz data that is explained below.

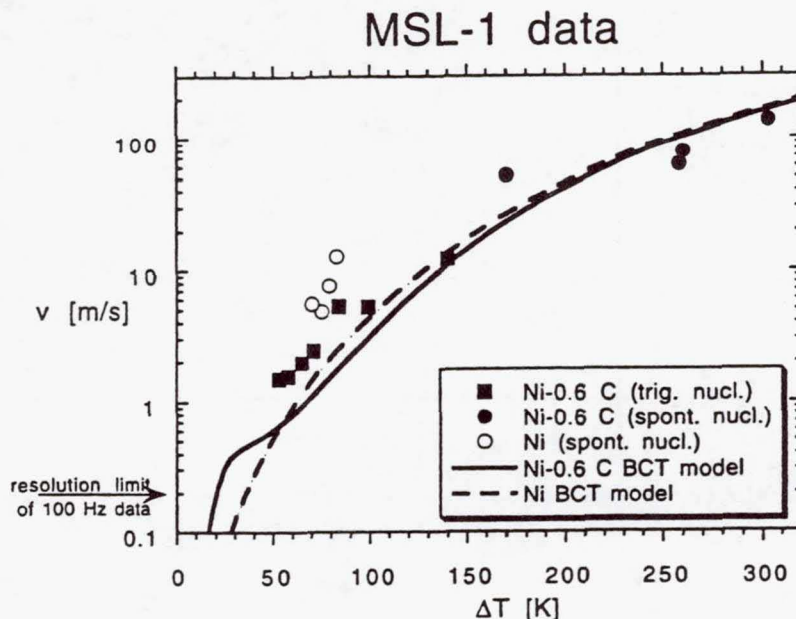


Figure 2: Dendrite growth velocity V versus undercooling ΔT data on pure Ni (open symbols) and a dilute Ni-0.6 at.% C alloy (black symbols), obtained during the MSL-1 Spacelab mission. Squares refer to triggered nucleation events with high accuracy of measurements, circles/dots to spontaneous nucleation events with reduced accuracy. All data plotted in figure 2 have been derived from an evaluation of the 1 MHz temperature data channel. An arrow marks the resolution limit of 100 Hz temperature data (cf. figure 3). Calculated curves according to the predictions of the BCT model [1] are plotted for Ni (dashed line) as well as for Ni-C (full line).

For the dilute Ni-C alloy, μg -data on an extended undercooling range up to $\Delta T = 305$ K have been obtained, whereas the μg -data points on Ni are restricted to the most interesting regime of small undercoolings up to $\Delta T = 85$ K. Seven stimulated and six spontaneous nucleation events were evaluated for Ni-C, and four recalescence profiles following spontaneous nucleations of Ni were saved with sufficient time resolution. Those latter data are only rough estimations of growth velocity, but the seven data points on Ni-C with triggered nucleation are of excellent reliability.

Fig. 3 shows a 100 Hz temperature-time profile during recalescence of the pure Ni sample at a representative small undercooling level of 25 K. Since the release of the latent heat was too weak for this level of ΔT , compared to the height of the signal noise, the automatic recalescence detection failed. The fast 1 MHz pyrometer data would have only been saved and down-linked from the ringmemory if the algorithm had recognised a more pronounced temperature rise of at least 35 K. Nevertheless, 100 Hz temperature data are available for the whole duration of the experiment independent on success or failure of recalescence detection. According to fig. 3, recalescence looks instantaneous on the time scale of 10^{-2} s even at $\Delta T = 25$ K because no data point is recorded. The crystal

growth velocity V therefore exceeds, as an estimation, the limit of resolution of the 100 Hz channel that is $V = 0.2 \text{ ms}^{-1}$.

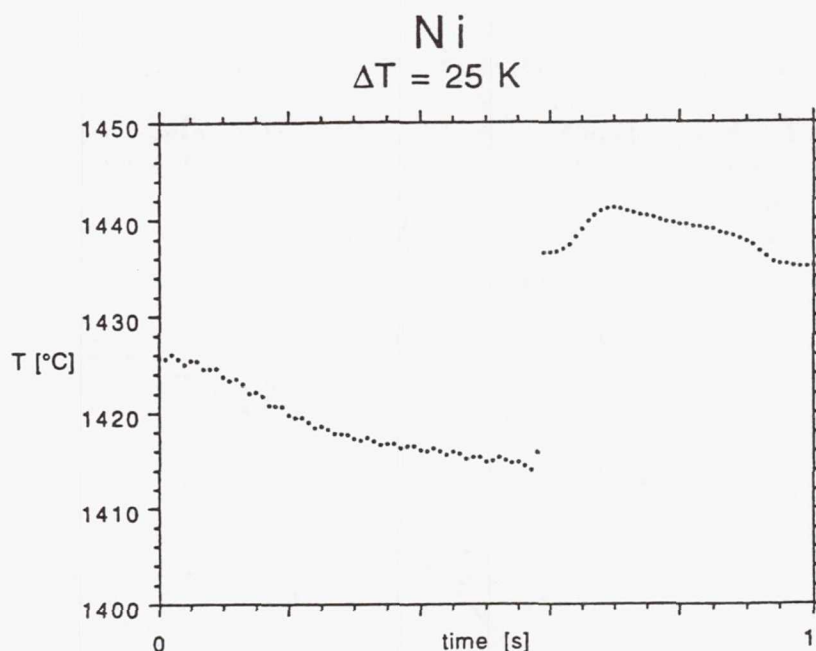


Figure 3: Temperature-time profile during recalescence of the Ni specimen at a small level of undercooling of $\Delta T = 25 \text{ K}$. On the 100 Hz time scale (cf. figure 2), recalescence is instantaneous.

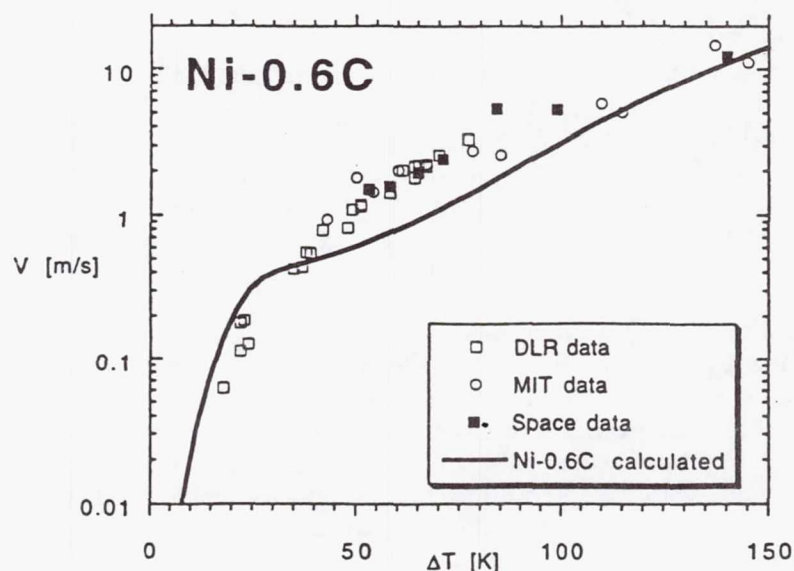


Figure 4: Comparison of space data (black symbols) on Ni-0.6 at.% C to terrestrial data (open symbols) on the same alloy. The full line refers to calculations on Ni-C according to the BCT model [1].

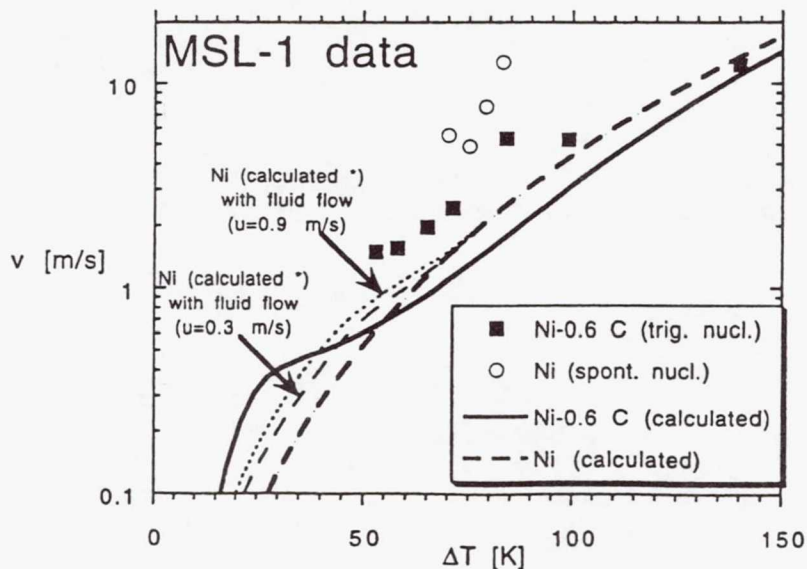
During the space experiments, a particle contamination was observed while monitoring the surface of both specimens by video. Post-flight SEM/EDX, EPMA and XPS surface studies as well as a quantitative chemical analysis revealed that the main impurity in the samples was Zr. Impurity levels of 0.02 at.% Zr in the originally pure Ni sample and of 0.035 at.% Zr in the dilute Ni-C alloy

were found. Furthermore, the analysis of the as-flown samples indicated a C composition of 0.69 at.% in the Ni-C specimen, and of 0.0005 at.% in Ni, respectively.

Grain size and morphology of the microstructure of the flown Ni-C sample undercooled 53 K prior to its last solidification event was identical to that of a specimen crystallized on earth upon about the same amount of undercooling (cf. ref. [4]). A grain-refined equiaxed structure was found, and no primarily grown dendrites could be preserved owing to fragmentation. The Ni flight sample showed an unusual large shrinkage pore near the center of the solidified droplet.

Fig. 4 shows a comparison of the most accurate μ g-data on Ni-C to former 1g-results and to the predictions by the BCT model. In particular at small undercoolings, all μ g-data are located above the theoretical curves, and growth velocities in space are throughout similar to those measured in terrestrial experiments. Thus, either the reduction of fluid flow motion in liquid samples processed in TEMPUS during MSL-1-R mission compared to levitation experiments on earth was not sufficient to detect an influence in the measured velocity-undercooling relationship within the uncertainty of measurements, or theoretical predictions lead to an overestimation of the respective effect. Possibly, the measured growth velocities are high compared to the calculated fluid flow velocities (see below), and the effect of convection is non-negligible only in the regime $\Delta T < 50$ K where no high accuracy data were measured during the space experiments.

As derived from fig. 3, the growth velocity of pure Ni at $\Delta T = 25$ K is estimated to be at least 0.2 ms^{-1} or higher. In contrast to that, the BCT dendrite growth model predicts 0.05 ms^{-1} at the same level of undercooling, as can be deduced or extrapolated from fig. 2.



* according to model of Ananth et al. (1991)

Figure 5: Comparison of space data on Ni (open circles) and Ni-0.6 at.% C (black squares) to theoretical predictions with and without considering convection. Calculated curves according to the predictions of the BCT model [1] are plotted for Ni (dashed line) as well as for Ni-C (full line). The thin dashed line refers to the prediction of the model by Ananth and Gill [10] for pure Ni under the assumption of a fluid flow velocity $u_{\infty} = 0.3 \text{ m/s}$, the thin dotted line has been calculated for $u_{\infty} = 0.9 \text{ m/s}$.

The model of Ananth et al. [10] has been applied in the present work for a first attempt to describe the velocity versus undercooling data on pure Ni as measured on earth and in space. This model assumes a uniform approaching fluid flow, in opposite direction of crystal growth and with velocity u_{∞} . The interface undercooling terms were calculated according to the BCT model. Fig. 5 shows calculated curves, taken from ref. [3], under the assumptions of fluid flow velocities of 0.3 and 0.9 ms^{-1} that are reasonable values for terrestrial levitation experiments. It is, however, unrealistic to assume a uniform

approaching flow since the flows induced by eddy currents in electromagnetic levitation experiments are circular. Obviously, there is no quantitative agreement between both calculated curves and the data although the deviations have become slightly smaller compared to the predictions without convection. The coupling of convection and solidification speed is strongest if the fluid flow velocities are of the same order of magnitude or smaller than the crystal growth velocity. Therefore, calculations on the remaining flow conditions in TEMPUS are of importance. Fluid flow velocities in the order of only about 0.01 ms^{-1} have been estimated [11] that are far below the experimentally measured crystal growth rates. Therefore, it is justified to assume that nearly convection-free conditions prevailed.

The growth velocity as measured under microgravity being comparable to those measured under terrestrial conditions and larger as predicted by theory might be, in principle, caused by Zr-contaminations in both samples. The Zr contamination has been found to be less than 0.1 at.%. Calculations of dendrite growth velocities assuming such contaminations in the flight samples show that only a minor impact on the solidification kinetics is expected. A maximum effect in the enhancement of the growth velocity due to an impurity of a strongly partitioning element would occur for a composition of about 0.5 at.% Zr.

Solvability theory has been developed so far that describes dendrite growth in three dimensions for pure metals as well as for alloys [12]. In contrast to the marginal stability hypothesis solvability theory delivers a self-consistent unique solution for the operating point of a growing dendrite in an undercooled melt by taking into account the anisotropy during the growth of a crystal. The radius of the tip of a dendrite as predicted by solvability theory differs from that of marginal stability theory only by the anisotropy parameter.

A promising future experiment program in an Advanced TEMPUS facility for studies of dendrite growth may be the development of new experimental techniques to measure dendrite growth velocity at small undercoolings with high accuracy e.g. by introducing the capacity sensor method [3] or a high-speed video technique [8] to TEMPUS. TEMPUS offers the advantage that the fluid flow conditions are altered in a systematic way by the variation of the positioning and heating fields of the quadrupole and dipole fields of the coil systems. Those experiments would deliver the growth velocity not only as a function of melt undercooling, but also in dependence on the strength of electromagnetic stirring.

(6) CONCLUSIONS INCLUDING SIGNIFICANCE AND FUTURE PLANS

Dendrite growth velocities of undercooled dilute Ni-C and pure Ni melts have been measured in containerless microgravity experiments. The measurements that have been performed in the TEMPUS facility during the Spacelab flight STS-94 deliver for the first time quantitative data of crystal growth velocity as a function of undercooling as measured in space on metallic systems under the conditions of significant reduction of natural and forced convection. However, the space results compare well with results of terrestrial experiments and no significant differences were observed in the undercooling range covered by the TEMPUS experiments. Future space experiments in the area of dendrite growth in undercooled melts of metals and alloys may be directed towards an improvement of the measuring accuracy, the access of the very small undercooling range for external triggering crystallization and a systematic change of fluid flow conditions under microgravity. High accuracy measurements of dendrite growth velocity at small undercoolings on melts in a highly quiescent state form experimental conditions capable to measure the anisotropy parameter for metals. Such investigations may be a challenge for future space experiments.

(7) ARTICLES/PRESENTATIONS RESULTING FROM THE FLIGHT

"IN SPACE'97"-conference in Tokyo, November 1997

TMS Fall Meeting in Chicago, October 1998

Publications in scientific journals are currently under preparation.

(8) NON-TECHNICAL SUMMARY

The purpose of the current investigations was to verify theoretical predictions on dendritic growth behavior and to study the influence of melt convection on crystal growth velocities of pure nickel and dilute nickel-carbon alloy melts. On earth, convection produces fluid flow velocities in the melt of approximately the same order of magnitude as the dendritic growth velocities. In microgravity, however, convection is reduced, and the expected influence of melt convection on solidification kinetics can be proven. Excellent growth velocity data were obtained during the mission that did surprisingly not show any decrease in solidification velocities compared to ground-based data. Future experiments on Spacehab or the International Space Station are planned to clarify more systematically these unexpected results.

ACKNOWLEDGEMENTS

The authors thank the entire TEMPUS team for the outstanding co-operation, i.e. the involved members of MUSC (Microgravity User Support Center of DLR), NASA and DARA (former German Space Agency), Dornier (facility developer) and all other scientific groups using the TEMPUS facility.

REFERENCES

- [1] W. J. Boettinger, S. R. Coriell and R. Trivedi, in R. Mehrabian and P. A. Parrish (eds.), *Rapid Solidification Processing, Principles and Technologies IV*, Claitor's, Baton Rouge, 13 (1988).
- [2] J. S. Langer and H. Müller-Krumbhaar, *Acta metall.* 26, 1681 (1978).
- [3] K. Eckler and D. M. Herlach, *Mat. Sci. Eng. A178*, 159 (1994).
- [4] K. Eckler, A. F. Norman, F. Gärtner, A. L. Greer and D. M. Herlach, *J. of Crystal Growth* 173, 528 (1997).
- [5] N. El-Kaddah and J. Szekely, in G. E. Rindone (ed.), *Mat. Proc. in the Reduced Gravity Environment of Space*, Elsevier, Amsterdam, 191 (1982).
- [6] M. E. Glicksman, M. B. Koss and E. A. Winsa, *Phys. Rev. Letters* 73, 573 (1994).
- [7] X. Tong, C. Beckermann and A. Karma, submitted for publication (1998).
- [8] D. M. Matson, A. Shokuhfar, J. W. Lum, and M. C. Flemings, in *Solidification Science and Processing*, I. Ohnaka and D. M. Stefanescu (eds.), TMS meeting, Warrendale PA, 19 (1996).
- [9] R. Knauf, J. Piller, A. Seidel, M. Stauber, U. Zell and W. Dreier, in R. Schiffman (ed.), *Int. Symposium on Experimental Methods for Microgravity Mat. Sci.*, The TMS Society, Warrendale, 43 (1994).
- [10] R. Ananth and W. N. Gill, *J. of Crystal Growth* 91, 587 (1988).
- [11] G. Trapaga, *International Workshop on "Nucleation and Thermophysical Properties of Undercooled Melts"*, Physikzentrum Bad Honnef, 4th-6th of March (1998).
- [12] A. Karma, private communication (1998).

Page intentionally left blank

523-26

434 859

10P.

Electromagnetic Containerless Processing Facility (TEMPUS)

362429

Undercooled Melts of Alloys with Polytetrahedral Short-Range Order

Principal Investigator:

Dr. Dieter Herlach
DLR
Cologne, Germany

FINAL SCIENCE REPORT

UNDERCOOLED MELTS OF ALLOYS WITH POLYTETRAHEDRAL SHORT-RANGE ORDER

D. Holland-Moritz^{1,2}, D.M. Herlach², K.F. Kelton³, H. Bach¹ and B. Feuerbacher²

- ¹ Ruhr-Universität Bochum, Institut für Experimentalphysik/Festkörperphysik, D-44780 Bochum, Germany
- ² Institut für Raumsimulation, DLR, D-51170 Köln, Germany
- ³ Washington University, Department of Physics, One Brookings Drive, St. Louis, MO 63130, U.S.A.

1. Abstract

Molecular-dynamics investigations [1-4] predict that an icosahedral short-range order prevails in the undercooled melt. Such a short-range order in the undercooled melt is expected to have consequences for the specific heat of the melt and for the nucleation of solid phases. Because the icosahedral symmetry is incompatible with the translational invariance of simple crystalline phases it is expected that the nucleation of these phases is hindered leading to a high undercoolability of the melt [5]. On the other hand, quasicrystals and Frank-Kasper phases [6] are characterized by a more or less pronounced degree of polytetrahedral short-range order, which is similar to that anticipated for the undercooled melt. Therefore a low interfacial energy between melt and polytetrahedral nucleus is expected, which leads to a low activation threshold for nucleation of the polytetrahedral phase and by means of this to a low undercoolability of the melt [7].

It was intended to investigate the maximum level of undercooling, the specific heat and the viscosity as a function of temperature at melts which form different quasicrystalline and Frank-Kasper phases in the TEMPUS facility on the MSL-1/MSL-1R missions in 1997.

2. Objectives

The investigations aimed to study the nucleation behaviour and the thermophysical properties as a function of the undercooling for melts forming polytetrahedral phases.

3. Background

As it was experimentally observed by Turnbull [8] in the early 1950's, metallic melts can be deeply undercooled below their melting temperature. For several metallic elements the undercoolings reported typically amount to about 20% of the melting temperature. Frank [5] suggested that these high levels of undercooling might be a result of an icosahedral short-range order, which should be energetically favored in undercooled melts of systems consisting of atoms of spherelike geometrical symmetry. Icosahedral short-range order is incompatible with the translational symmetry of crystalline phases. This should give rise to an increase of the nucleation threshold for crystalline solids, because crystal nucleation requires a breakup of the icosahedral short-range order. Later, Frank's prediction of an icosahedral short-range order in undercooled melts was confirmed by several molecular dynamic computer calculations on Lennard-Jones liquids [1-4].

On the other hand, a different nucleation behaviour is expected for icosahedral quasicrystalline phases. These phases are characterized by icosahedral atom correlations in the solid state, which are similar to those anticipated in undercooled melts. Therefore the interfacial energy between quasicrystalline nucleus and melt should be low, resulting in a comparatively low activation energy for the nucleation of the icosahedral quasicrystal and a bad undercoolability of the melt [7].

Apart from the icosahedral quasicrystals other phases exist which exhibit a more or less pronounced degree of polytetrahedral short-range order. Examples for this type of solids are the decagonal quasicrystals, which are quasiperiodic in two dimensions and periodic in the third dimension. Furthermore the Frank-Kasper phases [6], are crystalline phases characterized by a large unit cell and polytetrahedral symmetry-elements inside this cell. Depending on the grade of icosahedral short-range order we expect an activation threshold for the nucleation of these phases that lies somewhere in between that of icosahedral quasicrystals and simple crystals.

Up to now only a few investigations on the undercoolability of melts of alloys forming polytetrahedral phases have been reported. Most of these alloys consist of elements which are highly reactive with respect to oxidation such as Al, Ti, and/or Mg. Therefore, undercooling techniques based upon a containment in a crucible such as the fluxing method are very difficult to apply in order to obtain reliably and reproducibly large undercoolings of quasicrystal-forming alloys. To study the *intrinsic* effect of volume nucleation of crystalline and quasicrystalline phases it is mandatory to circumvent possible disturbing effects by *extrinsic* heterogeneous nucleation on the surface of the sample as far as possible. The special conditions of containerless processing are most favorable to overcome such difficulties, since any reaction between the melt and a containment is completely avoided [9].

4. Methods of data acquisition and analysis

4.1 Ground based experiments

Electromagnetic levitation [9,10] is applied to process massive samples with diameters of about 7mm in the containerless state. The experimental setup consists of an HF- generator with a two-coil-levitation system operating in a frequency range of 150-400 kHz at a maximum power output of 9 kW. The coil system and the sample are integrated into an ultra-high-vacuum (UHV) chamber which is evacuated to a pressure of 10^{-8} mbar before backfilling with He or He-10%H₂ cooling gas of a purity better than 99.9999%. The metallic sample is levitated and inductively heated by the HF-field. Cooling of the levitated sample requires forced convection by a flow of cooling gas over the sample surface. The temperature of the sample is contactlessly measured by a pyrometer with an accuracy of ± 10 K and recorded with a sampling rate of 100 Hz.

4.2 Space experiments

The TEMPUS facility is an electromagnetic positioning device that has been designed for containerless processing of metallic melts under microgravity conditions [11]. It consists of two different HF-generators with an maximum output of 0.85 and 1.08 kW powering a positioning and a heating coil at frequencies of 150 and 350 kHz respectively. For positioning

of the specimen a quadrupole field is applied, while for heating a dipole field is used. The sample temperature is measured contactlessly with a two-color pyrometer at sampling rates of 100 Hz. By use of a ring memory data-rates of up to 1 MHz are achievable within short time intervals. Video observation of the sample is possible from the top and from the side with frame rates of 120 and 30 Hz respectively.

5. Results

5.1 Ground results

First experiments on the maximum undercoolability of droplets of quasicrystal-forming alloys about 7 mm in diameter by application of the containerless technique of electromagnetic levitation were reported in [12]. In that work the undercooling behaviour of melts forming the icosahedral I-phase in Al-Cu-Fe and the decagonal D-phase in Al-Cu-Co was studied. Meanwhile similar experiments were performed in which the nucleation behaviour of the I-phase in Al-Pd-Mn [13,14], the D-phase in Al-Ni-Co [14,15], the metastable D-phase in Al-Co [14,16], the polytetrahedral phases λ -Al₁₃Fe₄ [13,14,17,18] and μ -Al₅Fe₂ [13,14,17,18] and - for comparison - the crystalline CsCl-type β -phase in Al-(Cu-)Co [14,17,18] was investigated.

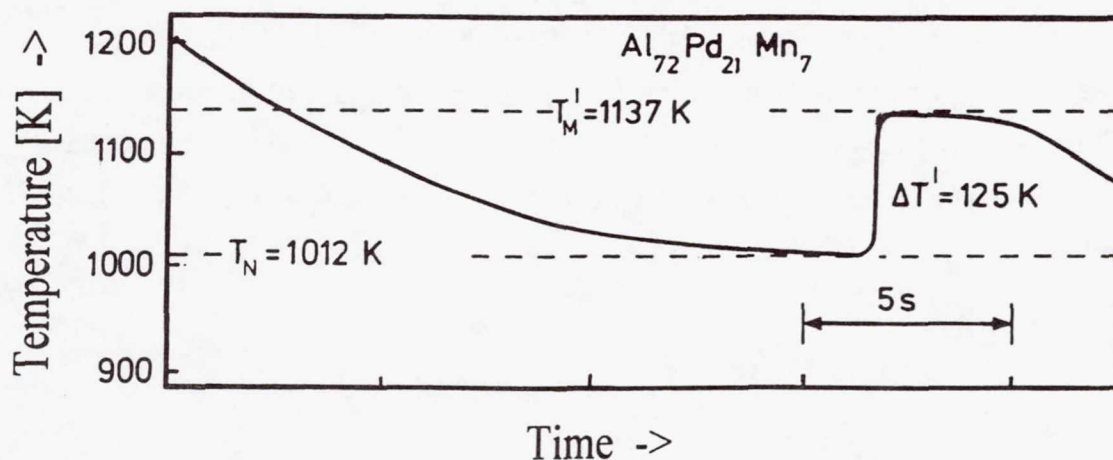


Fig. 1 Temperature-time profile of a levitation-undercooling experiment on an Al₇₂Pd₂₁Mn₇ sample where the maximum level of undercooling was achieved.

As an example a temperature-time profile of an undercooling experiment performed on an $\text{Al}_{72}\text{Pd}_{21}\text{Mn}_7$ specimen that forms an icosahedral quasicrystalline I-Phase is shown in Fig. 1. The sample is first molten and subsequently, the melt is undercooled below its liquidus temperature T_L . Nucleation sets in at the temperature T_N . The release of the heat of fusion during crystallization leads to a temperature rise (recalescence) up to the melting temperature of the I-phase. After recalescence, the solidified sample cools down. The undercooling ΔT is inferred from the measured difference of the nucleation and the liquidus temperature, $\Delta T = T_L - T_N$.

The maximum relative undercoolings achievable by electromagnetic levitation for the I-phases both in Al-Cu-Fe and Al-Pd-Mn amount to $\Delta T'/T_L' \approx 0.1$ [12,13,14,17], while for the D-phases in Al-Cu-Co, Al-Ni-Co and Al-Co values of $\Delta T^D/T_L^D \approx 0.15$ [12-17] are obtained. For the crystalline polytetrahedral phase, relative undercoolings were measured of $\Delta T'/T_L' \approx 0.13$ for the λ -phase in Al(-Cu)-Fe and of $\Delta T^\mu/T_L^\mu \approx 0.14$ for the μ -phase in Al-Fe [13,14,17,18]. The maximum undercooling of the crystalline β -phase in Al-Cu-Co was the largest ($\Delta T^\beta/T_L^\beta \approx 0.25$) [14,17,18]. This behaviour is described by the relation

$$\Delta T'/T_L' < \Delta T^\lambda/T_L^\lambda < \Delta T^\mu/T_L^\mu < \Delta T^D/T_L^D < \Delta T^\beta/T_L^\beta$$

Obviously, the maximum undercoolings achieved by the levitation experiments are strongly dependent on the structure of the primarily nucleating phases.

Recently, a numerical estimation of the interfacial energy of the solid-liquid interface was performed for the I-Phase in Al-Pd-Mn and the polytetrahedral phases m and l, which implies the same sequence for the undercoolability of the different phases [14,19].

These results indicate that the activation energy for the formation of a critical nucleus decreases with increasing degree of polytetrahedral short-range order of the nucleating phase. This can be explained under the assumption of a polytetrahedral short-range order in the undercooled melt [7].

5.2 Flight results

Two quasicrystal-forming samples of the compositions $\text{Al}_{60}\text{Cu}_{34}\text{Fe}_6$ and $\text{Al}_{65}\text{Cu}_{25}\text{Co}_{10}$ were processed in the TEMPUS facility during the MSL-1R mission. However due to contamination problems no significant undercoolings of the specimens were achieved. The

post-flight analysis of the flight samples by scanning electron microscopy (SEM) in combination with energy dispersive X-ray analysis (EDX) and by X-ray photoemission spectroscopy (XPS) indicated a contamination of the samples by material from another specimen processed in TEMPUS.

In order to solve the problem of contamination during the experiment, we attempted to clean the specimens by heating to high temperatures. Such a treatment was in many cases successfully employed to remove contamination sites during earthbound levitation experiments. Although this procedure was able to partly remove the contamination sites, before a sufficient cleaning was obtained, the FO's were terminated because of heavy sample rotations leading to disintegration of the samples by centrifugal force. These rotations are most likely due to the interaction of inhomogeneities of the electromagnetic field with inhomogeneities in the specimen. Thus samples with a large interval between solidus and liquidus temperature are most sensitive to spinning, because during heating these samples consist for a considerably long time of a solid-liquid phase mixture. $\text{Al}_{60}\text{Cu}_{34}\text{Fe}_6$ and $\text{Al}_{65}\text{Cu}_{25}\text{Co}_{10}$ are characterized by an extremely wide interval between solidus and liquidus temperature of several hundred K.

In this context it should be emphasized that we - aware of this problem - proposed experiments on the congruently melting binary alloy $\text{Al}_{13}\text{Fe}_4$. However, this alloy was rejected by the review board.

6. Conclusions

In ground-based studies melts of alloys forming polytetrahedral phases were containerlessly undercooled by electromagnetic levitation. The nucleation behavior of various solid phases with a different degree of polytetrahedral short-range order was investigated. The analysis of the undercooling experiments within classical nucleation theory results in the conclusion that the energy of the interface between the liquid and a solid nucleus is the lowest, the larger the degree of polytetrahedral short-range order of the primarily nucleating solid phases is. This observation is consistent with numerical estimations of the solid-liquid interfacial energy.

7. Bibliographic citations of articles/presentations resulting from the flight

none

8. Non-technical summary suitable for Public Affairs Office use

The maximum undercoolability of melts forming polytetrahedral phases was studied by containerless processing in an electromagnetic levitation facility. The investigations exhibit a systematic dependence of the undercoolability on the structure of the primarily nucleating phases. The observations are in favour of the assumption of a polytetrahedral short-range order prevailing in undercooled melts.

Acknowledgements

The authors thank the whole TEMPUS team for the excellent cooperation, i.e. the involved members of DLR-MUSC, NASA, DLR-BO (former DARA), Daimler-Benz Aerospace (Dornier) and the other scientific groups using TEMPUS.

References

- [1] P.J. Steinhardt, D.R. Nelson, and M. Ronchetti, *Phys. Rev. B* **28**, 784 (1984)
- [2] H. Jónsson und H.C. Andersen; *Phys. Rev. Lett.* **60**, 2295 (1988)
- [3] S. Nosé, and F. Yonezawa, *J. Chem. Phys.*, **84**, 1803 (1986)
- [4] S. Nosé und F. Yonezawa; *Solid State Commun.* **56**, 1005 (1985); **56**, 1009 (1985)
- [5] F.C. Frank, *Proc. R. Soc. London A* **215**, 43 (1952)
- [6] F.C. Frank, and J.S. Kasper, *Acta Cryst.* **11**, 184 (1958)
- [7] D.R. Nelson and F. Spaepen; *Solid State Phys.*, edited by H. Ehrenreich, F. Seitz, and D. Turnbull (Academic, New York, 1989), Vol.42, p.1
- [8] D. Turnbull, *J. Appl. Phys.* **21**, 1022 (1950)
- [9] D.M. Herlach, R.F. Cochrane, I. Egry, H.-J. Fecht and A.L. Greer, *International Materials Review* **38**, 2473 (1993).
- [10] D.M. Herlach; *Ann. Rev. Mater. Sci.* **21**, 23 (1991)
- [11] R. Knauf, J. Piller, A. Seidel, M. Stauber, U. Zell and W. Dreier in R. Schiffman (ed.), *Int. Symposium on Experimental Methods for Microgravity Mat. Sci.*, The TMS Society, Warrendale, 43 (1994)
- [12] D. Holland-Moritz, D.M. Herlach, and K. Urban, *Phys. Rev. Lett.* **71**, 1196 (1993)

- [13] J. Schroers, Thesis, RWTH Aachen (1997)
- [14] D. Holland-Moritz, accepted for publication in *J. Non-Equilibrium Processing*
- [15] T. Schenk, D. Holland-Moritz and B. Grushko; to be published
- [16] J. Schroers, D. Holland-Moritz, D.M. Herlach, B. Grushko and K. Urban; *Mat. Sci. Eng. A* **226-228**, 990 (1997)
- [17] D. Holland-Moritz, J. Schroers, D.M. Herlach, B. Grushko and K. Urban; *Acta Mater.* **46**, 1601 (1998)
- [18] D. Holland-Moritz, J. Schroers, D.M. Herlach, B. Grushko and K. Urban; *Proceedings of the 5th International Conference on Quasicrystals, Avignon (1995)*
- [19] D. Holland-Moritz; *Proceedings of the 6th International Conference on Quasicrystals, Tokyo (1997)*, ed. S. Takeuchi and T. Fujiwara, 293-296, World Scientific, Singapore (1998)

Page intentionally left blank

524-27
434860

Electromagnetic Containerless Processing Facility (TEMPUS)

362730

10P.

Thermal Expansion of Glass Forming Metallic Alloys in the Undercooled State

Principal Investigator:

Dr. Konrad Samwer
University of Augsburg
Augsburg, Germany

Thermal Expansion of Glass Forming Metallic Alloys in the Undercooled State

Final Science Report

Konrad Samwer, Bernd Damaschke

Institut für Physik, Universität Augsburg, 86135 Augsburg, Germany

in cooperation with

Ivan Egry

Institut für Raumsimulation, DLR, 5000 Köln, Germany

August 1998

Abstract

The thermal expansion of liquid samples of glass forming metallic alloys was measured under microgravity conditions. The experiments were performed in an electromagnetic levitation facility (TEMPUS facility) on board the space orbiter Columbia (mission MSL-1). The sample was imaged by a high resolution CCD camera with on-board recording. After the mission the video tapes were analyzed by digital image processing.

The values found for the thermal expansion coefficients are between $1.8 \cdot 10^{-5} \text{K}^{-1}$ and $32 \cdot 10^{-5} \text{K}^{-1}$ which complements nicely experiments done earlier at lower temperatures. The volume jump at the melting point is $\leq 2\%$. In some cases structural changes occur leading to different regimes for thermal expansion.

Objectives

Metallic glasses are a new class of materials showing no long range order in their microstructure like conventional metals and alloys. The loss of the crystalline structure give these materials physical properties which are interesting for scientific investigations but also for technical application. Some of the most famous metallic glasses are Zr-Cu-Al, Zr-Ni-Al [1] and Zr-Ti-Ni-Cu-Be [2].

The measurement of the thermodynamic properties is an important step to get a basic understanding of the physics of the glassy metals. Especially in the melt and in the undercooled state only some of these properties could be measured in the last years. Because of the reactivity of the samples at high temperatures the experiments have to be made containerless under ultra high vacuum conditions.

Within the TEMPUS-project at MSL-1 the thermal properties of various metals and alloys could be investigated under microgravity conditions. The positioning of the samples was made using electromagnetic levitation and heating was achieved with an additional heating coil [3].

Our group has performed the thermal expansion measurements. For this purpose we developed a suitable method based on optical imaging of the sample with a new measuring camera. After the mission the on board recorded pictures were analyzed with digital image processing giving the volume of the sample as a function of time and temperature [4].

The thermal expansion data give insight into the structure of the samples and can be interpreted and related to the glass transition within the 'free volume model' [5, 6]. The volume as a function of temperature also is sensitive to structural and compositional changes which is important for the understanding of the physical processes running in the sample.

Method

While the sample was processed in the TEMPUS-facility it was imaged by a CCD measuring camera with resolution 659×494 pixels. The camera has an electronic shutter with exposure times between 1/60 and 1/2000000s allowing sample temperatures from about 700 to 2500 °C. It is equipped with a telecentric lens system with a focal length of 160mm.

Because of the limited bandwidth of the video transtion channel of the space orbiter the camera divided the original picture in 4 partial pictures (and an additional testcard). The frequency of 30Hz lead to an effective repetition rate of 6Hz for the whole information. The partial pictures were recorded on board with a video recorder.

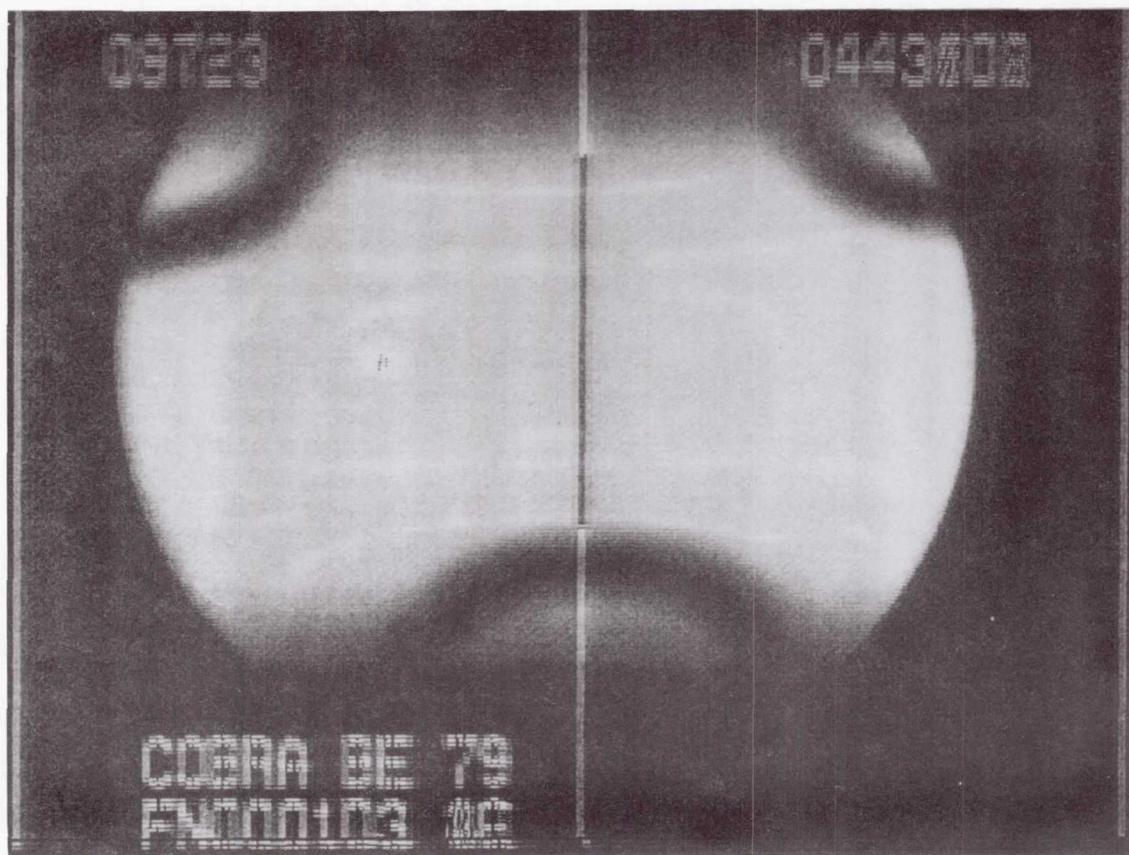


Fig. 1: Composed picture of a $\text{Pd}_{78}\text{Cu}_6\text{Si}_{16}$ sample at a temperature of 1053 °C. Inserted are marks for synchronization of the digitized picture (3 vertical stripes), the Greenwich mean time (top), the hexadecimal values for automatic gain control (BE) the temperature of the camera hardware (79) and a frame counter (bottom).

After the mission the partial pictures were digitized and composed to reconstruct the original picture. Marks were inserted in the original picture to eliminate synchronization problems in the digitization process (see Fig. 1).

After getting the composite picture the edges of the sample were detected first by searching the maximum slope and subsequently by fitting a polynomial of 3rd degree to the transition and taking the half height (resolution 1/10 pixel). At least the resulting contour list was fitted to the equation of an ellipse giving the midpoint, angle and, under the assumption of rotational symmetry, the volume V of the sample.

The theoretical resolution of the system and the evaluation procedure $\Delta V/V = 3.75 \times 10^{-4}$ cannot be reached in reality because of sample movements, covering of parts of the sample by wires of the sample holder (see Fig. 1) and worsening of the edges by the transition channels and the recording. More experimental details can be found in [4].

Results

In mission MSL-1 experiments were made with the following samples in cooperation with other groups: Zr (Bayuzick, Hofmeister, Vanderbilt Univ., Nashville), $\text{Zr}_{57}\text{Cu}_{15.4}\text{Ni}_{12.6}\text{Nb}_5\text{Al}_{10}$, $\text{Zr}_{11}\text{Cu}_{47}\text{Ti}_{34}\text{Ni}_8$ (Johnson, Caltech, Pasadena), $\text{Zr}_{65}\text{Cu}_{17.5}\text{Al}_{7.5}\text{Ni}_{10}$, $\text{Zr}_{60}\text{Cu}_{18}\text{Al}_{10}\text{Ni}_9\text{Co}_3$ (Fecht, Wunderlich, TU Berlin), $\text{Pd}_{78}\text{Cu}_6\text{Si}_{16}$ (Egry, DLR, Cologne) and $\text{Pd}_{82}\text{Si}_{18}$ (Trapaga, Hyers, MIT, Boston).

As an example the evaluated data in the case of $\text{Zr}_{11}\text{Cu}_{47}\text{Ti}_{34}\text{Ni}_8$ are shown.

First the temperature is raised to melt the sample (8mm diameter), then the sample cooled down to a measuring temperature at which a temperature modulation for a specific-heat measurement (Johnson) was performed. After about 500s the heater was switched off and the sample again cooled down until the solidification takes place. In this melting cycle we observed an undercooling of 43°C (T_m : 842°C). At least the sample became solid and the temperature decreased until the end of the cycle was reached. The volume follows the temperature but there are some disturbances due to sample movements.

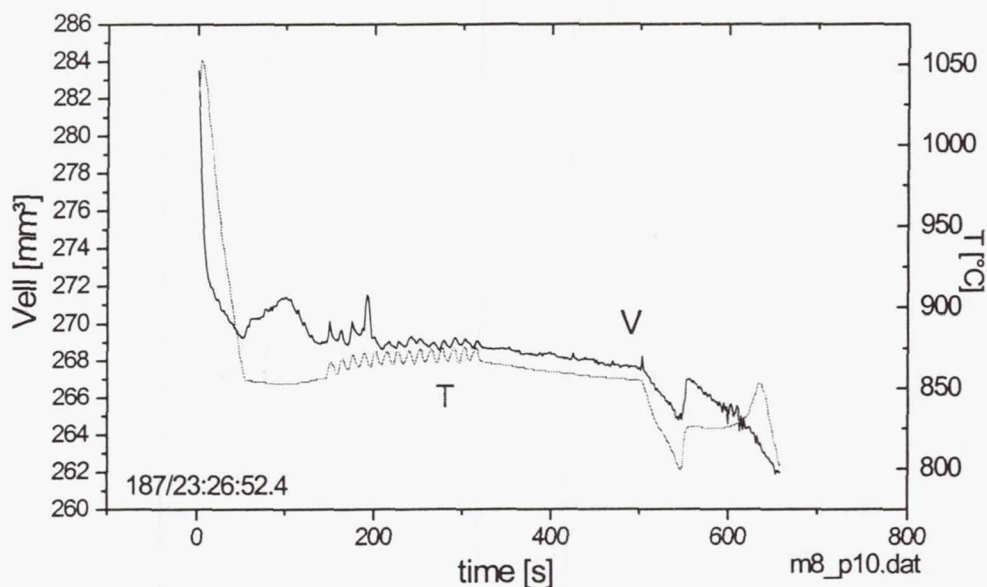


Fig. 2: $\text{Zr}_{11}\text{Cu}_{47}\text{Ti}_{34}\text{Ni}_8$, volume and temperature as a function of processing time. The Greenwich Mean Time of the measurement is inserted (bottom, left).

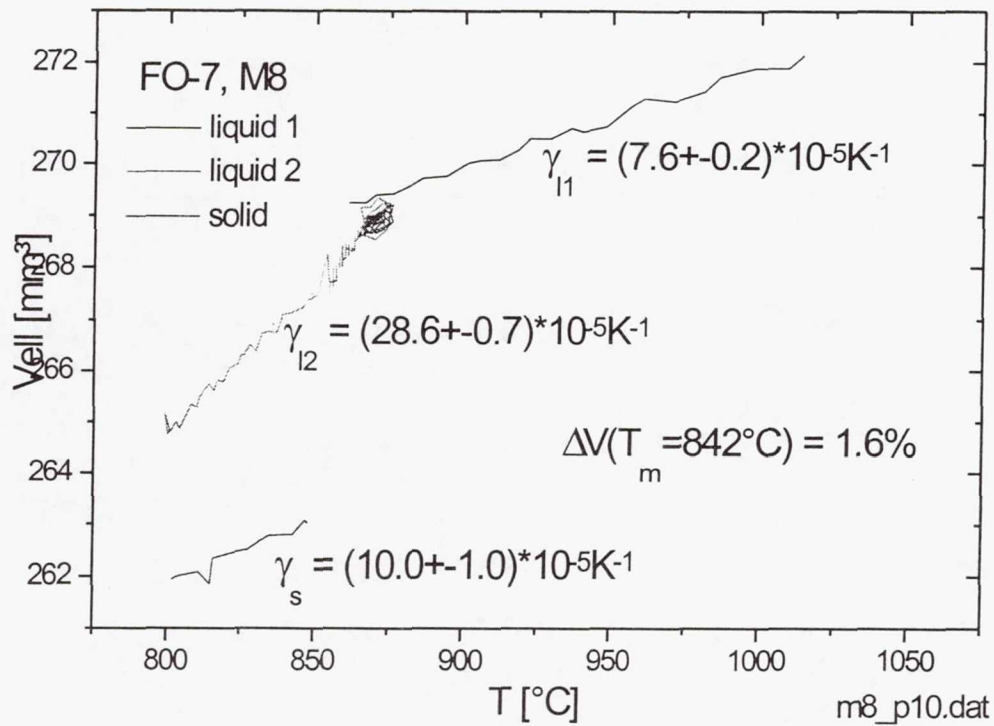


Fig. 3: $Zr_{11}Cu_{47}Ti_{34}Ni_8$, volume as a function of temperature. The thermal expansion coefficients are given for two different linear ranges in the liquid and one in the solid. ΔV is the volume jump at the melting point.

In Fig. 3 the volume is shown as a function of temperature. The given coefficient of volumetric thermal expansion $\gamma = (1/V(T=0^\circ\text{C}))(\partial V/\partial T)$ was calculated from a linear fit. In this case we have two different linear ranges with different thermal expansion coefficients. The system is most likely still in the liquid since we see no recalescence event. The volume jump at the thermodynamic melting point is 1.6% (of the volume of the melt) [6]. The very high value of the thermal expansion coefficient in the solid may be an artefact of the measurement due to the poor contrast for low temperatures (dark samples). Further investigations with background illumination are necessary. The other data evaluated so far are summarized in Table 1. The Zr-data could not be evaluated due to strong sample movements and a limited view caused by a special sample holder. Because of the large amount of data and the complexity of the evaluation not all cycles are evaluated until now and so the table contents only preliminary values.

For $\text{Pd}_{78}\text{Cu}_6\text{Si}_{16}$ the results can be compared with values measured on earth: Between 797 and 923 °C the thermal expansion coefficient was given by $8.0 \cdot 10^{-5} \text{K}^{-1}$ [8] (recalculated with our definition of γ given above).

Table 1: Thermal expansion in the liquid state (preliminary values)

Sample	FO-No.	γ [10^{-5}K^{-1}]	T-range [°C]	T_m [°C]	$\Delta V(T_m)$ [%]
$\text{Zr}_{57}\text{Cu}_{15.4}\text{Ni}_{12.6}\text{Nb}_5\text{Al}_{10}$	4	5.9 ± 1.8	800-1200	819	not eval.
$\text{Zr}_{65}\text{Cu}_{17.5}\text{Al}_{7.5}\text{Ni}_{10}$	6	1.9 ± 0.1	750-925	837	≤ 0.7
$\text{Zr}_{11}\text{Cu}_{47}\text{Ti}_{34}\text{Ni}_8$	7	7.7 ± 0.5	830-1125	842	2.0 ± 0.4
		32.0 ± 13.2	795-875		
$\text{Zr}_{60}\text{Cu}_{18}\text{Al}_{10}\text{Ni}_9\text{Co}_3$	8	5.5 ± 0.7	830-1200	860	1.0 ± 0.4
$\text{Pd}_{78}\text{Cu}_6\text{Si}_{16}$	24	7.9 ± 0.3	920-1200	760	not eval.
		1.8 ± 0.3	780-920		

For the Zr-based alloys only few results were known. For $\text{Zr}_{65}\text{Cu}_{17.5}\text{Al}_{7.5}\text{Ni}_{10}$ measurements above the glass transition lead to $\gamma = 6 \cdot 10^{-5} \text{K}^{-1}$ at 650°C [9]. For the similar alloy $\text{Zr}_{41.2}\text{Ti}_{13.8}\text{Cu}_{12.5}\text{Ni}_{10.0}\text{Be}_{22.5}$ values of $5.32 \cdot 10^{-5} \text{K}^{-1}$ [10] and $5.43 \cdot 10^{-5} \text{K}^{-1}$ [11] had been observed. Further investigations on earth have to be made to look for the discrepancies.

Conclusions

In the mission MSL-1 the thermal expansion which is one of the important thermophysical properties of glass forming metallic alloys was measured in the TEMPUS facility. The samples were imaged with a high resolution measuring camera and after the mission the pictures were analyzed with digital image processing. The values found for the thermal expansion coefficients are between $1.8 \cdot 10^{-5} \text{K}^{-1}$ and $32 \cdot 10^{-5} \text{K}^{-1}$ which complements nicely experiments done earlier at lower temperatures. The volume jump at the melting point is $\leq 2\%$. In some cases structural changes occur leading to different regimes for thermal expansion.

The method newly developed for the TEMPUS facility worked successfully. For the future we plan to work on industrial related systems where the knowledge of the thermal expansion coefficient and volume change during solidification is important for casting and other applications.

Non-technical summary

Metallic glasses are a new class of materials showing no long range crystalline order in their atomic structure like conventional metals and alloys. The loss of the crystalline structure give these materials physical properties which are interesting for scientific investigations but also for technical application.

If the melt of metallic alloys is cooled down below the melting point it can remain in the liquid state when the experiment is controlled under special pure conditions. In this temperature regime it is called to be in the undercooled state. The glassy state can be reached by cooling very fast below the glass transition temperature. In this case the liquid structure is frozen in and mechanical behavior changes dramatically. However, if the cooling is not fast enough the alloys crystallize and do not show the glassy structure.

To understand the undercooled liquid and the glass transition it is necessary to measure the thermophysical properties like specific heat and thermal expansion of the samples. Understanding is not only the base for scientific knowledge but also for the development of new materials for special applications.

Our group has performed the thermal expansion measurements. For this purpose we developed a suitable method based on optical imaging of the sample with a new measuring camera. After the mission the on board recorded pictures were analyzed with digital image processing giving the volume of the sample as a function of time and temperature.

The method newly developed for the TEMPUS facility worked successfully. We got values for the thermal expansion coefficients for nearly all samples in the high temperature range. For the future we plan to install a background illumination necessary for experiments at lower temperatures with dark samples.

References

- 1.) T. Zhang, A. Inoue, T. Masumoto, Mater. Trans. JIM **32**, 1005 (1991)
- 2.) A. Peker, W.L. Johnson, Appl. Phys. Lett **63**, 2342 (1993)
- 3.) G. Lohöfer, P. Neuhaus, and I. Egry, High Temp.-High Press. **23**, 333 (1991)
- 4.) B. Damaschke, D. Oelgeschlaeger, E. Ehrich, E. Dietzsch, and K. Samwer, Rev. Sci. Instrum. **69**, 2110 (1998)
- 5.) M.H. Cohen and G.S. Grest, Phys. Rev. B **20**, 1077 (1979)
- 6.) B. Damaschke and K. Samwer, to be published
- 7.) A. van den Beukel and J. Sietsma, Acta metall. mater. **38**, 383 (1990)
- 8.) L.F. Chua, C.W. Yuen, and H.W. Kui, Appl. Phys. Lett. **67**, 614 (1995)
- 9.) N. Geier and K. Samwer, submitted to Appl. Phys. Lett. 5/1998
- 10.) K. Ohsaka, S.K. Chung, W.K. Rhim, A. Peker, D. Scruggs, and W.L. Johnson, Appl. Phys. Lett. **70**, 726 (1997)
- 11.) Y. He, R.B. Schwarz, D. Mandrus and L. Jacobson, J. Non Cryst. Solids **205-207**, 602 (1996)

Articles and presentations resulting from the flight

Articles

- 1.) B. Damaschke, D. Oelgeschlaeger, E. Ehrich, E. Dietzsch, and K. Samwer, Rev. Sci. Instrum. **69**, 2110 (1998)
- 2.) Article in University-Press 1/97, Univ. Augsburg
- 3.) Article in public newspaper (Augsburger Allgemeine, spring 97)
- 4.) B. Damaschke and K. Samwer, to be published

Presentations (1997 and 1998)

- 1.) Seminar-talk in Augsburg, 2/97
- 2.) Talk in Köln, TEMPUS-Meeting, 6/97
- 3.) Seminar-talk in Sion, 10/97
- 4.) Talk in Augsburg, 'Tage der Forschung', 11/97
- 5.) Talk in Augsburg, IHK, 12/97
- 6.) Seminar-talk in Göttingen, 12/97
- 7.) Talk in Bad Honnef, TEMPUS-Meeting, 3/98
- 8.) Talk in Regensburg, DFG-Spring Meeting, 3/98

5-5-26
434861
8p.

Electromagnetic Containerless Processing Facility (TEMPUS))

362731

Experiment on Nucleation in Different Flow Regimes

Principal Investigator:

Dr. Robert J. Bayuzick
Vanderbilt University
Nashville, Tennessee

Experiments on Nucleation in Different Flow Regimes
R. J. Bayuzick, W.H. Hofmeister, and C.M. Morton
Department of Chemical Engineering, Vanderbilt University
M.B. Robinson
Space Sciences Laboratory, MSFC

Introduction

The vast majority of metallic engineering materials are solidified from the liquid phase. Understanding the solidification process is essential to control microstructure, which in turn, determines the properties of materials. The genesis of solidification is nucleation, where the first stable solid forms from the liquid phase. Nucleation kinetics determine the degree of undercooling and phase selection. As such, it is important to understand nucleation phenomena in order to control solidification or glass formation in metals and alloys.

Early experiments in nucleation kinetics were accomplished by droplet dispersion methods [1-6]. Dilatometry was used by Turnbull and others, and more recently differential thermal analysis and differential scanning calorimetry have been used for kinetic studies. These techniques have enjoyed success; however, there are difficulties with these experiments. Since materials are dispersed in a medium, the character of the emulsion/metal interface affects the nucleation behavior. Statistics are derived from the large number of particles observed in a single experiment, but dispersions have a finite size distribution which adds to the uncertainty of the kinetic determinations. Even though temperature can be controlled quite well before the onset of nucleation, the release of the latent heat of fusion during nucleation of particles complicates the assumption of isothermality during these experiments.

Containerless processing has enabled another approach to the study of nucleation kinetics [7]. With levitation techniques it is possible to undercool one sample to nucleation repeatedly in a controlled manner, such that the statistics of the nucleation process can be derived from multiple experiments on a single sample. The authors have fully developed the analysis of nucleation experiments on single samples following the suggestions of Skripov [8]. The advantage of these experiments is that the samples are directly observable. The nucleation temperature can be measured by noncontact optical pyrometry, the mass of the sample is known, and post processing analysis can be conducted on the sample. The disadvantages are that temperature measurement must have exceptionally high precision, and it is not possible to isolate specific heterogeneous sites as in droplet dispersions.

Experimental Method

Levitation processing of refractory materials in ultra high vacuum provides an avenue to conduct kinetic studies on single samples. Two experimental methods have been identified where ultra high vacuum experiments are possible; electrostatic levitation in ground based experiments and electromagnetic processing in low earth orbit on TEMPUS [9]. Such experiments, reported here, were conducted on zirconium. Liquid zirconium is an excellent solvent and has a high solubility for contaminants contained in the bulk material as well as those contaminants found in the vacuum environment. Oxides, nitrides, and carbides do not exist in the melt, and do not form on the surface of molten zirconium, for the materials and vacuum levels used in this study.

Ground based experiments with electrostatic levitation have shown that the statistical nucleation kinetic experiments are viable and yield results which are consistent with classical nucleation theory [9]. The advantage of low earth orbit experiments is the ability to vary the flow conditions in the liquid prior to nucleation. The purpose of nucleation experiments in TEMPUS was to examine the effects of fluid flow on nucleation.

The primary evidence for a change in nucleation behavior is a shift in the mean undercooling. It is not necessary to know the functional form of the nucleation rate equation, or the operative mechanism to make the comparison of nucleation behavior under two different flow conditions. Simply stated, if the nucleation rate is different for two experimental conditions, then the parent distribution of nucleation events is different and the mean undercooling is different.

Null hypothesis testing is used to determine if the difference in means of two samples reflects a significant difference in the means of parent distributions for two experimental conditions. Two sets of data (A and B) can be compared by analysis of means using the null hypothesis.

The null hypothesis (H_0) is:

The mean nucleation temperature in experiment A and experiment B are identical.

and, the alternate hypothesis (H_1) is:

The mean nucleation temperature in experiment A and experiment B are different.

If H_0 is rejected and H_1 supported, then the means of the parent distributions are different and therefore the nucleation rate as a function of temperature is different.

The central limit theorem states that the means of samples from a population will be distributed normally, even if the population is not normally distributed. Nucleation temperature distributions, particularly those at low activation energies, are not normally distributed. However, in invoking the central limit theorem, no assumptions about the underlying distributions are necessary, and the means of two samples can be compared by using Student's "t" distribution [10].

Results and Conclusions

Statistical distributions of undercoolings were generated in "free cooling" experiments on TEMPUS. During free cooling the heater power is set to the lowest value, and the power input to the sample comes from the positioning field. One sample was repeatedly melted and cooled to freezing, holding all experimental variables constant except for the positioner power settings on cooling. Two different power supply settings were used; the lowest positioner power capable of stable positioning of the sample, and a high positioner power. The pure radiation cooling rate for this sample is 53Ks^{-1} . At the low positioner power the cooling rate was 50Ks^{-1} , and at the high positioner power the cooling rate was 48Ks^{-1} . Fluid flow calculations for the lower positioner power indicate the undercooled liquid is in the laminar flow regime with flows of approximately 4 cm s^{-1} and Reynolds numbers of about 200[11]. Modeling is continuing to characterize the flow regime corresponding to the higher positioner power which is known to be greater than the low

power. The experiments were interspersed to minimize any effect of sample history on the comparison.

The distributions of undercoolings for these experiments and the nucleation kinetic fits are shown in figure 1. A t-test for mean undercooling at the 95% confidence level supports the null hypothesis and rejects the alternate hypothesis. These experiments revealed there is no significant change in the nucleation behavior in the range of flow conditions tested.

The kinetic determinations made from the distributions, assuming the classical nucleation expression [12] are given in table I. These kinetic determinations are consistent with ground based experiments on zirconium using the electrostatic levitator. The kinetic values are similar to those for arc melted samples, and are lower than the maximum values ($\Delta T_{\text{mean}}=348\text{K}$, $K_v=10^{43}$, $\Delta G^*=88\text{kJ}$) obtained on a machined sample in the electrostatic levitator. The kinetic determinations are believed to be lower because of the temperature measurement uncertainty caused by sample translations on MSL-1. The maximum mean undercoolings from MSL-1 scale to the maximum achieved in the ESL if volume and cooling rate are considered.

Other experiments were conducted to determine the surface tension and viscosity of the undercooled melt [13], and to examine the heat capacity by noncontact modulation calorimetry [14]. To accomplish these experiments in the undercooled melt, the heater power was used to hold liquid samples at the desired temperature and pulsing or modulation of the heater was used to excite surface oscillations or to modulate the temperature of the sample. Experiments at low temperatures (and heater powers) were followed by free cooling to the nucleation temperature, which, in all cases was within the bounds of the distributions in the previous experiments. In experiments near the melting temperature, at heater voltages above 220 V, the undercooling of the samples was significantly limited as shown in figure 2. At 220 V heater the flows are estimated to be 50 cm s^{-1} . Initial analysis by Hyers and Trapaga indicates that at these flows the dynamic pressure is equal to the static pressure in the samples, a condition which is known to cause cavitation in fluid flows [15]. The collapse of cavitation bubbles creates sufficient pressures to raise the melting point of the material through the Clapyeron equation such that nucleation of the solid occurs [16-18].

Additional evidence of nucleation by cavitation can be found in the modulation experiments. A compilation of specific heat/total hemispherical emissivity (C_p/ϵ) determinations from the drop tube, electrostatic levitator and TEMPUS is shown in figure 3. The drop tube data was derived by measuring the release temperature of Zr pendant drops, the free fall time to recalescence in vacuum, and the nucleation temperature. In 135 experiments with masses around 0.23 g, the average ratio of specific heat to total hemispherical emissivity was 1.57 with a one sigma standard deviation of 0.03. In the electrostatic levitator, 332 cooling curves (four samples, mass range from 0.013 to 0.057 g) were evaluated by a sliding boxcar fit of the cooling curves to the radiation cooling equation solving for C_p/ϵ . The average value over the temperature range was 1.54 ± 0.12 (1σ). The TEMPUS modulation C_p/ϵ data falls within the bounds of these other determinations except for the experiment at the melting temperature. This determination is apparently 13-15% higher than the rest of the data. Other determinations indicate that there is no temperature dependence of C_p/ϵ in the measured range and do not support the findings of the TEMPUS

modulation experiment at the melting temperature. In essence, the melting temperature data showed a smaller modulation in temperature for the applied power modulation. The temperature modulations in this experiment were 10K above below the melting temperature at a frequency of 0.1Hz. A cyclic phase transformation including nucleation by cavitation and subsequent remelting provides a heat source during cooling and a heat sink during melting which explains the decrease in the temperature modulation around the melting point. This explanation is consistent with the above fluid flow calculations.

These experiments indicate that fluid flow has no effect on nucleation until the cavitation phenomenon occurs, and that cavitation induced nucleation is responsible for limiting bulk undercooling in the higher flow regimes.

References

1. D. Turnbull, J. Chem. Phys., **20** (3), 411 (1952).
2. D. Turnbull, J. Chem. Phys. **18**, 198 (1950).
3. J.J. Richmond, J.H. Perepezko, S.E. LeBeau, and K.P. Cooper, in "Rapid Solidification Processing: Principles and Technologies III" (R. Mehrabian, ed.), pp. 90-95, NBS, Gaithersburg, MD, 1982.
4. J.H. Perepezko, S.E. LeBeau, B.A. Mueller, and G.J. Hildeman, in "ASTM Conference on Rapidly Solidified Powder Aluminum Alloys" (M.E. Fine and E.A. Starke, Jr., eds.), pp. 118-136, ASTM-STP 890. Philadelphia, PA, 1985.
5. W.T. Kim, D.L. Zhang and B. Cantor, Met. Trans. A **22A**, 2487 (1991).
6. G.A. Merry and H. Reiss, Acta. Metall. V. 32, no. 9 (1984) p. 1447.
7. C.W. Morton, W.H. Hofmeister, R.J. Bayuzick, and M.B. Robinson, Mat. Sci. Eng. **A178** (1-2), 209 (1994).
8. V.P. Skripov, in "Current Topics in Materials Science, Crystal Growth in Materials, Vol. 2" (E. Kaldis and H.J. Scheel, eds.), p. 328, North Holland Publishing Co., New York, 1977.
9. C.W. Morton, W.H. Hofmeister, R.J. Bayuzick, A. Rulison, J. Watkins; submitted to Acta Materialia.
10. G.K. Bhattacharyya and R.A. Johnson; "Statistical Methods and Concepts", John Wiley and Sons, New York, 1977.
11. R. W. Hyers and G. Trapaga, MIT, personal communication.
12. D. Turnbull, and J.C. Fisher, J. Chem. Phys., **17** (1), 71 (1949).
13. I. Egry; J. Mat. Sci. **26** (1991) 2997-3003.
14. H.J. Fecht and W.L. Johnson; Rev. Sci. Instrum. V. 65, no. 5 (1991) p. 1299.
15. I.S. Pearsall; I. Mech. E., CME, July 1974, p. 79.
16. J.D. Hunt and K.A. Jackson; J. Appl. Phys. V. 37, no. 1 (1966) p.254.
17. R. Hickling; Nature, v. 206, no.4987 (1965) p. 915.
18. J.J. Frawley and W.J. Childs; Trans. AIME, v. 242, Feb. 1968, p.256.

Table I: Results of kinetic determinations of nucleation distributions from MSL-1R. The Classical Turnbull-Fisher expression was used to fit the distributions.

Positioner Power	Mean Undercooling $\Delta T_{\text{avg}} \pm 1\sigma$ (K)	$\log K_v$ ($\sigma \approx 3.0$)	ΔG^* (kT) ($\sigma \approx 7.0$)
Low	333.8 ± 4.8	29	62
High	334.7 ± 3.2	34	72

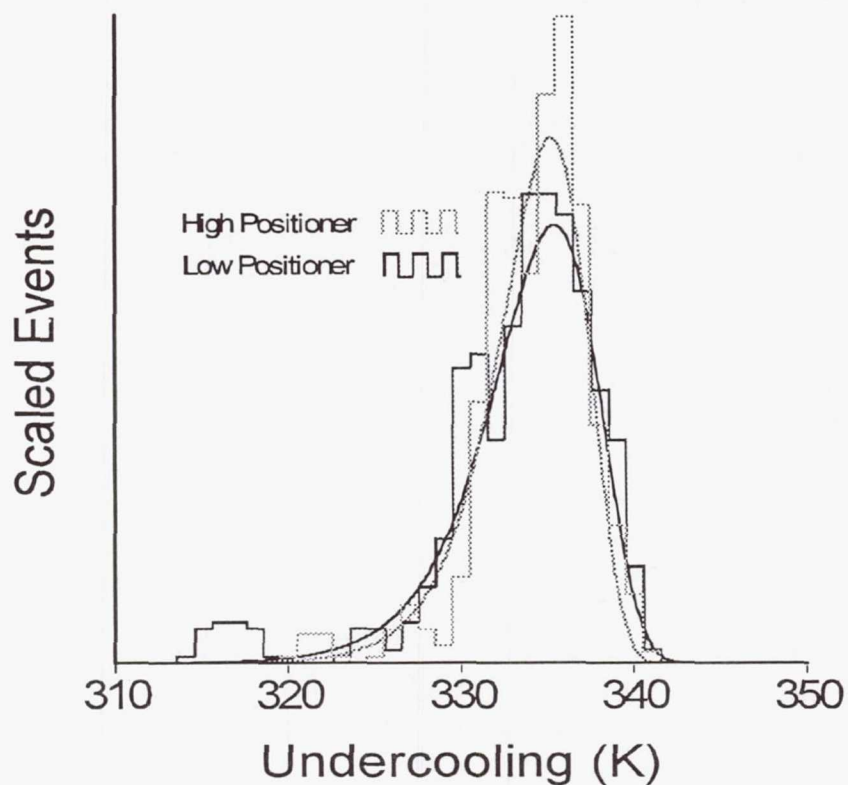


Figure 1: Two distributions from “free cooling” experiments on MSL-1R. The Low Positioner distribution is in the laminar flow regime and the High Positioner is believed to be in a transitional flow regime.

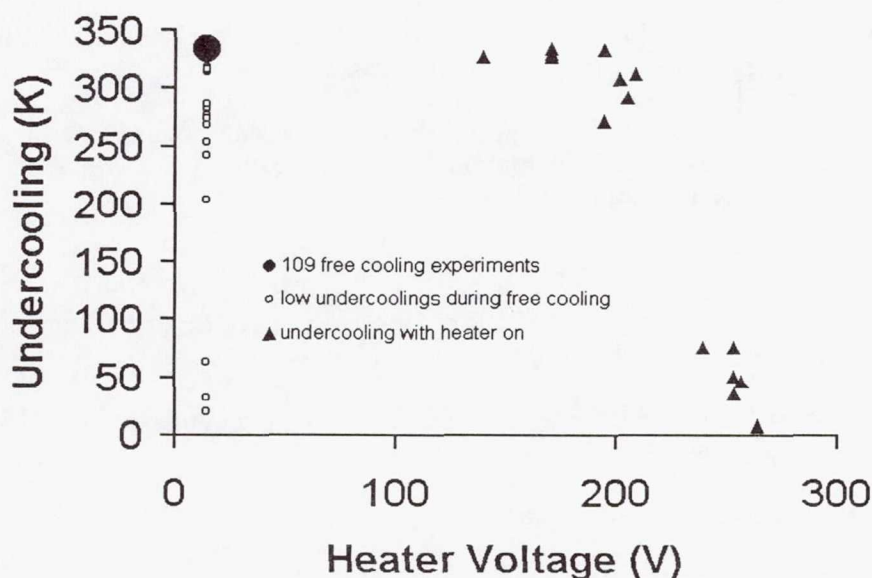


Figure 2: All zirconium undercoolings from two samples are compiled in this graph as a function of heater voltage applied during the cycle. Both distributions in figure 1 are contained in the large circle at the upper left. Samples processed above 220 V heater would not undercool to the same level as those cooled with less heater voltage applied.

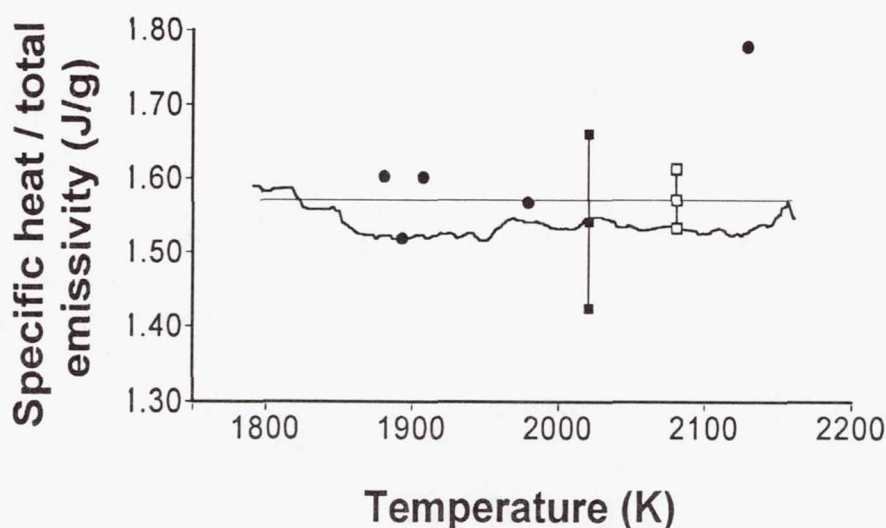


Figure 3: The ESL data as a function of temperature is plotted as the thick black line. The average ESL data over the temperature range is represented with filled squares. The drop tube data temperature range is represented with a thin straight line and the mean and one sigma points as open squares. The modulation calorimetry results from TEMPUS are given as filled circles.

Presentations of Flight Results:

"Nucleation in Metallic Melts," Chemical Engineering Seminar, Vanderbilt University, January, 1998.

"Effects of Fluid Flow on Nucleation," International Workshop on Nucleation and Thermophysical Properties of Undercooled Melts, Bad Honnef, Germany, March, 1998.

"Containerless Processing of Metallic Melts in Space," in special session on "Advancing Technology Through Space Experiments," International Conference on Powder Metallurgy and Particulate Materials, Las Vegas, NV, June, 1998.

Presentations in near future:

"State of the Art Materials Research using TEMPUS and Its Prospective Contributions to Industrial Applications," IN SPACE '98, Tokyo, Japan, September, 1998.

"Nucleation Experiments on TEMPUS in Low Earth Orbit," TEMPUS symposium, TMS, Rosemont, IL, October, 1998.

Related Flight Publications (not necessarily flight results):

"Evaluation of Statistical Analysis of Nucleation by Monte Carlo Simulation," W.H. Hofmeister, C.W. Morton, and R.J. Bayuzick; *Acta Metall.*, 46, 6 (1998) pp.1903-1908.

"The Kinetics of Solid Nucleation in Zirconium," C.W. Morton, W.H. Hofmeister, R.J. Bayuzick, A.J. Rulison, and J.L. Watkins; accepted for publication in *Acta Metall.*

526-26
434862

362732

Electromagnetic Containerless Processing Facility (TEMPUS)

101

Alloy Undercooling Experiments

Principal Investigator:

Dr. Merton C. Flemings
Massachusetts Institute of Technology
Cambridge, Massachusetts

ALLOY UNDERCOOLING EXPERIMENTS IN A MICROGRAVITY ENVIRONMENT

"Final results from the first Microgravity Sciences Laboratory (MSL-1R) mission"

Merton C. Flemings and Douglas M. Matson
Department of Materials Science and Engineering
Massachusetts Institute of Technology
77 Massachusetts Avenue Room 8-407
Cambridge, MA 02139

Phone : (617) 253-3233
E-mail : flemings@mit.edu, matson@mit.edu

Abstract

Molten samples of ternary steel alloys were successfully processed in a containerless fashion using the TEMPUS electromagnetic levitator during the first Microgravity Sciences Laboratory (MSL-1R) mission aboard the shuttle Columbia. Transformation from the metastable ferritic to the stable austenitic phase was observed following either spontaneous or triggered nucleation. Although the growth velocity of either phase in microgravity does not significantly differ from ground-based results (to greater than 88% confidence), a significant difference is seen in the delay between nucleation events (99% confidence). The possible reasons for deviation are discussed based on a new model for phase selection based on growth competition. Suppression of melt convection in microgravity is proposed as a potential explanation for the differences in delay times seen at low undercoolings.

Objectives

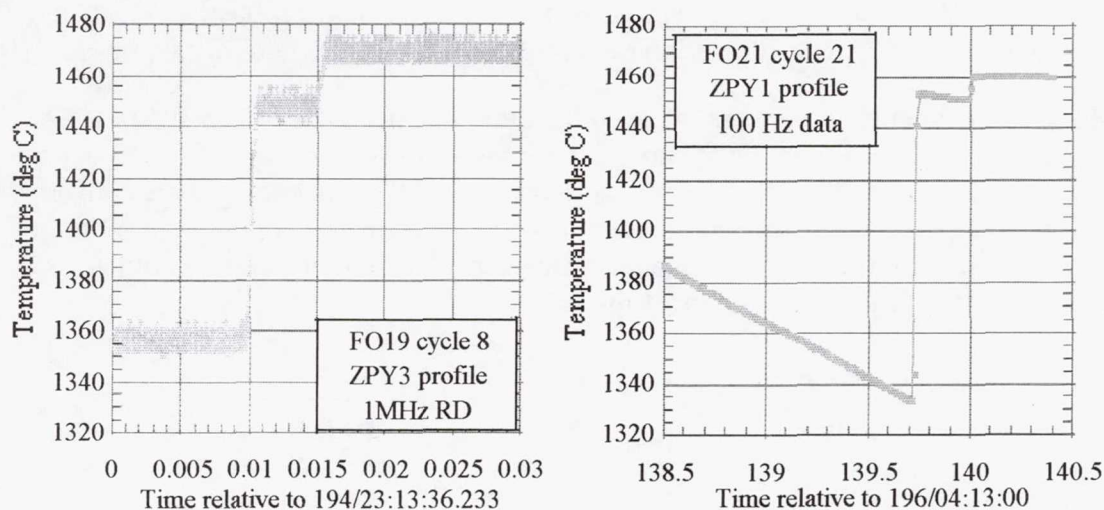
The focus of this program is the study of the effect of microgravity on metastable solidification of ternary steel alloys. By observing changes in the mechanism for nucleation of the stable phase following primary recalescence from undercooled melts, the role of convection in phase selection may be evaluated.

Background

Undercooling in containerless processing has shown promise in producing metastable phases and materials that exhibit improved chemical homogeneity and ultra-fine grain sizes. One aim of this research is to develop an understanding of the role of convection in the metastable to stable transition that has been observed in multi-component systems, notably in Fe-Ni and Fe-Cr-Ni alloys. The mechanism for nucleation of the second phase and the delay time observed in this transformation appear to be dependent on solid movement and coalescence, probably the result of convective flow.¹ Ground-based electromagnetic (EM) levitation experiments require maintaining a balance between the levitation force and gravity, while space experiments need far less energy to position the sample. With a reduction in melt convection² in μg , we have investigated the apparent changes in phase selection for these two different environments. Microgravity is thus an integral requirement for the successful attainment of the goals of this program.

Methods of Data Acquisition and Analysis

In collaboration with our Co-Investigator Wolfgang Löser of Institut für Metallische Werkstoffe (IFW-Dresden), the rapid solidification of two ternary steel alloys, a Fe-12wt%Cr-16wt%Ni and a Fe-16wt%Cr-12wt%Ni alloy, were investigated under containerless processing conditions. A high-speed digital video technique was used to image growth into the undercooled melt for both the metastable ferritic phase and the stable austenitic phase³⁻⁴. Above a critical undercooling, the metastable δ -phase nucleates first and, after a delay, a second thermal rise is observed during transformation to the stable γ -phase. This two step, or double recalescence phenomenon is highly compositionally dependent as seen in Figure 1 for the two different flight ternary steel alloys.



(a) Fe-12wt%Cr-16wt%Ni

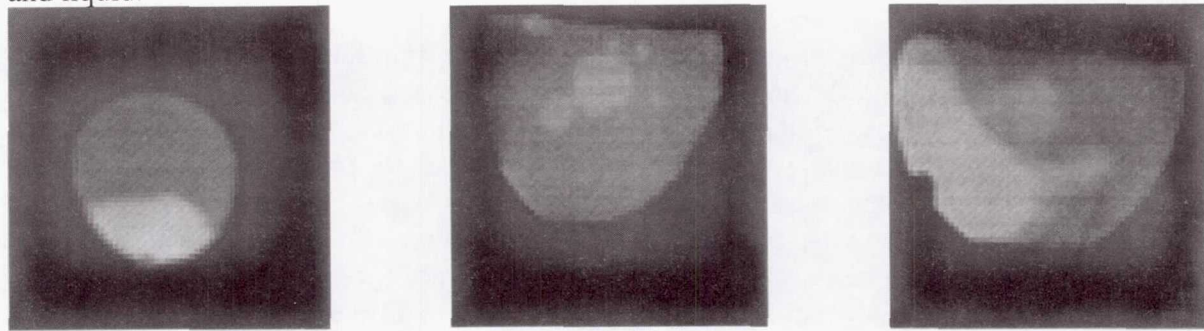
(b) Fe-16wt%Cr-12wt%Ni

Figure 1 - Double recalescence events observed during the MSL-1 mission

In the lower chromium hypoeutectic alloy, the transformation occurs on a time scale of microseconds while for the higher chromium eutectic composition the delay time is far longer. Double recalescence events were observed at temperatures consistent with the T_0 temperature of the bcc phase defining a value of the critical undercooling for metastable nucleation which is significantly lower than previously predicted.^{1, 5-8}

Figure 2 contains digital images taken at an acquisition rate of 40,500 frames/second during steel alloy double recalescence events⁹. In the first image, primary metastable phase nucleation was initiated at a known site using a stimulation trigger with subsequent growth into the undercooled liquid; growth of the second phase follows soon thereafter from the same nucleation site. In the second image, spontaneous nucleation of the second phase is seen, both from the primary nucleation site (in the center) and in other sites distributed within the semi-solid. The third image shows nucleation of the stable phase at the growing metastable phase front with subsequent competitive growth of both phases into the undercooled liquid. As seen in these images, ground-based double recalescence events show three types of mechanisms for nucleation

of the second phase, two within the semi-solid and one at the interface between primary phase and liquid.



(a) Triggered nucleation undercooled $\Delta T=145^\circ$ (b) γ growth in semi-solid undercooled $\Delta T=218^\circ$ (c) edge nucleation event undercooled $\Delta T=130^\circ$

Figure 2 - Digital images of growth competition in ground-based steel alloy solidification

For ground-based experiments, the growth of each phase into the melt is measured by tracking the position of the interface as a function of time as the front crosses the surface of the levitated droplet. The two dimensional video pixel (x, y) coordinates from the video images are converted into three dimensional (x', y', z') surface coordinates using a simple matrix technique.³ With knowledge of the position of the front in sequential frames and knowing the location of the nucleation point, the growth velocity may be evaluated.

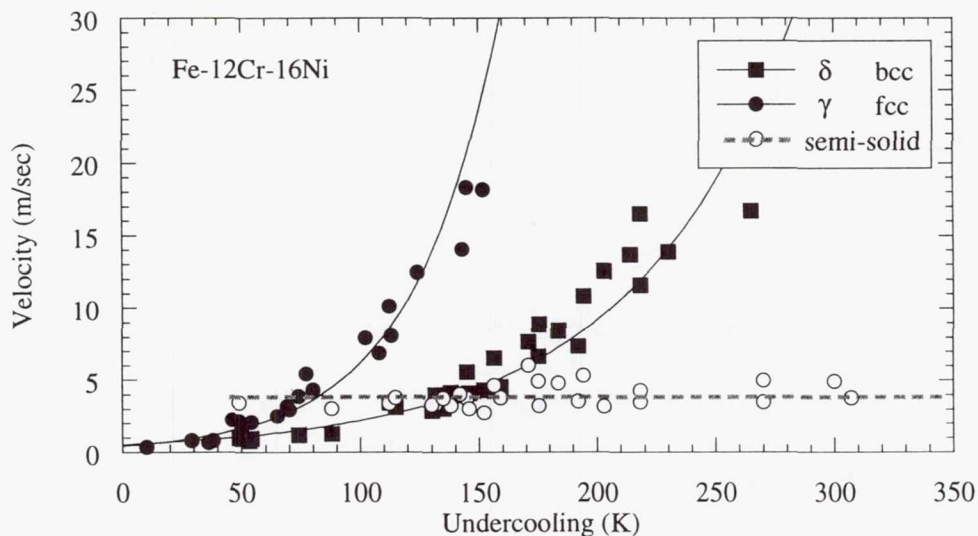


Figure 3 - Growth rate of each phase as measured in ground-based EM levitation testing

Solid symbols indicate growth into undercooled liquid

Open symbols indicate growth into the semi-solid following primary recalescence

As shown in Figure 3, at a given temperature the rate of growth into the undercooled liquid for the fcc gamma phase is greater than for the bcc delta phase. The velocity of the stable phase growing into the semi-solid which forms during primary metastable recalescence was also measured and, as seen in Figure 3, is independent of the initial undercooling. This effect has previously been observed in other ternary steel alloys⁹. The behavior arises because the driving

force for growth under these conditions is approximately constant given that the temperature following primary recalescence is always nearly the same at a given composition.

Depending upon the delay time between nucleation events, the bcc phase may be growing into the liquid at the same time as the fcc phase is growing into the semi-solid. During simultaneous growth at temperatures below the undercooling where the velocities of the two phases are equal, the metastable phase grows into the liquid faster than the stable phase grows within the semi-solid and thus a distinct double recalescence event is observed. Above this temperature, the equilibrium phase can overwhelm the slower metastable phase and break into the undercooled liquid. Such a double recalescence event can therefore appear as a single event. A model based on competitive growth of the two phases successfully predicts the limit where double recalescence events may be detected as a function of the geometric relationship between the sensor and the nucleation site.

Flight Results

Molten samples of the ternary steel alloys were successfully processed in a containerless fashion using the TEMPUS electromagnetic levitation facility aboard the shuttle Columbia during the MSL-1R/STS-94 mission. The solidification rate was measured as a function of undercooling using a combination of live video downlink and the onboard recording of a perpendicular set of two high-speed pyrometers. Growth velocities were measured by taking the spot size of the pyrometer target and dividing by the rise time. Nucleation was induced at a known site within the field of view using a ZrO_2 -coated stimulation needle.

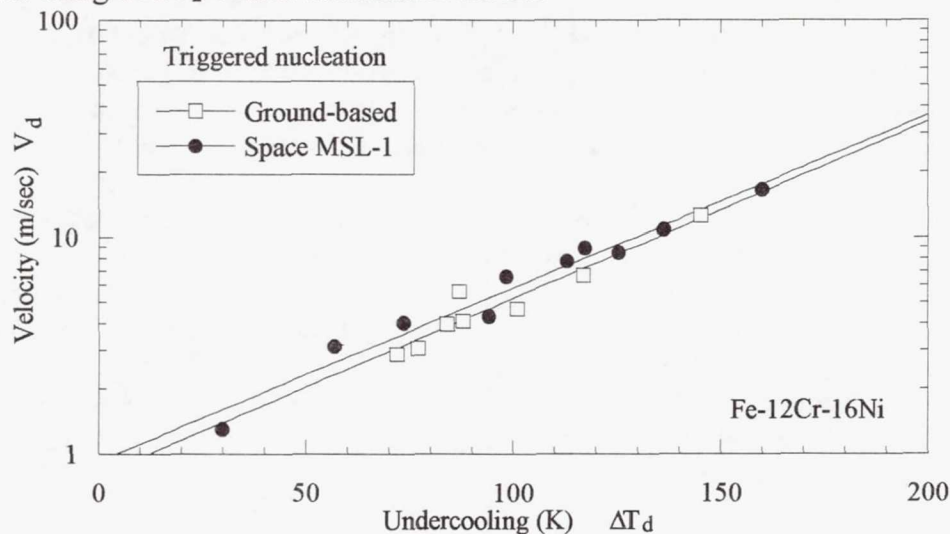


Figure 4 - Growth rate of the metastable phase into the liquid during primary recalescence

Figure 4 shows a comparison between the growth rate of the metastable phase into the undercooled liquid for ground-based and MSL-1 microgravity experiments. By employing a two-sided t-test we found that there is no significant difference between these two conditions to a confidence level of 88%. In a similar manner, the velocity for growth of the stable phase into the semi-solid following primary recalescence was also evaluated and found to be the same in space and on the ground with a confidence level of 97%.

Figure 5 shows a comparison between the observed delay times measured adjacent to the nucleation stimulation point in space and on the ground; significant positive deviation (to a confidence level of 99%) is observed in space. These results are consistent with our hypothesis that convection may influence the formation of secondary nucleation sites.

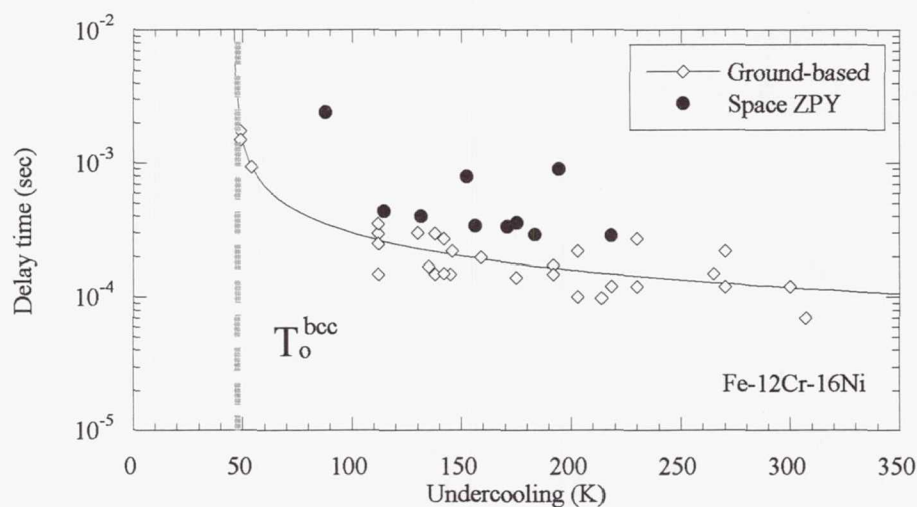


Figure 5 - Delay times under ground-based and space conditions

A growth competition model was developed to predict which phase would be seen, given a known relationship between the nucleation site and the location of the sensor used to monitor the passage of each of the fronts during recalescence. This model was based on ground-based measurements of the propagation velocities and delay times and includes the assumption that secondary nucleation will occur within the semi-solid – either at the primary site or distributed within the semi-solid. The model was intentionally designed to fail to include edge nucleation events as these are assumed statistical in nature. In the case where a single recalescence event is detected when a double recalescence event was predicted, ground-based results show that this occurrence is associated with the edge nucleation mechanism. In terrestrial tests on the flight Fe-12Cr-16Ni master alloy this was observed to occur in 71% of the tests below an undercooling of 150° and in none above this undercooling. In μg tests during MSL-1, this was never observed at any undercooling level and we therefore associate the occurrence of the edge nucleation mechanism with ground-based conditions.

In addition to being able to predict which phase will be observed, the growth competition model allows prediction of what the delay time should be, as a function of sensor position relative to the nucleation site. Using the growth competition model, we have defined a deviation parameter,

$$\theta_d = \left(\frac{\tau_o}{\tau_p} \right) - 1$$

based on the ratio of the observed, τ_o , to predicted, τ_p , delay times. This parameter may then be used to compare the ground-based and space results to a common theoretical baseline.

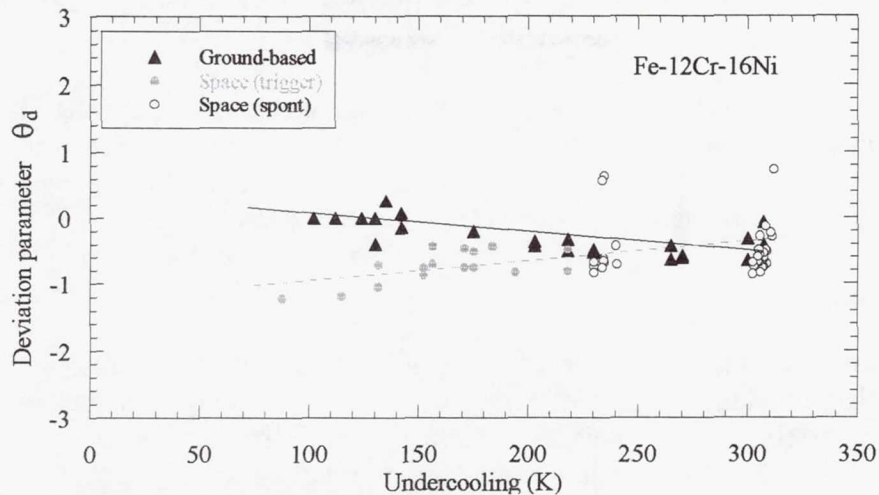


Figure 6 - Variation of the deviation parameter

This comparison is shown in Figure 6 where significant negative deviation is seen for flight experiments at low undercoolings. This effect is due to the increased delay times observed during MSL-1 compared to those measured in ground-based tests, as seen earlier in Figure 5.

Four possible reasons for the difference between the deviation parameter observed in ground-based and in space experiments have been identified. These are :

- (1) Method of data collection
- (2) Alloy composition
- (3) Cooling rate
- (4) Melt convection

The use of the deviation parameter allows comparison of sensors at different orientations and of differing geometry – results are based on deviation from a common basis and thus not due to simple changes in the data collection technique. The use of either pyrometer or a video camera can thus be normalized since they both rely on a rise in radiative intensity resulting from passage of the thermal front through the field of view during recalescence. The deviation between ground and flight data can thus not be associated with this difference through careful design of the analysis technique.

Alloy composition and cooling rate can also be eliminated by experimental design. Three data sets exist for the Fe-12wt%Cr-16wt%Ni alloy, two were obtained from measurements conducted in ground-based testing and one in space. The ground testing at Dresden was conducted on the same master alloy material as was flown during MSL-1 (and in fact was accomplished on flight spare samples following the mission); there was no significant difference in either composition or in oxygen/trace metal contamination detected. Ground testing at MIT was conducted on samples prepared to obtain the identical baseline composition but with significantly less oxygen - 10 ppm as compared to the flight sample value of 25 ppm. There was no significant difference between the two ground test series based on observed delay times while there was a difference when either is compared to the space data. In a like manner, the flight and MIT tests were conducted at a nominal cooling rate of 50 degrees/second while the Dresden tests were run at a

cooling rate of 5-10 degrees/second. Again, no difference was seen between ground-based data sets.

Melt convection remains as the only source of difference in delay times identified during this test program. It is interesting to note that the difference is most pronounced at low undercoolings and appears to have two distinct sources – the occurrence of edge nucleation events in ground based tests and a significant shift to longer delay times in space.

Conclusions

Double recalescence events were observed in hypoeutectic ternary steel alloys at much lower undercoolings than previously reported. Using a high speed imaging technique, we are able to identify and characterize the mechanism for nucleation of the stable phase after the initiation of metastable phase growth. We have shown evidence that nucleation of the stable phase at the interface between the growing metastable phase and the liquid may be suppressed in microgravity.

When comparing the growth rate under ground-based and microgravity conditions, there is no significant difference for the observed growth of the metastable phase into the undercooled liquid over the range of undercoolings investigated. There is also no significant difference in the growth rate of the stable phase into the semi-solid that formed during primary recalescence. There is, however, a significant difference in the delay between primary and secondary recalescence.

We have successfully developed a model that combines :

- (1) simultaneous growth of competing phases,
- (2) the delay between recalescence events,
- (3) assumptions on the mechanism for secondary nucleation of the stable phase, and
- (4) given a known relationship between the sensor and the nucleation events

to explain the role of growth competition in phase selection during rapid solidification of undercooled hypoeutectic Fe-Cr-Ni alloys. Using this model, we have demonstrated that a difference exists between the high convective environment of ground based electromagnetic levitation and that attainable in microgravity.

In the future, we will be developing models to explain the role of convection in selection of the mechanism for nucleation of the second phase - either along the growing metastable interface or within the semi-solid. We will also be investigating the growth rate of the stable phase into the semi-solid, which forms following primary solidification.

References

1. T. Koseki and M.C. Flemings, *Met. Trans.*, **26A**, 2991 (1995).
2. G. Trapaga, D.M. Matson, R. W. Hyers, and M.C. Flemings, in **Proc. Julian Szekely Memorial Symposium on Materials Processing**, H. Y. Sohn, J. W. Evans, and D. Apelian, eds., TMS Warrendale PA, 453 (1996).
3. D.M. Matson, in **Solidification 1998**, S.P. Marsh *et al.*, eds., TMS Warrendale PA, 233 (1998).
4. J.W. Lum, D.M. Matson, and M.C. Flemings, *Met. Trans.*, **28B**, 865 (1996).
5. T. Koseki and M.C. Flemings, *Met. Trans.*, **27A**, 3226 (1996).
6. T. Volkman, W. Löser, and D.M. Herlach, *Met. Trans.*, **28A**, 453 (1997).
7. T. Volkman, W. Löser, and D.M. Herlach, *Met. Trans.*, **28A**, 461 (1997).
8. S. Moir and D.M. Herlach, *Acta Mater.*, **45**(7), 2827 (1997).
9. D.M. Matson, A. Shokuhfar, J.W. Lum, and M.C. Flemings, in **Solidification science and processing**, I. Ohnaka and D.M. Stefanescu, eds., TMS Warrendale PA, 19 (1996).

Bibliographic Citations

Articles

- G. Trapaga, D.M. Matson, R. W. Hyers, and M.C. Flemings, "Mathematical Modeling of Electromagnetically Levitated Metallic Melts in the Observation of Solidification Phenomena", in **Proc. Julian Szekely Memorial Symposium on Materials Processing**, H. Y. Sohn, J. W. Evans, and D. Apelian, eds., TMS Warrendale PA, 453 (1996).
- U. Thiedemann, M. Roesner-Kuhn, D. M. Matson, G. Kuppermann, K. Drewes, M. C. Flemings, and M. G. Froberg, "Mixing Enthalpy Measurements in the Liquid Ternary System Iron-Nickel-Chromium and its Binaries", *Steel Research*, **69**[1], pp. 3-7, (1998).
- D.M. Matson, "The Measurement of Dendrite Tip Propagation Velocity During Growth into Undercooled Metallic Melts", in **Solidification 1998**, S.P. Marsh *et al.*, eds., TMS Warrendale PA, 233 (1998).
- W. Hofmeister, R. J. Bayuzick, G. Trapaga, D. M. Matson, and M. C. Flemings, "Observation of Thermal Profiles during Impact and Solidification of Nickel Drops", in **Solidification 1998**, S. Marsh *et al.*, eds., TMS Warrendale PA, pp. 375-387, (1998).
- M. Roesner-Kuhn, D. M. Matson, K. Drewes, U. Thiedemann, G. Kuppermann, M. C. Flemings, and M. G. Froberg, "Enthalpies and Heat Capacities of Liquid Fe-Cr-Ni Alloys with the Focus on Pure Liquid Chromium", *Thermochimica Acta*, **314**, pp. 123-129, (1998).
- D. M. Matson and M. C. Flemings, "Phase selection and rapid solidification of undercooled Fe-Cr-Ni steel alloys in microgravity", TMS conference proceedings, Rosemont IL, (1998).
- M. Barth, D. Holland-Moritz, D. M. Herlach, D. M. Matson, and M. C. Flemings, "Dendrite growth velocity measurements in undercooled Ni and Ni-C melts in space", TMS conference proceedings, Rosemont IL, (1998).

Presentations

- "Alloy Undercooling Experiments", NASA/DARA International Working Group Review Meeting, February 29, Regensburg GDR, (1996).
- "Developing a High-speed Scanning Pyrometer to Image Metallic Droplet Solidification", Invited Departmental Seminar, Department of Metallurgy and Materials Engineering, University of Connecticut, April 30, Storrs CT, (1997).
- "The Measurement of Dendrite Tip Propagation Velocity During Growth into Undercooled Metallic Melts", Invited Seminar, 1998 TMS Annual Meeting, February 17, San Antonio TX, (1998).
- "Delay times and Critical Undercooling", NASA/DLR Conference on Nucleation and Thermophysical Properties of Undercooled Melts, March 4, Bad Honnef GDR, (1998).
- "Growth competition during double recalescence in Fe-Cr-Ni alloys", Invited Seminar, Laboratoire de Metallurgie Mecanique, June 2, Ecole Polytechnique Federale Lausanne, Suisse CH, (1998).
- "Recent results from the STS-83 and STS-94 missions" NASA microgravity Materials Science Conference, July 15, Huntsville AL, (1998).

Program Summary

Samples of steel alloys were investigated using the TEMPUS containerless processing technique aboard Columbia during the first Microgravity Science Laboratory (MSL-1) mission. The samples were electromagnetically melted and then the molten metal was allowed to cool to below its melting point. Pictures of how the samples solidified and measurements of the thermal profile were transmitted to the operations center on the ground in near real-time to control the progress of the experiment. A significant difference was seen between experiments that were run in space and on the ground based on which crystal phase was observed to grow. A change was also seen in both when and where the transformation from one phase to another begins. It is now thought that this apparent difference in phase selection may be influenced by melt convection.

omit the
PAGE

Electromagnetic Containerless Processing Facility (TEMPUS)

Measurement of Surface Tension Viscosity of Undercooled Liquid Metals

Principal Investigators:

Dr. Merton C. Flemings
Dr. Gerardo Trapaga
Massachusetts Institute of Technology
Cambridge, Massachusetts

THE MEASUREMENT OF THE VISCOSITY AND SURFACE TENSION OF UNDERCOOLED MELTS UNDER MICROGRAVITY CONDITIONS AND SUPPORTING MHD CALCULATIONS

Robert Hyers, Gerardo Trapaga, and Merton C. Flemings

Department of Materials Science and Engineering

Massachusetts Institute of Technology

(617) 253-3236

rwhyers@mit.edu, trapaga@navier.mit.edu, flemings@mit.edu

10P.

362733

SINGLE SCAN

527-29

434863

Abstract

Successful containerless measurement of the viscosity of a liquid metal was demonstrated for the first time during these microgravity experiments, both for the superheated and undercooled regimes. Also, high-precision containerless measurements of surface tension were performed as a part of these experiments.

These measurements were performed in TEMPUS as a part of the MSL-1 Space Shuttle missions (STS-83 and -94). Electromagnetically levitated metal samples were melted and surface oscillations excited. The frequency of the oscillations is determined by the surface tension of the liquid metal, and the damping of the oscillations by the viscosity. Results were obtained for pure metals (Zr), glass-forming alloys (PdSi, 4 Zr-based alloys), and steels (FeCrNi). Results for PdSi are presented here; the results for the other materials will be published later.

Objectives of the Investigation

The scientific and technical objective of our experiment in the MSL-1 space shuttle mission was to utilize the electromagnetic levitation (EML) system, TEMPUS, for the experimental determination of the surface tension and the viscosity of metallic melts, in both the superheated and the undercooled state, using the unique attributes of microgravity. This objective was achieved on both the STS-83 and STS-94 shuttle missions for several different metals.

In addition, the development of a mathematical model aimed at representing the magnetohydrodynamic phenomena in levitated samples represented an important component of the project. This model has provided the means for the understanding of the role of the different processing parameters on the behavior of the samples during the experiments, as well as an important tool for the design of the actual experiments.

Significance

The containerless measurement of viscosity has been demonstrated for the first time on a liquid metal. The ability to measure surface tension and viscosity while avoiding the contamination and heterogeneous nucleation of container walls enables measurement of the properties of undercooled liquid metals. Accurate knowledge of thermophysical properties of liquid metals

over a wide temperature range is important to a number of fields, including process modeling, studies of nucleation and growth, and theories of the liquid state.

Necessity of Microgravity

Ground based experiments with the oscillating droplet technique introduce an inherent systematic error in the measurement of surface tension. In addition, the perfect symmetry of the samples, possible only in microgravity conditions, eliminates the splitting of oscillation modes that is observed in ground-based experiments. Based on purely theoretical grounds, Cummings and Blackburn^[1] have developed a correction for gravitational and electromagnetic effects on the apparent surface tension; one of the accomplishments of the IML-2 flight was to provide the first experimental results suggesting the validity of the correction factor. Surface tension data from the MSL-1 flights suggest that this correction factor, while only about 1-3% for microgravity experiments, is still relevant even for these experiments.

The reason for performing measurements of viscosity under microgravity conditions is quite different. Under earthbound conditions, the levitation forces needed are quite high and the associated rotational component of that force (the curl of $\mathbf{J} \times \mathbf{B}$) gives rise to transitional or turbulent flows, making the measurement of viscosity impossible for normal metals. However, in microgravity, this internal flow velocity may be greatly reduced because much smaller positioning forces (i.e., about 300 times smaller than under earthbound conditions) are needed to contain the sample. These reduced forces allow a laminar flow condition which will not interfere with the droplet oscillations.

Experimental Method and Data Analysis

In a typical experiment, a thermal cycle is prescribed where a sample is heated, melted and superheated, and then allowed to cool. As the droplet cools, the heating field is pulsed to excite surface oscillations. This sample processing is illustrated in Fig. 1 where seven pulses are shown during the cooling step. Each of these pulses represents a measuring point providing surface tension and viscosity data for a particular temperature range.

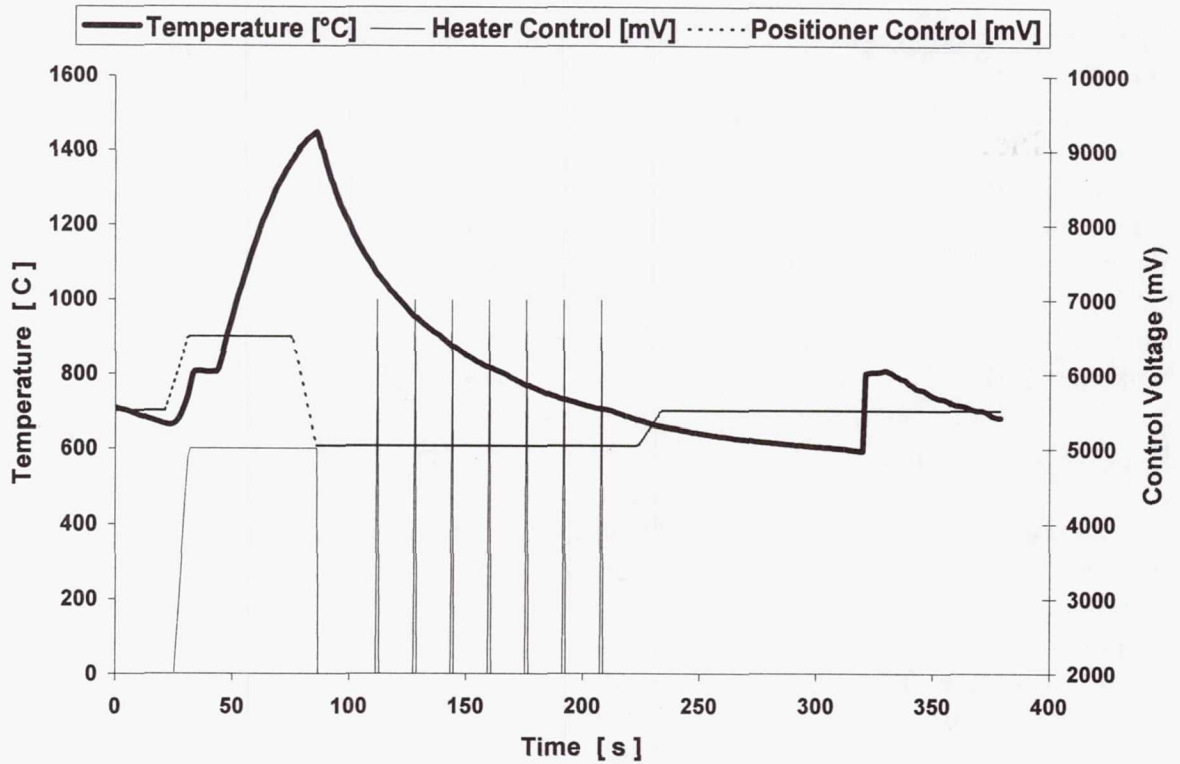


Fig 1: Typical thermal profile for droplet oscillation experiments in TEMPUS. Sample is melted As the droplet cools, the heating field is pulsed to excite surface oscillations. The sample recalesces and is fully solidified, then mechanically damped in preparation for the next cycle.

The surface oscillation are recorded on video. The apparent area of the droplet is measured for each frame yielding the measured area-time signal (Fig. 2.a). A Fourier power spectrum is taken of this signal to find the frequency of the surface oscillation (Fig. 2.b) which is related to the surface tension by Rayleigh's equation:

$$\omega_l^2 = \frac{l(l-1)(l+2)\gamma}{\rho R_o^3} \quad (\text{eq. 1})$$

where ω_l is the angular frequency of oscillation mode l , for a droplet of surface tension γ , density ρ , and radius R_o . The mode $l = 2$ is the fundamental mode of surface oscillations.

A band-pass filter (flat-topped Hamming widow) is used to isolate the component of the area-time signal which is due to surface oscillations (Fig. 2.c). The damping time τ of these oscillations is related to the viscosity, μ , by Lamb's equation:

$$\tau_l = \frac{\rho R_o^2}{(l-1)(2l+1)\mu} \quad (\text{eq. 2})$$

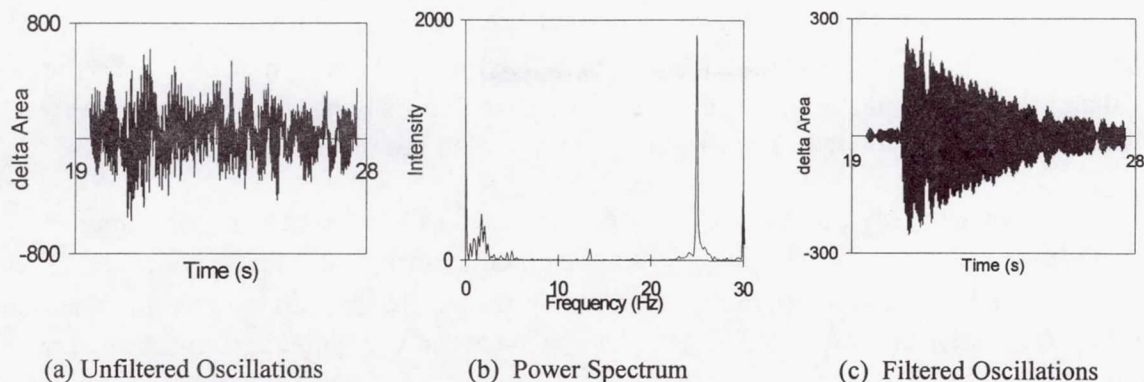


Fig 2: MSL-1(STS-83) experimental data Pd-18Si sample, excited oscillations at 1215C. Power Spectrum of the unfiltered oscillation shows a surface tension peak visible at 25.0 Hz, which corresponds to a surface tension of 1.7 N/m and (c) filtered oscillations with exponential damping constant of 3.42s, giving viscosity 9.0 mPa-s.

Flight Results

Surface tension and viscosity data are presented in Figs. 3 and 4 for a Pd-18Si alloy for a wide range of temperatures (725 - 1425C), covering up to 100 C of undercooling and 650 C of superheat.

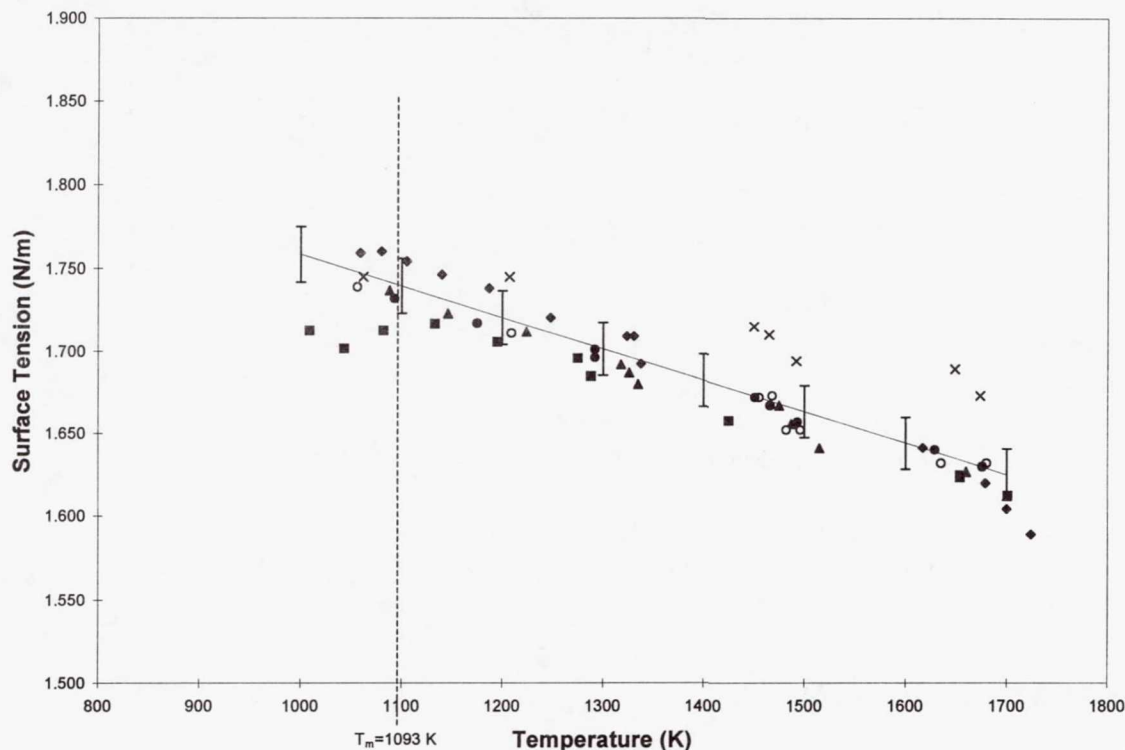
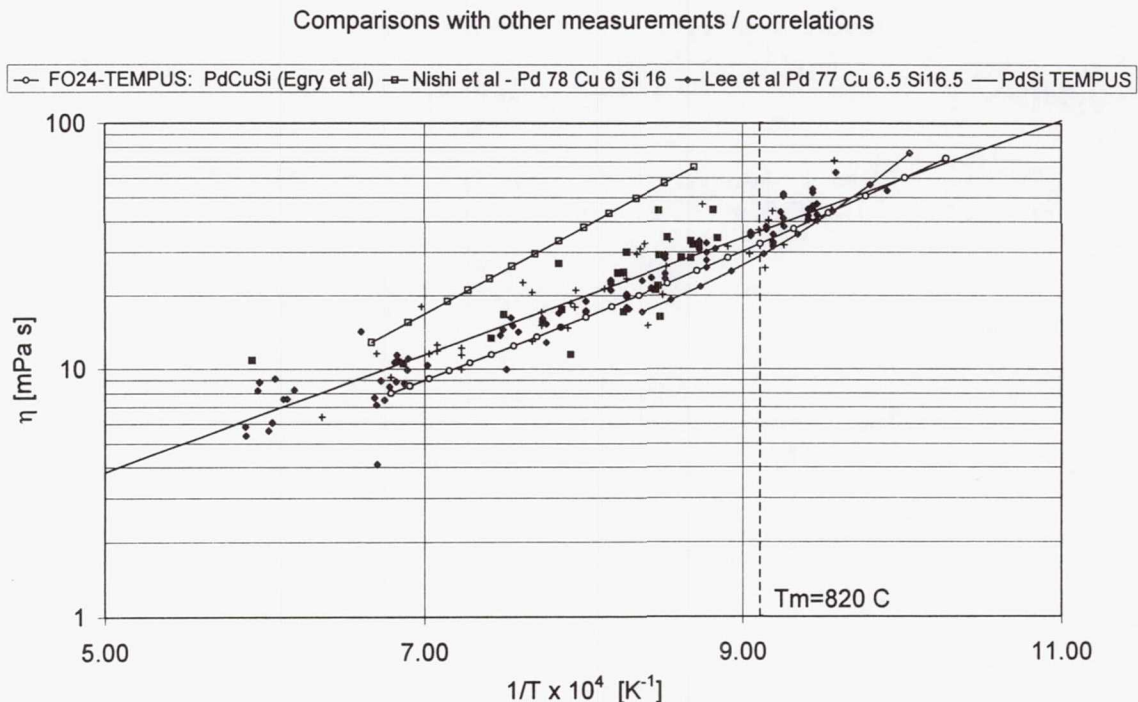


Fig 3: Corrected surface tension data for Pd-18Si.

Surface tension data are corrected and fitted as a function of temperature as $\gamma = 1.949 - 1.91 \times 10^{-4} T$, for surface tension γ in N/m and T in Kelvin, to a standard error of better than 1%. The application of Cummings and Blackburn's correction for electromagnetic forces to these points provides a significant improvement in the scatter of these data.

Measurements of viscosity for this alloy may be correlated as a function of temperature, as $\mu = 0.1917 \exp(5754/T)$, for viscosity μ in mPa-s and temperature T in Kelvin. The viscosity data presented in Fig 4, are compared with experimental correlations reported by other authors [2]-[4] for this and similar glass-forming alloys. These data are in very good agreement and prove that the oscillation drop technique is capable of providing containerless measurements of viscosity.



The results described above represent a small portion of the data acquired on the MSL-1 missions. Additional results are forthcoming for other alloy systems: Zr, FeCrNi, ZrNiCuAlNb and TiZrCuNi

Magnetohydrodynamic Calculations

Calculations of the magnetohydrodynamic flow in the droplets allow comparison of flow conditions between different experiments and samples. These calculations were an important part of the planning of these experiments, and contributed significantly to the importance and utility of the results. Due to lack of space only two illustrations are presented in this report.

Characteristic internal flow patterns in the droplet are determined depending on the parameters employed during specific experiments. Fig.5 shows calculated flow fields for a 7mm Zr sample in TEMPUS for a constant coil positioner current (100A) and various coil heating currents. These computed results illustrate possible control regimes of the flow and the transition from positioning- dominated to heating-dominated flow, within this range of parameters.

The figure indicates that as the current in the heating coil is increased, the forces from the heating field oppose the flow of the positioner's equatorial recirculating loops and augment the flow of the positioner's polar loops. Because the force due to the heating field is directed inward at the equator, this force should augment loops with flow inward near the equator and out at the poles and suppress circulations with the opposite direction. Thus, the original four-loop (positioner-dominated) flow pattern, becomes a two-loop (heater dominated) pattern, as the heater current is increased and the outward-flowing equatorial loops of the positioner-dominated pattern slow to extinction. During this flow transition, the droplet mean and maximum velocities undergo a decrease, as the faster loop of the positioner-dominated pattern is slowed, but when the heater forces become dominant, the velocity resumes the expected increase with increasing heater current.

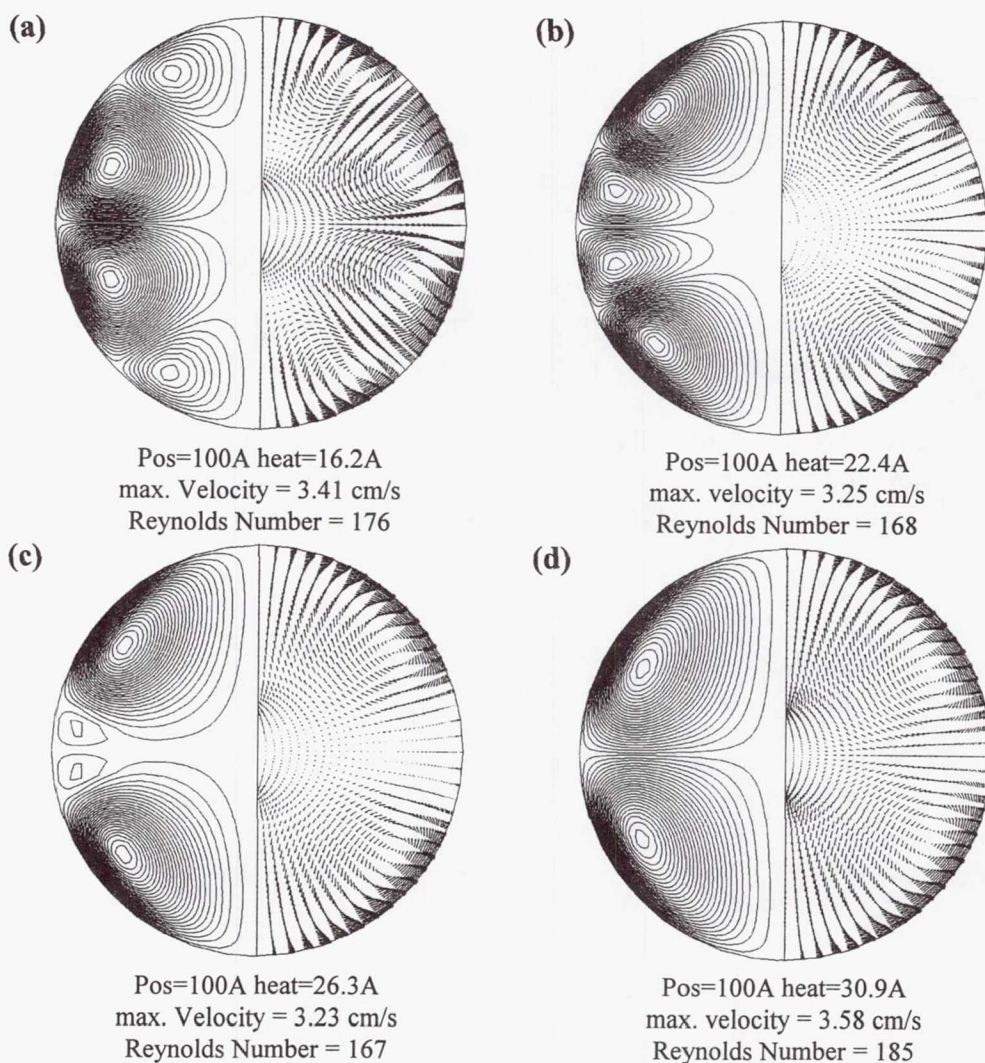


Fig 5: Development of flow pattern for increasing heating current at constant positioning current of 100A for 7mm Zr sample. The heating forces oppose the rotation of the faster positioner loop, so the increasing heating forces cause the faster loop of the positioner flow to slow and disappear, while the slower positioner loop becomes faster.

Another important result of the modeling work involves the analysis of the role of fluid flow during nucleation experiments in microgravity for Zr samples (in collaboration with the Vanderbilt team^[5]). These experiments found that the maximum undercooling was independent of the applied heating field only up to about 200V in the heater oscillating circuit, and that undercooling was inhibited at higher voltages.

The MHD model suggests that this effect was caused by cavitation. The calculations show a locally reduced pressure in the recirculation loops; this reduction would give a negative local pressure for a heating field corresponding to 225V (Fig. 6). This local state of hydrostatic

tension provides a driving force for cavitation. The collapse of bubbles then promotes the nucleation of the solid phase.

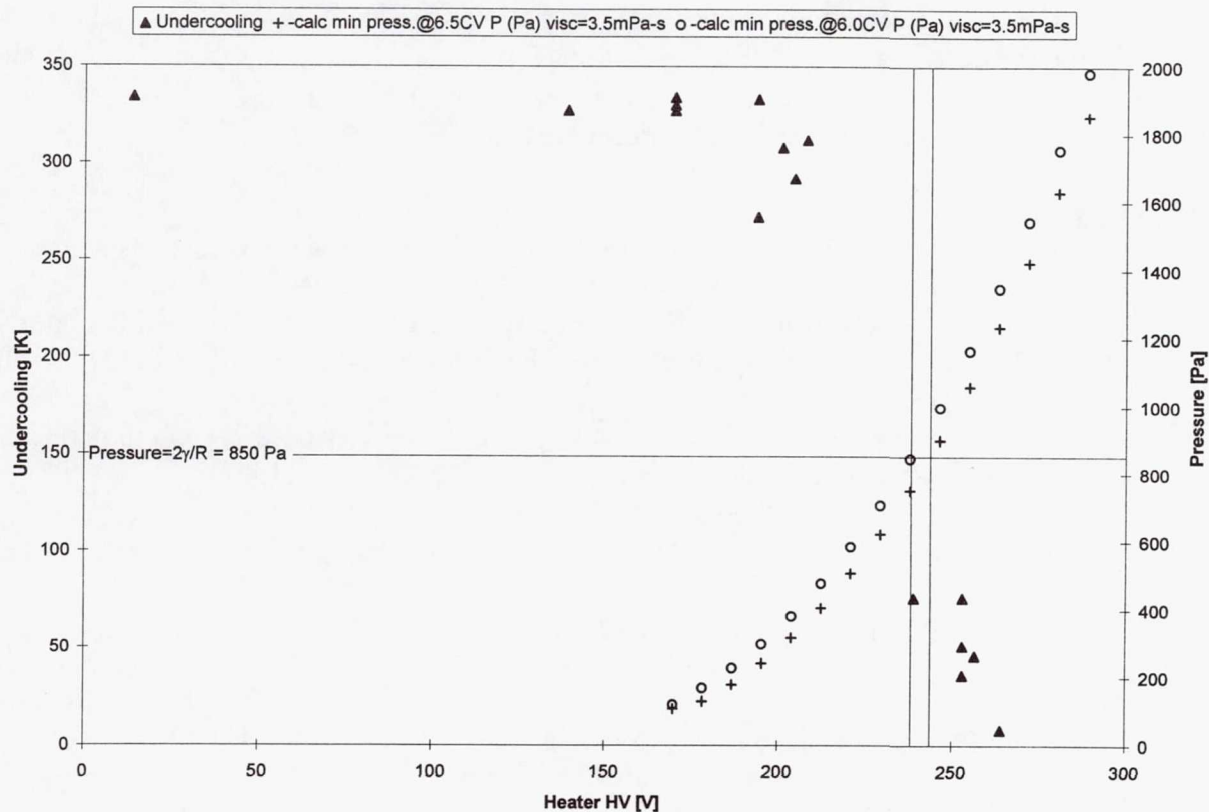


Fig 6: Undercooling as a function of applied heater voltage for a 7mm Zr sample.

Conclusion

Experiments carried out during the STS83 and STS94 mission provided successful containerless viscosity measurements using EML for a wide range of temperatures and viscosities. Also resulted precise, containerless measurement of surface tension and its temperature dependence over a wide temperature range. Analysis of surface tension data indicated that Cummings and Blackburn's correction, while only 1-3 % for these microgravity experiments, is still important.

The theoretical analysis, based on the use of mathematical modeling techniques, proved to be very useful to provide important information for the design and analysis of EML experiments. As illustrated in this report, the modeling work allowed to obtain some important insight into the role of internal flows on the behavior of the droplet for different samples and type of experiments, for example by providing a plausible explanation of the occurrence of dynamic nucleation in nucleation experiments for Zr.

Future Work

- Characterize the limits of this technique in terms of operational parameters.
- Extend to electrostatic levitation (ESL).
- Detailed analysis of the sources and magnitudes of error.
- New measurements on these and other materials of interest, including more pure metals, industrial alloys, and semiconductors.

References

- [1] D.L. Cummings and D.A. Blackburn, "Oscillations of Magnetically levitated Aspherical Droplets", *J. Fluid Mech.*, Vol. 224, 395-416 (1991).
- [2] Y. Nishi, N. Kayama, S. Kiuchi, K. Suzuki and T. Masumoto, "Viscosities and Glass Formation of $\text{Pd}_{84}\text{Si}_{16}$ Alloy and $\text{Pd}_{78}\text{Cu}_6\text{Si}_{16}$ Alloy" *J. Japan Inst. Metals*, Vol. 44, No. 12, pp. 1336-1341 (1980).
- [3] S.K. Lee, K.H. Tsang and H.W. Kui, "Viscosity of molten $\text{Pd}_{77}\text{Cu}_{6.5}\text{Si}_{16.5}$ and the Principle of Corresponding States", *J. Appl. Phys.*, Vol. 70, No. 9, pp. 4842 (1991).
- [4] I. Egry, G. Lohöfer, *et al.*, MSL-1 Results for PdCuSi , priv. comm.
- [5] R. Bayuzick, W. Hofmeister, *et al.*, MSL-1 Results for Zr, priv. comm.

Articles and Presentations Resulting from this Work

- R.W. Hyers, G. Trapaga, and M.C. Flemings, "The Measurement of the Viscosity and Surface Tension of Undercooled Melts Under Microgravity Conditions and Supporting MHD Calculations", NASA Microgravity Materials Science Conference, Huntsville, AL, July 1998.
- G. Trapaga, R.W. Hyers and M.C. Flemings, "Measurements of Surface Tension and Viscosity Using TEMPUS: Preliminary Results and Future Directions", Workshop on nucleation and thermophysical properties of undercooled melts, Bad Honnef, Germany, 1998.
- R.W. Hyers, G. Trapaga, and M.C. Flemings, "Mathematical Modeling of Electromagnetically Levitated Metallic Melts for Thermophysical Property Measurements", Materials Day 1997, MIT, Cambridge, MA, October 1997 (poster presentation).
- G. Trapaga, D.M. Matson, R.W. Hyers, and M.C. Flemings, "Mathematical Modeling of Electromagnetically Levitated Metallic Melts in the Observation of Solidification Phenomena", in *Proceedings of the Julian Szekely Memorial Symposium*, H.Y. Sohn, J.W. Evans, and D. Apelian, *Eds.*, TMS, Cambridge, MA, October 1997.
- M.C. Flemings, G. Trapaga, and R.W. Hyers, "The Measurement of the Viscosity and Surface Tension of Undercooled Melts Under Microgravity Conditions and Supporting MHD Calculations", NASA Microgravity Materials Science Conference (*NASA Conference Publication 3342*), Huntsville, AL, June 1996.
- Szekely, J., E. Schwartz, and R. Hyers, "Electromagnetic Levitation – a Useful Tool in Microgravity Research", *JOM*, vol. 47, no. 5, May 1995, pp.50-53.

Non-technical Summary

Characterization of materials is a critical part of materials science. Accurate knowledge of the properties of liquid metals will allow more efficient production and manufacturing, as well as providing a basis for comparison with theories about the fundamental nature of liquids.

This investigation employs a unique method for measuring two of the properties of liquid metals: surface tension and viscosity. Surface tension is a force which tries to minimize the surface area of a liquid. This force allows water bugs to “skate” on the surface of a pond. Viscosity, on the other hand, is a fluid’s resistance to flow; water has a low viscosity, but honey has a much higher viscosity.

These experiments are the first successful demonstration of the use of electromagnetic levitation to measure the viscosity of a liquid metal. Also, the surface tension measurements made with this technique are much more accurate than is possible in ground-based experiments.

The major advantage of the technique used in this investigation is that it is containerless: a drop of liquid metal is supported by magnetic forces and does not touch any kind of container. The advantages of this technique are many, including reduced contamination, more spherical samples, and the ability to cool liquid metals below their freezing point without causing them to solidify. However, the experiments must be done in zero gravity so that the magnetic forces do not interfere with the measurement of viscosity.

Page intentionally left blank

omit
this
page

Electromagnetic Containerless Processing Facility (TEMPUS)

AC Calorimetry and Thermophysical Properties of Bulk Glass-Forming Metallic Liquids

Principal Investigator:

Dr. William L. Johnson
California Institute of Technology
Pasadena, California

SINGLESCAN

528-27

434864

362735

Final Science Report MSL-1

11P.

Thermo-physical Properties of Undercooled
Metallic Glass Forming Alloys

Prof. Dr. W. L. Johnson

Dr. D. S. Lee

S. C. Glade

Keck Laboratory of Engineering Materials
California Institute of Technology

Abstract

Thermo-physical properties of two bulk metallic glass forming alloys, $\text{Ti}_{34}\text{Zr}_{11}\text{Cu}_{47}\text{Ni}_8$ (VIT 101) and $\text{Zr}_{57}\text{Nb}_5\text{Ni}_{12.6}\text{Al}_{10}\text{Cu}_{15.4}$ (VIT 106), were investigated in the stable and undercooled melt. Our investigation focused on measurements of the specific heat in the stable and undercooled liquid using the method of AC modulation calorimetry. The experiments were conducted in close collaboration with the group of Prof. Samwer, University of Augsburg, for measurement of the specific volume, the groups of Prof. I. Egry, DLR Cologne and Prof. M.G. Froberg, Technical University of Berlin, for measurements of surface tension and high temperature viscosity, and the group of Prof. H. J. Fecht, University of Ulm, Germany, for coordination of sample selection and specific heat measurements. The VIT 106 exhibited a maximum undercooling of 140 K in free radiative cooling. Specific heat measurements could be performed in stable melt down to an undercooling of 80 K. Analysis of the specific heat data indicate an anomaly near the equilibrium liquidus temperature. This anomaly is also observed in the temperature dependencies of the external relaxation time, the specific volume, and the surface tension; it is tentatively attributed to a phase separation in the liquid state. The VIT 101 specimen exhibited a small undercooling of about 50 K. Specific heat measurements were performed in the stable and undercooled melt. These various results will be combined with ground based work such as the measurement of T-T-T curves in the electrostatic levitator and low temperature viscosity and specific heat measurements for modeling the nucleation kinetics of these alloys.

2. Objectives

The primary scientific objective of the experiments conducted in the MSL-1 spacelab mission was the measurement of the specific heat capacity in the stable and undercooled liquid of the two bulk metallic glass forming alloys

$\text{Ti}_{34}\text{Zr}_{11}\text{Cu}_{47}\text{Ni}_8$ VIT 101

$\text{Zr}_{57}\text{Nb}_5\text{Ni}_{12.6}\text{Al}_{10}\text{Cu}_{15.4}$ VIT 106

From the free temperature decay of the specimen between bias temperature T_1 and T_2 , the rate of radiative heat loss was measured from which the total hemispherical emissivity of the specimen as function of temperature can be inferred if the specific heat is known. Furthermore, the method of AC modulation calorimetry employed for the measurement of the specific heat allows the determination of the effective thermal conductivity of the liquid alloy.

In cooperation with different scientific groups participating in the TEMPUS experiment on MSL-1, it was also planned to share these specimens for the measurement of the temperature dependencies of specific volume, surface tension, and viscosity.

3. Background

In recent years, bulk metallic glass forming alloys, which can be produced with dimensions relevant for their use as structural materials, have attracted considerable attention. This is in part due to their improved mechanical properties, such as increased tensile strength, hardness, and corrosion resistance, making these materials interesting candidates for engineering applications. On the other hand, the exceptional stability of these materials in the metastable undercooled melt makes the undercooled liquid amenable to physical investigations not possible before. The formation of metallic glasses by cooling the liquid alloy from temperatures well above the equilibrium melting point depends critically on the cooling rate, or equivalently on the stability of undercooled melt with regard to crystallization. Following classical nucleation theory,

the nucleation rate is determined by kinetic factors such as the viscosity, expressing the mobility of atoms or groups of atoms, and by thermodynamic factors, expressing the driving force for the formation of a crystalline nucleus in the melt. The latter is composed of a surface energy term and the difference in the Gibbs free energy between the undercooled liquid and the competing crystalline phase. The Gibbs free energy difference can be obtained from measurements of the specific heat capacity, in the metastable liquid and crystalline phase, and the heat of fusion. Combining the specific heat and viscosity data with measurements of the nucleation kinetics, such as T-T-T curves, can serve to model nucleation kinetics. Thus, differences in the nucleation kinetics and glass forming ability of different alloy compositions may be systematically assessed. Investigations of the nucleation kinetics of these alloys have been performed in a ground based program with the electrostatic levitator (ESL). These experiments also allow the determination of the ratio of the specific heat to the total hemispherical emissivity.

In addition to the factors mentioned above, it has been shown that for one alloy composition, ZrTiCuNiBe, phase separation in the stable or slightly undercooled melt strongly influences the undercooling, phase selection, and crystallization microstructure. This effect can be detected as discontinuities in the second derivative of the Gibbs free energy, such as the specific heat and the coefficient of thermal expansion.

Another factor affecting the critical cooling rate for glass formation is the ability of a given alloy composition to either dissolve or passivate possible heterogeneous nucleants present in the melt. This question can be addressed by comparing the Gibbs free energy and viscosity of different alloy compositions together with careful investigation of impurity content on phase selection and undercooling behavior.

4. Methods of data acquisition and analysis

Measurements of the specific heat capacity were performed on 8 mm diameter specimens with the containerless electromagnetic processing device TEMPUS. Specimens are positioned by an radio-frequency (rf) electromagnetic quadrupole field and heated by a dipole field. Containerless conditions are required to avoid heterogeneous nucleation of the undercooled melt

by contact of the specimen with container walls. Furthermore, heating due to the strong levitation forces required for containerless electromagnetic processing would not allow one to perform these experiments under clean ultrahigh vacuum conditions in a 1-g environment.

The heat capacity of the specimen is determined by AC modulation calorimetry. In short, the heating power input to specimen at bias temperature T_0 is sinusoidally modulated at frequency ω . This results in a temperature response at ω with amplitude ΔT_{mod} such that $\Delta T_m / T_0 \ll 1$, with c_p given by:

$$c_P = \frac{P_{\text{mod}}}{\omega \Delta T_{\text{mod}}} f(\omega, \tau_1, \tau_2)$$

P_{mod} is the amplitude of modulated power component. $f(\omega, \tau_1, \tau_2)$ is a correction function accounting for the finite thermal conductivity, with internal relaxation time τ_2 , and heat loss, with external relaxation time τ_1 . Due to the typically large difference in the external and internal relaxation times for metallic specimens, there is a frequency where $\Delta T_{\text{mod}}(\omega)$ is position independent, characterizing the isothermal regime with $1 - f(\omega, \tau_1, \tau_2) < 10^{-2}$. Experimentally, this regime can be identified by a phase shift of 90° between the heater current modulation and the temperature response. Calibration of P_{mod} is performed by application AC modulation calorimetry to the crystalline phase with known specific heat. The temperature dependence of the calorimeter constant thus obtained can be determined from measurement of the specific volume and the resistivity, as obtained from the current and voltage data from the rf-generator. Fig. 1 shows a typical experimental run with the VIT 106 alloy depicting melting and overheating (1), rapid cooling into the undercooled melt (2), and performing AC modulation calorimetry (3). The sample subsequently recalesces (4), possibly into a metastable crystalline phase.

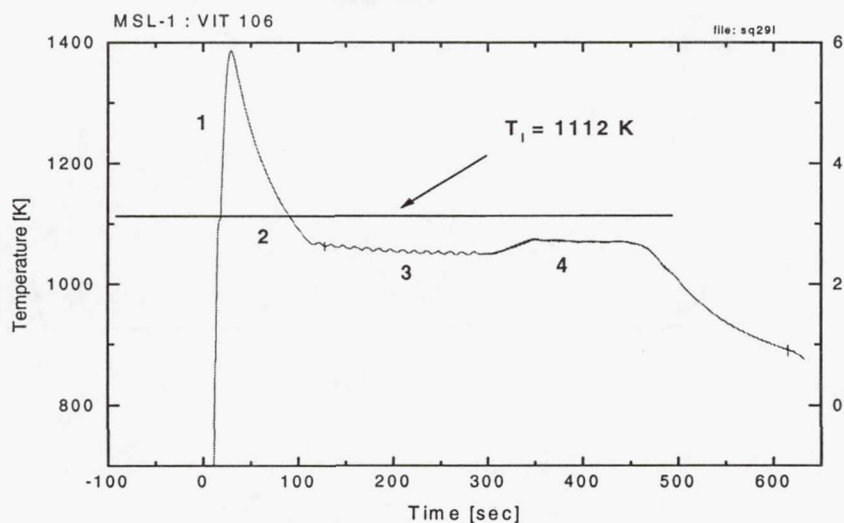


Fig. 1. Typical MSL-1 experiment with VIT 106

Determination of ΔT_{mod} is performed by application of a baseline drift correction, with external relaxation time τ_1 , and subsequent Fourier analysis, as shown in Fig.2. The frequency components at 1.2 and 1.5 Hz are due to harmonic motions of the specimen in the potential well of the positioning field and do not represent true temperature variation. Alternatively, a FFT low pass filter is applied to the raw signal and a running average over modulation cycles is performed. The two methods agree within the statistical error of the running average, typically to within 0.1 K. As such, with $\Delta T_{\text{mod}} \approx 3$ K, a relative error in c_p determination of $< 4\%$ is obtained. From a step function change in the heating power input, τ_1 can also be determined from the transient behavior of the modulation signal. The data shown in Fig. 3 can be very well represented by a single exponential fit as expected for transients with a small temperature difference.

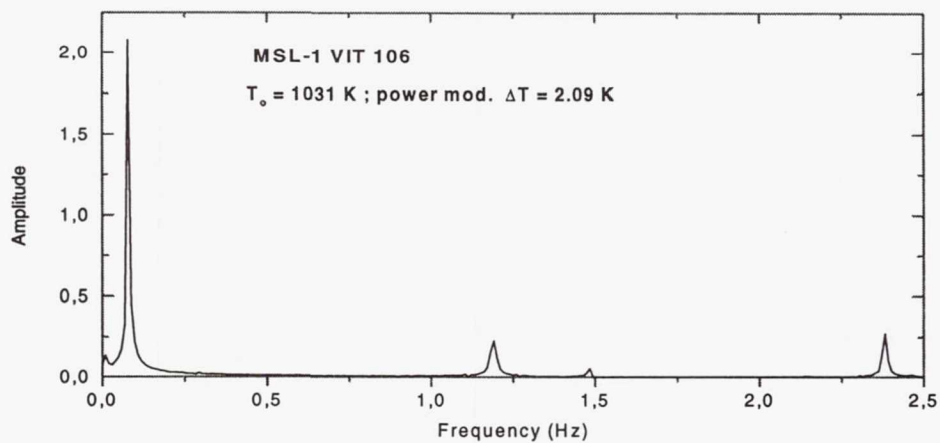


Fig. 2. Fourier transform of temperature signal (3) from Fig.1 after correcting for signal drift

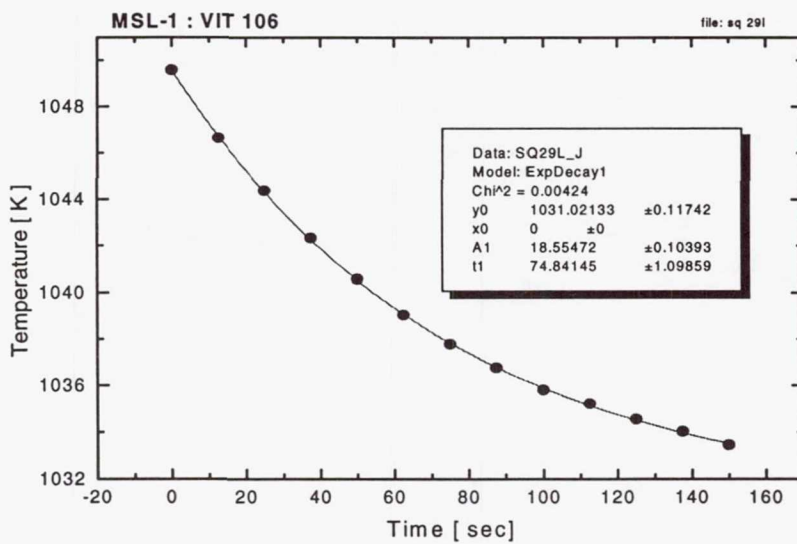


Fig3. Position of modulation maxima as function of time for τ_1 determination. ● data points, — single exponential fit

5. Flight results compared with ground results

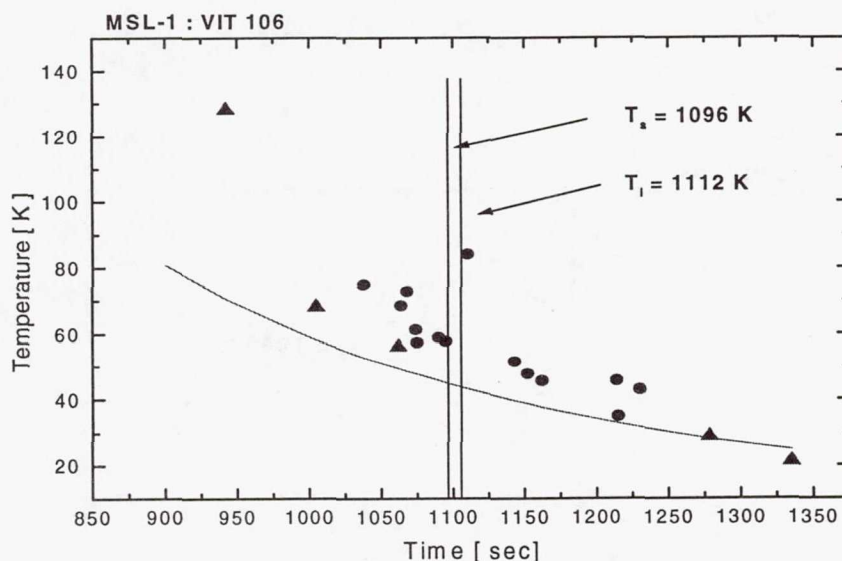


Fig. 4. External relaxation time as a function of temperature for VIT 106
 ●: MSL-1, Δ: ESL- ground based results.

Fig. 4 shows results for the external relaxation time τ_1 obtained in the flight experiment for VIT 106 together with similar values obtained in the ESL. The good agreement between these values demonstrates the consistency of the experimental approach. The solid line represents a T^{-3} scaling of τ_1 for constant specific heat capacity. As such, the deviation of the experimental data from this scaling reflects the strong increase of the specific heat with decreasing temperature for the undercooled melt. Furthermore, a singular point near T_l is observed suggesting an unusual behavior in c_p . Further evidence is provided in Fig. 5, with values of the specific heat from AC modulation calorimetry normalized to the heater coupling coefficient. The temperature dependence of the coupling coefficient has not yet been taken into account. Nonetheless, the anomaly exhibited in the external relaxation time is also present in the specific heat in the same temperature range. Furthermore, the temperature dependence of the specific volume also appears to change in this temperature range. This behavior is suggestive of a phase separation just above the liquidus temperature. In order to test this hypothesis further, laboratory experiments to analyze the solidification microstructure after rapidly quenching the liquid from different

temperatures are under way. AC modulation calorimetry could be performed for this alloy up to an undercooling of 70 K. The agreement of data points at similar temperatures is very good and demonstrates the precision of this method.

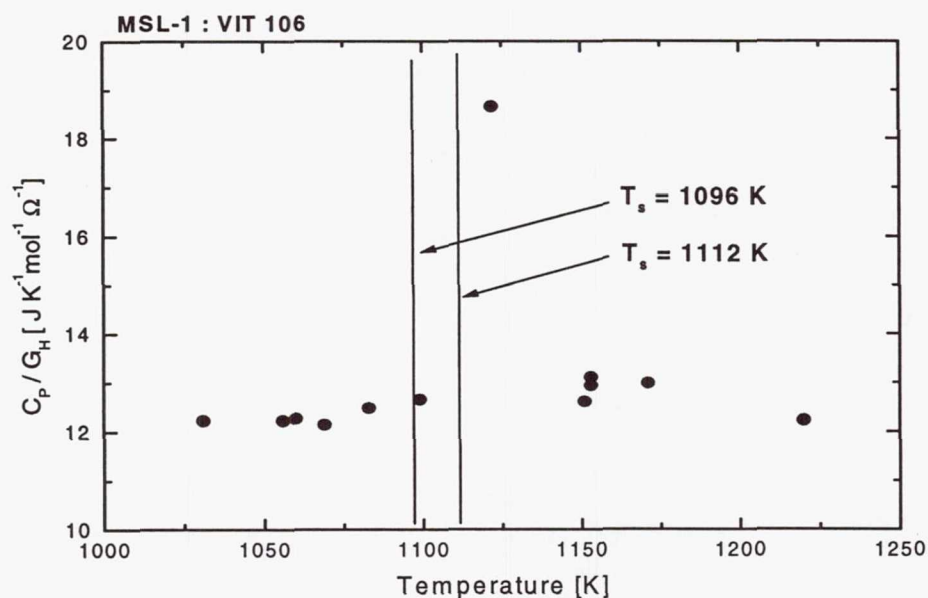


Fig 5. Specific heat capacity of VIT 106 normalized to heater coupling coefficient G_H .

As compared to ESL ground based experiments where undercooling of over 200 K could be obtained, the VIT 101 flight specimen showed only an undercooling of 45 K, which is attributed to the presence of minor impurities. Specific heat capacity data in the stable melt and the slightly undercooled melt were obtained. It should be pointed out that no anomaly in τ_1 or c_p similar to VIT 106 could be observed. The same holds for the measurements performed by the Fecht group on two bulk glass forming alloys of different composition.

Other ground based work includes analysis of solidification microstructure and phase selection in the flight specimen (VIT 101) solidified from the undercooled liquid under μg conditions. Comparison will be made with a 1-g reference specimen, as well with those phases crystallizing at high undercooling by heating the glass into the undercooled melt. Results of an

electron microprobe analysis are shown in Table 1, exhibiting two phases of almost complementary composition in $(\text{ZrTi}) \approx 50 \text{ at\%}$ and $(\text{NiCu}) \approx 50 \text{ at\%}$. We will further identify the structure of these phases and investigate the dependence of their formation on impurity levels.

Tab. 1 EDX spot analysis of $\text{Ti}_{34}\text{Zr}_{11}\text{Cu}_{47}\text{Ni}_8$ (VIT 101) flight specimen

Phase	Zr at%	Ti at%	Ni at%	Cu at%
1	7.45	36	12.97	36.42
2	18.99	22.44	8.12	50.44
3	3.27	47.44	3.05	46.24

6. Conclusions

The specific heat capacity of two glass forming metallic alloys was measured by AC modulation calorimetry in the stable and undercooled (for VIT 106) melt. The temperature dependence of the specific heat as well of the external relaxation time and the specific volume appear to exhibit an anomaly tentatively identified as phase separation in the liquid. This would constitute an important finding as phase separation is suggested to occur frequently in glass forming metallic melts. However, with a few exceptions, experimental evidence of this is rare.

Further work will include investigation of the phase selection in these alloys as well as viscosity measurements at high undercooling. These data can be combined with high temperature viscosity data and undercooling experiments with the ESL to model the nucleation kinetics in these alloys. Future perspectives also include the implementation of AC modulation calorimetry in the ESL.

Thermo-physical Properties of Undercooled Metallic Glass Forming Alloys

W. L. Johnson, D. S. Lee, and S. C. Glade

Keck Laboratory of Engineering Materials, California Institute of Technology

Metallic glasses are a relatively new class of materials. Discovered in 1967 by Duwez *et al.* using rapid quenching methods, metallic glasses lack the long range atomic order that is present in crystalline metals. Over the past several years, advances in this field have resulted in the discovery of many new metallic glass forming compositions, some with substantially improved glass forming ability. With rapid cooling techniques, yielding cooling rates as high as 10^5 K/s, only metallic glass specimens of very small dimensions can be produced. The recently discovered metallic glass compositions, some requiring cooling rates as low as 1 K/s, can be cast into bulk parts, making them feasible for use in engineering applications.

In the MSL-1 spacelab mission, we performed experiments on two bulk glass forming alloys, $\text{Ti}_{34}\text{Zr}_{11}\text{Cu}_{47}\text{Ni}_8$ and $\text{Zr}_{57}\text{Nb}_5\text{Ni}_{12.6}\text{Al}_{10}\text{Cu}_{15.4}$, using TEMPUS, an electromagnetic containerless processing facility. This facility allowed us to perform experiments in the undercooled liquid regime that are not possible to perform on earth. Using the AC modulation calorimetry technique, we measured the specific heat capacity of these two alloys in the stable melt and the undercooled liquid. The 5-component alloy exhibited an anomaly in the specific heat capacity near the equilibrium liquidus temperature. This is possibly due to phase separation in the liquid, but further investigation is needed.

In collaboration with other science teams, other thermo-physical properties of these two alloys were measured, including viscosity, surface tension, coefficient of thermal expansion, thermal conductivity, and total hemispherical emissivity. This data, along with data from ground based experiments, will help us in determining why these new alloys have such an enhanced glass forming ability as well as aide us in the search for new bulk metallic glass forming alloys.

omit
T1415
PAGE

Accelerometers

Orbital Acceleration Research Experiment (OARE) Space Acceleration Measurement System (SAMS) Microgravity Measurement Assembly (MMA)

Mr. Richard Delombard
NASA Lewis Research Center
Cleveland, Ohio

Mr. Maurizio Nati
European Space Research and Technology Center
Noordwijk, The Netherlands

Final Science Report for OARE and SAMS on STS-94 / MSL-1

Milton Moskowitz, Kenneth Hrovat
Tal-Cut Company, North Olmsted, Ohio

Kevin McPherson, Peter Tschen, Richard DeLombard
NASA Lewis Research Center, Cleveland, Ohio

Maurizio Nati
European Space Research and Technology Center
Noordwijk, The Netherlands

529-29
434 865
9P.

362437

ABSTRACT

Four microgravity acceleration measurement instruments were included on MSL-1 to measure the accelerations and vibrations to which science experiments were exposed during their operation on the mission. The data were processed and presented to the principal investigators in a variety of formats to aid their assessment of the microgravity environment during their experiment operations.

Two accelerometer systems managed by the NASA Lewis Research Center (LeRC) supported the MSL-1 mission: the Orbital Acceleration Research Experiment (OARE), and the Space Acceleration Measurement System (SAMS). In addition, the Microgravity Measurement Assembly (MMA) and the Quasi-Steady Acceleration Measurement (QSAM) system, both sponsored by the Microgravity Research Division, collected acceleration data as a part of the MSL-1 mission. The MMA was funded and designed by the European Space Agency in the Netherlands (ESA/ESTEC), and the QSAM system was funded and designed by the German Space Agency (DLR).

The Principal Investigator Microgravity Services (PIMS) project at the NASA Lewis Research Center (LeRC) supports Principal Investigators (PIs) of the microgravity science community as they evaluate the effects of acceleration on their experiments. PIMS' primary responsibility is to support NASA-sponsored investigators in the area of acceleration data analysis and interpretation.

A mission summary report was prepared and published by PIMS in order to furnish interested experiment investigators with a guide for evaluating the acceleration environment during the MSL-1 mission.

OBJECTIVE(S)

The objective of microgravity measurement instruments manifested on MSL-1 was to measure the accelerations and vibrations to which science experiments were exposed during their operation on the mission. The data were processed and presented to the principal investigators in a variety of formats to aid their assessment of the microgravity environment during their experiment operations.

BACKGROUND

Two accelerometer systems managed by the NASA Lewis Research Center (LeRC) supported the MSL-1 mission: the Orbital Acceleration Research Experiment (OARE), and the Space Acceleration Measurement System (SAMS). These accelerometers were funded by the Microgravity Research Division (MRD) of the NASA Office of Life and Microgravity Sciences and Applications. In addition, the Microgravity Measurement Assembly (MMA) and the Quasi- Steady Acceleration Measurement (QSAM) system, both sponsored by the Microgravity Research Division, collected acceleration data as a part of the MSL- 1 mission. The MMA was funded and designed by the European Space Agency in the Netherlands (ESA/ESTEC), and the QSAM system was funded and designed by the German Space Agency (DLR).

The Principal Investigator Microgravity Services (PIMS) project at the NASA Lewis Research Center (LeRC) supports Principal Investigators (PIs) of the microgravity science community as they evaluate the effects of acceleration on their experiments. PIMS' primary responsibility is to support NASA-sponsored investigators in the area of acceleration data analysis and interpretation.

Numerous activities occurred during the MSL-1 mission that are of interest to the low-gravity community. Specific activities of interest during STS-94 were:

1. crew activities
2. experiment operations,
3. orbiter attitude
4. venting operations
5. microgravity glovebox (MGBX) circulation fans
6. crew exercise
7. Public Affairs Office (PAO) events/quiet periods
8. Physics of Hard Spheres Experiment (PHaSE) activation/ deactivation
9. PHaSE mixer

10. Combustion Module-1 (CM-1) mallet pounding for setup
11. CM-1 gas chromatograph vacuum pump
12. effect of leaving free drift
13. accelerations related to the Astro/Plant Generic Bioprocessing Apparatus (ASTRO/PGBA)
14. accelerations related to the Droplet Combustion Experiment (DCE)
15. accelerations related to the electromagnetic containerless processing facility (TEMPUS)

The low-gravity environment related to these activities is discussed in the summary report prepared by PIMS for the mission (see Bibliography). Disturbances which are common to Orbiter missions were also apparent, including the Ku band antenna dither, orbital maneuvering system and primary reaction control system firings, and attitude changes.

METHODS OF DATA ACQUISITION AND ANALYSIS

DATA ACQUISITION

Four accelerometer systems measured the microgravity and vibration environment of the Orbiter Columbia during the MSL-1 mission: the Orbital Acceleration Research Experiment (OARE), the Space Acceleration Measurement System (SAMS), the Microgravity Measurement Assembly (MMA), and the Quasi-Steady Acceleration Measurement (QSAM) System.

OARE measured quasi-steady accelerations from below 1×10^{-8} g up to 2.5×10^{-3} g at a location on the Shuttle keel, near the center of mass.

SAMS measured the low-gravity environment of the Orbiters in support of microgravity science payloads. The SAMS configuration for MSL-1 consisted of two remote triaxial sensor heads (TSHs), connecting cables, and a central processing unit with a data recording system using standard commercial hard drives that have been upgraded for space use. The main unit was located in the center aisle of the Spacelab module. The locations of the SAMS sensor heads were in the Combustion Module rack and on the Microgravity Glovebox. The data from one of the two active TSHs was deemed unusable due to a high number of sporadic gain changes. Therefore, the data used for the post-mission analysis was predominantly that from the MMA.

MMA measured the low-gravity environment of the Orbiters in support of microgravity science payloads. These sensor heads consist of six Microgravity Sensor Packages (MSPs) and one Accelerometre Spatiale Triaxiale Electrostatique (ASTRE).

The ASTRE and one MSP resided within the MMA unit, one MSP was located on the Droplet Combustion Experiment, and one MSP was located on the Large Isothermal Furnace.

QSAM measured accelerations from quasi-steady up to 50 Hz. QSAM was located in Rack 3 (next to the TEMPUS facility). In order to assess the quasi-steady acceleration level, QSAM suppresses the sensor's bias and noise by rotating the sensor's sensitive axis. QSAM utilizes four rotating sensors to allow for a three-dimensional quasi-steady acceleration detection.

DATA ANALYSES

PIMS had the opportunity to work closely with the Structure of Flame Balls at Low Lewis-number (SOFBALL) and the Coarsening in Solid-Liquid Mixtures (CSLM) experiment teams during the pre-mission Investigator Working Group meetings.

During the mission, the PIMS group analyzes the data available via downlink and forwarded the analysis results to the PIs.

The SAMS real-time displays on the Internet included acceleration versus time plots (for the X-, Y-, and Z-axes), and a color spectrogram for the root-sum-of-squares (RSS) combination of the three axes for the TSH B (MGBX), and TSH C (LIF) data. The color spectrograms served as an overview of the recent microgravity environment. These plots allowed the PIMS team to determine exercise activity, and alert the TEMPUS experiment team in near-real-time when exercise was currently underway. This real-time feedback allowed the TEMPUS group to closely monitor and control their critical experiment activities, attempting to minimize the impact of acceleration disturbances on their experiment.

In addition, a customized analysis display was developed for the CSLM experiment. This customized analysis contained plots of root-mean-square (RMS) acceleration versus time for five different frequency intervals. The total range of these frequency intervals was from 0.05 to 25 Hz. The specific intervals were chosen based upon discussions between the CSLM and PIMS groups.

Post-mission, the data were analyzed via time-domain and frequency-domain analysis tools. Time-domain tools used were acceleration versus time and trimmean acceleration versus time. The frequency-domain analysis tools were the power spectral density (PSD) versus frequency and the power spectral density versus frequency versus time (spectrogram).

Additionally, the quasi-steady data were analyzed via a histogram method called the Quasi-steady Three-Dimensional Histogram.

FLIGHT RESULTS COMPARED WITH GROUND RESULTS

This item does not apply to the accelerometer instruments on-board this mission.

CONCLUSIONS

This report describes the acceleration environment recorded during the STS-94 flight of Columbia, including accelerations related to Orbiter attitude, Orbiter venting operations, a variety of experiment-specific fans, pumps, and compressors, crew exercise, and crew quiet periods.

Low-frequency acceleration variations result from changes in the Orbiter's attitude. Primarily, these accelerations are due to aerodynamic drag, gravity gradient, and rotational effects within the Orbiter. Atmospheric density changes resulting from day/night transitions cause variations, which have been seen in the past, and have been noted for this mission. Vehicle venting operations (such as water dumps) produce a quasi-steady shift of the acceleration vector, related to the venting force and direction. As seen in figure 1, typical acceleration changes are on the order of $-1.5 \mu\text{g}$ for the Y_b -axis, and $1.7 \mu\text{g}$ for the Z_b -axis, for simultaneous supply and waste water dump operations.

Accelerations related to crew activity and Orbiter system operations have been noted. Specifically, crew exercise produced acceleration disturbances resulting from a shoulder-sway motion (1-1.5 Hz), the fundamental pedaling frequency (2.5-3 Hz), and harmonics of these frequencies. Exercise for this mission were typically on the order of $100\text{-}200 \mu\text{g}_{\text{RMS}}$. PAO events and crew conferences were shown (figure 2) to be quieter microgravity periods, lasting for up to 30 minutes at a time, with a nominal $40 \mu\text{g}_{\text{RMS}}$ quieting of the acceleration environment. The 17 Hz dither of the Orbiter's Ku-band communication antenna was present throughout the mission, with magnitudes around $75\text{-}105 \mu\text{g}_{\text{RMS}}$. The distributed nature of the three MMA sensor heads allowed the magnitude variations of this signal to be seen as a function of distance from the disturbance source.

A number of acceleration sources were identified which were related to experiment or facility operations. Some of note include the MGBX work area circulation fans (63.5, 66.5, 98.6, and 127.0 Hz with magnitudes up to $180 \mu\text{g}_{\text{RMS}}$), the PHaSE mixer (2000-3000 μg vector magnitude increase), the CM-1 gas chromatograph vacuum pump (46 and 55 Hz, $170 \mu\text{g}_{\text{RMS}}$ magnitude), the Astro/ PGPA air circulation pump (31.8, 44.4, 45.0, and 63.5 Hz, ranging between 5 and $750 \mu\text{g}_{\text{RMS}}$ in magnitude), and

the TEMPUS water pump (42.5-43 Hz, 250 μg_{RMS} magnitude). Some other sources include one or more unidentified components on the PHaSE and the DCE experiments.

Direct correlations were made by the SOFBALL team between their radiometry data and firing of the VRCS thrusters, figure 3.

PIMS provided an analysis showing the microgravity effects of leaving free drift. This showed there were an increased number of thruster firings as the Orbiter maneuvered back to the desired attitude.

Correlations between the MMA ASTRE sensor were made with the OARE instrument. For the venting operations (water dumps), both instruments measured approximately the same magnitude and direction for the acceleration vector.

Utilization of high-frequency data from three MMA sensor heads enabled a unique opportunity for the localization and identification of a number of disturbance sources. This proved to be an invaluable tool for the analysis and interpretation of the MSL-1 microgravity environment.

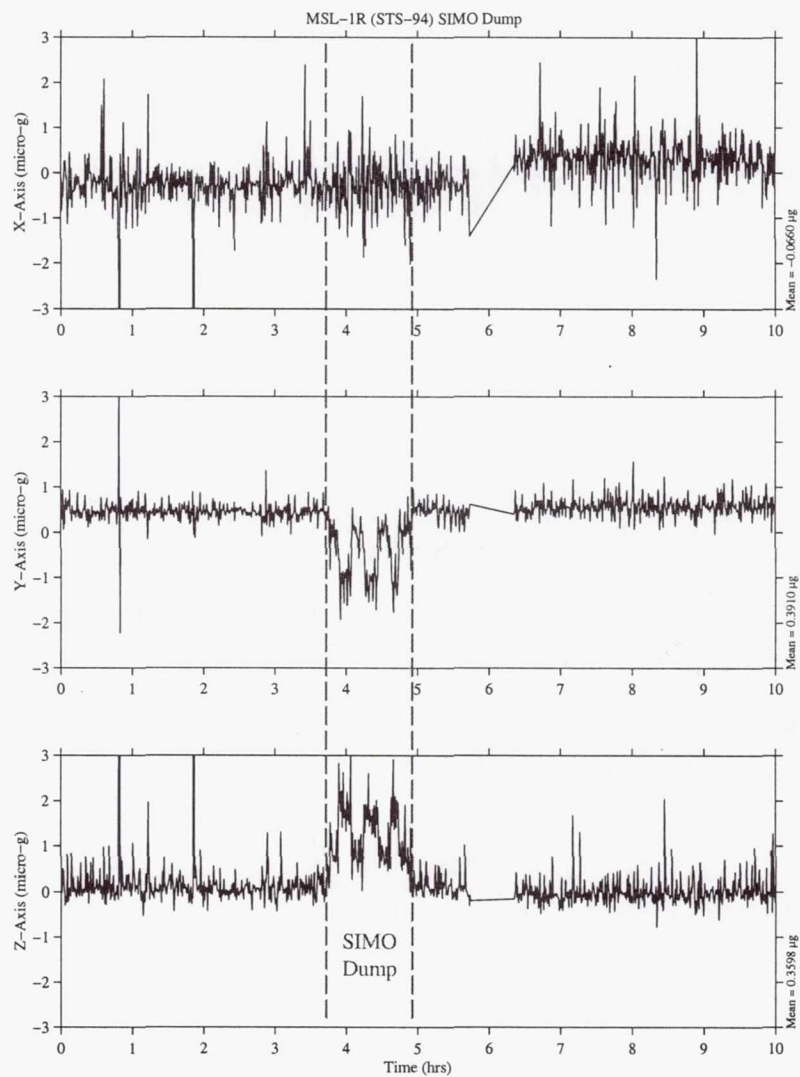
BIBLIOGRAPHY

1. Moskowitz, M. E.; Hrovat, K.; Tschen, P.; McPherson, K.; Nati, M.; and Reckart, T. A.: Summary Report of Mission Acceleration Measurements for MSL-1, NASA TM-1998-206979, 1998
2. Canopus Systems, Inc., OARE Technical Report 151, STS-94 (MSL-1) Final Report. CSI-9704, August 1997

OARE, Trimmed Mean Filtered
OARE Location

MET Start at 005/15:00:07.920

Frame of Reference: Orbiter
MSL-1R
Body Coordinates



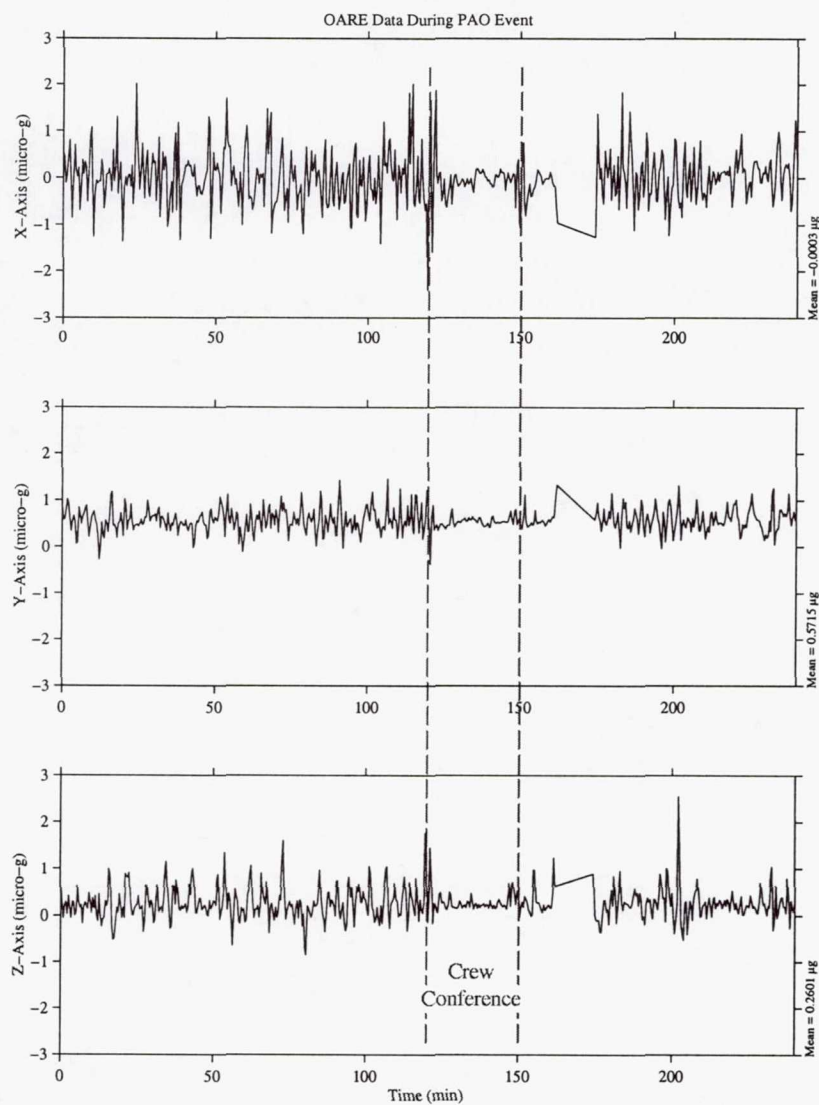
MATLAB: 2D-View 1998, 06/02 p04

Figure 1. OARE Data Collected During a Simultaneous Supply and Waste Water Dump at MET 005/15:00.

OARE, Trimmed Mean Filtered
OARE Location

MET Start at 013/10:45:00.000

Frame of Reference: Orbiter
MSL-1R
Body Coordinates



MATLAB: 27-Sep-1996, 16:17 pm

Figure 2. Trimmean Filtered OARE Data Collected During an STS-94 Crew Conference, MET 013/10:45.

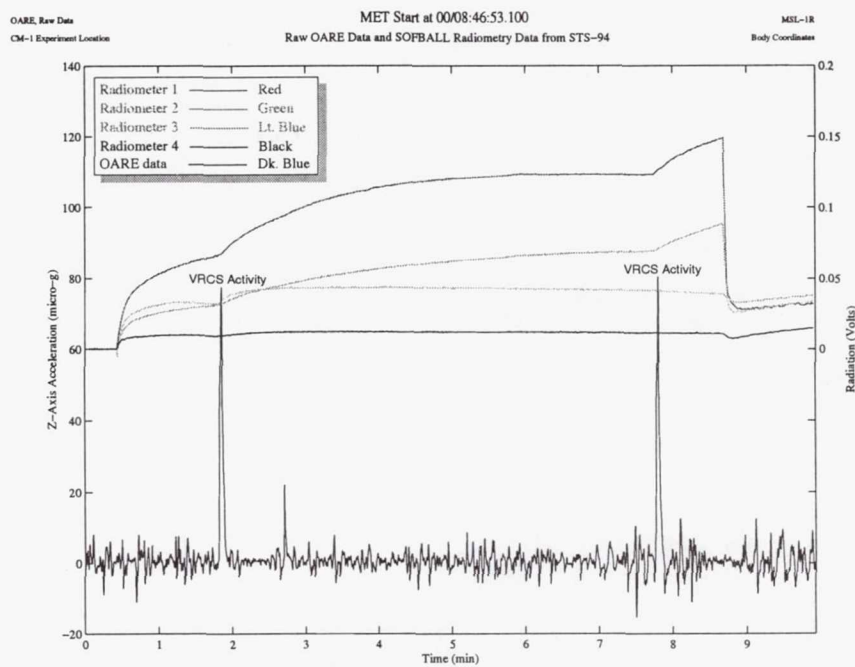


Figure 3. Raw (10 samples per second) OARE Data with SOFBALL Radiometry Data from STS-94, SOFBALL Test Point 14A. MET Start 007/08:46:53.

omit
THIS
PAGE

Accelerometer

Quasi-Steady Acceleration Measurement System (QSAM)

Project Scientist:

Dr. Hans Hamacher
DLR
Cologne, Germany

Microgravity Measurements of QSAM on Spacelab MSL-1

H. Hamacher¹⁾, R. Jilg²⁾, H. E. Richter¹⁾, S. Drees¹⁾

1) German Aerospace Center (DLR), Koeln, Germany

2) Acsys, Rimsting, Germany

362438

530-29 101.
434866

Abstract

The residual acceleration (or microgravity) of a space laboratory is a perturbation to experiments intended to be executed under weightlessness. Detailed knowledge of the microgravity is therefore indispensable for the analysis of the experiment results. Measurements of the residual acceleration are required at various locations of the spacecraft. According to the spectral sensitivity of experiments, frequencies from static (0 Hz) to high frequency contributions of the order of 100 Hz has to be detected. The low amplitude levels of the static and quasi-static acceleration (typically 1 μ g and below) requires inflight sensor calibration. The Quasi-Steady Acceleration Measurement system (QSAM), developed by DLR, is an instrument especially designed to detect acceleration in the entire range between 0 and 50 Hz. Continuous sensor calibration is achieved by signal modulation. The MSL-1 mission was the third spaceflight of QSAM. Data analysis started during the mission in the HOSC based on QSAM's real-time data processing capability. Post mission analyses concentrated mainly on investigations of characteristic perturbation pattern like those, induced by crew interaction with the orbiter (exercises), the oscillations of samples in the TEMPUS facility, shuttle induced disturbances (water dumps, thruster firings) and orbit-attitude induced residual accelerations(solar inertial attitude).

1 Scientific Objectives

The motivation for doing science in space is to take advantage of orbital factors in experimental investigations. One of the unique space flight conditions is the state of weightlessness which is approximated to a high degree in a freely drifting spacecraft. The MSL-1 mission was devoted particularly to experimentation under weightlessness. Some inherent 'disturbing' effects are the reasons, that ideal weightlessness (or zero gravity) cannot be achieved completely. It has been shown, however, that physical effects, intended for study under the conditions of weightlessness, tolerate a finite level of residual acceleration (or 'microgravity') [1, 2]. This tolerated level depends

1. on the physical phenomenon itself, and
2. on the history of the residual acceleration vector at the location of the experiment, i.e. on its magnitude, direction and frequency composition.

A detailed knowledge of the residual acceleration during the experiment running time is therefore indispensable for a thorough analysis of the scientific results. To measure the residual acceleration, the MSL-1 payload was equipped with various accelerometer packages. The Quasi-Steady Acceleration Measurement system QSAM, developed by DLR, was part of this instrumentation along with NASA's Space Acceleration Measurement System (SAMS) and Orbital Acceleration Research Experiment (OARE, in the cargobay) and ESA's Microgravity Measurement Assembly (MMA). QSAM made use of a novel measurement principle designed to cover the experiments most significant frequency range between real 0 Hz and 50 Hz. Figure 1 shows the QSAM hardware, Fig. 2 indicates its location within the Spacelab module. After a first test flight on IML-2, and a second on the prematurely ended original MSL-1 mission, MSL-1R was the third

orbital flight of QSAM with the main objective to verify the power of the measurement principle. QSAM also allowed real-time data analysis in the HOSC to supply experimenters and mission operation managers with relevant acceleration data .

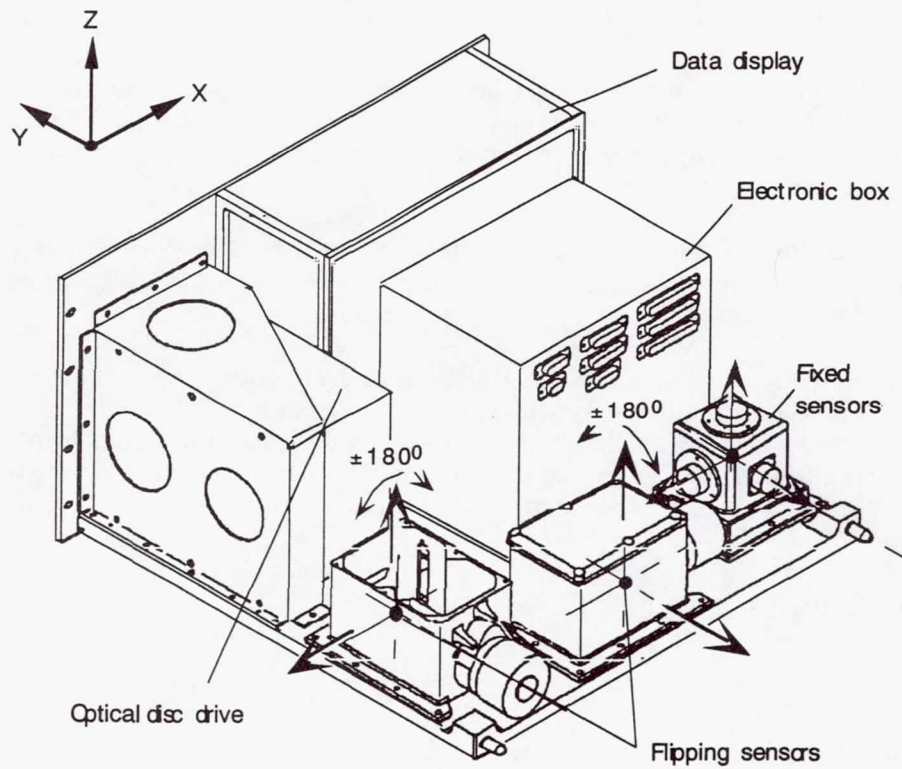


Fig. 1. QSAM hardware (back view). The low frequency acceleration vector is detected by the two flipping sensor packages , the g-jitter range by the tri-axial fixed sensor package

2 Residual Accelerations, Causes and Characteristics

The disturbing effects can be grouped in two main categories [3, 4].

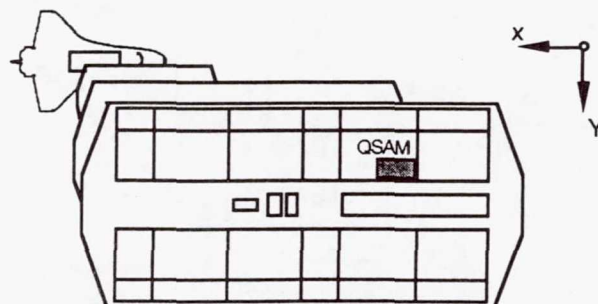


Fig. 2. Location of QSAM within the Spacelab Module in Rack 3.

2.1 First Category: Low Frequency Accelerations

External forces. Residual external forces prevent the spacecraft from being in an ideal free fall state (Fig. 3). The residual atmosphere is the dominating external force.

Gravity gradient effect. Due to the gradient of the Earth's gravitational field, even a free fall system applies weightlessness only at the location of its center of mass. At other places gravity is not completely compensated by inertia which causes gravity gradient or tidal acceleration.

Spacecraft rotation. Simulation of weightlessness in free fall requires true translational motion. In practice the spacecraft may rotate around its center of mass which generates rotational accelerations.

These three effects cause static or quasi-static (low frequency) accelerations. Their levels are the lowest in the frequency spectrum and are typically of the order of $1 \mu g$ or less. This is reflected in Fig. 3 by the step curve which indicates the upper limit of periodic accelerations allowed for ISS. Since the Orbiter's fundamental (i.e. lowest) frequency is between $f_f = 0.1$ and 1 Hz, the spacecraft reacts as a rigid body to the low frequency excitations.

2.2 Second Category: g-Jitter

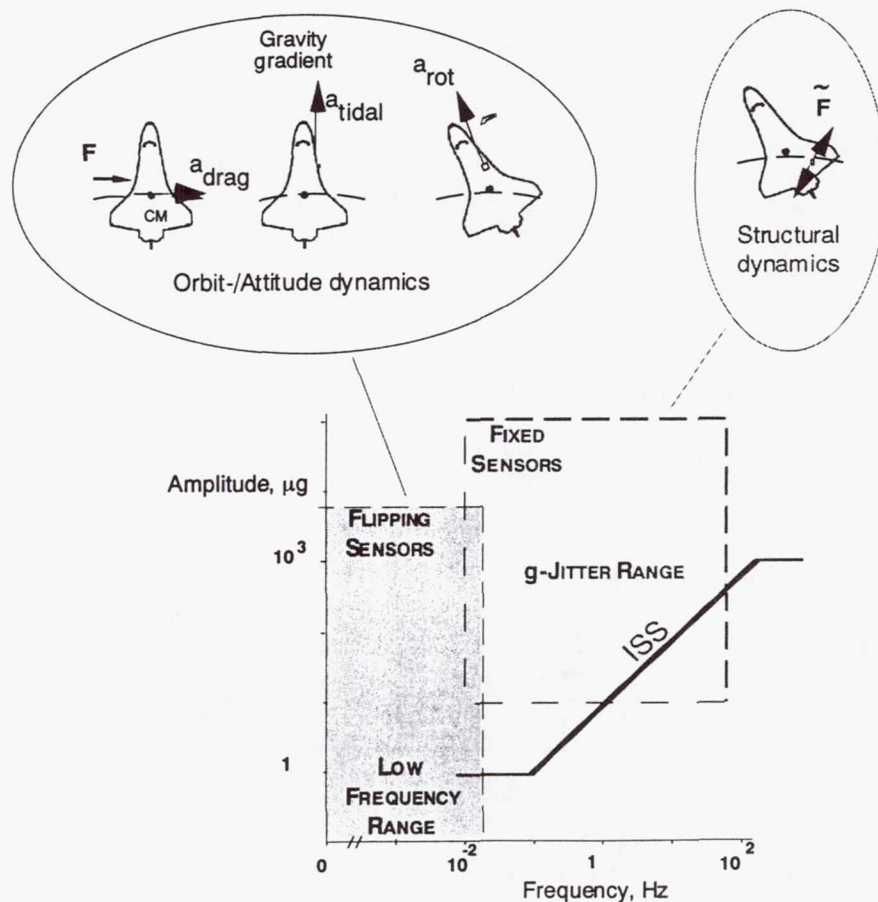


Fig. 3. Perturbation effects and related frequency ranges

The second group of perturbing forces is dynamic in character and excite the spacecraft structure to vibrate causing high frequency accelerations or the 'g-jitter'. Excitation sources are running machines, thruster firings, astronauts push-offs, etc. The g-jitter amplitudes are usually much higher than those of the first category as indicated by the ISS curve in Fig. 3. Most experiments, however, tolerate higher g-jitter amplitudes than low frequency perturbations. The range of accelerations to which experiments are susceptible is mostly limited towards higher frequencies due to the increasing tolerance. Based on results of ref. [2], QSAM has an upper detection range of 50 Hz.

High frequency acceleration typically vary with time and spatially as a result of the flexibility of the spacecraft structure. Thus, g-jitter measurements have to be performed as closely to the experiments as possible. The g-jitter acceleration is a local state whereas low frequency acceleration has a global character.

2 Concept of QSAM

The QSAM system is designed to detect the low-frequency and g-jitter range which is achieved by two different types of sensor packages: flipping sensors to detect the low frequency acceleration and a tri-axial fixed package for the g-jitter range (Fig. 1). The flipping sensors detect the components between 0 Hz and 0.02 Hz. Continuous suppression of bias and noise, needed in this range, is accomplished by signal modulation as the result of flipping. The g-jitter are detected by conventional fixed sensors. For a detailed description of the QSAM system see refs. [5, 6].

3 Results

From the huge amount of data stored during the mission and analyzed, few of general interest are discussed in the following.

3.1 Water Dumps and induced Thruster Firings

The space shuttle has dumping capabilities for potable and waste water. These dumps are performed using nozzles on the port side of the space shuttle, along the positive y-axis in the dynamic orbiter body coordinate system. The effect is shown in figures 4 and 5.

While the supply water dumps are performed continuously, the waste water dumps are cycled on and off. As can be seen from figure 4, the thruster firings to compensate the dump momentum, dominate the disturbance level, even when averaged over 36 s. This is due to the high acceleration amplitude, of approximately up to $250 \mu\text{g}$ measured over a 1 Hz lowpass, that compensates for their short duration of minimal 85 ms.

The quasi-static effect of the supply water dump is approximately $-1.5 \mu\text{g}$ in Y_B direction and $+1.5 \mu\text{g}$ along Z_B .

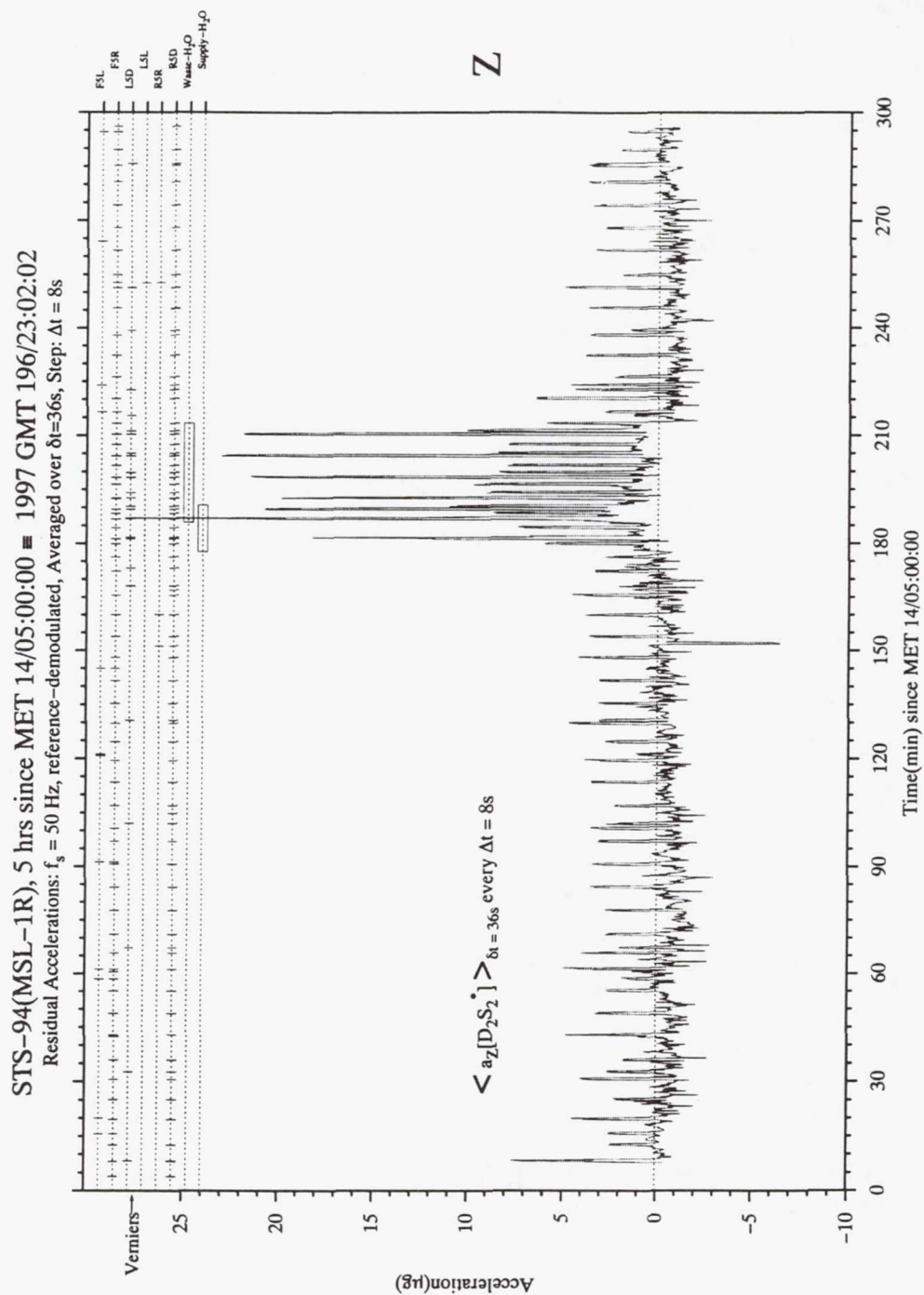


Fig. 4. Disturbances caused by a supply water and/or a waste water dump, and the induced thruster firings. Top: Event timeline from SAPH (Spacelab Ancillary Parameter History) Bottom: Low-frequency acceleration along Z_b as seen by an experiment of 36 seconds duration. Moving average with a window base of 36 seconds, evaluated every 8 seconds.

Running Average
Base: $\Delta t = 144s$
Step: $\delta t = 1s$

Frame of Reference: Orbiter Body Coordinates
Location: QSAM, Rack 3

QSAM on STS-94(MSL-1R), Acceleration vs. Time

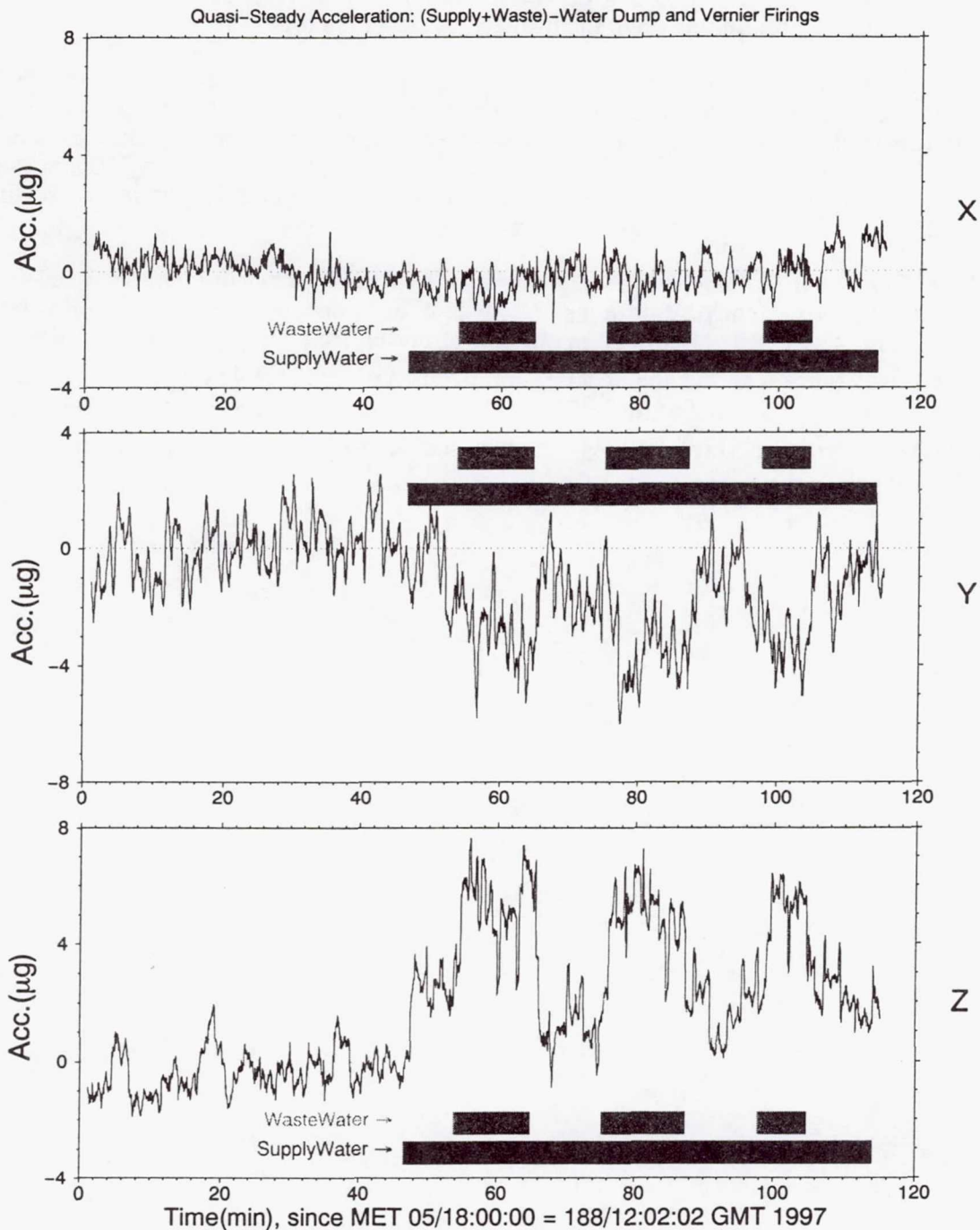


Fig. 5. SIMO-dump (simultaneous supply and waste water dump). Shown are the scalar low frequency accelerations in the dynamic system. Here - as compared to figure 4 the base of the moving average window is 144 seconds, plotted every second.

3.2 Solar Inertial Attitude





The low-frequency microgravity environment also depends on the attitude and the position on orbit. Atmospheric drag is experienced by the orbiter due to the varying atmosphere and attitudes. The amount of drag is primarily determined by the orbiter frontal area, which is dependent on the attitude of the space shuttle relative to its direction of flight. This area is a maximum when the orbiter is oriented belly or cargo forward, and is a minimum when the orbiter nose or tail is forward.

As opposed to an earth oriented attitude, a solar inertial attitude orients the orbiter attitude relative to the sun. This attitude then results in a variable frontal area during its orbital period, thus causing a variable atmospheric drag acceleration. Even with constant frontal area there will be a variation in drag in these altitudes of typically 300 km, due to variations of the atmosphere. For an orbit of constant altitude, the major variation in density stems from the day/night variation.

The effects of the atmospheric drag on the microgravity environment are seen in the quasi-steady frequency regime as a constant acceleration vector with a variable component. The main variable component is at orbital frequency (approx. 90 minutes or 185 μHz). Figure 6 shows the acceleration levels measured while the space shuttle was oriented in a solar inertial attitude. The major variation in the acceleration levels are due to the large variation in frontal area. The maximal levels in X_B -direction are about $1\mu g$.

Running Average
Base: $\Delta t = 144s$
Step: $\delta t = 1s$

Frame of Reference: Orbiter Body Coordinates
Location: QSAM, Rack 3

QSAM-Coverage:    
QSAM-State: Data Stop1 StopAll NoData

QSAM on STS-94(MSL-1R), QS-Acceleration vs. Time

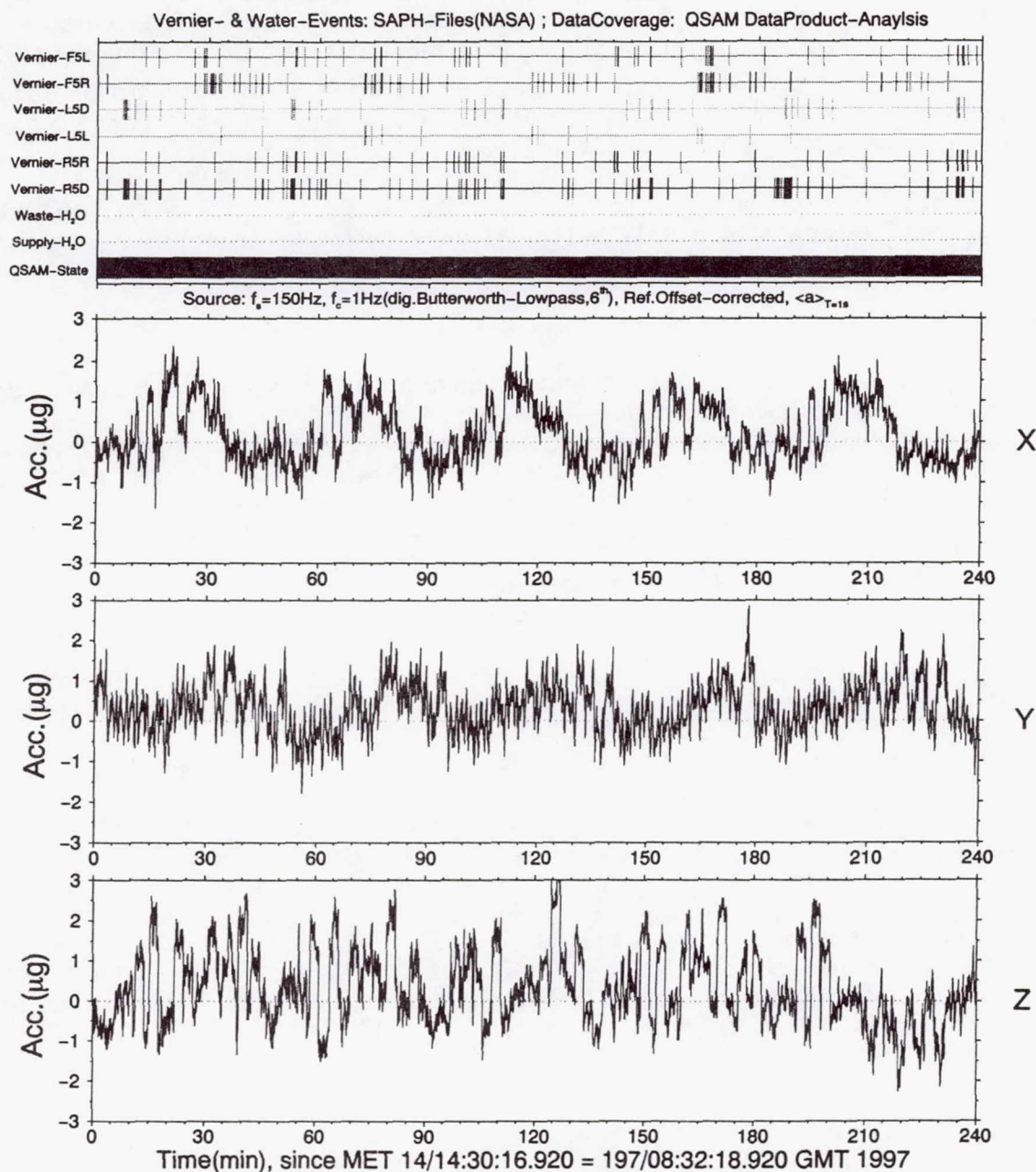


Fig. 6 Quasi-steady acceleration environment whilst flying in solar inertial attitude on MSL-1R. Again the time window of the moving average is 144 s sampled every second. The event data is from SAPH-files. The constant contribution stems from attitude, the modulation from density variations along the orbital trajectory of space shuttle.

4 Conclusions

The MSL-1 Mission was the third flight of the QSAM system. The QSAM data gave, together with the SAMS, OARE and MMA measurements, a detailed picture of the residual acceleration of the Spacelab Module covering the complete frequency range of interest to the experimenter. The significance of microgravity measurements as a means of monitoring and therefore assuring the quality of the microgravity environment aboard Spacelab to support experimenters was confirmed. The MSL-1 Mission also demonstrated the unique role of microgravity measurement for controlling the payload and facility operations. MSL-1 carried μ y-detection instruments with different measurement approaches. Few results of QSAM have been discussed. Others are being compared with the results especially of OARE.

QSAM's next flight will be again on the Russian free flying capsule FOTON (FOTON-12). The first flight aboard FOTON-11 in October 1997 was successful.

References

- [1] Alexander, J. I. D., "Low gravity experiment sensitivity to residual acceleration: a review", *Microgravity Science and Technology*, 3 (1990), pp 52 - 68
- [2] Monti, R., Langbein, D., Favier, J. J., "Influence of residual accelerations on fluid physics and materials science experiments", *Fluid Sciences and Materials Science in Space*, H. U. Walter (ed.), Springer-Verlag, Berlin, 1987, pp 637 - 680.
- [3] Hamacher, H., "Spacecraft low frequency acceleration", *Journal on Spacecraft and Rockets*, 32 (1995), pp. 324 - 327
- [4] Hamacher, H., Fitton, B., Kingdon, J., "The environment of Earth-orbiting systems", *Fluid Sciences and Materials Science in Space*, H. U. Walter (ed.), Springer-Verlag, Berlin, 1987, pp 1 - 50.
- [5] Hamacher, H., Jilg, R., Feuerbacher, B., "QSAM- A measurement system to detect quasi-steady accelerations aboard a spacecraft", IAF paper 90-377, October 1990, 8p
- [6] Hamacher, H., Jilg, R., Richter, H. E., "An approach to detect low-frequency acceleration", 24th International Conference on Environmental Systems and 5th European Symposium on Space Environmental Control Systems, Friedrichshafen, Germany, June 20.23, 1994, paper no. 941362, 5 pp
- [7] Krueder, J., "Microgravity conditions of Spacelab, a case study based on the IML-2 Mission", Diploma Thesis, Technical University of Munich, Dpt. of Aeronautics and Astronautics, 1995, 155 pp. (in German)
- [8] Hamacher, H., Bluemel, U., Jilg, R., "Spacelab's microgravity environment-a characterization based on D-1 and D-2 data", 9th European Symp. "Gravity-Dependent Phenomena in Physical Sciences", Berlin, 1995, pp. 343-344

REPORT DOCUMENTATION PAGE			Form Approved OMB No. 0704-0188	
Public reporting burden for this collection of information is estimated to average 1 hour per response, including the time for reviewing instructions, searching existing data sources, gathering and maintaining the data needed, and completing and reviewing the collection of information. Send comments regarding this burden estimate or any other aspect of this collection of information, including suggestions for reducing this burden, to Washington Headquarters Services, Directorate for Information Operation and Reports, 1215 Jefferson Davis Highway, Suite 1204, Arlington, VA 22202-4302, and to the Office of Management and Budget, Paperwork Reduction Project (0704-0188), Washington, DC 20503				
1. AGENCY USE ONLY (Leave Blank)	2. REPORT DATE November 1998	3. REPORT TYPE AND DATES COVERED Conference Publication		
4. TITLE AND SUBTITLE Microgravity Science Laboratory (MSL-1) Final Report		5. FUNDING NUMBERS		
6. AUTHORS M.B. Robinson, Compiler				
7. PERFORMING ORGANIZATION NAME(S) AND ADDRESS(ES) George C. Marshall Space Flight Center Marshall Space Flight Center, Alabama 35812		8. PERFORMING ORGANIZATION REPORT NUMBER M-900		
9. SPONSORING/MONITORING AGENCY NAME(S) AND ADDRESS(ES) National Aeronautics and Space Administration Washington, DC 20546-0001		10. SPONSORING/MONITORING AGENCY REPORT NUMBER NASA/CP-1998-208868		
11. SUPPLEMENTARY NOTES Proceedings of the Microgravity Science Laboratory (MSL-1) One Year Science Review Meeting held at Marshall Space Flight Center, Huntsville, Alabama, August 25-26, 1998				
12a. DISTRIBUTION/AVAILABILITY STATEMENT Unclassified-Unlimited Subject Category 88 Standard Distribution		12b. DISTRIBUTION CODE		
13. ABSTRACT (Maximum 200 words) This document reports the results and analyses presented at the Microgravity Science Laboratory (MSL-1) One Year Science Review meeting held at Marshall Space Flight Center August 25-26, 1998. The MSL-1 payload first flew on the Space Shuttle Columbia (STS-83) April 4-8, 1997. Due to a fuel cell problem, the mission was cut short, and the payload flew again on Columbia (STS-94) July 1-17, 1997. The MSL-1 investigations were performed in a pressurized Spacelab module and the Shuttle middeck. Twenty-nine experiments were performed and represented disciplines such as fluid physics, combustion, materials science, biotechnology, and plant growth. Four accelerometers were used to record and characterize the microgravity environment. The results demonstrate the range of quality science that can be conducted utilizing orbital laboratories in microgravity.				
14. SUBJECT TERMS MSL-1, Spacelab, microgravity research, materials science, combustion, fluid physics, isothermal furnace, protein crystal growth, biotechnology, containerless processing, space acceleration measurement		15. NUMBER OF PAGES 340		
		16. PRICE CODE A15		
17. SECURITY CLASSIFICATION OF REPORT Unclassified	18. SECURITY CLASSIFICATION OF THIS PAGE Unclassified	19. SECURITY CLASSIFICATION OF ABSTRACT Unclassified	20. LIMITATION OF ABSTRACT Unlimited	